



**Università
degli Studi
di Ferrara**



**INTERNATIONAL DOCTORAL COURSE IN
"EARTH AND MARINE SCIENCES (EMAS)"**

CYCLE XXXIII

COORDINATOR Prof. COLTORTI MASSIMO

**Geological and petrological investigation of the western
North Makran ophiolites (SE Iran): new constraints for
the Late Jurassic – Cretaceous tectono-magmatic and
geodynamic evolution of the Neo-Tethys Ocean**

Scientific/Disciplinary Sector (SDS) GEO/07

Candidate

Dott. Edoardo Barbero

Supervisor

Prof. Emilio Sacconi

Co-Supervisors

Prof. Luca Pandolfi

Years 2017/2020

Table of contents

| | |
|--|------------|
| Abstract | i |
| Riassunto | iii |
| | |
| Chapter 1. Introduction | |
| 1-10 | |
| 1.1. General introduction..... | 2 |
| 1.2. The significance and the importance of ophiolite to reconstruct geodynamic evolution of the accretionary prism..... | 4 |
| 1.3. Study area and research methodology | 6 |
| 1.4. Plan of the thesis..... | 8 |
| | |
| Chapter 2. Geological setting | |
| 11-22 | |
| 2.1. The Makran Accretionary Prism: geological and geophysical framework..... | 12 |
| 2.2. The North Makran domain..... | 14 |
| 2.3. Regional-scale structural setting of the studied area and its comparison with the eastern Makran..... | 19 |
| | |
| Chapter 3. Analytical methods | |
| 23-27 | |
| 3.1. Whole-rock geochemical analysis..... | 24 |
| 3.2. Mineral chemistry analysis..... | 24 |
| Appendix..... | 26-27 |
| | |
| Chapter 4. The Ganj Complex | |
| 28-80 | |
| 4.1. Geological features..... | 29 |
| 4.1.1. The dyke-swarm..... | 31 |
| 4.1.2. The volcano-sedimentary sequence..... | 33 |
| 4.1.3. The turbidite sequence..... | 34 |
| 4.2. Arenite petrography (courtesy of L. Pandolfi)..... | 36 |
| 4.3. Biostratigraphy (courtesy of R. Catanzariti)..... | 39 |
| 4.4. Petrography of volcanic and sub-volcanic rocks..... | 41 |
| 4.4.1. Sub-volcanic rocks..... | 42 |
| 4.4.2. Massive lava flows..... | 42 |
| 4.4.3. Pillow lavas..... | 44 |
| 4.5. Geochemistry of volcanic and sub-volcanic rocks..... | 45 |
| 4.5.1. Group 1 rocks..... | 46 |
| 4.5.2. Group 2 rocks..... | 49 |

| | |
|---|---------------|
| 4.5.3. Group 3 rocks..... | 52 |
| 4.6. Discussion..... | 54 |
| 4.6.1. Petrogenesis and tectonic setting of formation of the primary melts of the Ganj Complex..... | 54 |
| 4.6.1.1. Petrogenesis of Group 1 rocks..... | 58 |
| 4.6.1.2. Petrogenesis of Group 2 rocks..... | 59 |
| 4.6.1.3. Petrogenesis of Group 3 rocks..... | 60 |
| 4.6.2. Tectonic setting of formation of the Ganj Complex volcanic and subvolcanic rocks.... | 62 |
| 4.6.3. Geodynamic significance of the Ganj Complex..... | 65 |
| 4.7. Conclusion..... | 69 |
| Appendix..... | 72-80 |
| Chapter 5. The Band-e-Zeyarat | |
| | 81-148 |
| 5.1. The stratigraphy of the Band-e-Zeyarat ophiolite..... | 82 |
| 5.2. Sections sampled for plagiogranites suitable for zircon U-Pb geochronological dating..... | 86 |
| 5.2.1. The Chah Mirak section | 86 |
| 5.2.2. The Bandkouh section | 87 |
| 5.3. Petrography of the magmatic rocks..... | 90 |
| 5.4. Geochemistry of the magmatic rocks..... | 93 |
| 5.4.1. Intrusive complex | 93 |
| 5.4.2. Sheeted dyke complex, volcanic sequence, and individual dykes..... | 98 |
| 5.4.2.1. Type-I volcanic and subvolcanic rocks..... | 100 |
| 5.4.2.2. Type-II volcanic and subvolcanic rocks..... | 102 |
| 5.5. Mineral chemistry..... | 104 |
| 5.5.1 Olivine..... | 105 |
| 5.5.2 Plagioclase..... | 105 |
| 5.5.3 Clinopyroxene..... | 107 |
| 5.6. Geothermobarometry..... | 109 |
| 5.6.1. Intrusive complex..... | 110 |
| 5.6.2. Sheeted dyke complex..... | 112 |
| 5.7. Zircon U-Pb dating (courtesy of A. Langone)..... | 112 |
| 5.8. Discussion..... | 114 |
| 5.8.1. Melt petrogenesis..... | 114 |
| 5.8.1.1. Type-I..... | 117 |
| 5.8.1.2. Type-IIa..... | 118 |
| 5.8.1.3. Type-IIb..... | 119 |
| 5.8.1.4. Type-IIc..... | 120 |

| | |
|---|----------------|
| 5.8.1.5. <i>Type-II</i> | 120 |
| 5.8.2. <i>Tectono-magmatic setting of formation of the Band-e-Zeyarat ophiolite and geodynamic implications</i> | 122 |
| 5.9. <i>Conclusion</i> | 127 |
| Appendix..... | 129-148 |
| Chapter 6. The Durkan Complex | |
| | 149-233 |
| 6.1. <i>The Durkan Complex in the western North Makran: General field features and tectono-stratigraphic architecture</i> | 150 |
| 6.1.1. <i>The Zandan transect</i> | 153 |
| 6.1.2. <i>The Manujan transect</i> | 156 |
| 6.1.3. <i>The Chah Shahi 1 transect</i> | 158 |
| 6.1.4. <i>The Chah Shahi 2 transect</i> | 160 |
| 6.2. <i>Biostratigraphy</i> | 163 |
| 6.2.1. <i>Foraminifera (courtesy of V. Luciani)</i> | 164 |
| 6.2.2. <i>Calcareous nannofossils (courtesy of R. Catanzariti)</i> | 167 |
| 6.2.3. <i>Radiolarian (courtesy of M. Chiari)</i> | 168 |
| 6.2.3.1. <i>Manujan transect</i> | 169 |
| 6.2.3.2. <i>Chah Shahi 1 transect</i> | 171 |
| 6.3. <i>Petrography of the Durkan Complex magmatic rocks</i> | 172 |
| 6.3.1. <i>Magmatic texture</i> | 172 |
| 6.3.2. <i>Vesicles content</i> | 175 |
| 6.4. <i>Geochemistry of the Durkan Complex magmatic rocks</i> | 177 |
| 6.4.1. <i>Group 1 rocks</i> | 178 |
| 6.4.2. <i>Group 2 rocks</i> | 181 |
| 6.4.3. <i>Group 3 rocks</i> | 183 |
| 6.5. <i>Mineral chemistry of clinopyroxene from the Durkan Complex</i> | 185 |
| 6.5.1. <i>Clinopyroxene</i> | 185 |
| 6.5.2. <i>Comparison between clinopyroxene composition and whole rock geochemistry</i> | 191 |
| 6.6. <i>Discussion</i> | 193 |
| 6.6.1. <i>Reconstruction of the stratigraphy of the western Durkan Complex</i> | 193 |
| 6.6.1.1. <i>Type-I stratigraphic succession</i> | 193 |
| 6.6.1.2. <i>Type-II stratigraphic succession</i> | 194 |
| 6.6.1.3. <i>Type-III stratigraphic succession</i> | 196 |
| 6.6.2. <i>Stratigraphic implications for the regional geology of the North Makran</i> | 198 |
| 6.6.3. <i>Petrological implications: melt petrogenesis of the magmatic rocks</i> | 202 |
| 6.6.3.1. <i>Group 1 rocks</i> | 205 |

| | |
|---|----------------|
| 6.6.3.2. <i>Group 2 rocks</i> | 207 |
| 6.6.3.3. <i>Group 3 rocks</i> | 208 |
| 6.6.4. <i>New definition of the Late Cretaceous tectono-sedimentary and volcanic environment for the western Durkan Complex</i> | 210 |
| 6.6.5. <i>Tectono-magmatic significance of the basalts from the Durkan Complex</i> | 213 |
| 6.6.6. <i>The role of seamount accretion in controlling the physiography and tectonic evolution of the Makran convergent margin</i> | 218 |
| Appendix..... | 222-233 |
| Chapter 7. The Bajgan Complex | |
| | 234-264 |
| 7.1. <i>General field features</i> | 235 |
| 7.2. <i>Lithostratigraphy</i> | 236 |
| 7.3. <i>Petrography and geochemistry of the meta-volcanic and meta-intrusive rocks</i> | 237 |
| 7.3.1. <i>Petrography</i> | 238 |
| 7.3.2. <i>Geochemistry</i> | 240 |
| 7.3.2.1. <i>Ultramafic cumulitic protoliths</i> | 241 |
| 7.3.2.2. <i>Group 1 magmatic protoliths (N-MORB)</i> | 242 |
| 7.3.2.3. <i>Group 2 magmatic protoliths (E-MORB)</i> | 246 |
| 7.3.2.4. <i>Group 3 magmatic protoliths (alkaline basalts)</i> | 248 |
| 7.4. <i>U/Pb geochronology of the meta-intrusive rocks</i> | 249 |
| 7.5. <i>Discussion</i> | 251 |
| 7.5.1. <i>Tectono-magmatic significance</i> | 251 |
| 7.5.2. <i>The Bajgan Complex re-interpreted as remnants of an Late Jurassic - Early Cretaceous oceanic lithosphere</i> | 257 |
| Appendix..... | 260-264 |
| Chapter 8. Structural setting | |
| | 265-284 |
| 8.1. <i>Structural setting of the Band-e-Zeyarat ophiolite</i> | 266 |
| 8.2. <i>Structural setting of the Durkan Complex</i> | 270 |
| 8.3. <i>Post-Eocene deformation in the western North Makran</i> | 276 |
| 8.4. <i>Discussion: Structural evolution of the western North Makran</i> | 280 |
| Chapter 9. Geodynamic implications and concluding remarks | |
| | 285-300 |
| 9.1. <i>Summary of the new data from the Ganj Complex, the Band-e-Zeyarat ophiolite, the Durkan Complex, and the Bajgan Complex in the western North Makran</i> | 286 |
| 9.2. <i>Late Jurassic - Cretaceous tectono-magmatic and geodynamic model for the western North Makran domain</i> | 290 |
| 9.3. <i>Implications for the Cretaceous geodynamic of the Neo-Tethys realm</i> | 294 |
| 9.4. <i>Open problems and future perspective</i> | 300 |

| | | |
|--|-------------------|---------|
| | References | 301-319 |
| Acknowledgements | | 320 |
| Report of activities attended the during Ph.D. course | | 322 |

Abstract

The Makran Accretionary Prism (South Iran) is related to the convergence between the Arabia and Eurasia plates accommodated by the northward subduction of the Neo-Tethys Ocean since the Cretaceous. Mesozoic ophiolites, sedimentary successions, and minor continental-derived tectonic units are preserved in the North Makran domain.

This thesis is focused on field-based geological study, as well as petrological and geochemical characterization of the magmatic rocks of the Bajgan and Durkan Complexes, the Band-e-Zeyarat ophiolitic unit, and the Ganj Complex. The studied units are included in the North Makran domain and they are up to now interpreted as the remnants of a Mesozoic oceanic basin (the North Makran Ocean) and its southern continental margin. The aim of this thesis is to provide data for understanding the geodynamic significance of these units and new constraints for the Mesozoic geodynamic history of the North Makran Ocean.

The new multidisciplinary data documented a complex tectono-magmatic evolution for the different tectonic units. The Ganj Complex was interpreted in literature as an ophiolitic unit. The new data indicate that it represents a Late Cretaceous volcanic arc succession. The Ganj arc was likely built close or onto the southern margin of Eurasia plate. The Band-e-Zeyarat ophiolitic unit displays crustal architecture, geochemical fingerprints of magmatic rocks, and mineral chemistry of rock-forming minerals indicating its formation in a mid-oceanic ridge tectonic setting during Early Cretaceous. Petrogenetic evidence suggests a ridge-mantle plume interaction during the formation of this unit. The Bajgan and Durkan Complexes were up to now considered as the remnants of a microcontinental block deformed in the Makran. The multidisciplinary data provided by this thesis point out for a different interpretation of these complexes. The Durkan Complex records the interplay of alkaline magmatism and shallow water and pelagic sedimentation during the Late Cretaceous. The combination of stratigraphic and petrological data and mineral chemistry data suggest that the Durkan Complex represents the remnants of a Late Cretaceous seamounts chain tectonically disrupted in the Makran. The Bajgan Complex includes meta-serpentinites, meta-intrusive rocks, meta-volcanic rocks and meta-sedimentary rocks. This type of tectono-stratigraphic architecture is comparable with that of a typical subduction-unrelated oceanic succession. Whole-rock geochemistry of meta-magmatic rocks and petrogenetic study indicate a subduction-unrelated chemical affinity. Dating of magmatic zircon from meta-intrusive rocks testifies for Late Jurassic – Early Cretaceous age. These data indicate that the Bajgan Complex corresponds to an assemblage of Mesozoic meta-ophiolitic tectonic slices. Structural data on the Band-e-Zeyarat ophiolitic unit

and Durkan Complex provide evidence for a multiphase deformation history occurred during the latest Late Cretaceous – Paleocene-earliest Eocene accretion and subsequent exhumation within the frontal accretionary wedge.

In conclusion this thesis provides significant constraints for the understanding of the Late Jurassic - Cretaceous geodynamic and tectono-magmatic significance of the North Makran Ocean and its role during the convergent tectonic stages starting from the latest Late Cretaceous. The outstanding conclusion is that, in contrast to any previous interpretation, this ocean likely represented a mature and wide oceanic basin rather than a marginal basin or a back-arc basin as previously thought. The implications of these new findings are also discussed in the framework of the regional-scale Cretaceous evolution of the Neo-Tethys realm.

Riassunto

Il Prisma di Accrezione del Makran (Iran meridionale) è legato alla convergenza tra la placca Araba e quella Euroasiatica, che è accomodata, a partire dal Cretacico, dalla subduzione verso Nord dell'oceano della Neo-Tetide. Nel dominio tettonico del North Makran sono preservate ofioliti mesozoiche, successioni sedimentarie e minori resti di rocce di derivazione continentale.

La presente tesi è focalizzata sui complessi di Bajgan e Durkan, sull'unità di Band-e-Zeyarat e sul complesso di Ganj e comprende un dettagliato studio geologico di queste unità sul terreno così come un dettagliato studio geochimico-petrologico delle rocce magmatiche. Le unità studiate fanno parte del dominio del North Makran e sono state interpretate come i resti del bacino oceanico Mesozoico, noto in letteratura come Oceano del North Makran, e il suo margine continentale meridionale. Lo scopo di questa tesi è di presentare nuovi dati per meglio comprendere il significato geodinamico dei complessi di Bajgan e Durkan, dell'unità di Band-e-Zeyarat e del complesso di Ganj e vincolare l'evoluzione geodinamica dell'Oceano del North Makran.

I dati presentati nella presente tesi documentano una complessa evoluzione tettono-magmatica per le diverse unità tettoniche. Il complesso di Ganj rappresenta una successione di arco vulcanico del Cretacico Superiore, probabilmente formatasi vicino alla placca Euroasiatica. L'ofiolite di Band-e-Zeyarat mostra un'architettura crostale, un'affinità geochimica delle rocce magmatiche e la composizione chimica delle fasi mineralogiche compatibile con la genesi in una dorsale medio oceanica durante il Cretacico Inferiore. I nuovi dati petrologici suggeriscono che l'ofiolite di Band-e-Zeyarat si sia formata durante l'interazione tra dorsale e plume di mantello. Il complesso di Durkan registra magmatismo alcalino coevo con sedimentazione pelagica e in ambiente di piattaforma carbonatica durante il Cretacico Superiore. La combinazione dei dati stratigrafici e petrologici indica che il Complesso di Durkan rappresenta i resti di una catena di seamounts deformata nel prisma di accrezione del Makran. Il complesso di Bajgan è costituito da meta-serpentiniti, varie tipologie di rocce metamorfiche da protoliti magmatici e rocce meta-sedimentarie. Questa tipologia di associazione litologica e la composizione chimica delle rocce magmatiche sono confrontabili con le ofioliti di tipo MOR (mid ocean ridge). Le datazioni di zirconi separati da meta-gabbri e meta-plagiograniti hanno fornito età comprese tra il Giurassico Superiore e il Cretacico Inferiore. I nuovi dati sul Complesso di Bajgan suggeriscono che corrisponda a un insieme di scaglie tettoniche di ofioliti Mesozoiche. I dati strutturali sull'ofiolite di Band-e-Zeyarat e il Complesso di Durkan indicano che queste unità hanno subito una storia

deformativa polifasica tra il tardo Cretacico Superiore e il Paleocene-Eocene inferiore durante la loro accrezione e successiva esumazione nei settori frontali del prisma del Makran.

In conclusione, i risultati della presente tesi forniscono importanti vincoli per comprendere l'evoluzione geodinamica dell'Oceano del North Makran durante il tardo Giurassico e il Cretacico, così come il suo ruolo nella tettonica convergente attiva a partire dal tardo Cretacico Superiore. Il risultato principale è che i nuovi dati multidisciplinari suggeriscono che l'Oceano del North Makran rappresentasse un bacino oceanico maturo piuttosto che un bacino marginale o un back-arc come precedentemente suggerito in letteratura. Sono inoltre discusse le implicazioni dei nuovi dati nel contesto dell'evoluzione a scala regionale della Neo-Tetide durante il Cretacico.

Chapter 1. Introduction

1.1. General introduction and aim of the thesis

The Makran Accretionary Prism (SE Iran, Fig. 1.1) is related to the long-lived and complex geodynamic evolution of the Neo-Tethys Domain and it is mainly dominated since the Cretaceous by the northward subduction of the Neo-Tethyan oceanic lithosphere below the Eurasian margin (i.e., Lut and Afghan Block) (McCall & Kidd, 1982; Glennie et al., 1990; Dercourt et al., 1986; Barrier et al., 2018; Burg, 2018; Saccani et al., 2018). This prism has been subdivided in four tectono-stratigraphic domains, namely from north to south the North Makran, the Inner Makran, the Outer Makran, and the Coastal Makran (Fig. 1.1; Dolati, 2010; Burg et al., 2013).

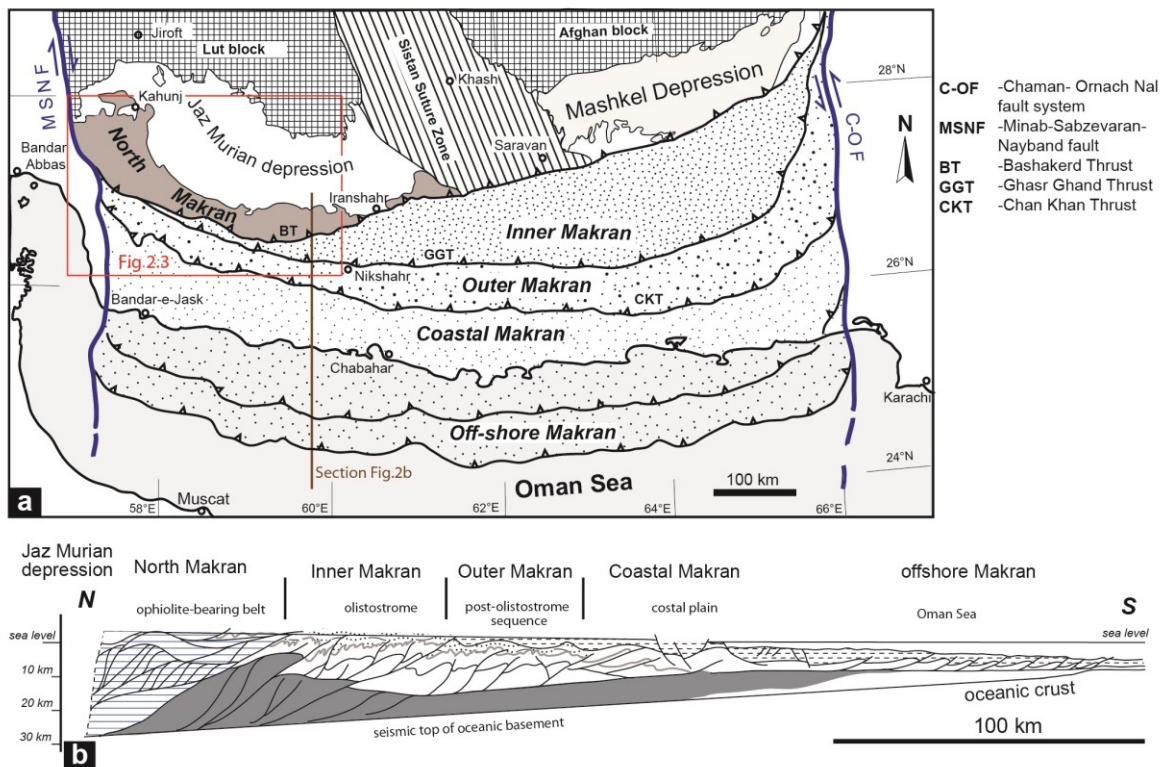


Figure 1.1. Structural sketch map (a) of the Makran accretionary wedge and related cross section (b) (modified from Burg et al., 2013) The box in Panel a) indicates the area shown in Fig. 2.3

The North Makran domain represents the innermost tectonic domain of the Makran and it is an imbricated stack of tectonic units that, in the western sector, include Mesozoic ophiolite units (i.e., the North Makran Ophiolite; McCall & Kidd, 1982; Hunziker et al., 2015), fragments of

continental crust and related sedimentary cover (i.e., the Bajgan-Durkan Complexes, [McCall & Kidd, 1982](#); [Hunziker et al., 2015](#)), slices of ultramafic mantle and lower crust sequence (i.e., Sorkhband and Rudan slices; [Delavari et al., 2016](#)), and an ophiolitic mélange (i.e., the Coloured Mélange, [McCall & Kidd, 1982](#); [Saccani et al., 2018](#)). Recent research on the Coloured Mélange in the western sector of the North Makran outlined the occurrence of basaltic rocks that show various geochemical affinity including undated mid-oceanic ridge basalt (MORB), Late Cretaceous oceanic island basalt (OIB), as well as Early to Late Cretaceous island arc tholeiites (IAT) and calc-alkaline basalt (CAB) ([Saccani et al., 2018](#); [Esmaeili et al., 2019](#)). These data suggest an extremely complex tectono-magmatic evolution for the Makran sector of the Neo-Tethys during the Cretaceous. In addition, the North Makran Ophiolite was interpreted as the remnants of the North Makran Ocean, which corresponded to a neo-Tethyan seaway that opened during the latest Late Jurassic and separated the Lut-Afghan continental block, to the north, and a microcontinental block, to the south, that is believed to be represented by the Bajgan-Durkan complexes ([McCall & Kidd, 1982](#); [Hunziker, 2014](#); [Hunziker et al., 2015](#); [Monsef et al., 2019](#)). The geodynamic significance of this oceanic basin is still debated as few data are available from the North Makran ophiolites and its conjugate continental margins. On the basis of these few data, this basin has been interpreted as either an Early Cretaceous back-arc basin related to the northward subduction of the Neo-Tethys ([McCall & Kidd, 1982](#)) or a marginal basin opened during Late Jurassic - Early Cretaceous at the southern margin of the Central Iran Block ([Hunziker et al., 2015](#); [Burg, 2018](#)).

In this framework, a detailed study of the North Makran Ophiolite and the Bajgan-Durkan Complexes in the western North Makran has the potential to improve the knowledge on this part of the Makran and provide constraints to reconstruct the complex Cretaceous tectono-magmatic evolution of the North Makran Ocean. This thesis is focused on the study of a sector in the north-western North Makran domain ([Fig. 1.1](#)) through geological investigations and petrological and

geochemical characterization of the magmatic rocks of three different tectonic units outcropping in this area, namely the Band-e-Zeyarat ophiolite, the Ganj Complex, the Durkan Complex, and the Bajgan Complex. According to the available data and interpretations, the Band-e-Zeyarat ophiolite and the Ganj Complex are interpreted as the remnants of the oceanic lithosphere of the North Makran Ocean, whereas the Durkan and Bajgan Complexes are believed to represent the remnants of the sedimentary cover and the continental basement, respectively, of the southern continental margin of this basin (McCall & Kidd, 1982). The final aim of this thesis is to provide data for a better understanding of the geodynamic significance of these four units and provide new constraints to unveil the history of the North Makran Ocean and its southern paleo-margin during the Cretaceous. Finally, these data will be used to discuss the role of the North Makran Ocean during the Late Cretaceous – pre Eocene convergent tectonics of the Makran Accretionary Prism.

1.2. The significance and the importance of ophiolite for reconstructing the geodynamic evolution of accretionary prisms

Subduction complexes develop at convergent plate boundaries when oceanic and continental material is transferred between the subducting oceanic plate and the overlying plate through tectonic accretion and erosion (e.g., Davis et al., 1983; Moore et al. 1990; Charvet & Ogawa, 1994; Meneghini et al., 2009; Kusky et al., 2013; Festa et al., 2018). Among the different material incorporated within subduction complexes, ophiolites are quite revealing for the reconstruction of the geological history of the oceanic basins and their associated continental margins as they record a prolonged tectonic evolution, from rifting to spreading, and the subsequent subduction and continental collision phases (e.g., Shervais, 2001; Kusky et al., 2013; Dilek & Furnes, 2014). In fact, ophiolites represent fragments of ancient oceanic crust and upper mantle that were tectonically

emplaced into collisional and accretionary belts (Dewey & Bird, 1971; Coleman, 1977; Wakabayashi & Dilek, 2003; Dilek & Furnes, 2011; 2014). They consist of a suite of ultramafic, mafic, and felsic rocks that can be petrogenetically and geochronologically related and represent the products of multiple mantle melting events and magmatic differentiation processes (Dilek & Furnes, 2011; Fig. 1.2). Early studies interpreted the ophiolites as fragments of fossil mid-oceanic ridge tectonic setting (Moores & Vine, 1971; Anonymous, 1972; Coleman, 1977). However, since

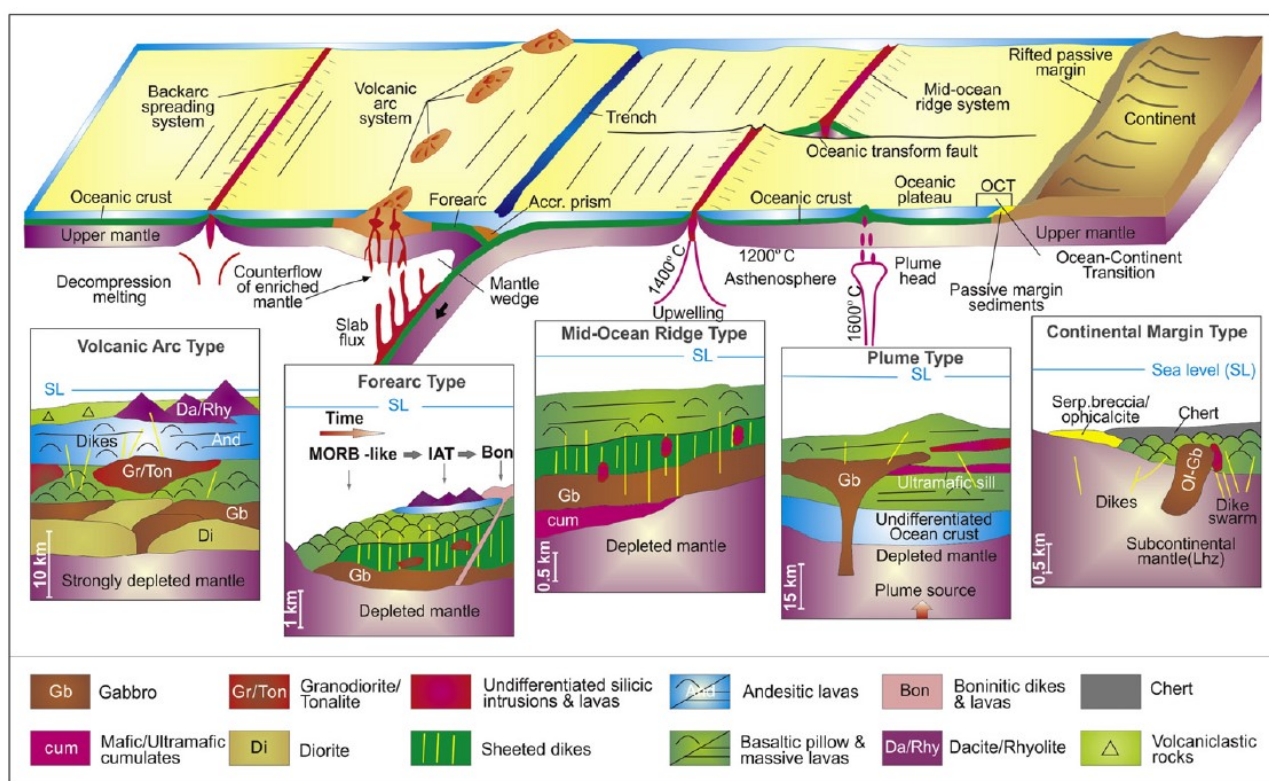


Figure 1.2. Schematic cartoons showing the major tectonic settings of magmatic construction of the oceanic lithosphere and the stratigraphic-structural of the main types of oceanic lithosphere formed in these different settings (from Dilek & Furnes, 2011; Furnes & Dilek, 2017).

1970s geochemical studies challenged this view of mid-oceanic ridge origin of ophiolites and suggested in many cases a magmatic evolution related to subduction zone (Miyashiro, 1973; Pearce, 1983). After many years of scientific debate on the genesis of ophiolites, it is now widely accepted that ophiolites can be distinguished in subduction-unrelated and subduction-related ophiolite (Fig. 1.2; Dilek & Furnes, 2011). Indeed, they may form in a wide variety of plate tectonic settings

including mid-ocean ridges, oceanic hot spots and plume-proximal ridges, as well as supra-subduction zone environments, within intra-oceanic arcs, forearcs and back-arcs settings (Fig. 1.2; Dilek & Furnes, 2011; Furnes & Dilek, 2017). For each setting of origin, the ophiolites show distinctive features in term of stratigraphic architecture and/or geochemical fingerprinting of magmatic rocks that are fundamental for identifying their tectono-magmatic setting of formation (Fig. 1.2; Dilek & Furnes, 2011; Pearce, 1996, 2014; Saccani, 2015; Xia & Li, 2019). In conclusion, the ophiolite incorporated in collisional and accretionary belts can provide robust constraints for the geodynamic reconstructions of ancient oceanic basins and their related continental margins.

1.3. Study area and research methodology

The study area is located in the north-western sector of the Makran Accretionary Prism (SE Iran; Fig. 1.3), in the neighbourhood of the Manujan city. The area extends for ~ 80 km to the west of the Jaz Murian desertic depression and in N-S direction for ~ 110 km to the south of Kahnuj city (Fig. 1.3). The thesis is focused on the Band-e-Zeyarat ophiolites, the Ganj Complex, as well as the Durkan and Bajgan Complexes and aim to study in detail these tectonic units in the western sector of the North Makran domain through multidisciplinary approach. The geological features of this area are poorly known and have only been investigated by the Paragon-Contech and the Geological Survey of Iran during a geological mapping program in the 70s. The results of this program consist of 1:250,000 scale geological maps and reports, which are available through the Geological Survey of Iran. The studied area is part of the 1:250,000 scale Minab sheet of the Geological Map of Iran (Samini Namin, 1983), and consists of arid to semi-arid region characterized by relative high mountain ranges crossed by several fluvial valleys. The permanent rivers are few and concentrated in the larger valleys. In this area, small cities are rather well connected by asphalt roads whereas

sparsely distributed villages are in general linked through motorable dirty roads. However, still many outcrops are difficult to be reached by car and, often, a long-time walk is needed to reach them. Therefore, the field work in this area is rather complex and always required a detailed planning with satellite images for both the geological and logistic aspects.

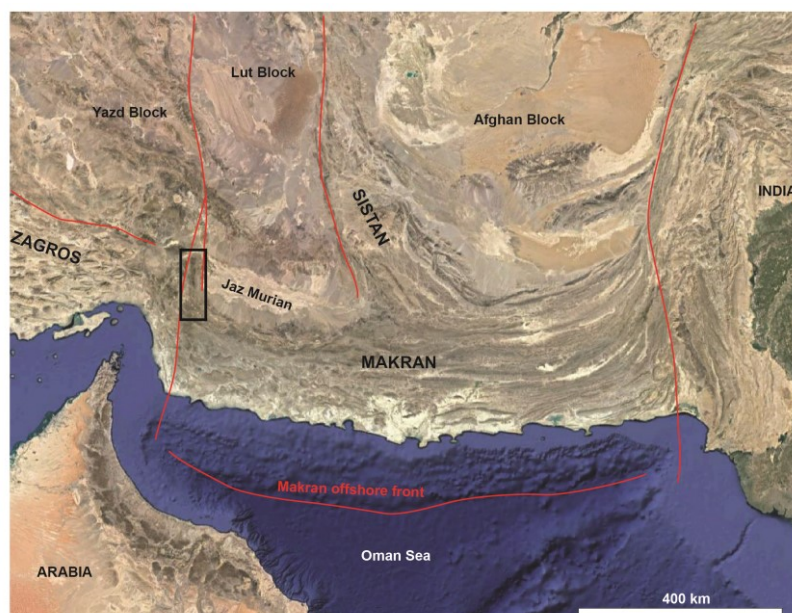


Figure 1.3. Satellite image showing the studied area (black box) and the main plates and accretionary-collisional belts.

This thesis is part of a wider research project on Makran Accretionary Prism, which involves an international research group from University of Ferrara (Italy), University of Pisa (Italy), Kaharazmi University (Theran, Iran), Italian Research Council (Firenze and Pisa, Italy), Leoben Mountain University (Austria), and University of Pavia (Italy). This thesis follows a multidisciplinary approach and combines field and analytical works spanning in different Earth Science disciplines. For each studied tectonic unit, stratigraphic and structural data have been collected to reconstruct and describe the stratigraphic architecture of each unit. These field data are coupled with a considerable amount of petrographic and geochemical analyses of the magmatic rocks from the different units as well as selected mineral chemistry analyses. These investigations aim to characterize the geochemical affinity of these rocks and discuss their petrogenesis and

tectono-magmatic setting of formation. The chronological constraints for the magmatic events are given by both biostratigraphic analyses of the sedimentary rocks associated to volcanic sequence and U-Pb zircon dating of magmatic rocks. These constraints have been provided by geoscientists who are expert in such disciplines. In my research project I focused only in some of these disciplines; in detail, I performed both field investigations, such as geological mapping, stratigraphic and structural analyses, and lab-based research that includes petrographic and geochemical studies of the magmatic rocks, and mineral chemical analyses of primary magmatic mineral phases. In contrast, for the others research disciplines, such as petrography of sedimentary rocks, biostratigraphy and radiometric dating, I contributed to the sampling, the best choice of samples to be analysed, and the discussion of the results of these analyses. Indeed, these types of data were collected by various researchers of the team. However, I reported in this thesis these results since they are fundamental to support the conclusion of my PhD research. To be completely clear, I choose to state the chapter that derived from analyses not performed by myself, indicating the name of the research who kindly provided these data.

1.4. Plan of the thesis

In addition to this first introductory chapter, this thesis is composed of eight chapters. After the second and third chapters that deal with the geological setting and the analytical methods, it follows the presentation of the data and the results of this thesis (from chapter four to eight). Each of these chapters deals with a specific topic and provides the presentation of the data and their discussion. A final discussion of the whole data presented in the thesis is given in chapter nine. The detailed topic of each chapter will be briefly summarized in the following:

Chapter 2 introduces the geodynamic and geological setting of the Makran Accretionary

Prism, a detail explanation of the previous data and interpretation for the North Makran domain, and finally a brief introduction to the regional-scale structural setting of the western North Makran and its comparison with the eastern sector, recently studied by [Burg et al. \(2008, 2013\)](#) and [Burg, \(2018\)](#).

Chapter 3 provides the description of the analytical methods employed during this thesis.

Chapter 4 deals with the Ganj Complex. It is described the stratigraphic succession, the petrographic compositions of the arenites interlayered in the sequence, the paleontological dating, and the petrographic and geochemical features of the magmatic rocks. The meaning of these dataset is discussed in the framework of the geodynamic significance of this Complex.

Chapter 5 deals with the Band-e-Zeyarat ophiolite and their sedimentary covers. At first it includes a description of the stratigraphic succession of this unit and the section sampled for zircon geochronology on the basis of field data. It follows detailed a description of the petrographic and geochemical features of the magmatic rocks, the results of mineral chemistry analysis on rock-forming minerals of these rocks, as well as the results on zircon geochronology. These data are then discussed focusing on the petrogenesis of the magmatic rocks and the tectono-magmatic significance of the Band-e-Zeyarat ophiolite.

Chapter 6 deals with the Durkan Complex presenting a multidisciplinary dataset. It is described in detail the tectono-stratigraphic architecture of this complex in four key transects, focusing on the description of the stratigraphic sequence and the relationships of volcanic rocks and the sedimentary successions. It follows a paleontological study aiming at providing age constraints for the volcanic activity recorded in the Durkan Complex, dating the sedimentary rocks associated with the volcanic rocks. A detailed and exhaustive description of the petrographic features of the volcanic rocks, the geochemistry, and the composition of the clinopyroxene is then presented. This multidisciplinary dataset is then discussed to propose the tectono-stratigraphic

setting of formation of this Complex, the petrogenesis of the volcanic rocks and their tectono-magmatic setting of formation, and finally the role of this Complex for the tectonic evolution of the North Makran.

Chapter 7 deals with the Bajgan Complex and after a brief description of the lithostratigraphy of this metamorphic complex, it follows a detailed petrographic and geochemical investigation of the meta-intrusive and meta-volcanic rocks. The final aim is to discuss the tectono-magmatic setting of formation of the Bajgan Complex. The data presented are, therefore, focused on the protoliths formation rather than the study of the metamorphic overprint.

Chapter 8 deals with the structural setting of the studied area providing a detailed structural study of the Band-e-Zeyarat ophiolite and the Durkan Complex, as well as a brief and preliminary introduction to the post-Eocene deformation of the western North Makran. The meaning of these data for the structural evolution of the North Makran is then discussed.

Chapter 9 deals with final geodynamic model for the Mesozoic evolution of the Makran Accretionary Prism integrating the new data of this thesis and those published in literature. Finally it is discussed a comparison of this model and those published for the neighbouring collisional belts in the general context of the Cretaceous – Eocene geodynamic and paleogeographic reconstruction of the Middle East and western Asia.

Chapter 2. Geological setting

2.1. The Makran Accretionary Prism: geological and geophysical framework

The Makran Accretionary Prism resulted from the Cretaceous to Present-day convergence between the Arabian and the southern margin(s) of Eurasian plates. This convergence was associated with northward subduction of the Neo-Tethys Ocean below the Eurasia margin(s) (McCall & Kidd, 1982; Dercourt et al., 1986; Platt et al., 1985; Ricou, 1994; Saccani et al., 2018; Burg, 2018; Monsef et al., 2019). This subduction started in the Early Cretaceous as a consequence of the migration of the Arabian Plate toward the southern margin(s) of Eurasia (Dercourt et al., 1986; Barrier et al., 2018), and it is still active in the Makran (Figs. 2.1, 2.2a). This is indicated by

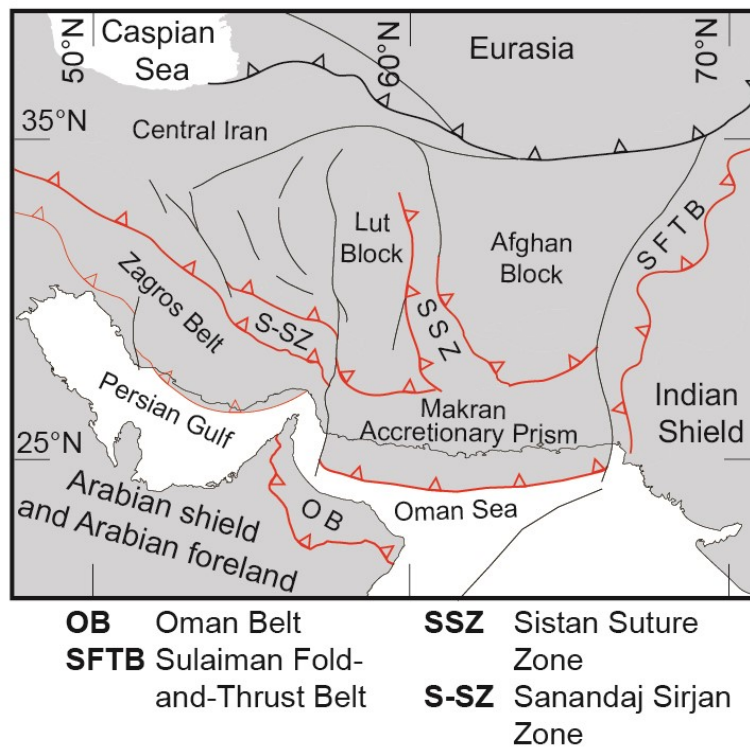


Figure 2.1. Tectonic sketch map of the Middle East area showing the main tectonic plates and convergent zones (modified from Bagheri & Stampfli, 2008; Zanchetta et al., 2013; Mohammadi et al., 2016; Pirnia et al., 2020).

both geophysical data (White & Klitgord, 1976; Kopp et al., 2000; Grando & McClay, 2007; Entezar-Saadat et al., 2017; Motaghi et al., 2020) and earthquake focal mechanisms (Engdahl et al., 2006; Penney et al., 2017). The Makran is an E-W trending accretionary wedge that is bounded by

two major strike-slip fault systems (Figs. 2.1, 2.2a). In fact, the Makran Accretionary Prism is separated from the Zagros fold-and-thrust belt (to the west) by the dextral Zendan-Minab faults system and from the Himalaya continent-continent collision zone (to the east) by the sinistral Chaman-Ornach-Nal faults system (e.g., Kopp et al., 2000; Regard et al., 2010; Penney et al., 2015; Riaz et al., 2019). Its northern boundary with the Lut and Afghan blocks is masked by the Quaternary cover of the Jaz Murian and Mashkel depressions, whereas, to the south it is bounded by the north-dipping active subduction of the Oman Sea Plate (Figs. 2.1, 2.2). In the Iranian sector, the Jaz Murian represents a large sag basin (also known as Jaz Murian depression) that is regarded as a forearc located south of the volcanic arc, which is now active onto the southern margin of the Lut block (Fig. 2.2a), as a result of the present-day subduction (Abdetedal et al., 2015).

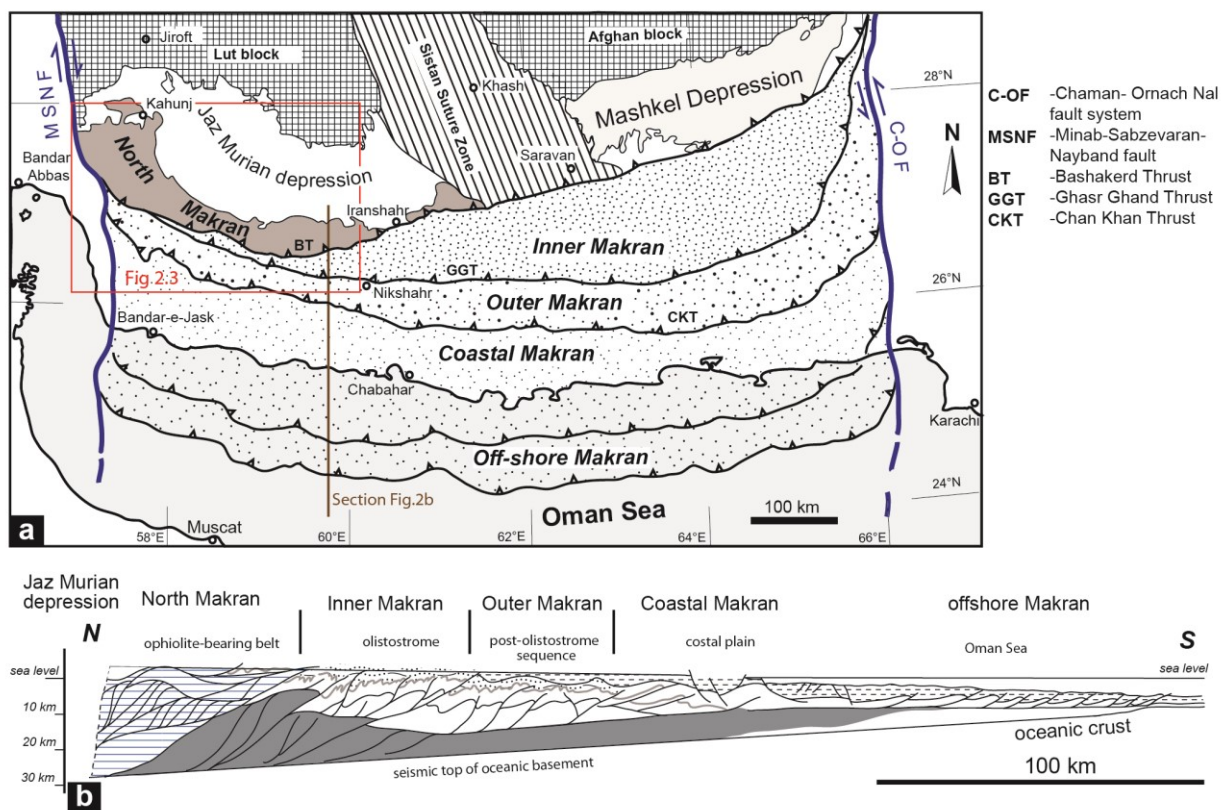


Figure 2.2. Structural sketch map (a) of the Makran accretionary wedge and related cross section (b) (modified from Burg et al., 2013) The box in Panel a) indicates the area shown in Fig. 2.3.

The Makran Accretionary Prism includes an active, southernmost offshore wedge and an

exhumed onshore prism (Fig. 2.2). The onshore prism includes four major tectono-stratigraphic domains (Fig. 2.2), which are, from the structural top to the bottom (i.e., from north to south): i) the North Makran; ii) the Inner Makran; iii) the Outer Makran; iv) the Coastal Makran (Dolati, 2010; Burg et al., 2013). These domains are tectonically juxtaposed through regional-scale and N-dipping thrust zones, showing progressively younger ages toward the south (e.g., Bashakerd, Ghasr Ghand and Chan Khan thrusts, see Fig. 2.2a, see also Dolati, 2010; Dolati & Burg, 2013; Burg et al., 2013). The Bashakerd Thrust (Fig. 2.2a) is a mainly E-W striking regional scale fault zone separating southward the North Makran from the Eocene - present day accretionary complex, which is represented by the Inner, Outer and Coastal Makran (Burg et al., 2013; Burg, 2018). The North Makran consists of an imbricate stack of both metamorphic and non-metamorphic continental and oceanic units (e.g., McCall & Kidd, 1982; Burg, 2018). These stacks were formed during the pre-Eocene geodynamic history of the Makran Accretionary Prism, as constrained by the unconformable deposition onto this domain of lower Eocene deposits (e.g., Samimi Namin, 1983; McCall, 1985, 1997, 2002). In contrast, the Inner Makran, Outer Makran and Coastal Makran domains include Eocene to Pleistocene mainly siliciclastic sedimentary successions that have been progressively incorporated in the frontal part of the accretionary prism (e.g., Platt et al., 1985; Dolati, 2010; Burg et al., 2008; 2013; Mohammadi et al., 2016; Burg, 2018).

2.2. The North Makran domain

The North Makran tectono-stratigraphic domain has been subdivided into several major tectonic units (Fig. 2.3) bounded by either high angle faults or low angles shear zones (McCall, 1985; Samimi Namin, 1983; Eftekhar-Nezhad et al. 1979). These units are from the north to the south and from the uppermost to the lowermost one (Fig. 2.3): i) the Ganj Complex; ii) the North

Makran Ophiolites (Inner Makran Spreading Zone of McCall & Kidd, 1982); iii) the Bajgan and Durkan Complexes; iv) the Deyader Metamorphic Complex; v) the Sorkhband – Rudan tectonic slices; vi) the Coloured Mélange (Imbricate Zone of Burg et al., 2013).

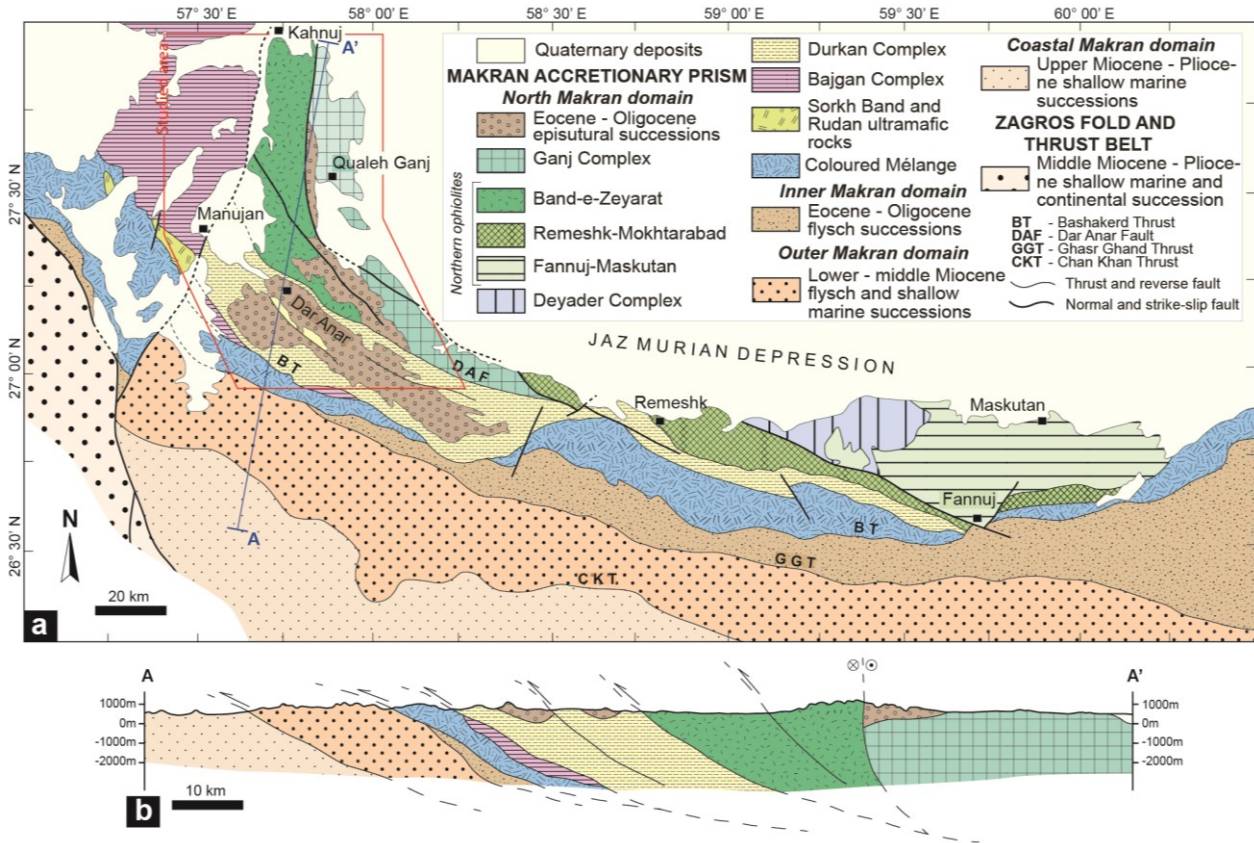


Figure 2.3. Simplified geological-structural map (a) and geological cross section (b) of the North Makran Domain showing the different tectonic units (modified from Eftekhar-Nezhad et al., 1979; Burg, 2018; Samimi Namin, 1982, 1983). Red polygon indicates the studied area.

According to the available literature, the North Makran ophiolites (Fig. 2.3) are represented by four distinct tectonic units, which are: 1) the Band-e-Zeyarat / Dar Anar (Kananian et al., 2001; Ghazi et al., 2004); 2) the Ganj Complex (Shaker-Ardakani et al., 2009); 3) the Remeshk-Mokhtarabad ophiolite (Moslempour et al., 2015; Monsef et al., 2019); 4) the Fannuj-Maskutan ophiolite (Desmons & Beccaluva, 1983). The Ganj Complex is poorly known. Only large-scale investigations have been carried out by McCall and co-workers during the geological mapping of the Makran performed in the 1970s by the Paragon Contech Company (McCall & Kidd, 1982;

McCall, 1985). McCall (1985) describes the Ganj Complex as an Albian-Maastrichtian ophiolite sequence, noting however that this unit shows some remarkable differences if compared with the classical ophiolite sequences observed in the other units in the North Makran. In particular, McCall (1985) observed that it is dominated by sub-volcanic rocks of intermediate to acidic composition and includes volcanic rocks showing calc-alkaline affinity. The Band-e-Zeyarat, Remeshk-Mokhtarabad, and the Fannuj-Maskutan ophiolites show Early Cretaceous and Late Cretaceous ages and are characterized by magmatic rocks mostly showing enriched-type mid-ocean ridge basalts (E-MORB) geochemical affinity and supra-subduction zone geochemical affinity, respectively (Desmond & Beccaluva, 1983; Ghazi et al., 2004; Burg, 2018, Monsef et al., 2019; Sepidbar et al., 2020). The North Makran Ophiolites are collectively considered as remnants of the North Makran Ocean (Fig. 2.4), which has been interpreted as either an Early Cretaceous back-arc basin related to the northward subduction of the Neo-Tethys (McCall & Kidd, 1982) or a marginal basin opened during Late Jurassic - Early Cretaceous at the southern margin of the Central Iran Block (Hunziker et al., 2015; Burg, 2018). Regardless of these different interpretations, it is commonly suggested that the opening of this basin led to the drift of a microcontinental block (the so called Bajgan-Durkan microcontinent) from the Lut Block (Fig. 2.4; McCall & Kidd, 1982; McCall, 2002; Hunziker, et al., 2015; Burg, 2018).

The Bajgan and Durkan Complexes are regarded as a narrow (~40 km wide) block with continental affinity (Fig. 2.3). Some authors suggested that the Bajgan and Durkan Complexes represent the south-eastward continuation of the Sanandaj-Sirjan Zone (e.g., McCall & Kidd, 1982; McCall, 1985). However, these two complexes are characterized by completely different rock assemblages. The Bajgan Complex is an assemblage of metamorphic rocks that includes schists, paragneisses, amphibolites, and marbles, as well as basic and acidic meta-intrusive rocks and rare glaucophane-bearing schists (McCall, 1985; McCall, 2002; Dorani et al., 2017). The tectono-

metamorphic evolution and the age of this complex is poorly known. McCall (1985) and Dorani et al. (2017) estimated metamorphic conditions characterized by a moderately high pressures and relatively high temperatures. In contrast, the Durkan Complex is non metamorphic or only slightly

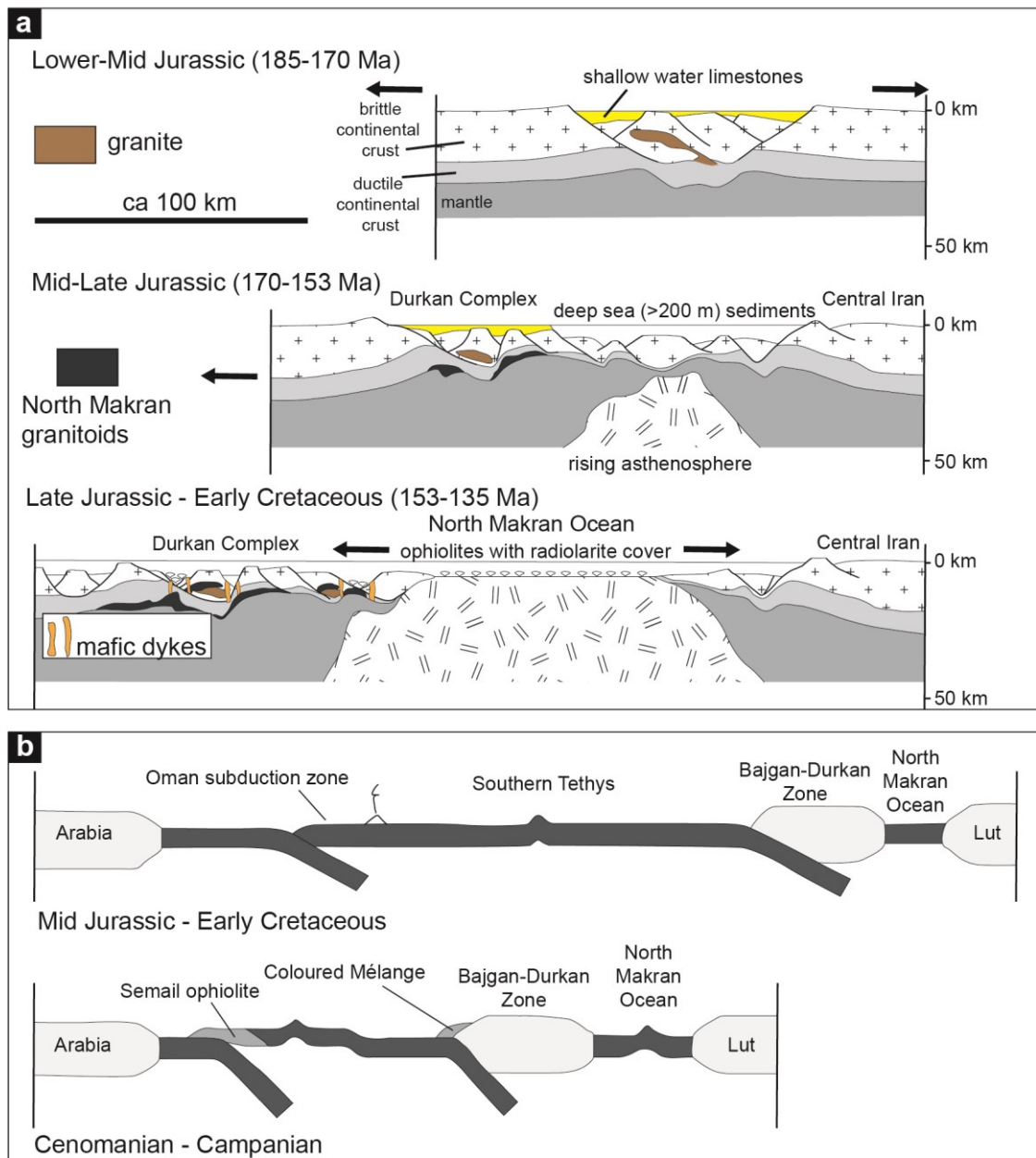


Figure 2.4. Different geodynamic reconstruction proposed in literature for the North Makran Ocean: a) geodynamic model interpreting the North Makran Ocean as a subduction-unrelated oceanic basin opened at the southern margin of the Lut Block (redrawn from Hunziker et al., 2015); b) geodynamic model interpreting the North Makran Ocean as a subduction-related marginal basin (back-arc?) related to the north-ward subduction of the Neo-Tethys oceanic lithosphere (redrawn from McCall & Kidd, 1982).

recrystallized (i.e., from diagenetic condition to subgreenschist facies) and it has been considered as the original sedimentary cover of the metamorphic Bajgan Complex (McCall, 1985, 2002). In the North Makran domain, the Durkan Complex is a ~250 km long and up to ~30 km wide complex, and crops out from Manujan to Fannuj, showing a gradual thinning toward both the west and east (Fig. 2.3). It consists of an assemblage of different tectonic slices showing different stratigraphic successions, including: i) Lower Cretaceous to Paleocene shallow-water limestones and thick sequences of alternating limestones, sandstones, shales, cherts, volcanics and volcanoclastics; ii) rare tectonic slices of Carboniferous, Permian, and Jurassic shelf carbonate rocks, and iii) subordinate marbles and schists (McCall, 1985, 2002; Hunziker et al., 2015). In addition, different types of granitoids have been intruded into Permian and Jurassic shelf limestones in the eastern sector of the Durkan Complex (Hunziker et al., 2015; Burg, 2018). They progressively range from Early Jurassic granites to Middle -Late Jurassic diorite-trondhjemite-plagiogranite suite. According to Hunziker et al. (2015), this lithological variation records the chemical evolution of the different magmatic pulses associated with the extensional tectonics of the southern margin of the Central Iranian Block, which led to the Late Jurassic – Early Cretaceous opening of the North Makran Ocean (Fig. 2.4).

The Deyader Metamorphic Complex outcrop in the eastern sector of the North Makran (Fig. 2.3). It is a metamorphic complex showing HP-LT metamorphism and consisting of meta-limestones, meta-volcanics and meta-gabbros affected by HP-LT metamorphism (Delaloye & Desmons, 1980; McCall, 1985; Hunziker et al., 2015; Omrani et al., 2017).

The Coloured Mélange consists of an assemblage of lozenge-shaped, metric- to decametric-thick slices that includes volcanic rocks, cherts, limestones, serpentinites, gabbros, shales, as well as various types of metamorphic rocks (e.g., Gansser, 1955; McCall 1983, 2002; Saccani et al., 2018; Esmaili et al., 2019, 2020). The formation of the Coloured Mélange was associated with the

Cretaceous subduction of the Neo-Tethys ocean and it includes a great variety of volcanic rocks from both the subducting oceanic plate and the subduction-related upper plate (Fig. 2.5; Saccani et al., 2018). Remnants of the subducting plates consist of Late Cretaceous oceanic plateau basalts,

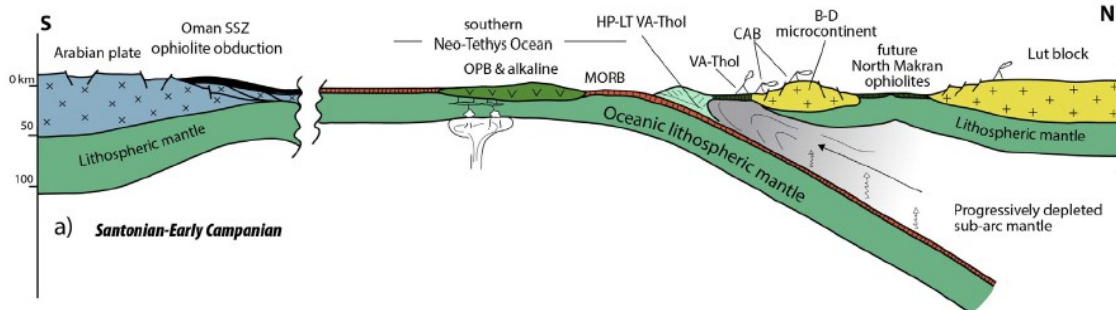


Figure 2.5. Geodynamic reconstruction at Late Cretaceous showing the tectono-magmatic setting of formation of the different rock types forming the Coloured Mélange as a consequence of the tectonic deformation during late Paleocene (from Saccani et al., 2018).

normal-type mid-ocean ridge basalts (N-MORB), and alkaline within-plate basalts (OIB) (Fig. 2.5). Moreover, remnants of the upper plate include Early to Late Cretaceous island arc tholeiites and calc-alkaline basalts likely formed in a forearc-arc tectonic setting (Fig. 2.5). McCall (2002) and Saccani et al. (2018) suggested a late Paleocene age of formation for this mélange.

The Sorkhband and Rudan tectonic slices crop out between the Coloured Mélange and the Bajgan Complex (McCall, 2002; Delavari et al., 2016). They consist of slices of ultramafic and mafic rocks, which are up to 4 km thick. The Sorkhband tectonic slice includes gabbros derived from a mid-ocean ridge tectonic setting tectonically juxtaposed to mantle peridotites and lower crust rocks generated at a supra-subduction zone setting (Delavari et al., 2016). A Mesozoic age has been proposed for these rocks by Delavari et al. (2016).

2.3. Regional-scale structural setting of the studied area and its comparison with the eastern Makran

The studied area is in the western sector of the North Makran domain in the neighbourhood of

Manujan city (Fig. 2.3). The available structural data for this area dates back to more than thirty-five years ago and were collected during the Makran 1:250,000 scale geological mapping program (Samini Namin, 1983; McCall, 1985). These data are mainly focused on the map relationships between the different tectonic unit, whereas the mesoscale structural setting is poorly known. The studied area is dominated by the complex interference between the mainly NW-SE and locally N-S striking thrusts and reverse faults juxtaposing the different tectonic units and the NNE-SSW to NNW-SSE striking high angle strike-slip and normal fault zones (Fig. 2.3; McCall, 1985; Regard et al., 2004). During the mapping program, the crosscutting relationships between these different fault systems allowed to grossly recognize their time-relationships. In detail, the tectonic contact between the different units is crosscut by strike-slip and normal faults, suggesting that the latter are younger than thrusts and reverse faults (Samini Namin, 1983; McCall, 1985). However, these authors also hypothesised that thrust and reverse faults can be related to different deformation stages and/or multiple reactivations occurred from Late Cretaceous to middle Miocene, and possibly also during younger ages. Differently, the strike-slip and normal faults are thought to be mainly related to the late Miocene-Quaternary tectonic activity in the area (McCall, 1985). The successions of the different tectonic units in the studied area show also multiple folding stages (McCall, 1985). McCall (1985) clearly stated the difficulties in discriminating pre-Eocene folding from those occurred during the post-Eocene deformation of the accretionary prism.

Recent structural studies have been carried out by Burg and co-workers (Dolati, 2010; Haghypour et al., 2012; Dolati & Burg, 2013; Burg et al., 2013; Hunziker, 2014; Hunziker et al., 2015; Mohammadi et al., 2016; Burg, 2018) eastward to the studied area, in the sector comprised between Remeshk and Espakeh cities and in the area to the south of Fannuj city (Fig. 2.3). These authors described in detail the complex structural evolution of this area suggesting multiple stages of deformation. To summarize, the accretionary prism in this sector is characterized by E-W

trending thrust zones and folds (Dolati, 2010; Dolati & Burg, 2013; Hunziker, 2014;). The thrusts show a younging age from the N to S, from the Bashakerd Thrust to the Chan Khan Thrust, and show southward vergence (Dolati, 2010; Dolati & Burg, 2013; Burg et al., 2013). Both thrusts and folds are generally offset by NE-SW left-lateral and NW-SE right-lateral fault systems, which are interpreted as representing conjugate strike-slip fault systems related to N-S shortening during Arabian and Eurasian convergence (Burg, 2018). The age of these faults is hypothesised as younger than early Eocene since they crosscut the pre-Eocene thrusts in the North Makran (Hunziker, 2014). By contrast, some strike slip-faults are related to the post-Eocene thrusts and possibly represent transfer lateral ramp of the compressive structures (Dolati & Burg, 2013). Finally, normal faults with E-W trending are described in this sector and they cut sedimentary rocks younger than late Miocene as well as the older thrusts contacts between the different units.

These literature data point out for a clockwise rotation of the trending of the main thrusts and folds from east to west in the Makran, i.e., from the Fannuj-Remeshk-Espake sector to the Manujan sector (Fig. 2.3). In fact, moving from east to west these structures gradually change from E-W strike toward NE-SW and N-S striking. This strike variation is thought to be controlled by the NNW-striking Minab-Sabzevaran-Nayband fault system (also known as Minab-Zandan-Palami Fault system), which accommodated right-lateral displacement (McCall, 1985; Stoneley, 2005; Burg, 2018). This Fault system is believed to represent a wide and still in part active deformation zone that separates the active Makran subduction zone from the Zagros continent-continent collisional zone (Kopp et al., 2000; Stoneley, 2005; Regard et al., 2010; Penney et al., 2015). The Minab-Sabzevaran-Nayband fault system has likely been active since the Miocene to accommodate different tectonic styles of deformation between the Makran and the Zagros belts (Regard et al., 2010).

In conclusion, the studied area corresponds to an extremely complex portion of the Makran

Accretionary. Its structural setting mainly resulted from a long-lived deformation history related to the tectonic stages in the accretionary prism followed by intense dextral strike-slip faulting stages associated to the activity of the tectonic boundary between the Makran and Zagros belts.

Chapter 3. Analytical methods

3.1. Whole-rock geochemical analysis

Whole-rock major and selected trace elements were analysed by X-ray fluorescence (XRF) on pressed-powder pellets using an ARL Advant-XP automated X-ray spectrometer. The matrix correction method proposed by [Lachance & Trail \(1966\)](#) was applied. Volatile elements content was determined as loss on ignition (LOI) at 1000°C. In addition, trace elements, such as Rb, Sr, Y, Zr, Nb, Hf, Ta, Th, U, and the rare earth elements (REE) were determined by inductively coupled plasma-mass spectrometry (ICP-MS) using a Thermo Series X-I instrument. The accuracy of the data and detection limits were evaluated using results for international standard rocks run as unknown. Accuracies and detection limits for both XRF and ICP-MS analyses are reported in [Table 3.1](#) and [3.2](#), respectively. In these tables are also shown the trace elements analyzed with different methods. All whole-rock analyses were performed at the Department of Physics and Earth Sciences, Ferrara University.

3.2. Mineral chemistry analysis

Silicates were analyzed by electron microprobe using a Superprobe Jeol JXA 8200 (JEOL, Tokyo, Japan) at the Eugen F. Stumpfl Laboratory at the University of Leoben, Austria, using both ED and WD systems. During the quantitative analyses of silicates, the electron microprobe was operated in the WDS mode, with an accelerating voltage of 15 kV and beam current of 10 nA. The diameter of the beam was about 1 µm. Counting times were 20 s on the peak and 10 s on the left and right backgrounds. Standards (element, emission line) were: adularia (Al and Si, K α), rutile (Ti, K α), chromite (Cr, K α), almandine (Fe, K α), rhodonite (Mn, K α), olivine (Mg, K α), wollastonite (Ca, K α), albite (Na, K α), and sanidine (K, K α). The following diffracting crystals

were selected: TAP for Na, Mg, and Al; PETJ for K, Si, and Ca; and LIFH for Ti, Cr, Mn and Fe. The detection limits were automatically calculated by the Jeol microprobe software and they are listed in the following as ppm: Na, Al, Mg, K, Ca (100), Si, Cr, Fe, Mn (150) and Ti (200). As a consequence of the severe ocean-floor hydrothermal alteration that affected the studied rocks, a few samples were suitable for electron microprobe analysis. Only one type of mineral phase (plagioclase or clinopyroxene) was fresh enough to be analysed in only three samples of the sheeted dyke and volcanic complexes. In four samples from the intrusive complex we found two or more different types of fresh mineral phases, including olivine, plagioclase, clinopyroxene. The composition of Fe^{2+} and Fe^{3+} for clinopyroxene was calculated from the measured FeO according to the method of [Droop \(1987\)](#).

Appendix Table 3.1. Comparison of major and trace element concentrations in reference samples analysed using X-Ray Fluorescence spectrometry and detection limits. Recommended values for international reference materials BE-N and BHVO-1 are from Govindaraju (1994). Abbreviations: Recomm. = recommended values; n.d. = not detected. Detection limits were estimated.

| | | BE-N | | | BHVO-1 | | | Detection limits |
|---------------------------------------|--------------------------------|---------|-----------------------------|--------------------|---------|-----------------------------|--------------------|------------------|
| | | Recomm. | Measured Mean Values (n=30) | Relative Error (%) | Recomm. | Measured Mean Values (n=13) | Relative Error (%) | |
| X-Ray Fluorescence spectrometry (XRF) | (wt%) | | | | | | | |
| | SiO ₂ | 38.48 | 38.58 | -0.3 | 49.94 | 49.57 | 0.74 | 0.05 |
| | TiO ₂ | 2.63 | 2.62 | 0.3 | 2.71 | 2.75 | -1.48 | 0.01 |
| | Al ₂ O ₃ | 10.14 | 9.81 | 3.3 | 13.80 | 14.02 | -1.59 | 0.05 |
| | Fe ₂ O ₃ | 12.93 | 12.78 | 1.2 | 12.23 | 12.52 | -2.37 | 0.10 |
| | MnO | 0.20 | 0.19 | 7.4 | 0.17 | 0.17 | 0.00 | 0.05 |
| | MgO | 13.25 | 13.60 | -2.7 | 7.23 | 6.90 | 4.56 | 0.01 |
| | CaO | 13.97 | 13.73 | 1.7 | 11.40 | 11.52 | -1.05 | 0.04 |
| | Na ₂ O | 3.20 | 3.30 | -3.0 | 2.26 | 2.36 | -4.42 | 0.01 |
| | K ₂ O | 1.40 | 1.36 | 2.9 | 0.52 | 0.50 | 3.85 | 0.01 |
| | P ₂ O ₅ | 1.06 | 1.00 | 5.4 | 0.27 | 0.25 | 7.41 | 0.01 |
| | (ppm) | | | | | | | |
| | Zn | 120 | 116 | 3.3 | 105 | 98 | 6.67 | 2 |
| | Cu | 72 | 73 | -0.8 | 136 | 140 | -2.94 | 3 |
| | Sc | 22 | 21 | 2.3 | 31.8 | 32 | -0.63 | 3 |
| | Ga | 17 | 16 | 4.4 | 21 | 22 | -4.76 | 3 |
| | Ni | 267 | 260 | 2.6 | 121 | 124 | -2.48 | 2 |
| | Co | 60 | 63 | -5.0 | 45 | 46 | -2.22 | 2 |
| | Cr | 360 | 351 | 2.5 | 289 | 298 | -3.11 | 2 |
| | V | 235 | 231 | 1.7 | 317 | 312 | 1.58 | 2 |
| | Rb | 47 | 47 | 0.2 | 11 | 10 | 9.09 | 1 |
| | Ba | 1025 | 999 | 2.5 | 139 | 145 | -4.32 | 3 |
| | Pb | 4 | n.d. | | 2.6 | n.d. | | 5 |
| | Sr | 1370 | 1360 | 0.7 | 403 | 408 | -1.24 | 2 |
| | Zr | 260 | 268 | -3.1 | 179 | 172 | 3.91 | 2 |
| | Y | 30 | 28 | 5.3 | 27.6 | 28 | -1.45 | 1 |
| | La | 82 | 79 | 3.7 | 15.8 | 18 | -13.9 | 5 |
| | Ce | 152 | 160 | -5.3 | 39 | 42 | -7.69 | 5 |
| Nd | 67 | 65 | 3.7 | 25.2 | 24 | 4.76 | 3 | |
| Nb | 105 | 105 | -0.1 | 19 | 18 | 5.26 | 1 | |
| Th | 10.4 | 11 | -2.7 | 1.08 | 1 | 7.41 | 1 | |

Appendix Table 3.2. Comparison trace element concentrations in reference samples analysed using Inductively Coupled Plasma-Mass Spectrometry and detection limits. Recommended values for international reference materials BHVO-1 are from Govindaraju (1994). Abbreviations: Recomm. = recommended values; n.d. = not detected. Detection limits were estimated

| | | BHVO-1 | | | Detection limits |
|---|-------|---------|-----------------------------|--------------------|------------------|
| | | Recomm. | Measured Mean Values (n=13) | Relative Error (%) | |
| Inductively Coupled Plasma-Mass Spectrometry (ICP-MS) | (ppm) | | | | |
| | Rb | 11 | 10.9 | 1.4 | 0.020 |
| | Sr | 403 | 410 | -1.7 | 0.020 |
| | Y | 27.6 | 28.4 | -2.8 | 0.003 |
| | Zr | 179 | 190 | -6.1 | 0.020 |
| | La | 15.8 | 16.0 | -1.3 | 0.010 |
| | Ce | 39 | 37.6 | 3.7 | 0.002 |
| | Pr | 5.7 | 5.57 | 2.3 | 0.004 |
| | Nd | 25.2 | 26.1 | -3.7 | 0.002 |
| | Sm | 6.2 | 6.53 | -5.3 | 0.006 |
| | Eu | 2.06 | 2.10 | -1.9 | 0.002 |
| | Gd | 6.4 | 6.25 | 2.3 | 0.001 |
| | Tb | 0.96 | 0.93 | 3.6 | 0.002 |
| | Dy | 5.2 | 5.42 | -4.2 | 0.001 |
| | Ho | 0.99 | 1.05 | -6.1 | 0.002 |
| | Er | 2.4 | 2.57 | -7.1 | 0.001 |
| | Tm | 0.33 | 0.32 | 4.5 | 0.003 |
| | Yb | 2.02 | 2.16 | -6.9 | 0.001 |
| | Lu | 0.291 | 0.31 | -6.9 | 0.005 |
| | Nb | 19 | 18.5 | 2.7 | 0.001 |
| Hf | 4.38 | 4.29 | 2.1 | 0.001 | |
| Ta | 1.23 | 1.30 | -5.7 | 0.005 | |
| Th | 1.08 | 1.13 | -4.6 | 0.0015 | |
| U | 0.42 | 0.45 | -7.1 | 0.002 | |

Chapter 4. The Ganj Complex

Associated manuscript:

Barbero E., Delavari M., Dolati A., Saccani E., Marroni M., Catanzariti R., Pandolfi L., 2020. The Ganj Complex reinterpreted as a Late Cretaceous volcanic arc: Implications for the geodynamic evolution of the North Makran domain (southeast Iran). *Journal of Asian Earth Sciences*, 195, <https://doi.org/10.1016/j.jseaes.2020.104306>

4.1. Geological features

The Ganj Complex occurs as a tectonic unit along a discontinuous belt of 38 km-long and 15 km-wide in the North Makran area in correspondence of the southwestern border of the Jaz Murian depression. Toward west and southwest, the Ganj Complex is separated from the Band-e-Zeyarat/Dar Anar and Fannuj-Maskutan ophiolites by the Jiroft fault (Figs. 4.1, 4.2a), a sub-vertical shear zone ranging in strike from N-S to NW-SE.

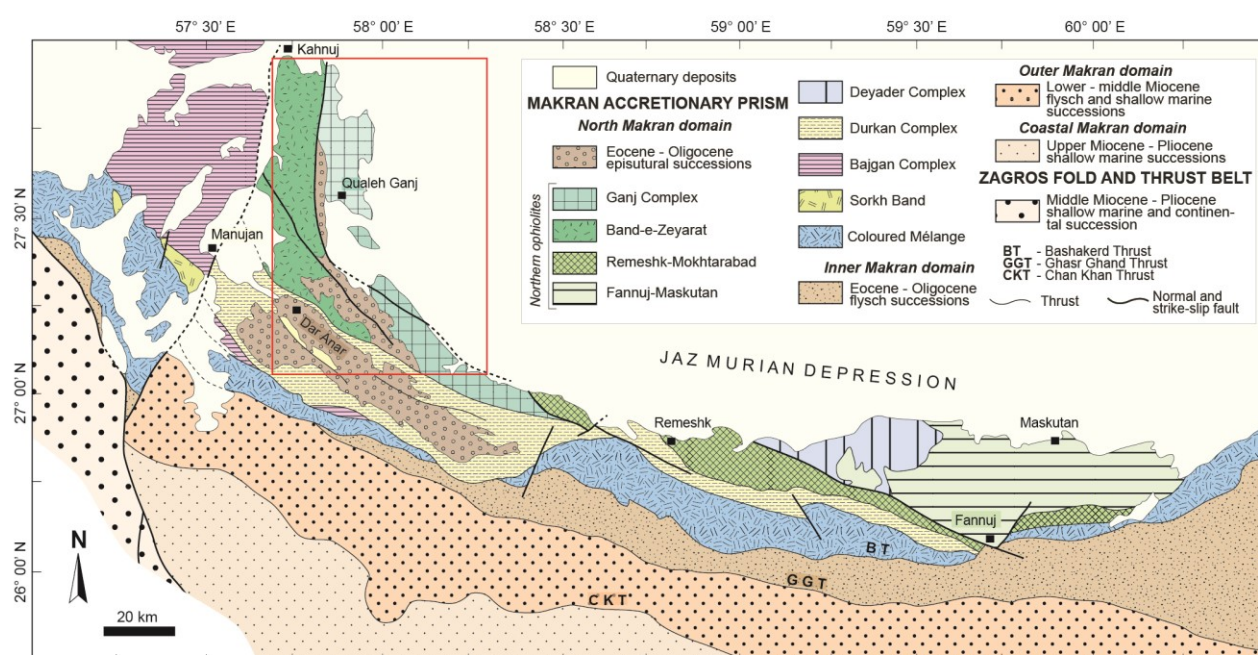


Figure 4.1. Simplified geological map of the North Makran Domain, modified from *Eftekhari-Nezhad et al. (1979)*; *Eftekhari-Nejad & McCall (1993)*; *Burg (2018)*; *Samimi Namin (1982, 1983)*. The box indicates the area expanded in Fig. 4.2.

The Ganj Complex is unconformably covered by the Eocene deposits represented by nummulite-bearing limestones and siliciclastic turbidites (Figs. 4.1a, b, d). A panoramic field view of this unconformity is shown in the [Appendix Figure 4.1](#). Both the Ganj Complex and the Eocene deposits are in turn affected first by a gentle folding phase and then by a faulting phase represented by high angle strike-slip and normal faults. No evidence of pre-Eocene deformations or orogenic metamorphism has been found in the Ganj Complex.

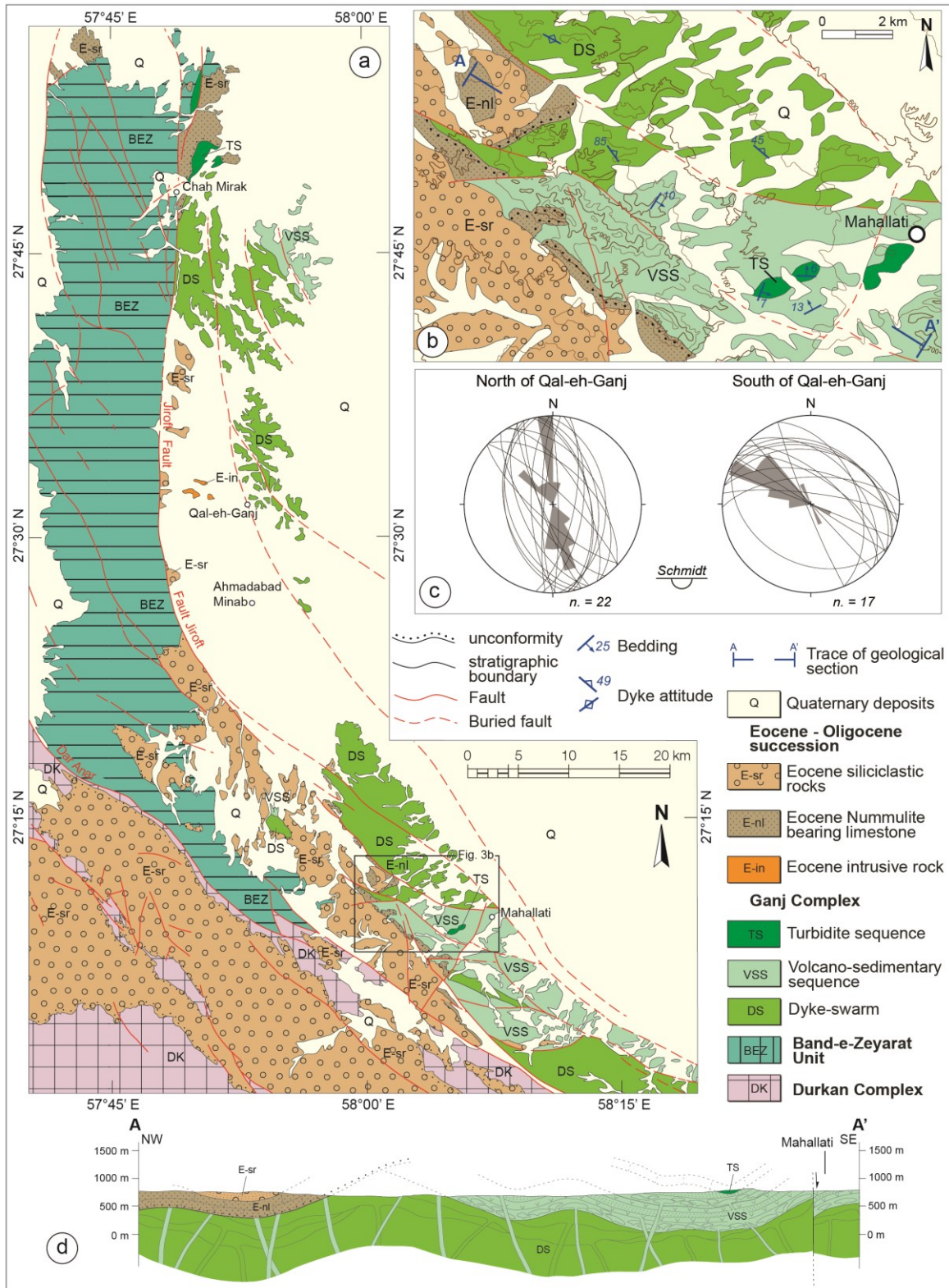


Figure 4.2. a) Geological scheme of the Ganj Complex; b) Geological map of the Mahallati Village area; c) mesoscale data (Schmidt net, lower hemisphere) showing the dykes attitude and their orientation (rose diagram); d) cross-section of the Mahallati Village area (trace of section is indicated in panel b). a): modified from Samimi Namin, (1983) integrated with original field observations and mapping; b), c), and d): based on original data.

Detailed field work allowed us to recognize that the Ganj Complex is dismembered into several tectonic slices bounded by high angle faults. The slices are undeformed in their core where the pristine stratigraphic features of the Ganj Complex are fully preserved. In one of these slices cropping out close to the Mahallati Village a complete section, from the magmatic rocks to the sedimentary cover, has been recognized (Figs. 4.2b, c). The log of this section has been integrated by the stratigraphic features observed in the other tectonic slices. The reconstructed stratigraphic sequence is shown in Figure 4.3a.

According to McCall (1985) and Shafaii Moghadam & Stern (2015), the base of the Ganj Complex is characterized by a gabbroic complex that, however, has not been recognized during the detailed field work. We propose that the stratigraphy of the Ganj Complex can be subdivided into three main parts (Fig. 4.3a): (1) the basal dyke swarm showing a transition to (2) the volcano-sedimentary sequence that grade-up, in turn, to (3) the turbidite sequence. As shown in the geological cross-sections (Fig. 4.2d) the thickness of the entire sequence can be estimated as not less than 2000 m.

4.1.1. The dyke-swarm

Sub-volcanic rocks are widespread in the sequence of the Ganj Complex and mostly occur as dyke-swarms that is, major groups of sub-parallel or crosscutting dykes. Nonetheless, in the northern part of the Ganj Complex well-developed sheeted dykes, consisting of groups of perfectly parallel dykes, can locally be observed. The basal part of the dyke-swarm sequence is mainly represented by parallel and sub-parallel dykes. The dykes show variable thickness, ranging from 0.5 to more than 3 m (Figs. 4.3b, c). They are represented by a great variety of rock-types, including andesites, dacites, rhyolites and subordinate basaltic rocks. These different rock types are

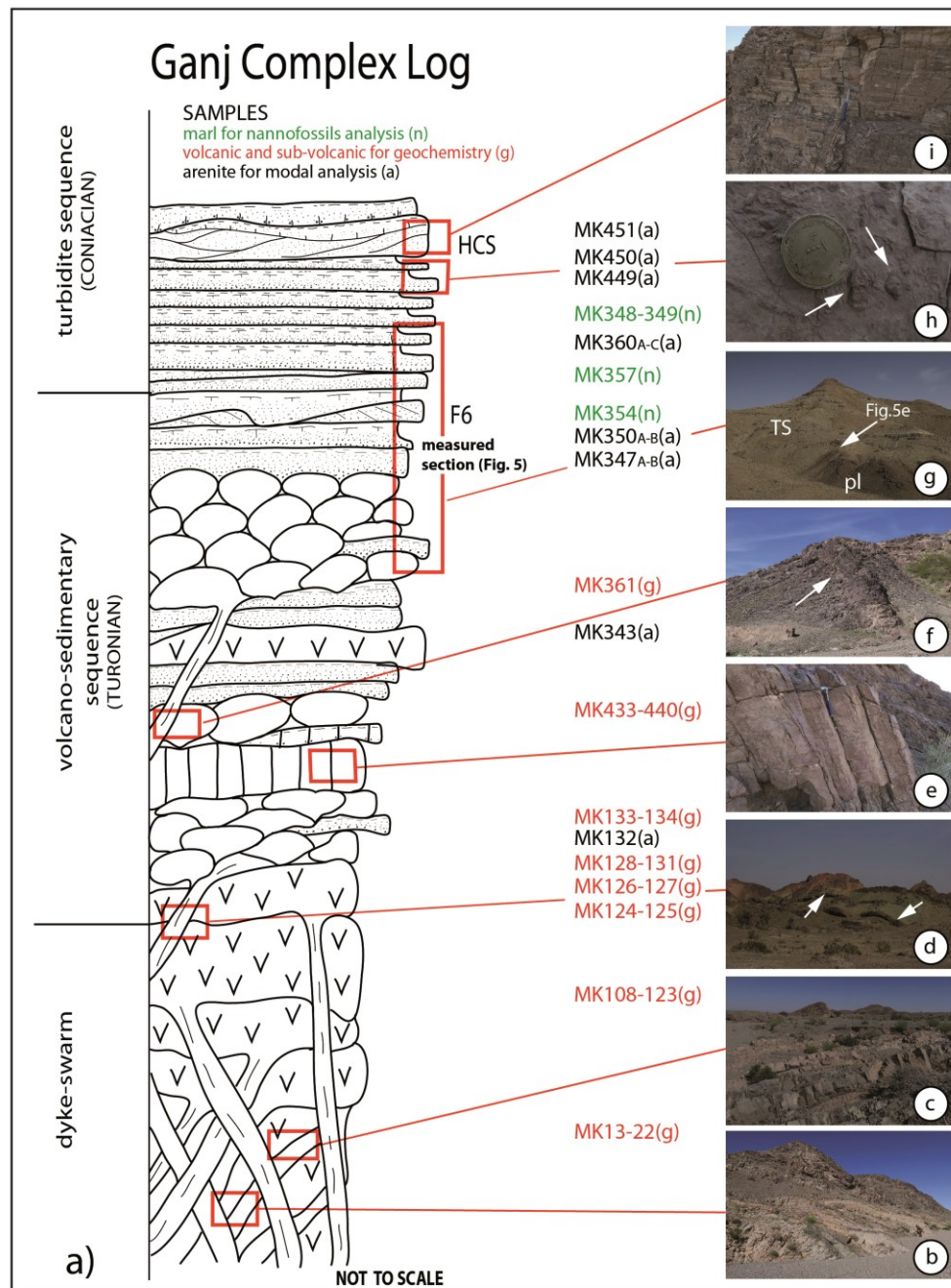


Figure 4.3. a) Stratigraphic log of the Ganj Complex succession. The sample positions with respect to the log is also indicated. b-i) Most significant outcrop views with reference to the log. b) and c) dyke-swarm complex; d) lava flow crosscut by andesitic dykes (arrows); e) columnar basalts; f) pillow lava crosscut by a plurimetric dyke (arrow); g) stratigraphic relationships between the pillow lavas (pl) of the volcano-sedimentary sequence and the turbidite sequence (TS). The area expanded in Fig. 4.4e is indicated; h) reworked fragments of shells and gastropods (arrows) in the turbiditic strata of the upper part of the turbidite sequence; i) hummocky-cross stratification structures in the uppermost part of the turbidite sequence. Abbreviations, HCS: hummocky-cross stratification structures; F6: facies F6 according to Mutti (1992). The position of the log shown in Fig. 4.4 is also indicated. Only the marly samples with the most significant and best-preserved taxa are shown in this Figure. For a full list of the marls analyzed for biostratigraphy, see Appendix Table 4.1.

evenly distributed in the study area. No relationship between rock type and spatial distribution can be observed. Likewise, no relative chronological evolution from basalts to differentiated dacites and rhyolites can be recognized based on crosscutting relationships between different dykes. In the uppermost part of the dyke-swarm, the occurrence of sills crosscutting massive lava flows marks the transition to the volcano-sedimentary sequence (Fig. 4.3d).

4.1.2. The volcano-sedimentary sequence

The volcano-sedimentary sequence consists of an assemblage of massive lava flows, pillow lavas, lava breccias and minor sedimentary deposits (Fig. 4.4a), represented by coarse-grained volcanoclastic turbidites showing comparable sedimentological features and composition of the turbidites detected in the turbidite sedimentary cover sequence (see next paragraph). Massive lava flows are volumetrically the most abundant and widespread volcanic facies.

The lower part of the volcano-sedimentary sequence is dominated by massive lava flows rarely intercalated with pillow lavas, lava breccias and rare turbidite beds. Massive lava flows are mainly represented by intermediate to acidic rock-types (i.e., dacites and rhyolites) and minor andesites, whereas basaltic rocks are subordinate. In this part of the succession, columnar basalts (Fig. 4.3e) associated with volcanic scoria are observed suggesting that they were erupted in sub-aerial or, eventually, very shallow water (e.g., lacustrine or lagoon) settings environments. In the middle part of the volcano-sedimentary sequence, lava flows, pillow lavas and minor turbidite beds are equally widespread. The pillow and massive lava flows are sometimes crosscut by dykes, as shown in Fig. 4.3f. The upper part of the volcano-sedimentary sequence is dominated by pillow lavas mainly consisting of basalts and basaltic andesites, interfingering with lava flows and turbidite beds (Figs. 4.3a, g). Remnants of unconsolidated silty marls and marly limestones have been recognized as soft

clasts squeezed among the pillow lavas. The general features of the sedimentary rocks suggest that the associated lava flows were most likely erupted in relatively shallow water (<300 m) marine setting.

In order to better constrain the primary relationships between the volcano-sedimentary sequence and the turbidite sequence, a 30 m detailed stratigraphic section (Figs. 4.3a, 4.3g and 4.4a) has been measured along the transition between these two stratigraphic sequences. The bottom of the measured log is characterized by ~12 m of pillow-lavas (Fig. 4.4b) and subordinate pillow-breccias. Inside the pillow lava sequence a bed of volcanoclastic coarse-grained arenites (sample MK343 in Fig. 4.4c) has been recognized. The inter-pillow space is often filled by squeezed soft clasts of marly limestones (Fig. 4.4d) that indicates the emplacement of the pillow lava into a non-consolidated fine-grained turbidite carbonatic mud. The marly limestones indeed contain large amounts of small clasts of volcanic glass (see Fig. 4.5a), which further indicate that the emplacement of the lava flow and the sedimentation were almost contemporaneous. The top of the pillow lavas is covered by coarse-grained turbidite beds (see arenite petrography paragraph, samples MK347A/B and MK350A/B), characterized by F8+F9a and subordinate F6 facies of Mutti (1992) (Fig. 4.4e). These volcanoclastic beds mark the boundary between the lava-dominated volcano-sedimentary sequence and the turbidite sequence.

4.1.3. The turbidite sequence

The turbidite sequence is formed by a sequence of medium to thin-bedded low-density turbidites (F8+F9a and F9a facies of Mutti, 1992; Ta-e and Tc-e facies of Bouma, 1962; Figs. 4.4f, g). The turbidites consist of basal medium- to coarse-grained arenites (F8 interval) that pass into fine-grained laminated silty marls and marly limestones (F9 interval) with ripples and plane lamina

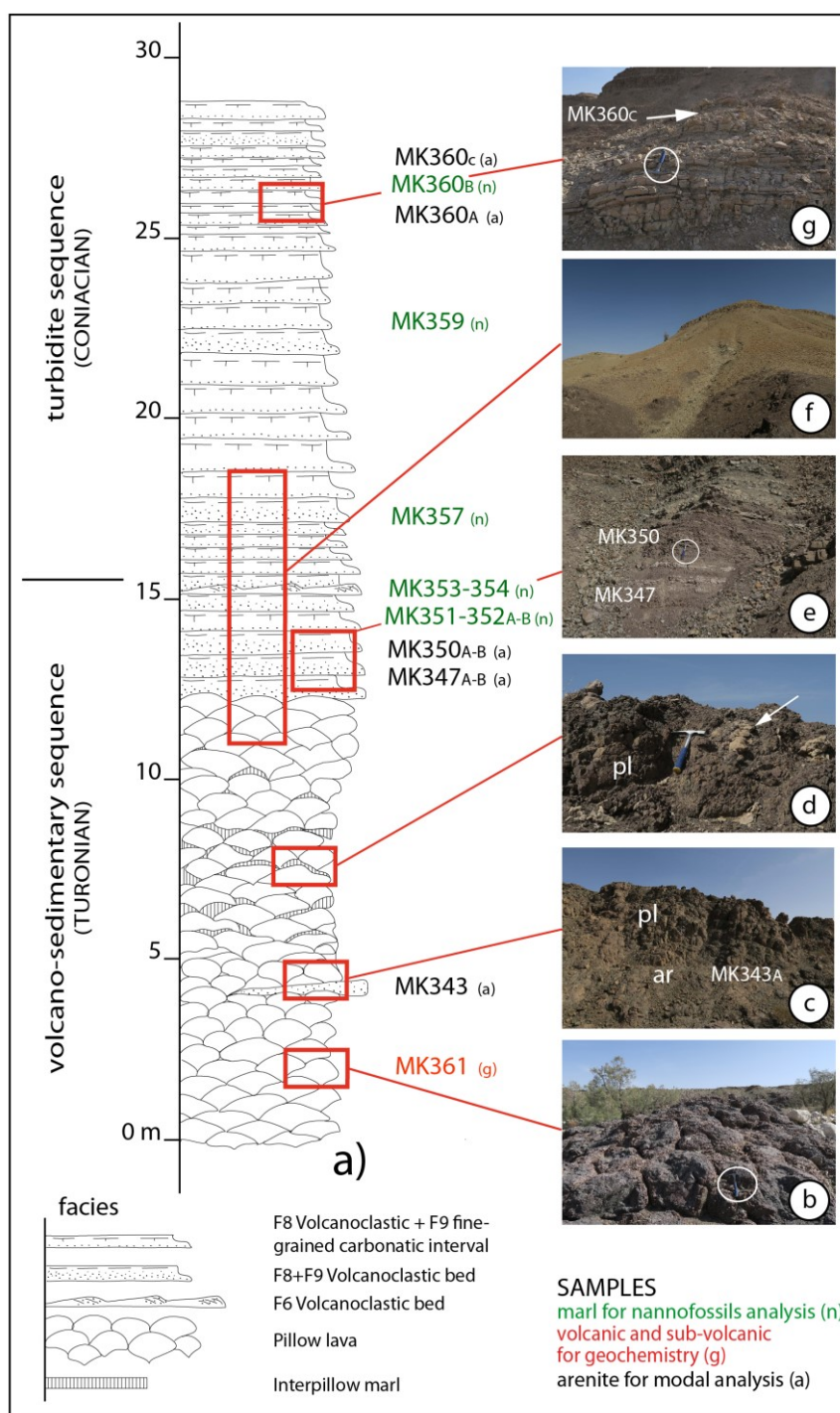


Figure 4.4. a) Detailed stratigraphic log of the transition between the volcano-sedimentary and the turbidite sequences. The sample positions with respect to the log is also indicated. b – g) Most significant outcrop views with reference to the log. b) pillow lavas (hammer for scale); c) volcaniclastic coarse-grained arenites (ar) interfingering in the pillow lava flows (pl); d) non-consolidated soft clasts of marly limestones (arrow) within the pillow lava flows (pl); e) coarse-grained volcaniclastic turbidite beds characterizing the uppermost part of the volcano-sedimentary sequence (hammer for scale); f); stratigraphic relationships between the volcano-sedimentary (pillow lava) and the turbidite sequences; g) medium- to thin-bedded low-density turbidites characterizing the uppermost part of the turbidite sequence (hammer for scale). Only the marly samples with the most significant and best preserved taxa are shown in this Figure. For a full list of the marls analysed for biostratigraphy, see [Appendix Table 4.1](#).

highlighted by pelagic foraminifera and minor benthic foraminifera [Figs. 4.4g, 4.5b](#)). In the coarse-grained arenites the occurrence of fragments of both carbonate and volcanic rocks can be clearly detected in the field as well as in thin section (see the next chapter for further details). In a coarse-grained stratum it has been recognized the presence of reworked fragments of shell and gastropods ([Fig. 4.3h](#)) that indicate a coeval outer platform environment as source area for the turbidites.

The presence, in the uppermost part of the sequence, of arenitic beds ([Fig. 4.3i](#)) showing hummocky cross stratification structures seems to point to a river-delta influenced outer platform environment ([Tinterri et al., 2011](#)). As a whole, the turbidite sequence can be regarded as a shallowing upward sequence.

4.2. Arenite petrography (courtesy of L. Pandolfi)

In order to better understand the provenance of sediments from the volcano-sedimentary sequence and the turbidite sequence, several arenite samples have been collected mainly in the Mahallati Village, where both these sequences are well exposed. Among these, twenty-three thin sections have been studied using polarizing microscope. The modal analysis was performed on eleven samples of medium- to coarse-grained arenites showing a well- to moderately-sorted texture. The modal analysis was performed by counting 500 grains using the Gazzi-Dickinson technique ([Gazzi, 1966](#); [Dickinson, 1970](#); [Ingersoll et al., 1984](#); [Zuffa, 1987](#)) in order to minimize the dependence of arenite composition on grain size. The modal analysis results are shown in the [Appendix Table 4.2](#) and plotted on the triangular diagrams in [Fig. 4.6](#).

No significant differences can be recognized in the framework composition of arenites from both volcano-sedimentary sequence and the turbidite sequence of the Ganj Complex ([Fig. 4.6](#)). They range from pure volcanic litharenites ([Fig. 4.5c](#)) to volcanic-rich litharenites to quartz-poor

arkoses (Fig. 4.5d) in which the siliciclastic fine-grained lithic composition is dominated by volcanic rock fragments or mixed with carbonate framework fragments (Fig. 4.5e). The triangular diagrams (Fig. 4.6) show no compositional evolution-trend along the reconstructed stratigraphic log and no significant differences can be recognized between the arenites sampled in the volcano-sedimentary sequence or in the turbidite sequence (Fig 4.6).

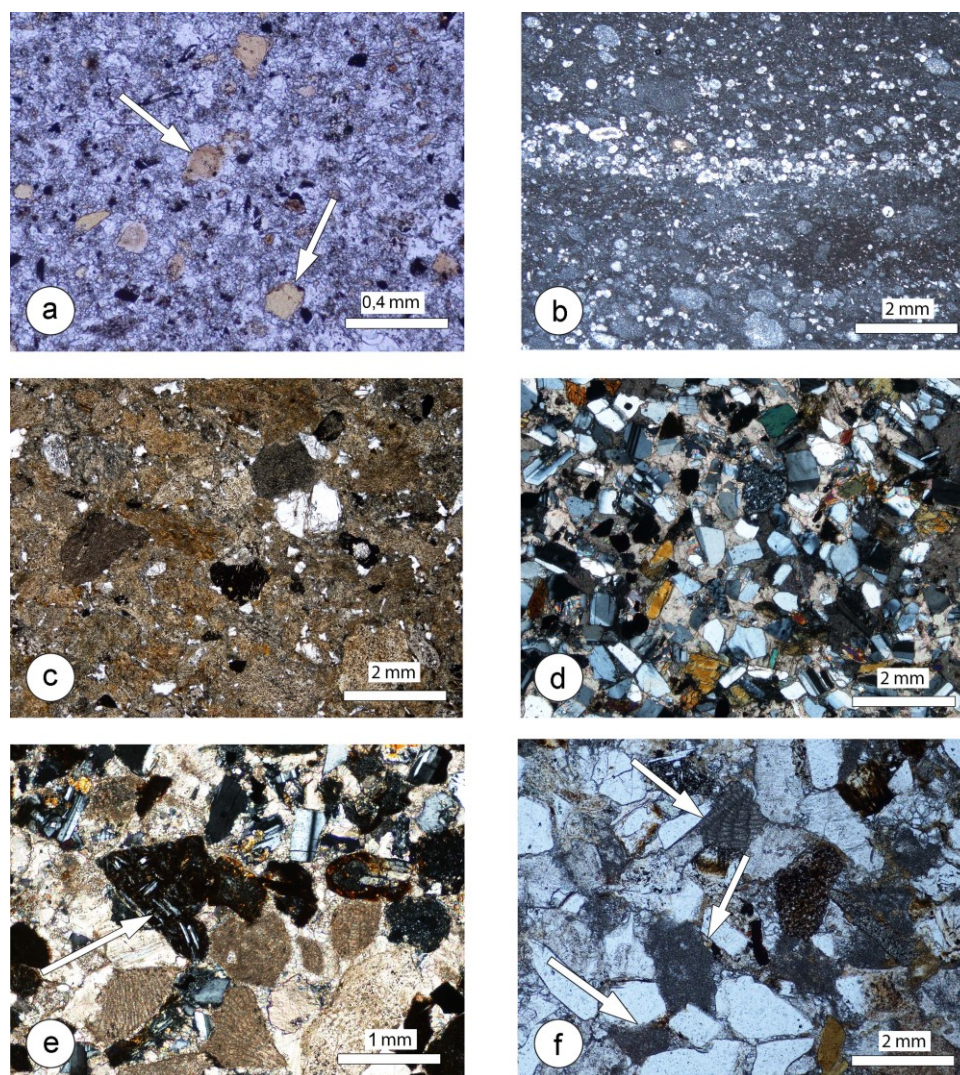


Figure 4.5. Photomicrographs of the studied sedimentary rocks from the Ganj Complex: a) detail of an inter-pillow turbidite marly limestone soft clast including small fragments of volcanic glass (arrows); b) fine-grained laminated silty marls and marly limestones. The laminae are highlighted by pelagic foraminifera and minor benthic foraminifera; c) pure volcanic litharenites, (sample MK343, upper part of the volcano-sedimentary sequence); d) quartz-poor arkose (sample MK347A, upper part of the volcano-sedimentary sequence), where the siliciclastic composition is dominated by plagioclase and clinopyroxene crystals; e) mixed siliciclastic-carbonate petrofacies (sample MK450, upper part of the turbidite sequence). Arrow indicate an intermediate volcanic lithic fragment; f) intrabasinal and coeval carbonate rock fragments (arrows) represented by mudstones and wackestones with deformed and squeezed soft margins, and by isolated bioclasts (sample MK360, turbidite sequence).

The siliciclastic framework is characterized by common plagioclase single crystals (1-42%, Fig. 4.5d) and by rare mono- and polycrystalline quartz (1-8% of the total framework) and K-feldspar (1-11%). Fine-grained lithic fragments are dominated by volcanic rock (6-74% of the total framework). It is worth noting that all the magmatic fragments belong to volcanic or subvolcanic rocks. In arenites from both the volcano-sedimentary sequence and the turbidite arenites of perfectly euhedral plagioclase crystals (Figs. 4.5d, e) suggest that the sedimentary reworking of the volcanic debris was very limited.

During the point counting, felsic (rhyolites and rhyodacites), intermediate (dacites and andesites) and mafic (andesitic-basalts and basalts) volcanic fragments have been distinguished. The triangular diagram of Fig. 4.6d indicates that the intermediate volcanic and subvolcanic fragments represent the dominant clasts ranging from 38% to 98% of the total volume of volcanic fragments.

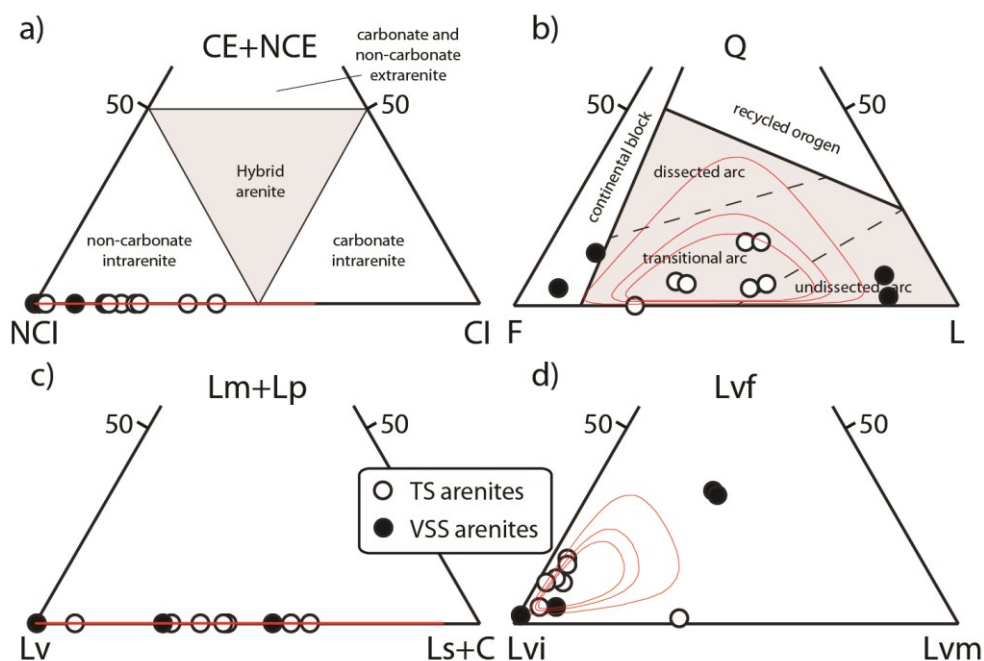


Figure 4.6. Ternary plots showing framework modes of arenites from the Ganj Complex sequence: a) CE+NCE CI NCI (Zuffa, 1980); b) Q F L (Dickinson et al., 1983); c) Lm Lv Ls+C (Ingersoll & Suzcek, 1979); d) Lv (felsic volcanic) Lvi (intermediate volcanic) Lvm (mafic volcanic) total rock fragments. Solid circles: arenites from the volcano-sedimentary sequence. Open circles: arenites from the turbidite sequence. The thin lines indicate 90, 95 and 99% confidence regions using the software CoDaPack (Comas-Cufi & Thio-Henestrosa, 2011).

The carbonate framework of the Ganj Complex arenites is formed by intrabasinal and coeval carbonate rock fragments (Fig. 4.5f). They are mainly represented by mudstones and wackestones with deformed and squeezed soft margins and by isolated bioclasts, mainly pelagic and minor benthic foraminifera and macrofossils fragments (undeterminable lamellibranchia, rudista and algae fragments). According to Zuffa (1980) the total framework is characterized by a coeval intrabasinal composition (Fig. 4.6a) where the carbonatic intrabasinal contribution (CI less than 30% of the total framework) led to classify these rocks as non-carbonate intrarenite (Fig. 4.6a).

4.3. Biostratigraphy (courtesy of R. Catanzariti)

A total of seventeen samples from the Ganj Complex were collected for biostratigraphy. We sampled the marly limestone interval representing the uppermost level (Td and Te Bouma intervals) of the turbidite beds. The position of samples with respect to the stratigraphic log is shown in Figs. 4.3a, 4.4a. In brief, five samples were taken from the transition between the volcano-sedimentary sequence and the turbidite sequence, three from the lower part of the turbidite sequence, and nine from the middle-upper part of the turbidite sequence.

Taxa were identified on smear slides (see Bown & Young, 1998) by the optical microscope at 1250X in cross polarized light. Species relative abundances were classified as R-Rare (less than 1 specimen per FOV-Field of View) and C-Common (1 or more than 1 specimen per FOV). Rarity of diagnostic species due to high dissolution effect was the main problem. In fact, only the taxa more resistant to dissolution were preserved, which made a challenge for identification at specific levels.

The main nannofossil species recognized during the study are shown in the Appendix Figure 4.2, whereas biostratigraphic data are shown in Appendix Table 4.1. Figure 4.7 shows the

distribution model of calcareous nannofossil taxa in which the chronostratigraphy and the age of

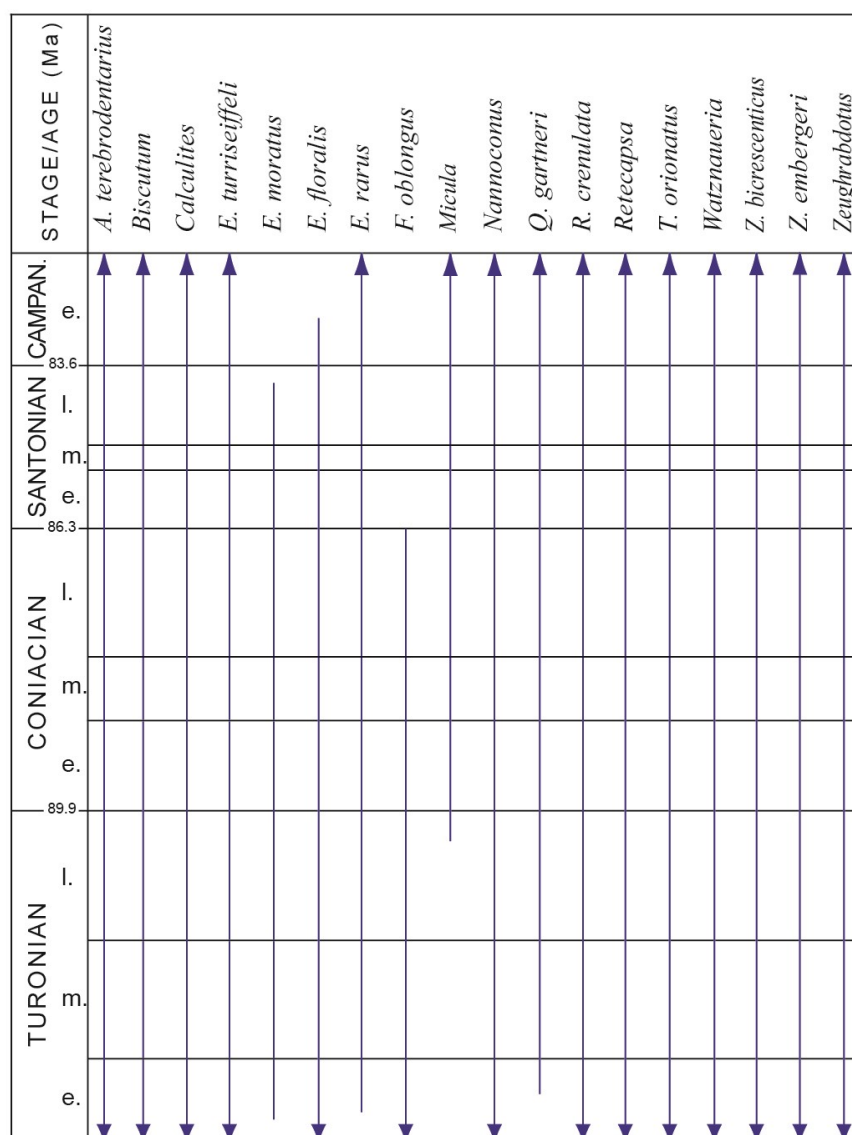


Figure 4.7. Range chart showing distribution of selected calcareous nannofossil taxa recognized in the Ganj Complex sequence, with chronostratigraphy and the age of the stage boundaries after [Gradstein et al. \(2012\)](#). Abbreviations, e.: early; m.: middle; l.: late.

the stage boundaries are from [Gradstein et al. \(2012\)](#). All taxa are referenced in [Bown \(1998\)](#), and their distribution is after [Burnett \(1998\)](#). The transition from the volcano-sedimentary sequence to the turbidite sequence contains assemblages consisting of *Quadrum gartneri*, *Eprolithus floralis*, *Eiffellithus turriseiffeli*, *Retecapsa crenulata*, *Biscutum* sp. and *Watznaueria* spp. The presence of *Q. gartneri* and *E. floralis* suggests a Turonian age. The turbidite sequence contains *Eprolithus*

eptapetalus, *Eprolithus* cf. *rarus*, *E. floralis*, *Q. gartneri*, and some specimens of cf. *Micula*, that allow us to propose a Turonian-Coniacian age.

4.4. Petrography of volcanic and sub-volcanic rocks

The volcanic and sub-volcanic rocks of the Ganj Complex are affected by low-grade hydrothermal alteration, which resulted in variable degree of replacement of the primary magmatic phases. No relationships exist between the degree of alteration and any particular rock type (i.e., basalt, rhyolite, etc.) or any volcanic facies (i.e., dykes, lava flows, etc.). Regardless of the secondary recrystallization, the primary magmatic texture is commonly preserved in most of both volcanic and sub-volcanic rocks. Olivine crystals are very rare and occur only in volcanic rocks as small phenocrysts, commonly replaced by iddingsite. Fresh plagioclase is almost absent, as it is usually replaced by albite, calcite, and sericite. Clinopyroxenes are always pseudomorphosed by chlorite and actinolitic amphibole. In the most differentiated samples (i.e., from andesite to rhyolite), primary amphibole and biotite, as well as quartz are found as both phenocrysts and groundmass crystals. Generally, brown hornblende is pseudomorphosed by chlorite and actinolitic amphibole, whereas biotite is usually replaced by a fine-grained assemblage of clay minerals and oxides. K-feldspar (sanidine) altered in sericite, occurs as phenocryst in dacites and rhyolites. Volcanic glass is deeply altered into a fine-grained aggregate mainly consisting of chlorite and clay minerals and minor chalcedony. Massive and pillow lava samples frequently exhibit amygdaloidal texture, with rounded- to ovoidal-shaped amygdules filled by quartz, calcite, chlorite or zeolite. The following petrographic description will be made according to the volcanic primary igneous phases and textures, regardless of the secondary mineralogical alterations.

4.4.1. Sub-volcanic rocks

Sub-volcanic rocks studied in this thesis were taken from both the dyke-swarm, particularly from its lowermost part and from isolated dykes in the volcano-sedimentary sequence (Fig. 4.3a). They are characterized by a great variety of rock types, including basalts, basaltic andesites, andesites, dacites, and rhyolites (Figs. 4.3b, c). They consist of fine- to medium-grained dykes, with textures ranging from aphyric to porphyritic (Fig. 4.8a) with porphyritic index (PI) ranging from ~10 to ~35 and, locally, glomeroporphyritic texture. The phenocryst assemblage varies depending on the rock-type. In fact, it consists of: a) plagioclase and clinopyroxene in basalts; b) plagioclase, clinopyroxene, opaque minerals, as well as minor biotite and amphibole in basaltic andesites and andesites; c) plagioclase, sanidine, amphibole, biotite, opaque mineral and quartz in dacitic-rhyolitic rocks (Fig. 4.8a). Groundmass displays intergranular to subophitic texture in most of the basaltic rocks and consists of microlites of plagioclase, clinopyroxene, and Fe-Ti oxides. In addition to these minerals, minor biotite occurs in the groundmass of andesites. In dacitic and rhyolitic dykes, the groundmass texture ranges from microcrystalline (with plagioclase, quartz, biotite and Fe-Ti oxides; Figs. 4.8a, b) to hypohyaline and hypocrySTALLINE. The crystallization order in basaltic dykes is: clinopyroxene + Fe-Ti oxide → plagioclase → biotite.

4.4.2. Massive lava flows

Massive lava flows are mainly from the volcano-sedimentary sequence and subordinately from the upper part of the dyke-swarm (Fig. 4.3a). They are represented mainly by dacites and rhyolites, and subordinate andesites and basaltic rocks showing a variety of textures and mineral assemblages. Dacites and rhyolites, show porphyritic (Fig. 4.8c) and glomeroporphyritic texture

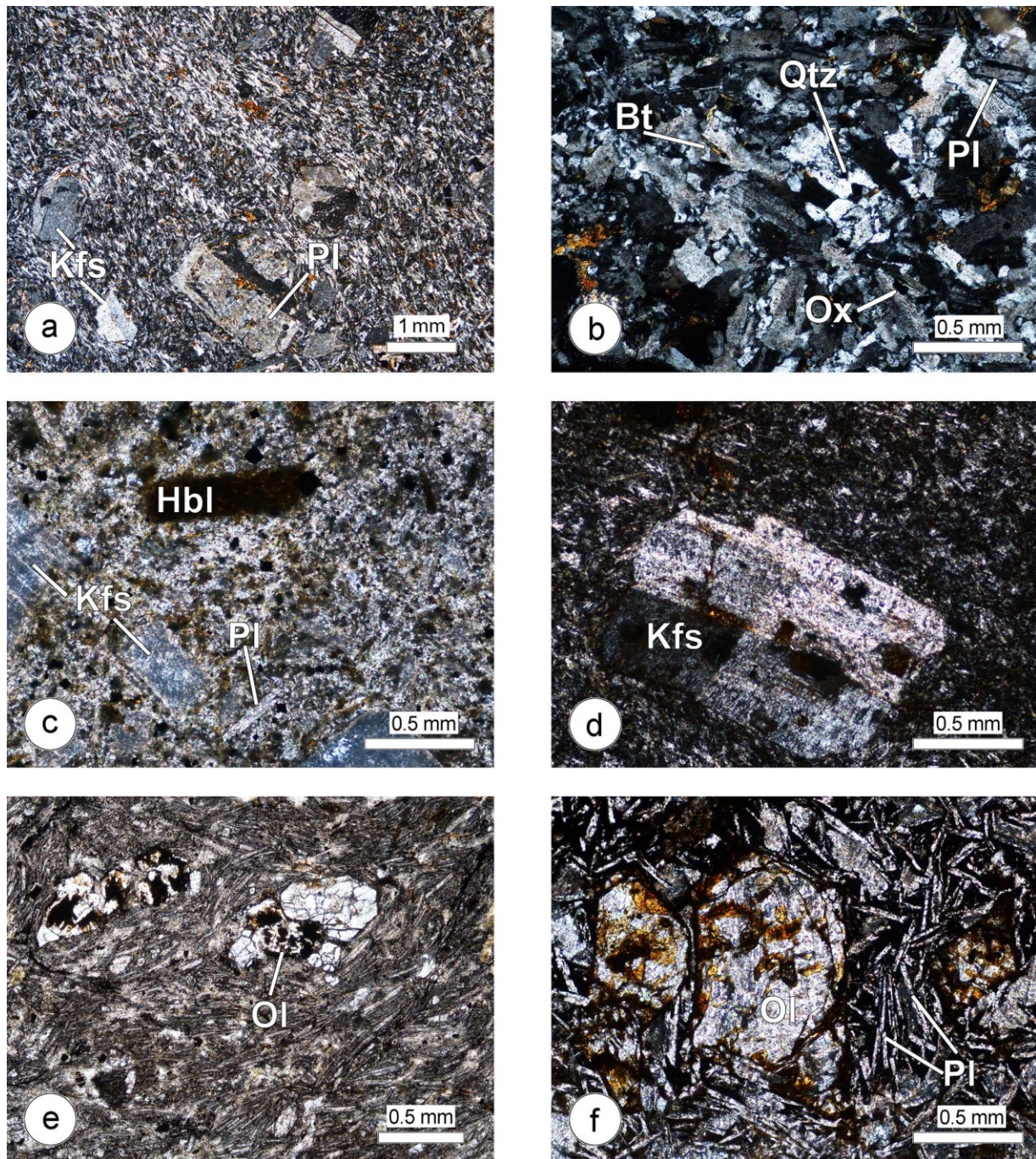


Figure 4.8. Photomicrographs of sub-volcanic (a-b) and volcanic (c-f) rocks from the Ganj Complex: a) Porphyritic texture in a dacitic dyke (sample MK19) consisting of K-feldspar (Kfs) and plagioclase (Pl) phenocrysts in a groundmass composed of plagioclase, quartz, K-feldspar and biotite; b) Quartz (Qtz), K-feldspar, biotite (Bt) and Fe-Ti oxides (Ox) in the microcrystalline groundmass of a rhyolitic dyke (sample MK115); c) Weakly porphyritic massive lava flow (sample MK21) with K-feldspar and altered hornblende (Hbl) phenocrysts set in a microcrystalline groundmass with plagioclase, Fe-Ti oxides and amphibole; d) K-feldspar phenocryst sets in a hypohyaline microcrystalline groundmass (sample MK126); e) Basaltic andesite pillow lava (sample MK361) showing olivine (Ol) phenocrysts set in a hyalopilitic to intergranular groundmass composed of laths of plagioclase, and small clinopyroxene and olivine rains. The groundmass show fluidal texture; f) Detail of the groundmass of pillow lava (samples MK434) showing plagioclase laths and volcanic glass enclosing small olivine phenocrysts.

(PI >10), though very few dacitic samples show aphyric texture. The phenocrysts are mainly represented by laths of plagioclase, K-feldspar, and prismatic-elongated altered amphibole (brown hornblende), as well as minor microcrystalline to hypohyaline and holohyaline (Figs. 4.8c, d). Very few samples show a hyalopilitic or vitrophyric textures. Plagioclase, quartz and opaque minerals can be recognized in the microcrystalline groundmasses. Textures in basalts and andesites vary from aphyric to porphyritic. Phenocrysts consist of plagioclase and clinopyroxene in all rock-types, whereas euhedral olivine phenocrysts occur only in basalts. In addition, subordinate phenocrysts of altered amphibole and biotite can be observed in basaltic andesites and andesites. The groundmass shows hypohyaline, intersertal texture with plagioclase laths and intergranular clinopyroxenes, glass, and very rare olivine. Fluidal texture is very common in the groundmass and is defined by the sub-parallel orientation of the plagioclase laths.

4.4.3. *Pillow lavas*

Pillow lavas were exclusively taken from the volcano-sedimentary sequence. They consist of basalts and basaltic andesites showing slightly porphyritic (PI = 5-10) to aphyric texture (Fig. 4.8e). Phenocrysts consist of euhedral olivine, clinopyroxene, and minor plagioclase set in a groundmass showing hyalopilitic to intersertal and intergranular texture, in which laths of plagioclase and minor clinopyroxene and olivine, are surrounded by altered volcanic glass (Figs. 4.8e, f). The groundmass commonly shows a fluidal texture defined by the orientation of small laths of plagioclase (Fig. 4.8e). All pillow lavas are characterized by amygdules filled by calcite and/or quartz, which become relatively more abundant in the lavas from the upper part of the volcano-sedimentary sequence.

4.5. Geochemistry of volcanic and sub-volcanic rocks

In this section, the geochemical features of the magmatic rocks of the Ganj Complex will be described. I anticipate, for the sake of clarity, that three main groups of rocks have been distinguished based on their overall geochemical features. It is worth to outline that rocks of these three geochemical groups can equally be found in the dyke-swarm and in the volcano-sedimentary sequence, and as dykes or lava flows (see [Appendix Table 4.3](#) for further details about the distribution of the different rocks). In addition, no relative chronological relationships exist between the different rock groups. For these reasons, the geochemical features of the distinct rock groups will be described in detail in the next sections regardless of their distribution or occurrence.

Many incompatible trace elements (e.g., Ti, P, Zr; Y, Sc, Nb, Ta, Hf, Th), as well as middle and heavy rare earth elements (MREE and HREE, respectively) and some transitional metals (e.g., Ni, Co, Cr, V) are considered to be virtually immobile during low-temperature alteration. By contrast, large ion lithophile elements, such as K, Sr, Rb, Ba, Pb, and many major elements are commonly mobilized during alteration processes (e.g., [Pearce & Norry 1979](#)). In addition, light rare earth elements (LREE) may also be affected to some degree of alteration-induced mobilization, particularly in the presence of carbonate-rich fluids (e.g., [Valsami & Cann, 1992](#)). The petrographic study has evidenced that most of the studied samples were affected by moderate to severe alteration. In order to estimate the general amount of remobilization of these elements, mobility tests were made for each geochemical rock group by plotting several mobile elements versus immobile elements (e.g., Zr, Y) and then calculating the correlation coefficient (r^2). These tests indicate that SiO_2 (r^2 vs. Y < 0.19), CaO (r^2 vs. Y < 0.065), Na_2O (r^2 vs. Y < 0.454), K_2O (r^2 vs. Y < 0.418), Rb (r^2 vs. Y < 0.19), U (r^2 vs. Y < 0.40) experienced high degree of alteration-induced mobilization in all rock-groups. Al_2O_3 and FeO display different results, being mobilized

in Group 1 rocks (r^2 vs. $Y < 0.23$), whereas they suffered moderately to little mobilization in Group 2 rocks (r^2 for Al_2O_3 vs. $Y = 0.75-0.89$; r^2 for FeO vs. $Y = 0.61 - 0.87$). As a consequence, these elements will not be used in the following discussion. Ba (r^2 vs. $Y = 0.65-0.88$), La (r^2 vs. $Y = 0.74 - 0.96$), and Ce (r^2 vs. $Y = 0.75 - 0.99$), as well as Sr (r^2 vs. $Y = 0.63-0.80$, with the exception of some samples) have experienced limited amount of mobilization in all rock groups. Therefore, though with some caution, these elements will be used in the following discussion.

4.5.1. Group 1 rocks

This group of rocks includes both dykes and massive lavas. They consist mainly of dacites and rhyolites, and minor basaltic andesites and andesites ([Appendix Table 4.3](#)). In general, Group 1 rocks display extremely variable Mg# (66.6-8.1) [$Mg\# = 100 \times MgO / (MgO+FeO)$], as well as SiO_2 (56.82-74.35 wt.%), MgO (0.16-6.04 wt.%), and CaO (0.52-7.41 wt.%) contents. They show a clear sub-alkaline nature, as exemplified by low Nb/Y ratio (0.07-0.28, [Appendix Table 4.3](#), [Fig. 4.9](#)). Group 1 rocks are characterized by variable but generally low TiO_2 (0.24-1.59 wt.%), P_2O_5 (0.02-0.45 wt.%), Zr (76-236 ppm), and Y (15-49 ppm) contents. These very variable Mg# values and element contents likely reflect different degree of fractionation of these rocks. Compatible elements contents (e.g., Cr = <53 ppm; Ni <18 ppm) are very low ([Appendix Table 4.3](#)).

[Figure 4.10](#) shows that TiO_2 and FeO_t contents decrease with increasing Y content, where the increase in Y content is observed to represent increasing magmatic differentiation in the studied data set (i.e., from basaltic andesites to rhyolites). Such elemental behaviour strongly suggests a calc-alkaline (CA) affinity for these rocks. This CA affinity is also indicated by the strong increase in Y/Sc ratios with increasing Y, which points out for a magmatic evolution characterized by fractionation of mainly clinopyroxene, and hornblende, and magnetite with respect to plagioclase

(Fig. 4.10). Accordingly, Group 1 rocks show relatively high Th contents (Fig. 4.10).

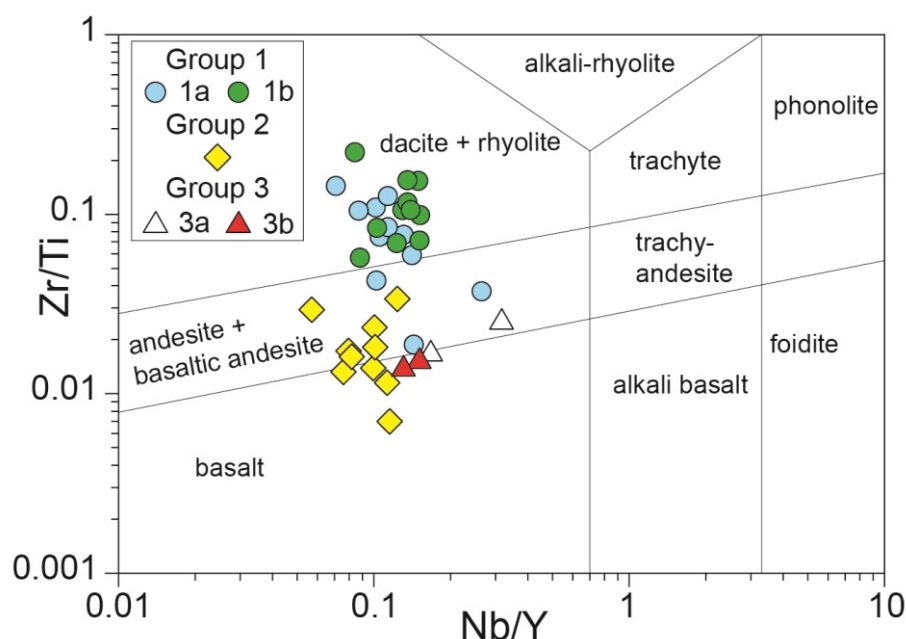


Figure 4.9. Nb/Y vs. Zr/Ti discrimination diagram of Winchester & Floyd (1977) modified by Pearce (1996) for sub-volcanic and volcanic rocks of the Ganj Complex.

In N-MORB normalized incompatible element patterns, Group 1 rocks display a great enrichment in Th, U, La, and Ce coupled with Ta, Nb, P, and Ti negative anomalies (Figs. 4.11a, b). The basaltic andesite MK440 also shows these anomalies except that of Ti, which is due to the crystallization of Fe-Ti-oxides in this rock. The enrichment in Th of Group 1 rocks is particularly significant (9 – 30 times N-MORB composition) and, together with the overall geochemistry of these rocks, is consistent with a calc-alkaline affinity (e.g., Pearce, 1983). This is clearly supported by the discrimination diagram in Figure 4.12, where Group 1 rocks plot indeed in the field for calc-alkaline rocks. The chondrite-normalized REE abundances of the Group 1 rocks are also consistent with the calc-alkaline nature of these rocks but show two different type of REE patterns that are characterized by different MREE and LREE enrichments with respect to HREE (Figs. 4.11c, d). In fact, based on the different MREE/HREE and LREE/HREE ratios (Appendix Table 4.3), Group 1 rocks can be subdivided into two distinct sub-groups. The first sub-group (1a) displays regularly

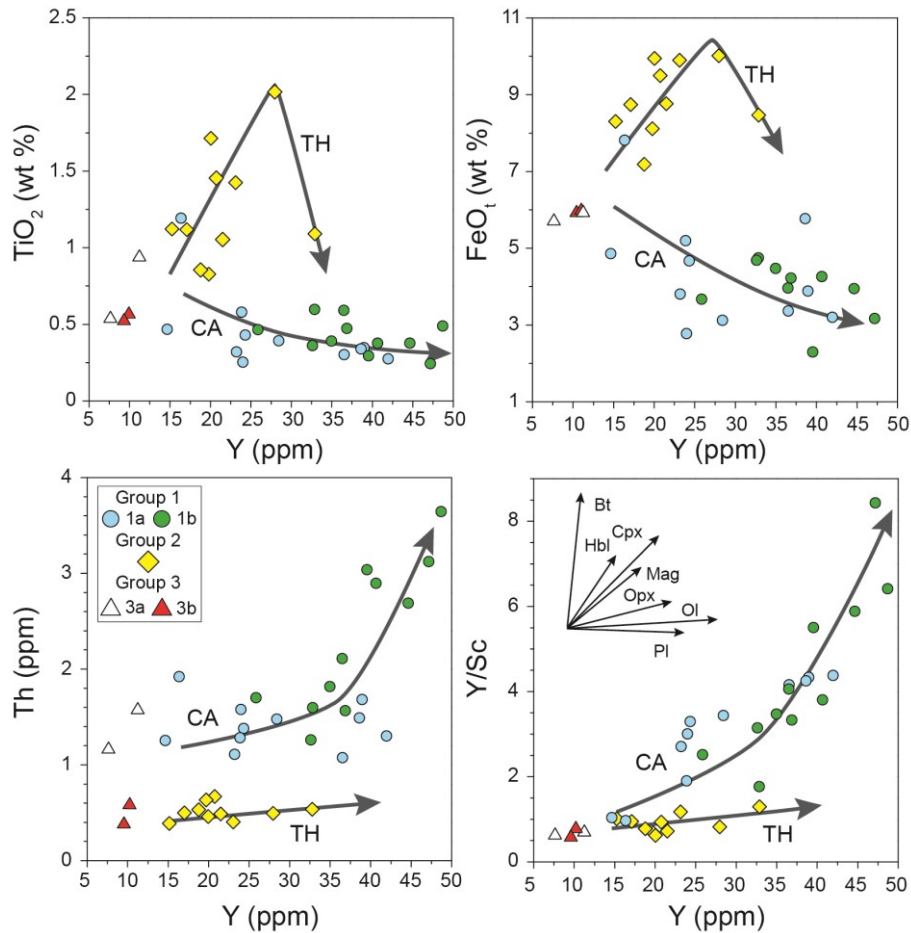


Figure 4.10. Variation of selected major and trace elements vs. Y (assumed here as fractionation index) for volcanic and sub-volcanic rocks of the Ganj Complex. Major element oxides are recalculated on anhydrous bases. Arrows generally indicate the fractionation trends for tholeiitic-type (TH) and calc-alkaline-type (CA) magmatic series. The CA-type magmatic series is characterized by the early crystallization of Fe-Ti oxides, which result in the gradual decrease of Ti and Fe with increasing Y. The TH-type series is characterized by the late crystallization of Fe-Ti oxides, which result in an increase of these elements with increasing Y, followed by a sharp decrease in the most evolved rocks. The fractional crystallization trends for mineral phases are shown in panel Y/Sc-Y. Abbreviations, Ol: olivine; Cpx: clinopyroxene; Pl: plagioclase; Opx: orthopyroxene; Hbl: hornblende; Bt: biotite; Mag: magnetite.

decreasing patterns from LREE to HREE (Fig. 4.11c) with relatively high $(La/Yb)_N$ (3.26 – 5.50) and $(Sm/Yb)_N$ (1.86 – 2.29) ratios (Fig. 4.13a). In contrast, the second sub-group of rocks (1b) show moderate enrichment of LREE respect to HREE, and rather flat pattern from MREE to HREE (Fig. 4.11d). Accordingly, the $(La/Yb)_N$ (1.67 – 2.31) and $(Sm/Yb)_N$ (1.10 – 1.64) ratios are lower than those observed in sub-Group 1a (Fig. 4.13a). The different enrichments in LREE and MREE with respect to HREE shown by sub-Group 1a and sub-Group 1b rocks (Fig. 4.13a) are independent from the different fractionation degrees of these rocks, as testified by different

(La/Yb)_N ratios at similar Zr/Ti ratios ([Appendix Table 4.3](#)).

4.5.2. Group 2 rocks

Group 2 rocks include both dykes, massive lavas and pillow lavas. They are represented by basalt, basaltic andesite and andesite ([Appendix Table 4.3](#)), showing a clear sub-alkaline nature as suggested by the low Nb/Y ratio (0.06-0.12; [Fig. 4.9](#)). Group 2 rocks are characterized by quite variable SiO₂ (42.13-58.28 wt.%), Al₂O₃ (11.16-16.12 wt.%), MgO (3.75-12.38 wt.%) contents, which reflect different degrees of fractionation. These rocks have higher TiO₂ (0.53-2.02 wt.%), Cr (12-336), and Co (19-40 ppm), and lower Y (9.5-32.89 ppm) with respect to Group 1 rocks, at comparable degrees of fractionation ([Appendix Table 4.3](#)). Group 2 rocks show a clear tholeiitic nature exemplified by a sharp increase in TiO₂ and FeO_t contents from basalt to basaltic andesite, followed by a significant decrease in the most differentiated andesite ([Fig. 4.10](#)). Group 2 rocks display N-MORB normalized incompatible element patterns with significant Ta and Nb negative anomalies coupled with Th and Ba relative enrichment ([Figs. 4.11e, f](#)). However, these rocks show lower abundance in both Th (see [Fig. 4.11](#)) and Nb and do not show any Ti and P negative anomalies compared with Group 1 rocks ([Figs. 4.11e, f](#)). The geochemical features of Group 2 rocks are similar to those of island arc tholeiites (IAT) (e.g. [Pearce, 1983](#); [Saccani et al., 2011](#)). In the discrimination diagram in [Figure 4.12](#) all samples plot in the field for IAT, and are clearly distinct from the calc-alkaline rocks of Group 1. This conclusion is also supported by the most common discrimination diagrams. The IAT affinity for these rocks is also evidenced by the variation of the Y/Sc ratios ([Fig. 4.10](#)), which points out for the predominance of plagioclase crystallization with respect to clinopyroxene and magnetite, as typically observed in the IAT

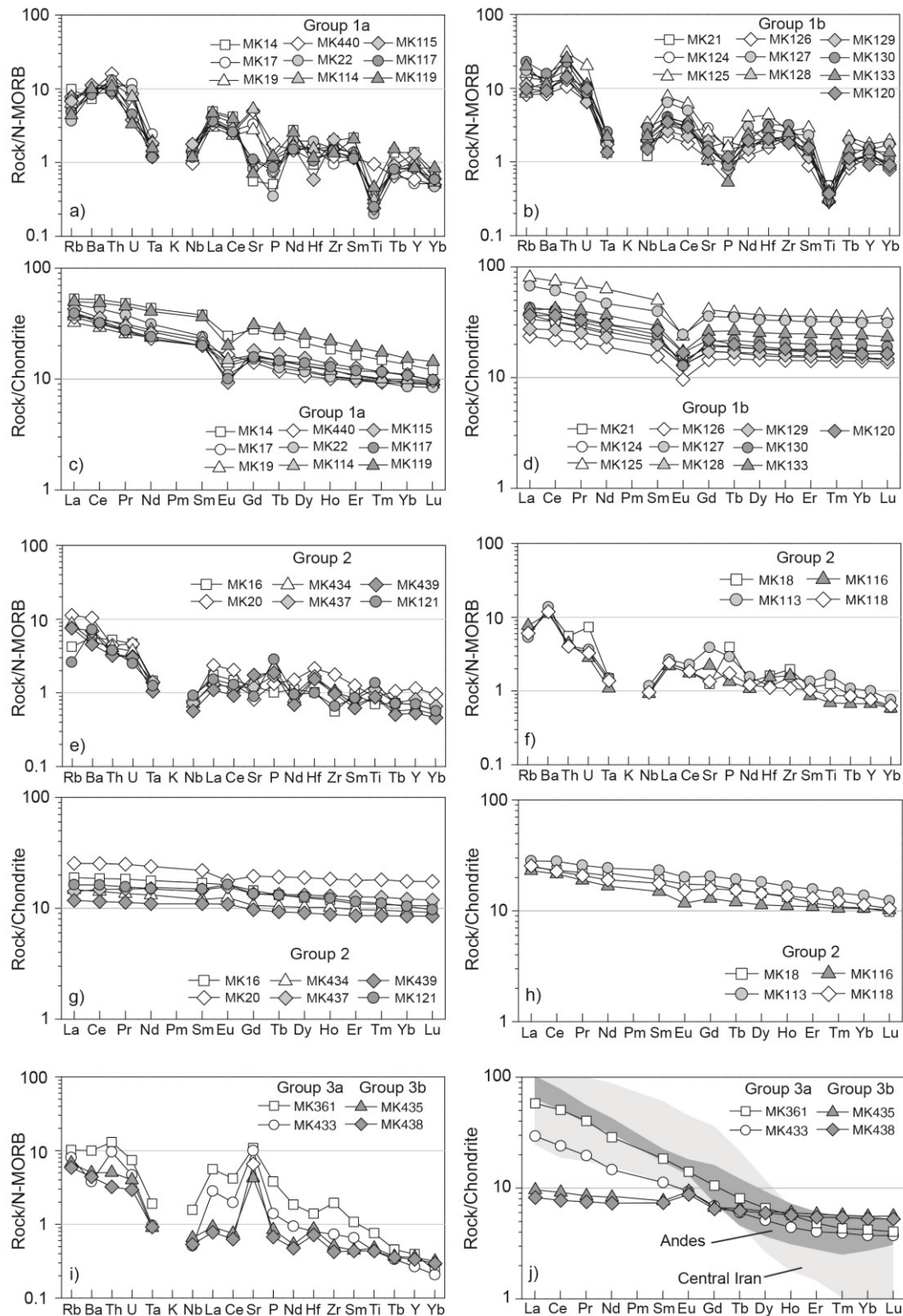


Figure 4.11. N-MORB (normal-type mid-ocean ridge basalt) normalized incompatible element patterns and Chondrite-normalized rare earth element (REE) patterns for volcanic and sub-volcanic rocks from the Ganj Complex. In panel j), the composition of mafic-intermediate Miocene adakites from the Central Iran (Rossetti et al., 2014) and adakite-like rocks from the Andes (Richards & Kerrich, 2007) are shown for comparison. Normalizing values are from Sun & McDonough (1989).

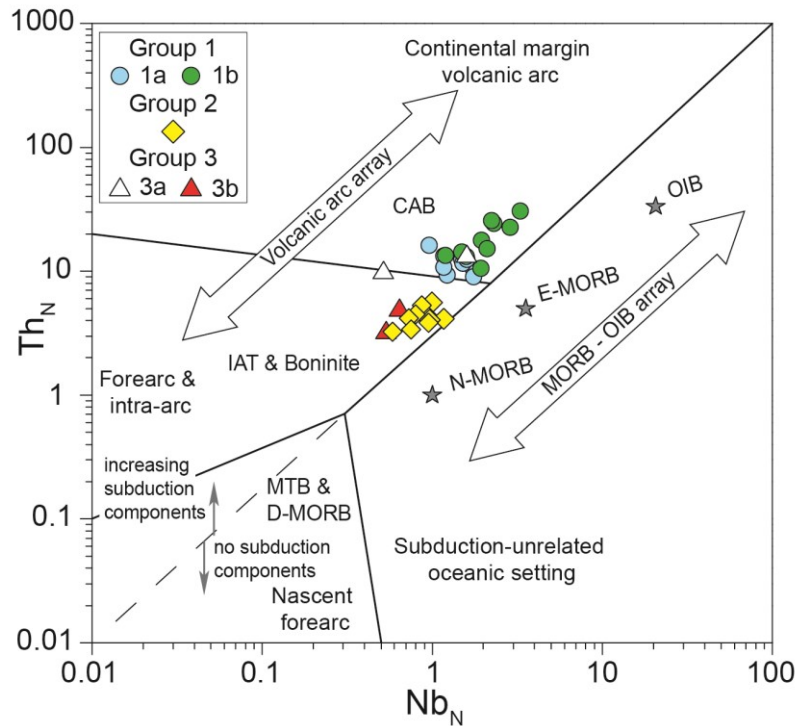


Figure 4.12. N-MORB normalized Th vs. Nb discrimination diagram of *Saccani (2015)* for volcanic and sub-volcanic rocks from the Ganj Complex. Abbreviations, MORB: mid-ocean ridge basalt, N-: normal type, E-: enriched type, D-: depleted type, IAT: island arc tholeiite, CAB: calc-alkaline basalt; OIB: alkaline oceanic within-plate basalt; MTB: medium titanium basalt. Normalizing values, as well as the composition of typical N-MORB, E-MORB, and OIB (grey stars) are from *Sun & McDonough (1989)*.

magmatic series (see *Beccaluva et al., 1983*). Group 2 rocks show chondrite-normalized REE patterns slightly decreasing from LREE to HREE. HREE varies from ~9 to ~20 times Chondrite abundance (*Fig. 4.11g, h*). Either slightly positive or negative, Eu anomalies is observed in most samples. All samples are characterized by nearly flat patterns from MREE to HREE with $(\text{Sm}/\text{Yb})_N$ ratios ranging from 1.21 to 1.80 (*Figs. 4.11g, h*). In contrast to Group 1 and Group 3 rocks, Group 2 volcanic rocks and dykes cannot be unequivocally subdivided into different subgroups on the basis of their REE contents and ratios (*Fig. 4.13a*). Most samples show low LREE/MREE and LREE/HREE ratios, as exemplified by the $(\text{La}/\text{Yb})_N$ ratios, which are in the range 1.17-1.74 (*Fig. 4.11g*). A few samples, however, show slightly higher LREE contents compared to HREE; with $(\text{La}/\text{Yb})_N$ ratios >2 (*Fig. 4.11h*).

4.5.3. Group 3 rocks

This group includes one basaltic pillow lava and three massive lava flows showing basaltic to basaltic andesitic composition ([Appendix Table 4.3](#)). SiO₂ and Al₂O₃ contents, as well as Mg# are in the range of 49.0-52.3, 16.0-16.9, and 70.5-64.7, respectively, suggesting relatively low degrees of fractionation for these rocks. Group 3 rocks show a sub-alkaline nature with low Nb/Y ratio (0.13 – 0.33; [Fig. 4.9](#)). These rocks have relatively low TiO₂ (0.53-0.94 wt.%) and very low Y (7.64-11.2 ppm) contents, as well as relatively low compatible elements abundances (e.g., Cr = 62-144 ppm; Co = 20 – 25 ppm; Ni = <31 ppm). A distinctive feature of Group 3 rocks is an exceptionally high abundance of Sr (380-982 ppm) compared with that of the other rock groups ([Appendix Table 4.3](#)). N-MORB normalized incompatible element patterns show a marked Th and Sr enrichment with respect to Nb and Ta, as well as very low contents of high field strength elements (HFSE) from Hf to Yb ([Fig. 4.11i](#)). In particular, Sr contents range from 4 to 11 times N-MORB composition, whereas Nb and Ta are in the range 0.5-1.6 and 1-1.9 times N-MORB contents, respectively. Another distinctive feature of these rocks is a very low HREE content with Yb_N values ranging from 3.8 to 5.7 times Chondrite abundance ([Sun & McDonough, 1989](#)) ([Fig. 4.11j](#)). Based on the REE contents Group 3 rocks can be subdivided into two different sub-groups. The first sub-Group (3a) shows La_N ranging from 30 to 60 times Chondrite abundance coupled with REE patterns strongly decreasing from La to Yb ([Fig. 4.11j](#)). The (La/Yb)_N and (Sm/Yb)_N ratios of these rocks are the highest in the studied data set, ranging from 8 to 14 and from 3 to 4 ([Fig. 4.13a](#)). In contrast, the second sub-Group (3b) shows low LREE contents with La_N ranging from 8 to 10 times Chondrite abundance, as well as REE patterns slightly decreasing from La to Yb. The (La/Yb)_N (~1.6) and (Sm/Yb)_N (~1.4) ratios of these rocks are consequently very different from those of Group 3a samples, as also shown in ([Fig. 4.13a](#)).

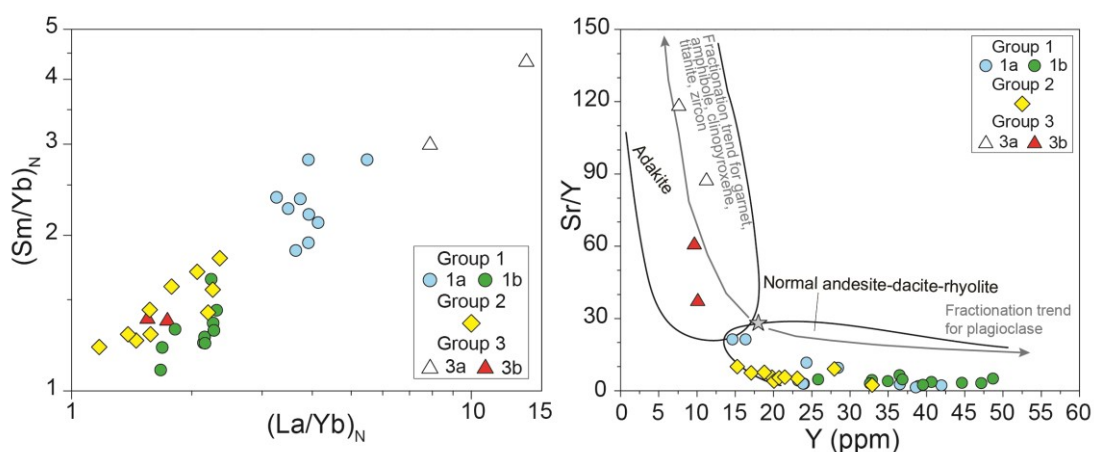


Figure 4.13. (a) Chondrite-normalized $(Sm/Yb)_N$ vs. $(La/Yb)_N$ diagrams for volcanic and sub-volcanic rocks from the Ganj Complex. Normalizing values are from Sun & McDonough (1989); (b) Sr/Y vs. Y diagram (Defant & Drummond, 1990) for volcanic and sub-volcanic rocks from the Ganj Complex. The compositional variation of adakite (from Richards & Kerrich (2007) and “normal” andesite-dacite-rhyolite (from Defant & Drummond (1993), are shown for comparison. Grey arrows schematically indicate the differentiation paths resulting from fractionation of various, different minerals (from Castillo et al., 1999). The star indicates the average composition of medium-K andesites (data from Gill, 1981).

In the discrimination diagram in Fig. 4.12, sub-Group 3a rocks plot in the field for calc-alkaline rocks, whereas sub-Group 3b basaltic andesites plot in the field for IATs. The overall geochemical features of Group 3 basalts and basaltic andesites show many differences compared to those of Group 1 (CA) and Group 2 (IAT) rocks, whereas they show some broad similarities with adakitic rocks. However, these rocks show rather unusual chemical characteristics and cannot be classified as adakites. Indeed, typical adakites (or “high silica adakites”) are characterized by $SiO_2 \geq 56$ wt.% (but commonly >60 wt.%), $Al_2O_3 \geq 15$ wt.%, $MgO < 3$ wt.%, low Y (≤ 18 ppm) and HREE ($Yb \leq 1.8$ ppm), high Sr (>400 ppm), and La/Yb values greater than 20 (e.g., Defant & Drummond, 1990; Castillo et al., 1999; Richards & Kerrich, 2007). In addition, Martin et al. (2005) described as “low-silica adakites” rocks with $50 \text{ wt.}\% < SiO_2 < 60 \text{ wt.}\%$, and Sr/Y and La/Yb values extremely high (100–300 and 40–80, respectively). Apart from their Al_2O_3 , Sr, Y, and Yb contents, as well as Sr/Y ratios, Group 3 rocks do not match the definition of both “high silica” and “low silica” adakites. Nonetheless, the Sr-Y-Yb systematics of these rocks strongly suggests an adakite-like chemical signature for Group 3 rocks (Fig. 4.14b).

4.6. Discussion

4.6.1. Petrogenesis and tectonic setting of formation of the primary melts of the Ganj Complex

Our petrogenetic discussion will be focused to the identification of the possible mantle sources of the different volcanic rock-groups cropping out in the Ganj Complex in order to constrain their tectono-magmatic setting of formation (e.g., [Pearce & Norry, 1979](#); [Pearce, 1983](#)).

[Figure 4.12](#) shows that the volcanic and subvolcanic rocks from the Ganj Complex plot in the fields for volcanic arc basalts. Volcanic arc rocks are commonly interpreted as originating from partial melting of sub-arc residual peridotites that experienced Nb and Ti depletion during previous partial melting events followed by Ba, Th, and LREE enrichment carried by subduction-derived fluids or melts (e.g., [Pearce, 1983](#); [Gribble et al., 1996](#); [Parkinson & Pearce, 1998](#)). Compatible element abundance is not significantly modified during the progressive mantle source depletion (i.e., progressive degree of partial melting), whereas the abundance of incompatible elements is closely related to source depletion and degree of melting ([Pearce, 1983](#)). We therefore use the Cr (compatible element) vs. Y (incompatible element) diagram shown in [Figure 4.14](#) ([Pearce, 1983](#), [Murton, 1989](#)) for inferring the composition of mantle sources and the degrees of partial melting generating the different magmatic rock-types. In this figure, three possible, typical sub-arc mantle sources are assumed according to [Saccani et al. \(2017\)](#): 1) a depleted mantle lherzolite, which represents residual mantle after ~12% MORB-type melt extraction (lherzolite EP22 from the Pindos ophiolite in Greece); 2) a comparatively more depleted mantle lherzolite, which represents residual mantle after ~20% MORB-type melt extraction (lherzolite A19 from the Othrys ophiolite in Greece); 3) a rather depleted mantle lherzolite, which represents residual mantle after ~12% MORB-type melt extraction followed by ~12% IAT-type melt extraction (lherzolite EP7 from the

Pindos ophiolite in Greece). All these lherzolites were chosen because they well represent compositions of depleted sub-arc mantle rocks, which did not undergo detectable enrichment in subduction components (Saccani et al., 2017). However, the model in Figure 4.14 does not give information about the nature of the possible contribution of subduction-derived components to the mantle sources and therefore, for qualitatively evaluating the different chemical contributions from subduction-derived components, ratios of Ba/Th against Th/Nb are used (Fig. 4.15). Finally, REE modeling has been applied in order to: a) better constrain the mantle peridotite compositions; b) estimate the nature and extent of enrichments in LREE due to subduction-related fluids and/or melts; c) estimate the partial melting degrees that best fit the compositions of the primary melts for each magmatic groups (Fig. 4.16). In primitive to moderately fractionated rocks, ratios of incompatible elements (e.g., Nb/Yb, Th/Ta, Th/Nb, Ba/Th and REE ratios) are assumed to represent those of the associated mantle source (e.g., Allègre & Minster, 1978; Beker et al., 1997). However, Group 1 and Group 2 samples are represented by fairly fractionated products, as shown in Figure 4.14. A detailed study of the magmatic evolution of these rocks (i.e., the petrogenetic processes that occurred in the magma chamber) is beyond the scope of this thesis. Nonetheless, in order to model the different mantle sources generating the primary melt of these distinct rock-groups, it has inferred the composition of the possible primary melts (with hypothetical MgO = 8 wt.%) assuming various degrees of fractional crystallization for the relatively fractionated rocks based on the Cr-Y model shown in Figure 4.14. The degree of fractional crystallization estimated for each sub-group of rocks is shown in Figure 4.16. It should be noted that in supra-subduction zone settings, the fluid/melt flux from a subducted slab is dependent on a number of factors, such as (among others): localized or pervasive fluxing, addition of fluid-mobile trace elements at every melting increment, the mineralogical compositions of the subducting rocks, temperatures, pressures, and distance from a subduction zone (e.g., Pearce & Parkinson, 1993; Gribble et al.,

1996; Barth et al, 2003; Elliott, 2003, Mibe et al., 2011). Given these uncertainties, a rigorous quantification of the melting processes (i.e., composition of mantle sources and degrees of partial melting) generating the different rock-types is not possible. Nonetheless, the semi-quantitative modeling of REE shown in Figure 4.16 can place some solid constraints on the petrogenesis of basaltic rocks in subduction-related settings. The input parameters for REE modeling are given in Appendix Table 4.4.

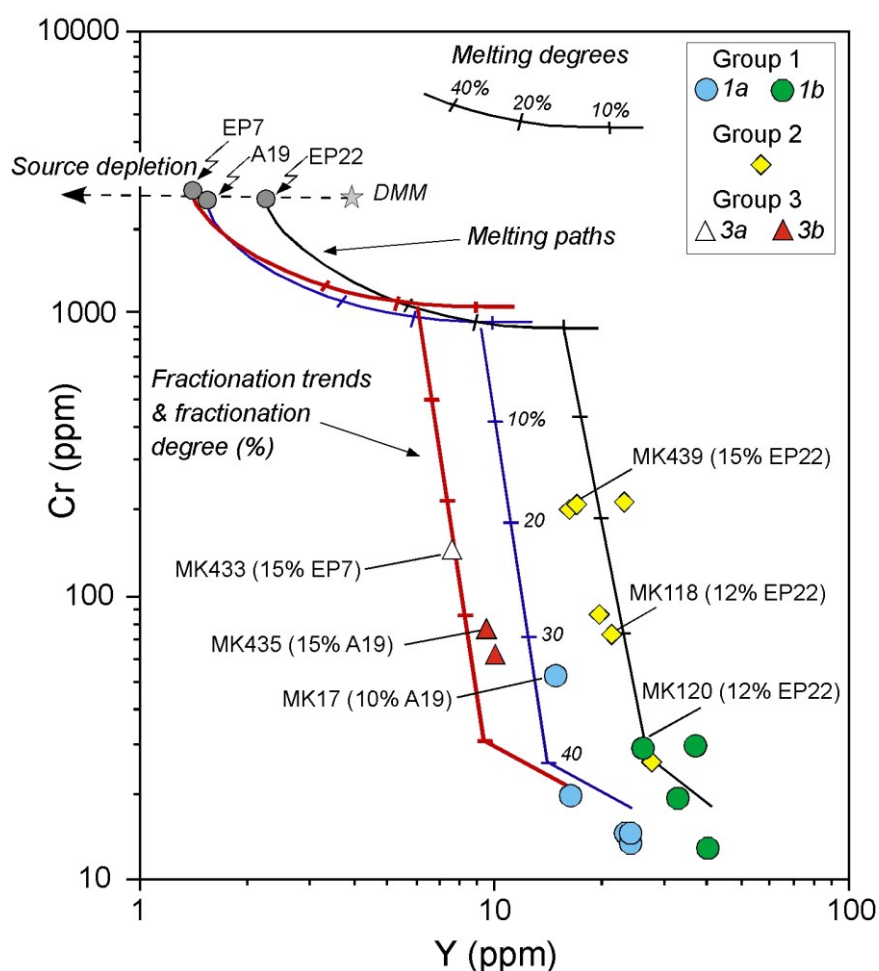


Figure 4.14. Cr vs. Y diagram of Pearce (1983) and melting models for volcanic and sub-volcanic rocks from the Ganj Complex. Abbreviations, DMM: depleted MORB mantle (Workman & Hart, 2005). Melting paths (with partial melting degrees) for incremental batch melting are calculated according to Murton (1989). The composition of depleted mantle lherzolites assumed as possible mantle sources (EP7, A19, and EP22) are from Saccani et al. (2017). Depleted lherzolites EP22 and A19 represent residual mantle after 12% and 20% MORB melt extraction from the DMM source, respectively, whereas the depleted lherzolite EP7 represents residual mantle after 12% island arc tholeiitic melt extraction from a depleted mantle residual, in turn, after 12% MORB melt extraction from the DMM. The fractional crystallization trends are also shown (tick marks indicate 10% fractional crystallization steps). Samples used in the REE models in Figure 4.16 are identified in this Figure. For each of these sample is shown the mantle source composition and the percent of partial melting.

Two main distinct components from the slab can commonly contribute to the chemistry of IAT and CA volcanic arc lavas and dykes, such as those cropping out in the Ganj Complex. One component is argued to be a melt of the sedimentary cover of the down-going slab, while the second is a fluid flux derived from the dehydration of the down-going oceanic crust (e.g., Hochstaedter et al., 2001; Elliott, 2003; Ikeda et al., 2016). For these reasons, in the models in Figure 4.16, the possible contributions from a melt derived from oceanic pelagic sediments (Taylor & McLennan, 1985), and from seawater (Li, 2000) are taken into account for Group 1 and Group 2 rocks.

Group 3 rocks show a clear adakite-like signature (i.e., very high Sr contents coupled with very low HREE and Y contents; Figs. 4.11i, j and 4.13b), which probably point out for the involvement of garnet in their petrogenesis (see Richards & Kerrich, 2007). These features are indeed similar to those of typical adakites generated as partial melts of subducted, garnetiferous (i.e., eclogitized) oceanic crust (i.e., slab melting; Defant & Drummond, 1990). However, Group 3 rocks, when compared to typical adakites, show higher MgO, Cr, and Ni contents and Mg# values coupled with lower SiO₂ contents, which did not simply fit a slab-melting model (Richards & Kerrich, 2007). Rather, these characteristics are consistent with mantle-derived melts. We therefore hypothesize that the unusual chemistry of Group 3 rocks is consistent with an origin from partial melting of depleted sub-arc mantle metasomatized by slab-derived adakitic melts, as suggested for analogous rocks (e.g., Martin et al., 2005; Castillo, 2006; Richards & Kerrich, 2007; König et al., 2007). For consistency, the depleted peridotites used in the models in Figure 4.16 are the same used in the model in Figure 4.14. REE modeling has been performed for a number of different combinations of mantle compositions, type and amount of subduction-derived components, and partial melting degrees. For simplicity, only the REE modeling results that best fit the primary magma compositions of the Ganj Complex rocks will be presented in the next sections.

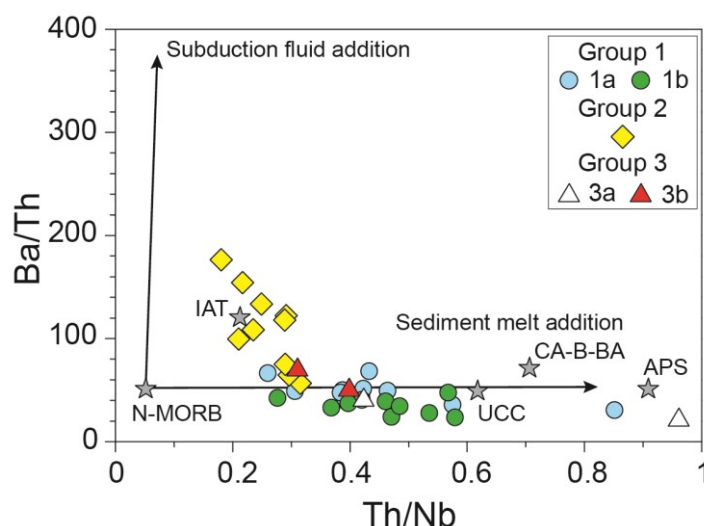


Figure 4.15. Ba/Th vs. Th/Nb diagram for volcanic and sub-volcanic rocks from the Ganj Complex. The composition of average pelitic sediments (APS); upper continental crust (UCC); average calc-alkaline basalts and basaltic andesites (CA-B-BA); average island arc tholeiitic basalts (IAT); normal-type mid-ocean ridge basalt (N-MORB) are also shown. Data source: N-MORB are from [Sun & McDonough \(1989\)](#); APS and UCC are from [Taylor & McLennan \(1985\)](#); IAT, and CA-B-BA are calculated from 249, and 244 samples, respectively of basaltic rocks from various ophiolitic complexes (see [Saccani, 2015](#) for references).

4.6.1.1. Petrogenesis of Group 1 rocks

Although Group 1 volcanic rocks and dykes represent fractionated melts, the Cr-Y model shows that these rocks are compatible with partial melting of different mantle sources ([Fig. 4.14](#)). In detail, sub-Group 1a rocks are compatible with ~10-12% partial melting of the depleted lherzolite A19 (residual after ~20% MORB-type melt extraction). In contrast, Group 1b rocks are compatible with ~10% partial melting of the lherzolite EP22 (residual after ~12% MORB-type melt extraction). The Th/Nb enrichment relative to Ba/Th suggests that both the mantle sources of Group 1 rocks were predominantly influenced by a subduction component significantly enriched in Th, which is compatible with sediment melt addition ([Fig. 4.15](#)). For the REE models, the possible theoretical mantle source compositions have been calculated by modeling various proportions of sediment melt addition to the depleted lherzolites shown in [Fig. 4.14](#). Our model shows that the REE composition of the calculated primary melt for Group 1a rocks can best be explained by 10%

partial melting of the lherzolite A19 with the addition of 0.5% of a sediment melt component (Fig. 4.16a). In contrast, the REE composition of the inferred primary melt for sub-Group 1b rocks can best be explained by 12% partial melting of the lherzolite EP22 with 0.7% sediment melt component (Fig. 4.16b). The low MREE/HREE fractionation of both the inferred primary melts for Group 1 rocks ($Sm_N/Yb_N < 1.9$) suggests that partial melting occurred in the spinel-facies mantle. In fact, the Sm/Yb ratios calculated for partial melting in the garnet-facies mantle starting from the same mantle compositions would be comparatively much higher ($Sm_N/Yb_N > 4.0$).

4.6.1.2. Petrogenesis of Group 2 rocks

Although Group 2 volcanic rocks and dykes represent slightly to moderately fractionated melts, the Cr-Y model shows that they are compatible with 12 – 15% partial melting of the lherzolite EP22 (Fig. 4.14). The Th/Nb and Ba/Th covariation (Fig. 4.15) suggests that both sediment melt addition and subduction-derived fluids have contributed, though with variable mutual proportions, to the subduction components that have enriched the assumed mantle lherzolite source.

The different enrichment in LREE with respect to HREE observed in Group 2 rocks (Figs. 4.11g, h) also suggests that sediment melt component and subduction-derived fluids were added in different proportions to the mantle source. For the REE models, the possible theoretical mantle source compositions have been calculated by modeling various proportions of sediment melt and subduction fluids addition to the depleted lherzolite EP22. Our model shows that the REE composition of the calculated primary melt for Group 2 rocks with low LREE/HREE ratios can best be explained by 17% partial melting of the lherzolite EP22 with the addition of 0.2% of a sediment melt component and 0.3% of aqueous fluid component (Fig. 4.16c). The comparatively

higher LREE/HREE ratios of some Group 2 samples (Fig. 4.11h) suggest however a comparatively higher transfer of LREE-enriched subduction zone components to the sub-arc mantle wedge (e.g., Barth et al., 2003). In fact, the REE composition of the inferred primary melt for Group 2 rocks showing relatively high LREE/HREE ratios can best be explained by 12% partial melting of the lherzolite EP22 with the addition of 0.5% sediment melt component and 0.5% aqueous fluid component (Fig. 4.16d). Similar to what observed in Group 1 rocks, the low MREE/HREE fractionation of the inferred primary melts for Group 2 rocks ($Sm_N/Yb_N < 1.5$) suggests that partial melting occurred in the spinel-facies mantle.

4.6.1.3. Petrogenesis of Group 3 rocks

The Cr-Y model shows that Group 3 volcanic rocks are likely compatible with partial melting of different mantle sources (Fig. 4.14). Sub-Group 3a rocks are compatible with either ~20% partial melting of the depleted lherzolite A19 or, alternatively, ~15% partial melting of the very depleted lherzolite EP7 (residual after ~12% MORB-type + ~12% IAT-type melt extraction). Likewise, sub-Group 3b rocks are compatible with either ~15% partial melting of the depleted lherzolite A19, or ~12% partial melting of the lherzolite EP7.

As described above, the chemistry of Group 3 is consistent with an origin from partial melting of depleted sub-arc mantle metasomatized by slab-derived adakitic melts. For the REE models, the possible theoretical mantle source compositions have been calculated by modeling various proportions of adakitic melt addition to the depleted lherzolites used in the model in Fig. 4.14. The adakitic melt has been calculated assuming low degree of partial melting of an N-MORB type eclogite. Our model shows that the REE composition of the relatively less fractionated sub-Group 3a basalt can best be explained by 15% partial melting of the very depleted lherzolite EP7 with the

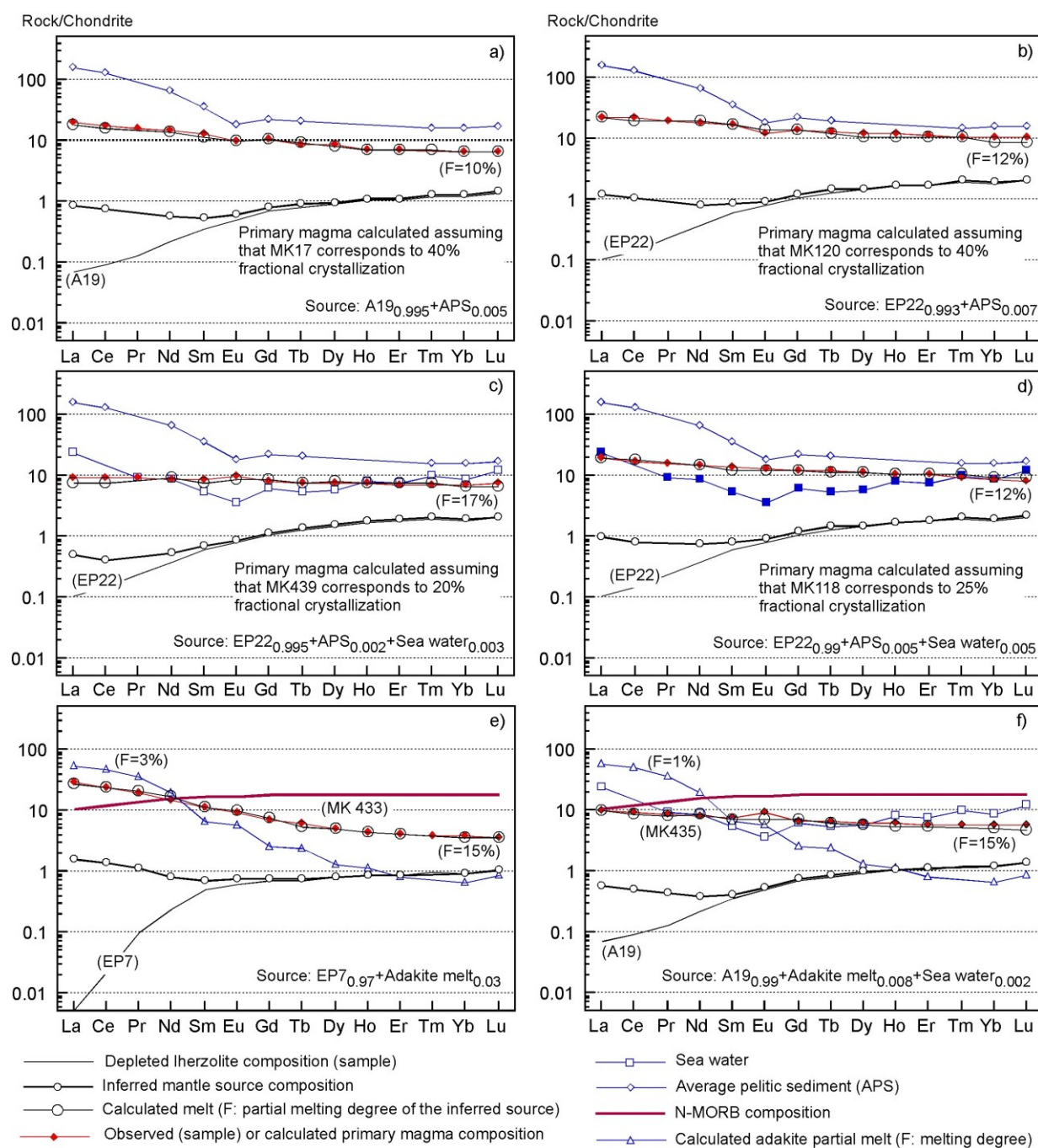


Figure 4.16. Calculated chondrite-normalized (Sun & McDonough, 1989) rare earth element (REE) patterns for parental melts derived from different mantle sources, assuming various degrees of non-modal fractional melting. Input parameters for the REE models (source modes, melting proportions, partition coefficients, etc.), as well as the compositions of the different inferred mantle sources and the compositions of the different slab-derived chemical components are shown in Appendix Table 4.4.

addition of 3% of an adakitic melt component (Fig. 4.16e). In contrast, the REE composition of the relatively less fractionated sub-Group 3b basalts can best be explained by 15% partial melting of

the depleted lherzolite A19 with 0.8% adakitic melt component plus 0.2% aqueous fluid component (Fig. 4.16f).

4.6.2. Tectonic setting of formation of the Ganj Complex volcanic and subvolcanic rocks

A first order conclusion shown by the Cr-Y and REE models (Figs. 4.14 and 4.16, respectively) is that all rock-types forming the Ganj Complex are compatible with a genesis in a volcanic arc tectonic setting. Nonetheless, the different nature of the subduction components (i.e., water, sediment melts, and adakitic melts) that are inferred to have been added to the sub-arc mantle wedge suggests that they were most likely added through different processes and at different depths beneath the arc-forearc system.

The possible tectono-magmatic setting of formation of the Ganj Complex volcanic arc rocks and dykes and the processes of mantle metasomatism due to subduction-derived fluids and melts are summarized in the simplified scheme in Fig. 4.17a. Water, which is initially represented by seawater released during the compaction in sediments and altered oceanic crust, and then by dehydration of clay minerals is argued to be the subduction-derived component that is added at relatively shallower depths. In contrast, the contribution from sediment melts is commonly observed at relatively greater depths beneath the arc (e.g., Hochstaedter et al., 2001; Elliott, 2003; Kelley et al., 2005; Saffer & Tobin, 2011; Ikeda et al., 2016). A wealth of experimental data have shown that the adakitic melts with severe depletion in HREE-and Y can be formed by partial melting of mafic rocks, within the field of garnet stability that is, at depths greater than 1.0–1.2 GPa, at least (see an exhaustive review in Moyen & Stevens, 2006). In fact, melts generated from melting of metabasalt at depths below the blueschist-eclogite transition, where garnet is stable, have intermediate to felsic (dacitic) compositions and characteristic “adakitic” HREE- and Y-

depleted geochemistry (see [Richards & Kerrich, 2007](#) and references therein). However, the adakitic pristine melts have been documented to form in a range of situations and processes (see Fig. 12 in [Moyen, 2009](#) and references therein, for an exhaustive review). The main points are: a) subduction environments with abnormally hot thermal regimes. Most of them are indeed associated

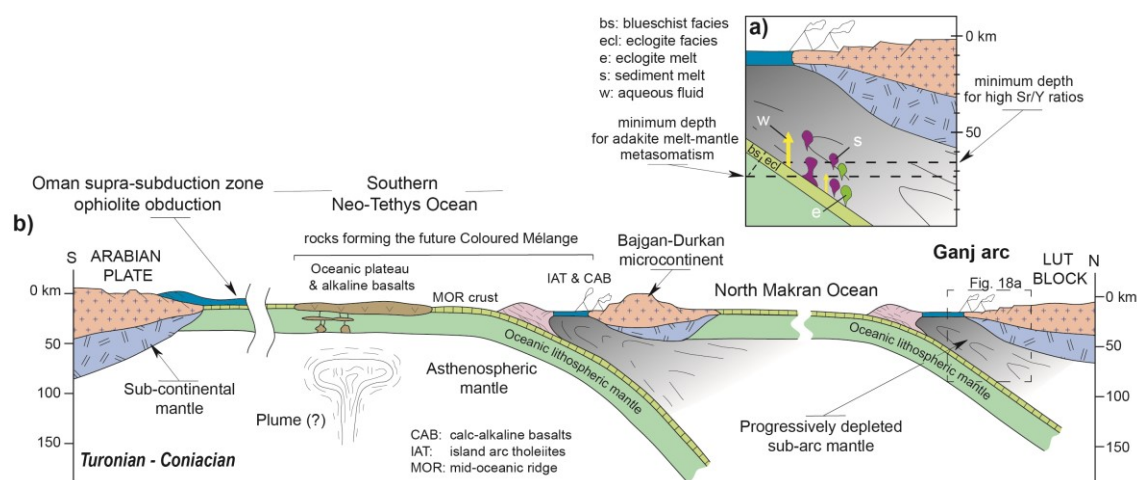


Figure 4.17. a) Tectono-magmatic model for the formation of the volcanic and subvolcanic rocks in the Ganj volcanic arc setting; b) Tectonic reconstruction along N-S profile of the Makran-Oman system in the Turonian-Coniacian time. See discussion into the text. The reconstruction of the profile in the sector from the Bajgan-Durkan microcontinents to the Lut block is based on the data presented in this thesis. The reconstruction of the profile in the sector from the Bajgan-Durkan microcontinents to the Arabian plate is modified from [Saccani et al. \(2018\)](#), and references therein) and [Burg \(2018\)](#), and references therein) The question mark on the plume indicate that there is no general consensus about the existence of a mantle plume in this area during the Cretaceous

to “hot” subductions, where a young (generally less than 20 Ma), hot lithosphere (possibly a ridge) is subducted. Adakites were indeed documented in a typical subduction zones such as “fast” subductions characterized by abnormally hot thermal regimes. Likewise, slab breakoff and/or formation of “slab windows” can permit melting of the slab at the edge of the “window”; b) Medium Sr/Y adakites are high pressure melts (i.e., more than 0.1 GPa), of different sources including underplated mafic rocks in the lower crust (of a continental arc) or lower collisional crust. c) High-pressure crystal fractionation (i.e., garnet fractionation) of basaltic magma (see [Castillo, 2006](#)). In addition, the so-called “adakitic signature” observed in melts generated at volcanic arcs can also form by different processes (see [Castillo, 2006](#); [Richards & Kerrich, 2007](#);

Moyen, 2009 for a review). They include: a) partial melting of the sub-arc depleted mantle metasomatized by pristine adakite melts formed, in turn, after slab melting. b) mixing of mantle-derived mafic melts with pristine slab-derived adakite melts. c) mixing between mantle-derived basaltic melts and adakitic melts generated by partial melting of the garnetiferous lower crust, where partial melting is facilitated by the high temperatures of the ascending mafic melts. An identification of the processes that led to the formation of the Group 3 rocks of the Ganj Complex cannot straightforwardly be made with the available data. However, I can exclude the formation of Group 3 rocks by mixing of CA or IAT melts with adakitic melts originated from partial melting of either garnet amphibolite or eclogite from the lower crust or eclogite from the subducting slab. In fact, REE models considering variable extents of mixing between either CA or IAT mafic rocks and partial melts from either garnet (lower crust) compositions do not reproduce the REE compositions of the observed Group 3 rocks (not shown). In particular, these mixing processes cannot reproduce the HREE patterns observed in Group 3 rocks.

Experiments on partial melting of adakite-metasomatized mantle (Rapp et al., 2000) have shown that garnet is stable above 2.5 GPa in metasomatized peridotites; this therefore places a minimum depth on the site of the interactions between adakitic melts and mantle peridotites, which has to be at ≥ 70 km (Fig. 4.17a), and therefore the slab melting forming the adakitic melt that will subsequently interact with the mantle must occur around or below this depth (Moyen, 2009). This is in agreement with the minimum depth for generating high Sr/Y ratios, which can roughly be placed at ≥ 65 km (see Moyen, 2009 and references therein) (Fig. 4.17a). From the above discussion it follows that the favoured hypothesis for explaining the adakitic signature shown by Group 3 rocks implies partial melting of the subducted mafic crust in the eclogite facies (Fig. 4.17a). Partial melting of the eclogite at the zone of “normal” arc magma generation resulted in adakite melt(s) that formed a distinct subduction slab-contribution to the sub-arc mantle wedge.

REE modeling (Figs. 4.16a-d) shows partial melting of depleted sub-arc mantle metasomatized by various proportions of aqueous fluids and sediment melts (Fig. 4.17a) can reproduce the REE compositions of the main Group 1 (CA) and Group 2 (IAT) primary melts. The stratigraphic alternation of volcanic rocks with CA and IAT affinities implies that the distinct volcanic eruptions tapped melts generated in portions of the sub-arc mantle that were metasomatized by different slab-derived components, possibly in different times. The occurrence of volcanic rocks with adakitic signature suggests a progressive deepening of the subducting slab, up to the eclogite facies of hot (i.e., young) oceanic lithosphere (Fig. 4.17a).

4.6.3. Geodynamic significance of the Ganj Complex

The tectono-magmatic model discussed in Section 4.6.2 shows that the volcanic rocks and dykes forming the Ganj Complex represent remnants of a volcanic arc (the Ganj volcanic arc) dominated by calc-alkaline and island arc tholeiitic magmatisms associated, in the upper part of the sequence, with eruptions of volcanic arc lavas showing adakitic signature. Accordingly, the volcano-sedimentary sequence and turbidite sequence show the typical stratigraphic features observed in many volcanic arc settings (Dickinson, 1995; Draut & Clift, 2013). This conclusion is in contrast to the previous interpretation of the Ganj Complex as an ophiolite unit (McCall & Kidd, 1982; McCall, 1997, 2002). The arenites forming the sedimentary cover range in composition from volcanic-rich litharenites to quartz-poor arkoses. According to Dickinson et al. (1983), the source area was located in a “transitional to undissected arc” tectonic setting (Fig. 4.6b). These sedimentary rocks were derived from distinct but coeval and intrabasinal source rocks (*sensu* Zuffa, 1980). The first source was represented by either rocks forming the volcanic edifice, or by volcanic fragments directly erupted from the volcano(s) (e.g., reworked pyroclastic material). The

second source rock was probably represented by platform carbonates located in the basin margin. Our new biostratigraphic data show that the Ganj Complex is Turonian-Coniacian in age (94-90 Ma), which is in agreement with the Albian-Senonian age obtained from K-Ar radiometric dating on sub-volcanic felsic rocks (McCall, 1985).

According to the tectonic reconstructions proposed in literature for the North Makran in the Mesozoic, a volcanic arc was active onto the southern margin of the Central Iranian blocks during Cretaceous times and was associated with the north-dipping subduction of the Southern Neo-Tethys Ocean. Remnants of this volcanic arc are represented within the Coloured Mélange Complex. The southern margin of the Central Iranian blocks is represented in the Makran area by the Bajgan-Durkan terranes (see Fig.17 in Saccani et al., 2018, as well as Glennie et al., 1990; Ricou, 1994; Burg, 2018). As a consequence of this subduction, the North Makran Ocean opened in the Early Cretaceous as a backarc basin, thus leading to the separation of the Bajgan-Durkan continental block from the Central Iranian blocks; namely, from the Lut Block (McCall & Kidd, 1982; Saccani et al., 2018; Monsef et al., 2019). The continental rift between the Bajgan-Durkan and the Lut block most likely occurred in the Late Jurassic (Hunziker et al., 2015). The present-day tectonic position of the Ganj Complex and the general sense of shear of the tectonic units of the North Makran indicate that the formation of the Ganj volcanic arc was not associated with the subduction of the Southern Neo-Tethys Ocean below the Bajgan-Durkan continental block. In fact, in the northwestern part of the North Makran domain the pile of tectonic units includes, from south to north and from bottom to top (Fig. 4.1c): 1) the Coloured Mélange Complex; 2) the Bajgan-Durkan Complex; 3) the North Makran ophiolites (i.e., the remnants of the North Makran Ocean); 4) the Ganj Complex. A simple retro-deformation based on the top-to-the-south sense of shear of the deformations (Burg et al., 2013) in the different units allow us to suggest that the original location of the Ganj volcanic arc was to the north of the North Makran Ocean that, in turn, was

bounded to the south by the Bajgan-Durkan continental block.

A possible geodynamic model that can explain the formation of the Ganj volcanic arc at the northern rim of the North Makran Ocean is shown in [Figure 4.17b](#). This model is based on the existence of two different subducting oceanic basins associated with two distinct volcanic arcs, along S-N Arabia – Makran-Lut block transect during the Late Cretaceous. Our new model implies that, differently from the volcanic arc located onto the Bajgan-Durkan microcontinent, the Ganj volcanic arc was developing at the northernmost side of the North Makran Ocean, possibly close, or onto, the southern Lut continental margin ([Fig. 4.17b](#)). In contrast to the geodynamic models that have so far been proposed (e.g., [Saccani et al., 2018](#); [Burg, 2018](#); [Monsef et al., 2019](#)), the proposed model implies that the Ganj volcanic arc formed in consequence of the subduction of the North Makran oceanic basin below the Lut continental margin ([Fig. 4.17b](#)). According to [Omrani et al. \(2017\)](#), the HP-LT metamorphic rocks of the Deyader Metamorphic Complex, which discontinuously crops out at the northern rim of the North Makran domain, can be interpreted as related to the subduction of the Makran Ocean below the Lut Block. Unfortunately, the sedimentary cover of the Jaz Murian depression and the Cenozoic-Quaternary tectonics do not allow the substrate onto which the Ganj volcanic arc was built to be recognized ([Fig. 4.1](#)). Hence, it is not possible to establish whether this volcanic arc was placed onto a thinned continental crust or, alternatively, at ocean-continent transition zone ([Fig. 4.17b](#)).

The appearance of volcanic arc rocks with “adakitic-melt signature” in the upper part of the volcano-sedimentary sequence implies local partial melting of eclogites in the subducting slab during the late stages of arc magmatism ([Fig. 4.17a](#)). The available data do not allow us to constrain in detail the processes responsible for adakite melt formation. The formation of adakitic melts is associated with abnormally hot thermal regimes in the subducting slab ([Castillo, 2006](#); [Richards & Kerrich, 2007](#); [Moyen, 2009](#)). These hot thermal regimes are, in turn, commonly

associated with subduction of a young (generally less than 20 Ma), hot lithosphere. Unfortunately, the available data do not allow us to constrain in detail the age of the subducting lithosphere. Nonetheless, the available data suggest that the birth and death of the North Makran Ocean took place between the Valanginian (Ghazi et al., 2004) and the Coniacian; that is in a relatively short time span. Therefore, it is reasonable to assume that the subducting oceanic lithosphere was relatively hot. An alternative hypothesis that can explain the abnormally hot thermal regime necessary for adakite melt formation implies the existence of a mantle plume activity in the North Makran area during the Cretaceous, as suggested by Esmaeili et al. (2019).

Some features of the Ganj Complex allow us to better constrain the tectonic setting in which this Complex was formed. The occurrence of columnar basalts and volcanic scoriae indicates that at least some of the volcanic flows were erupted in submarine environments at relatively shallow depth. Sedimentary rocks are formed exclusively by intrabasinal debris, whereas extrabasinal (i.e., continental crust-derived debris) is absent all along the whole sequence, suggesting then that no debris from the continental margin has reached the basin(s) in which the volcano-sedimentary sequence and the turbidite sequence were formed. In addition, the intrabasinal debris only consists of volcanic and minor carbonatic debris. Dykes showing “sheeted” nature within the dyke-swarm are much more abundant in volume and widespread (particularly in the northern part of the Ganj Complex), with respect to what observed in many volcanic arc complexes (e.g., Gill, 1981; Dilek & Furnes, 2011). The formation of sheeted dykes in volcanic arc settings implies extensional tectonic regimes (e.g., Dilek & Furnes, 2011). All these features seem to suggest that the Ganj Complex was formed in an intra-arc tectonic setting or, eventually, a proximal (i.e., shallow water) forearc environment (see Draut & Clift, 2013 for an exhaustive review of the volcanic arc settings). According to these authors, intra-arc basins are commonly characterized by smaller extension and shallower water depths than forearc or backarc basins. Intra-arc basins are usually bounded by

volcanic edifices or by faults, which hamper the feeding of the sedimentary debris from the exposed continental area. As a consequence, intra-arc sedimentation consists of proximal (i.e., intrabasinal) volcanic and volcanoclastic material derived from the arc massif, fining away from the eruptive centers into turbidite and deep-water facies. Intra-arc volcanic and volcanoclastic deposits may be associated with reef or platform carbonates, reflecting changes in the intensity of eruption history and in relative sea level (local uplift and subsidence) that lead to episodic carbonate formation and destruction during arc activity and basin sedimentation (e.g., [Hoffmann et al., 2009](#); [Draut & Clift, 2013](#); [Zanchetta et al., 2013](#)). In contrast to forearc settings, where compressional tectonics prevail, the intra-arc zone is characterized by arc-normal extension that may generate new basins within the arc massif ([Draut & Clift, 2013](#)). Extensional tectonics may favour the formation of sheeted dykes in intra-arc settings compared to forearc settings. However, it should be noted that distinguishing between intra-arc and proximal forearc deposits in the geologic record could be problematic ([Dickinson, 1995](#)). In addition, one cannot exclude that the Ganj Complex includes subvolcanic, volcano-sedimentary and sedimentary sequences formed in similar, but distinct intra-arc basins separated by volcanic edifices and faults. Similar basin configuration is observed in many modern volcanic arc settings, as, for example the Aegean Sea ([Mezzadri & Saccani, 1989](#)).

4.7. Conclusion

The Ganj Complex consists of a > 2000 m-thick sequence, which starts with a dyke swarm, locally sheeted that shows a transition to a volcano-sedimentary sequence topped by a turbidite sequence. This Complex has so far been considered as one of the Cretaceous ophiolitic tectonic units cropping out in the North Makran domain that, in turn, represents the backstop of the Makran

accretionary wedge. In this chapter I present the results of a multidisciplinary study that was performed on the Ganj Complex through detailed fieldwork, structural, sedimentological, biostratigraphic, and geochemical investigations. The new data obtained from this study can be summarized as follows.

1) The Ganj Complex represents a typical volcanic arc succession mainly consisting of a dyke swarm complex (locally sheeted) followed by a well-developed volcano-sedimentary sequence characterized by the predominance of massive lava flows in its lower part and by pillow lava flows alternating with coarse-grained turbiditic beds in its upper part. The turbiditic beds become progressively more abundant toward the top of the volcano-sedimentary sequence and then pass to the turbiditic sequence forming the uppermost sequence of the Ganj Complex.

2) Compositionally, the turbiditic arenites are characterized by ubiquitous volcanic-derived minerals and rock fragments associated with variable, but generally moderate, amounts of calcareous rock fragments and bioclasts. This composition indicates sediment provenance from coeval, intrabasinal volcanic arc and carbonatic platform source areas.

3) Calcareous nannofossil biostratigraphy indicates that the volcano-sedimentary sequence and the turbidite have a Turonian-Coniacian age.

4) Volcanic rocks and dykes are represented mainly by intermediate and acidic rocks and subordinate basaltic rocks. These rocks mainly show calc-alkaline and island arc tholeiitic affinities. Nonetheless, minor volcanic arc rocks showing adakitic chemical signature occur in the upper part of the volcano-sedimentary sequence. REE modeling shows that they were originated from partial melting of depleted peridotites metasomatized by adakitic melts generated, in turn, by partial melting of eclogites forming the subducting slab melt.

In contrast to previous interpretations, all these data clearly indicate that the Ganj Complex represents a volcanic arc whose youngest age can be constrained to Turonian-Coniacian times.

The new data presented herein allow us to propose a new model for the Mesozoic geodynamic evolution of the North Makran. In contrast to previous interpretations, the proposed model implies that the Ganj volcanic arc was not associated with the subduction of the main Southern Neo-Tethys Ocean below the Bajgan-Durkan microcontinent. Rather, it formed in the southern margin of the Lut block during Late Cretaceous times as a consequence of the subduction of the North Makran Ocean, which existed since the Early Cretaceous between the Bajgan-Durkan (to the south) and the Lut (to the north) continental margins. This model implies that the Southern Neo-Tethys Ocean and the North Makran Ocean were both affected in the Late Cretaceous by north-dipping subduction, which resulted in the formation of two separate volcanic arcs whose remnants are today preserved in the Coloured Mélange Complex and in the Ganj Complex, respectively. The lithostratigraphic features of the whole succession suggest that the Ganj volcanic arc sequence was forming in a relatively shallow marine environment in an extensional intra-arc setting along the southern rim of the Lut block continental margin.

APPENDIX

Appendix Table 4.1. Calcareous nannofossils taxa with their relative abundances. R-Rare (less than 1 specimen per FOV-Field of View), C-Common (1 or more than 1 specimens per FOV). All taxa are referenced in [Young et al. \(2017\)](#).

| Sample | <i>Assipetra terebrentarius</i> | <i>Biscutum</i> sp. | <i>Calculites</i> sp. | <i>Eiffellithus turrisseiffelii</i> | <i>Eprolithus moratus</i> | <i>Eprolithus floralis</i> | <i>Eprolithus rarus</i> | <i>cf. Flabellites oblongus</i> | <i>cf. Micula</i> | <i>Nannoconus</i> sp. | <i>Quadrum gartneri</i> | <i>Quadrum cf. gartneri</i> | <i>Retecapsa crenulata</i> | <i>Retecapsa</i> sp. | <i>Tranolithus orionatus</i> | <i>Watznaueria</i> spp. | <i>Zeugrhabdotus diplogrammus</i> | <i>Zeugrhabdotus embergeri</i> | <i>Zeugrhabdotus</i> sp. |
|--------|---------------------------------|---------------------|-----------------------|-------------------------------------|---------------------------|----------------------------|-------------------------|---------------------------------|-------------------|-----------------------|-------------------------|-----------------------------|----------------------------|----------------------|------------------------------|-------------------------|-----------------------------------|--------------------------------|--------------------------|
| MK448 | \ | \ | \ | \ | \ | \ | \ | \ | \ | \ | \ | \ | \ | \ | \ | \ | \ | \ | \ |
| MK447 | \ | \ | \ | \ | \ | \ | \ | \ | \ | \ | \ | \ | \ | \ | \ | \ | \ | \ | \ |
| MK446 | \ | \ | \ | \ | \ | \ | \ | \ | \ | \ | \ | \ | \ | \ | \ | \ | \ | \ | \ |
| MK445 | \ | \ | \ | \ | \ | \ | \ | \ | \ | \ | \ | \ | \ | \ | \ | C | \ | \ | \ |
| MK444 | \ | \ | \ | R | R | R | \ | \ | \ | \ | \ | \ | \ | \ | \ | C | \ | \ | \ |
| MK443 | \ | \ | \ | \ | \ | \ | \ | \ | \ | \ | \ | \ | \ | \ | \ | \ | \ | \ | \ |
| MK442 | R | \ | \ | \ | R | R | \ | \ | R | \ | \ | \ | \ | \ | R | C | R | R | \ |
| MK349 | \ | \ | \ | \ | \ | R | R | \ | R | \ | R | R | \ | R | \ | C | R | R | \ |
| MK348 | \ | \ | \ | \ | R | R | R | R | R | R | R | R | \ | \ | \ | C | \ | R | \ |
| MK360B | \ | \ | \ | \ | \ | \ | \ | \ | \ | \ | \ | \ | \ | \ | \ | R | \ | \ | \ |
| MK359 | \ | \ | \ | \ | \ | \ | \ | \ | \ | \ | \ | \ | \ | \ | \ | \ | \ | \ | \ |
| MK357 | \ | \ | \ | \ | \ | \ | \ | \ | \ | \ | \ | \ | \ | \ | \ | R | \ | \ | \ |
| MK354 | \ | R | R | R | \ | R | \ | \ | \ | \ | R | R | R | \ | R | C | \ | \ | \ |
| MK353 | \ | \ | \ | \ | \ | \ | \ | \ | \ | \ | \ | \ | \ | \ | \ | R | \ | \ | R |
| MK352B | \ | \ | \ | \ | \ | \ | \ | \ | \ | \ | \ | \ | \ | \ | \ | R | \ | \ | \ |
| MK352A | \ | \ | \ | \ | \ | \ | \ | \ | \ | \ | \ | \ | \ | \ | \ | R | \ | \ | \ |
| MK351 | \ | \ | \ | \ | \ | \ | \ | \ | \ | \ | \ | \ | \ | R | \ | R | \ | \ | \ |

Appendix Table 4.2. Modal analysis of the Ganj Complex arenites. Point counting (500 points) on the selected arenites was performed using the Gazzi-Dickinson technique (Gazzi, 1966; Dickinson, 1970; Ingersoll et al., 1984; Zuffa, 1987) to minimize the dependence of arenite composition on grain size. Abbreviations, Amg: medium-coarse grained arenites; Am: medium grained arenites; VSS: Volcano Sedimentary Sequence; TSCS: Turbidite Sedimentary Cover Sequence.

| SAMPLE | | MK132 | MK343 | MK347A | MK347B | MK350A | MK350b | MK360A | MK360B | MK449 | MK450 | MK451 |
|---|---|---------------------------------|--------|--------|--------|--------|--------|--------|--------|--------|--------|--------|
| Formation | | | | | | | | | | | | |
| Arenite grain size | | Amg | Amg | Amg | Amg | Am | Amg | Am | Am | Amg | Amg | Amg |
| Sorting (according Longiaru et. alii, 1987) | | B | B/C | B | B | B/C | B/C | B | B | B | B/C | B |
| Counted points | | 500 | 500 | 500 | 500 | 500 | 500 | 500 | 500 | 500 | 500 | 500 |
| Petrofacies | | VSS | VSS | VSS | VSS | TSCS | TSCS | TSCS | TSCS | TSCS | TSCS | TSCS |
| NCE | Non Carbonatic Extrabasinal fragment | 0.00 | 0.00 | 0.00 | 0.00 | 0.00 | 0.00 | 0.00 | 0.00 | 0.00 | 0.00 | 0.00 |
| Q | Q medium quartz single crystal | 2.73 | 1.41 | 2.35 | 5.84 | 1.93 | 1.93 | 2.75 | 2.88 | 4.36 | 2.79 | 0.00 |
| | Q medium quartz polycrystalline | 3.64 | 0.00 | 0.70 | 0.23 | 0.48 | 0.24 | 0.25 | 0.72 | 3.15 | 5.12 | 0.00 |
| | Q quartz in felsic volcanic r.f | 0.91 | 0.70 | 0.23 | 2.80 | 1.20 | 0.72 | 0.75 | 0.72 | 1.69 | 0.70 | 0.00 |
| K | K-feldspar single crystal | 2.73 | 0.23 | 10.80 | 9.58 | 3.13 | 5.56 | 3.75 | 4.56 | 5.33 | 3.49 | 9.98 |
| | K-feldspar in felsic volcanic r.f. | 0.23 | 0.70 | 2.11 | 1.17 | 0.72 | 0.24 | 1.00 | 0.72 | 0.48 | 0.00 | 0.23 |
| | K-feldspar in intermediate volcanic r.f. | 0.68 | 1.64 | 1.17 | 0.23 | 2.17 | 1.93 | 1.50 | 2.64 | 1.69 | 2.56 | 2.49 |
| P | P plagioclase single crystal | 0.68 | 3.75 | 41.78 | 31.07 | 12.77 | 15.22 | 24.50 | 22.78 | 10.65 | 9.30 | 34.24 |
| | P plagioclase in felsic volcanic r.f. | 1.14 | 0.00 | 2.58 | 0.93 | 1.20 | 0.48 | 1.50 | 0.24 | 0.00 | 0.00 | 0.00 |
| | P plagioclase in intermediate volcanic r.f. | 5.91 | 7.49 | 2.11 | 2.80 | 6.51 | 8.45 | 6.75 | 7.91 | 3.63 | 3.02 | 3.40 |
| | P plagioclase in mafic volcanic r.f. | 0.23 | 0.00 | 1.17 | 1.87 | 0.24 | 0.00 | 0.50 | 1.20 | 0.24 | 0.70 | 2.72 |
| L | Lv Felsic volcanic r.f. | 1.14 | 0.00 | 1.17 | 3.04 | 4.34 | 3.62 | 3.00 | 0.00 | 1.94 | 2.79 | 0.00 |
| | Lv Intermediate volcanic r.f. | 65.68 | 73.77 | 3.52 | 3.97 | 29.40 | 31.64 | 20.75 | 22.30 | 21.79 | 20.93 | 12.70 |
| | Lv Mafic volcanic r.f. | 5.45 | 0.47 | 0.94 | 0.70 | 2.17 | 0.97 | 0.75 | 0.24 | 0.97 | 1.16 | 7.48 |
| Fill. | Phyllosilicate single crystal | 0.00 | 0.00 | 0.23 | 0.00 | 0.00 | 0.48 | 0.00 | 0.48 | 0.24 | 0.00 | 0.45 |
| | Phyllosilicate in intermediate volcanic r.f | 0.45 | 0.00 | 0.00 | 0.47 | 0.00 | 0.00 | 0.25 | 0.24 | 0.48 | 0.00 | 0.23 |
| Pes. | Olivine in mafic volcanic r.f. | 0.00 | 0.00 | 0.00 | 0.23 | 0.00 | 0.24 | 0.25 | 0.00 | 0.48 | 0.00 | 0.45 |
| | Px and/or Amph single crystal | 0.23 | 2.11 | 13.15 | 9.11 | 3.86 | 4.59 | 1.75 | 4.32 | 0.48 | 0.70 | 13.15 |
| | Px and/or Amph in mafic volcanic r.f. | 0.45 | 0.00 | 2.82 | 4.44 | 0.00 | 0.24 | 0.25 | 0.00 | 0.24 | 0.00 | 1.59 |
| | Px and/or Amph in intermediate volcanic r.f. | 1.36 | 1.87 | 0.00 | 1.40 | 1.93 | 2.90 | 1.25 | 0.24 | 2.66 | 1.63 | 0.91 |
| | Heavy mineral single crystal (apatite, zircon rutile) | 0.00 | 0.47 | 0.00 | 0.23 | 0.48 | 0.00 | 0.25 | 0.00 | 0.73 | 0.00 | 0.00 |
| | Oxide single crystal | 2.95 | 0.94 | 5.63 | 3.04 | 2.65 | 1.69 | 2.50 | 5.76 | 0.97 | 1.16 | 4.76 |
| | Oxide in intermediate volcanic r.f. | 1.36 | 1.64 | 0.00 | 0.23 | 0.00 | 0.24 | 0.25 | 1.92 | 0.00 | 0.47 | 0.45 |
| | Glaucanites | 0.00 | 0.00 | 0.00 | 0.23 | 0.00 | 0.97 | 1.25 | 0.72 | 1.45 | 2.09 | 0.00 |
| | CE | Carbonate extrabasinal fragment | 0.00 | 0.00 | 0.00 | 0.00 | 0.00 | 0.00 | 0.00 | 0.00 | 0.00 | 0.00 |
| Cl | Bioclast | 0.00 | 0.00 | 1.41 | 3.74 | 12.53 | 8.21 | 7.50 | 4.56 | 22.28 | 28.84 | 0.45 |
| | Mudstone (soft clast) r.f. | 0.00 | 0.00 | 0.94 | 4.91 | 8.92 | 6.76 | 11.00 | 11.51 | 7.99 | 7.67 | 1.59 |
| | Grainstone r.f. | 0.00 | 0.00 | 0.00 | 0.00 | 0.00 | 0.48 | 0.00 | 0.48 | 1.21 | 2.79 | 0.00 |
| | Wackstone r.f. | 0.00 | 0.00 | 0.00 | 0.23 | 0.00 | 0.97 | 0.50 | 0.00 | 2.18 | 1.16 | 0.00 |
| U | Undetermined framework fragment | 2.05 | 2.81 | 4.93 | 7.48 | 0.96 | 0.72 | 2.00 | 0.96 | 2.66 | 0.00 | 2.72 |
| | Limeclast | 0.00 | 0.00 | 0.23 | 0.00 | 2.41 | 0.48 | 3.25 | 1.92 | 0.00 | 0.93 | 0.00 |
| Total framework % | | 100.00 | 100.00 | 100.00 | 100.00 | 100.00 | 100.00 | 100.00 | 100.00 | 100.00 | 100.00 | 100.00 |
| F Framework | | 88.00 | 85.40 | 85.20 | 85.60 | 83.00 | 82.80 | 80.00 | 83.40 | 82.60 | 86.00 | 88.20 |
| M Non carbonatic matrix | | 7.20 | 7.20 | 7.40 | 5.60 | 1.80 | 2.20 | 3.20 | 3.60 | 1.80 | 1.60 | 7.40 |
| M Carbonatic matrix | | 0.00 | 0.00 | 1.60 | 0.60 | 2.80 | 3.60 | 5.60 | 4.40 | 3.60 | 4.20 | 0.00 |
| P Primary porosity | | 0.00 | 0.00 | 0.00 | 0.00 | 0.60 | 2.40 | 3.20 | 3.60 | 5.60 | 1.00 | 0.00 |
| P Pore filling calcite cement | | 0.00 | 0.00 | 0.00 | 0.40 | 5.60 | 6.20 | 3.60 | 1.40 | 3.20 | 3.40 | 0.00 |
| U Patchy calcite | | 4.80 | 7.40 | 5.80 | 7.80 | 6.20 | 2.80 | 4.20 | 3.60 | 3.20 | 3.80 | 4.40 |
| TOTALE % | | 100.00 | 100.00 | 100.00 | 100.00 | 100.00 | 100.00 | 100.00 | 100.00 | 100.00 | 100.00 | 100.00 |

Appendix Table 4.3 (1/3). Major and trace element analyses of sub-volcanic and volcanic rocks from the Ganj Complex. Abbreviations, bas: basalt; bas and: basaltic andesite; and: andesite; dac: dacite; rhy: rhyolite; MLF: massive lava flow; CA: calc-alkaline; IAT: island arc tholeiite; L(La/Yb)_N: low La/Yb chondrite-normalized ratio; H(La/Yb)_N: high La/Yb chondrite-normalized ratio; XRF: X-ray fluorescence spectrometry; ICP-MS: inductively coupled plasma-mass spectrometry; n.d.: not detected. Mg# = 100 x Mg/(Mg+Fe). Fe₂O₃=0.15 x FeO. Normalizing values for REE ratios are from Sun & McDonough (1989).

| Unit | Group I (CA) | | | | | | | | | | |
|--------------------------------|------------------------------|---------|-------|-------|-------|---------|------------|-------|-------|--------|--------|
| | Group Ia | | | | | | Dyke-swarm | | | | |
| | Volcano-sedimentary sequence | | | | | | | | | | |
| Sample | MK13 | MK15 | MK14 | MK17 | MK19 | MK440 | MK22 | MK114 | MK115 | MK117 | MK119 |
| Rock | dac | dac | dac | and | dac | bas and | rhy | dac | rhy | dac | dac |
| Note | MLF | MLF | dyke | dyke | dyke | MLF | dyke | dyke | dyke | dyke | dyke |
| <i>XRF analyses:</i> | | | | | | | | | | | |
| SiO ₂ | 67.89 | 64.77 | 65.80 | 61.64 | 63.04 | 56.82 | 73.03 | 68.26 | 72.65 | 70.96 | 68.33 |
| TiO ₂ | 0.34 | 0.27 | 0.34 | 0.47 | 0.43 | 1.19 | 0.25 | 0.39 | 0.30 | 0.32 | 0.58 |
| Al ₂ O ₃ | 13.46 | 13.36 | 18.73 | 16.89 | 15.69 | 15.47 | 13.04 | 14.06 | 12.63 | 13.24 | 13.30 |
| Fe ₂ O ₃ | 0.49 | 0.40 | 0.73 | 0.62 | 0.60 | 1.02 | 0.36 | 0.40 | 0.44 | 0.50 | 0.68 |
| FeO | 3.30 | 2.65 | 4.84 | 4.14 | 4.01 | 6.79 | 2.40 | 2.69 | 2.94 | 3.31 | 4.51 |
| MnO | 0.10 | 0.18 | 0.22 | 0.18 | 0.07 | 0.07 | 0.03 | 0.06 | 0.04 | 0.07 | 0.06 |
| MgO | 0.16 | 0.23 | 1.03 | 4.64 | 2.22 | 2.86 | 1.61 | 1.92 | 0.89 | 1.30 | 2.95 |
| CaO | 3.61 | 5.68 | 1.77 | 3.02 | 2.58 | 7.41 | 0.52 | 2.14 | 1.35 | 1.48 | 0.93 |
| Na ₂ O | 7.01 | 6.39 | 0.56 | 4.57 | 8.40 | 6.21 | 6.41 | 4.81 | 7.97 | 7.57 | 7.27 |
| K ₂ O | 0.10 | 0.06 | 1.20 | 0.64 | 0.40 | 0.65 | 0.41 | 3.24 | 0.02 | 0.03 | 0.01 |
| P ₂ O ₅ | 0.07 | 0.06 | 0.02 | 0.08 | 0.13 | 0.21 | 0.04 | 0.13 | 0.09 | 0.10 | 0.14 |
| LOI | 3.67 | 5.99 | 4.69 | 3.05 | 2.24 | 1.05 | 1.58 | 1.58 | 0.54 | 1.14 | 1.39 |
| Total | 100.20 | 100.03 | 99.94 | 99.93 | 99.81 | 99.75 | 99.68 | 99.70 | 99.86 | 100.01 | 100.14 |
| Mg# | 8.1 | 13.2 | 27.6 | 66.6 | 49.7 | 42.9 | 54.4 | 56.0 | 35.1 | 41.2 | 53.8 |
| Zn | 59 | 78 | 184 | 220 | 46 | 54 | 30 | 26 | 8 | 36 | 47 |
| Cu | n.d. | 5 | n.d. | 135 | 27 | 17 | n.d. | 9 | n.d. | 59 | 67 |
| Sc | 9 | 10 | 9 | 14 | 7 | 17 | 8 | 8 | 9 | 9 | 13 |
| Ga | 18 | 15 | 22 | 17 | 19 | 19 | 15 | 17 | 19 | 18 | 15 |
| Ni | n.d. | n.d. | 18 | 4 | n.d. | 5 | n.d. | 2 | n.d. | n.d. | n.d. |
| Co | n.d. | n.d. | 3 | 14 | 8 | 20 | n.d. | 6 | 2 | 2 | 11 |
| Cr | 7 | 6 | 4 | 53 | 13 | 20 | 15 | 17 | 24 | 15 | 14 |
| V | 6 | 8 | 10 | 94 | 43 | 191 | 5 | 30 | 9 | 20 | 38 |
| Ba | 75 | 88 | 76 | 61 | 68 | 58 | 56 | 58 | 71 | 52 | 63 |
| Pb | 14 | 10 | 8 | 12 | 10 | 12 | 9 | 8 | 10 | 9 | 12 |
| <i>ICP-MS analyses:</i> | | | | | | | | | | | |
| Rb | (XRF) 2 | (XRF) 2 | 5.55 | 2.78 | 3.52 | 4.33 | 2.06 | 4.34 | 3.80 | 2.72 | 2.47 |
| Sr | 71 | 91 | 49.7 | 312 | 281 | 352 | 67.3 | 269 | 96.7 | 96.9 | 66.4 |
| Y | 39 | 42 | 38.7 | 14.7 | 24.4 | 16.4 | 24.0 | 28.5 | 36.6 | 23.3 | 23.9 |
| Zr | 145 | 166 | 146 | 76.2 | 108 | 86.7 | 114 | 130 | 145 | 109 | 99.9 |
| Nb | 4 | 3 | 3.51 | 4.08 | 3.55 | 2.25 | 2.74 | 3.76 | 4.12 | 2.88 | 2.75 |
| La | 10 | 12 | 12.4 | 9.23 | 7.53 | 8.39 | 11.0 | 8.60 | 10.0 | 9.13 | 11.7 |
| Ce | 28 | 34 | 31.4 | 20.3 | 17.6 | 19.0 | 25.9 | 20.8 | 21.5 | 19.4 | 29.3 |
| Pr | | | 4.51 | 2.60 | 2.39 | 2.52 | 3.54 | 2.94 | 2.82 | 2.57 | 4.26 |
| Nd | 9 | 8 | 20.0 | 10.9 | 10.9 | 10.7 | 14.4 | 12.7 | 12.0 | 11.0 | 18.7 |
| Sm | | | 5.69 | 3.04 | 3.13 | 3.01 | 3.61 | 3.48 | 3.18 | 3.01 | 5.46 |
| Eu | | | 1.40 | 0.755 | 0.797 | 0.948 | 0.620 | 0.854 | 0.536 | 0.572 | 1.14 |
| Gd | | | 5.66 | 3.09 | 3.27 | 2.86 | 3.06 | 3.34 | 3.66 | 3.19 | 6.23 |
| Tb | | | 0.910 | 0.498 | 0.545 | 0.433 | 0.465 | 0.538 | 0.619 | 0.540 | 1.02 |
| Dy | | | 5.28 | 3.03 | 3.31 | 2.68 | 2.93 | 3.28 | 3.85 | 3.48 | 6.19 |
| Ho | | | 1.04 | 0.594 | 0.680 | 0.562 | 0.581 | 0.668 | 0.765 | 0.717 | 1.23 |
| Er | | | 2.69 | 1.64 | 1.73 | 1.57 | 1.62 | 1.78 | 2.07 | 1.93 | 3.17 |
| Tm | | | 0.370 | 0.243 | 0.249 | 0.235 | 0.236 | 0.252 | 0.291 | 0.284 | 0.435 |
| Yb | | | 2.26 | 1.60 | 1.55 | 1.53 | 1.43 | 1.65 | 1.83 | 1.79 | 2.57 |
| Lu | | | 0.300 | 0.230 | 0.226 | 0.225 | 0.211 | 0.239 | 0.241 | 0.245 | 0.357 |
| Hf | 3 | 3 | 1.94 | 3.17 | 3.19 | 3.47 | 3.96 | 3.14 | 1.22 | 2.16 | 2.39 |
| Ta | | | 0.220 | 0.321 | 0.183 | 0.157 | 0.169 | 0.252 | 0.242 | 0.154 | 0.208 |
| Th | 2 | 1 | 1.49 | 1.25 | 1.38 | 1.92 | 1.58 | 1.48 | 1.07 | 1.11 | 1.28 |
| U | | | 0.220 | 0.546 | 0.254 | 0.403 | 0.452 | 0.364 | 0.178 | 0.211 | 0.156 |
| Nb/Y | 0.10 | 0.07 | 0.09 | 0.28 | 0.15 | 0.14 | 0.11 | 0.13 | 0.11 | 0.12 | 0.12 |
| Zr/Ti | 0.108 | 0.143 | 0.104 | 0.037 | 0.059 | 0.019 | 0.074 | 0.077 | 0.125 | 0.084 | 0.042 |
| (La/Sm) _N | | | 1.40 | 1.96 | 1.55 | 1.80 | 1.97 | 1.59 | 2.03 | 1.96 | 1.38 |
| (Sm/Yb) _N | | | 2.80 | 2.11 | 2.25 | 2.19 | 2.79 | 2.35 | 1.93 | 1.86 | 2.36 |
| (La/Yb) _N | | | 3.92 | 4.14 | 3.49 | 3.93 | 5.50 | 3.74 | 3.92 | 3.65 | 3.26 |
| Sr/Y | 1.83 | 2.17 | 1.28 | 21.2 | 11.5 | 21.5 | 2.80 | 9.45 | 2.64 | 4.17 | 2.78 |

Appendix Table 4.3. (2/3)

| Rock type | Group 1 (CA) | | | | | | | | | | Group2 (IAT) | | | |
|--------------------------------|------------------------------|--------|-------|--------|--------|-------|-------|-------|-------|--------------|--------------|--------|-----------------|------|
| Unit | Group 1b | | | | | | | | | | Dyke-swarm | | Volc.-sed. seq. | |
| | Volcano-sedimentary sequence | | | | | | | | | | | | | |
| Sample | MK21 | MK12 | MK12 | MK12 | MK12 | MK12 | MK12 | MK12 | MK13 | MK13 | MK120 | MK12 | MK16 | MK20 |
| Rock | dac | dac | dac | dac | dac | dac | dac | dac | dac | rhy | dac | rhy | bas | and |
| Note | MLF | MLF | lava | lava | lava | lava | MLF | MLF | MLF | dyke | dyke | pillow | MLF | |
| SiO ₂ | 63.20 | 65.52 | 69.25 | 66.71 | 64.94 | 67.12 | 63.29 | 65.46 | 72.79 | 67.73 | 74.35 | 42.97 | 54.05 | |
| TiO ₂ | 0.60 | 0.59 | 0.49 | 0.36 | 0.38 | 0.39 | 0.47 | 0.38 | 0.29 | 0.46 | 0.24 | 0.83 | 1.09 | |
| Al ₂ O ₃ | 13.90 | 14.76 | 13.91 | 13.90 | 14.06 | 14.02 | 14.69 | 14.60 | 12.29 | 14.23 | 12.39 | 13.42 | 13.28 | |
| Fe ₂ O ₃ | 0.61 | 0.51 | 0.40 | 0.61 | 0.55 | 0.58 | 0.54 | 0.51 | 0.30 | 0.48 | 0.41 | 0.97 | 1.08 | |
| FeO | 4.05 | 3.43 | 2.66 | 4.05 | 3.65 | 3.86 | 3.59 | 3.39 | 1.99 | 3.18 | 2.76 | 6.47 | 7.18 | |
| MnO | 0.06 | 0.09 | 0.06 | 0.08 | 0.06 | 0.06 | 0.04 | 0.06 | 0.04 | 0.05 | 0.03 | 0.17 | 0.14 | |
| MgO | 3.25 | 2.74 | 1.91 | 2.13 | 1.71 | 1.97 | 2.95 | 1.42 | 0.90 | 3.47 | 0.86 | 12.38 | 7.45 | |
| CaO | 3.61 | 2.73 | 2.26 | 2.06 | 3.91 | 2.06 | 3.99 | 3.26 | 2.05 | 1.25 | 1.74 | 9.86 | 6.04 | |
| Na ₂ O | 6.49 | 5.84 | 5.30 | 7.09 | 6.61 | 6.87 | 5.79 | 6.73 | 4.89 | 5.83 | 6.45 | 3.24 | 4.26 | |
| K ₂ O | 0.94 | 1.83 | 2.06 | 1.03 | 1.41 | 1.04 | 1.17 | 1.55 | 3.03 | 1.62 | n.d. | 0.02 | 1.55 | |
| P ₂ O ₅ | 0.21 | 0.17 | 0.18 | 0.11 | 0.10 | 0.10 | 0.09 | 0.10 | 0.06 | 0.13 | 0.04 | 0.11 | 0.15 | |
| LOI | 2.92 | 1.85 | 1.30 | 1.93 | 2.67 | 1.87 | 3.15 | 2.29 | 1.28 | 1.50 | 0.59 | 9.65 | 3.42 | |
| Total | 99.83 | 100.06 | 99.78 | 100.06 | 100.04 | 99.93 | 99.77 | 99.74 | 99.91 | 99.93 | 99.88 | 100.08 | 99.69 | |
| Mg# | 58.8 | 58.8 | 56.1 | 48.4 | 45.5 | 47.6 | 59.4 | 42.8 | 44.6 | 66.0 | 35.7 | 77.3 | 64.9 | |
| Zn | 39 | 46 | 57 | 58 | 67 | 55 | 53 | 66 | 73 | 37 | n.d. | 125 | 66 | |
| Cu | 10 | 4 | 5 | 4 | 8 | 8 | 6 | 11 | 8 | 10 | n.d. | n.d. | 23 | |
| Sc | 19 | 9 | 8 | 10 | 11 | 10 | 11 | 8 | 7 | 10 | 6 | 29 | 25 | |
| Ga | 19 | 20 | 20 | 23 | 21 | 22 | 20 | 21 | 15 | 17 | 19 | 15 | 17 | |
| Ni | n.d. | n.d. | n.d. | n.d. | n.d. | n.d. | n.d. | n.d. | n.d. | n.d. | n.d. | 16 | 12 | |
| Co | 9 | 3 | 4 | 2 | 3 | 2 | 8 | n.d. | n.d. | 6 | n.d. | 30 | 26 | |
| Cr | 19 | 7 | 7 | 10 | 10 | 14 | 30 | 8 | 13 | 29 | 5 | 86 | 80 | |
| V | 40 | 30 | 22 | 12 | 14 | 12 | 36 | 9 | 15 | 35 | 6 | 177 | 171 | |
| Ba | 75 | 81 | 86 | 53 | 79 | 59 | 63 | 99 | 70 | 58 | 95 | 36 | 66 | |
| Pb | 10 | 12 | 9 | 10 | 10 | 12 | 9 | 11 | 13 | 9 | 9 | 9 | 6 | |
| <i>ICP-MS analyses:</i> | | | | | | | | | | <i>(XRF)</i> | | | | |
| Rb | 5.46 | 7.75 | 8.87 | 4.58 | 9.69 | 4.75 | 6.26 | 12.7 | 11.1 | 5.41 | 1 | 2.39 | 6.38 | |
| Sr | 142 | 233 | 242 | 97.9 | 142 | 134 | 171 | 142 | 94.1 | 119 | 147 | 111 | 75.8 | |
| Y | 32.9 | 36.5 | 52.7 | 32.7 | 40.7 | 35.0 | 36.9 | 44.7 | 39.6 | 25.9 | 47 | 19.8 | 32.9 | |
| Zr | 140 | 165 | 196 | 153 | 180 | 167 | 162 | 236 | 184 | 126 | 214 | 42.5 | 133 | |
| Nb | 2.80 | 4.56 | 7.73 | 4.54 | 5.40 | 4.92 | 3.72 | 6.76 | 5.24 | 3.50 | 4 | 2.02 | 1.85 | |
| La | 8.76 | 8.00 | 19.1 | 5.60 | 16.0 | 9.41 | 6.54 | 10.2 | 9.68 | 8.69 | 12 | 4.48 | 6.03 | |
| Ce | 19.6 | 19.5 | 45.5 | 13.4 | 37.3 | 22.3 | 16.6 | 24.8 | 25.7 | 22.3 | 28 | 11.3 | 15.5 | |
| Pr | 2.69 | 2.79 | 6.59 | 1.97 | 5.07 | 3.03 | 2.43 | 3.29 | 3.80 | 3.13 | | 1.75 | 2.36 | |
| Nd | 11.6 | 12.1 | 29.6 | 8.84 | 21.9 | 13.1 | 10.9 | 14.3 | 17.1 | 14.1 | 14 | 8.27 | 11.2 | |
| Sm | 3.27 | 3.08 | 7.62 | 2.37 | 6.06 | 3.49 | 3.05 | 3.75 | 4.48 | 4.11 | | 2.59 | 3.36 | |
| Eu | 0.823 | 0.747 | 1.37 | 0.558 | 1.41 | 0.802 | 0.751 | 0.744 | 0.993 | 0.976 | | 0.943 | 1.02 | |
| Gd | 3.95 | 3.58 | 8.44 | 2.98 | 7.34 | 4.07 | 3.51 | 4.36 | 5.36 | 4.54 | | 2.99 | 4.01 | |
| Tb | 0.703 | 0.628 | 1.45 | 0.553 | 1.31 | 0.711 | 0.634 | 0.811 | 0.992 | 0.750 | | 0.494 | 0.719 | |
| Dy | 4.59 | 4.02 | 9.40 | 3.67 | 8.47 | 4.63 | 4.23 | 5.31 | 6.49 | 4.84 | | 3.15 | 4.80 | |
| Ho | 0.987 | 0.873 | 2.04 | 0.810 | 1.86 | 1.00 | 0.899 | 1.17 | 1.41 | 1.03 | | 0.674 | 1.04 | |
| Er | 2.83 | 2.54 | 5.94 | 2.35 | 5.30 | 2.90 | 2.59 | 3.29 | 4.10 | 2.96 | | 1.83 | 2.95 | |
| Tm | 0.437 | 0.388 | 0.901 | 0.360 | 0.814 | 0.454 | 0.395 | 0.509 | 0.620 | 0.432 | | 0.275 | 0.461 | |
| Yb | 2.93 | 2.53 | 5.93 | 2.40 | 5.31 | 2.97 | 2.58 | 3.37 | 4.11 | 2.78 | | 1.81 | 2.98 | |
| Lu | 0.434 | 0.367 | 0.929 | 0.352 | 0.789 | 0.440 | 0.374 | 0.483 | 0.592 | 0.419 | | 0.267 | 0.444 | |
| Hf | 4.56 | 4.12 | 8.84 | 3.24 | 3.73 | 3.57 | 4.28 | 6.52 | 5.76 | 4.201 | 4 | 2.12 | 4.50 | |
| Ta | 0.175 | 0.257 | 0.296 | 0.251 | 0.331 | 0.262 | 0.229 | 0.338 | 0.292 | 0.179 | | 0.196 | 0.184 | |
| Th | 1.59 | 2.11 | 3.64 | 1.26 | 2.89 | 1.82 | 1.56 | 2.69 | 3.04 | 1.70 | 3 | 0.636 | 0.539 | |
| U | 0.341 | 0.383 | 0.948 | 0.305 | 0.504 | 0.343 | 0.307 | 0.404 | 0.522 | 0.464 | | 0.222 | 0.221 | |
| Nb/Y | 0.09 | 0.12 | 0.15 | 0.14 | 0.13 | 0.14 | 0.10 | 0.15 | 0.13 | 0.14 | 0.08 | 0.10 | 0.06 | |
| Zr/Ti | 0.057 | 0.069 | 0.098 | 0.104 | 0.116 | 0.105 | 0.083 | 0.152 | 0.154 | 0.071 | 0.219 | 0.012 | 0.029 | |
| (La/Sm) _N | 1.73 | 1.68 | 1.62 | 1.53 | 1.70 | 1.74 | 1.38 | 1.75 | 1.39 | 1.36 | | 1.12 | 1.16 | |
| (Sm/Yb) _N | 1.24 | 1.35 | 1.43 | 1.10 | 1.27 | 1.31 | 1.31 | 1.23 | 1.21 | 1.64 | | 1.59 | 1.25 | |
| (La/Yb) _N | 2.14 | 2.27 | 2.31 | 1.67 | 2.16 | 2.28 | 1.82 | 2.16 | 1.69 | 2.24 | | 1.78 | 1.45 | |
| Sr/Y | 4.31 | 6.38 | 4.59 | 3.00 | 3.48 | 3.84 | 4.64 | 3.19 | 2.38 | 4.59 | 3.10 | 5.63 | 2.30 | |

Appendix Table 4.3. (3/3)

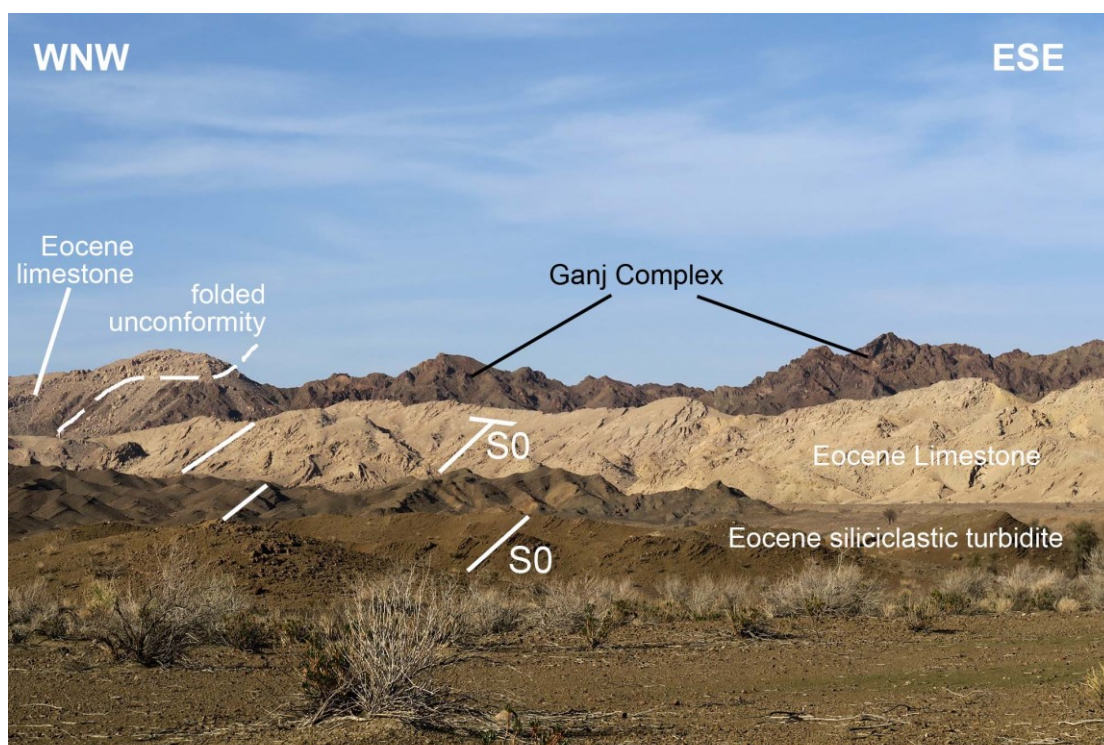
| Rock type | Group2 (IAT) | | | | | | | | Group 3 | | | |
|--------------------------------|------------------------------|--------|---------|-------|------------|-------|-------|---------|-----------------------------|--------|-----------------------------|--------|
| | Volcano-sedimentary sequence | | | | Dyke-swarm | | | | Group 3a Volc.-sed. seq. | | Group 3b Volc.-sed. seq. | |
| Unit | MK1 | | | | MK121 | MK113 | MK116 | MK118 | MK361 | MK433 | MK435 | MK438 |
| Sample | MK434 | MK437 | MK439 | 8 | | | | | | | | |
| Rock | bas and | bas | bas and | bas | bas | bas | and | bas and | bas and | bas | bas and | bas |
| Note | pillow | MLF | pillow | and | dyke | dyke | dyke | dyke | pillow | MLF | MLF | MLF |
| XRF | | | | dyke | | | | | | | | |
| analyses | | | | | | | | | | | | |
| SiO ₂ | 46.31 | 50.31 | 42.13 | 49.19 | 54.06 | 56.83 | 58.28 | 52.87 | 48.97 | 50.70 | 51.32 | 52.29 |
| TiO ₂ | 0.99 | 1.43 | 0.93 | 1.46 | 1.71 | 2.02 | 0.85 | 1.05 | 0.94 | 0.54 | 0.58 | 0.53 |
| Al ₂ O ₃ | 13.07 | 13.35 | 11.16 | 13.94 | 15.40 | 13.23 | 14.41 | 14.20 | 16.23 | 16.86 | 16.12 | 15.97 |
| Fe ₂ O ₃ | 1.01 | 1.29 | 0.90 | 1.17 | 1.28 | 1.30 | 0.92 | 1.11 | 0.75 | 0.72 | 0.76 | 0.76 |
| FeO | 6.71 | 8.57 | 5.99 | 7.78 | 8.51 | 8.68 | 6.15 | 7.38 | 5.02 | 4.82 | 5.05 | 5.04 |
| MnO | 0.12 | 0.19 | 0.12 | 0.16 | 0.18 | 0.22 | 0.12 | 0.13 | 0.08 | 0.09 | 0.09 | 0.09 |
| MgO | 3.75 | 5.54 | 5.55 | 6.48 | 8.33 | 5.91 | 7.18 | 10.48 | 5.94 | 4.96 | 5.22 | 6.75 |
| CaO | 19.34 | 12.64 | 22.56 | 8.33 | 2.64 | 5.21 | 3.31 | 3.53 | 10.43 | 10.84 | 9.06 | 8.72 |
| Na ₂ O | 5.50 | 4.33 | 4.56 | 3.73 | 4.62 | 4.07 | 4.71 | 4.49 | 6.95 | 5.97 | 6.91 | 5.47 |
| K ₂ O | 0.39 | 0.36 | 0.78 | 0.28 | n.d. | 0.54 | 1.04 | 0.05 | 0.54 | 0.40 | 0.22 | 0.35 |
| P ₂ O ₅ | 0.22 | 0.20 | 0.18 | 0.43 | 0.33 | 0.34 | 0.15 | 0.19 | 0.43 | 0.16 | 0.09 | 0.08 |
| LOI | 2.78 | 2.13 | 5.06 | 7.03 | 2.91 | 1.48 | 2.68 | 4.31 | 3.93 | 4.25 | 4.83 | 4.11 |
| Total | 100.19 | 100.33 | 99.92 | 99.96 | 99.97 | 99.82 | 99.81 | 99.80 | 100.22 | 100.31 | 100.24 | 100.16 |
| Mg# | 49.9 | 53.5 | 62.3 | 59.7 | 63.6 | 54.8 | 67.6 | 71.7 | 67.8 | 64.7 | 64.8 | 70.5 |
| Zn | 59 | 64 | 55 | 125 | 163 | 82 | 73 | 72 | 55 | 34 | 50 | 45 |
| Cu | 35 | 41 | 24 | n.d. | 105 | 3 | 21 | 54 | 36 | 69 | 15 | 36 |
| Sc | 18 | 20 | 15 | 22 | 32 | 34 | 24 | 30 | 16 | 12 | 15 | 18 |
| Ga | 12 | 16 | 11 | 23 | 19 | 21 | 18 | 19 | 25 | 15 | 14 | 15 |
| Ni | 58 | 60 | 87 | 4 | n.d. | 4 | 2 | 6 | 16 | 31 | n.d. | 4 |
| Co | 29 | 31 | 38 | 19 | 25 | 40 | 21 | 33 | 25 | 25 | 20 | 23 |
| Cr | 336 | 214 | 199 | 12 | 13 | 26 | 22 | 44 | 132 | 144 | 62 | 76 |
| V | 193 | 296 | 161 | 152 | 145 | 242 | 121 | 173 | 109 | 124 | 106 | 116 |
| Ba | 32 | 44 | 29 | 79 | 46 | 87 | 71 | 75 | 63 | 24 | 32 | 28 |
| Pb | 9 | 8 | 10 | 10 | 6 | 8 | 9 | 8 | 10 | 10 | 12 | 8 |
| <i>ICP-MS analyses:</i> | | | | | | | | | | | | |
| Rb | 4.86 | 4.32 | 4.27 | 3.21 | 1.48 | 3.00 | 4.30 | 3.39 | 5.74 | 4.53 | 3.83 | 3.32 |
| Sr | 127 | 120 | 153 | 113 | 81.4 | 348 | 208 | 122 | 983 | 904 | 380 | 585 |
| Y | 17.1 | 23.1 | 15.2 | 20.7 | 20.1 | 28.0 | 18.8 | 21.5 | 11.2 | 7.64 | 10.0 | 9.55 |
| Zr | 79.8 | 77.4 | 73.8 | 147 | 49.4 | 114 | 119 | 80.7 | 146 | 54.7 | 38.4 | 32.7 |
| Nb | 1.69 | 1.73 | 1.35 | 2.32 | 2.20 | 2.73 | 2.13 | 2.24 | 3.72 | 1.21 | 1.53 | 1.26 |
| La | 3.49 | 3.35 | 2.79 | 5.89 | 3.87 | 6.67 | 5.45 | 6.02 | 14.1 | 7.11 | 2.33 | 1.98 |
| Ce | 8.72 | 9.06 | 7.07 | 14.2 | 9.91 | 17.1 | 13.2 | 13.9 | 31.6 | 14.9 | 5.70 | 4.82 |
| Pr | 1.29 | 1.41 | 1.08 | 2.11 | 1.48 | 2.44 | 1.79 | 1.97 | 3.91 | 1.90 | 0.824 | 0.727 |
| Nd | 6.17 | 7.06 | 5.16 | 9.73 | 7.06 | 11.3 | 7.78 | 8.86 | 13.7 | 6.94 | 3.93 | 3.47 |
| Sm | 1.84 | 2.24 | 1.68 | 2.92 | 2.29 | 3.55 | 2.27 | 2.71 | 2.86 | 1.74 | 1.19 | 1.15 |
| Eu | 0.724 | 0.903 | 0.634 | 1.01 | 0.953 | 1.17 | 0.677 | 0.886 | 0.831 | 0.550 | 0.551 | 0.517 |
| Gd | 2.18 | 2.76 | 1.99 | 3.51 | 2.77 | 4.21 | 2.65 | 3.24 | 2.20 | 1.43 | 1.40 | 1.36 |
| Tb | 0.389 | 0.501 | 0.347 | 0.582 | 0.490 | 0.720 | 0.449 | 0.575 | 0.305 | 0.228 | 0.249 | 0.238 |
| Dy | 2.58 | 3.35 | 2.30 | 3.66 | 3.22 | 4.61 | 2.87 | 3.65 | 1.69 | 1.32 | 1.60 | 1.54 |
| Ho | 0.576 | 0.731 | 0.498 | 0.753 | 0.693 | 0.940 | 0.628 | 0.770 | 0.327 | 0.254 | 0.345 | 0.329 |
| Er | 1.60 | 2.11 | 1.42 | 1.95 | 1.90 | 2.59 | 1.80 | 2.15 | 0.814 | 0.682 | 0.982 | 0.920 |
| Tm | 0.246 | 0.322 | 0.219 | 0.279 | 0.282 | 0.370 | 0.267 | 0.313 | 0.113 | 0.102 | 0.148 | 0.141 |
| Yb | 1.59 | 2.05 | 1.45 | 1.80 | 1.77 | 2.32 | 1.78 | 1.92 | 0.734 | 0.646 | 0.961 | 0.918 |
| Lu | 0.234 | 0.303 | 0.215 | 0.249 | 0.247 | 0.312 | 0.259 | 0.266 | 0.104 | 0.095 | 0.144 | 0.136 |
| Hf | 3.27 | 3.48 | 3.20 | 3.29 | 2.10 | 2.35 | 3.15 | 2.28 | 2.90 | 1.66 | 1.79 | 1.50 |
| Ta | 0.158 | 0.189 | 0.142 | 0.195 | 0.167 | 0.197 | 0.144 | 0.182 | 0.253 | 0.130 | 0.121 | 0.123 |
| Th | 0.612 | 0.610 | 0.464 | 0.669 | 0.461 | 0.493 | 0.531 | 0.486 | 1.57 | 1.16 | 0.610 | 0.390 |
| U | 0.255 | 0.204 | 0.211 | 0.346 | 0.120 | 0.171 | 0.133 | 0.154 | 0.350 | 0.222 | 0.190 | 0.140 |
| Nb/Y | 0.10 | 0.07 | 0.09 | 0.11 | 0.11 | 0.10 | 0.11 | 0.10 | 0.33 | 0.16 | 0.15 | 0.13 |
| Zr/Ti | 0.017 | 0.013 | 0.016 | 0.023 | 0.007 | 0.014 | 0.034 | 0.018 | 0.025 | 0.016 | 0.016 | 0.014 |
| (La/Sm) _N | 1.22 | 0.97 | 1.08 | 1.30 | 1.09 | 1.21 | 1.55 | 1.44 | 3.18 | 2.64 | 1.26 | 1.12 |
| (Sm/Yb) _N | 1.29 | 1.21 | 1.29 | 1.80 | 1.43 | 1.70 | 1.42 | 1.57 | 4.33 | 2.99 | 1.38 | 1.39 |
| (La/Yb) _N | 1.57 | 1.17 | 1.39 | 2.35 | 1.57 | 2.06 | 2.20 | 2.25 | 13.7 | 7.89 | 1.74 | 1.55 |
| Sr/Y | 7.42 | 5.20 | 10.0 | 5.47 | 4.06 | 12.4 | 11.1 | 5.69 | 87.4 | 118 | 37.9 | 61.3 |

Appendix Table 4.4 (1/2). Input parameters for the partial melting models used for the different volcanic and subvolcanic rock-types from the Ganj Complex. The compositions of lherzolites EP22, A19, and EP7 are from [Saccani et al. \(2017\)](#). The compositions of average pelitic sediments (APS) and sea water are from [Taylor & McLennan \(1985\)](#) and [Li \(2000\)](#), respectively. The compositions of adakitic melts are calculated from partial melting of an hypothetical eclogite with: chemical composition = N-MORB of [Sun & McDonough \(1989\)](#); modal composition = cpx 0.5 - grt 0.5; melting proportions = cpx 0.7 - grt 0.3. Source mode and melting proportions for the peridotite partial melting are from [Kostopoulos & Murton \(1992\)](#). Abbreviations, ol: olivine; opx: orthopyroxene; cpx: clinopyroxene; spl: spinel; grt: garnet; REE: rare earth elements.

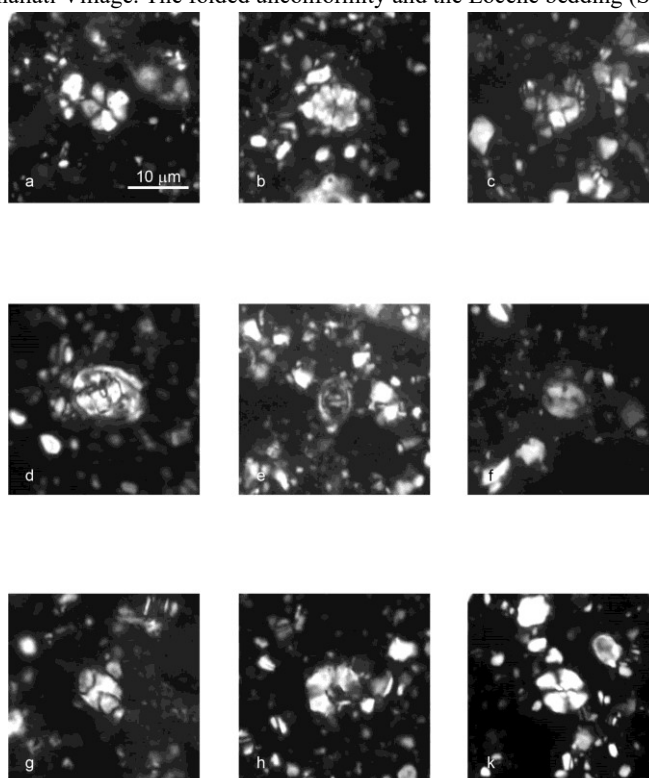
| | Composition of mantle peridotites and subduction-related additional components | | | | | | | Composition of the theoretical mantle sources calculated by the addition of various proportions of subduction-related components to depleted peridotities | | | | | | |
|--|--|------------------------------------|------------------------------|------|-----------|---|---|---|----------|---------------------|----------------------|----------------|----------------|----------------|
| | Slightly depleted lherzolite EP22 | Moderately depleted lherzolite A19 | Very depleted lherzolite EP7 | APS | Sea water | Adakite (1) melt from 3% eclogite melting | Adakite (2) melt from 1% eclogite melting | Group 1a | Group 1b | Group 2 (low La/Yb) | Group 2 (high La/Yb) | Group 3a | Group 3b | |
| | | | | | | | | Mantle peridotite | A19 | EP22 | EP22 | EP22 | EP7 | A19 |
| | | | | | | | | Fluid component | - | - | 0.3% Sea water | 0.5% Sea water | - | 0.5% Sea water |
| | | | | | | | | Melt component | 0.5% APS | 0.7% APS | 0.2% APS | 0.5% APS | 3% adakite (1) | 1% adakite (2) |
| La | 0.026 | 0.018 | 0.001 | 38 | 5.6 | 12.9 | 14.2 | 0.207 | 0.291 | 0.118 | 0.243 | 0.389 | 0.142 | |
| Ce | 0.090 | 0.059 | 0.014 | 80 | 1.6 | 28.9 | 30.9 | 0.459 | 0.649 | 0.254 | 0.497 | 0.881 | 0.309 | |
| Pr | 0.024 | 0.013 | 0.010 | | 0.87 | 3.39 | 3.51 | 0.013 | 0.023 | 0.026 | 0.028 | 0.111 | 0.043 | |
| Nd | 0.179 | 0.106 | 0.114 | 32 | 4.2 | 9.18 | 9.30 | 0.265 | 0.402 | 0.255 | 0.358 | 0.386 | 0.187 | |
| Sm | 0.097 | 0.055 | 0.078 | 5.6 | 0.84 | 1.04 | 1.03 | 0.083 | 0.135 | 0.110 | 0.128 | 0.107 | 0.065 | |
| Eu | 0.047 | 0.030 | 0.036 | 1.1 | 0.21 | 0.346 | 0.343 | 0.035 | 0.054 | 0.050 | 0.053 | 0.045 | 0.033 | |
| Gd | 0.221 | 0.148 | 0.148 | 4.7 | 1.3 | 0.526 | 0.521 | 0.171 | 0.253 | 0.233 | 0.249 | 0.160 | 0.153 | |
| Tb | 0.051 | 0.031 | 0.028 | 0.77 | 0.21 | 0.089 | 0.088 | 0.035 | 0.056 | 0.053 | 0.055 | 0.029 | 0.032 | |
| Dy | 0.384 | 0.246 | 0.204 | | 1.5 | 0.327 | 0.323 | 0.245 | 0.382 | 0.387 | 0.388 | 0.208 | 0.249 | |
| Ho | 0.098 | 0.060 | 0.051 | | 0.45 | 0.065 | 0.064 | 0.059 | 0.097 | 0.099 | 0.099 | 0.051 | 0.060 | |
| Er | 0.300 | 0.183 | 0.147 | | 1.3 | 0.139 | 0.138 | 0.182 | 0.298 | 0.302 | 0.303 | 0.142 | 0.184 | |
| Tm | 0.052 | 0.032 | 0.025 | 0.4 | 0.25 | | | 0.034 | 0.054 | 0.053 | 0.054 | | | |
| Yb | 0.320 | 0.214 | 0.163 | 2.8 | 1.5 | 0.116 | 0.115 | 0.227 | 0.338 | 0.329 | 0.338 | 0.161 | 0.215 | |
| Lu | 0.054 | 0.035 | 0.028 | 0.43 | 0.32 | 0.023 | 0.023 | 0.037 | 0.056 | 0.055 | 0.057 | 0.028 | 0.036 | |
| Cr | 2580 | 2464 | 2677 | | | | | 2568 | 2563 | 2568 | 2556 | 2597 | 2651 | |
| Y | 2.12 | 1.66 | 1.40 | | | | | 2.22 | 2.26 | 2.19 | 2.27 | 1.36 | 1.41 | |
| Source mode: ol 0.65 - opx 0.28 - cpx 0.06 - spl 0.08 | | | | | | | | | | | | | | |
| Melting proportions: ol 0.1 - opx 0.64 - cpx 0.25 - spl 0.02 | | | | | | | | | | | | | | |
| Partition coefficients for mantle peridotites, REE in ol and spl: McKenzie & O'Nions (1991) ; REE in opx and cpx: Fujimaki et al. (1984) ; Y: Ulmer (1989) ; Cr in ol, opx, cpx: Ewart et al. (1973) ; Cr in spl: Klemme et al. (2006) . Partition coefficients for eclogite, REE in cpx and grt: Irving & Frey (1984) . | | | | | | | | | | | | | | |

Appendix Table 4.4. (2/2) *Input parameters for the calculation of the primary melts for Group 1 and Group 2 rocks assuming fractional crystallization, as well as REE compositions of calculated primary melts.*

| | Group 1a | Group 1b | Group 2 (low La/Yb) | Group 2 (high La/Yb) |
|--|---|----------|---|-------------------------|
| Starting differentiated sample | MK17 | MK120 | MK349 | MK118 |
| Modal composition of primary melts | ol 0.5 - pl 0.38 - cpx 0.25 opx 0.2 - hbl 0.1 - spl 0.02 | | ol 0.8 - pl 0.45 - cpx 0.45 opx 0 - hbl 0 - spl 0.02 | |
| Fractionation degree | 40% | 40% | 20% | 25% |
| La | 5.67 | 5.38 | 2.27 | 4.60 |
| Ce | 12.6 | 13.9 | 5.75 | 10.7 |
| Pr | 1.56 | 1.91 | 0.87 | 1.49 |
| Nd | 6.93 | 8.88 | 4.21 | 6.82 |
| Sm | 1.96 | 2.64 | 1.38 | 2.11 |
| Eu | 0.597 | 0.750 | 0.565 | 0.764 |
| Gd | 2.14 | 2.95 | 1.65 | 2.54 |
| Tb | 0.338 | 0.512 | 0.294 | 0.464 |
| Dy | 2.15 | 3.24 | 1.93 | 2.91 |
| Ho | 0.398 | 0.696 | 0.419 | 0.617 |
| Er | 1.16 | 1.99 | 1.20 | 1.72 |
| Tm | 0.166 | 0.271 | 0.178 | 0.241 |
| Yb | 1.13 | 1.86 | 1.21 | 1.53 |
| Lu | 0.164 | 0.283 | 0.197 | 0.213 |
| Partition coefficients from Fujimaki et al. (1984) | | | | |



Appendix Figure 4.1. Geo-panorama showing the field relationships between the Ganj Complex and the unconformable Eocene deposits in the North of the Mahallati Village. The folded unconformity and the Eocene bedding (S_0) are indicated.



Appendix Figure 4.2. Photomicrograph of selected calcareous nannofossils taxa. Light Microscope photographs are in Cross polarized Light. a) *Eprolithus rarus*, sample MK348; b) *Eprolithus floralis*, sample MK348; c) *Quadrum gartneri*, sample MK348; d) *Zeugrhabdotus embergeri*, sample MK349; e) *Zeugrhabdotus diplogrammus*, sample MK349; f) *Tranolithus orinatus*, sample MK442; g) *Calculites sp.*, sample MK354; h) *Nannoconus sp.*, MK348; k) *Watznaueria barnesiae*, sample MK354.

Chapter 5. The Band-e-Zeyarat Ophiolite

Associated manuscript:

Barbero E., Delavari M., Dolati A., Vahedi L., Langone A., Marroni M., Pandolfi L., Zaccarini F., Saccani E., 2020. Early Cretaceous Plume–Ridge Interaction Recorded in the Band-e-Zeyarat Ophiolite (North Makran, Iran): New Constraints from Petrological, Mineral Chemistry, and Geochronological Data. *Minerals*, 10(12), 1100, doi:10.3390/min10121100

5.1. The stratigraphy of the Band-e-Zeyarat ophiolite

The Band-e-Zeyarat ophiolite is bordered by regional-scale strike-slip and reverse fault zones (Figs. 5.1, 5.2a; see also McCall, 1985, 2002). In detail, the dextral strike-slip Jiroft Fault separates this unit from the Ganj Complex to the east, whereas, the reverse Dar-Anar Fault juxtaposes the Band-e-Zeyarat ophiolite to the Durkan Complex in the southeast (Fig. 5.2a). To the west, this ophiolite is unconformably covered by Quaternary deposits, which mask its relationships with the Bajgan Complex (Fig. 5.2a). However, the Band-e-Zeyarat ophiolite is separated from the Bajgan Complex by the N-striking and dextral strike-slip Sabzevaran Fault (Figs. 5.1, 5.2a; McCall, 2002).

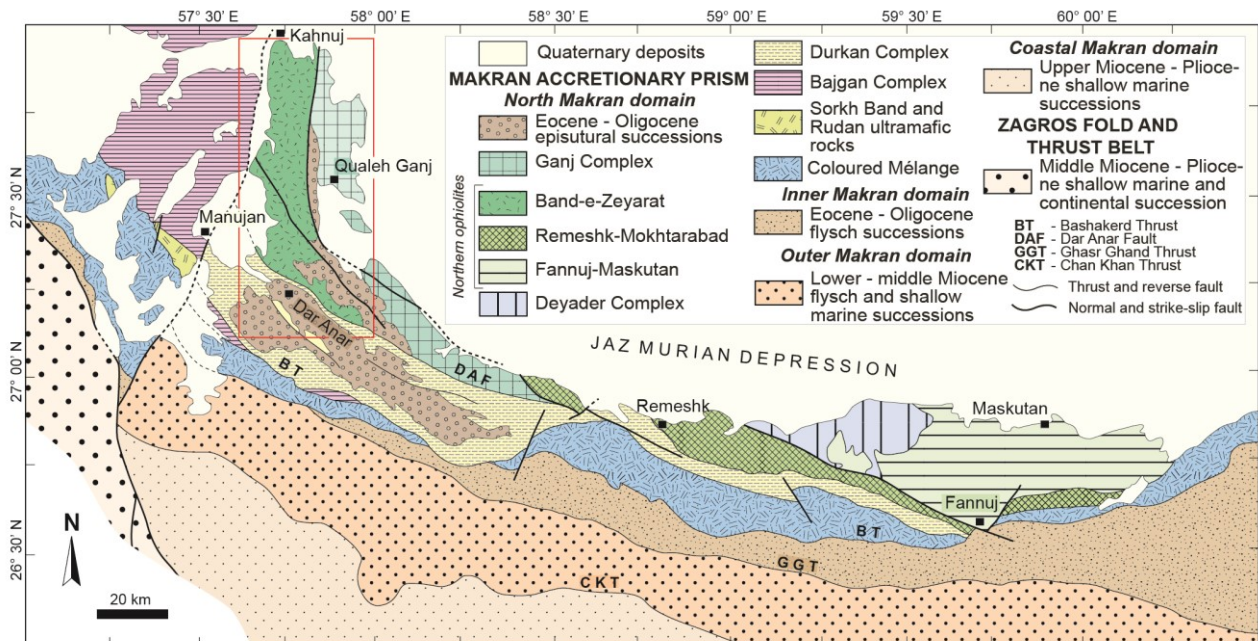


Figure 5.1. Simplified geological map of the North Makran Domain, modified from Eftekhari-Nezhad *et al.* (1979); Eftekhari-Nejad & McCall (1993); Burg (2018); Samimi Namin (1982, 1983). The box indicates the area expanded in Fig. 5.2.

The Band-e-Zeyarat ophiolite has classically been considered as a unique and coherent tectonic unit (e.g., McCall & Kidd, 1982; McCall, 1985; Ghazi *et al.*, 2004). However, it represents a N-S elongated tectonic element in the western North Makran domain, whose continuity is crosscut by several high angle and mainly strike-slip fault zones (Figs. 5.1, 5.2a).

These fault zones also involved the post Eocene siliciclastic successions, which unconformably cover the Band-e-Zeyarat unit (Figs. 5.1, 5.2a). Therefore, it is not possible to clearly understand if the post-Eocene tectonic activity of these faults juxtaposed different ophiolitic units or if these faults only interrupted the N-S continuity of a unique ophiolite unit.

The Band-e-Zeyarat ophiolite includes from bottom to top: 1) a rather thick (more than 5 km) intrusive complex consisting of layered gabbros (in the lower part) that gradually pass upward to isotropic gabbros; 2) a sheeted dyke complex (~1.5 – 2 km); 3) a volcanic sequence up to ~2-3 km thick (Fig. 5.2b). In addition, a mainly carbonatic, pelagic sedimentary cover stratigraphically overlays the volcanic sequence (Fig. 5.2b).

The layered gabbros consist of cumulitic rocks including alternating troctolites, olivine-gabbros, leucogabbros, as well as minor dunites (Fig. 5.2b). This alternation defines a cm- to m-thick magmatic layering (Figs. 5.2b, 5.3a). In addition, the gabbros show a well-developed magmatic foliation, which can be readily recognized in the field and it is defined by the iso-orientation of the mineral assemblages, especially plagioclase and pyroxene (Fig. 5.3b). The isotropic gabbro series mainly consists of isotropic rocks, but cumulitic layers are locally found. This series includes gabbros, olivine-gabbros, ferrogabbros, and diorites (Figs. 5.2b, 5.3c). In addition, small plagiogranitic bodies and dykes can be observed in this series (Fig. 5.2b). Plagiogranites are, however, particularly abundant at the top of the intrusive complex, close to the transition between gabbros and the sheeted dyke complex. In addition, the isotropic gabbros are frequently crosscut by basaltic dykes, which are particularly abundant at the top of the series (Fig. 5.2b).

The sheeted dyke complex consists of mutually intrusive, parallel and sub-parallel dykes showing different colours and grain-sizes (Fig. 5.3d). Their contacts are usually tectonized and fractured, then chilled margins are rarely preserved. Dykes show variable thickness, from

pluridecimeteric to plurimetric and are typically characterized by doleritic texture that can usually be easily recognized in the field (Fig. 5.3e). The volcanic sequence stratigraphically overlays the sheeted dyke complex through a transitional zone composed of pillow lavas and massive lava flows cut by abundant sills and dykes (Fig. 5.2b).

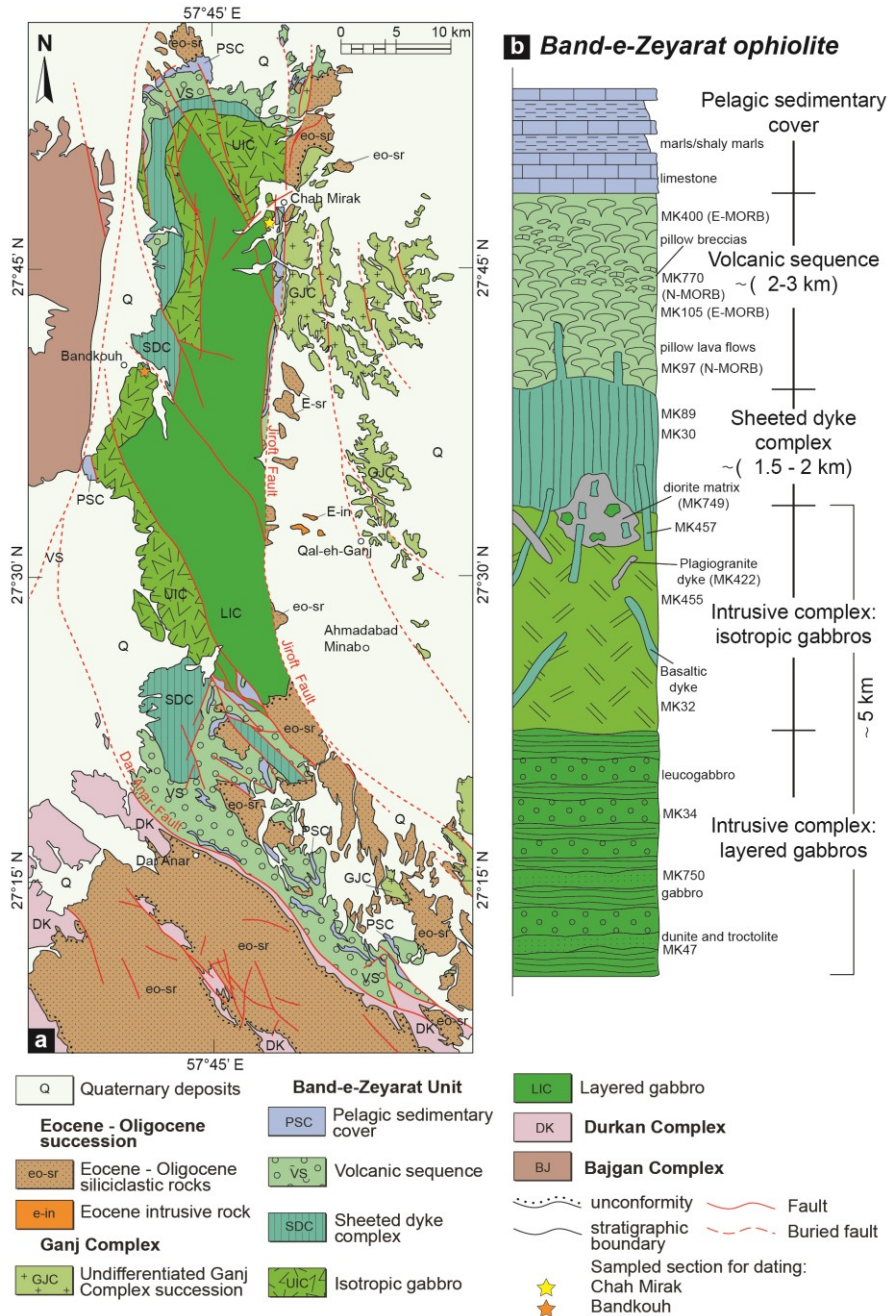


Figure 5.2. a) Simplified geological map of north-western sector of the North Makran domain showing the structural setting of the Band-e-Zeyarat ophiolite (based on Samimi Namin, 1983 and modified according to our original fieldwork and photointerpretation with satellite images); b) schematic stratigraphic column of the Band-e-Zeyarat ophiolite.

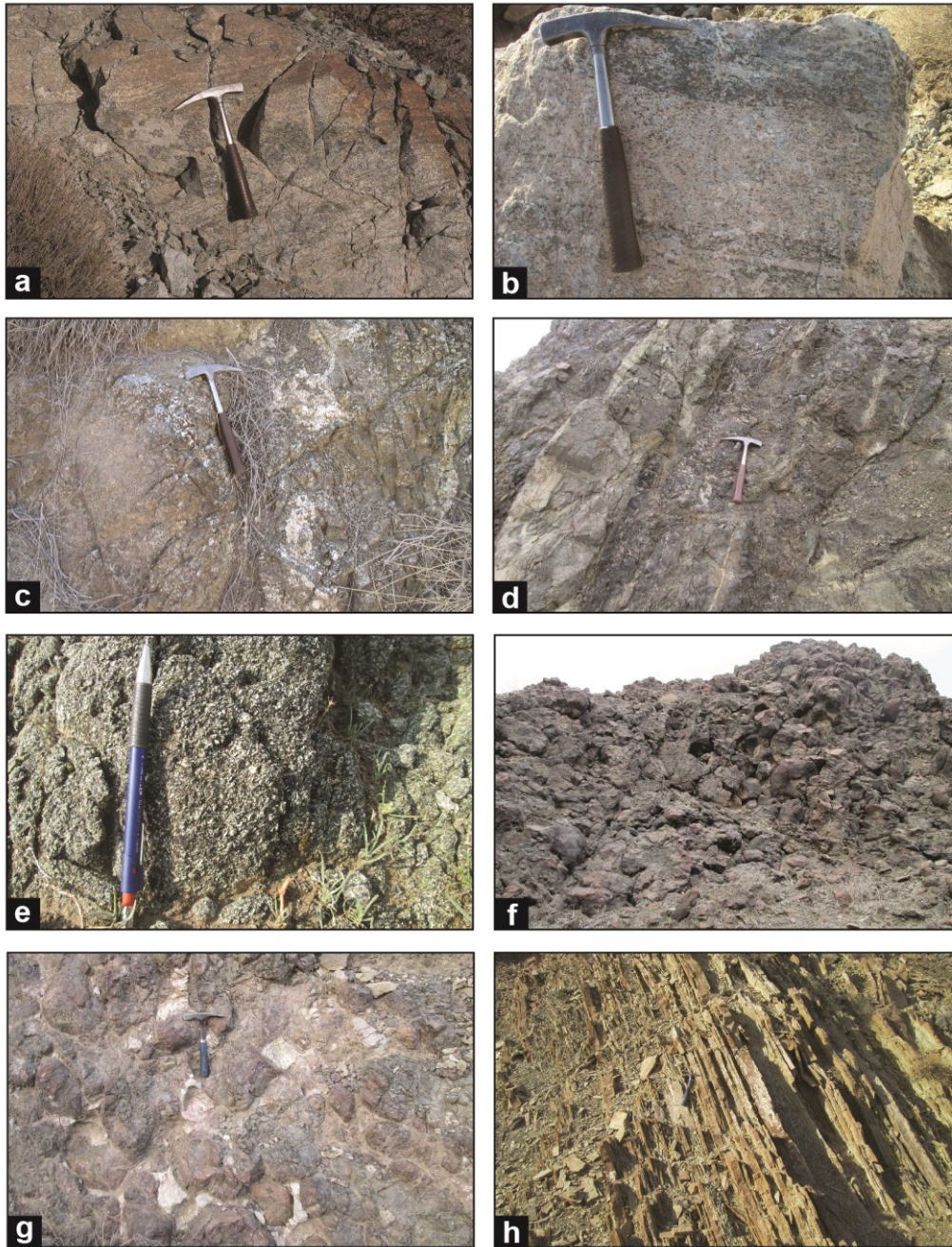


Figure 5.3. Field occurrence of the Band-e-Zeyarat ophiolite: a) cumulitic gabbros from the Layered gabbro (hammer for scale); b) close up of primary magmatic banding defined by the alternation of leucogabbro and gabbro (hammer for scale); c) gabbro from the Isotropic gabbro (hammer for scale); d) vertical and parallel dykes from the sheeted dyke (hammer for scale); e) close up of the doleritic texture of an individual dyke from the Sheeted dyke (pencil for scale); f) pillow lava flows from the Volcanic sequence; g) pillow breccia with clast of whitish limestone (hammer for scale); h) alternating thin beds of limestone and marl from the pelagic sedimentary cover (hammer for scale).

The volcanic sequence is characterized by alternating pillow lava flows up to plurimetric in thickness (Fig. 5.3f) and minor massive lava flows. In addition, pillow breccias are also

interlayered in the sequence at several stratigraphic levels (Fig. 5.2b). They consist of centimetric- to pluridecimetric-sized fragments of pillow basalts as well as pelagic limestones and cherts, which are set in a fine-grained glassy matrix (Fig. 5.3g). Finally, the volcanic sequence is crosscut by randomly distributed individual dykes.

The sedimentary cover consists of alternating whitish to brownish pelagic limestones, shaly marls and shales, as well as minor abundant pinkish limestones and red cherts (Figs. 5.2b, 5.3h). In addition, tabular beds of turbiditic limestone are interlayered in the sequence.

5.2. Sections sampled for plagiogranites suitable for zircon U-Pb geochronological dating

The field investigation was focused on the lithostratigraphic features of the Band-e-Zeyarat ophiolite. Particular attention has been paid for sampling plagiogranitic rocks suitable for zircon U-Pb geochronology. Unfortunately, the study area is affected by abundant acidic dykes associated with Tertiary calc-alkaline magmatism (McCall, 1985), which are sometimes hard to be distinguished in the field from the plagiogranite dykes of the ophiolitic sequence. Therefore, a detailed field investigation proved necessary for unequivocally distinguishing ophiolitic plagiogranites from the Cenozoic acidic dykes. The best plagiogranite outcrops occur at the transition between the gabbro and sheeted dyke complexes. Plagiogranites were sampled in two distinct areas, namely the Chah Mirak and Bandkouh areas (Fig. 5.2a), which were investigated in detail.

5.2.1. The Chah Mirak section

In the Chah Mirak section, the upper part of the intrusive complex is well exposed and crosscut

by both mafic and plagiogranite dykes (Figs. 5.4a, b). Two samples of plagiogranites were taken for geochronological analysis (samples MK422, and MK423). Mafic dykes are intruded into isotropic ferrogabbros (sample MK455) and are up to ~2m thick (Figs. 5.4a, b). They are characterized by porphyritic texture and show chilled margin, indicating intrusion in relatively cold gabbros. In contrast, the plagiogranite dykes show up to metric thickness and crosscut both gabbros and mafic dykes (Figs. 5.4a, b). Plagiogranite dykes commonly intruded along the contacts between gabbros and mafic dykes (Figs. 5.4a, b). Plagiogranite injections caused fragmentation of both gabbros and mafic dykes, producing breccias in which plagiogranite forms the matrix enclosing fragments of both gabbros and mafic dykes (Fig. 5.4c). These fragments are centimetric in size and show sub-angular to rounded margins (Fig. 5.4c). In thin section, the contact between plagiogranites and mafic dyke clasts is rather transitional, not sharp, and show a gradual decrease in grain-size toward the clasts (Fig. 5.4d).

The contact between the plagiogranite dykes and the gabbros is rather sharp but curvilinear. A decrease in the grain-size of plagiogranites toward the contact is locally observed (Fig. 5.4e). The relationships between plagiogranites and mafic dykes, as well as the nature of their contacts suggest that the plagiogranite dykes were emplaced after the mafic dykes, but when the latter were still able to react to the intrusion of the plagiogranite with a ductile behaviour. These data collectively support the primary magmatic relationships between the sampled plagiogranites and the intrusive complex.

5.2.2. The Bandkouh section

In the Bandkouh section, the base of the sheeted dyke complex is characterized by the occurrence of magmatic breccia showing a matrix of plagiogranitic to quartz-dioritic composition

(Fig. 5.2b). Samples MK748 and MK749 used for geochronological dating consist of quartz-

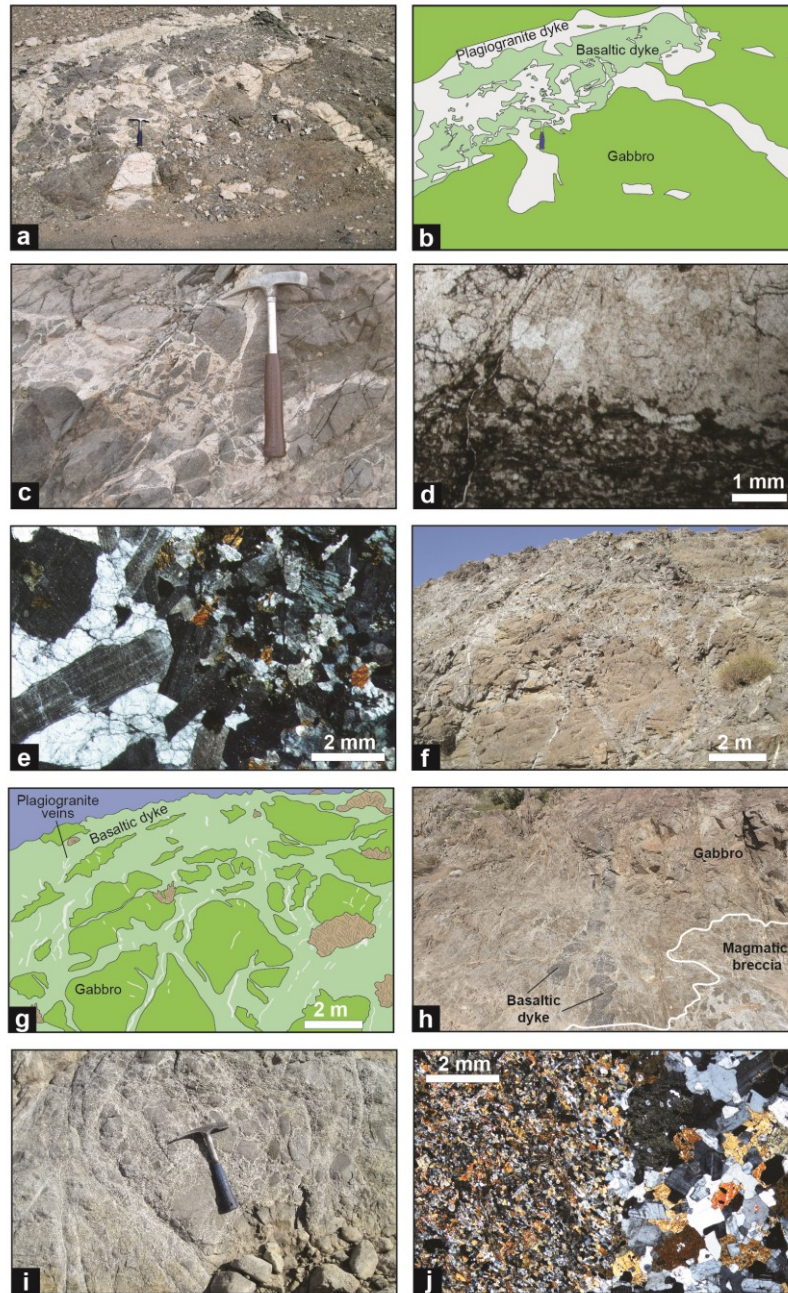


Figure 5.4. Field occurrence and photomicrographs of the sections sampled for zircon dating. (a-e) Chah Mirak section: a) view and (b) schematic sketch of the complex intrusive relationships between isotrope gabbro, mafic dyke and plagiogranite dyke (hammer for scale); c) magmatic breccia showing plagiogranite matrix enclosing sub-angular to rounded clast of both gabbro and mafic dyke (hammer for scale); d) photomicrographs of the contact between matrix and clast in the magmatic breccia; e) photomicrograph of the curvilinear contact between the plagiogranite and the gabbro; (f-j) Bandkouh section: f) view and (g) schematic explanatory drawing of the transition zone between the Isotropic gabbro and the sheeted dyke showing a network of basaltic dykes crosscutting the gabbro screen. White plagiogranite veinlets crosscut both the gabbro and the dykes; h) magmatic breccia bodies within the gabbro (hammer for scale); i) close-up view of the magmatic breccia showing sub-angular to rounded clasts set within plagiogranite matrix. Plagiogranite veinlets are injected in the clasts from the matrix (hammer for scale); j) gradual intrusive contact between plagiogranite matrix and micro-gabbro clasts in the magmatic breccia.

diorites taken from the matrix of this breccia. The lower part of this section shows lens-shaped bodies of magmatic breccias, which can reach up to tens of metres in thickness (Fig. 5.4f). The upper part of this section is characterized by a network of mafic dykes crosscutting the gabbro screens (Figs. 5.2b, 5.4g, h). Dykes gradually increase in abundance upward and progressively replace the gabbros up to form a pure sheeted dyke complex. The magmatic breccias show anastomosed contacts with the gabbros (Fig. 5.4f), and consist of plagiogranite matrix, which enclose up to metric enclaves of gabbros and mafic dykes (Fig. 5.4i). The mafic enclaves show lobate to sub-angular shape, and their margins are quite sharp but generally rounded (Fig. 5.4i). The enclaves are locally cut by a network of millimetric veins of plagiogranite, which are clearly injected from the matrix (Fig. 5.4i). In this case, the contacts between veins and enclaves are curvilinear with no clear grain variation and chilled margin (Fig. 5.4j). In addition, in this portion of the transition zone, the gabbros are characterized by small (<few cm) veins of plagiogranite that are clearly injected into the gabbros from the breccia matrix. These observations suggest primary magmatic relationship between plagiogranites and mafic rocks. Plagiogranite melts were localized in the uppermost part of the intrusive complex and were injected into the transition zone between the intrusive and the sheeted dyke complexes. This process produced magmatic breccias and plagiogranite veinlets into the already crystallized but likely still hot gabbros. Similar magmatic breccias are found in the Oman ophiolites at the transition between the intrusive and sheeted dyke complexes, as well as in other ophiolitic complex. They have been interpreted as forming in a typical mid-oceanic ridge magma chamber, in consequence of the interaction of coeval different magmatic liquids (Stake & Taylor, 2009; Rollinson, 2009).

5.3. Petrography of the magmatic rocks

Most of the studied rocks are affected by various degrees of low-grade ocean-floor hydrothermal alteration. Alteration has produced the replacement of the primary igneous phases, whereas the primary igneous textures are always well preserved. In general, olivine is completely replaced by iddingsite and/or serpentine in volcanic and subvolcanic rocks, whereas it is preserved only in intrusive rocks. Plagioclase is commonly pseudomorphosed by albite and/or phyllosilicate aggregates, even though some samples of intrusive rocks show fresh plagioclase. Clinopyroxene alteration normally occurs as pseudomorphic replacement by brown amphibole. This is more common in volcanic and subvolcanic rocks, whereas fresh pyroxene generally occurs in the intrusive rocks. However, rims of crystals are locally replaced by amphibole also in the intrusive rocks. The volcanic glass in the groundmass of volcanic rocks is commonly replaced by fine-grained assemblages of chlorite and clay minerals.

In the layered intrusive complex, rocks are characterized by holocrystalline, medium- to coarse-grained, cumulitic texture. They range in composition from dunites to troctolites, olivine-gabbros, gabbros, and leucogabbros. Dunites consist of completely serpentinized olivine crystals, usually bordered by oxide rims (Fig. 5.5a). In addition, relicts of altered clinopyroxene occur and they likely represent intercumulus phases. Troctolites show rounded olivine crystals (40-60%), subhedral plagioclase (60-40%) together with minor clinopyroxenes and rare altered spinels (Fig. 5.5b). Plagioclase crystals locally enclose olivine, whereas anhedral clinopyroxene crystals occur in interstitial spaces (Fig. 5.5b). The crystallization order is: olivine + plagioclase + clinopyroxene that is the typical crystallization order of MORB-type rocks (Beccaluva et al., 1983).

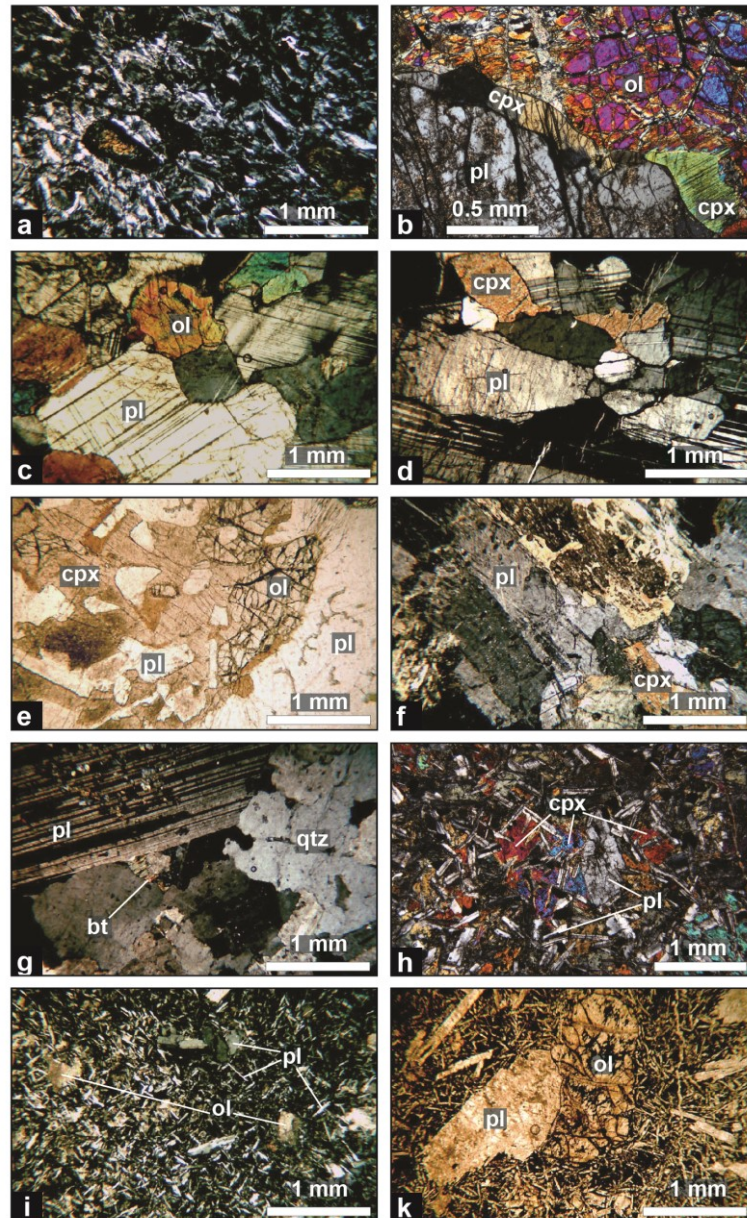


Figure 5.5. Photomicrographs of intrusive (a-g), sub-volcanic (h), and volcanic (i-j) rocks from the Band-e-Zeyarat ophiolite: a) serpentinized dunites showing relicts of magmatic olivine; b) cumulitic texture in troctolite showing large olivine and plagioclase crystals and intercumulus clinopyroxene; c) cumulitic texture in gabbro showing rounded olivine crystals and subhedral plagioclase; d) cumulitic leucogabbro showing intercumulus clinopyroxene and magmatic foliation define by preferential orientation of plagioclase crystals; e) hypidiomorphic texture in gabbro showing crystallization order olivine + plagioclase + clinopyroxene; f) autoallotriomorphic texture showing subhedral plagioclase and clinopyroxene; g) euhedral plagioclase and anhedral quartz in plagiogranite; h) subophitic texture in basaltic dyke from the sheeted dyke; i) aphyric and weakly porphyritic (k) pillow lava showing intersertal texture with plagioclase microlite set in altered volcanic glass. Abbreviations, ol: olivine; pl: plagioclase; cpx: clinopyroxene; bt: biotite; qtz: quartz.

Gabbros range from olivine-gabbro to gabbro and leucogabbro according to the modal contents of olivine and plagioclase. Olivine crystals (from 10 to 30% in volume) show rounded shape and

are surrounded by subhedral plagioclases (Fig. 5.5c) and anhedral clinopyroxene. In addition, subordinate Fe-Ti oxides also occur in interstitial positions. Leucogabbros are composed by subhedral plagioclase (70-80% of the modal composition) and interstitial clinopyroxene (30-10%) (Fig. 5.5d), as well as subordinate olivine and spinel (<10%). They commonly show magmatic foliation defined by the parallel orientation of plagioclase laths (Fig. 5.5d). The rocks from the isotropic gabbro show a wide range of variation in grain-size, from coarse- to fine-grained. They include gabbros, ferrogabbros and diorites showing granular texture ranging from hypidiomorphic to autoallotriomorphic. Hypidiomorphic gabbros show euhedral olivine, often enclosed in subhedral plagioclase crystals (Fig. 5.5e). In addition, large (i.e., plurimillimetric) clinopyroxene oikocrysts enclose both olivine and plagioclase (Fig. 5.5e), defining the crystallization order as: olivine + plagioclase + clinopyroxene. Autoallotriomorphic textures are characterized by subhedral plagioclase and clinopyroxene and minor olivine (Fig. 5.5f). The ferrogabbros typically show interstitial Fe-Ti oxides, whereas diorites have biotite and rare quartz in interstitial position. The plagiogranite dykes are medium-grained and show holocrystalline and hypidiomorphic texture (Fig. 5.5g). They are composed of euhedral plagioclase, surrounded by anhedral quartz and minor amphibole (Fig. 5.5g), usually pseudomorphosed by chlorite. In addition, rare small crystal of epidote, biotite and zircon occur in interstitial position.

Basaltic dykes, either individual dykes in the intrusive complex or sheeted dykes, show medium- to fine-grained holocrystalline texture. Commonly, these rocks are characterized by subophitic texture with plagioclase laths partially enclosed within clinopyroxene crystals, as well as interstitial Fe-Ti oxides and rare altered olivine crystals (Fig. 5.5h). Some samples show intergranular texture with plagioclase laths and granular clinopyroxene. Basaltic pillow lavas show both aphyric and weakly porphyritic (PI ~10) textures (Figs. 5.5i, k). The aphyric varieties are hypocrystalline and show intersertal texture with plagioclase laths and minor olivine set in an

altered volcanic glass (Fig. 5.5i). In contrast, the porphyritic basaltic rocks show plagioclase and olivine phenocrysts, up to 3 mm in size, set in a hypocrystalline groundmass (Fig. 5.5k). The groundmass commonly shows intersertal texture with plagioclase laths and olivine microliths surrounded by altered volcanic glass (Fig. 5.5k). Few samples also show amygdaloidal texture defined by rounded vesicles filled by calcite.

5.4. Geochemistry of the magmatic rocks

The description of the geochemical features of the magmatic rocks studied in this Chapter is based on those elements considered virtually immobile during alteration processes (Pearce & Norry, 1979; Pearce, 2014). They include some incompatible elements (e.g., Ti, P, Zr, Y, Nb, Ta, Hf, Th), middle (MREE) and heavy (HREE) rare earth elements (REE), as well as some transitional metal, such as Ni, Cr, V, Co. In contrast, light REE (LREE), large ion lithophile elements (LILE, e.g., Ba, Sr, Rb) and most major elements are usually sensitive to secondary alteration processes. Therefore, these elements were plotted against immobile elements (e.g., Zr or Y) and the correlation coefficients were calculated in order to check their amount of mobilization (not shown). These tests returned fairly good correlation for LILE, CaO, and MgO in most of the samples, suggesting that these elements can be used, though with some caution. In contrast, the good correlation coefficients for LREE suggest no or very little re-mobilization of these elements during secondary alteration processes.

5.4.1. Intrusive complex

As outlined in the previous sections, the intrusive complex includes a variety of different rock-

types showing either cumulitic or isotropic texture. Cumulitic rocks range from dunites to troctolites, olivine-gabbros, gabbros, and leucogabbros, whereas the isotropic varieties include gabbros, ferrogabbros, diorites, quartz-diorites, and plagiogranites (Appendix Table 5.1). The large variation in the geochemistry of these rocks suggests that they were formed at different stages of magmatic fractionation. In fact, the variation of their geochemistry is in accordance with the variation of the modal composition, as also evidenced by the co-variation of $\text{Al}_2\text{O}_3/\text{TiO}_2$ against $\text{Ti}/1000$ (assumed here as an indicator of differentiation) shown in Figure 5.6. In this figure and in

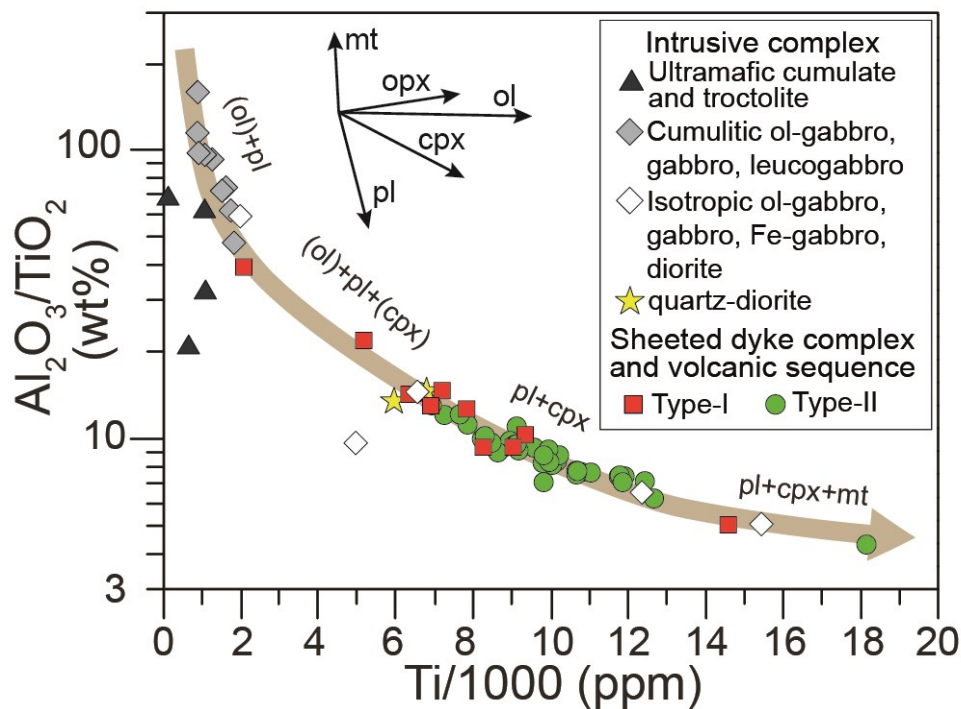


Figure 5.6. $\text{Al}_2\text{O}_3/\text{TiO}_2$ vs. $\text{Ti}/1000$ diagram for magmatic rocks from the Band-e-Zeyarat ophiolite. Arrows show the fractional crystallization trends of magnetite (mt), orthopyroxene (opx), olivine (ol), clinopyroxene (cpx), and plagioclase (pl).

agreement with petrographic observations, the intrusive rocks plot along a differentiation trend defined by the crystallization of olivine + plagioclase + clinopyroxene + magnetite (Fig. 5.6), which is the typical crystallization order of tholeiitic magma series with mid oceanic ridge (MOR) affinity (Beccaluva et al., 1983).

Ultramafic cumulates and troctolites display low TiO_2 , P_2O_5 , and incompatible element contents, such as Nb, Y, and Zr, whereas MgO, Cr, Co, and Ni contents are particularly high (Appendix Table 5.1). The troctolites MK750 and MK781 display a wide range of variation in the contents of Al_2O_3 (5.50 – 10.60 wt%), MgO (23.50 – 32.07 wt%), CaO (4.20 – 8.00 wt%), and Cr (683 – 1926 ppm), which are depending on the mutual abundance of plagioclase and olivine, as observed by the petrographic study. Ultramafic cumulates consist of dunites with high MgO (37.83 – 38.03 wt%) and Cr (2287 – 3146 ppm). The dunite MK47 shows severe depletion in incompatible elements (about 0.01 times N-MORB composition) and REE (about 0.1 times Chondrite abundance (Figs. 5.7a, b)). In contrast, dunite MK40 shows comparatively higher incompatible elements and REE contents, which are broadly comparable to those of the cumulitic gabbros (Fig. 5.7a). Both dunite samples do not show any Eu anomaly (Fig. 5.7b). Cumulitic gabbros show a wide range of variation in the contents of many major and trace elements, which clearly reflect the variation of the modal amounts of rock-forming minerals. In particular, Al_2O_3 (14.50 – 23.60 wt%), MgO (7.50 – 17.34 wt%), and Cr (337 – 1927 ppm) are among those elements showing the largest variations. Mg# is also variable (91 - 76), but generally high (around 84 in most sample). In contrast, TiO_2 , P_2O_5 , and other incompatible elements contents are low, showing values by far lower than 1 times N-MORB composition (Sun & McDonough, 1989). In the chondrite-normalized REE diagram all gabbroic rocks show marked Eu positive anomalies (Fig. 5.7b), reflecting large amount of plagioclase early crystallization and accumulation (Fig. 5.6). The REE patterns for the leucogabbros and gabbros MK32 and MK35 are quite flat with slight LREE and MREE enrichment with respect to HREE (Fig. 5.7b), as testified by $(\text{La}/\text{Yb})_N$ and $(\text{Sm}/\text{Yb})_N$ ratios slightly higher than 1 (Appendix Table 5.1). In contrast, gabbro MK44 shows an LREE-depleted pattern that is comparable with the REE patterns of typical N-MORB (Sun & McDonough, 1989).

The isotropic mafic rocks range from gabbro to ferrogabbro and diorite with Mg# ranging from 83 to 51. They show a wide variation of TiO₂, P₂O₅, Zr, Nb, and Y contents, likely reflecting different, progressive degrees of fractionation (Appendix Table 5.1, Fig. 5.6). This is also suggested by the high variation of compatible elements contents, such as Cr, Co, and Ni (Appendix Table 5.1). In addition, V contents are extremely variable in the isotropic intrusive rocks, showing the lowest values in olivine-gabbro and a very high value in the ferrogabbro (Appendix Table 5.1). N-MORB normalized incompatible elements spider diagrams show two distinct patterns for the

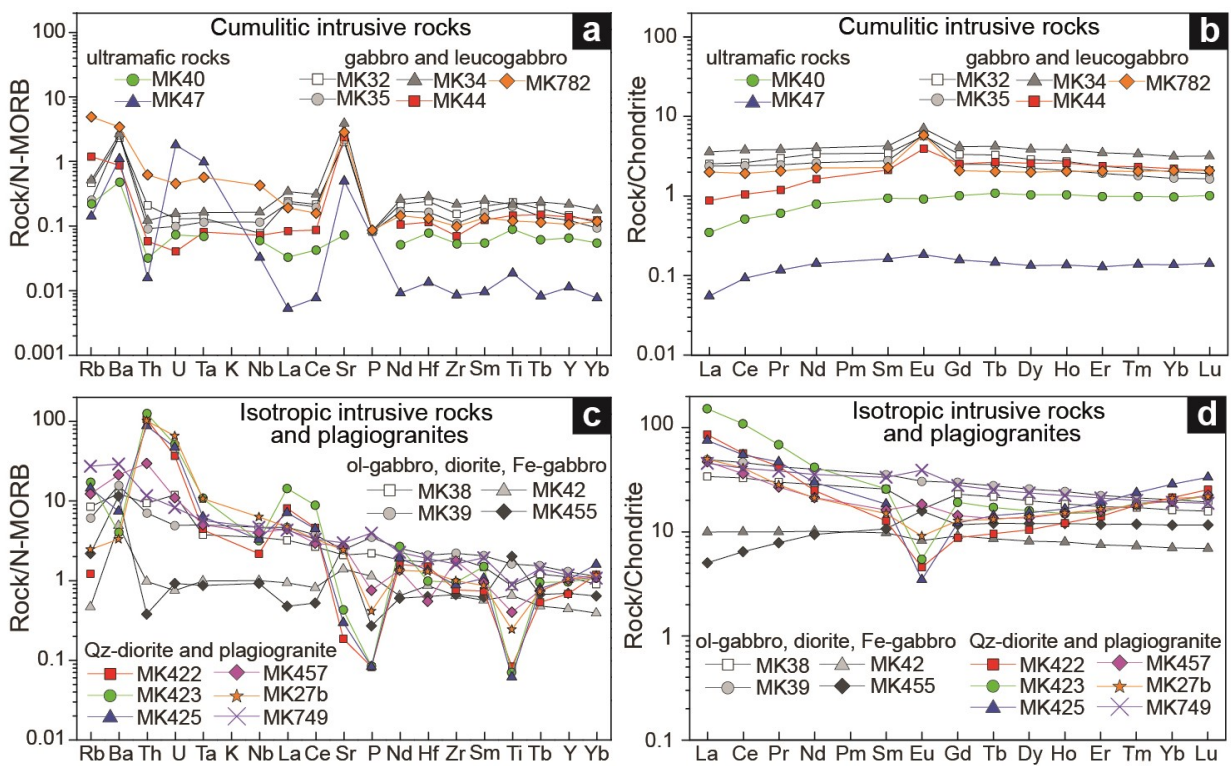


Figure 5.7. N-MORB (normal-type mid-ocean ridge basalt) normalized incompatible element patterns (a, c) and Chondrite-normalized rare earth element (REE) patterns (b, d) for mafic and ultramafic cumulates, isotropic mafic rocks, Quartz-diorites, and plagiogranites from the intrusive complex (Layered gabbro and Isotropic gabbro) from the Band-e-Zeyarat ophiolite. Normalizing values are from Sun & McDonough (1989)

isotropic intrusive rocks (Fig. 5.7c). In detail, ferrogabbro MK455 show rather flat patterns, with normalized values lower than 1 times N-MORB composition (Fig. 5.7c), whereas the olivine-gabbro MK42 and diorites MK38, MK39 display regularly decreasing pattern from LILE to HFSE

(high field strength elements) (Fig. 5.7c). Accordingly, ferrogabbro MK455 shows a chondrite-normalized REE pattern with marked depletion of LREE with respect to MREE and HREE (Fig. 5.7d). Samples MK42, MK38, and MK39 show REE pattern, gradually decreasing from LREE to HREE (Fig. 5.7d). Different extents of negative anomalies of Eu are observed in all these samples, likely reflecting different amount of early crystallization and fractionation of plagioclase (Fig. 5.7d).

The plagiogranitic rocks range in composition from quartz-diorites ($\text{SiO}_2 = 56.50 - 58.30$ wt%; $\text{Mg\#} = 61 - 49$) to highly differentiated plagiogranites ($\text{SiO}_2 = 63.60 - 74.20$ wt%, $\text{Mg\#} = 56 - 32$). Accordingly, the contents of many major and trace elements show a wide range of variation. For example, TiO_2 , P_2O_5 , MgO , Ni, Cr, and Co contents are relatively high in the quartz-diorites and very low in plagiogranites (Appendix Table 5.1). In the N-MORB normalized incompatible elements spider diagrams, plagiogranites show different patterns (Fig. 5.7c). The majority of the samples show different extents of Ti, P, Nb negative anomalies, as well as LILE enrichment with respect to HFSE. HFSE display rather low values ranging from 0.8 to 1.9 times N-MORB composition (Fig. 5.7c). In the chondrite-normalized REE diagram (Fig. 5.7d), the quartz-diorite MK749 displays a regularly decreasing pattern from La to Yb, whereas the plagiogranites show U-shaped patterns with MREE depletion with respect to LREE and HREE, which is likely associated with the fractional crystallization of amphibole. In addition, most of the samples display Eu negative anomalies (Fig. 5.7d), suggesting abundant crystallization and removal of plagioclase before their formation.

In conclusion, the geochemistry of the cumulitic rocks from the Band-e-Zeyarat ophiolite is mainly controlled by the amount of cumulus minerals and, therefore, does not represent the composition of a magmatic liquid. Nonetheless, the overall geochemical features of these rocks point out for crystallization and mineral removal from parental liquids with MORB affinity

(Beccaluva et al., 1983). In contrast the chemistry of isotropic gabbros most likely reflect the composition of magmatic liquids, as particularly suggested by the REE compositions with HREE composition >10 times chondrite abundance (Fig. 5.7d). The overall geochemical features indicate that some of the studied gabbroic rocks are comparable with the composition of N-MORBs (MK431 and MK455), whereas some other intrusive rocks have compositions similar to those of enriched-type MORB (E-MORB) rocks (MK42, MK38, and MK39).

The overall geochemical features of quartz-diorites and plagiogranites indicate that they represent differentiated products from primitive MORB-type tholeiitic melts, whose composition was similar to those of the Band-e-Zeyarat basalts. This hypothesis well agrees with field observation, which point out for co-magmatic relationships between plagiogranites and isotropic gabbros. However, plagiogranites represent the product of crystallization of extremely fractionated melts. Therefore, it is impossible to assess if they bear normal-type or enriched-type MORB affinity. In contrast, quartz-diorites MK748 and MK749 show overall geochemical features and REE compositions that are well comparable with those of E-MORB type rocks (Fig. 5.7d).

5.4.2. *Sheeted dyke complex, volcanic sequence, and individual dykes*

No geochemical differences can be observed between the individual dykes intruded into the intrusive complex, the dolerites forming the sheeted dyke complex, and the basaltic rocks in the volcanic sequence (Appendix Table 5.2); therefore, in this section I describe together their geochemical features regardless of their distribution in the stratigraphic succession. Subvolcanic and volcanic rocks are mainly represented by basalts, subordinate basaltic andesites and andesites, as well as one rhyolitic dyke (Fig. 5.8). They show variable but relatively low Nb/Y ratios that suggest a sub-alkaline nature (Fig. 5.8). Mg# (76.1 – 40.6), CaO (2.1 – 12.5 wt%), Al₂O₃ (11.4 –

18.4 wt%), MgO (1.2 – 14.4 wt%), TiO₂ (0.35 – 3 wt%), and P₂O₅ (0.06 – 0.54 wt%) are extremely variable, suggesting that these rocks represent melts at different stages of fractionation. This feature is also suggested by the high variability of compatible elements (e.g., Cr, Ni, Co, and V) contents, which generally decrease in abundance from the basalts to the more differentiated basaltic andesites and rhyolites (Appendix Table 5.2). In detail, the co-variation diagram of Al₂O₃/TiO₂ against Ti/1000 mainly point out for a fractionation trend dominated by the progressive crystallization of olivine, plagioclase, plagioclase + clinopyroxene, and finally, magnetite (Fig. 5.6). This evidence, combined with the low Nb/Y ratios, suggest the same sub-alkaline and tholeiitic nature for all the magmatic rocks from the sheeted dyke complex and the volcanic sequence. However, based on incompatible elements and REE compositions, two geochemical types can be distinguished (hereafter Type-I, and Type-II). These different geochemical types are observed in both the volcanic sequence and the sheeted dyke complex. However, it is worth to outline that we observed, as a general tendency, that the Type-II rocks are more abundant than the Type-I rocks in the upper part of the volcanic sequence.

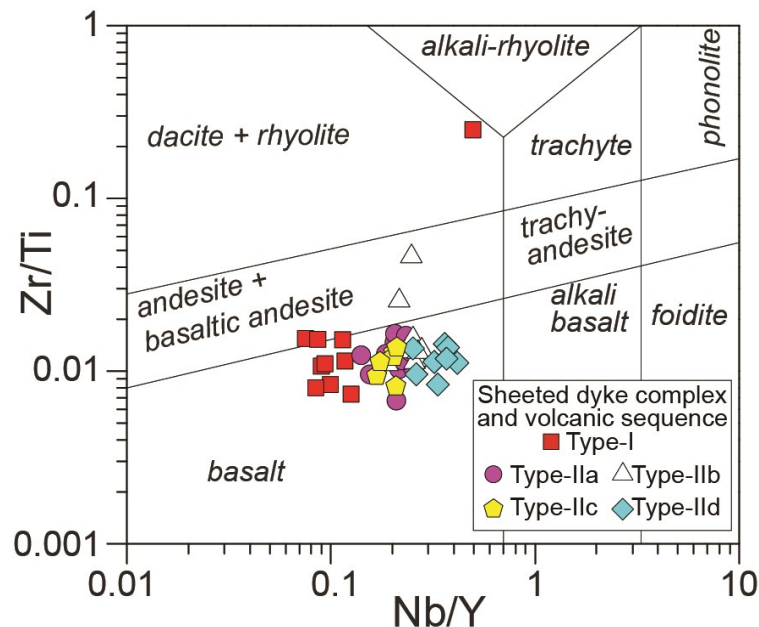


Figure 5.8. Nb/Y vs. Zr/Ti discrimination diagram of Winchester & Floyd (1977) modified by Pearce (1996) for sub-volcanic and volcanic rocks from the sheeted dyke complex and volcanic sequence of the Band-e-Zeyarat ophiolite.

5.4.2.1. Type-I volcanic and subvolcanic rocks

Type-I includes basaltic rocks and one rhyolitic dyke (Appendix Table 5.2; Fig. 5.8). The basaltic rocks display relatively low Nb/Y ratio (0.08 – 0.11) and they are characterized by generally low abundance of Y (15.0 – 50.7 ppm), Zr (55.4 – 143 ppm), Nb (1.36 – 5 ppm), Th (0.063 – 0.611) and Ta (0.090 – 0.440 ppm) (Appendix Table 5.2). The rhyolite MK92 has, in contrast, higher concentration of these incompatible elements, reflecting its differentiated nature (Appendix Table 5.2). In the N-MORB normalized incompatible elements spider diagram (Fig. 5.9a), the basaltic rocks show rather flat pattern, with slightly positive anomalies in Ti, and low concentration of HFSE and LILE, which range from ~0.35 to 1.51 and 0.55 to 5 times the N-MORB composition (Sun & McDonough, 1989), respectively. Chondrite-normalized REE patterns of basaltic rocks (Fig. 5.9b) are rather flat from MREE to HREE, whereas LREE are characterized by variable extent of depletion in comparison with MREE (Figs. 5.9b, 5.10a). These features are exemplified by the Sm_N/Yb_N and La_N/Sm_N ratios, which are in the range 0.93 - 1.41 and 0.34 – 0.97, respectively. Samples MK29 and MK713 show positive Eu anomaly and slightly negative Eu anomaly, respectively (Fig. 5.9b). These features are well comparable with those of typical N-MORB (Sun & McDonough, 1989). The rhyolite MK92 is characterized by marked Eu negative anomaly, reflecting early crystallization of plagioclase. It shows a rather flat MREE - HREE pattern, with HREE contents of ~1.8 times chondrite abundance, whereas the LREE are strongly enriched with respect to MREE, as testified by the high $(La/Sm)_N$ ratios (Fig. 5.9b; Appendix Table 5.2). These geochemical features suggest that the rhyolite can represent the product of differentiation processes of a N-MORB-like primary melt. In the discrimination diagram in Figure 5.10b, the Type-I basalts plot close to the composition of N-MORBs (Saccani, 2015), whereas the differentiated rocks (i.e., the basaltic andesites and rhyolite) plot at higher $Nb_N - Th_N$ values, along

the trend calculated for fractional crystallization starting from an N-MORB primary melt.

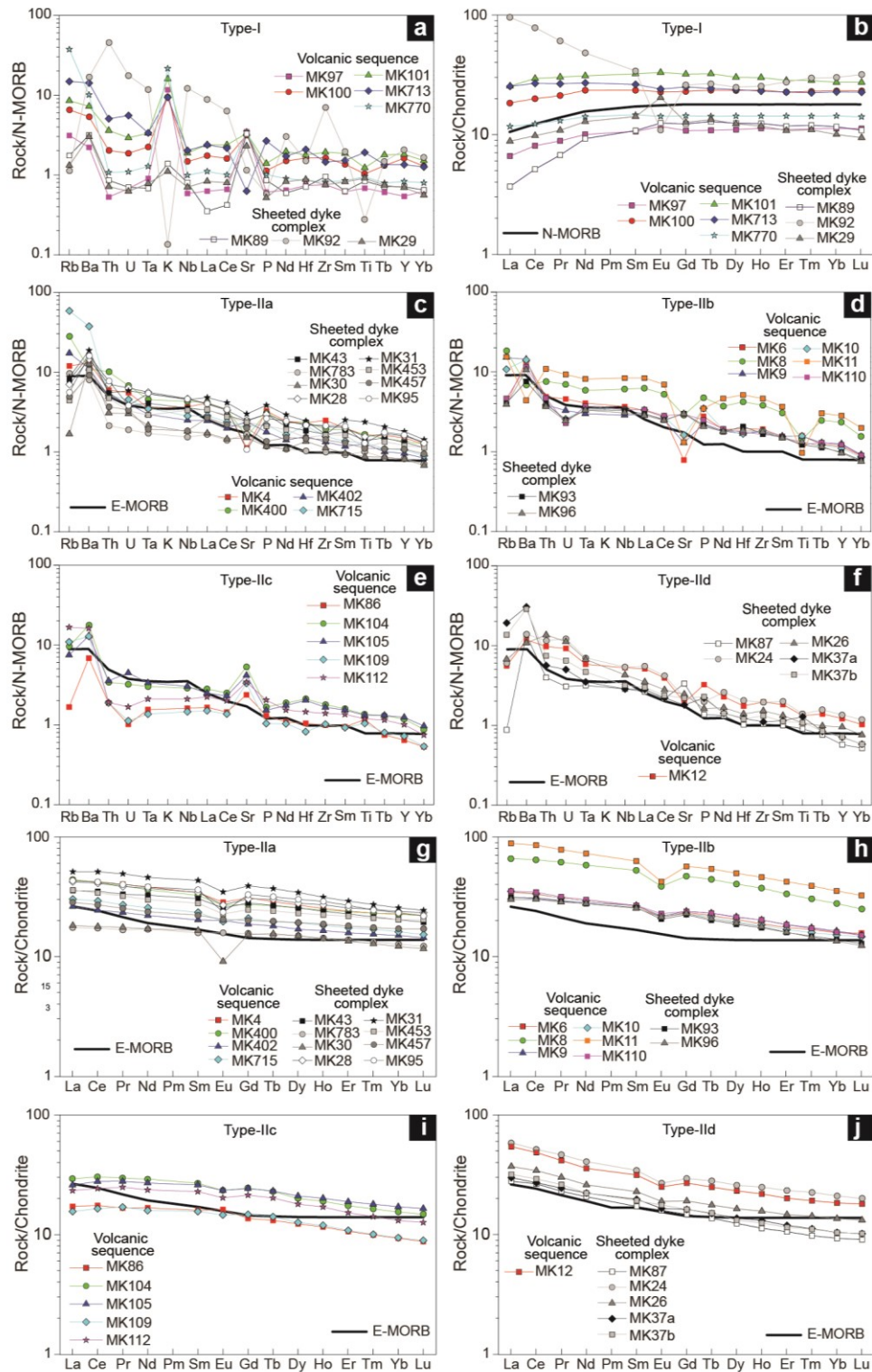


Figure 5.9. N-MORB (normal-type mid-ocean ridge basalt) normalized incompatible element patterns (a, c-f) and Chondrite-normalized rare earth element (REE) patterns (b, g-j) for volcanic and sub-volcanic rocks from the sheeted dyke complex and volcanic sequence of the Band-e-Zeyarat ophiolite. Normalizing values and N-MORB and E-MORB compositions are from [Sun & McDonough \(1989\)](#).

5.4.2.2. Type-II volcanic and subvolcanic rocks

Type-II volcanic rocks include mainly basalts and subordinate basaltic andesites and andesites (Fig. 5.8). Type-II is characterized by Nb/Y ratios ranging from 0.14 to 0.42 (Fig. 5.8). Nb (3.59 – 19.46 ppm), Zr (72.3 – 340 ppm), Th (0.22 – 1.31 ppm), Ta (0.18 – 1.07 ppm), and Y (17.8 – 78.2 ppm) contents are generally higher than those of Type-I rocks.

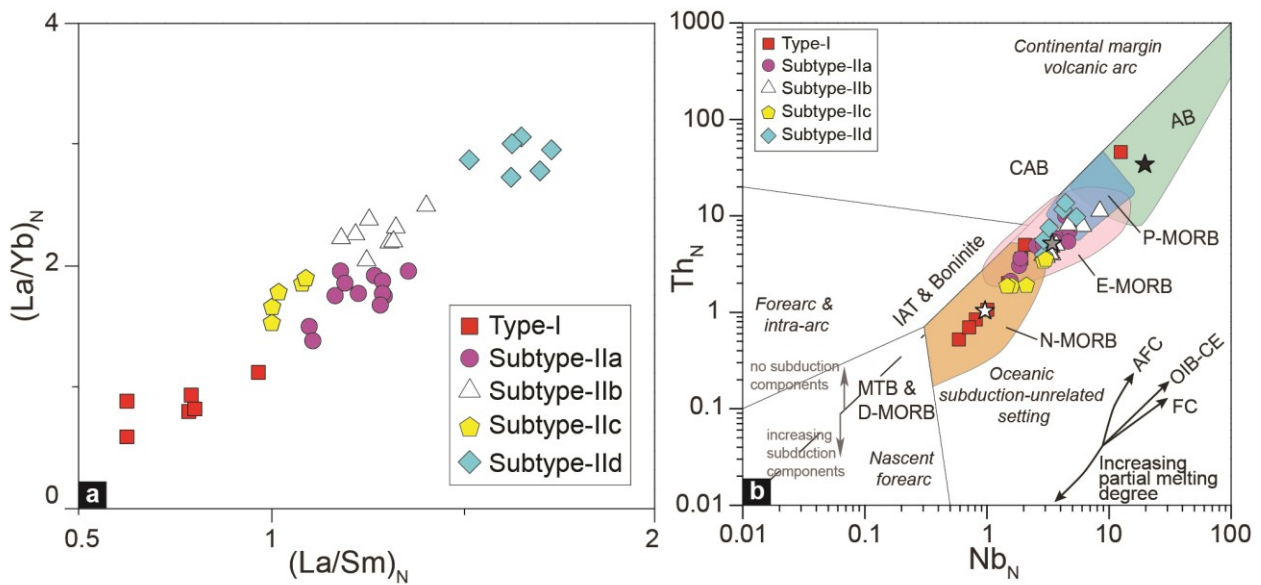


Figure 5.10. Chondrite-normalized $(La/Sm)_N$ vs. $(La/Yb)_N$ diagram (a) and N-MORB normalized Th vs. Nb discrimination diagram of Saccani (2015) (b) for volcanic and subvolcanic rocks from the sheeted dyke complex and volcanic sequence of the Band-e-Zeyarat ophiolite. Vectors in (b) indicate the trends of compositional variations due to the main petrogenetic processes. Abbreviations: AFC: assimilation-fractional crystallization; OIB-CE: ocean island-type (plume-type) component enrichment; FC: fractional crystallization; MORB: mid-ocean ridge basalt; N-: normal type; E-: enriched type; P-: plume type; D-: depleted type; IAT: island arc tholeiite; CAB: calc-alkaline basalt; AB: alkaline oceanic within-plate basalt; MTB: medium titanium basalt. Normalizing values, as well as the composition of typical N-MORB (white star), E-MORB (grey star), and OIB (black star) are from Sun & McDonough (1989).

The N-MORB normalized incompatible element patterns are characterized by LILE enrichment with respect to HFSE, with regularly decreasing pattern from Th to Y (Figs. 5.9c, d, e, f). These elements range from 2 to 14 and 0.5 to 3 times N-MORB abundance, respectively. Only few differentiated samples display different extents of negative anomalies in Ti, likely reflecting the fractionation of Fe-Ti oxides (Figs. 5.9c, d). The N-MORB normalized incompatible element

patterns (Figs. 5.9c, d, e, f) strongly resemble those of the typical E-MORB composition (Sun & McDonough, 1989). Accordingly, in the discrimination diagram in Figure 5.10b, Type-II rocks plot in the field for subduction-unrelated settings, within the compositional field for rocks with E-MORB affinity (Sun & McDonough, 1989).

The chondrite-normalized REE patterns generally show enrichment of LREE with respect to MREE and HREE with $(La/Yb)_N = 1.3-3.1$ and $(La/Sm)_N = 1.2 - 1.9$. However, the different samples show crosscutting REE patterns (Figs. 5.9g-j) that coupled with slightly different incompatible element contents and ratios point out for magmatic differentiation starting from primary melts with distinct REE compositions. These slightly different compositions of primary melts point out, in turn, for their origin from partial melting of distinct mantle source compositions and partial melting conditions (Pearce & Norry, 1979; Allègre & Minster, 1978). Therefore, though these geochemical differences are minor, some subtypes of rocks mainly based on REE contents can be distinguished (Fig. 5.10a).

Subtype-IIa basalts show chondrite-normalized REE with Eu negative anomalies, which are progressively more marked in the relatively more differentiated rocks (Fig. 5.9g). This suggests early fractionation of plagioclase as commonly observed in tholeiitic volcanic series. These rocks are characterized by gently decreasing patterns from LREE to MREE and HREE (Fig. 5.9g), as exemplified by similar $(La/Sm)_N$ and $(La/Yb)_N$ ratios, which are in the range 1.10-1.29 and 1.38-1.87, respectively (Fig. 5.10a). Subtype-IIa basalts can be distinguished from the other Type-II rocks by their relatively high Ta/Hf (>6.3) and Th/Nb (>0.07) ratios.

Subtype-IIb volcanic rocks and dykes show steeper chondrite-normalized REE patterns with respect to Subtype-IIa (Fig. 5.9h). In fact, compared to Subtype-IIa rocks, they show similar $(La/Sm)_N$ ratios (1.18-1.40), but higher $(La/Yb)_N$ ratios, which are in the range 2.04-2.50 (Fig. 5.10a). However, similar to Subtype-IIa, they display Eu negative anomalies, whose values are

positively correlated with the degree of fractionation of the different differentiated rocks. Subtype-IIb basalts can be distinguished from Subtype-IIa basalts by their relatively low Ta/Hf (<6.3) and Th/Nb (<0.07) ratios.

Subtype-IIc basalts show chondrite-normalized REE patterns (Fig. 5.9i) characterized by no or very little enrichment of LREE with respect to MREE, that is, almost flat patterns from La to Sm (Fig. 5.9i). In fact, their La_N/Sm_N ratios range from 1.00 to 1.09 (Fig. 5.10a). However, these basalts show moderate LREE/HREE enrichment with $(La/Yb)_N$ ratios (1.53-1.89) that are comparable to those of Subtype-IIa basalts (Fig. 5.10a). It follows that they display a marked enrichment in MREE with respect to HREE, as exemplified by relatively high Sm_N/Yb_N ratios (1.46 – 1.74). These basalts also show the lowest Th, Nb values within Type-II rocks, whereas other trace element contents and ratios (e.g., Ce/Y, Zr/Nb) are comparable with those of Type-II rocks (Appendix Table 5.2).

Subtype-IId basalts show the highest LREE/MREE and LREE/HREE enrichment (Fig. 5.9j). Their $(La/Sm)_N$ and $(La/Yb)_N$ ratios range from 1.51 to 1.70 and from 2.33 to 3.06, respectively (Fig. 5.10). Slightly negative anomalies in Eu can be seen in the slightly differentiated samples (Fig. 5.9j). These basalts also display relatively high contents of Nb and Th (Fig. 5.10b) and the highest Nb/Y and the lowest Zr/Nb ratios within the Type-II rocks.

5.5. Mineral chemistry

As a consequence of the severe ocean-floor hydrothermal alteration that affected the studied rocks, a few samples were suitable for electron microprobe analysis. Only one type of mineral phase (plagioclase or clinopyroxene) was fresh enough to be analysed in only three samples of the sheeted dyke and volcanic complexes. In four samples from the intrusive complex I found two or

more different types of fresh mineral phases, including olivine, plagioclase, clinopyroxene. The composition of Fe^{2+} and Fe^{3+} for clinopyroxene was calculated from the measured FeO according to the method of Droop (1987). Representative analyses are shown in Appendix Tables 5.3, 5.4, and 5.5.

5.5.1 Olivine

The olivine crystals are unzoned and show quite homogeneous composition from core to rim (Appendix Table 5.3). In the cumulitic gabbro MK750 from the layered gabbros, the olivine crystals display MgO ranging from 39.4 to 41.4 wt% and forsterite contents in the range of 76.1 – 78.2%. In contrast, the olivine from the cumulitic gabbros MK32 and MK35 from the isotropic gabbros shows comparatively lower MgO content (36.5 - 38.0 wt% in sample MK32; 37.9 - 38.7 wt% in sample MK35) and forsterite content (71.2 – 72.6% in samples MK32; 73.0 – 74.1% in sample MK35). The different contents in forsterite and MgO observed in gabbros from the layered and isotropic gabbros likely reflect the segregation of the different olivine compositions from melts at different fractionation stages. The co-variation of olivine forsterite content against anorthite content of the coexisting plagioclase likely suggests a fractionation trend comparable with that described for MOR cumulates (Fig. 5.11a).

5.5.2 Plagioclase

Plagioclase was analysed in cumulitic gabbros, namely in samples MK32 and MK35 from the isotropic complex and samples MK750 and MK752 from the layered complex. In addition this mineral was also analyzed in sample MK93 from the sheeted-dyke complex. Plagioclases from

cumulitic gabbros are commonly unzoned as outlined by the low (less than 2%) variation in anorthite contents from core to rim (Appendix Table 5.4). Collectively, they show relatively low anorthite content (58.1 - 75.6 %). However, the plagioclase crystals of each sample have quite homogeneous composition in term of anorthite content (MK32 = 64.1 – 67.9 %; MK35 = 60.0 – 66.5 %; MK750 = 74.4 – 75.6 %; MK752 = 58.1 – 60.9 %). Plagioclase from the sheeted-dyke complex shows anorthite contents ranging from 62.3 to 67.3 % (Appendix Table 5.4). In the rocks

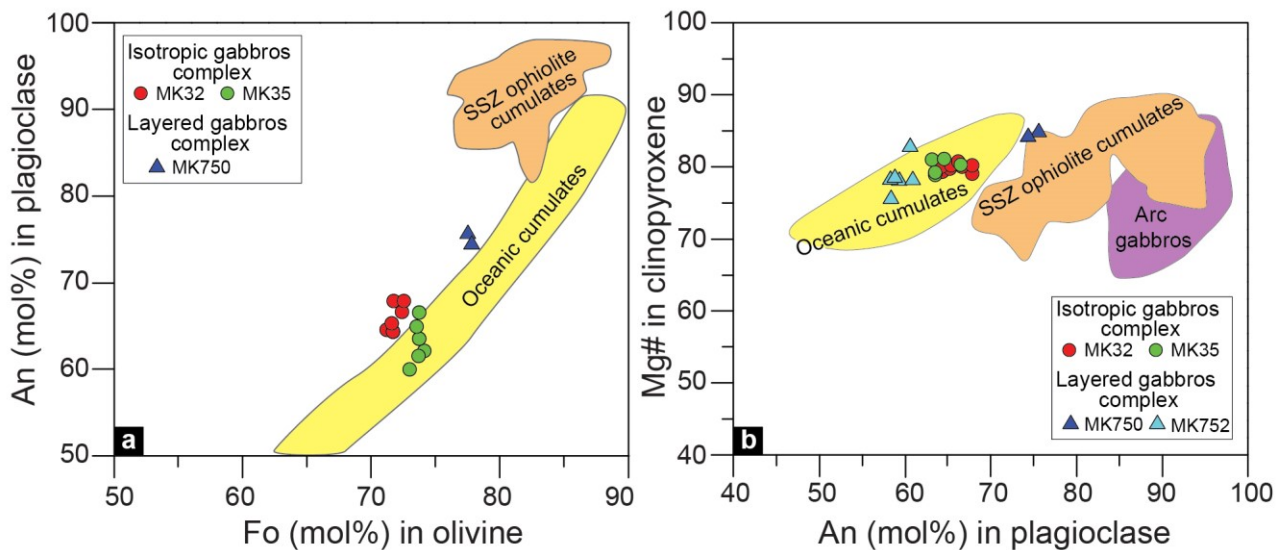


Figure 5.11. Forsterite (Fo) in olivine vs. anorthite (An) in plagioclase (a) and anorthite (An) in plagioclase vs. Mg# in clinopyroxene (b) diagrams for cumulitic gabbros from the layered and isotropic gabbro of the Band-e-Zeyarat ophiolite. Field for compositional variations of supra-subduction zone ophiolites, arc gabbros, and oceanic cumulates are shown for comparisons (Burns, 1985; Hébert & Laurent, 1990; Parlak et al., 2020).

from both the layered and isotropic complex, the anorthite contents plotted against forsterite contents of the co-existing olivine overlap the compositional field for MOR-type cumulitic rocks, showing lower anorthite percentage with respect to plagioclase of cumulitic rocks from supra-subduction zone ophiolites (Fig. 5.11a). Accordingly, the co-variation of anorthite contents in plagioclase vs. the Mg# in co-existing clinopyroxene from the Band-e-Zeyarat cumulitic gabbros are comparable with those of MORB-type gabbros (Fig. 5.11b). Low anorthite content is commonly related to the crystallization of plagioclase from water-poor magma, whereas high anorthite content suggests crystallization from a water-rich magma (Sisson & Groove, 1993; Parlak et al., 2020). The

low anorthite content observed in the studied plagioclases (Fig. 5.11b) suggests that they crystallized from a tholeiitic liquid at low H₂O contents, as commonly observed in typical MORBs.

5.5.3 Clinopyroxene

Clinopyroxene was analyzed in four cumulitic gabbros (i.e., MK32, MK35, MK750, and MK752), as well as in Type-II basalts MK10 and MK105 from the volcanic sequence (Appendix Table 5.5). The former sample represents a dyke crosscutting the lower part of the volcanic sequence whereas sample MK105 corresponds to a pillow lava. The compositions of clinopyroxenes from cumulitic gabbros plot mainly in the augite field with enstatite contents ranging from 38.4 to 44.0 % (Fig. 5.12a). Most of the crystals are unzoned (Appendix Table 5.5). In fact, Mg#, TiO₂, Cr₂O₃, and Al₂O₃ contents, do not show significant variation from core to rim (Appendix Table 5.5). Mg# is generally high ranging from 75.6 to 84.8 and its variation in each sample is lower than 3%, with the only exception of the sample MK752 in which it ranges from 75.6 to 82.8 (Appendix Table 5.5).

Cr₂O₃ positively correlates with Mg# value and is generally low in all samples (0.13 - 0.47 wt.%), except for the cumulitic gabbro MK750 (0.55 – 0.78 wt.%). TiO₂ (0.33-1.20 wt.%) and Al₂O₃ (1.98 – 3.93 wt.%) contents are relatively high and negatively correlate with Mg#. In Figure 5.11b the clinopyroxene from the Band-e-Zeyarat ophiolite overlap the compositional field for clinopyroxene and plagioclase from MOR-gabbros from modern settings (Burns, 1985; Ross & Elthon, 1993; Parlak et al., 2020). The clinopyroxene from basalts show augitic composition with enstatite contents in the range 36.1-49.7% (Fig. 5.12a). They display Mg# ranging from 64.6 to 81.4 in the basaltic dyke MK10 and from 70.4 to 84.1 in the pillow basalt MK105. TiO₂ (0.57 – 1.93 wt.%) and Al₂O₃ (1.71 – 4.65 wt.%) are relatively high and negatively correlate with Mg#. In contrast,

Cr₂O₃ contents (0.01 - 0.98 wt.%) show positive correlation with Mg#. Some clinopyroxenes in basalts are weakly zoned showing both normal and reverse zoning (Appendix Table 5.5). In detail, the normal-zoned crystals show a decrease of Mg# and Cr₂O₃ contents and an increase of TiO₂ contents from core to rim. By contrast, the reverse-zoned crystals have core characterized by higher TiO₂ contents and lower Mg# and Cr₂O₃ contents with respect to the crystals rim (Appendix Table 5.5). The amount of TiO₂ in clinopyroxene is related to the Ti activity in the parental melt, as well as the degree of depletion of the mantle source (Pearce & Norry, 1979).

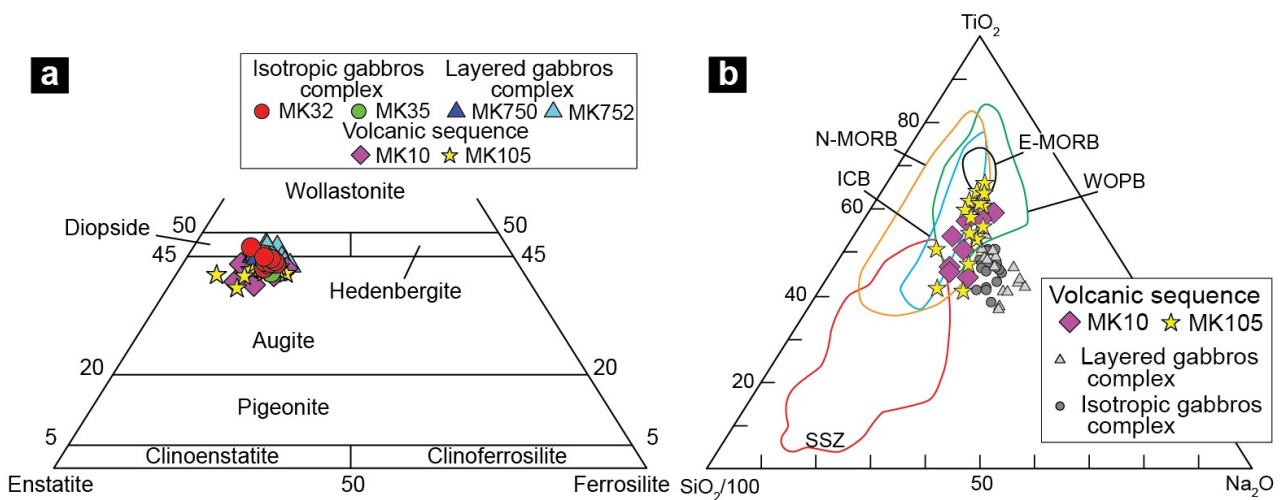


Figure 5.12. Pyroxene quadrilateral diagram (Morimoto, 1988) (a) and TiO₂-Na₂O-SiO₂/100 diagram for discriminating clinopyroxenes in basalts from different oceanic settings (Beccaluva et al., 1989) (b). Clinopyroxene from the intrusive complex of Band-e-Zeyarat ophiolite are also plotted for comparison in (b). Abbreviations, E-MORB: enriched mid-ocean ridge basalt; N-MORB: normal mid-ocean ridge basalt; WOPB: within oceanic plate basalts; ICB: Iceland basalts; and SSZ: supra-subduction zone basalts.

The relatively high TiO₂ contents in clinopyroxenes from the Band-e-Zeyarat ophiolite suggest their crystallization from primary magmas generated from mantle sources that did not experienced significant previous partial melting events, as those commonly observed in mid-ocean ridge settings (Pearce, 1996; Dilek & Furnes, 2011; Saccani, 2015). This is also suggested by the discrimination diagram shown in Figure 5.12b in which the clinopyroxenes from basalts plot in field for MOR setting, showing clearly distinct compositions from those of supra-subduction zone setting.

5.6. Geothermobarometry

Thermobarometric methods were applied in order to estimate pressure (P) and temperature (T) of crystallization of the intrusive and sheeted dyke complexes. We applied the method proposed by [Putirka et al. \(2007\)](#) to estimate the temperature of crystallization of olivine, the methods proposed by [Putirka \(2008\)](#) to estimate T and P condition of crystallization of plagioclase, and the methods of [Putirka et al. \(1996\)](#), and [Putirka et al. \(2003\)](#) for estimating P-T crystallization conditions for clinopyroxene. The method proposed by [Putirka et al. \(2007\)](#) allow to calculated T of crystallization of olivine using a P input estimated independently. The analysed olivine crystals are hosted in samples from the layered gabbros (MK750) and the isotropic gabbros (MK32 and MK35). Therefore, it is assumed as the possible P of crystallization of olivine 0.3 GPa for the stratigraphically lower layered gabbros and 0.25 GPa for the upper isotropic gabbros, which correspond to ~10 km and 8 km, respectively. The choice of these P was made according to the stratigraphic position in the sequence, as well as using the results of P-T calculation for the crystallization conditions of clinopyroxene. The methods of [Putirka \(2008\)](#) for estimating the P-T conditions of crystallization of plagioclase require the input of the content of H₂O in the melt. The studied rocks show a clear MORB tholeiitic affinity. The water content in this type of rocks is estimated as extremely low, and therefore in our calculation it is assumed a negligible H₂O contents in the melts. All the above listed methods are based on the mineral phase vs. whole-rock equilibrium. Some of the thermobarometric estimations were performed on mineral phases from cumulitic rocks and are therefore unlike to be in equilibrium with the bulk composition of their hosting rock. Indeed, whole-rock compositions of cumulitic rocks rarely correspond to parental melt composition, rather they are strictly dependent on the amount of cumulus minerals, which were progressively removed from the crystallizing melts at various stages of magmatic

fractionation (Casetta et al., 2018). Therefore, in order to apply the thermobarometric calculations I carefully selected melt compositions that could be in equilibrium with the chemical compositions of mineral phases from the rocks studied in this thesis. In Appendix Figure 5.1 it is graphically shown the re-equilibration processes and the whole-rock composition in equilibrium with each mineral phase. Another problem for the thermobarometric calculations for the studied rocks is that geothermobarometers proposed in literature are based on cation exchange of elements that are very mobile during ocean-floor alteration (e.g., Na, Ca). Therefore, considering the severe alteration of the studied rocks, I carefully chose minerals suitable for thermobarometric calculations.

5.6.1. Intrusive complex

The results of the thermobarometric calculations in samples from the layered gabbros indicate that olivine from sample MK750 crystallized at $\sim 1250^{\circ}\text{C}$, whereas plagioclase ($T = 1170^{\circ}\text{C}$) and clinopyroxene ($T = 1126^{\circ}\text{C} - 1159^{\circ}\text{C}$) crystallized at lower temperature than olivine (Fig. 5.13a). P estimated for these rocks shows that in sample MK752 plagioclase and clinopyroxene crystallized at average pressures of about 0.4 GPa and 0.33 GPa, respectively, whereas the same minerals in sample MK750 gave calculated average P of 0.27 GPa for plagioclase and 0.13 GPa for clinopyroxene (Fig. 5.13b).

Thermobarometric calculations for minerals in rocks from the isotropic gabbros indicate an average T of crystallization for olivine of 1188°C and 1153°C in samples MK35 and MK32, respectively. However, the T of crystallization estimated for the olivine from the sample MK32 is slightly lower than the T estimated for plagioclase in the same sample, suggesting that it can be influenced by not perfect mineral – whole-rock equilibrium and/or sub-solidus re-equilibration. The average T calculated using plagioclase compositions shows similar results ($T_{\text{MK32}} = 1168$

°C; T MK35 = 1154 °C) (Fig. 5.13a). The T estimated using clinopyroxene compositions are very similar to those obtained from plagioclase (T MK32 = 1120 °C; T MK35 = 1153 °C (Fig. 5.13a). The clinopyroxenes from the samples MK32 crystallized at an estimated average P of 0.17 GPa, whereas the average P estimated for clinopyroxenes from sample MK35 is 0.33 GPa (Fig. 5.13b). These data agree with average P estimated for plagioclases, which are P = 0.28 GPa for sample MK32 and P = 0.26 GPa for sample MK35 (Fig. 5.13b).

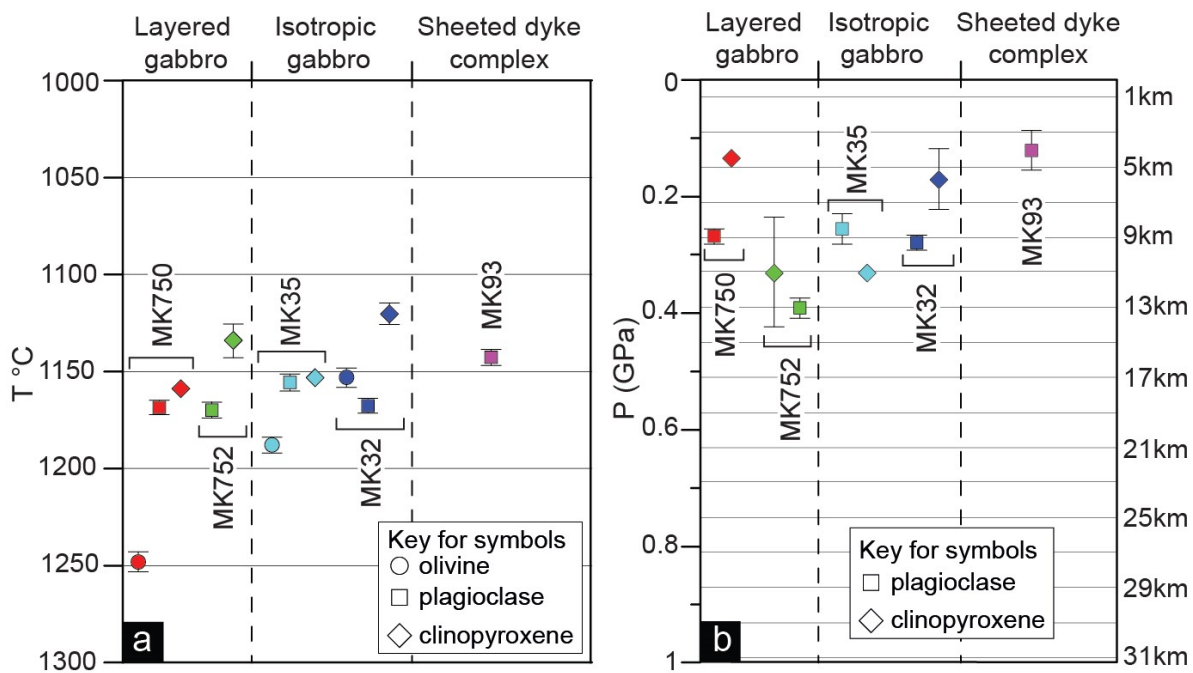


Figure 5.13. Schematic diagram showing the estimated temperature (a) and pressure (b) of crystallization for olivine, plagioclase and clinopyroxene in different samples from the intrusive and sheeted dyke complexes of the Band-e-Zeyarat ophiolite. Pressure is estimated only for plagioclase and clinopyroxene. Symbols indicate average values, bars indicate standard deviation.

In summary, in samples from both the layered and isotropic gabbro complexes there is a general correlation between P and T of crystallization, that is the decreasing of T is coupled with a decrease in P (Fig. 5.13b). The layered gabbros show estimated P-T higher than those estimated for isotropic gabbros suggesting crystallization at deeper crustal levels compared to isotropic gabbros. These results are consistent with the stratigraphic evidence from the Band-e-Zeyarat ophiolite. In addition, the P-T estimated for the layered and isotropic gabbros of the Band-e-Zeyarat ophiolite

(Fig. 5.13b) are consistent with P-T data for similar rocks from worldwide ophiolites (Dilek & Furnes, 2011) and modern oceanic setting (Wanless & Behn, 2017). Another general conclusion from our thermobarometric calculations is that the T of crystallization decreases from olivine to plagioclase and clinopyroxene (Fig. 5.13a). This evidence is in agreement with the crystallization order olivine + plagioclase + clinopyroxene observed by the petrographic analyses.

5.6.2. Sheeted dyke complex

The thermobarometric calculations for the sheeted dyke complex are based only on plagioclase from sample MK93 (Fig. 5.13). Our estimations indicate average T and P of crystallization of 1142 °C and 0.12 GPa, respectively. The estimated values are slightly lower than those calculated for the isotropic gabbros (Fig. 5.13) and are perfectly in agreement with the relatively upper stratigraphic position of the sheeted dyke with respect to the underlying gabbros in the Band-e-Zeyarat unit.

5.7. Zircon U-Pb dating (courtesy of A. Langone)

Zircon grains from the quartz-diorite MK748 are generally euhedral and small (<100 µm) with low aspect ratios. They are characterised by broad banding and oscillatory zoning. Inclusions of apatite are common. Thirteen U-Pb analyses on thirteen zircon grains were performed on this sample. Ten data yield a concordance better than 92% (Fig. 5.14), with a weighted average $^{206}\text{Pb}/^{238}\text{U}$ age of $125\pm 6\text{Ma}$ (Appendix Table 5.6). Similarly, zircon grains from the quartz-dioritic sample MK749 are generally euhedral and small (<100 µm) with low aspect ratios. They are characterised by darker core surrounded by brighter rims locally showing oscillatory zoning. Fourteen data yield a concordance better than 92% (Fig. 5.14) with a weighted average $^{206}\text{Pb}/^{238}\text{U}$

age of $122\pm 2\text{Ma}$ (Appendix Table 5.6).

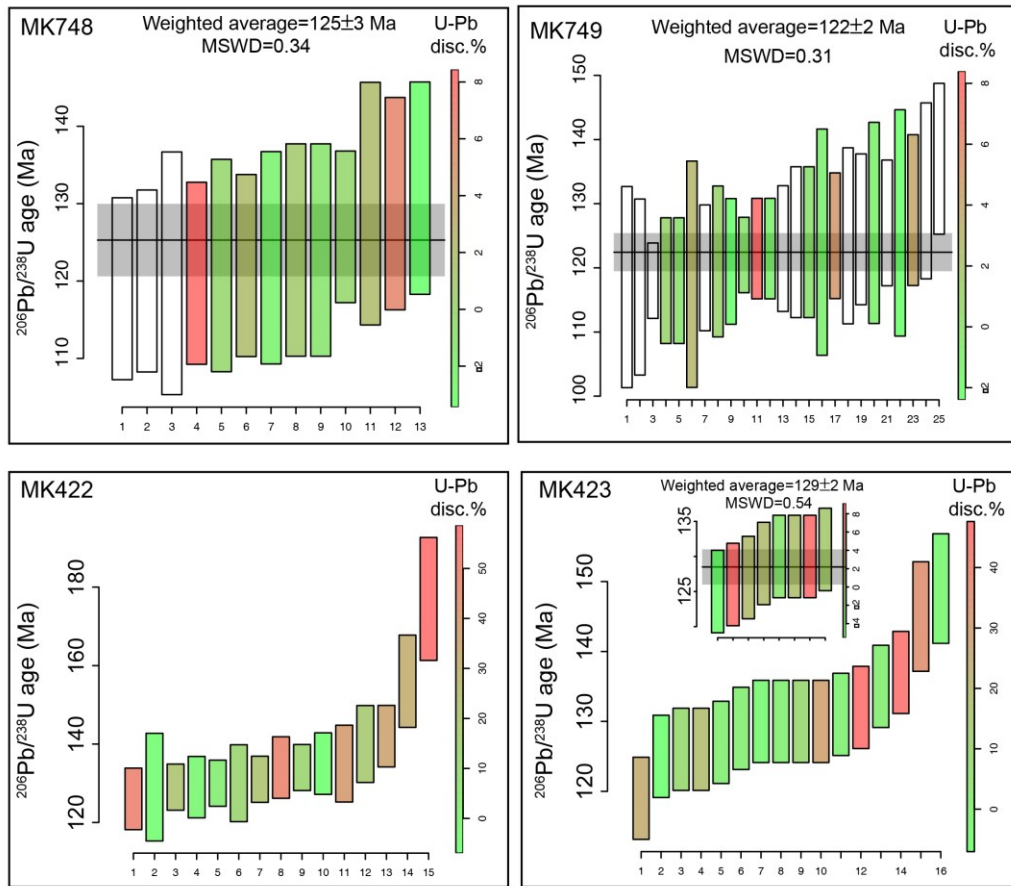


Figure 5.14. $^{206}\text{Pb}/^{238}\text{U}$ age distribution of concordant and sub-concordant (discordance $< \pm 8\%$) data and discordant data (unfilled bars). The weighted average age and the relative Mean Square Weighted Deviates (MSWD) are also reported and refer only to filled bars.

Zircon grains from the plagiogranite MK422 are generally euhedral and small ($< 75\ \mu\text{m}$) with low aspect ratios. They are characterized by sector and oscillatory zoning. Euhedral grains without apparent zoning also occur. Inclusions of apatite are common. Fifteen U-Pb analyses on fifteen zircon grains were collected for the MK422 sample. All data resulted severely discordant with only four sub-concordant data without a significant cluster (Fig. 5.14). Zircon grains from the plagiogranite MK423 are generally euhedral and small ($< 75\ \mu\text{m}$) with low aspect ratios. They are characterized by oscillatory zoning. Sixteen U-Pb analyses were performed on sixteen grains. Some of the U-Pb data resulted discordant. Nonetheless, eight concordant and sub-concordant

(concordance better than 92%) data provided a weighted average $^{206}\text{Pb}/^{238}\text{U}$ age of $129\pm 2\text{Ma}$ (Fig. 5.14; Appendix Table 5.6).

5.8. Discussion

5.8.1. Melt petrogenesis

Our petrogenetic discussion will be focused on the identification of the possible mantle sources and their melting conditions (e.g., degree of partial melting and melting depth) with the aim of better constraining the tectono-magmatic setting of formation of the Band-e-Zeyarat ophiolite. Incompatible elements and REE composition of basaltic rocks is thought to be largely dependent on the composition of the mantle source and its degree of partial melting, rather than fractional crystallization processes (Pearce & Norry, 1979). In addition, even in the presence of moderate amounts of fractional crystallization of mainly olivine + plagioclase + clinopyroxene, ratios of incompatible elements (e.g., Zr/Nb, Nb/Y, Th/Ta, Th/Tb, and REE) in magmatic rocks are assumed to represent those of the associated mantle source (Allègre & Minster, 1978). For these reasons, the following petrogenetic discussion will be based on the relatively less fractionated basalts for each geochemical type. Our data show that the magmatic rocks from the Band-e-Zeyarat ophiolite basically include two geochemical types: Type-I showing N-MORB affinity and Type-II showing E-MORB affinity. According to their chemical features, Type-I and Type-II rocks were likely originated from partial melting of chemically different mantle sources. Information about the possible mantle sources can be obtained using ratios of hygromagmatophile element ratios, such as Th/Ta and Th/Tb ratios. In fact, Th, Ta and Tb are weakly fractionated during either fractional crystallization or partial melting and, therefore, their ratios in the basaltic rocks are

mainly controlled by the elemental ratios of the mantle source (Allègre & Minster, 1978; Rollinson, 1993). A first discrimination of the possible mantle sources associated with the different Type-I and Type-II rocks can be obtained from Figure 5.15a, which shows that Type-I basalts have (Th/Tb)/(Th/Ta) ratios overlapping those of N-MORBs, whereas Type-II basalts show ratios similar to those of E-MORBs. Accordingly, Figure 5.15b shows that Type-I primary basalts plot close to the composition of the typical N-MORB (Saccani et al., 2013a, b), suggesting that they were generated from a depleted MORB-type sub-oceanic mantle source. In contrast, Type-II basalts plot along the N-MORB – OIB mixing line suggesting that these rocks are generally compatible with a genesis from depleted MORB-type mantle, which was metasomatized by OIB-type (plume-type) chemical components. Further informations on petrogenesis of the studied rocks can be derived from the Nb/Yb-TiO₂/Yb co-variation (Fig. 5.15c). This diagram highlights depth of melting and mantle source composition (i.e., depletion vs. enrichment), as the variance of TiO₂/Yb values is almost entirely depending on garnet residues during melting, whereas the Nb/Yb variation mainly depends on source composition and melting degree (Pearce, 2008). In fact, on the TiO₂/Yb-Nb/Yb diagram (Fig. 5.15c), Type-I and Subtype-IIa relatively primitive basalts plot in the MORB array, suggesting that they originated from partial melting at relatively shallow depths (i.e., spinel-facies mantle). In contrast, Subtypes-IIb, -IIc, and -IId basalts have higher TiO₂/Yb ratios than MORB suggesting deeper melting with involvement of a garnet-bearing mantle source (Fig 5.15c). The Nb/Yb ratios further suggest that Type-I basalts were generated from a depleted N-MORB type mantle source without any influence of plume-type chemical components, whereas Type-II basalts show Nb/Yb ratios higher than Type-I rocks, as well as a co-variation of TiO₂/Yb and Nb/Yb ratios, which indicates plume–ridge interaction (Fig. 5.15c).

Given this evidence, it is performed non-modal, batch partial melting modelling using both Nb/Yb-Th co-variation, as well as REE composition (Figs. 5.16, 5.17). Plots of Th vs. Nb/Yb are

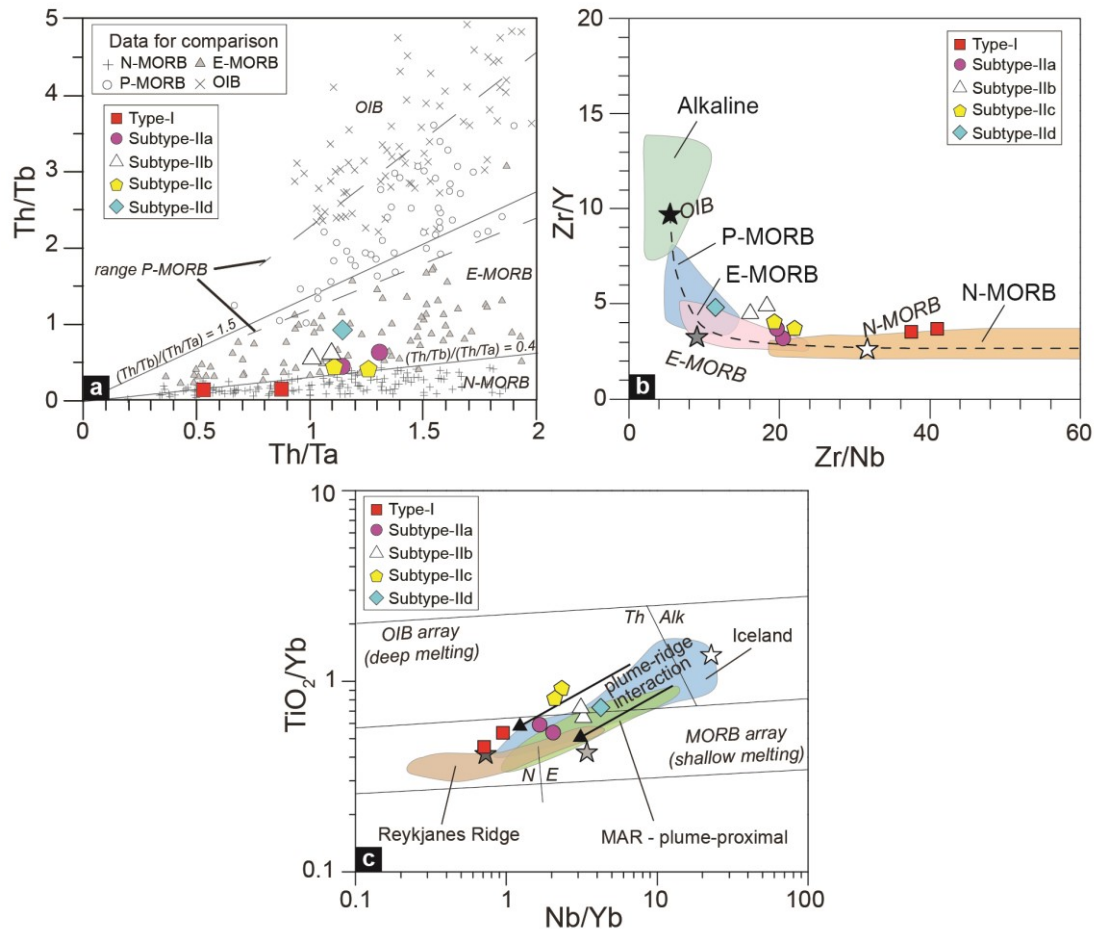


Figure 5.15. Diagrams showing the co-variation of some trace element ratios for subvolcanic and volcanic rocks from the sheeted dyke complex and volcanic sequence of the Band-e-Zeyarat ophiolite. (a) Th/Tb vs. Th/Ta diagram for primitive basalts for each geochemical Type and Subtype. Compositions of oceanic subduction-unrelated rocks are shown for comparison (Saccani et al., 2003; Bortolotti et al., 2004; Chiari et al., 2011; Saccani, 2015). (b) Zr/Nb vs. Zr/Y diagram for primitive basalts for each geochemical Type and Subtype. N-MORB, E-MORB and OIB end-members are from Sun & McDonough (1989). Fields indicate compositional variation for different types of basalts from subduction-unrelated ophiolites and modern oceanic setting. Data source (Le Roex et al., 1983; Hanan et al., 2000; Saccani et al., 2003; Bortolotti et al., 2004; Chiari et al., 2011; Chauvet et al., 2011; Saccani et al., 2013a, b; Saccani et al., 2014). The dashed line represents the mixing curve calculated using OIB and N-MORB end-members (from Le Roex et al. (1983)). (c) Nb/Yb vs. TiO_2/Yb diagram from Pearce (2008) for primitive basalts for each geochemical Type. Compositional fields for basalts erupted in modern plume-ridge interaction are shown for comparison (Pearce, 2008). Composition of typical N-MORB (dark grey star), E-MORB (light grey star), and OIB (white star) are from Sun & McDonough (1989).

particularly useful for distinguishing between melting in the spinel and garnet stability fields (Thirlwall et al., 1994), whereas the abundance of Th and Nb is particularly useful for evaluating the enrichment of the source (Saccani et al., 2013a; Saccani, 2015). In this model, two compositionally different mantle sources are considered based on the diagrams in Figure 5.15: (1)

a depleted MORB mantle (DMM) source (Workman & Hart, 2005) melting in the spinel-facies; (2) a theoretical DMM source enriched in LREE and incompatible elements by a plume-type chemical component (i.e., plume-influenced source of Saccani (2015) or plume-proximal ridge of Pearce (2008)) that melts either in the spinel- or garnet-facies mantle (source S2 in Figs. 5.16, 5.17). It should however be noted that the composition of the enriched source S2 cannot be precisely constrained. In the proposed model the theoretical composition of the enriched source S2 is calculated starting from a DMM slightly metasomatized and enriched in LREE, Th, and Nb by OIB-type chemical component. An enriched mantle source typical for alkaline basalts (Lustrino et al., 2002) was used for representing the OIB-type chemical component (Figs. 5.17b-d). This assumption agrees with petrogenetic studies on E-MORB basalts from both modern oceanic setting and ophiolites, which are interpreted as possibly derived from a DMM source that was metasomatized to varying degrees by an OIB-type component (Le Roux et al., 1983; Thirlwall et al., 1994; Haase & Devey, 1996; Saccani et al., 2013b; Saccani et al., 2014; Bortolotti et al., 2017). The composition in terms of REE, Th, and Nb of the DMM source, the OIB-type mantle source, and the theoretical enriched mantle source S2, as well as their modal compositions and melting proportions (Kinzler, 1997), and partition coefficients (McKenzie & O’Nions, 1991; Ewart & Griffin, 1994; Horn et al., 1994; Dunn & Sen, 1994; Kinzler, 1997; Salters & Longhi, 1999; Green et al., 2000; Klemme et al., 2006;) used in the models in Figures 5.16, 5.17 are given in Appendix Table 5.7.

5.8.1.1. Type-I

Depletion of LREE with respect of MREE and HREE (Fig. 5.9b) and low Nb/Yb and TiO₂/Yb ratios (Fig. 5.15c) displayed by Type-I rocks suggest a melt generation from a depleted, sub-

oceanic mantle source (DMM) in the spinel stability field. The model in Figure 5.16 shows indeed that the Th-Nb-Yb composition of Type-I primitive basalts can be explained by 15-18% of partial melting of a DMM source (Saccani et al., 2013a) in the spinel-facies. The REE modelling (Fig. 5.17a) fully confirms the results obtained from the Th vs. Nb/Yb model. In fact, the REE composition of the relatively primitive basalt MK97 fit well with the liquid composition calculated for ~ 15% of partial melting of a DMM source in the spinel-facies (Fig. 5.17a).

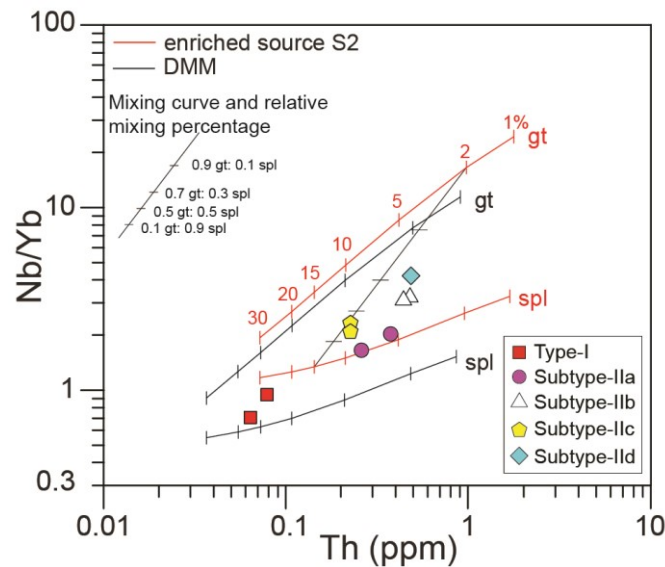


Figure 5.16. Melt curve models based on Th vs. Nb/Yb and compositions of the relatively more primitive basalts for each rock types and subtypes. Melt curves are calculated using non-modal, batch partial melting of DMM (Workman & Hart, 2005) and a theoretically enriched mantle source (S2). Ticks on all melting curve indicate the same percentages of partial melting as shown for the melting curve of source S2 in the garnet-facies. The thin black line represents the mixing line of various melt fractions from garnet- and spinel-facies mantle. Input parameters for the REE models (source modes, melting proportions, and partition coefficients), as well as compositions of the mantle sources are shown in Appendix Table 5.7.

5.8.1.2. Type-IIa

The Subtype-IIa rocks have clear E-MORB geochemical affinity with different extent of LREE/HREE enrichment (Figs. 5.9g, 5.10a), as well as low TiO₂/Yb ratios (Fig. 5.15c), which suggest a melting of an enriched sub-oceanic mantle source in the spinel stability field. The chemical features of Subtype-IIa basalts cannot be modelled by very low degrees of partial melting

of a DMM mantle source. In fact, Subtype-IIa primitive rocks clearly plot at higher values of both Th and Nb/Yb with respect to the calculated melting curve for partial melting of DMM source (Fig. 5.16). In contrast, the Th-Nb/Yb composition of Subtype-IIa relatively primitive basalts is compatible with 6-8% partial melting in the spinel-facies of the enriched mantle source S2 (Fig. 5.16). Accordingly, results of the REE modelling indicate that the REE composition of Subtypes-IIa primitive basalts is compatible with the ~9% partial melting of the S2 source in the spinel-facies (Figs. 5.17b). In agreement with the Th-Nb-Yb modelling, higher and lower degrees of partial melting fail to reproduce the REE composition of the primitive basalts of the Type-IIa. Likewise, very low degrees (<3%) partial melting of a DMM source cannot reproduce the REE patterns of Subtype-IIa basalts (not shown).

5.8.1.3. Type-IIb

Subtype-IIb rocks show higher LREE/HREE enrichment (Figs. 5.9g, h and 5.10a) and TiO₂/Yb ratios (Fig. 5.15c) compared to Subtype-IIa rocks. These features, particularly the TiO₂/Yb ratios, suggest an involvement of residual garnet during partial melting. In fact, the model in Figure 5.16 shows that Th-Nb-Yb composition of Subtype-IIb relatively primitive basalts cannot be explained by partial melting in the spinel-facies alone. Rather, the composition of these basalts can be explained by ~2% partial melting of mantle source S2 in the garnet-facies and ~4% partial melting of the same source in the spinel facies. Accordingly, the REE composition of these basalts is compatible with partial melting of the mantle source S2 that starts to melt at low degrees (~2%) in the garnet-facies and continues to melt to larger extents (~5%) in the spinel facies (Figs. 5.17c). The mixing proportion between melts generated at spinel- and garnet-facies that best fit the REE composition of the primitive basalt MK93 is 8:2 (Figs. 5.17c). In Figure 5.17c it is also shown that

calculations involving different degrees of partial in the garnet- and spinel-facies, as well as different mixing proportions of melts generated at spinel- and garnet-facies fails to reproduce the REE composition of Subtype-IIb basalts.

5.8.1.4. *Type-IIc*

Subtype-IIc rocks show a general LREE/HREE enrichment, which is comparable to that of Subtype-IIa basalts, but show the lowest LREE/MREE and MREE/HREE enrichment within Type-II rocks (Figs. 5.9i, 5.10a). Primitive basalts show relatively high TiO_2/Yb ratios (Fig. 5.15c) and the low HREE contents (e.g., $\text{YbN} = 9.5$), which suggest an involvement of residual garnet during partial melting. Though the REE patterns of these rocks are appreciably different from those of other Type-II basalts, ratios of hygromagmatophile element ratios are comparable with those of Subtypes-IIa and -IIb basalts (Fig. 5.15a), suggesting a compositionally similar mantle source. Therefore, I postulate that the different REE patterns of these rocks are most likely due to different melting condition of the enriched source S2. In fact, the model in Figure 5.16 shows that the Th-Nb-Yb composition of Subtypes-IIc primitive basalts can be explained by 2-4% and 10-14% partial melting of the theoretical source S2 in the garnet- and spinel-facies, respectively. The REE composition of Subtype-IIc primitive basalt MK109 can be explained by mixing with proportion 8:2 of liquids generated from 4% and 12% partial melting of mantle source S2 in the garnet and spinel stability fields, respectively (Fig. 5.17d).

5.8.1.5. *Type-IId*

Subtype-IId rocks show the highest enrichment in LREE with respect to MREE and HREE

observed within the Type-II rocks (Figs. 5.9j, 5.10a). Primitive basalts show TiO_2/Yb ratios (Fig. 5.15c) and the low HREE absolute contents (e.g., $\text{Yb}_N = 9.3$), which suggest an involvement of residual garnet in the mantle source. In our model (Fig. 5.16), the Subtype-II_d primitive basalt MK87 plots very close to Subtype-II_b basalts. In fact, similar to Subtype-II_b, the Th-Nb-Yb composition of sample MK87 is compatible with ~2% partial melting of the theoretical source S2 in the garnet-facies, and ~7-8% partial melting of S2 in the spinel-facies. Accordingly, REE model shows that the REE composition of the relatively more primitive Subtype-II_d basalt is compatible with partial melting of the mantle source S2 that melts in the garnet-facies for 2% partial melting and continues to melt in the spinel-facies for about 10% (Fig. 5.17e). The mixing proportion between melts generated at spinel- and garnet-facies that best fit the REE composition of the primitive basalt MK87 is 7:3 (Figs. 5.17e). It follows that the relatively high LREE/HREE and MREE/HREE ratios displayed by Subtype-II_d rocks (Fig. 5.10a) are most likely due to a slightly higher contribution of melt formed in the garnet-facies mantle with respect to Subtype-II_b and Subtype-II_c rocks. Nonetheless, it cannot be excluded that the relatively higher LREE enrichment displayed by Subtype-II_d basalts may result from partial melting of a mantle source slightly more enriched in LREE than the theoretical source S2. The (Th/Tb)/(Th/Ta) ratios of the primitive Subtype-II_d basalt are indeed slightly higher than those of other Subtypes-II basalt (Fig. 5.15a). However, the differences in (Th/Tb)/(Th/Ta) ratios in the distinct Subtypes-II basalt are so small that it is difficult to unequivocally confirm this hypothesis.

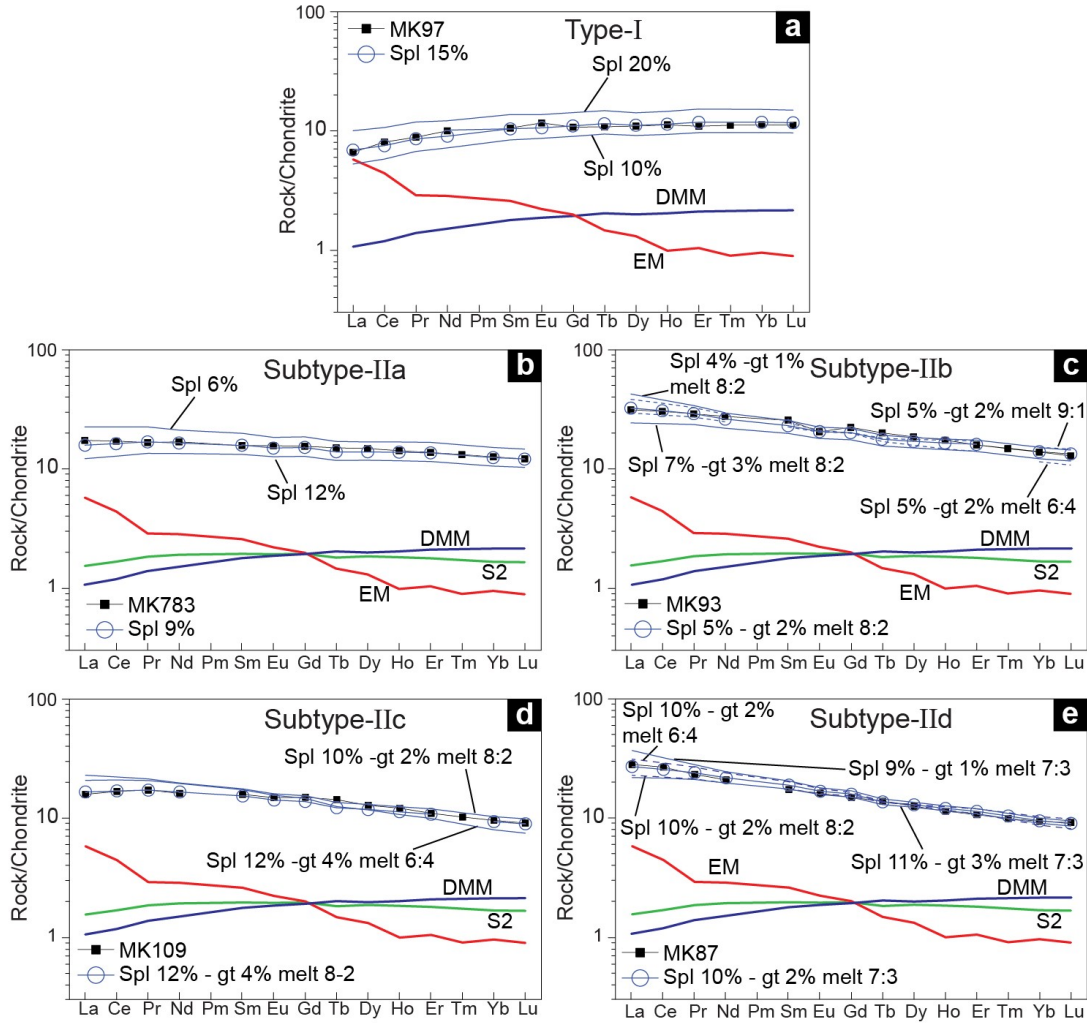


Figure 5.17. Calculated chondrite-normalized (Pearce & Norry, 1979) rare earth element (REE) liquid composition for parental melts derived from different mantle sources, assuming various degrees of non-modal batch partial melting. Abbreviations: EM: enriched mantle source (from Lustrino et al., 2002); DMM: depleted MORB mantle (Workman & Hart, 2005); S2: enriched mantle source S2. Input parameters for the REE models (source modes, melting proportions, and partition coefficients), as well as compositions of the different mantle sources are shown in Appendix Table 5.7.

5.8.2. Tectono-magmatic setting of formation of the Band-e-Zeyarat ophiolite and geodynamic implications

Previous studies have suggested that the rocks from the Band-e-Zeyarat ophiolite were derived from mafic melts with E-MORB composition and show an Early Cretaceous age (141 – 143 Ma,

based on ^{40}Ar – ^{39}Ar methods; Ghazi et al., 2004). Our new whole-rock geochemical data, and geochronological data, as well as the mineral chemistry data are in agreement with this conclusion. In fact, they highlight that the oceanic basin in which the Band-e-Zeyarat ophiolite was formed (i.e., the North Makran Ocean), was characterized by an Early Cretaceous chemically composite upper oceanic crust consisting of N-MORBs and different varieties of E-MORBs. The petrological evidence presented in Section 5.8.1 clearly indicates that the Band-e-Zeyarat ophiolite was generated in a mid-ocean ridge setting from partial melting of mantle sources showing a combination of distinct compositions and different partial melting degrees and melting depths. Accordingly, our thermobarometric calculations indicate that the different rock-forming minerals crystallized at temperatures and depths that are compatible with those of magma chambers beneath sub-oceanic ridges. The absolute ages of 122 – 129 Ma obtained in this work combined with previously published ages of 141 - 143 Ma (Ghazi et al., 2004) suggest that a spreading ridge characterized by enriched-type mantle sources was active in the North Makran Ocean from the lowermost Early Cretaceous.

In Figure 5.18 it is presented a schematic tectono-magmatic model that can explain the formation of the Band-e-Zeyarat composite upper crustal sequence. Type-I (N-MORB) rocks were generated from the partial melting in the spinel-facies of a depleted sub-oceanic asthenosphere without influences of OIB-type components (Figs. 5.16, 5.17a, 5.18). Type-II (E-MORB) rocks derived from the partial melting of a comparatively more enriched mantle source (S2 source), which corresponds to an asthenospheric depleted sub-oceanic mantle bearing OIB-type chemical components (Figs. 5.16, 5.17b-e, 5.18). However, it has been shown in the petrogenetic discussion (Figs. 5.15c, 5.16, 5.17) that the different Subtypes-II rocks are compatible with different melting conditions in terms of partial melting degree and depth of melting of the enriched mantle source S2.

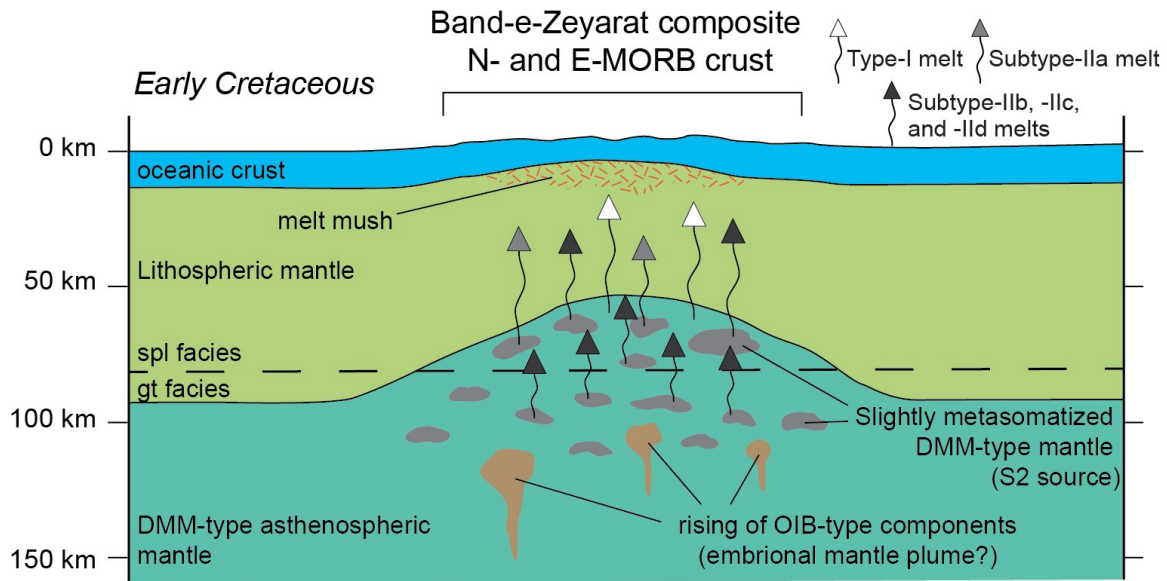


Figure 5.18. Conceptual two-dimensional cartoon showing the petrogenetic processes responsible for the formation of the N- and E-MORB composite crust of the Band-e-Zeyarat ophiolite in a mid-oceanic ridge tectono-magmatic setting. Abbreviations: N-MORB: normal mid-oceanic ridge basalt; E-MORB: enriched mid-oceanic ridge basalt; OIB: oceanic island basalt; DMM: depleted MORB mantle.

The tectono-magmatic setting shown in Figure 5.18 can explain the formation of these slightly different E-MORBs forming the Band-e-Zeyarat ophiolite. We propose that Type-IIa melts were generated from the partial melting of the enriched mantle source S2 in the spinel-facies. By contrast, the Type-IIb, -IIc, -II d rocks may have been generated from variable degrees of partial melting of the same S2 source, which started to melt in the garnet-facies and continued to melt in the spinel-facies (Fig. 5.18). The tectono-magmatic model proposed in Figure 5.18 is compatible with two different mid-ocean ridge settings: 1) a mid-ocean ridge proximal to a mantle plume that was active during the formation of the Band-e-Zeyarat ophiolite; 2) a mid-ocean ridge associated with a heterogeneous sub-oceanic asthenospheric mantle bearing inherited portions enriched by ancient mantle plume activity. The discriminations between these two distinct tectono-magmatic settings based only on petrogenetic data from the Band-e-Zeyarat ophiolite is difficult to be made. To this purpose, some useful constraints can be obtained from the comparison with the tectono-magmatic events occurring in the Makran area and, more generally, in the Middle East – Tibet area

during Cretaceous times. The Band-e-Zeyarat ophiolite, together with the Fannuj - Maskutan and Remesk - Moktarabad ophiolites, has classically been interpreted as an Early Cretaceous ophiolite, which represents the remnants of the North Makran Ocean (McCall & Kidd, 1982; Hunziker et al., 2015). Recent works on the eastern ophiolites of the North Makran domain have shown that the Fannuj - Maskutan ophiolites (Fig. 5.1) consist of island arc tholeiitic gabbros and E-MORB basalts. These ophiolites are interpreted as formed in a supra-subduction zone basin (backarc basin) located between the Lut Block and the Bajgan-Durkan microcontinent during the Late Jurassic - Early Cretaceous (Sepidbar et al., 2020). On the other hand, data from the Ganj Complex in the western North Makran indicate that the subduction-related magmatism in the western North Makran is Late Cretaceous in age (Chapter 4) and, therefore, it is much younger than the Early Cretaceous N- to E-MORB magmatism recorded by the Band-e-Zeyarat ophiolite. This evidence allow to exclude that the Band-e-Zeyarat ophiolite was formed in the same Late Jurassic - Early Cretaceous supra-subduction zone tectonic setting of formation of the eastern North Makran ophiolites. Recent works have documented the widespread occurrence of Late Cretaceous alkaline and oceanic plateau basalts, as well as P-MORB in the Makran area, namely in the Coloured Mélange and in the Durkan Complex. The genesis of these rocks has been related either to oceanic within-plate mantle plume magmatism (Saccani et al., 2018; Chapter 6) or to a plume-ridge interaction (Esmaeili et al., 2019). In any case, these data point out that during the Late Cretaceous a mantle plume activity strongly influenced the magmatic history of the Northern Makran Ocean. Accordingly, mantle plume activity has been documented in the Early Cretaceous at a regional scale from the Caucasus to Tibet (Yang & Dilek, 2015; Rolland et al., 2020).

Given this regional evidence, it is suggested that the N-MORB - E-MORB association in the Band-e-Zeyarat ophiolite can most likely be related to a mantle plume activity rather than an inherited metasomatized asthenospheric mantle. However, an active mantle plume close to a MOR

setting commonly results in abundant eruptions of E-MORB, P-MORB, and alkaline basalts formed through polybaric melting, as well as a time-dependent magmatic evolution from depleted N-MORB to enriched E-MORB, P-MORB and alkaline basalts (Pearce, 2008; Saccani et al., 2013a, b; Yang & Dilek, 2015). By contrast, in the case of melting of sub-oceanic mantle showing inherited OIB-type metasomatism the volume of E-MORB, P-MORB and alkaline basalts is commonly subordinate with respect to N-MORB and partial melting is by far limited to the spinel-facies mantle, as observed in modern oceanic settings (Warren, 2016), as well as in many ophiolitic settings (Thirlwall et al., 1994; Pearce, 2008; Dilek & Furnes, 2011; Saccani et al., 2013b; Saccani, 2015; Saccani et al., 2015 Bortolotti et al., 2017). In the Band-e-Zeyarat ophiolite, the E-MORB rocks are volumetrically largely prevailing compared to N-MORBs. In addition, it can be observed, as a general tendency, the increase of the abundance of E-MORBs toward the top of the sequence. Therefore, I postulate that the Band-e-Zeyarat ophiolite most likely represents an excellent fossils example of a plume-proximal mid-oceanic ridge, which recorded plume-ridge interaction during an embryonic stage of a mantle plume activity in the Early Cretaceous. In our model, this embryonic plume activity was characterized by the rising of OIB-type chemical components from a deep and enriched mantle source, which metasomatized the existing asthenospheric sub-oceanic mantle (Fig. 5.18).

Recent works in the Makran area (Saccani et al., 2018; Esmaeili et al., 2019) demonstrated the occurrence of E-MORBs, P-MORBs, and alkaline OIBs formed in seamounts and oceanic plateaux settings associated with Late Cretaceous mantle plume activity. The new evidence of Early Cretaceous plume-ridge interaction in the Band-e-Zeyarat ophiolite is, therefore, highly significant as it represents, up to now, the earliest witness of mantle plume activity in the Makran sector of the Neo-Tethys. This conclusion fits well and improves the extant literature data from Makran (Saccani et al., 2018; Esmaeili et al., 2019) and neighbouring collisional belts (Saccani et al.,

2013a, 2014; Yang et al., 2015; Rolland et al 2020), which point out for a plume activity starting in the Early Cretaceous and continuing in the Late Cretaceous in the Neo-Tethys realm. This data well agree with the evidence for two major pulses of mantle plume activities at a worldwide scale during the Early and Late Cretaceous (i.e., from 122 Ma to 70 Ma, see Kerr, 2014); in fact example of oceanic plateau and continental flood basalts associated with Cretaceous mantle plume are well known in the Indian Ocean (e.g., Kerguelen Plateau, Coffin et al., 2002), in the Pacific Ocean (e.g., Ontong Java Plateau, Kerr et al., 2000, Fitton & Godard, 2004; Hikurangi Plateau, Hoernle et al., 2010), and in the Caribbean region (Caribbean Plateau, Kerr et al., 2000). Our new findings suggest that the worldwide Cretaceous plume activity also affected the Makran sector of the Neo-Tethys. Therefore, the Band-e-Zeyarat ophiolite may represent a potential natural laboratory to unveil the processes responsible for crustal growth during plume activities at a global scale.

5.9. Conclusion

1. The Band-e-Zeyarat ophiolite consists of (from bottom to top): ultramafic cumulates, layered gabbros, isotropic gabbros, as well as a sheeted dyke complex and a volcanic series including mainly basalts and subordinate andesites and rhyolites.

2. Whole-rock chemical compositions of basaltic rocks show both N-MORB and E-MORB affinities.

3. The compositions of rock-forming minerals (i.e., olivine, plagioclase, and clinopyroxene) also point out for a general MORB-type affinity of both gabbros and basalts.

4. Geothermobarometric estimations show that the rock-forming minerals crystallized at temperatures and pressures that are compatible with those commonly observed in sub-oceanic magma chambers beneath mid-ocean ridges.

5. LA–ICP–MS zircon U–Pb dating showed the age of the Band-e-Zeyarat gabbros at ~122–129 Ma.
6. Band-e-Zeyarat N-MORBs formed from partially melting of a depleted sub-oceanic mantle peridotite in the spinel-facies.
7. Band-e-Zeyarat E-MORBs formed from partial melting of a depleted sub-oceanic mantle peridotite that was metasomatized by OIB-type (plume-type) components. They show different LREE, Th, Nb, TiO₂, and Ta contents, which point out for different partial melting conditions, in terms of partial melting degrees, and melting depths.
8. It is suggested that the Band-e-Zeyarat ophiolite represents a chemically composite upper oceanic crust, which records an Early Cretaceous plume-ridge interaction in the Makran Neo-Tethys.
9. The plume activity that affected the Makran sector of the Neo-Tethys can be framed into the plume activities observed worldwide during the Cretaceous.

APPENDIX

Appendix Table 5.1. (1/2) Major (wt.%) and trace (ppm) element composition of representative magmatic rocks from the intrusive complex of the Band-e-Zeyarat ophiolite. Abbreviations: *serp dun*: serpentinized dunite; *troct*: troctolite; *gb*: gabbro; *ol-gb*: olivine-gabbro; *Fe-gb*: ferrogabbros; *pl gran*: plagiogranite; *qz-diorite*: quartz-diorite XRF: X-ray fluorescence spectrometry; ICP-MS: inductively coupled plasma-mass spectrometry; *n.d.*: not detected. $Mg\# = 100 \times MgO / (MgO + FeO)$. $Fe_2O_3 = 0.15 \times FeO$. Normalizing values for REE ratios from Sun & McDonough (1989).

| Unit Rock type Sample rock Note Age | Layered gabbros | | | | | | | | | | Isotropic gabbro | | |
|--|-------------------------------------|----------|--------|-------|-----------------|----------|----------|--------|--------|-----------------|------------------|----------------|---------|
| | ultramafic cumulates and troctolite | | | | mafic cumulates | | | | | mafic cumulates | | cumulitic rock | |
| | MK40 | MK47 | MK781 | MK750 | MK33 | MK34 | MK41 | MK44 | MK751 | MK752 | MK782 | MK32 | MK35 |
| | serp dun | serp dun | troct | troct | leuco gb | leuco gb | leuco gb | gb | ol-gb | Ol-gb | leuco gb | gb | pl rich |
| XRF analyses: | | | | | | | | | | | | | |
| SiO ₂ | 39.0 | 40.0 | 40.0 | 42.2 | 46.5 | 48.9 | 44.7 | 47.6 | 45.0 | 49.1 | 46.9 | 48.4 | 47.6 |
| TiO ₂ | 0.10 | 0.02 | 0.17 | 0.17 | 0.21 | 0.27 | 0.14 | 0.18 | 0.15 | 0.30 | 0.15 | 0.29 | 0.25 |
| Al ₂ O ₃ | 2.06 | 1.41 | 5.54 | 10.6 | 19.3 | 19.9 | 16.4 | 17.2 | 14.8 | 14.5 | 23.6 | 18.3 | 18.5 |
| Fe ₂ O ₃ | | | | | 0.52 | 0.56 | 0.33 | 0.51 | 0.71 | 0.77 | 0.35 | 0.86 | 0.97 |
| FeO | 8.23 | 6.00 | 9.53 | 8.79 | 3.47 | 3.77 | 2.21 | 3.42 | 4.74 | 5.11 | 2.34 | 5.75 | 6.49 |
| MnO | 0.10 | 0.09 | 0.14 | 0.14 | 0.07 | 0.08 | 0.05 | 0.08 | 0.10 | 0.10 | 0.05 | 0.12 | 0.13 |
| MgO | 38.0 | 37.8 | 32.1 | 23.2 | 10.2 | 7.48 | 12.5 | 11.2 | 17.3 | 13.2 | 7.34 | 10.1 | 11.1 |
| CaO | 0.18 | 2.37 | 4.21 | 8.0 | 13.5 | 13.3 | 17.3 | 14.9 | 11.4 | 12.9 | 14.4 | 13.6 | 11.7 |
| Na ₂ O | 0.03 | 0.04 | 0.45 | 1.06 | 2.53 | 3.37 | 1.32 | 1.93 | 1.78 | 2.06 | 2.53 | 2.51 | 2.78 |
| K ₂ O | n.d. | n.d. | 0.01 | 0.04 | 0.02 | 0.05 | 0.08 | 0.05 | 0.03 | 0.05 | 0.05 | 0.03 | 0.04 |
| P ₂ O ₅ | n.d. | n.d. | n.d. | 0.01 | 0.01 | 0.01 | n.d. | n.d. | n.d. | n.d. | 0.01 | 0.01 | 0.01 |
| LOI | 12.3 | 12.2 | 8.00 | 5.68 | 3.71 | 2.37 | 5.01 | 2.99 | 3.95 | 1.94 | 2.37 | 0.22 | 0.48 |
| Total | 100.00 | 99.91 | 100.15 | 99.92 | 100.06 | 100.05 | 100.01 | 100.05 | 100.04 | 100.04 | 100.08 | 100.11 | 100.10 |
| Mg# | 90.3 | 91.8 | 85.7 | 84.2 | 84.0 | 78.0 | 91.0 | 85.4 | 86.7 | 82.2 | 84.8 | 75.8 | 75.3 |
| Zn | 34 | 33 | 54 | 42 | 19 | 22 | 4 | 14 | 36 | 21 | 10 | 35 | 45 |
| Cu | 211 | 4 | 50 | 23 | 114 | 57 | 124 | 139 | 16 | 88 | 9 | 90 | 69 |
| Sc | 15 | 4 | 13 | 13 | 23 | 22 | 22 | 30 | 23 | 36 | 12 | 28 | 17 |
| Ga | 3 | n.d. | 5 | 8 | 12 | 16 | 7 | 10 | 9 | 11 | 12 | 13 | 13 |
| Ni | 1823 | 2166 | 986 | 545 | 129 | 59 | 403 | 129 | 279 | 101 | 69 | 177 | 162 |
| Co | 82 | 102 | 96 | 79 | 25 | 20 | 23 | 25 | 48 | 51 | 18 | 45 | 45 |
| Cr | 3146 | 2287 | 1926 | 683 | 711 | 337 | 1927 | 466 | 1579 | 401 | 507 | 461 | 391 |
| V | 63 | 28 | 61 | 56 | 81 | 84 | 85 | 128 | 63 | 115 | 43 | 100 | 69 |
| Ba | 3 | 7 | 6 | 10 | 20 | 17 | 33 | 5 | 6 | 33 | 21 | 14 | 16 |
| Pb | 7 | 6 | 9 | 9 | 9 | 9 | 8 | 8 | 9 | 11 | 9 | 13 | 10 |
| ICP-MS analyses:* | | | (XRF) | (XRF) | (XRF) | | (XRF) | | (XRF) | (XRF) | | | |
| Rb | 0.123 | 0.078 | 2 | 2 | n.d. | 0.284 | n.d. | 0.654 | n.d. | 2 | 2.71 | 0.257 | 0.139 |
| Sr | 6.46 | 44.1 | 159 | 160 | 263 | 344 | 425 | 210 | 249 | 243 | 251 | 176 | 191 |
| Y | 1.81 | 0.312 | 4 | 6 | 5 | 5.99 | 5 | 3.81 | 4 | 9 | 2.93 | 4.05 | 3.39 |
| Zr | 3.92 | 0.626 | 7 | 10 | 7 | 15.9 | 4 | 5.09 | 2 | 8 | 7.21 | 11.3 | 8.05 |
| La | 0.082 | 0.013 | n.d. | n.d. | n.d. | 0.841 | n.d. | 0.207 | n.d. | n.d. | 0.472 | 0.596 | 0.560 |
| Ce | 0.314 | 0.057 | n.d. | n.d. | n.d. | 2.29 | 6 | 0.641 | n.d. | 7 | 1.17 | 1.60 | 1.46 |
| Pr | 0.058 | 0.011 | | | | 0.362 | | 0.112 | | | 0.194 | 0.284 | 0.232 |
| Nd | 0.371 | 0.066 | n.d. | n.d. | n.d. | 1.86 | n.d. | 0.759 | n.d. | n.d. | 1.04 | 1.57 | 1.22 |
| Sm | 0.142 | 0.025 | | | | 0.65 | | 0.323 | | | 0.347 | 0.526 | 0.420 |
| Eu | 0.054 | 0.011 | | | | 0.406 | | 0.226 | | | 0.335 | 0.327 | 0.343 |
| Gd | 0.207 | 0.032 | | | | 0.849 | | 0.516 | | | 0.427 | 0.678 | 0.510 |
| Tb | 0.040 | 0.005 | | | | 0.156 | | 0.099 | | | 0.075 | 0.122 | 0.093 |
| Dy | 0.262 | 0.034 | | | | 0.973 | | 0.650 | | | 0.502 | 0.727 | 0.565 |
| Ho | 0.059 | 0.008 | | | | 0.214 | | 0.145 | | | 0.115 | 0.152 | 0.118 |
| Er | 0.162 | 0.021 | | | | 0.574 | | 0.391 | | | 0.337 | 0.391 | 0.316 |
| Tm | 0.025 | 0.004 | | | | 0.086 | | 0.059 | | | 0.052 | 0.055 | 0.045 |
| Yb | 0.165 | 0.023 | | | | 0.531 | | 0.371 | | | 0.352 | 0.341 | 0.280 |
| Lu | 0.026 | 0.004 | | | | 0.080 | | 0.053 | | | 0.053 | 0.048 | 0.042 |
| Nb | 0.138 | 0.075 | 2 | 3 | n.d. | 0.375 | n.d. | 0.165 | 3 | 3 | 0.979 | 0.178 | 0.265 |
| Hf | 0.159 | 0.027 | n.d. | n.d. | n.d. | 0.572 | n.d. | 0.233 | n.d. | n.d. | 0.264 | 0.488 | 0.332 |
| Ta | 0.009 | 0.127 | | | | 0.021 | | 0.010 | | | 0.074 | 0.017 | 0.015 |
| Th | 0.004 | 0.002 | n.d. | n.d. | n.d. | 0.014 | n.d. | 0.007 | n.d. | n.d. | 0.074 | 0.025 | 0.011 |
| U | 0.003 | 0.083 | | | | 0.007 | | 0.002 | | | 0.021 | 0.006 | 0.005 |
| Nb/Y | 0.08 | 0.24 | 0.67 | 0.48 | | 0.06 | | 0.04 | 0.76 | 0.39 | 0.33 | 0.04 | 0.08 |
| (La/Sm) _N | 0.37 | 0.34 | | | | 0.84 | | 0.41 | | | 0.88 | 0.73 | 0.86 |
| (Sm/Yb) _N | 0.96 | 1.19 | | | | 1.35 | | 0.97 | | | 1.09 | 1.71 | 1.66 |
| (La/Yb) _N | 0.36 | 0.41 | | | | 1.14 | | 0.40 | | | 0.96 | 1.25 | 1.43 |

Appendix Table 5.1. (2/2)

| Unit Rock type | Isotropic gabbro | | | | | | | | | | | |
|--------------------------------|----------------------|----------------|-----------------|-----------------|---------------|------------------|------------------|------------------|------------------|------------------|---------------------|---------------------|
| | isotropic mafic rock | | | | | acidic rock | | | | | | |
| Sample rock | MK431 gb | MK455 Fe-gb | MK38 diorite | MK39 diorite | MK42 ol-gb | MK422 pl gran | MK423 pl gran | MK425 pl gran | MK456 pl gran | MK27B pl gran | MK748 qz-diorite | MK749 qz-diorite |
| Note | N-MORB | N-MORB | E-MORB | E-MORB | E-MORB | | | | | | E-MORB | E-MORB |
| Age | | | | | | 1295±2Ma | | | | | 125±6Ma | 122±2Ma |
| <i>XRF analyses:</i> | | | | | | | | | | | | |
| SiO ₂ | 54.5 | 47.1 | 54.8 | 51.1 | 43.8 | 77.0 | 77.2 | 76.4 | 63.6 | 74.2 | 58.3 | 56.5 |
| TiO ₂ | 0.33 | 2.51 | 1.08 | 2.05 | 0.80 | 0.11 | 0.09 | 0.08 | 0.51 | 0.31 | 0.98 | 1.11 |
| Al ₂ O ₃ | 19.5 | 12.8 | 15.9 | 13.5 | 7.81 | 10.5 | 11.0 | 11.6 | 18.0 | 12.1 | 13.4 | 16.4 |
| Fe ₂ O ₃ | 0.48 | 1.74 | 1.13 | 1.66 | 1.38 | 0.14 | 0.14 | 0.13 | 0.41 | 0.25 | 1.00 | 0.99 |
| FeO | 3.23 | 11.6 | 7.52 | 11.1 | 9.21 | 0.91 | 0.96 | 0.85 | 2.75 | 1.67 | 6.69 | 6.58 |
| MnO | 0.06 | 0.17 | 0.14 | 0.21 | 0.17 | 0.01 | 0.01 | 0.01 | 0.04 | 0.02 | 0.15 | 0.14 |
| MgO | 4.37 | 8.86 | 4.75 | 6.38 | 25.53 | 0.27 | 0.25 | 0.22 | 1.26 | 1.22 | 5.82 | 3.53 |
| CaO | 9.61 | 11.0 | 7.97 | 9.85 | 6.70 | 4.09 | 1.50 | 2.97 | 3.68 | 3.02 | 7.94 | 6.42 |
| Na ₂ O | 5.47 | 1.81 | 4.56 | 3.18 | 1.05 | 6.40 | 5.28 | 5.45 | 7.67 | 6.42 | 3.61 | 5.06 |
| K ₂ O | 0.99 | 0.21 | 0.96 | 0.42 | 0.06 | n.d. | 2.07 | 1.80 | 1.47 | 0.18 | 0.84 | 0.75 |
| P ₂ O ₅ | 0.04 | 0.03 | 0.26 | 0.41 | 0.13 | 0.01 | 0.01 | 0.01 | 0.09 | 0.05 | 0.13 | 0.45 |
| LOI | 1.71 | 1.40 | 0.99 | 0.35 | 3.41 | 0.97 | 1.71 | 0.87 | 0.90 | 0.60 | 1.01 | 1.69 |
| Total | 100.33 | 99.14 | 100.04 | 100.07 | 100.08 | 100.47 | 100.25 | 100.37 | 100.37 | 100.10 | 99.87 | 99.55 |
| Mg# | 70.7 | 57.6 | 53.0 | 50.7 | 83.2 | 34.6 | 32.0 | 31.8 | 44.9 | 56.5 | 60.8 | 48.8 |
| Zn | 20 | 57 | 78 | 123 | 72 | n.d. | n.d. | n.d. | 15 | 9 | 57 | 67 |
| Cu | 13 | 81 | 15 | 50 | 81 | 7 | 21 | 4 | n.d. | 6 | 13 | 14 |
| Sc | 13 | 51 | 31 | 48 | 27 | 5 | 4 | 5 | 5 | 6 | 28 | 16 |
| Ga | 18 | 17 | 23 | 24 | 9 | 10 | 12 | 15 | 27 | 17 | 18 | 23 |
| Ni | 4 | 32 | 9 | 33 | 850 | n.d. | n.d. | n.d. | n.d. | n.d. | 17 | 3 |
| Co | 13 | 61 | 23 | 32 | 85 | n.d. | n.d. | n.d. | 7 | 4 | 27 | 14 |
| Cr | 91 | 54 | 49 | 180 | 1361 | n.d. | n.d. | n.d. | 4 | 44 | 155 | 17 |
| V | 77 | 715 | 204 | 320 | 148 | 6 | 4 | 4 | 29 | 30 | 191 | 94 |
| Ba | 70 | 73 | 78 | 99 | 31 | n.d. | 26 | 47 | 134 | 21 | 149 | 184 |
| Pb | 9 | 7 | 11 | 10 | 5 | 9 | 9 | 11 | 12 | 9 | 12 | 11 |
| <i>ICP-MS analyses:*</i> | | | | | | | | | | | | |
| Rb | 7 | 1.23 | 4.76 | 3.40 | 0.263 | 0.687 | 9.69 | 8.12 | 6.92 | 1.38 | 17.0 | 15.4 |
| Sr | 441 | 240 | 190 | 220 | 126 | 16.8 | 38.6 | 26.8 | 243 | 218 | 206 | 269 |
| Y | 15 | 19.5 | 31.3 | 36.4 | 12.4 | 19.2 | 27.1 | 28.8 | 29.0 | 29.4 | 34 | 33.2 |
| Zr | 43 | 49.5 | 142 | 164 | 48.1 | 56.9 | 70.7 | 65.4 | 131 | 74.1 | 86 | 120 |
| La | 8 | 1.20 | 8.06 | 11.7 | 2.36 | 20.4 | 36.0 | 17.9 | 11.2 | 11.8 | n.d. | 10.8 |
| Ce | 18 | 3.94 | 20.1 | 28.4 | 6.12 | 34.8 | 66.7 | 33.6 | 22.2 | 25.1 | 12 | 25.0 |
| Pr | | 0.746 | 2.85 | 4.01 | 0.950 | 4.04 | 6.52 | 4.46 | 2.56 | 2.69 | | 3.64 |
| Nd | n.d. | 4.41 | 13.3 | 18.7 | 4.72 | 11.7 | 19.5 | 14.0 | 9.95 | 9.90 | 13 | 16.6 |
| Sm | | 1.64 | 3.94 | 5.41 | 1.50 | 1.95 | 3.96 | 2.83 | 2.49 | 2.29 | | 5.12 |
| Eu | | 0.921 | 0.954 | 1.78 | 0.478 | 0.265 | 0.319 | 0.201 | 1.07 | 0.528 | | 2.27 |
| Gd | | 2.41 | 4.72 | 6.12 | 1.88 | 1.81 | 3.95 | 2.50 | 2.94 | 2.63 | | 5.74 |
| Tb | | 0.451 | 0.812 | 1.03 | 0.322 | 0.359 | 0.640 | 0.536 | 0.504 | 0.492 | | 0.945 |
| Dy | | 3.06 | 5.06 | 6.55 | 2.07 | 2.66 | 4.06 | 3.88 | 3.46 | 3.56 | | 6.00 |
| Ho | | 0.682 | 1.05 | 1.38 | 0.452 | 0.685 | 0.846 | 0.940 | 0.854 | 0.857 | | 1.26 |
| Er | | 1.95 | 2.89 | 3.71 | 1.24 | 2.34 | 2.53 | 3.16 | 2.64 | 2.74 | | 3.50 |
| Tm | | 0.302 | 0.437 | 0.541 | 0.186 | 0.459 | 0.483 | 0.607 | 0.465 | 0.454 | | 0.512 |
| Yb | | 1.97 | 2.76 | 3.46 | 1.19 | 3.63 | 3.30 | 4.88 | 3.37 | 3.56 | | 3.28 |
| Lu | | 0.296 | 0.401 | 0.491 | 0.176 | 0.646 | 0.563 | 0.847 | 0.572 | 0.551 | | 0.477 |
| Nb | 2 | 2.16 | 8.18 | 10.9 | 2.34 | 5.10 | 7.39 | 7.73 | 9.34 | 14.7 | 5 | 10.9 |
| Hf | n.d. | 1.30 | 3.50 | 4.30 | 1.78 | 3.10 | 2.04 | 2.78 | 1.13 | 2.68 | 3 | 3.90 |
| Ta | | 0.115 | 0.499 | 0.664 | 0.131 | 0.588 | 1.45 | 0.837 | 0.670 | 1.42 | | 0.752 |
| Th | 2 | 0.046 | 1.13 | 0.852 | 0.118 | 12.9 | 15.1 | 10.6 | 3.58 | 12.3 | n.d. | 1.41 |
| U | | 0.043 | 0.564 | 0.232 | 0.035 | 1.73 | 2.43 | 2.22 | 0.518 | 3.10 | | 0.391 |
| Nb/Y | 0.13 | 0.11 | 0.26 | 0.30 | 0.19 | 0.27 | 0.27 | 0.27 | 0.32 | 0.50 | 0.16 | 0.33 |
| (La/Sm) _N | | 0.47 | 1.32 | 1.40 | 1.02 | 6.76 | 5.87 | 4.09 | 2.90 | 3.33 | | 1.36 |
| (Sm/Yb) _N | | 0.92 | 1.59 | 1.74 | 1.39 | 0.60 | 1.33 | 0.64 | 0.82 | 0.72 | | 1.73 |
| (La/Yb) _N | | 0.44 | 2.10 | 2.43 | 1.42 | 4.03 | 7.83 | 2.63 | 2.38 | 2.38 | | 2.36 |

Appendix Table 5.2. (1/4) Major (wt.%) and trace (ppm) element composition of representative sub-volcanic and volcanic rocks from the sheeted dyke complex and volcanic sequence of the Band-e-Zeyarat ophiolite. Abbreviations: bas: basalt; bas and: basaltic andesite; rhy: rhyolite; Fe-bas: ferrobasalt; and: andesite; MLF: massive lava flow; XRF: X-ray fluorescence spectrometry; ICP-MS: inductively coupled plasma-mass spectrometry; n.d.: not detected. $Mg\# = 100 \times MgO / (MgO + FeO)$. $Fe_2O_3 = 0.15 \times FeO$. Normalizing values for REE ratios from Sun & McDonough (1989).

| Rock type | Type-I (N-MORB) | | | | | | | | | | Type-IIa (E-MORB) | | | |
|--------------------------------|-------------------|---------|---------|--------|--------|--------|--------------|--------|--------|---------|-------------------|---------|---------|--------|
| | Volcanic sequence | | | | | | Sheeted dyke | | | | Volcanic sequence | | | |
| Stratigraphic unit | MK97 | MK100 | MK101 | MK108 | MK713 | MK770 | MK29 | MK89 | MK92 | MK94 | MK4 | MK7 | MK106 | MK400 |
| Sample rock | bas | bas and | bas and | bas | bas | bas | bas | bas | rhy | bas | bas | bas | bas | bas |
| Note | pillow | pillow | pillow | MLF | pillow | pillow | dyke | dyke | dyke | dyke | MLF | MLF | pillow | pillow |
| <i>XRF analyses:</i> | | | | | | | | | | | | | | |
| SiO ₂ | 46.7 | 53.1 | 54.0 | 50.9 | 49.2 | 48.1 | 47.7 | 49.4 | 71.8 | 49.6 | 50.4 | 48.9 | 52.0 | 55.1 |
| TiO ₂ | 0.83 | 1.28 | 1.53 | 1.35 | 2.32 | 1.16 | 1.13 | 1.04 | 0.35 | 1.48 | 2.01 | 1.60 | 1.64 | 2.08 |
| Al ₂ O ₃ | 18.4 | 16.3 | 15.9 | 12.7 | 11.7 | 17.2 | 14.9 | 14.9 | 13.8 | 13.9 | 14.4 | 13.7 | 13.4 | 13.0 |
| Fe ₂ O ₃ | 1.04 | 1.34 | 1.37 | 1.43 | 1.51 | 1.28 | 1.65 | 1.11 | 0.21 | 1.43 | 1.32 | 1.32 | 1.16 | 1.02 |
| FeO | 6.93 | 8.93 | 9.10 | 9.57 | 10.1 | 8.55 | 11.0 | 7.39 | 1.39 | 9.54 | 8.82 | 8.83 | 7.72 | 6.81 |
| MnO | 0.15 | 0.45 | 0.51 | 0.23 | 0.21 | 0.49 | 0.18 | 0.25 | 0.02 | 0.15 | 0.19 | 0.20 | 0.17 | 0.19 |
| MgO | 8.36 | 4.82 | 3.49 | 9.74 | 4.94 | 6.71 | 9.12 | 10.1 | 1.20 | 9.73 | 8.33 | 8.80 | 7.42 | 4.09 |
| CaO | 10.0 | 6.81 | 6.05 | 8.52 | 10.4 | 8.59 | 10.6 | 11.2 | 2.08 | 8.67 | 7.14 | 8.11 | 8.55 | 8.86 |
| Na ₂ O | 3.32 | 4.16 | 5.03 | 2.62 | 4.18 | 3.18 | 2.21 | 2.42 | 8.62 | 2.95 | 3.20 | 3.22 | 5.44 | 5.83 |
| K ₂ O | 0.82 | 0.68 | 1.15 | 0.90 | 0.65 | 1.53 | 0.08 | 0.10 | 0.01 | 0.41 | 0.93 | 0.85 | 0.24 | 1.37 |
| P ₂ O ₅ | 0.07 | 0.13 | 0.16 | 0.15 | 0.30 | 0.11 | 0.06 | 0.10 | 0.07 | 0.27 | 0.37 | 0.28 | 0.28 | 0.36 |
| LOI | 3.35 | 1.98 | 1.78 | 1.93 | 4.20 | 2.99 | 1.53 | 2.02 | 0.45 | 1.85 | 2.92 | 4.11 | 2.08 | 0.80 |
| Total | 100.04 | 100.02 | 100.04 | 100.08 | 99.69 | 99.86 | 100.08 | 100.04 | 100.00 | 100.00 | 100.00 | 99.91 | 100.09 | 99.46 |
| Mg# | 68.2 | 49.0 | 40.6 | 64.5 | 46.7 | 58.3 | 59.7 | 70.8 | 60.7 | 64.5 | 62.7 | 64.0 | 63.1 | 51.7 |
| Zn | 57 | 106 | 93 | 59 | 87 | 53 | 89 | 79 | 12 | 60 | 88 | 92 | 75 | 90 |
| Cu | 147 | 107 | 77 | 4 | 31 | 130 | 24 | 13 | n.d. | 8 | 43 | 51 | 32 | 42 |
| Sc | 26 | 22 | 23 | 44 | 30 | 26 | 33 | 41 | 6 | 41 | 33 | 34 | 26 | 19 |
| Ga | 16 | 17 | 15 | 14 | 16 | 15 | 17 | 16 | 17 | 20 | 16 | 17 | 15 | 9 |
| Ni | 146 | 116 | 63 | 64 | 6 | 74 | 50 | 76 | n.d. | 68 | 31 | 44 | 61 | 34 |
| Co | 43 | 45 | 33 | 44 | 58 | 50 | 46 | 32 | 2 | 27 | 48 | 38 | 45 | 35 |
| Cr | 359 | 231 | 278 | 312 | 20 | 261 | 162 | 367 | 6 | 214 | 117 | 182 | 197 | 92 |
| V | 156 | 166 | 220 | 270 | 311 | 176 | 284 | 210 | 10 | 275 | 211 | 240 | 194 | 214 |
| Ba | 14 | 34 | 46 | 108 | 90 | 64 | 19 | 20 | 107.1 | 43 | 83 | 85 | 81.7 | 69.7 |
| Pb | 7 | 10 | 17 | 7 | 9 | 9 | 8 | 8 | 9 | 8 | 8 | 9 | 11 | 8 |
| <i>ICP-MS analyses:*</i> | | | | | | | | | | | | | | |
| Rb | 1.76 | 3.68 | 4.81 | 18 | 8.40 | 21.2 | 0.736 | 0.982 | 0.631 | (XRF) 3 | (XRF) 6.76 | (XRF) 7 | (XRF) 4 | 15.9 |
| Sr | 314 | 285 | 299 | 288 | 56.2 | 315 | 208 | 297 | 103 | 290 | 101 | 354 | 113 | 141 |
| Y | 15.0 | 45.3 | 50.7 | 34 | 37.6 | 23.2 | 19.4 | 19.90 | 57.7 | 44 | 41.8 | 41 | 27 | 37.9 |
| Zr | 55.7 | 121 | 143 | 95 | 107 | 60.4 | 55.4 | 70.4 | 523 | 138 | 184 | 165 | 124 | 142 |
| La | 1.56 | 4.34 | 5.99 | 5 | 5.97 | 2.76 | 2.08 | 0.872 | 22.4 | 6 | 10.3 | 10 | 6 | 10.4 |
| Ce | 4.93 | 12.1 | 17.9 | 15 | 16.3 | 7.49 | 5.97 | 3.14 | 47.6 | 20 | 25.5 | 28 | 20 | 25.5 |
| Pr | 0.838 | 2.00 | 2.86 | | 2.51 | 1.24 | 1.03 | 0.638 | 5.71 | | 3.82 | | | 3.71 |
| Nd | 4.67 | 10.9 | 14.4 | 3 | 12.5 | 6.56 | 5.98 | 4.31 | 22.2 | 12 | 17.7 | n.d. | 14 | 16.8 |
| Sm | 1.62 | 3.58 | 4.89 | | 3.99 | 2.23 | 2.15 | 1.65 | 5.18 | | 5.23 | | | 4.96 |
| Eu | 0.676 | 1.31 | 1.90 | | 1.39 | 0.819 | 1.17 | 0.720 | 0.628 | | 1.64 | | | 1.55 |
| Gd | 2.21 | 4.69 | 6.54 | | 5.10 | 2.94 | 2.59 | 2.52 | 5.31 | | 6.37 | | | 5.60 |
| Tb | 0.405 | 0.874 | 1.20 | | 0.905 | 0.529 | 0.496 | 0.478 | 0.991 | | 1.07 | | | 0.991 |
| Dy | 2.79 | 5.90 | 7.61 | | 5.98 | 3.61 | 3.11 | 3.15 | 6.28 | | 6.82 | | | 6.45 |
| Ho | 0.636 | 1.32 | 1.68 | | 1.30 | 0.805 | 0.664 | 0.698 | 1.43 | | 1.42 | | | 1.38 |
| Er | 1.81 | 3.73 | 4.68 | | 3.73 | 2.36 | 1.78 | 1.94 | 4.53 | | 3.96 | | | 3.91 |
| Tm | 0.285 | 0.584 | 0.717 | | 0.567 | 0.362 | 0.278 | 0.305 | 0.751 | | 0.586 | | | 0.585 |
| Yb | 1.91 | 3.92 | 4.61 | | 3.84 | 2.42 | 1.69 | 1.97 | 5.08 | | 3.85 | | | 3.83 |
| Lu | 0.284 | 0.585 | 0.691 | | 0.570 | 0.355 | 0.239 | 0.275 | 0.800 | | 0.562 | | | 0.556 |
| Nb | 1.36 | 3.42 | 4.39 | 4 | 4.73 | 2.31 | 1.64 | 1.87 | 28.7 | 5 | 8.59 | 9 | 6 | 10.0 |
| Hf | 1.51 | 3.34 | 3.65 | 3 | 4.28 | 1.75 | 1.80 | 1.46 | 3.09 | 4 | 4.79 | n.d. | n.d. | 4.86 |
| Ta | 0.119 | 0.297 | 0.440 | | 0.445 | 0.169 | 0.103 | 0.090 | 1.57 | | 0.468 | | | 0.601 |
| Th | 0.063 | 0.244 | 0.434 | n.d. | 0.611 | 0.129 | 0.086 | 0.078 | 5.56 | n.d. | 0.716 | n.d. | n.d. | 1.22 |
| U | 0.032 | 0.088 | 0.138 | | 0.263 | 0.051 | 0.029 | 0.033 | 0.839 | | 0.262 | | | 0.320 |
| Nb/Y | 0.09 | 0.08 | 0.09 | 0.12 | 0.13 | 0.10 | 0.08 | 0.09 | 0.50 | 0.11 | 0.21 | 0.21 | 0.23 | 0.26 |
| (La/Sm) _N | 0.62 | 0.78 | 0.79 | | 0.97 | 0.80 | 0.62 | 0.34 | 2.79 | | 1.27 | | | 1.36 |
| (Sm/Yb) _N | 0.94 | 1.01 | 1.18 | | 1.16 | 1.02 | 1.41 | 0.93 | 1.13 | | 1.51 | | | 1.44 |
| (La/Yb) _N | 0.59 | 0.80 | 0.93 | | 1.12 | 0.82 | 0.88 | 0.32 | 3.17 | | 1.92 | | | 1.95 |
| Th/Ta | 0.53 | 0.82 | 0.99 | | 1.37 | 0.76 | 0.83 | 0.87 | 3.54 | | 1.53 | | | 2.03 |

Appendix Table 5.2. (2/4)

| Rock type | Type-Ia (E-MORB) | | | | | | | | | | | Type-Ib (E-MORB) | | |
|--------------------------------|------------------------|------------------------|------------------------|---------------------|---------------------|----------------------|---------------------|---------------------|---------------------|----------------------|----------------------|-------------------|-------------------------|----------------------|
| Stratigraphic unit | Volcanic sequence | | | Sheeted dyke | | | | | | | | Volcanic sequence | | |
| Sample rock Note | MK402 bas pillow | MK714 bas pillow | MK715 bas pillow | MK30 bas dyke | MK43 bas dyke | MK783 bas dyke | MK28 bas dyke | MK31 bas dyke | MK95 bas dyke | MK453 bas dyke | MK457 bas dyke | MK6 bas MLF | MK8 Fe-bas pillow | MK9 bas pillow |
| <i>XRF analyses:</i> | | | | | | | | | | | | | | |
| SiO ₂ | 47.8 | 55.6 | 49.4 | 38.8 | 49.3 | 48.4 | 50.0 | 49.5 | 52.1 | 51.0 | 49.3 | 48.1 | 53.6 | 45.6 |
| TiO ₂ | 1.55 | 1.75 | 1.56 | 1.06 | 1.74 | 1.25 | 1.96 | 3.00 | 1.61 | 1.41 | 1.39 | 1.92 | 1.76 | 1.88 |
| Al ₂ O ₃ | 14.5 | 13.7 | 13.4 | 15.5 | 13.2 | 15.3 | 13.9 | 13.0 | 11.4 | 12.8 | 13.5 | 14.3 | 13.6 | 14.0 |
| Fe ₂ O ₃ | 1.33 | 1.04 | 1.13 | 2.36 | 1.87 | 1.07 | 1.58 | 2.04 | 1.39 | 1.42 | 1.33 | 1.52 | 1.51 | 1.66 |
| FeO | 8.87 | 6.93 | 7.54 | 15.7 | 12.5 | 7.14 | 10.5 | 13.6 | 9.29 | 9.48 | 8.85 | 10.1 | 10.0 | 11.1 |
| MnO | 0.18 | 0.26 | 0.21 | 0.14 | 0.18 | 0.12 | 0.19 | 0.26 | 0.24 | 0.17 | 0.17 | 0.17 | 0.25 | 0.31 |
| MgO | 7.71 | 6.54 | 7.07 | 14.4 | 7.67 | 9.51 | 7.00 | 5.39 | 10.90 | 8.39 | 9.55 | 9.01 | 5.96 | 10.73 |
| CaO | 11.1 | 6.44 | 8.71 | 6.32 | 7.70 | 12.5 | 10.0 | 8.68 | 7.14 | 10.2 | 11.1 | 7.38 | 6.78 | 7.52 |
| Na ₂ O | 3.29 | 4.20 | 3.12 | 1.12 | 3.23 | 2.60 | 3.03 | 3.13 | 3.51 | 2.83 | 2.53 | 3.73 | 3.82 | 2.98 |
| K ₂ O | 0.49 | 2.12 | 2.50 | 0.09 | 0.34 | 0.21 | 0.59 | 0.41 | 0.17 | 0.43 | 0.59 | 0.22 | 0.00 | 0.02 |
| P ₂ O ₅ | 0.20 | 0.26 | 0.24 | 0.13 | 0.34 | 0.13 | 0.35 | 0.45 | 0.30 | 0.24 | 0.16 | 0.31 | 0.54 | 0.25 |
| LOI | 3.00 | 1.19 | 4.46 | 4.45 | 1.95 | 1.64 | 0.81 | 0.50 | 2.01 | 1.11 | 1.03 | 3.20 | 2.13 | 3.92 |
| Total | 100.08 | 99.98 | 99.27 | 100.07 | 100.03 | 99.91 | 99.98 | 99.91 | 100.06 | 99.44 | 99.52 | 100.04 | 99.95 | 99.98 |
| Mg# | 60.8 | 62.7 | 62.5 | 62.0 | 52.3 | 70.3 | 54.2 | 41.4 | 67.6 | 61.2 | 65.8 | 61.3 | 51.4 | 63.4 |
| Zn | 75 | 79 | 88 | 103 | 17 | 34 | 106 | 178 | 145 | 87 | 78 | 112 | 122 | 197 |
| Cu | 60 | 50 | 47 | n.d. | n.d. | 192 | 65 | 13 | 5 | 85 | 45 | 48 | n.d. | 49 |
| Sc | 25 | 27 | 28 | 36 | 42 | 32 | 44 | 53 | 46 | 37 | 35 | 36 | 25 | 36 |
| Ga | 17 | 15 | 15 | 17 | 23 | 15 | 22 | 25 | 21 | 19 | 16 | 20 | 24 | 18 |
| Ni | 90 | 43 | 53 | 181 | 24 | 76 | 41 | 1 | 21 | 41 | 75 | 45 | 7 | 61 |
| Co | 48 | 43 | 49 | 66 | 38 | 47 | 43 | 34 | 13 | 46 | 52 | 38 | 24 | 51 |
| Cr | 203 | 200 | 172 | 302 | 80 | 280 | 156 | 29 | 118 | 209 | 301 | 198 | 25 | 255 |
| V | 252 | 215 | 218 | 272 | 346 | 210 | 324 | 474 | 230 | 295 | 248 | 262 | 129 | 273 |
| Ba | 70.8 | 184 | 239.1 | 80.1 | 102 | 50.7 | 92.2 | 119 | 102 | 67.3 | 58 | 85 | 43 | 90 |
| Pb | 11 | 10 | 10 | 12 | 15 | 9 | 9 | 8 | 8 | 9 | 9 | 9 | 9 | 9 |
| <i>ICP-MS analyses:*</i> | | | | | | | | | | | | | | |
| Rb | 9.76 | 37 | 33.3 | 0.942 | 4.51 | 5.46 | 3.95 | 4.87 | 3.15 | 2.48 | 2.76 | 2.27 | 10.3 | 8.47 |
| Sr | 217 | 235 | 189 | 136 | 221 | 151 | 223 | 270 | 96 | 213 | 180 | 69.8 | 256 | 114 |
| Y | 26.7 | 32 | 29.7 | 22.7 | 36.9 | 23.1 | 44.2 | 50.5 | 46.0 | 33.7 | 30.4 | 32.0 | 65.0 | 34.8 |
| Zr | 98.9 | 115 | 115 | 83 | 123 | 74 | 154 | 123 | 159 | 120 | 105 | 140 | 281 | 131 |
| La | 6.19 | n.d. | 7.14 | 4.29 | 8.42 | 4.13 | 9.96 | 12.1 | 10.2 | 8.51 | 6.73 | 8.17 | 15.6 | 7.87 |
| Ce | 14.9 | 21 | 17.8 | 10.9 | 21.4 | 10.5 | 25.0 | 31.2 | 25.8 | 20.7 | 16.5 | 20.2 | 39.2 | 18.9 |
| Pr | 2.22 | | 2.57 | 1.66 | 3.15 | 1.59 | 3.66 | 4.66 | 3.80 | 3.04 | 2.40 | 2.92 | 5.81 | 2.78 |
| Nd | 10.3 | 18 | 12.0 | 7.95 | 15.2 | 7.90 | 17.4 | 21.4 | 17.8 | 14.0 | 11.1 | 13.6 | 27.0 | 13.1 |
| Sm | 3.09 | | 3.58 | 2.52 | 4.66 | 2.41 | 5.24 | 6.61 | 5.52 | 4.26 | 3.39 | 4.04 | 8.00 | 4.07 |
| Eu | 1.16 | | 1.14 | 0.528 | 1.48 | 0.912 | 1.56 | 2.00 | 1.36 | 1.32 | 1.18 | 1.23 | 2.23 | 1.25 |
| Gd | 3.84 | | 4.28 | 3.14 | 5.76 | 3.19 | 6.21 | 7.98 | 6.76 | 5.07 | 4.12 | 4.78 | 9.58 | 4.89 |
| Tb | 0.673 | | 0.729 | 0.579 | 1.00 | 0.565 | 1.12 | 1.38 | 1.18 | 0.900 | 0.736 | 0.820 | 1.64 | 0.859 |
| Dy | 4.29 | | 4.84 | 3.78 | 6.48 | 3.78 | 7.07 | 8.70 | 7.62 | 5.84 | 4.87 | 5.16 | 10.2 | 5.42 |
| Ho | 0.929 | | 1.03 | 0.795 | 1.35 | 0.808 | 1.53 | 1.77 | 1.63 | 1.26 | 1.06 | 1.06 | 2.10 | 1.14 |
| Er | 2.61 | | 2.87 | 2.22 | 3.75 | 2.29 | 4.21 | 4.79 | 4.43 | 3.60 | 2.98 | 2.88 | 5.49 | 3.04 |
| Tm | 0.392 | | 0.430 | 0.326 | 0.546 | 0.338 | 0.633 | 0.692 | 0.623 | 0.534 | 0.446 | 0.426 | 0.767 | 0.442 |
| Yb | 2.55 | | 2.73 | 2.06 | 3.45 | 2.15 | 4.04 | 4.44 | 3.94 | 3.45 | 2.88 | 2.68 | 4.69 | 2.76 |
| Lu | 0.365 | | 0.387 | 0.294 | 0.492 | 0.309 | 0.592 | 0.628 | 0.556 | 0.514 | 0.431 | 0.396 | 0.631 | 0.383 |
| Nb | 5.81 | 8 | 6.60 | 4.22 | 8.29 | 3.59 | 10.9 | 10.6 | 10.7 | 7.79 | 4.30 | 8.51 | 14.1 | 6.62 |
| Hf | 3.21 | 4 | 4.38 | 2.77 | 3.78 | 2.11 | 4.63 | 5.02 | 4.45 | 3.09 | 3.04 | 3.97 | 8.55 | 3.43 |
| Ta | 0.391 | | 0.460 | 0.284 | 0.539 | 0.226 | 0.745 | 0.713 | 0.722 | 0.382 | 0.254 | 0.533 | 0.768 | 0.391 |
| Th | 0.598 | n.d. | 0.614 | 0.371 | 0.664 | 0.258 | 0.849 | 0.664 | 0.937 | 0.568 | 0.443 | 0.583 | 0.907 | 0.457 |
| U | 0.189 | | 0.214 | 0.142 | 0.180 | 0.090 | 0.299 | 0.276 | 0.180 | 0.154 | 0.159 | 0.214 | 0.327 | 0.153 |
| Nb/Y | 0.22 | 0.25 | 0.22 | 0.19 | 0.22 | 0.16 | 0.25 | 0.21 | 0.23 | 0.23 | 0.14 | 0.27 | 0.22 | 0.19 |
| (La/Sm) _N | 1.29 | | 1.29 | 1.10 | 1.17 | 1.11 | 1.23 | 1.18 | 1.19 | 1.29 | 1.28 | 1.31 | 1.25 | 1.25 |
| (Sm/Yb) _N | 1.35 | | 1.46 | 1.36 | 1.50 | 1.24 | 1.44 | 1.65 | 1.56 | 1.37 | 1.30 | 1.67 | 1.90 | 1.64 |
| (La/Yb) _N | 1.74 | | 1.87 | 1.49 | 1.75 | 1.38 | 1.77 | 1.95 | 1.85 | 1.77 | 1.67 | 2.19 | 2.38 | 2.04 |
| Th/Ta | 1.53 | | 1.34 | 1.30 | 1.23 | 1.14 | 1.14 | 0.93 | 1.30 | 1.48 | 1.75 | 1.09 | 1.18 | 1.17 |

Appendix Table 5.2. (3/4)

| Rock type | Type-IIb (E-MORB) | | | | | | Type-IIc (E-MORB) | | |
|--------------------------------|-------------------|-------|--------|--------------|--------|--------|-------------------|--------|--------|
| | Volcanic sequence | | | Sheeted dyke | | | Volcanic sequence | | |
| Stratigraphic unit | MK10 | MK11 | MK110 | MK88 | MK93 | MK96 | MK86 | MK104 | MK105 |
| Sample | bas | and | bas | bas | bas | bas | bas | bas | bas |
| rock | dyke | MLF | dyke | dyke | dyke | dyke | MLF | pillow | pillow |
| Note | | | | | | | | | |
| <i>XRF analyses:</i> | | | | | | | | | |
| SiO ₂ | 47.8 | 58.7 | 47.5 | 50.6 | 49.0 | 50.4 | 49.5 | 47.3 | 44.9 |
| TiO ₂ | 1.92 | 1.19 | 1.48 | 1.50 | 1.50 | 1.64 | 1.44 | 1.65 | 1.60 |
| Al ₂ O ₃ | 14.4 | 14.4 | 13.6 | 14.4 | 14.4 | 13.7 | 13.5 | 14.6 | 14.8 |
| Fe ₂ O ₃ | 1.65 | 1.18 | 1.55 | 1.27 | 1.32 | 1.35 | 1.40 | 1.38 | 1.54 |
| FeO | 11.0 | 7.86 | 10.4 | 8.48 | 8.80 | 8.98 | 9.37 | 9.19 | 10.3 |
| MnO | 0.18 | 0.09 | 0.16 | 0.19 | 0.14 | 0.20 | 0.24 | 0.20 | 0.20 |
| MgO | 8.21 | 5.33 | 10.92 | 8.46 | 9.50 | 8.60 | 9.22 | 9.61 | 10.90 |
| CaO | 8.57 | 3.27 | 8.34 | 10.9 | 10.9 | 10.5 | 10.8 | 8.86 | 9.19 |
| Na ₂ O | 3.75 | 5.62 | 2.85 | 3.29 | 2.43 | 2.89 | 2.58 | 3.68 | 2.65 |
| K ₂ O | 0.13 | 0.06 | 0.11 | 0.12 | 0.22 | 0.19 | 0.17 | 0.36 | 0.38 |
| P ₂ O ₅ | 0.40 | 0.40 | 0.28 | 0.26 | 0.25 | 0.24 | 0.15 | 0.19 | 0.17 |
| LOI | 1.89 | 1.84 | 2.87 | 0.60 | 1.65 | 1.42 | 1.64 | 2.99 | 3.42 |
| Total | 99.94 | 99.93 | 100.03 | 100.02 | 100.04 | 100.04 | 100.03 | 100.03 | 100.07 |
| Mg# | 57.0 | 54.7 | 65.3 | 64.0 | 65.8 | 63.0 | 63.7 | 65.1 | 65.4 |
| Zn | 82 | 111 | 46 | 82 | 36 | 50 | 125 | 86 | 91 |
| Cu | 23 | 34 | n.d. | 30 | 52 | 45 | 7 | 86 | 80 |
| Sc | 33 | 18 | 37 | 37 | 38 | 43 | 42 | 40 | 42 |
| Ga | 21 | 26 | 18 | 18 | 19 | 19 | 18 | 17 | 19 |
| Ni | 46 | 4 | 104 | 61 | 106 | 61 | 70 | 34 | 47 |
| Co | 39 | 10 | 46 | 34 | 42 | 36 | 37 | 43 | 46 |
| Cr | 155 | 27 | 240 | 203 | 225 | 221 | 332 | 276 | 207 |
| V | 277 | 44 | 262 | 238 | 272 | 290 | 289 | 240 | 260 |
| Ba | 89 | 28 | 72 | 95 | 48 | 66 | 43 | 111 | 82 |
| Pb | 7 | 13 | 6 | 10 | 7 | 8 | 8 | 6 | 6 |
| <i>ICP-MS analyses:*</i> | | | | | | | | | |
| <i>(XRF)</i> | | | | | | | | | |
| Rb | 6.01 | 8.61 | 2.59 | 1 | 2.26 | 2.16 | 0.930 | 5.39 | 4.19 |
| Sr | 144 | 116 | 263 | 392 | 268 | 267 | 212 | 479 | 373 |
| Y | 30.5 | 78.2 | 33.8 | 36 | 27.3 | 26.5 | 17.8 | 32.8 | 34.4 |
| Zr | 135 | 340 | 121 | 142 | 124 | 131 | 72.4 | 132 | 121 |
| La | 8.26 | 20.8 | 8.30 | 8 | 7.39 | 7.06 | 4.11 | 6.97 | 6.20 |
| Ce | 20.4 | 51.9 | 21.0 | 29 | 18.5 | 18.3 | 10.8 | 18.7 | 17.1 |
| Pr | 2.91 | 7.40 | 2.98 | | 2.74 | 2.69 | 1.60 | 2.85 | 2.66 |
| Nd | 13.6 | 33.7 | 13.9 | 8 | 12.8 | 12.9 | 7.9 | 13.6 | 12.7 |
| Sm | 4.03 | 9.58 | 4.07 | | 3.91 | 3.85 | 2.46 | 4.13 | 3.99 |
| Eu | 1.28 | 2.44 | 1.32 | | 1.18 | 1.23 | 0.946 | 1.36 | 1.36 |
| Gd | 4.65 | 11.6 | 4.87 | | 4.57 | 4.68 | 2.82 | 5.06 | 5.02 |
| Tb | 0.804 | 2.013 | 0.856 | | 0.748 | 0.769 | 0.495 | 0.863 | 0.870 |
| Dy | 4.93 | 12.6 | 5.37 | | 4.69 | 4.82 | 3.14 | 5.12 | 5.38 |
| Ho | 1.04 | 2.59 | 1.14 | | 0.981 | 1.00 | 0.662 | 1.08 | 1.15 |
| Er | 2.76 | 6.96 | 3.03 | | 2.62 | 2.63 | 1.77 | 2.91 | 3.14 |
| Tm | 0.402 | 0.987 | 0.437 | | 0.375 | 0.368 | 0.255 | 0.420 | 0.461 |
| Yb | 2.56 | 5.98 | 2.71 | | 2.35 | 2.27 | 1.59 | 2.64 | 2.92 |
| Lu | 0.370 | 0.820 | 0.379 | | 0.325 | 0.312 | 0.224 | 0.379 | 0.422 |
| Nb | 7.86 | 19.5 | 7.80 | 9 | 7.61 | 7.09 | 3.72 | 6.69 | 7.01 |
| Hf | 3.39 | 10.5 | 3.56 | 3 | 4.19 | 3.73 | 2.12 | 4.30 | 4.12 |
| Ta | 0.458 | 1.07 | 0.490 | | 0.435 | 0.434 | 0.203 | 0.396 | 0.440 |
| Th | 0.460 | 1.31 | 0.560 | n.d. | 0.476 | 0.438 | 0.224 | 0.406 | 0.425 |
| U | 0.119 | 0.434 | 0.196 | | 0.117 | 0.113 | 0.047 | 0.150 | 0.209 |
| Nb/Y | 0.26 | 0.25 | 0.23 | 0.25 | 0.28 | 0.27 | 0.21 | 0.20 | 0.20 |
| (La/Sm) _N | 1.32 | 1.40 | 1.32 | | 1.22 | 1.18 | 1.08 | 1.09 | 1.00 |
| (Sm/Yb) _N | 1.75 | 1.78 | 1.67 | | 1.85 | 1.88 | 1.71 | 1.74 | 1.52 |
| (La/Yb) _N | 2.31 | 2.50 | 2.20 | | 2.26 | 2.23 | 1.85 | 1.89 | 1.52 |
| Th/Ta | 1.00 | 1.22 | 1.14 | | 1.09 | 1.01 | 1.11 | 1.03 | 0.97 |

Appendix Table 5.2. (4/4)

| Rock type | Type-Ilc (E-MORB) | | | Type-IId (E-MORB) | | | | | | | |
|--------------------------------|-------------------|-------|-------|-------------------|--------|--------|--------|--------|-------------------|--------|--------|
| | Volcanic sequence | | | Sheeted dyke | | | | | Volcanic sequence | | |
| Stratigraphic unit | MK109 | MK111 | MK112 | MK37A | MK37B | MK24 | MK26 | MK87 | MK3 | MK12 | MK779 |
| Sample | bas | bas | bas | bas | bas | bas | bas | bas | bas | bas | bas |
| Note | MLF | MLF | MLF | dyke | dyke | dyke | dyke | dyke | pillow | pillow | pillow |
| <i>XRF analyses:</i> | | | | | | | | | | | |
| SiO ₂ | 49.3 | 48.9 | 48.2 | 49.8 | 51.3 | 49.0 | 51.3 | 48.2 | 53.4 | 47.5 | 51.4 |
| TiO ₂ | 1.28 | 1.60 | 1.46 | 1.62 | 1.37 | 1.76 | 1.35 | 1.13 | 1.82 | 1.65 | 1.50 |
| Al ₂ O ₃ | 14.5 | 13.3 | 14.5 | 14.2 | 14.0 | 13.7 | 13.6 | 14.9 | 13.9 | 13.9 | 16.7 |
| Fe ₂ O ₃ | 1.27 | 1.56 | 1.39 | 1.42 | 1.29 | 1.55 | 1.32 | 1.07 | 1.12 | 1.73 | 1.05 |
| FeO | 8.50 | 10.4 | 9.28 | 9.49 | 8.61 | 10.3 | 8.77 | 7.12 | 7.44 | 11.5 | 7.03 |
| MnO | 0.19 | 0.20 | 0.17 | 0.17 | 0.16 | 0.18 | 0.17 | 0.18 | 0.38 | 0.14 | 0.14 |
| MgO | 8.89 | 8.51 | 9.53 | 8.55 | 8.02 | 9.00 | 8.79 | 12.70 | 5.18 | 8.99 | 5.05 |
| CaO | 11.1 | 10.4 | 9.47 | 9.72 | 9.69 | 9.52 | 8.96 | 10.4 | 8.81 | 6.35 | 10.5 |
| Na ₂ O | 2.36 | 2.62 | 2.55 | 2.51 | 3.12 | 2.90 | 3.63 | 2.08 | 4.50 | 4.82 | 3.79 |
| K ₂ O | 0.44 | 0.34 | 0.90 | 1.03 | 0.89 | 0.57 | 0.50 | 0.07 | 1.96 | 0.30 | 1.29 |
| P ₂ O ₅ | 0.12 | 0.20 | 0.23 | 0.26 | 0.27 | 0.23 | 0.19 | 0.16 | 0.31 | 0.37 | 0.20 |
| LOI | 2.05 | 1.95 | 2.28 | 1.15 | 1.27 | 1.29 | 1.48 | 2.06 | 1.09 | 2.89 | 1.31 |
| Total | 100.03 | 99.97 | 99.92 | 99.92 | 100.05 | 100.05 | 100.03 | 100.09 | 99.93 | 100.10 | 99.94 |
| Mgf# | 65.1 | 59.3 | 64.7 | 61.6 | 62.4 | 60.8 | 64.1 | 76.1 | 55.4 | 58.2 | 56.1 |
| Zn | 33 | 84 | 30 | 91 | 88 | 91 | 86 | 60 | 50 | 86 | 57 |
| Cu | 6 | 46 | 126 | 41 | 52 | 70 | 43 | 9 | 30 | 67 | 50 |
| Sc | 43 | 44 | 36 | 39 | 38 | 43 | 36 | 31 | 22 | 29 | 31 |
| Ga | 17 | 19 | 17 | 18 | 19 | 20 | 17 | 15 | 13 | 15 | 16 |
| Ni | 77 | 46 | 77 | 86 | 63 | 75 | 67 | 163 | 46 | 53 | 29 |
| Co | 39 | 42 | 43 | 43 | 28 | 43 | 40 | 33 | 38 | 38 | 33 |
| Cr | 301 | 228 | 236 | 260 | 223 | 226 | 260 | 261 | 137 | 208 | 205 |
| V | 268 | 284 | 257 | 258 | 251 | 287 | 226 | 194 | 228 | 231 | 216 |
| Ba | 81 | 112 | 102 | 195 | 183 | 89 | 69 | 86 | 335 | 75 | 179 |
| Pb | 9 | 9 | 9 | 9 | 10 | 9 | 10 | 7 | 7 | 12 | 9 |
| <i>ICP-MS analyses:*</i> | | | | | | | | | | | |
| | | (XRF) | | | | | | | (XRF) | | (XRF) |
| Rb | 6.12 | 8 | 9.35 | 10.9 | 7.75 | 3.39 | 3.81 | 0.495 | 23 | 3.16 | 22 |
| Sr | 297 | 399 | 306 | 163 | 200 | 205 | 223 | 304 | 164 | 176 | 357 |
| Y | 20.1 | 37 | 27.9 | 20.0 | 20.2 | 38.2 | 26.9 | 16.1 | 30 | 34.3 | 28 |
| Zr | 74.5 | 135 | 102 | 82.5 | 98.5 | 145 | 113 | 77.9 | 106 | 147 | 103 |
| La | 3.72 | 8 | 5.56 | 7.12 | 7.57 | 13.9 | 8.83 | 6.65 | 11 | 12.9 | n.d. |
| Ce | 10.2 | 21 | 14.9 | 16.7 | 17.9 | 31.7 | 21.1 | 16.3 | 26 | 29.8 | 21 |
| Pr | 1.62 | | 2.38 | 2.34 | 2.50 | 4.42 | 2.88 | 2.20 | | 3.98 | |
| Nd | 7.5 | 15 | 11.1 | 10.4 | 10.4 | 19.1 | 12.2 | 9.7 | n.d. | 16.8 | 13 |
| Sm | 2.40 | | 3.52 | 3.03 | 2.96 | 5.29 | 3.51 | 2.64 | | 4.84 | |
| Eu | 0.853 | | 1.18 | 0.964 | 1.03 | 1.57 | 1.10 | 0.929 | | 1.46 | |
| Gd | 3.05 | | 4.42 | 3.35 | 3.36 | 6.06 | 3.94 | 3.05 | | 5.56 | |
| Tb | 0.530 | | 0.762 | 0.563 | 0.570 | 1.06 | 0.664 | 0.514 | | 0.937 | |
| Dy | 3.23 | | 4.60 | 3.50 | 3.37 | 6.58 | 4.19 | 3.17 | | 5.92 | |
| Ho | 0.681 | | 0.968 | 0.744 | 0.71 | 1.42 | 0.892 | 0.642 | | 1.25 | |
| Er | 1.80 | | 2.53 | 1.98 | 1.92 | 3.88 | 2.44 | 1.75 | | 3.34 | |
| Tm | 0.258 | | 0.362 | 0.287 | 0.284 | 0.578 | 0.366 | 0.251 | | 0.493 | |
| Yb | 1.61 | | 2.24 | 1.78 | 1.78 | 3.60 | 2.32 | 1.59 | | 3.14 | |
| Lu | 0.229 | | 0.322 | 0.259 | 0.260 | 0.510 | 0.336 | 0.231 | | 0.460 | |
| Nb | 3.37 | 8 | 4.87 | 6.71 | 7.47 | 12.7 | 10.1 | 6.73 | 8 | 12.4 | 9 |
| Hf | 1.66 | 3 | 2.96 | 2.51 | 2.48 | 4.21 | 2.87 | 2.10 | n.d. | 3.63 | 3 |
| Ta | 0.178 | | 0.275 | 0.466 | 0.621 | 0.934 | 0.892 | 0.420 | | 0.779 | |
| Th | 0.224 | n.d. | 0.227 | 0.682 | 0.904 | 1.39 | 1.65 | 0.480 | n.d. | 1.18 | n.d. |
| U | 0.052 | | 0.078 | 0.237 | 0.308 | 0.578 | 0.532 | 0.146 | | 0.437 | |
| Nb/Y | 0.17 | 0.21 | 0.17 | 0.34 | 0.37 | 0.25 | 0.38 | 0.42 | 0.26 | 0.36 | 0.32 |
| (La/Sm) _N | 1.00 | | 1.02 | 1.51 | 1.65 | 1.70 | 1.62 | 1.63 | | 1.73 | |
| (Sm/Yb) _N | 1.65 | | 1.74 | 1.90 | 1.85 | 1.64 | 1.68 | 1.85 | | 1.71 | |
| (La/Yb) _N | 1.66 | | 1.78 | 2.87 | 3.06 | 2.78 | 2.73 | 3.00 | | 2.95 | |
| Th/Ta | 1.26 | | 0.82 | 1.46 | 1.46 | 1.80 | 1.85 | 1.14 | | 1.52 | |

Appendix Table 5.3. (1/2) Representative analyses of olivine from intrusive rocks forming the intrusive complex of the Band-e-Zeyarat ophiolite. Atoms per formula units (a.p.f.u.) are calculated on the bases of four cations. $Mg\# = 100 \times Mg / (Mg + Fe^{2+})$. Abbreviations, Fo: forsterite; Fa: fayalite; Te: tephroite.

| Unit | Isotropic gabbro | | | | | | | | | | | | | | | | | | | |
|--------------------------------|------------------|---------|---------|---------|---------|---------|---------|----------|----------|----------|---------|---------|---------|---------|----------|----------|---------|---------|---------|---------|
| Rock type | cumulitic gabbro | | | | | | | | | | | | | | | | | | | |
| Sample | MK32 | MK32 | MK32 | MK32 | MK32 | MK32 | MK32 | MK32 | MK32 | MK32 | MK32 | MK32 | MK32 | MK32 | MK32 | MK32 | MK35 | MK35 | MK35 | MK35 |
| Mineral-site | cr1-an1 | cr1-an5 | cr2-an3 | cr2-an5 | cr3-an1 | cr4-an3 | cr4-an5 | cr5--an1 | cr5--an4 | cr6--an1 | cr8-an5 | cr8-an8 | cr9-an1 | cr9-an5 | cr10-an5 | cr11-an1 | cr1-an6 | cr2-an3 | cr3-an3 | cr4-an1 |
| Position | | | | | | | | c | r | | | | | | | | | | | |
| SiO ₂ | 37.66 | 37.37 | 37.67 | 37.74 | 37.72 | 37.60 | 38.39 | 37.83 | 38.37 | 38.13 | 38.16 | 38.09 | 38.25 | 37.91 | 37.57 | 37.82 | 38.37 | 38.09 | 38.48 | 38.41 |
| TiO ₂ | 0.00 | 0.00 | 0.00 | 0.01 | 0.00 | 0.00 | 0.00 | 0.03 | 0.00 | 0.05 | 0.00 | 0.00 | 0.07 | 0.01 | 0.03 | 0.02 | 0.03 | 0.00 | 0.04 | 0.02 |
| Al ₂ O ₃ | 0.03 | 0.01 | 0.01 | 0.01 | 0.02 | 0.00 | 0.00 | 0.01 | 0.00 | 0.00 | 0.01 | 0.00 | 0.03 | 0.01 | 0.01 | 0.02 | 0.02 | 0.00 | 0.00 | 0.00 |
| Cr ₂ O ₃ | 0.01 | 0.00 | 0.03 | 0.00 | 0.00 | 0.02 | 0.00 | 0.04 | 0.00 | 0.00 | 0.00 | 0.00 | 0.01 | 0.01 | 0.00 | 0.00 | 0.02 | 0.00 | 0.06 | 0.00 |
| FeO | 25.90 | 25.24 | 25.46 | 25.42 | 25.60 | 25.16 | 25.04 | 24.78 | 25.43 | 25.39 | 25.09 | 25.29 | 24.71 | 25.79 | 25.58 | 25.22 | 24.10 | 24.68 | 23.74 | 23.96 |
| MnO | 0.37 | 0.38 | 0.32 | 0.37 | 0.40 | 0.40 | 0.41 | 0.40 | 0.30 | 0.32 | 0.50 | 0.35 | 0.26 | 0.28 | 0.38 | 0.33 | 0.34 | 0.35 | 0.37 | 0.45 |
| MgO | 36.51 | 36.52 | 36.65 | 36.73 | 36.82 | 37.00 | 37.35 | 37.39 | 37.34 | 37.22 | 37.71 | 38.03 | 37.14 | 37.18 | 36.57 | 37.41 | 38.49 | 38.01 | 38.75 | 38.43 |
| CaO | 0.00 | 0.00 | 0.01 | 0.00 | 0.00 | 0.00 | 0.00 | 0.00 | 0.00 | 0.00 | 0.00 | 0.00 | 0.00 | 0.00 | 0.00 | 0.00 | 0.00 | 0.00 | 0.00 | 0.00 |
| NiO | 0.00 | 0.02 | 0.00 | 0.04 | 0.07 | 0.04 | 0.08 | 0.02 | 0.06 | 0.00 | 0.04 | 0.00 | 0.05 | 0.02 | 0.03 | 0.03 | 0.06 | 0.08 | 0.04 | 0.00 |
| CoO | 0.10 | 0.14 | 0.03 | 0.00 | 0.12 | 0.04 | 0.06 | 0.09 | 0.10 | 0.06 | 0.10 | 0.07 | 0.05 | 0.06 | 0.12 | 0.01 | 0.08 | 0.01 | 0.11 | 0.07 |
| Total | 100.57 | 99.67 | 100.18 | 100.31 | 100.74 | 100.25 | 101.32 | 100.59 | 101.60 | 101.17 | 101.62 | 101.83 | 100.57 | 101.28 | 100.29 | 100.86 | 101.52 | 101.20 | 101.59 | 101.34 |
| <i>a.p.f.u.</i> | | | | | | | | | | | | | | | | | | | | |
| Si | 0.992 | 0.992 | 0.993 | 0.994 | 0.990 | 0.991 | 0.998 | 0.991 | 0.996 | 0.994 | 0.990 | 0.987 | 1.000 | 0.990 | 0.991 | 0.989 | 0.992 | 0.990 | 0.992 | 0.994 |
| Ti | 0.000 | 0.000 | 0.000 | 0.000 | 0.000 | 0.000 | 0.000 | 0.001 | 0.000 | 0.001 | 0.000 | 0.000 | 0.001 | 0.000 | 0.001 | 0.000 | 0.001 | 0.000 | 0.001 | 0.000 |
| Al | 0.001 | 0.000 | 0.000 | 0.000 | 0.001 | 0.000 | 0.000 | 0.000 | 0.000 | 0.000 | 0.000 | 0.000 | 0.001 | 0.000 | 0.000 | 0.001 | 0.001 | 0.000 | 0.000 | 0.000 |
| Cr | 0.000 | 0.000 | 0.001 | 0.000 | 0.000 | 0.000 | 0.000 | 0.001 | 0.000 | 0.000 | 0.000 | 0.000 | 0.000 | 0.000 | 0.000 | 0.000 | 0.000 | 0.000 | 0.001 | 0.000 |
| Fe ²⁺ | 0.571 | 0.560 | 0.562 | 0.560 | 0.562 | 0.554 | 0.544 | 0.543 | 0.552 | 0.554 | 0.545 | 0.548 | 0.540 | 0.563 | 0.564 | 0.552 | 0.521 | 0.537 | 0.512 | 0.518 |
| Mn | 0.008 | 0.008 | 0.007 | 0.008 | 0.009 | 0.009 | 0.009 | 0.009 | 0.007 | 0.007 | 0.011 | 0.008 | 0.006 | 0.006 | 0.009 | 0.007 | 0.007 | 0.008 | 0.008 | 0.010 |
| Mg | 1.434 | 1.444 | 1.441 | 1.441 | 1.441 | 1.453 | 1.447 | 1.460 | 1.445 | 1.447 | 1.459 | 1.468 | 1.447 | 1.447 | 1.438 | 1.459 | 1.483 | 1.473 | 1.489 | 1.482 |
| Ca | 0.000 | 0.000 | 0.000 | 0.000 | 0.000 | 0.000 | 0.000 | 0.000 | 0.000 | 0.000 | 0.000 | 0.000 | 0.000 | 0.000 | 0.000 | 0.000 | 0.000 | 0.000 | 0.000 | 0.000 |
| Ni | 0.000 | 0.000 | 0.000 | 0.001 | 0.001 | 0.001 | 0.002 | 0.001 | 0.001 | 0.000 | 0.001 | 0.000 | 0.001 | 0.001 | 0.001 | 0.001 | 0.001 | 0.002 | 0.001 | 0.000 |
| Co | 0.002 | 0.003 | 0.001 | 0.000 | 0.002 | 0.001 | 0.001 | 0.002 | 0.002 | 0.001 | 0.002 | 0.001 | 0.001 | 0.001 | 0.003 | 0.000 | 0.002 | 0.000 | 0.002 | 0.002 |
| Total | 3.007 | 3.008 | 3.005 | 3.005 | 3.008 | 3.009 | 3.001 | 3.008 | 3.004 | 3.004 | 3.008 | 3.013 | 2.997 | 3.009 | 3.007 | 3.009 | 3.007 | 3.009 | 3.006 | 3.006 |
| Mg# | 71.5 | 72.1 | 72.0 | 72.0 | 71.9 | 72.4 | 72.7 | 72.9 | 72.4 | 72.3 | 72.8 | 72.8 | 72.8 | 72.0 | 71.8 | 72.6 | 74.0 | 73.3 | 74.4 | 74.1 |
| Fo % | 71.2 | 71.8 | 71.7 | 71.7 | 71.6 | 72.1 | 72.3 | 72.6 | 72.1 | 72.1 | 72.4 | 72.6 | 72.6 | 71.8 | 71.5 | 72.3 | 73.7 | 73.0 | 74.1 | 73.7 |
| Fa % | 28.4 | 27.8 | 27.9 | 27.9 | 27.9 | 27.5 | 27.2 | 27.0 | 27.6 | 27.6 | 27.0 | 27.1 | 27.1 | 27.9 | 28.1 | 27.3 | 25.9 | 26.6 | 25.5 | 25.8 |
| Te % | 0.41 | 0.42 | 0.35 | 0.41 | 0.44 | 0.44 | 0.45 | 0.44 | 0.32 | 0.35 | 0.54 | 0.38 | 0.29 | 0.31 | 0.43 | 0.37 | 0.37 | 0.38 | 0.40 | 0.50 |
| Ca-OI | 0.00 | 0.00 | 0.01 | 0.00 | 0.00 | 0.00 | 0.00 | 0.00 | 0.00 | 0.00 | 0.00 | 0.00 | 0.00 | 0.00 | 0.00 | 0.00 | 0.00 | 0.00 | 0.00 | 0.00 |

Appendix Table 5.3. (2/2)

| Unit | Isotropic gabbro | | | | | | | | Layered gabbro | | | | | | | | | | |
|------------------------------------|------------------|------------------|-----------------|-----------------|-----------------|-----------------|-----------------|-----------------|------------------|-------------------|------------------|------------------|------------------|------------------|------------------|------------------|------------------|------------------|-------------------|
| Rock type | cumulitic gabbro | | | | | | | | troctolite | | | | | | | | | | |
| Sample Mineral-site Position | MK35 cr5-an3 | MK 35 cr5-an8 | MK35 cr5-an9 | MK35 cr6-an2 | MK35 cr7-an1 | MK35 cr8-an5 | MK35 cr8-an6 | MK35 cr9-an1 | MK750 cr1-an2 | MK 750 cr1-an4 | MK750 cr2-an3 | MK750 cr2-an4 | MK750 cr3-an2 | MK750 cr5-an5 | MK750 cr5-an9 | MK750 cr6-an1 | MK750 cr9-an2 | MK750 cr9-an3 | MK750 cr10-an2 |
| SiO ₂ | 38.12 | 38.01 | 38.66 | 37.99 | 38.26 | 38.31 | 38.07 | 38.18 | 38.61 | 38.99 | 38.61 | 37.94 | 37.75 | 38.52 | 38.48 | 38.34 | 38.53 | 38.59 | 38.66 |
| TiO ₂ | 0.00 | 0.00 | 0.00 | 0.07 | 0.00 | 0.01 | 0.02 | 0.03 | 0.00 | 0.00 | 0.02 | 0.00 | 0.01 | 0.04 | 0.00 | 0.03 | 0.02 | 0.00 | 0.00 |
| Al ₂ O ₃ | 0.00 | 0.00 | 0.00 | 0.00 | 0.01 | 0.00 | 0.00 | 0.00 | 0.00 | 0.02 | 0.01 | 0.00 | 0.00 | 0.00 | 0.01 | 0.00 | 0.01 | 0.01 | 0.01 |
| Cr ₂ O ₃ | 0.09 | 0.10 | 0.02 | 0.01 | 0.03 | 0.00 | 0.03 | 0.02 | 0.00 | 0.03 | 0.06 | 0.00 | 0.03 | 0.05 | 0.00 | 0.00 | 0.02 | 0.03 | 0.05 |
| FeO | 23.81 | 24.21 | 24.34 | 23.89 | 24.13 | 23.92 | 23.76 | 24.27 | 20.80 | 20.44 | 20.53 | 20.22 | 20.97 | 20.49 | 20.29 | 20.26 | 20.84 | 20.47 | 20.69 |
| MnO | 0.36 | 0.31 | 0.40 | 0.38 | 0.38 | 0.36 | 0.31 | 0.37 | 0.21 | 0.29 | 0.22 | 0.27 | 0.28 | 0.31 | 0.26 | 0.22 | 0.27 | 0.31 | 0.28 |
| MgO | 38.09 | 37.96 | 38.74 | 38.26 | 38.52 | 38.44 | 38.19 | 38.42 | 40.65 | 40.49 | 40.88 | 40.30 | 39.39 | 41.26 | 41.44 | 40.85 | 40.78 | 40.81 | 41.05 |
| CaO | 0.00 | 0.00 | 0.00 | 0.00 | 0.00 | 0.00 | 0.00 | 0.00 | 0.00 | 0.01 | 0.00 | 0.00 | 0.06 | 0.00 | 0.03 | 0.01 | 0.02 | 0.02 | 0.00 |
| NiO | 0.01 | 0.05 | 0.06 | 0.06 | 0.00 | 0.05 | 0.01 | 0.04 | 0.06 | 0.04 | 0.09 | 0.05 | 0.02 | 0.07 | 0.05 | 0.07 | 0.07 | 0.00 | 0.02 |
| CoO | 0.06 | 0.07 | 0.02 | 0.11 | 0.14 | 0.09 | 0.03 | 0.08 | 0.05 | 0.05 | 0.07 | 0.10 | 0.01 | 0.06 | 0.06 | 0.05 | 0.00 | 0.00 | 0.05 |
| Total | 100.54 | 100.72 | 102.23 | 100.76 | 101.46 | 101.18 | 100.43 | 101.40 | 100.39 | 100.34 | 100.48 | 98.88 | 98.51 | 100.81 | 100.61 | 99.84 | 100.57 | 100.24 | 100.81 |
| <i>a.p.f.u.</i> | | | | | | | | | | | | | | | | | | | |
| Si | 0.994 | 0.991 | 0.992 | 0.989 | 0.990 | 0.993 | 0.993 | 0.988 | 0.993 | 1.001 | 0.991 | 0.990 | 0.992 | 0.986 | 0.986 | 0.990 | 0.990 | 0.993 | 0.990 |
| Ti | 0.000 | 0.000 | 0.000 | 0.001 | 0.000 | 0.000 | 0.000 | 0.001 | 0.000 | 0.000 | 0.000 | 0.000 | 0.000 | 0.001 | 0.000 | 0.001 | 0.000 | 0.000 | 0.000 |
| Al | 0.000 | 0.000 | 0.000 | 0.000 | 0.000 | 0.000 | 0.000 | 0.000 | 0.000 | 0.001 | 0.000 | 0.000 | 0.000 | 0.000 | 0.000 | 0.000 | 0.000 | 0.000 | 0.000 |
| Cr | 0.002 | 0.002 | 0.000 | 0.000 | 0.001 | 0.000 | 0.001 | 0.000 | 0.000 | 0.001 | 0.001 | 0.000 | 0.001 | 0.001 | 0.000 | 0.000 | 0.001 | 0.001 | 0.001 |
| Fe ²⁺ | 0.519 | 0.528 | 0.522 | 0.520 | 0.522 | 0.518 | 0.518 | 0.525 | 0.447 | 0.439 | 0.441 | 0.441 | 0.461 | 0.439 | 0.435 | 0.438 | 0.448 | 0.440 | 0.443 |
| Mn | 0.008 | 0.007 | 0.009 | 0.008 | 0.008 | 0.008 | 0.007 | 0.008 | 0.005 | 0.006 | 0.005 | 0.006 | 0.006 | 0.007 | 0.006 | 0.005 | 0.006 | 0.007 | 0.006 |
| Mg | 1.481 | 1.476 | 1.481 | 1.485 | 1.485 | 1.485 | 1.485 | 1.483 | 1.558 | 1.549 | 1.564 | 1.568 | 1.543 | 1.575 | 1.583 | 1.572 | 1.562 | 1.565 | 1.567 |
| Ca | 0.000 | 0.000 | 0.000 | 0.000 | 0.000 | 0.000 | 0.000 | 0.000 | 0.000 | 0.000 | 0.000 | 0.000 | 0.002 | 0.000 | 0.001 | 0.000 | 0.001 | 0.001 | 0.000 |
| Ni | 0.000 | 0.001 | 0.001 | 0.001 | 0.000 | 0.001 | 0.000 | 0.001 | 0.001 | 0.001 | 0.002 | 0.001 | 0.000 | 0.002 | 0.001 | 0.002 | 0.002 | 0.000 | 0.001 |
| Co | 0.001 | 0.001 | 0.000 | 0.002 | 0.003 | 0.002 | 0.001 | 0.002 | 0.001 | 0.001 | 0.002 | 0.002 | 0.000 | 0.001 | 0.001 | 0.001 | 0.000 | 0.000 | 0.001 |
| Total | 3.005 | 3.007 | 3.007 | 3.008 | 3.009 | 3.007 | 3.006 | 3.009 | 3.006 | 2.998 | 3.007 | 3.009 | 3.006 | 3.012 | 3.013 | 3.009 | 3.009 | 3.007 | 3.009 |
| Mg# | 74.0 | 73.7 | 73.9 | 74.1 | 74.0 | 74.1 | 74.1 | 73.8 | 77.7 | 77.9 | 78.0 | 78.0 | 77.0 | 78.2 | 78.5 | 78.2 | 77.7 | 78.0 | 78.0 |
| Fo % | 73.7 | 73.4 | 73.6 | 73.7 | 73.7 | 73.8 | 73.9 | 73.5 | 77.5 | 77.7 | 77.8 | 77.8 | 76.7 | 77.9 | 78.2 | 78.0 | 77.5 | 77.8 | 77.7 |
| Fa % | 25.9 | 26.3 | 26.0 | 25.8 | 25.9 | 25.8 | 25.8 | 26.1 | 22.3 | 22.0 | 21.9 | 21.9 | 22.9 | 21.7 | 21.5 | 21.7 | 22.2 | 21.9 | 22.0 |
| Te % | 0.40 | 0.34 | 0.43 | 0.41 | 0.41 | 0.40 | 0.34 | 0.40 | 0.23 | 0.32 | 0.24 | 0.29 | 0.30 | 0.34 | 0.28 | 0.24 | 0.29 | 0.34 | 0.30 |
| Ca-OI | 0.00 | 0.00 | 0.00 | 0.00 | 0.00 | 0.00 | 0.00 | 0.00 | 0.00 | 0.01 | 0.00 | 0.00 | 0.08 | 0.00 | 0.04 | 0.01 | 0.03 | 0.03 | 0.00 |

Appendix Table 5.4. (1/2) Representative analyses of plagioclase from the intrusive and subvolcanic rocks forming the intrusive complex and the sheeted dyke complex of the Band-e-Zeyarat ophiolite. Atoms per formula units (a.p.f.u.) are calculated on the bases of five cations. Abbreviations, Ab: albite; An: anorthite; Or: orthoclase.

| Unit | Isotropic gabbro | | | | | | | | | | | | | | | | | | |
|--------------------------------|------------------|------------|---------|--------------|--------------|--------------|--------------|--------------|--------------|----------|--------------|--------------|---------|---------|---------|--------------|--------------|---------|----------|
| Rock type | cumulitic gabbro | | | | | | | | | | | | | | | | | | |
| Sample | MK32 | MK32 cr | MK32 | MK32 | MK32 | MK32 | MK32 | MK32 | MK32 | MK32 | MK35 | MK35 | MK35 | MK35 | MK35 | MK35 | MK35 | MK35 | MK35 |
| Mineral-site Position | cr 1an3 | 2an3 | cr 3an4 | cr 6an5 c | cr 6an6 r | cr 7an6 c | cr 7an9 r | cr 9an2 c | cr 9an4 r | cr 10an1 | cr 1an1 c | cr 1an7 r | cr 2an3 | cr 3an3 | cr 5an3 | cr 6an3 c | cr 6an5 r | cr 7an2 | cr 10an1 |
| SiO ₂ | 52.56 | 52.12 | 52.75 | 52.77 | 52.20 | 52.36 | 52.70 | 53.65 | 53.25 | 53.46 | 52.24 | 52.96 | 53.43 | 53.25 | 52.97 | 53.44 | 53.55 | 52.80 | 52.77 |
| TiO ₂ | 0.06 | 0.05 | 0.04 | 0.06 | 0.01 | 0.07 | 0.04 | 0.03 | 0.01 | 0.14 | 0.04 | 0.00 | 0.13 | 0.04 | 0.00 | 0.05 | 0.01 | 0.10 | 0.06 |
| Al ₂ O ₃ | 30.23 | 30.32 | 30.18 | 30.06 | 30.45 | 29.94 | 30.28 | 29.76 | 29.91 | 29.96 | 30.29 | 29.90 | 29.51 | 29.41 | 29.53 | 29.49 | 29.58 | 29.91 | 29.86 |
| Cr ₂ O ₃ | 0.00 | 0.00 | 0.00 | 0.00 | 0.00 | 0.00 | 0.00 | 0.00 | 0.00 | 0.00 | 0.00 | 0.00 | 0.00 | 0.00 | 0.00 | 0.00 | 0.00 | 0.00 | 0.00 |
| FeO | 0.20 | 0.15 | 0.25 | 0.12 | 0.20 | 0.16 | 0.17 | 0.17 | 0.18 | 0.24 | 0.17 | 0.18 | 0.22 | 0.14 | 0.23 | 0.17 | 0.27 | 0.17 | 0.26 |
| MnO | 0.00 | 0.00 | 0.03 | 0.00 | 0.00 | 0.00 | 0.00 | 0.06 | 0.00 | 0.00 | 0.01 | 0.00 | 0.03 | 0.00 | 0.00 | 0.00 | 0.00 | 0.00 | 0.00 |
| MgO | 0.00 | 0.00 | 0.01 | 0.02 | 0.03 | 0.01 | 0.02 | 0.00 | 0.02 | 0.01 | 0.00 | 0.01 | 0.02 | 0.02 | 0.02 | 0.00 | 0.00 | 0.01 | 0.00 |
| CaO | 13.53 | 14.21 | 13.37 | 14.08 | 14.24 | 13.74 | 13.94 | 13.61 | 13.85 | 13.59 | 13.86 | 13.12 | 12.44 | 12.98 | 13.35 | 13.50 | 12.83 | 13.55 | 13.66 |
| Na ₂ O | 4.07 | 3.67 | 4.06 | 3.85 | 3.69 | 3.98 | 3.88 | 4.11 | 4.03 | 4.16 | 3.79 | 4.17 | 4.52 | 4.32 | 4.19 | 4.24 | 4.38 | 4.06 | 4.03 |
| K ₂ O | 0.05 | 0.07 | 0.06 | 0.06 | 0.06 | 0.05 | 0.07 | 0.08 | 0.06 | 0.05 | 0.08 | 0.08 | 0.09 | 0.07 | 0.05 | 0.06 | 0.07 | 0.08 | 0.06 |
| Total | 100.70 | 100.59 | 100.75 | 101.03 | 100.87 | 100.31 | 101.09 | 101.46 | 101.30 | 101.61 | 100.48 | 100.42 | 100.38 | 100.24 | 100.35 | 100.96 | 100.70 | 100.67 | 100.69 |
| <i>a.p.f.u.</i> | | | | | | | | | | | | | | | | | | | |
| Si | 2.372 | 2.358 | 2.378 | 2.375 | 2.355 | 2.373 | 2.370 | 2.401 | 2.389 | 2.390 | 2.364 | 2.392 | 2.412 | 2.409 | 2.397 | 2.404 | 2.411 | 2.383 | 2.382 |
| Ti | 0.002 | 0.002 | 0.001 | 0.002 | 0.000 | 0.002 | 0.001 | 0.001 | 0.000 | 0.005 | 0.001 | 0.000 | 0.004 | 0.001 | 0.000 | 0.002 | 0.000 | 0.003 | 0.002 |
| Al | 1.608 | 1.616 | 1.603 | 1.595 | 1.619 | 1.599 | 1.605 | 1.570 | 1.581 | 1.579 | 1.615 | 1.592 | 1.570 | 1.568 | 1.575 | 1.563 | 1.570 | 1.591 | 1.589 |
| Cr | 0.000 | 0.000 | 0.000 | 0.000 | 0.000 | 0.000 | 0.000 | 0.000 | 0.000 | 0.000 | 0.000 | 0.000 | 0.000 | 0.000 | 0.000 | 0.000 | 0.000 | 0.000 | 0.000 |
| Fe ²⁺ | 0.007 | 0.006 | 0.009 | 0.005 | 0.008 | 0.006 | 0.006 | 0.006 | 0.007 | 0.009 | 0.006 | 0.007 | 0.008 | 0.005 | 0.009 | 0.006 | 0.010 | 0.006 | 0.010 |
| Mn | 0.000 | 0.000 | 0.001 | 0.000 | 0.000 | 0.000 | 0.000 | 0.002 | 0.000 | 0.000 | 0.000 | 0.000 | 0.001 | 0.000 | 0.000 | 0.000 | 0.000 | 0.000 | 0.000 |
| Mg | 0.000 | 0.000 | 0.001 | 0.001 | 0.002 | 0.001 | 0.001 | 0.000 | 0.001 | 0.001 | 0.000 | 0.001 | 0.001 | 0.002 | 0.001 | 0.000 | 0.000 | 0.001 | 0.000 |
| Ca | 0.654 | 0.689 | 0.646 | 0.679 | 0.688 | 0.667 | 0.672 | 0.652 | 0.666 | 0.651 | 0.672 | 0.635 | 0.601 | 0.629 | 0.648 | 0.651 | 0.619 | 0.655 | 0.661 |
| Na | 0.356 | 0.322 | 0.355 | 0.336 | 0.323 | 0.350 | 0.338 | 0.357 | 0.350 | 0.361 | 0.333 | 0.365 | 0.396 | 0.379 | 0.368 | 0.370 | 0.383 | 0.355 | 0.353 |
| K | 0.003 | 0.004 | 0.004 | 0.003 | 0.003 | 0.003 | 0.004 | 0.004 | 0.003 | 0.003 | 0.005 | 0.005 | 0.005 | 0.004 | 0.003 | 0.004 | 0.004 | 0.004 | 0.003 |
| Total | 5.002 | 4.996 | 4.998 | 4.996 | 4.998 | 5.001 | 4.997 | 4.994 | 4.997 | 4.998 | 4.996 | 4.997 | 4.999 | 4.997 | 5.001 | 4.999 | 4.997 | 4.998 | 5.000 |
| Ab % | 35.1 | 31.7 | 35.3 | 33.0 | 31.8 | 34.3 | 33.4 | 35.2 | 34.4 | 35.6 | 33.0 | 36.4 | 39.5 | 37.4 | 36.1 | 36.1 | 38.0 | 35.0 | 34.7 |
| An % | 64.6 | 67.9 | 64.3 | 66.7 | 67.9 | 65.4 | 66.3 | 64.4 | 65.3 | 64.2 | 66.6 | 63.2 | 60.0 | 62.2 | 63.6 | 63.5 | 61.5 | 64.6 | 65.0 |
| Or % | 0.3 | 0.4 | 0.4 | 0.3 | 0.3 | 0.3 | 0.4 | 0.4 | 0.3 | 0.3 | 0.5 | 0.5 | 0.5 | 0.4 | 0.3 | 0.4 | 0.4 | 0.4 | 0.3 |

Appendix Table 5.4. (2/2)

| Unit | Layered gabbro | | | | | | | | | | | | Sheeted dyke complex | | | |
|--------------------------------|----------------|---------|----------------|---------|---------|---------|---------|---------|----------------|---------|----------|----------|----------------------|---------|---------|----------|
| | troctolite | | olivine-gabbro | | | | | | olivine-gabbro | | | | basaltic dyke | | | |
| Rock type | MK750 | MK750 | MK752 | MK752 | MK752 | MK752 | MK752 | MK752 | MK752 | MK752 | MK752 | MK752 | MK93 | MK93 | MK93 | MK93 |
| Mineral-site | cr 1an3 | cr 2an3 | cr 1an3 | cr 1an4 | cr 2an4 | cr 4an5 | cr 5an5 | cr 6an2 | cr 7an5 | cr 8an8 | cr 10an7 | cr 11an4 | cr 1an5 | cr 4an3 | cr 5an1 | cr 10an4 |
| Position | | | c | r | | | | | | | | | | | | |
| SiO ₂ | 50.11 | 50.66 | 54.01 | 53.23 | 54.18 | 53.84 | 54.60 | 53.87 | 54.29 | 53.65 | 54.46 | 53.80 | 52.83 | 53.68 | 53.22 | 52.64 |
| TiO ₂ | 0.04 | 0.02 | 0.02 | 0.08 | 0.06 | 0.07 | 0.09 | 0.00 | 0.06 | 0.00 | 0.04 | 0.05 | 0.06 | 0.04 | 0.14 | 0.08 |
| Al ₂ O ₃ | 31.91 | 31.55 | 29.24 | 29.24 | 29.22 | 28.85 | 28.98 | 28.91 | 28.74 | 29.22 | 28.82 | 29.30 | 29.63 | 28.91 | 29.17 | 30.04 |
| Cr ₂ O ₃ | 0.00 | 0.00 | 0.00 | 0.00 | 0.00 | 0.00 | 0.00 | 0.00 | 0.00 | 0.00 | 0.00 | 0.00 | 0.00 | 0.00 | 0.00 | 0.00 |
| FeO | 0.12 | 0.17 | 0.11 | 0.11 | 0.16 | 0.13 | 0.08 | 0.09 | 0.12 | 0.05 | 0.11 | 0.07 | 0.52 | 0.71 | 0.81 | 0.50 |
| MnO | 0.04 | 0.03 | 0.01 | 0.05 | 0.00 | 0.00 | 0.00 | 0.10 | 0.00 | 0.05 | 0.00 | 0.00 | 0.05 | 0.00 | 0.07 | 0.04 |
| MgO | 0.00 | 0.00 | 0.00 | 0.00 | 0.00 | 0.04 | 0.00 | 0.00 | 0.00 | 0.00 | 0.02 | 0.02 | 0.14 | 0.17 | 0.31 | 0.16 |
| CaO | 15.84 | 15.62 | 12.47 | 12.03 | 12.14 | 12.49 | 12.39 | 12.23 | 12.56 | 12.71 | 12.45 | 12.81 | 13.65 | 12.85 | 13.14 | 13.98 |
| Na ₂ O | 2.81 | 2.94 | 4.65 | 4.70 | 4.79 | 4.65 | 4.86 | 4.75 | 4.69 | 4.50 | 4.74 | 4.48 | 3.84 | 4.21 | 3.98 | 3.71 |
| K ₂ O | 0.02 | 0.05 | 0.09 | 0.08 | 0.07 | 0.10 | 0.08 | 0.10 | 0.08 | 0.09 | 0.11 | 0.08 | 0.10 | 0.13 | 0.17 | 0.06 |
| Total | 100.89 | 101.04 | 100.61 | 99.52 | 100.62 | 100.16 | 101.07 | 100.04 | 100.54 | 100.27 | 100.74 | 100.62 | 100.81 | 100.69 | 101.01 | 101.21 |
| <i>a.p.f.u.</i> | | | | | | | | | | | | | | | | |
| Si | 2.271 | 2.291 | 2.430 | 2.421 | 2.436 | 2.435 | 2.445 | 2.438 | 2.445 | 2.424 | 2.447 | 2.422 | 2.385 | 2.422 | 2.399 | 2.368 |
| Ti | 0.001 | 0.001 | 0.001 | 0.003 | 0.002 | 0.002 | 0.003 | 0.000 | 0.002 | 0.000 | 0.001 | 0.002 | 0.002 | 0.001 | 0.005 | 0.003 |
| Al | 1.704 | 1.681 | 1.551 | 1.567 | 1.548 | 1.538 | 1.529 | 1.542 | 1.526 | 1.556 | 1.526 | 1.555 | 1.577 | 1.537 | 1.550 | 1.593 |
| Cr | 0.000 | 0.000 | 0.000 | 0.000 | 0.000 | 0.000 | 0.000 | 0.000 | 0.000 | 0.000 | 0.000 | 0.000 | 0.000 | 0.000 | 0.000 | 0.000 |
| Fe ²⁺ | 0.005 | 0.006 | 0.004 | 0.004 | 0.006 | 0.005 | 0.003 | 0.003 | 0.004 | 0.002 | 0.004 | 0.003 | 0.019 | 0.027 | 0.030 | 0.019 |
| Mn | 0.002 | 0.001 | 0.000 | 0.002 | 0.000 | 0.000 | 0.000 | 0.004 | 0.000 | 0.002 | 0.000 | 0.000 | 0.002 | 0.000 | 0.003 | 0.002 |
| Mg | 0.000 | 0.000 | 0.000 | 0.000 | 0.000 | 0.002 | 0.000 | 0.000 | 0.000 | 0.000 | 0.001 | 0.001 | 0.009 | 0.012 | 0.021 | 0.011 |
| Ca | 0.769 | 0.757 | 0.601 | 0.586 | 0.585 | 0.605 | 0.594 | 0.593 | 0.606 | 0.615 | 0.599 | 0.618 | 0.660 | 0.621 | 0.635 | 0.674 |
| Na | 0.247 | 0.257 | 0.406 | 0.414 | 0.418 | 0.407 | 0.422 | 0.416 | 0.409 | 0.394 | 0.413 | 0.391 | 0.336 | 0.368 | 0.348 | 0.323 |
| K | 0.001 | 0.003 | 0.005 | 0.005 | 0.004 | 0.006 | 0.004 | 0.006 | 0.005 | 0.005 | 0.006 | 0.005 | 0.006 | 0.007 | 0.010 | 0.004 |
| Total | 5.000 | 4.998 | 4.999 | 5.002 | 4.999 | 5.000 | 5.001 | 5.002 | 4.997 | 4.998 | 4.998 | 4.997 | 4.996 | 4.996 | 5.000 | 4.996 |
| Ab % | 24.3 | 25.3 | 40.1 | 41.2 | 41.5 | 40.0 | 41.4 | 41.0 | 40.1 | 38.9 | 40.5 | 38.6 | 33.5 | 36.9 | 35.0 | 32.3 |
| An % | 75.6 | 74.4 | 59.4 | 58.3 | 58.1 | 59.4 | 58.2 | 58.4 | 59.4 | 60.6 | 58.8 | 61.0 | 65.9 | 62.3 | 64.0 | 67.3 |
| Or % | 0.1 | 0.3 | 0.5 | 0.5 | 0.4 | 0.6 | 0.4 | 0.5 | 0.5 | 0.5 | 0.6 | 0.5 | 0.6 | 0.7 | 1.0 | 0.4 |

Appendix Table 5.5. (1/4) Representative analyses of clinopyroxene from the intrusive rocks, subvolcanic and volcanic rock forming the Intrusive complex (layered gabbro and isotropic gabbro) and the volcanic sequence of the Band-e-Zeyarat ophiolite. Atoms per formula units (a.p.f.u.) are calculated on the bases of four cations. The compositions of Fe³⁺ and Fe²⁺ were calculated from the measured total FeO according to Droop (1987); Mg# = 100 x Mg / (Mg + Fe²⁺). Abbreviations, Wo: wollastonite; En: enstatite; Fs: ferrosilite; Acm: acmite.

| Unit Rock type | Isotropic gabbro | | | | | | | | | | | | | | | | | | | |
|------------------------------------|------------------|-----------------------|-----------------------|----------------------|----------------------|----------------------|----------------------|-----------------|-----------------|-----------------|----------------------|----------------------|----------------------|----------------------|-----------------|----------------------|----------------------|-----------------|-----------------|-----------------|
| | cumulitic gabbro | | | | | | | | | | | | | | | | | | | |
| Sample Mineral-site position | MK32 cr1-an2 | MK32 cr2--an5 c | MK32 cr2--an2 c | MK32 cr2-an1 c | MK32 cr2-an3 r | MK32 cr3-an4 c | MK32 cr3-an5 r | MK32 cr4-an1 | MK32 cr6-an3 | MK32 cr7-an3 | MK32 cr8-an2 r | MK32 cr8-an3 c | MK32 cr8-an4 c | MK32 cr8-an5 c | MK32 cr9-an1 | MK35 cr1-an3 c | MK35 cr1-an5 r | MK35 cr2-an3 | MK35 cr3-an1 | MK35 cr4-an4 |
| SiO ₂ | 49.86 | 50.51 | 50.24 | 50.46 | 50.76 | 50.69 | 50.45 | 49.98 | 50.05 | 50.20 | 50.28 | 50.43 | 50.89 | 50.28 | 50.76 | 51.24 | 51.09 | 50.18 | 50.27 | 50.15 |
| TiO ₂ | 1.11 | 0.98 | 0.92 | 0.92 | 0.67 | 0.76 | 0.97 | 1.00 | 0.96 | 1.09 | 1.15 | 1.07 | 0.95 | 0.87 | 0.88 | 0.48 | 0.70 | 0.84 | 0.97 | 0.73 |
| Al ₂ O ₃ | 3.43 | 3.02 | 3.22 | 2.95 | 2.54 | 2.70 | 2.88 | 2.94 | 3.00 | 3.19 | 3.17 | 3.07 | 3.02 | 2.76 | 2.92 | 2.28 | 2.47 | 2.71 | 3.17 | 2.81 |
| Cr ₂ O ₃ | 0.31 | 0.13 | 0.21 | 0.23 | 0.17 | 0.18 | 0.36 | 0.29 | 0.28 | 0.22 | 0.29 | 0.25 | 0.19 | 0.28 | 0.30 | 0.19 | 0.17 | 0.24 | 0.33 | 0.47 |
| FeO | 6.95 | 7.43 | 7.17 | 6.87 | 6.53 | 6.87 | 6.85 | 7.11 | 6.47 | 6.83 | 6.68 | 6.60 | 6.52 | 6.45 | 6.89 | 6.74 | 6.44 | 7.48 | 6.86 | 6.35 |
| MnO | 0.15 | 0.21 | 0.19 | 0.21 | 0.23 | 0.18 | 0.20 | 0.17 | 0.18 | 0.16 | 0.20 | 0.15 | 0.14 | 0.15 | 0.20 | 0.19 | 0.25 | 0.25 | 0.19 | 0.22 |
| MgO | 15.12 | 15.58 | 15.49 | 15.26 | 15.51 | 15.46 | 15.08 | 15.12 | 15.12 | 15.05 | 15.02 | 15.01 | 14.86 | 15.24 | 15.16 | 15.46 | 15.42 | 15.67 | 14.75 | 15.29 |
| CaO | 22.06 | 21.47 | 22.25 | 22.94 | 23.13 | 22.37 | 22.46 | 22.14 | 22.84 | 22.48 | 22.59 | 22.83 | 22.64 | 23.10 | 22.67 | 23.17 | 23.53 | 21.48 | 22.80 | 23.00 |
| Na ₂ O | 0.61 | 0.66 | 0.50 | 0.54 | 0.58 | 0.55 | 0.67 | 0.63 | 0.65 | 0.57 | 0.63 | 0.56 | 0.56 | 0.51 | 0.55 | 0.42 | 0.49 | 0.62 | 0.62 | 0.54 |
| K ₂ O | 0.00 | 0.00 | 0.00 | 0.00 | 0.00 | 0.00 | 0.00 | 0.00 | 0.02 | 0.00 | 0.00 | 0.00 | 0.02 | 0.00 | 0.01 | 0.00 | 0.00 | 0.00 | 0.00 | 0.01 |
| Total | 99.60 | 99.98 | 100.19 | 100.38 | 100.12 | 99.75 | 99.91 | 99.38 | 99.56 | 99.79 | 100.00 | 99.98 | 99.77 | 99.65 | 100.34 | 100.16 | 100.55 | 99.46 | 99.95 | 99.54 |
| <i>a.p.f.u.</i> | | | | | | | | | | | | | | | | | | | | |
| Si | 1.842 | 1.857 | 1.844 | 1.850 | 1.862 | 1.868 | 1.858 | 1.851 | 1.847 | 1.852 | 1.851 | 1.857 | 1.878 | 1.856 | 1.863 | 1.882 | 1.868 | 1.854 | 1.853 | 1.851 |
| Ti | 0.031 | 0.027 | 0.025 | 0.025 | 0.019 | 0.021 | 0.027 | 0.028 | 0.027 | 0.030 | 0.032 | 0.030 | 0.026 | 0.024 | 0.024 | 0.013 | 0.019 | 0.023 | 0.027 | 0.020 |
| Al | 0.149 | 0.131 | 0.139 | 0.128 | 0.110 | 0.117 | 0.125 | 0.128 | 0.130 | 0.139 | 0.137 | 0.133 | 0.131 | 0.120 | 0.126 | 0.099 | 0.106 | 0.118 | 0.138 | 0.122 |
| Cr | 0.009 | 0.004 | 0.006 | 0.007 | 0.005 | 0.005 | 0.010 | 0.009 | 0.008 | 0.006 | 0.008 | 0.007 | 0.005 | 0.008 | 0.009 | 0.006 | 0.005 | 0.007 | 0.010 | 0.014 |
| Fe ³⁺ | 0.141 | 0.144 | 0.150 | 0.154 | 0.166 | 0.139 | 0.142 | 0.150 | 0.160 | 0.131 | 0.134 | 0.126 | 0.095 | 0.149 | 0.131 | 0.135 | 0.149 | 0.163 | 0.137 | 0.160 |
| Fe ²⁺ | 0.074 | 0.085 | 0.070 | 0.057 | 0.034 | 0.072 | 0.069 | 0.070 | 0.039 | 0.080 | 0.071 | 0.077 | 0.106 | 0.050 | 0.080 | 0.072 | 0.048 | 0.068 | 0.074 | 0.036 |
| Mn | 0.005 | 0.007 | 0.006 | 0.006 | 0.007 | 0.006 | 0.006 | 0.005 | 0.006 | 0.005 | 0.006 | 0.005 | 0.004 | 0.005 | 0.006 | 0.006 | 0.008 | 0.008 | 0.006 | 0.007 |
| Mg | 0.833 | 0.854 | 0.848 | 0.834 | 0.848 | 0.849 | 0.828 | 0.835 | 0.832 | 0.828 | 0.824 | 0.824 | 0.817 | 0.838 | 0.830 | 0.846 | 0.841 | 0.863 | 0.811 | 0.841 |
| Ca | 0.873 | 0.846 | 0.875 | 0.901 | 0.909 | 0.883 | 0.886 | 0.878 | 0.903 | 0.889 | 0.891 | 0.901 | 0.895 | 0.913 | 0.891 | 0.912 | 0.922 | 0.850 | 0.901 | 0.910 |
| Na | 0.044 | 0.047 | 0.036 | 0.039 | 0.041 | 0.039 | 0.048 | 0.045 | 0.046 | 0.040 | 0.045 | 0.040 | 0.040 | 0.037 | 0.039 | 0.030 | 0.035 | 0.044 | 0.044 | 0.039 |
| K | 0.000 | 0.000 | 0.000 | 0.000 | 0.000 | 0.000 | 0.000 | 0.000 | 0.001 | 0.000 | 0.000 | 0.000 | 0.001 | 0.000 | 0.001 | 0.000 | 0.000 | 0.000 | 0.000 | 0.000 |
| Total | 4.000 | 4.000 | 4.000 | 4.000 | 4.000 | 4.000 | 4.000 | 4.000 | 4.000 | 4.000 | 4.000 | 4.000 | 4.000 | 4.000 | 4.000 | 4.000 | 4.000 | 4.000 | 4.000 | 4.000 |
| Al (IV) | 0.149 | 0.131 | 0.139 | 0.128 | 0.110 | 0.117 | 0.125 | 0.128 | 0.130 | 0.139 | 0.137 | 0.133 | 0.122 | 0.120 | 0.126 | 0.099 | 0.106 | 0.118 | 0.138 | 0.122 |
| Al (VI) | 0.000 | 0.000 | 0.000 | 0.000 | 0.000 | 0.000 | 0.000 | 0.000 | 0.000 | 0.000 | 0.000 | 0.000 | 0.009 | 0.000 | 0.000 | 0.000 | 0.000 | 0.000 | 0.000 | 0.000 |
| Wo % | 44.45 | 42.83 | 44.23 | 45.42 | 45.49 | 44.52 | 44.91 | 44.40 | 45.59 | 45.17 | 45.33 | 45.76 | 45.82 | 45.96 | 45.21 | 45.71 | 46.23 | 42.75 | 45.78 | 45.81 |
| En % | 42.39 | 43.24 | 42.85 | 42.03 | 42.43 | 42.82 | 41.96 | 42.20 | 42.00 | 42.07 | 41.93 | 41.88 | 41.84 | 42.18 | 42.08 | 42.42 | 42.15 | 43.40 | 41.21 | 42.37 |
| Fs % | 14.11 | 14.43 | 15.03 | 15.41 | 16.66 | 13.96 | 14.27 | 15.02 | 16.05 | 13.13 | 13.46 | 12.68 | 9.59 | 14.92 | 13.14 | 13.55 | 14.96 | 16.38 | 13.79 | 16.03 |
| Acm % | 2.23 | 2.36 | 1.80 | 1.95 | 2.05 | 1.98 | 2.44 | 2.28 | 2.33 | 2.06 | 2.28 | 2.03 | 2.05 | 1.84 | 1.99 | 1.50 | 1.74 | 2.23 | 2.26 | 1.96 |
| Mg# | 79.5 | 78.9 | 79.4 | 79.8 | 80.9 | 80.0 | 79.7 | 79.1 | 80.6 | 79.7 | 80.0 | 80.2 | 80.3 | 80.8 | 79.7 | 80.3 | 81.0 | 78.9 | 79.3 | 81.1 |

Appendix Table 5.5. (2/4)

| Unit Rock type | Layered gabbro | | | | | | | | | | | | | | | | | | |
|--------------------------------|------------------|------------------|------------------|-----------------------|-----------------------|-----------------------|-----------------------|------------------|-----------------------|-----------------------|-----------------------|-----------------------|------------------|------------------|------------------|------------------|------------------|------------------|------------------|
| | troctolite | | | | | | | | olivine-gabbro | | | | | | | | | | |
| | MK750 cr5-an2 | MK750 cr5-an3 | MK750 cr5-an9 | MK750 cr4-an4 r | MK750 cr4-an6 c | MK750 cr6-an2 c | MK750 cr6-an8 r | MK750 cr7-an3 | MK752 cr1-an3 c | MK752 cr1-an5 r | MK752 cr2-an2 c | MK752 cr2-an4 r | MK752 cr3-an6 | MK752 cr4-an4 | MK752 cr4-an6 | MK752 cr5-an4 | MK752 cr5-an5 | MK752 cr7-an6 | MK752 cr8-an7 |
| SiO ₂ | 52.78 | 52.88 | 53.28 | 50.41 | 50.79 | 50.53 | 50.08 | 50.88 | 49.97 | 49.41 | 50.83 | 49.39 | 51.34 | 51.54 | 50.41 | 49.79 | 50.96 | 49.33 | 49.45 |
| TiO ₂ | 0.57 | 0.41 | 0.41 | 1.06 | 1.04 | 0.97 | 1.20 | 1.11 | 0.79 | 1.09 | 0.98 | 0.93 | 0.68 | 0.33 | 0.82 | 0.96 | 0.65 | 0.97 | 1.01 |
| Al ₂ O ₃ | 1.45 | 1.55 | 1.43 | 2.93 | 2.80 | 2.71 | 3.17 | 2.91 | 3.11 | 3.66 | 3.09 | 3.35 | 2.42 | 1.98 | 2.87 | 3.46 | 2.66 | 3.93 | 3.61 |
| Cr ₂ O ₃ | 0.23 | 0.31 | 0.23 | 0.55 | 0.59 | 0.66 | 0.78 | 0.71 | 0.11 | 0.19 | 0.14 | 0.16 | 0.12 | 0.07 | 0.06 | 0.13 | 0.06 | 0.18 | 0.26 |
| FeO | 13.69 | 13.76 | 13.64 | 5.76 | 5.58 | 5.00 | 5.21 | 5.26 | 6.54 | 7.15 | 7.46 | 8.17 | 6.70 | 5.78 | 7.91 | 6.78 | 7.11 | 7.05 | 7.17 |
| MnO | 0.26 | 0.32 | 0.25 | 0.20 | 0.18 | 0.19 | 0.10 | 0.11 | 0.22 | 0.20 | 0.22 | 0.15 | 0.15 | 0.18 | 0.20 | 0.24 | 0.22 | 0.16 | 0.16 |
| MgO | 29.13 | 29.72 | 29.61 | 15.57 | 15.77 | 15.67 | 15.52 | 15.88 | 14.30 | 14.66 | 15.54 | 15.35 | 14.45 | 15.60 | 13.74 | 14.51 | 14.31 | 14.12 | 14.47 |
| CaO | 1.19 | 1.12 | 0.93 | 22.69 | 22.67 | 22.92 | 22.77 | 22.90 | 23.32 | 22.80 | 21.90 | 21.11 | 23.68 | 23.78 | 23.17 | 22.81 | 23.24 | 22.43 | 22.50 |
| Na ₂ O | 0.01 | 0.00 | 0.04 | 0.63 | 0.52 | 0.54 | 0.55 | 0.62 | 0.67 | 0.78 | 0.56 | 0.60 | 0.64 | 0.54 | 0.71 | 0.81 | 0.63 | 0.88 | 0.84 |
| K ₂ O | 0.00 | 0.01 | 0.00 | 0.02 | 0.00 | 0.00 | 0.01 | 0.00 | 0.00 | 0.01 | 0.00 | 0.00 | 0.00 | 0.00 | 0.00 | 0.00 | 0.00 | 0.01 | 0.00 |
| Total | 99.31 | 100.08 | 99.83 | 99.82 | 99.93 | 99.18 | 99.38 | 100.36 | 99.02 | 99.95 | 100.70 | 99.21 | 100.19 | 99.79 | 99.88 | 99.50 | 99.84 | 99.05 | 99.45 |
| <i>a.p.f.u.</i> | | | | | | | | | | | | | | | | | | | |
| Si | 1.894 | 1.879 | 1.898 | 1.852 | 1.864 | 1.867 | 1.848 | 1.857 | 1.858 | 1.819 | 1.858 | 1.833 | 1.889 | 1.893 | 1.868 | 1.840 | 1.884 | 1.833 | 1.830 |
| Ti | 0.015 | 0.011 | 0.011 | 0.029 | 0.029 | 0.027 | 0.033 | 0.031 | 0.022 | 0.030 | 0.027 | 0.026 | 0.019 | 0.009 | 0.023 | 0.027 | 0.018 | 0.027 | 0.028 |
| Al | 0.061 | 0.065 | 0.060 | 0.127 | 0.121 | 0.118 | 0.138 | 0.125 | 0.136 | 0.159 | 0.133 | 0.147 | 0.105 | 0.086 | 0.125 | 0.151 | 0.116 | 0.172 | 0.157 |
| Cr | 0.006 | 0.009 | 0.007 | 0.016 | 0.017 | 0.019 | 0.023 | 0.020 | 0.003 | 0.006 | 0.004 | 0.005 | 0.004 | 0.002 | 0.002 | 0.004 | 0.002 | 0.005 | 0.007 |
| Fe ³⁺ | 0.115 | 0.146 | 0.119 | 0.139 | 0.113 | 0.114 | 0.116 | 0.123 | 0.147 | 0.194 | 0.134 | 0.174 | 0.122 | 0.147 | 0.142 | 0.170 | 0.124 | 0.166 | 0.179 |
| Fe ²⁺ | 0.296 | 0.263 | 0.287 | 0.038 | 0.058 | 0.040 | 0.045 | 0.038 | 0.056 | 0.026 | 0.094 | 0.079 | 0.084 | 0.030 | 0.104 | 0.040 | 0.096 | 0.053 | 0.043 |
| Mn | 0.008 | 0.010 | 0.008 | 0.006 | 0.006 | 0.006 | 0.003 | 0.003 | 0.007 | 0.006 | 0.007 | 0.005 | 0.005 | 0.006 | 0.006 | 0.007 | 0.007 | 0.005 | 0.005 |
| Mg | 1.558 | 1.575 | 1.572 | 0.853 | 0.863 | 0.863 | 0.854 | 0.864 | 0.793 | 0.804 | 0.847 | 0.849 | 0.793 | 0.854 | 0.759 | 0.800 | 0.789 | 0.782 | 0.798 |
| Ca | 0.046 | 0.042 | 0.035 | 0.893 | 0.892 | 0.907 | 0.900 | 0.896 | 0.929 | 0.899 | 0.857 | 0.839 | 0.934 | 0.935 | 0.920 | 0.903 | 0.920 | 0.893 | 0.892 |
| Na | 0.001 | 0.000 | 0.003 | 0.045 | 0.037 | 0.039 | 0.039 | 0.044 | 0.048 | 0.056 | 0.040 | 0.043 | 0.046 | 0.038 | 0.051 | 0.058 | 0.045 | 0.063 | 0.060 |
| K | 0.000 | 0.000 | 0.000 | 0.001 | 0.000 | 0.000 | 0.000 | 0.000 | 0.000 | 0.001 | 0.000 | 0.000 | 0.000 | 0.000 | 0.000 | 0.000 | 0.000 | 0.000 | 0.000 |
| Total | 4.000 | 4.000 | 4.000 | 4.000 | 4.000 | 4.000 | 4.000 | 4.000 | 4.000 | 4.000 | 4.000 | 4.000 | 4.000 | 4.000 | 4.000 | 4.000 | 4.000 | 4.000 | 4.000 |
| Al (IV) | 0.061 | 0.065 | 0.060 | 0.127 | 0.121 | 0.118 | 0.138 | 0.125 | 0.136 | 0.159 | 0.133 | 0.147 | 0.105 | 0.086 | 0.125 | 0.151 | 0.116 | 0.167 | 0.157 |
| Al (VI) | 0.000 | 0.000 | 0.000 | 0.000 | 0.000 | 0.000 | 0.000 | 0.000 | 0.000 | 0.000 | 0.000 | 0.000 | 0.000 | 0.000 | 0.000 | 0.000 | 0.000 | 0.005 | 0.000 |
| Wo % | 2.27 | 2.10 | 1.75 | 45.39 | 45.42 | 46.21 | 46.08 | 45.61 | 47.09 | 45.42 | 43.48 | 42.29 | 47.19 | 46.65 | 46.58 | 45.83 | 46.62 | 45.62 | 45.24 |
| En % | 77.31 | 77.72 | 77.96 | 43.34 | 43.96 | 43.96 | 43.69 | 44.00 | 40.17 | 40.63 | 42.94 | 42.77 | 40.07 | 42.59 | 38.42 | 40.57 | 39.95 | 39.95 | 40.47 |
| Fs % | 11.67 | 14.73 | 12.06 | 13.96 | 11.34 | 11.45 | 11.60 | 12.31 | 14.76 | 19.46 | 13.43 | 17.43 | 12.22 | 14.71 | 14.21 | 16.98 | 12.47 | 16.66 | 17.93 |
| Acm % | 0.03 | 0.00 | 0.14 | 2.28 | 1.90 | 1.96 | 2.01 | 2.22 | 2.43 | 2.83 | 2.02 | 2.17 | 2.32 | 1.91 | 2.58 | 2.96 | 2.29 | 3.24 | 3.04 |
| Mg# | 79.1 | 79.4 | 79.5 | 82.8 | 83.4 | 84.8 | 84.2 | 84.3 | 79.6 | 78.5 | 78.8 | 77.0 | 79.4 | 82.8 | 75.6 | 79.2 | 78.2 | 78.1 | 78.2 |

Appendix Table 5.5. (3/4)

| Unit Rock type | Volcanic sequence | | | | | | | | | | | | | | |
|------------------------------------|----------------------|----------------------|----------------------|----------------------|----------------------|-----------------|-----------------|-----------------|-----------------|-----------------|----------------------|----------------------|-----------------------|-----------------------|------------------|
| | basaltic dyke | | | | | | | | | | | pillow basalt | | | |
| Sample Mineral-site position | MK10 cr1-an5 r | MK10 cr3-an1 c | MK10 cr3-an4 r | MK10 cr4-an5 c | MK10 cr4-an7 r | MK10 cr6-an4 | MK10 cr7-an2 | MK10 cr7-an7 | MK10 cr8-an1 | MK10 cr8-an5 | MK10 cr9-an3 c | MK10 cr9-an4 c | MK105 cr1-an3 c | MK105 cr1-an5 r | MK105 cr2-an4 |
| SiO ₂ | 48.79 | 49.02 | 49.21 | 49.45 | 51.45 | 48.85 | 50.65 | 50.71 | 50.25 | 51.15 | 49.09 | 48.97 | 48.54 | 51.60 | 51.74 |
| TiO ₂ | 1.49 | 1.49 | 1.60 | 1.17 | 0.74 | 1.33 | 0.91 | 0.95 | 0.73 | 0.70 | 1.59 | 1.64 | 1.40 | 0.57 | 0.79 |
| Al ₂ O ₃ | 3.35 | 3.39 | 2.83 | 2.99 | 2.02 | 3.76 | 2.05 | 1.71 | 3.13 | 2.72 | 3.81 | 3.58 | 4.17 | 2.19 | 2.10 |
| Cr ₂ O ₃ | 0.07 | 0.08 | 0.00 | 0.13 | 0.17 | 0.16 | 0.05 | 0.04 | 0.93 | 0.67 | 0.12 | 0.03 | 0.13 | 0.46 | 0.34 |
| FeO | 11.14 | 9.36 | 13.02 | 9.61 | 9.16 | 9.72 | 11.42 | 11.23 | 6.65 | 6.66 | 8.86 | 10.51 | 7.66 | 7.15 | 6.89 |
| MnO | 0.22 | 0.27 | 0.30 | 0.18 | 0.29 | 0.20 | 0.21 | 0.32 | 0.15 | 0.15 | 0.18 | 0.19 | 0.17 | 0.20 | 0.17 |
| MgO | 14.22 | 14.77 | 13.33 | 15.34 | 16.95 | 14.57 | 15.40 | 16.13 | 15.64 | 16.41 | 14.34 | 14.23 | 15.39 | 18.19 | 17.64 |
| CaO | 19.94 | 21.05 | 20.05 | 20.75 | 18.95 | 20.43 | 19.05 | 18.78 | 21.43 | 21.34 | 21.14 | 20.67 | 21.42 | 19.46 | 19.48 |
| Na ₂ O | 0.48 | 0.49 | 0.63 | 0.39 | 0.34 | 0.50 | 0.39 | 0.33 | 0.43 | 0.34 | 0.41 | 0.48 | 0.40 | 0.30 | 0.27 |
| K ₂ O | 0.00 | 0.00 | 0.02 | 0.01 | 0.00 | 0.02 | 0.00 | 0.00 | 0.00 | 0.00 | 0.01 | 0.00 | 0.00 | 0.00 | 0.02 |
| Total | 99.70 | 99.91 | 100.98 | 100.04 | 100.07 | 99.54 | 100.13 | 100.19 | 99.34 | 100.14 | 99.56 | 100.30 | 99.27 | 100.13 | 99.44 |
| <i>a.p.f.u.</i> | | | | | | | | | | | | | | | |
| Si | 1.826 | 1.819 | 1.831 | 1.831 | 1.894 | 1.821 | 1.882 | 1.879 | 1.861 | 1.875 | 1.831 | 1.819 | 1.801 | 1.882 | 1.904 |
| Ti | 0.042 | 0.041 | 0.045 | 0.033 | 0.020 | 0.037 | 0.025 | 0.027 | 0.020 | 0.019 | 0.045 | 0.046 | 0.039 | 0.016 | 0.022 |
| Al | 0.148 | 0.148 | 0.124 | 0.131 | 0.088 | 0.165 | 0.090 | 0.075 | 0.136 | 0.118 | 0.168 | 0.157 | 0.182 | 0.094 | 0.091 |
| Cr | 0.002 | 0.002 | 0.000 | 0.004 | 0.005 | 0.005 | 0.001 | 0.001 | 0.027 | 0.020 | 0.004 | 0.001 | 0.004 | 0.013 | 0.010 |
| Fe ³⁺ | 0.150 | 0.163 | 0.170 | 0.167 | 0.103 | 0.151 | 0.122 | 0.136 | 0.105 | 0.098 | 0.109 | 0.147 | 0.162 | 0.118 | 0.067 |
| Fe ²⁺ | 0.198 | 0.127 | 0.235 | 0.130 | 0.179 | 0.152 | 0.233 | 0.212 | 0.101 | 0.107 | 0.168 | 0.180 | 0.075 | 0.100 | 0.145 |
| Mn | 0.007 | 0.008 | 0.010 | 0.006 | 0.009 | 0.006 | 0.007 | 0.010 | 0.005 | 0.005 | 0.006 | 0.006 | 0.005 | 0.006 | 0.005 |
| Mg | 0.793 | 0.817 | 0.739 | 0.847 | 0.930 | 0.810 | 0.853 | 0.891 | 0.864 | 0.897 | 0.797 | 0.788 | 0.851 | 0.989 | 0.968 |
| Ca | 0.799 | 0.837 | 0.799 | 0.823 | 0.747 | 0.816 | 0.758 | 0.746 | 0.850 | 0.838 | 0.845 | 0.823 | 0.851 | 0.760 | 0.768 |
| Na | 0.035 | 0.035 | 0.045 | 0.028 | 0.024 | 0.036 | 0.028 | 0.023 | 0.031 | 0.024 | 0.030 | 0.035 | 0.028 | 0.021 | 0.019 |
| K | 0.000 | 0.000 | 0.001 | 0.001 | 0.000 | 0.001 | 0.000 | 0.000 | 0.000 | 0.000 | 0.000 | 0.000 | 0.000 | 0.000 | 0.001 |
| Total | 4.000 | 4.000 | 4.000 | 4.000 | 4.000 | 4.000 | 4.000 | 4.000 | 4.000 | 4.000 | 4.000 | 4.000 | 4.000 | 4.000 | 4.000 |
| Al (IV) | 0.148 | 0.148 | 0.124 | 0.131 | 0.088 | 0.165 | 0.090 | 0.075 | 0.136 | 0.118 | 0.168 | 0.157 | 0.182 | 0.094 | 0.091 |
| Al (VI) | 0.000 | 0.000 | 0.000 | 0.000 | 0.000 | 0.000 | 0.000 | 0.000 | 0.000 | 0.000 | 0.000 | 0.000 | 0.000 | 0.000 | 0.000 |
| Wo % | 40.46 | 42.27 | 40.19 | 41.25 | 37.68 | 41.53 | 38.03 | 37.13 | 43.59 | 42.69 | 43.36 | 41.73 | 43.24 | 38.23 | 39.06 |
| En % | 40.14 | 41.28 | 37.16 | 42.43 | 46.89 | 41.21 | 42.76 | 44.38 | 44.27 | 45.68 | 40.93 | 39.96 | 43.24 | 49.74 | 49.20 |
| Fs % | 15.10 | 16.40 | 17.10 | 16.79 | 10.37 | 15.16 | 12.31 | 13.66 | 10.53 | 9.81 | 10.95 | 14.79 | 16.27 | 11.88 | 6.78 |
| Acm % | 1.77 | 1.79 | 2.28 | 1.41 | 1.21 | 1.84 | 1.42 | 1.16 | 1.58 | 1.22 | 1.53 | 1.75 | 1.45 | 1.06 | 0.96 |
| Mg# | 69.5 | 73.8 | 64.6 | 74.0 | 76.7 | 72.8 | 70.6 | 71.9 | 80.7 | 81.4 | 74.3 | 70.7 | 78.2 | 81.9 | 82.0 |

Appendix Table 5.5. (4/4)

| Unit Rock type | Volcanic sequence | | | | | | | | | | | | |
|------------------------------------|-------------------|-----------------------|-----------------------|-----------------------|-----------------------|-----------------------|------------------|-----------------------|-----------------------|-----------------------|-----------------------|------------------------|------------------------|
| | pillow basalt | | | | | | | | | | | | |
| Sample Mineral-site position | MK105 cr3-an3 | MK105 cr4-an2 c | MK105 cr5-an3 c | MK105 cr5-an4 r | MK105 cr6-an1 c | MK105 cr6-an6 r | MK105 cr7-an3 | MK105 cr8-an5 c | MK105 cr8-an7 r | MK105 cr9-an1 c | MK105 cr9-an3 r | MK105 cr10-an1 c | MK105 cr10-an3 r |
| SiO ₂ | 49.07 | 49.71 | 47.93 | 48.14 | 50.99 | 48.83 | 48.58 | 48.33 | 48.82 | 49.54 | 48.26 | 49.08 | 50.43 |
| TiO ₂ | 1.10 | 1.07 | 1.64 | 1.93 | 0.63 | 1.53 | 1.50 | 1.25 | 1.23 | 0.81 | 1.73 | 1.26 | 1.10 |
| Al ₂ O ₃ | 4.06 | 3.83 | 4.65 | 4.22 | 2.48 | 4.36 | 4.40 | 4.21 | 4.22 | 3.85 | 4.32 | 4.10 | 3.13 |
| Cr ₂ O ₃ | 0.37 | 0.20 | 0.04 | 0.01 | 0.70 | 0.02 | 0.05 | 0.42 | 0.34 | 0.98 | 0.03 | 0.06 | 0.00 |
| FeO | 6.93 | 7.32 | 8.22 | 10.47 | 5.84 | 8.27 | 8.11 | 6.78 | 6.95 | 5.63 | 8.73 | 8.10 | 7.83 |
| MnO | 0.17 | 0.20 | 0.18 | 0.24 | 0.18 | 0.10 | 0.23 | 0.17 | 0.22 | 0.14 | 0.17 | 0.20 | 0.15 |
| MgO | 15.89 | 15.92 | 15.07 | 14.00 | 17.31 | 14.86 | 15.07 | 15.55 | 15.54 | 16.23 | 14.78 | 15.14 | 15.59 |
| CaO | 21.06 | 20.47 | 21.68 | 20.65 | 20.81 | 21.18 | 21.55 | 21.44 | 21.62 | 21.80 | 20.55 | 21.43 | 21.44 |
| Na ₂ O | 0.47 | 0.47 | 0.45 | 0.53 | 0.41 | 0.52 | 0.48 | 0.37 | 0.42 | 0.42 | 0.53 | 0.52 | 0.43 |
| K ₂ O | 0.00 | 0.00 | 0.00 | 0.00 | 0.00 | 0.01 | 0.01 | 0.00 | 0.02 | 0.00 | 0.00 | 0.01 | 0.01 |
| Total | 99.10 | 99.18 | 99.86 | 100.19 | 99.36 | 99.68 | 99.97 | 98.52 | 99.37 | 99.40 | 99.11 | 99.89 | 100.10 |
| <i>a.p.f.u.</i> | | | | | | | | | | | | | |
| Si | 1.817 | 1.840 | 1.771 | 1.790 | 1.873 | 1.808 | 1.792 | 1.803 | 1.806 | 1.824 | 1.801 | 1.811 | 1.856 |
| Ti | 0.030 | 0.030 | 0.045 | 0.054 | 0.017 | 0.043 | 0.042 | 0.035 | 0.034 | 0.022 | 0.049 | 0.035 | 0.030 |
| Al | 0.177 | 0.167 | 0.203 | 0.185 | 0.107 | 0.190 | 0.191 | 0.185 | 0.184 | 0.167 | 0.190 | 0.178 | 0.136 |
| Cr | 0.011 | 0.006 | 0.001 | 0.000 | 0.020 | 0.001 | 0.001 | 0.012 | 0.010 | 0.029 | 0.001 | 0.002 | 0.000 |
| Fe ³⁺ | 0.151 | 0.121 | 0.196 | 0.164 | 0.121 | 0.145 | 0.174 | 0.154 | 0.157 | 0.142 | 0.149 | 0.165 | 0.122 |
| Fe ²⁺ | 0.063 | 0.106 | 0.058 | 0.161 | 0.059 | 0.111 | 0.077 | 0.058 | 0.058 | 0.031 | 0.124 | 0.085 | 0.119 |
| Mn | 0.005 | 0.006 | 0.006 | 0.007 | 0.006 | 0.003 | 0.007 | 0.005 | 0.007 | 0.004 | 0.005 | 0.006 | 0.005 |
| Mg | 0.877 | 0.878 | 0.830 | 0.776 | 0.948 | 0.820 | 0.829 | 0.864 | 0.857 | 0.891 | 0.822 | 0.833 | 0.856 |
| Ca | 0.835 | 0.812 | 0.858 | 0.823 | 0.819 | 0.840 | 0.852 | 0.857 | 0.857 | 0.860 | 0.822 | 0.847 | 0.846 |
| Na | 0.033 | 0.034 | 0.032 | 0.038 | 0.029 | 0.037 | 0.034 | 0.027 | 0.030 | 0.030 | 0.038 | 0.037 | 0.030 |
| K | 0.000 | 0.000 | 0.000 | 0.000 | 0.000 | 0.001 | 0.000 | 0.000 | 0.001 | 0.000 | 0.000 | 0.000 | 0.000 |
| Total | 4.000 | 4.000 | 4.000 | 4.000 | 4.000 | 4.000 | 4.000 | 4.000 | 4.000 | 4.000 | 4.000 | 4.000 | 4.000 |
| Al (IV) | 0.177 | 0.160 | 0.203 | 0.185 | 0.107 | 0.190 | 0.191 | 0.185 | 0.184 | 0.167 | 0.190 | 0.178 | 0.136 |
| Al (VI) | 0.000 | 0.007 | 0.000 | 0.000 | 0.000 | 0.000 | 0.000 | 0.000 | 0.000 | 0.000 | 0.000 | 0.000 | 0.000 |
| Wo % | 42.62 | 41.61 | 43.46 | 41.93 | 41.45 | 43.00 | 43.34 | 43.72 | 43.75 | 44.00 | 42.04 | 43.07 | 42.87 |
| En % | 44.73 | 45.04 | 42.03 | 39.54 | 47.98 | 41.97 | 42.17 | 44.11 | 43.75 | 45.59 | 42.07 | 42.34 | 43.37 |
| Fs % | 15.16 | 12.16 | 19.63 | 16.51 | 12.09 | 14.56 | 17.42 | 15.44 | 15.68 | 14.26 | 14.93 | 16.52 | 12.23 |
| Acm % | 1.71 | 1.74 | 1.64 | 1.95 | 1.49 | 1.92 | 1.75 | 1.37 | 1.52 | 1.54 | 1.95 | 1.88 | 1.54 |
| Mg# | 80.3 | 79.5 | 76.6 | 70.4 | 84.1 | 76.2 | 76.8 | 80.3 | 79.9 | 83.7 | 75.1 | 76.9 | 78.0 |

Appendix Table 5.6. (1/2) Zircon U-Pb isotopic ratios and ages.

| 03th December 2019, IGG-CNR U.O.S. of Pavia | | | | Data for Wetherill plot ² | | | | | | | Ages ² | | | | | Concordant data | | | |
|---|-----------|---------------|--------|--------------------------------------|---------|-------------------------------------|---------|-------------------------------------|---------|------|--------------------------------------|--------|-------------------------------------|--------|-------------------------------------|-----------------|--------------------------|-----|--------|
| Identifier | Zrc# | Spot Position | Zoning | ²⁰⁷ Pb/ ²⁰⁶ Pb | 1s % | ²⁰⁷ Pb/ ²³⁵ U | 1s % | ²⁰⁶ Pb/ ²³⁸ U | 1s % | Rho | ²⁰⁷ Pb/ ²⁰⁶ Pb | 1s abs | ²⁰⁷ Pb/ ²³⁵ U | 1s abs | ²⁰⁶ Pb/ ²³⁸ U | 1s abs | % U-Pb disc ^d | age | 2s abs |
| MK748 | 037SMPL | 1 | core | 0.04834 | 0.00889 | 0.13307 | 0.02385 | 0.01997 | 0.00076 | 0.03 | 116 | 21 | 127 | 23 | 127 | 5 | 0 | 127 | 9 |
| MK748 | 038SMPL | 2 | rim | 0.05847 | 0.01915 | 0.15246 | 0.04875 | 0.01892 | 0.00125 | 0.03 | 547 | 179 | 144 | 46 | 121 | 8 | 16 | | |
| MK748 | 039SMPL | 4 | rim | 0.04951 | 0.01417 | 0.13939 | 0.03881 | 0.02042 | 0.00122 | 0.03 | 172 | 49 | 133 | 37 | 130 | 8 | 2 | 130 | 15 |
| MK748 | 040SMPL | 6 | rim | 0.04759 | 0.01216 | 0.12619 | 0.03131 | 0.01924 | 0.00105 | 0.03 | 79 | 20 | 121 | 30 | 123 | 7 | -2 | 123 | 13 |
| MK748 | 041SMPL | 7 | rim | 0.04868 | 0.01269 | 0.12770 | 0.03230 | 0.01903 | 0.00106 | 0.03 | 132 | 35 | 122 | 31 | 122 | 7 | 0 | 122 | 13 |
| MK748 | 043SMPL | 10 | rim | 0.04904 | 0.01274 | 0.13081 | 0.03308 | 0.01935 | 0.00104 | 0.03 | 150 | 39 | 125 | 32 | 124 | 7 | 1 | 124 | 13 |
| MK748 | 044SMPL | 11 | rim | 0.05267 | 0.01106 | 0.13788 | 0.02795 | 0.01899 | 0.00090 | 0.03 | 315 | 66 | 131 | 27 | 121 | 6 | 8 | | |
| MK748 | 045SMPL | 14 | rim | 0.04722 | 0.01273 | 0.13440 | 0.03546 | 0.02065 | 0.00105 | 0.03 | 60 | 16 | 128 | 34 | 132 | 7 | -3 | | |
| MK748 | 046SMPL | 20 | rim | 0.05709 | 0.01230 | 0.14610 | 0.03037 | 0.01857 | 0.00091 | 0.03 | 495 | 107 | 138 | 29 | 119 | 6 | 14 | | |
| MK748 | 047SMPL | 19 | rim | 0.05225 | 0.01387 | 0.14669 | 0.03777 | 0.02037 | 0.00117 | 0.03 | 296 | 79 | 139 | 36 | 130 | 7 | 6 | | |
| MK748 | 048SMPL | 18 | rim | 0.04798 | 0.01394 | 0.12804 | 0.03621 | 0.01936 | 0.00114 | 0.03 | 98 | 29 | 122 | 35 | 124 | 7 | -1 | 124 | 14 |
| MK748 | 049SMPL | 16 | rim | 0.05811 | 0.01331 | 0.15004 | 0.03320 | 0.01873 | 0.00097 | 0.03 | 534 | 122 | 142 | 31 | 120 | 6 | 16 | | |
| MK748 | 050SMPL | 15 | rim | 0.04973 | 0.01213 | 0.13097 | 0.03102 | 0.01911 | 0.00098 | 0.03 | 182 | 44 | 125 | 30 | 122 | 6 | 2 | | |
| MK749 | 006SMPL | 22 | core | 0.05147 | 0.01062 | 0.13935 | 0.02826 | 0.01964 | 0.00080 | 0.03 | 262 | 54 | 132 | 27 | 125 | 5 | 5 | | |
| MK749 | 007SMPL | 23 | core | 0.04856 | 0.00686 | 0.12824 | 0.01786 | 0.01915 | 0.00055 | 0.03 | 127 | 18 | 123 | 17 | 122 | 3 | 0 | 122 | 7 |
| MK749 | 008SMPL | 24 | rim | 0.07997 | 0.01514 | 0.22770 | 0.04174 | 0.02064 | 0.00104 | 0.02 | 1196 | 226 | 208 | 38 | 132 | 7 | 37 | | |
| MK749 | 009SMPL | 24 | core | 0.05458 | 0.00756 | 0.13859 | 0.01887 | 0.01841 | 0.00054 | 0.03 | 395 | 55 | 132 | 18 | 118 | 3 | 11 | | |
| MK749 | 010SMPL | 26 | rim | 0.10574 | 0.01887 | 0.31328 | 0.05422 | 0.02149 | 0.00100 | 0.02 | 1727 | 308 | 277 | 48 | 137 | 6 | 50 | | |
| MK749 | 011SMPL | 27 | rim | 0.06519 | 0.01731 | 0.17625 | 0.04571 | 0.01960 | 0.00116 | 0.03 | 780 | 207 | 165 | 43 | 125 | 7 | 24 | | |
| MK749 | 012SMPL | 29 | rim | 0.04811 | 0.01717 | 0.13163 | 0.04634 | 0.01984 | 0.00120 | 0.03 | 105 | 37 | 126 | 44 | 127 | 8 | -1 | 127 | 15 |
| MK749 | 013SMPL | 29 | core | 0.05310 | 0.00708 | 0.14055 | 0.01833 | 0.01920 | 0.00059 | 0.03 | 333 | 44 | 134 | 17 | 123 | 4 | 8 | | |
| MK749 | 014SMPL | 30 | core | 0.05077 | 0.01216 | 0.14193 | 0.03341 | 0.02027 | 0.00094 | 0.03 | 230 | 55 | 135 | 32 | 129 | 6 | 4 | | |
| MK749 | 015SMPL | 31 | core | 0.04789 | 0.00748 | 0.12717 | 0.01947 | 0.01926 | 0.00064 | 0.03 | 94 | 15 | 122 | 19 | 123 | 4 | -1 | | |
| MK749 | 016SMPL | 32 | core | 0.05378 | 0.01058 | 0.13971 | 0.02690 | 0.01884 | 0.00080 | 0.03 | 362 | 71 | 133 | 26 | 120 | 5 | 9 | | |
| MK749 | 017SMPL | 43 | core | 0.05454 | 0.01163 | 0.14834 | 0.03097 | 0.01972 | 0.00088 | 0.03 | 393 | 84 | 140 | 29 | 126 | 6 | 10 | | |
| MK749 | 018SMPL | 42 | core | 0.05396 | 0.00906 | 0.14841 | 0.02436 | 0.01994 | 0.00074 | 0.03 | 369 | 62 | 141 | 23 | 127 | 5 | 9 | | |
| MK749 | 019SMPL | 41 | rim | 0.04764 | 0.02089 | 0.13029 | 0.05644 | 0.01983 | 0.00141 | 0.02 | 81 | 36 | 124 | 54 | 127 | 9 | -2 | 127 | 18 |
| MK749 | 020SMPL | 41 | core | 0.04882 | 0.01075 | 0.12452 | 0.02690 | 0.01850 | 0.00080 | 0.03 | 139 | 31 | 119 | 26 | 118 | 5 | 1 | 118 | 10 |
| MK749 | 021SMPL | 40 | rim | 0.05684 | 0.01049 | 0.15053 | 0.02718 | 0.01921 | 0.00076 | 0.03 | 485 | 90 | 142 | 26 | 123 | 5 | 14 | | |
| MK749 | 022SMPL | 40 | core | 0.05396 | 0.01144 | 0.14464 | 0.03000 | 0.01944 | 0.00087 | 0.03 | 369 | 78 | 137 | 28 | 124 | 6 | 10 | | |
| MK749 | 028SMPL | 39 | core | 0.06156 | 0.02097 | 0.15541 | 0.05196 | 0.01831 | 0.00121 | 0.02 | 659 | 224 | 147 | 49 | 117 | 8 | 20 | | |
| MK749 | 029SMPL | 38 | rim | 0.04876 | 0.01142 | 0.12703 | 0.02907 | 0.01890 | 0.00090 | 0.03 | 136 | 32 | 121 | 28 | 121 | 6 | 1 | 121 | 11 |
| MK749 | 030SMPL | 38 | core | 0.04753 | 0.00955 | 0.12438 | 0.02436 | 0.01898 | 0.00080 | 0.03 | 76 | 15 | 119 | 23 | 121 | 5 | -2 | 121 | 10 |
| MK749 | 031SMPL | 37 | rim | 0.05349 | 0.01729 | 0.13509 | 0.04284 | 0.01832 | 0.00114 | 0.03 | 350 | 113 | 129 | 41 | 117 | 7 | 9 | | |
| MK749 | 032SMPL | 37 | core | 0.04983 | 0.01875 | 0.12813 | 0.04718 | 0.01865 | 0.00139 | 0.03 | 187 | 70 | 122 | 45 | 119 | 9 | 3 | | |
| MK749 | 033SMPL | 36 | rim | 0.04858 | 0.01043 | 0.12968 | 0.02709 | 0.01936 | 0.00088 | 0.03 | 128 | 27 | 124 | 26 | 124 | 6 | 0 | 124 | 11 |
| MK749 | 034SMPL | 35 | rim | 0.04803 | 0.01967 | 0.12828 | 0.05166 | 0.01937 | 0.00143 | 0.03 | 101 | 41 | 123 | 49 | 124 | 9 | -1 | 124 | 18 |
| MK749 | 036SMPL | 33 | core | 0.04846 | 0.00907 | 0.12378 | 0.02240 | 0.01853 | 0.00076 | 0.03 | 122 | 23 | 118 | 21 | 118 | 5 | 0 | 118 | 10 |
| 005SMPL | 91500 | | | 0.07698 | 0.00349 | 1.90020 | 0.08512 | 0.17904 | 0.00280 | 0.03 | 1121 | 51 | 1081 | 48 | 1062 | 17 | | | |
| 027SMPL | Plesovice | | | 0.05263 | 0.00404 | 0.39815 | 0.02944 | 0.05487 | 0.00112 | 0.04 | 313 | 24 | 340 | 25 | 344 | 7 | | | |

Appendix Table 5.6. (2/2)

| 24th January 2019, IGG-CNR U.O.S. of Pavia | | | | Data for Wetherill plot ¹ | | | | | | | Ages ² | | | | | Concordant data | | | |
|--|----------|---------------|--------|--------------------------------------|---------|-------------------------------------|---------|-------------------------------------|---------|-----|--------------------------------------|--------|-------------------------------------|--------|-------------------------------------|-----------------|--------------------------|-----|--------|
| Identifier | Zrc# | Spot Position | Zoning | ²⁰⁷ Pb/ ²⁰⁶ Pb | 1s % | ²⁰⁷ Pb/ ²³⁵ U | 1s % | ²⁰⁶ Pb/ ²³⁸ U | 1s % | Rho | ²⁰⁷ Pb/ ²⁰⁶ Pb | 1s abs | ²⁰⁷ Pb/ ²³⁵ U | 1s abs | ²⁰⁶ Pb/ ²³⁸ U | 1s abs | % U-Pb disc ⁴ | age | 2s abs |
| MK422 | Jn24e006 | 37 | | 0.04678 | 0.02157 | 0.12999 | 0.05967 | 0.02019 | 0.00104 | 0.1 | 38 | 18 | 124 | 57 | 129 | 7 | -3.8 | | |
| MK422 | Jn24e007 | 42 | | 0.12739 | 0.02276 | 0.48867 | 0.08552 | 0.02785 | 0.00130 | 0.3 | 2062 | 368 | 404 | 71 | 177 | 8 | 56.2 | | |
| MK422 | Jn24e008 | 46 | | 0.06128 | 0.01550 | 0.18553 | 0.04671 | 0.02199 | 0.00085 | 0.2 | 649 | 164 | 173 | 44 | 140 | 5 | 18.9 | | |
| MK422 | Jn24e009 | 38 | | 0.07765 | 0.00856 | 0.23754 | 0.02607 | 0.02220 | 0.00069 | 0.3 | 1138 | 125 | 216 | 24 | 142 | 4 | 34.6 | | |
| MK422 | Jn24e010 | 47b | | 0.04654 | 0.00557 | 0.13550 | 0.01624 | 0.02114 | 0.00061 | 0.2 | 26 | 3 | 129 | 15 | 135 | 4 | -4.5 | | |
| MK422 | Jn24e012 | 50 | | 0.09948 | 0.00771 | 0.28802 | 0.02215 | 0.02104 | 0.00065 | 0.4 | 1614 | 125 | 257 | 20 | 134 | 4 | 47.8 | | |
| MK422 | Jn24e013 | 51 | | 0.05724 | 0.00300 | 0.16499 | 0.00893 | 0.02093 | 0.00054 | 0.5 | 501 | 26 | 155 | 8 | 134 | 3 | 13.9 | | |
| MK422 | Jn24e014 | 52 | | 0.05036 | 0.00304 | 0.14124 | 0.00873 | 0.02036 | 0.00053 | 0.4 | 212 | 13 | 134 | 8 | 130 | 3 | 3.1 | | |
| MK422 | Jn24e015 | 53 | | 0.07353 | 0.01466 | 0.24800 | 0.04911 | 0.02448 | 0.00092 | 0.2 | 1029 | 205 | 225 | 45 | 456 | 6 | 30.7 | | |
| MK422 | Jn24e016 | 54 | | 0.10090 | 0.01209 | 0.27400 | 0.03246 | 0.01973 | 0.00067 | 0.3 | 1641 | 197 | 246 | 29 | 126 | 4 | 48.8 | | |
| MK422 | Jn24e017 | 55 | | 0.05693 | 0.01355 | 0.15987 | 0.03777 | 0.02043 | 0.00086 | 0.2 | 489 | 116 | 151 | 36 | 130 | 5 | 13.4 | | |
| MK422 | Jn24e018 | 58 | | 0.06273 | 0.00378 | 0.17529 | 0.01080 | 0.02028 | 0.00054 | 0.4 | 699 | 42 | 164 | 10 | 129 | 3 | 21.1 | | |
| MK422 | Jn24e019 | 59 | | 0.06271 | 0.00251 | 0.17793 | 0.00762 | 0.02058 | 0.00052 | 0.6 | 698 | 28 | 166 | 7 | 131 | 3 | 21.0 | | |
| MK422 | Jn24e020 | 61 | | 0.04810 | 0.00978 | 0.13439 | 0.02726 | 0.02029 | 0.00066 | 0.2 | 104 | 21 | 128 | 26 | 129 | 4 | -1.1 | | |
| MK422 | Jn24e021 | 62 | | 0.08236 | 0.01329 | 0.24085 | 0.03852 | 0.02124 | 0.00079 | 0.2 | 1254 | 202 | 219 | 35 | 135 | 5 | 38.2 | | |
| MK423 | Jn24e026 | 2 | | 0.05334 | 0.00229 | 0.14471 | 0.00660 | 0.01970 | 0.00049 | 0.6 | 343 | 15 | 137 | 6 | 126 | 3 | 8.4 | | |
| MK423 | Jn24e027 | 4 | | 0.04737 | 0.00156 | 0.13346 | 0.00489 | 0.02045 | 0.00050 | 0.7 | 68 | 2 | 127 | 5 | 130 | 3 | -2.6 | | |
| MK423 | Jn24e028 | 6 | | 0.04866 | 0.00100 | 0.13853 | 0.00367 | 0.02060 | 0.00049 | 0.9 | 131 | 3 | 132 | 3 | 131 | 3 | 0.2 | 132 | 6 |
| MK423 | Jn24e029 | 8 | | 0.06599 | 0.00207 | 0.16880 | 0.00593 | 0.01864 | 0.00046 | 0.7 | 806 | 25 | 158 | 6 | 119 | 3 | 24.8 | | |
| MK423 | Jn24e030 | 9 | | 0.04947 | 0.00195 | 0.13544 | 0.00575 | 0.01993 | 0.00050 | 0.6 | 170 | 7 | 129 | 5 | 127 | 3 | 1.4 | 127 | 6 |
| MK423 | Jn24e031 | 12 | | 0.04930 | 0.00187 | 0.13794 | 0.00567 | 0.02036 | 0.00051 | 0.6 | 162 | 6 | 131 | 5 | 130 | 3 | 1.0 | 130 | 7 |
| MK423 | Jn24e032 | 14 | | 0.04954 | 0.00121 | 0.14408 | 0.00428 | 0.02115 | 0.00051 | 0.8 | 173 | 4 | 137 | 4 | 135 | 3 | 1.3 | 135 | 7 |
| MK423 | Jn24e033 | 17 | | 0.06013 | 0.00288 | 0.16335 | 0.00817 | 0.01979 | 0.00051 | 0.5 | 608 | 29 | 154 | 8 | 126 | 3 | 17.8 | | |
| MK423 | Jn24e034 | 19 | | 0.09361 | 0.00243 | 0.27695 | 0.00849 | 0.02151 | 0.00054 | 0.8 | 1500 | 39 | 248 | 8 | 137 | 3 | 44.7 | | |
| MK423 | Jn24e035 | 22 | | 0.09476 | 0.00337 | 0.27047 | 0.01042 | 0.02073 | 0.00054 | 0.7 | 1523 | 54 | 243 | 9 | 132 | 3 | 45.6 | | |
| MK423 | Jn24e036 | 23 | | 0.04959 | 0.00143 | 0.13737 | 0.00459 | 0.02019 | 0.00050 | 0.7 | 176 | 5 | 131 | 4 | 129 | 3 | 1.4 | 129 | 6 |
| MK423 | Jn24e037 | 24 | | 0.05363 | 0.00218 | 0.15072 | 0.00655 | 0.02041 | 0.00052 | 0.6 | 356 | 14 | 143 | 6 | 130 | 3 | 8.6 | | |
| MK423 | Jn24e038 | 25 | | 0.04618 | 0.00176 | 0.12449 | 0.00515 | 0.01959 | 0.00048 | 0.6 | 7 | 0 | 119 | 5 | 125 | 3 | -5.0 | | |
| MK423 | Jn24e039 | 26 | | 0.07021 | 0.00349 | 0.19731 | 0.01016 | 0.02043 | 0.00054 | 0.5 | 935 | 46 | 183 | 9 | 130 | 3 | 28.7 | | |
| MK423 | Jn24e040 | 29 | | 0.04778 | 0.00478 | 0.15364 | 0.01544 | 0.02341 | 0.00068 | 0.3 | 88 | 9 | 145 | 15 | 149 | 4 | -2.8 | 149 | 9 |
| MK423 | Jn24e041 | 30 | | 0.07776 | 0.00382 | 0.24282 | 0.01234 | 0.02273 | 0.00061 | 0.5 | 1141 | 56 | 221 | 11 | 145 | 4 | 34.4 | | |
| Jn24e005 | STD(QC) | PLESOVICE | | 0.05266 | 0.00084 | 0.39559 | 0.00926 | 0.05448 | 0.00129 | 1.0 | 314 | 5 | 338 | 8 | 342 | 8 | | | |
| Jn24e025 | STD(QC) | PLESOVICE | | 0.05176 | 0.00095 | 0.38965 | 0.00981 | 0.05461 | 0.00131 | 1.0 | 275 | 5 | 334 | 8 | 343 | 8 | | | |
| Jn24e042 | STD(QC) | PLESOVICE | | 0.05255 | 0.00147 | 0.39263 | 0.01282 | 0.05420 | 0.00134 | 0.8 | 309 | 9 | 336 | 11 | 340 | 8 | | | |

Appendix Table 5.7. Input parameters for the partial melting models used for the different volcanic and subvolcanic rock-types from the Band-e-Zeyarat ophiolite.

| Mantle source compositions | | | | Partial melting parameters | | | | | | | |
|----------------------------|-------|-------|--------------|------------------------------|-------|----|-----|-----|-----|-----|-----|
| | DMM* | EM** | Calculate S2 | Source mode (Kinzler, 1997) | | | Ol | Opx | Cpx | Sp | Gt |
| La | 0.253 | 1.37 | 0.364 | Ol | 0.53 | La | (1) | (1) | (1) | (1) | (1) |
| Ce | 0.726 | 2.70 | 1.022 | Opx | 0.27 | Ce | (1) | (1) | (1) | (1) | (1) |
| Pr | 0.132 | 0.273 | 0.174 | Cpx | 0.17 | Pr | (1) | (1) | (1) | (1) | (1) |
| Nd | 0.703 | 1.33 | 0.891 | Sp | 0.03 | Nd | (1) | (1) | (1) | (1) | (1) |
| Sm | 0.273 | 0.396 | 0.298 | | | Sm | (1) | (1) | (1) | (1) | (1) |
| Eu | 0.108 | 0.128 | 0.112 | Melting mode (Kinzler, 1997) | | | Eu | (1) | (1) | (1) | (1) |
| Gd | 0.397 | 0.407 | 0.399 | Ol | -0.06 | Gd | (1) | (1) | (1) | (1) | (1) |
| Tb | 0.076 | 0.055 | 0.068 | Opx | 0.28 | Tb | (1) | (1) | (1) | (1) | (1) |
| Dy | 0.505 | 0.329 | 0.470 | Cpx | 0.67 | Dy | (1) | (1) | (1) | (1) | (1) |
| Ho | 0.115 | 0.056 | 0.103 | Sp | 0.11 | Ho | (1) | (1) | (1) | (1) | (1) |
| Er | 0.348 | 0.172 | 0.295 | | | Er | (1) | (1) | (1) | (1) | (1) |
| Tm | | 0.023 | 0.000 | | | Tm | (1) | (1) | (1) | (1) | (1) |
| Yb | 0.365 | 0.156 | 0.283 | | | Yb | (1) | (1) | (1) | (1) | (1) |
| Lu | 0.058 | 0.023 | 0.042 | | | Lu | (1) | (1) | (1) | (1) | (1) |
| Nb | 0.202 | 2.00 | 0.334 | | | Nb | (1) | (3) | (4) | (5) | (6) |
| Th | 0.011 | 0.100 | 0.022 | | | Th | (1) | (7) | (1) | (2) | (1) |

* Workman & Hart (2005)

** Lustrino et al. (2002)

(1): McKenzie & O'Nions (1991)

(2): Klemme et al (2006)

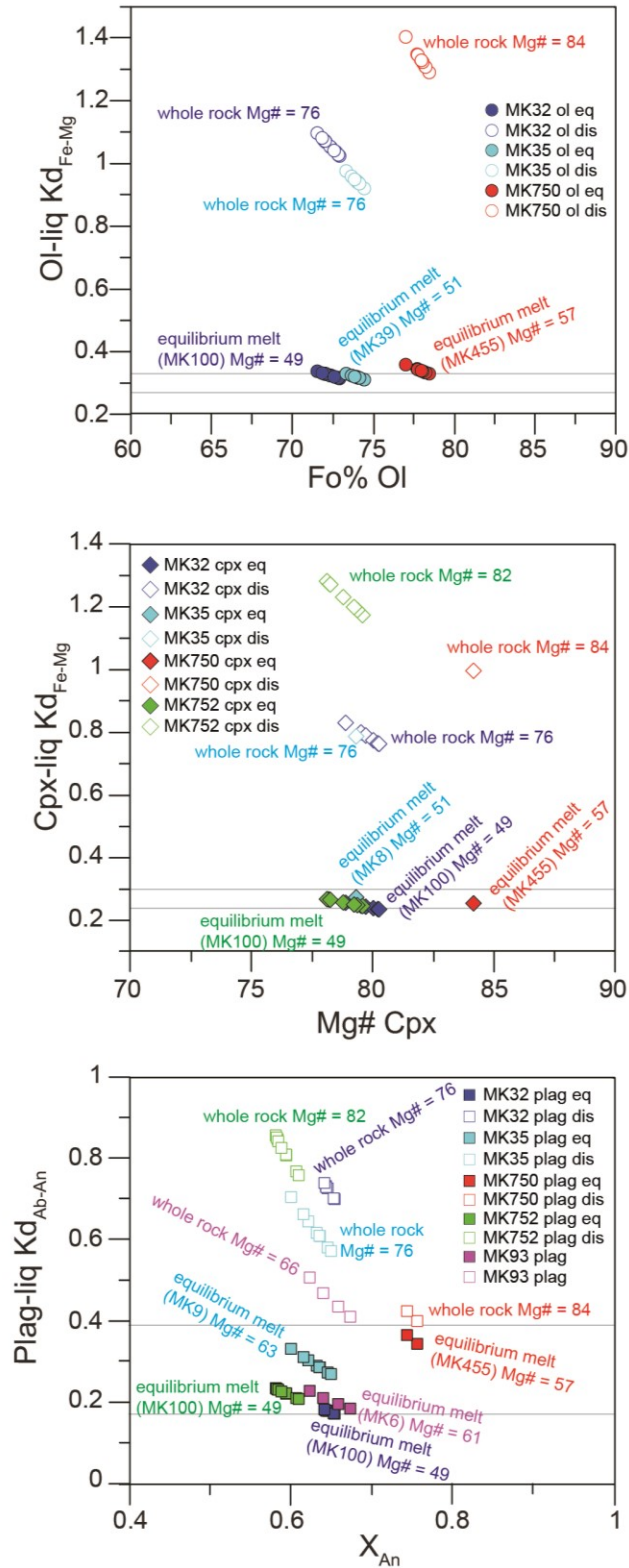
(3): Salters & Longhi (1999)

(4): Ewart & Griffin (1994)

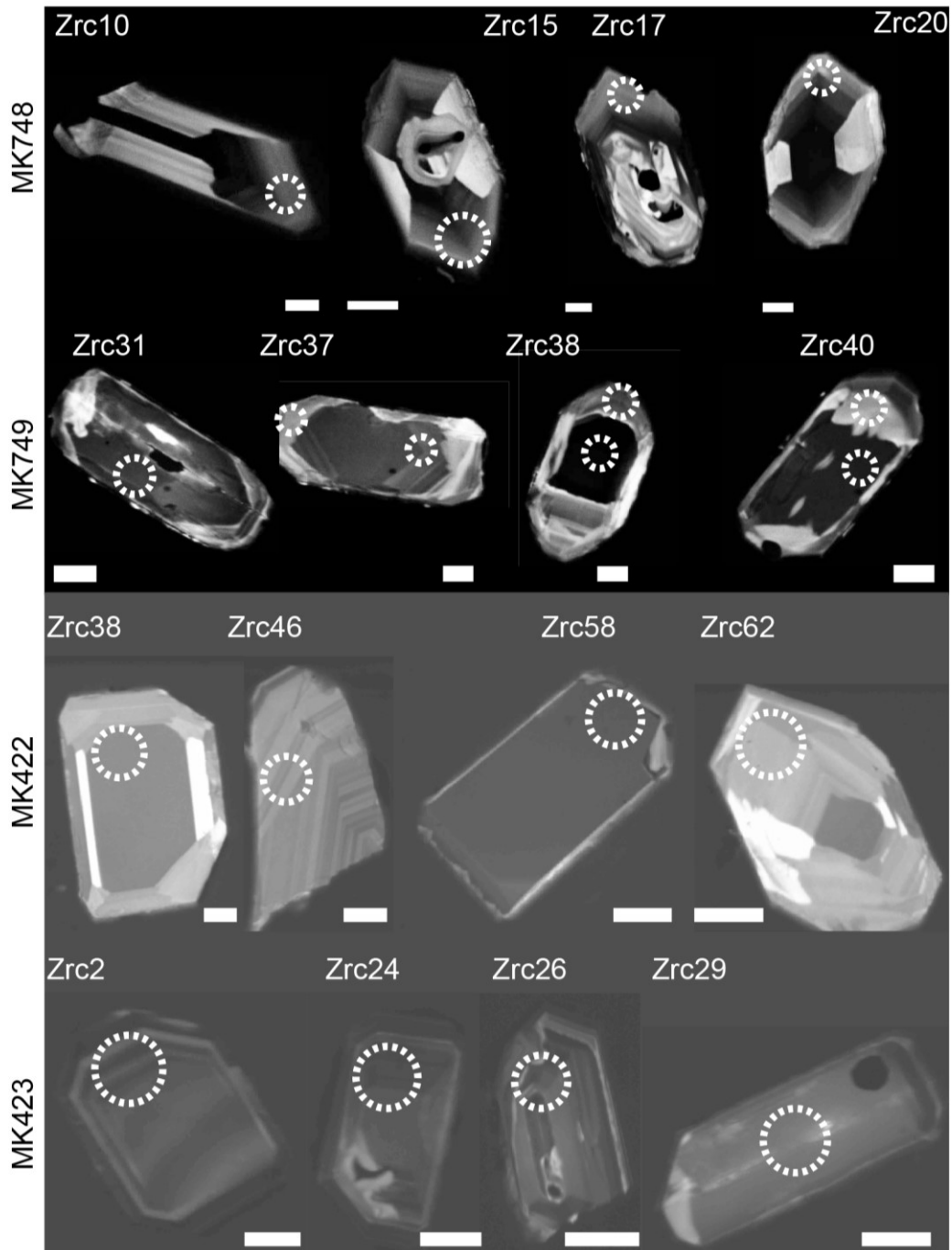
(5): Horn et al (1994)

(6): Green et al (2000)

(7): Dunn & Sen (1994)



Appendix Figure 5.1. $Fo\%$ vs. $Ol-Liq Kd_{Fe-Mg}$, $Mg\#$ vs. $Cpx-Liq Kd_{Fe-Mg}$, and X_{An} vs. $Plag-Liq Kd_{Ab-An}$ for olivine, clinopyroxene and plagioclase from the Band-e-Zeyarat ophiolite. The white symbols represent the disequilibrium between crystals and their host rock composition ($Mg\#$ indicated). The filled symbols represent the obtained equilibrium conditions after the selection of melt composition in equilibrium with the composition of mineral phase.



Appendix Figure 5.2. Representative cathodoluminescence (CL) features of zircons from MK422, MK423, MK749, and MK748 samples. White bar is 20 μ m. Dashed circles refer to LA-ICP-MS spot locations.

Chapter 6. The Durkan Complex

Associated manuscript:

Barbero E., Pandolfi L., Delavari M., Dolati A., Saccani E., Catanzariti R., Luciani V., Chiari M., Marroni M., The western Durkan Complex (Makran Accretionary Prism, SE Iran): a Late Cretaceous tectonically disrupted seamounts chain and its role in controlling deformation style. *Geoscience Frontiers*, First online, <https://doi.org/10.1016/j.gsf.2020.12.001>.

Barbero E., Delavari M., Dolati A., Marroni M., Saccani E., Pandolfi L., Zaccarini F., Tectonically disrupted remnants of a Late Cretaceous plume-influenced seamounts chain in the Neo-Tethys realm: new petrological constraints from the western Durkan Complex (Makran Accretionary Prism, SE Iran). In preparation

6.1. The Durkan Complex in the western North Makran: General field features and tectono-stratigraphic architecture

The Durkan Complex defines a NW-SE striking tectonic element, which is bounded by regional-scale fault zones (Fig. 6.1). To the north, the high angle and north dipping Dar-Anar Fault juxtaposes, with reverse kinematics, the Band-e-Zeyarat ophiolites and the Ganj Complex onto the Durkan Complex (Fig. 6.1). To the south, the deformation zone related to the Bashakerd thrust juxtaposes the Durkan Complex onto the Bajgan Complex, the Coloured Mélange, and the Inner Makran turbiditic sequences (Fig. 6.1). In the neighbourhood of Manujan, both the Durkan Complex and the Bashakerd thrust are abruptly truncated by the NNE-striking dextral Sabzevaran

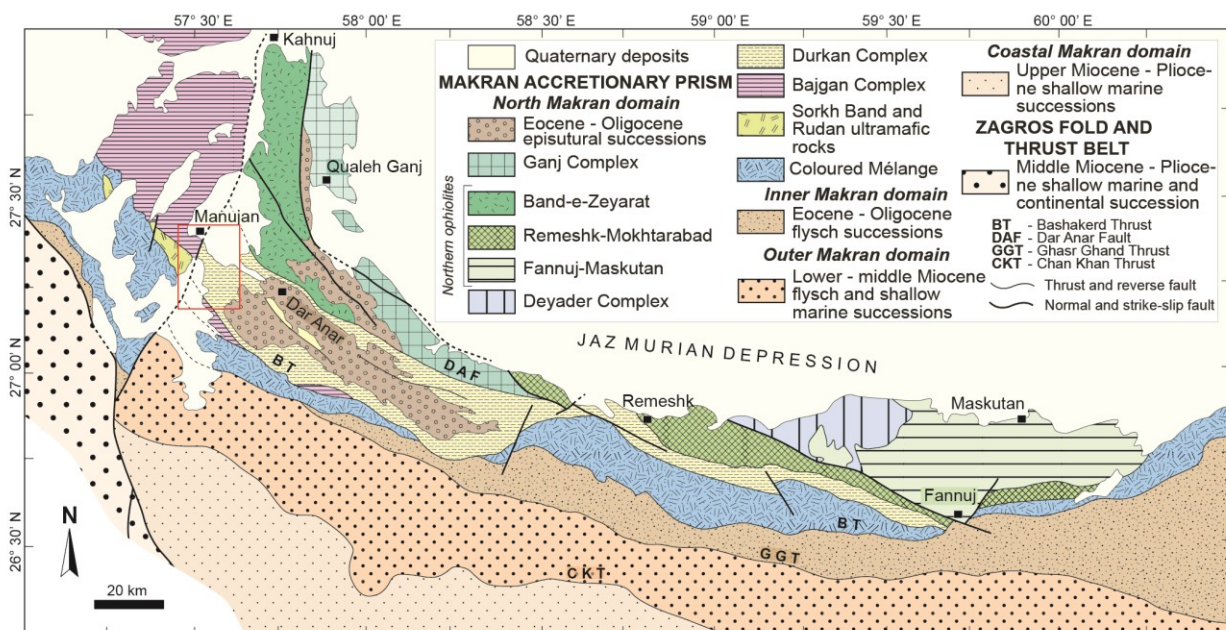


Figure 6.1. Simplified geological map of the North Makran Domain, modified from Eftekhari-Nezhad et al. (1979); Eftekhari-Nejad & McCall (1993); Burg (2018); Samimi Namin (1982, 1983). The box indicates the area expanded in Fig. 6.2.

Fault (Figs. 6.1, 6.2). The Durkan Complex consists of an assemblage of distinct fault-bounded slices (Figs. 6.3a-d). These slices are characterized by stratigraphic successions deformed by polyphase folding and thrusting phases (Fig. 6.4). In addition, several tectonic slices exhibit

various tectono-metamorphic overprints, which range from prehnite pumpellite to subgreenschist facies. The thickness of the successions in the different tectonic slices is difficult to be constrained

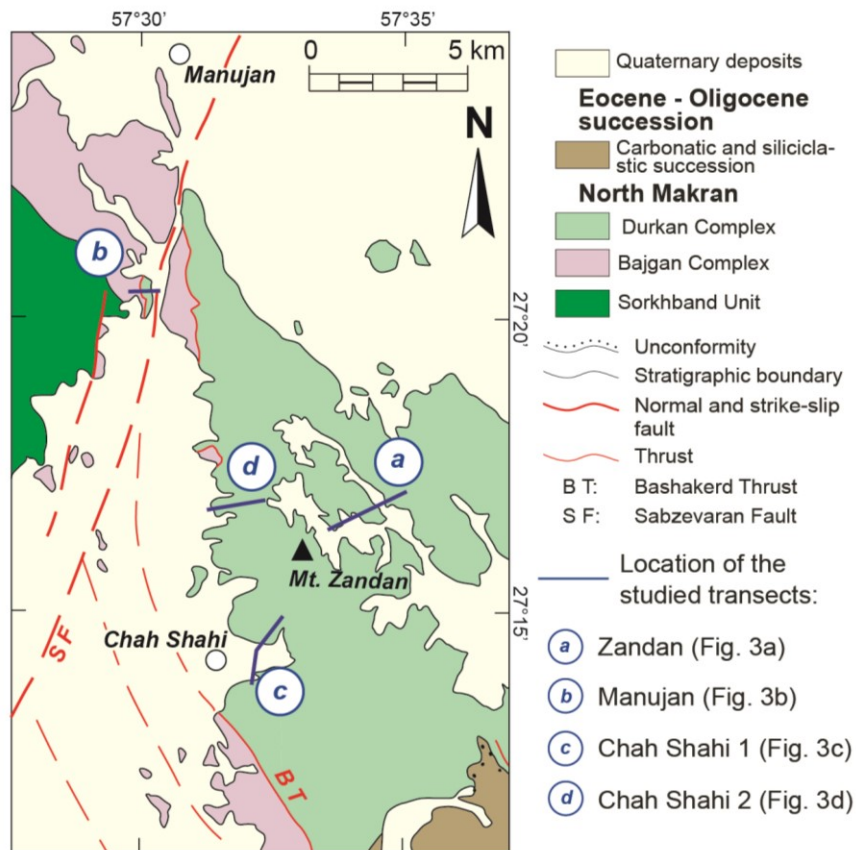


Figure 6.2. Simplified geological map of the Manujan sector showing the location of the studied transect (based on Samimi Namin (1983) and modified according to original fieldwork and photointerpretation with satellite images).

in detail due to the isoclinal folds duplicating the stratigraphic succession (Fig. 6.4). Nonetheless, their thickness can generally be estimated as at least several hundreds of metres.

This complicated structural setting resulted from multiple deformation stages, which occurred during the long-lived tectonic evolution of the Makran Accretionary Prism (McCall, 1985). In fact, the unconformable deposition of early Eocene successions onto the deformed and folded Durkan Complex (Figs. 6.1d, 6.2) indicates that this complex has been deformed during the pre-Eocene tectonic evolution of the North Makran (see also McCall, 1985, 2002). In addition, McCall (1985) suggested that the present-day structural setting of the Durkan Complex also resulted from the post-Eocene deformative stages. A detailed structural analysis and discussion of the structural

evolution of the Durkan Complex will be described in the chapter 7. Here, the general structural relationships among the different tectonic slices will be discussed. The tectono-stratigraphic architecture of the Durkan Complex will be investigated in detail by focusing on four key transects in which different stratigraphic successions are well preserved within distinct tectonic slices (Figs. 6.2, 6.3).

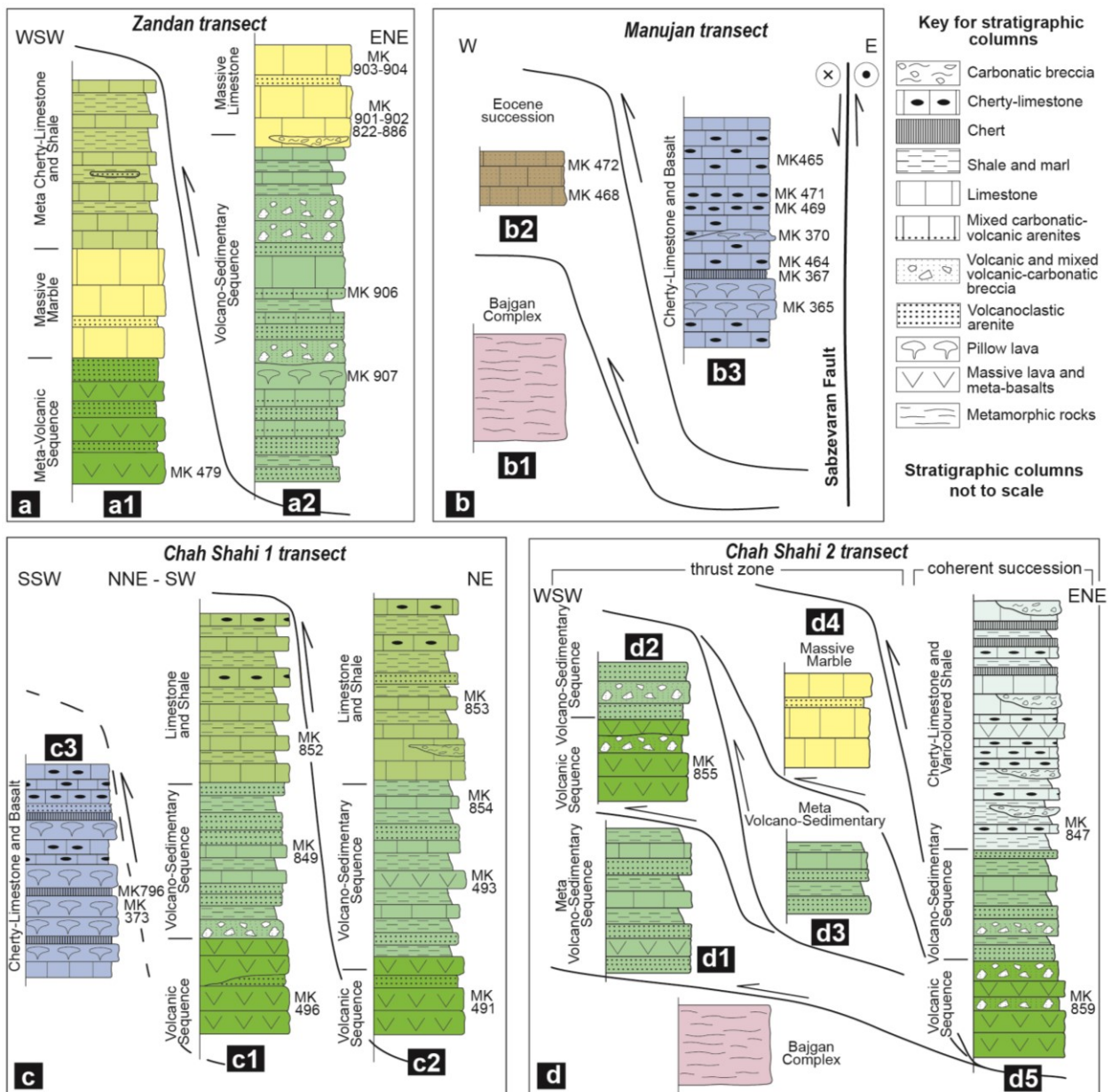


Figure 6.3. Schematic stratigraphic-structural setting and stratigraphic columns for the successions in the studied transects: Zandan transect (a), Manujan transect (b), Chah-Shahi 1 transect (c), and Chah-Shahi 2 transect (d). The location of the transects is shown in Figure 6.2.



Figure 6.4. Panoramic view of the polyphase folding deformation of the Durkan Complex successions showing W-verging isoclinal fold re-folded by E-verging open folds (axial planes and bedding are indicated in figure).

6.1.1. The Zandan transect

This transect is located to the east of the Mt Zandan (Fig. 6.2). Here, two tectonic slices are juxtaposed through an ENE-dipping medium-to-high angle reverse shear zone. They display different stratigraphic successions, as schematically shown in Fig. 6.3a. The succession of the lower unit has been metamorphosed under subgreenschist facies conditions. It consists of a Meta-Volcanic Sequence passing upward to a carbonatic meta-sedimentary succession; the latter can be further subdivided into two lithostratigraphic units, namely: the Massive Marble and the Meta Cherty-Limestone and Shale (Fig. 6.3a1). The Meta-Volcanic Sequence is characterized by massive meta-volcanic rocks showing primary stratigraphic relationships with the Massive Marble (Fig. 6.5a). These are alternated with coarse- and fine-grained meta-volcaniclastic arenites (Fig. 6.5b). Meta-volcanic rocks exhibit millimetre-spaced foliation characterized by fine-grained chlorite, epidote, actinolitic amphibole and minor albite. The Meta-Volcanic Sequence passes

upward to the Massive Marble (Figs. 6.3a1, 6.5a). The succession of the Massive Marble lithostratigraphic unit consists of massive whitish to yellowish marbles (Figs. 6.5a, c). Medium to thin beds of greenish meta-volcaniclastic arenites are locally interbedded within the marbles, suggesting primary stratigraphic relationships between the Massive Marble and the Meta-Volcanic Sequence (Figs. 6.3a1, 6.5d). The upper part of the meta-sedimentary succession consists of the Meta Cherty-Limestone and Shale (Fig. 6.3a1). This lithostratigraphic unit is made up of medium to thin beds of whitish to pinkish meta cherty-limestone and marble alternating with shaly marls, varicoloured shales (Fig. 6.5e), brownish- to yellowish meta-limestones, and subordinate meta-volcaniclastic arenites. The succession of the Meta Cherty-Limestone and Shale shows an upward thinning of the meta-limestone beds coupled with the increase in abundance of the shales, shaly-marls, and brownish meta-limestones (Fig. 6.3a1).

Although the stratigraphic succession of the upper tectonic slice shows intense folding and deformation, no metamorphic recrystallization can be observed and the primary sedimentary features are fairly well preserved. This succession includes two distinct lithostratigraphic units: the Volcano-Sedimentary Sequence and the overlying Massive Limestone (Fig. 6.3a2). The Volcano-Sedimentary Sequence is characterized by pillow lava flows and volcanic breccia (Fig. 6.5f), alternating with different types of sedimentary rocks. The pillow basalts commonly show amygdaloidal texture, characterized by rounded-shaped vesicles filled by calcite, and chlorite. Locally, pluri-centimetric limestone clasts are enclosed within the volcanic breccia, suggesting that the volcanic activity was coeval with the carbonatic sedimentation. The volcanic rocks are subordinate in volume and are interbedded within a sedimentary succession. This succession is mainly made up of volcaniclastic arenites (Fig. 6.5g) and calcareous turbidites alternating with greenish fine-grained shales. The calcareous turbidites display framework composition characterized by both carbonatic and volcanic lithic fragments, as well as fragments of bioclasts,

indicating a mixing between two distinct components. Lens-shaped massive limestones are

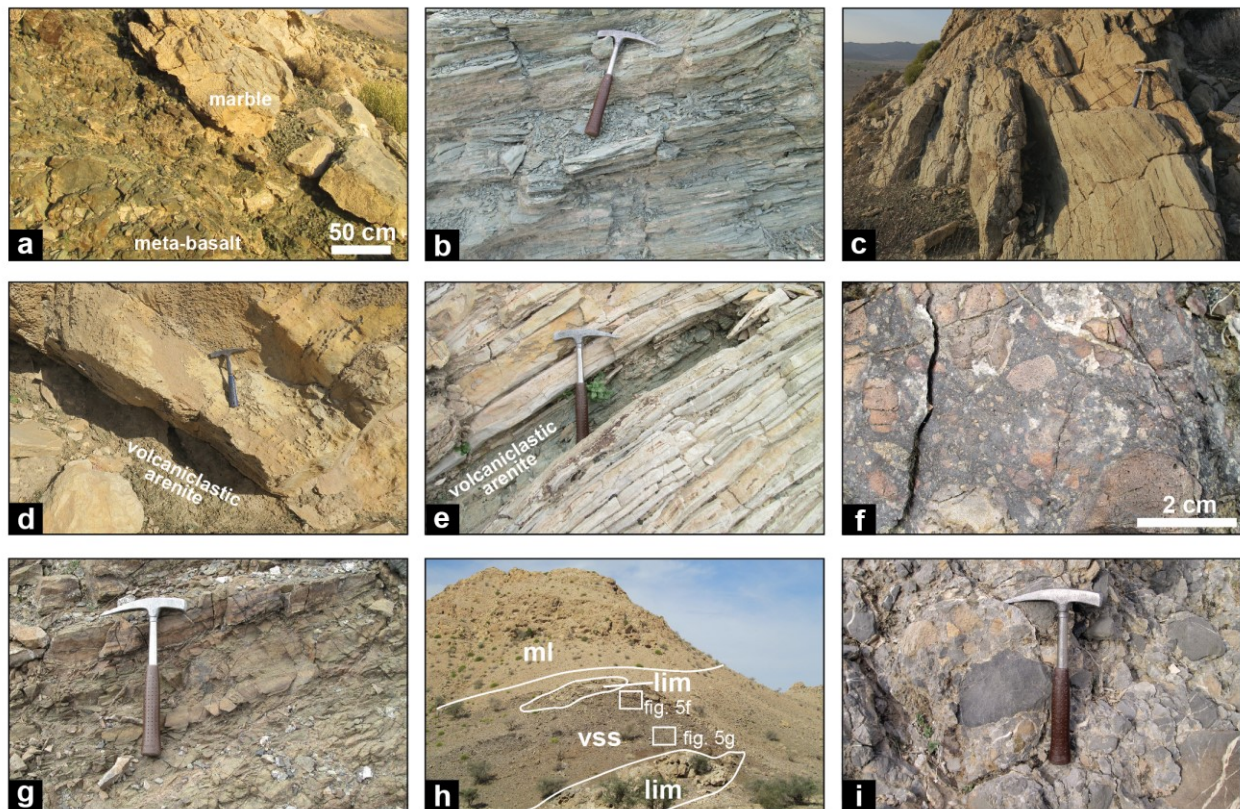


Figure 6.5. Field occurrence of the Durkan Complex in the Zandan transect: a) stratigraphic relationships between the Meta-Volcanic Sequence and the Massive Marble; b) foliated meta-volcaniclastic arenites; c) massive marble; d); intercalation of greenish meta-volcaniclastic arenites within the marble; e) medium-to – thin bedded meta-limestone alternating with shale and meta-volcaniclastic arenites ; f) volcanic breccia with clast of vesicular basaltic rocks set in fine-grained volcanic matrix; g) greenish volcaniclastic arenites; h) panoramic view of the contact between the Volcano-Sedimentary Sequence (VSS) and the Massive Limestone (ml) lithostratigraphic units. Intercalation of massive limestone (lim) occur in the VSS. The locations of Figures 6.5f and 6.5g are also indicated; i) clast-supported carbonatic breccias.

intercalated at different stratigraphic levels within the Volcano-Sedimentary Sequence (Figs. 6.3a2, 6.5h). This, again, indicates coeval volcanic activity and carbonatic sedimentation. The transition between the Volcano-Sedimentary Sequence and the overlying Massive Limestone succession is marked by alternating levels of shale and cherty limestone and, locally, by massive, lenticular bodies of carbonatic megabreccia (Fig. 6.3a2). The latter consists of sub-angular to rounded clasts of fossiliferous limestones embedded within a fine-grained greyish carbonatic matrix (Fig. 6.5i). The Massive Limestone succession (Fig. 6.5h) consists of alternating grainstones, packstones and

minor mudstones. The coarse-grained limestone varieties are characterized by abundant benthic foraminiferal bioclasts and green algae fragments set within a fine-grained recrystallized/micritic matrix indicating a shallow-water platform depositional environment.

6.1.2. The Manujan transect

This transect is located to the south of the town of Manujan (Fig. 6.2). In this area, the NNE-trending strike-slip Sabzevaran Fault truncates the low angle tectonic contact between the Durkan and Bajgan Complexes with dextral displacement (Figs. 6.2, 6.3b). This fault also shows a dip-slip displacement, causing the uplifting of the eastern fault block (Figs. 6.2, 6.3b). In this transect, the Durkan Complex occur, within a reverse fault zone, as lenticular and along strike discontinuous tectonic slices, which are several tens of meters thick (Figs. 6.3b, 6.6a). This fault zone juxtaposes the Durkan Complex onto the Bajgan Complex with the interposition of a tectonic slice of *Nummulites*-bearing siliciclastic rocks (Fig. 6.6b) of the Eocene succession (Figs. 6.3b, 6.6a). This evidence suggests a post-Eocene age for this reverse fault zone, which is, in turn, crosscut by the dextral Sabzevaran Fault (Figs. 6.2, 6.3b).

In the Manujan transect, the Durkan Complex consists of a non-metamorphic succession, which defines the Cherty-Limestone and Basalt lithostratigraphic unit of Figure 6.3b3. The sequence consists of a complex pelagic succession (Fig. 6.6c) composed by the alternation of pinkish to whitish cherty-limestones (Fig. 6.6d), thin- to medium-bedded silicified limestones (Fig. 6.6e), subordinate thin-bedded red cherts (Fig. 6.6f), reddish siliceous shales and marls. In addition, two levels of basaltic pillow lava are intercalated in the pelagic sequence (Fig. 6.3b3). The basaltic lava flows show clear primary stratigraphic relationships with sedimentary rocks and lateral sudden change in thickness, up to the pinch-out of the volcanic level into the pelagic

succession (Fig. 6.6g). The primary relationships among the pillow lava flows and the pelagic sequence are also indicated by soft clasts of the pelagic carbonate sequence inside the pillow lavas (Fig. 6.6h).

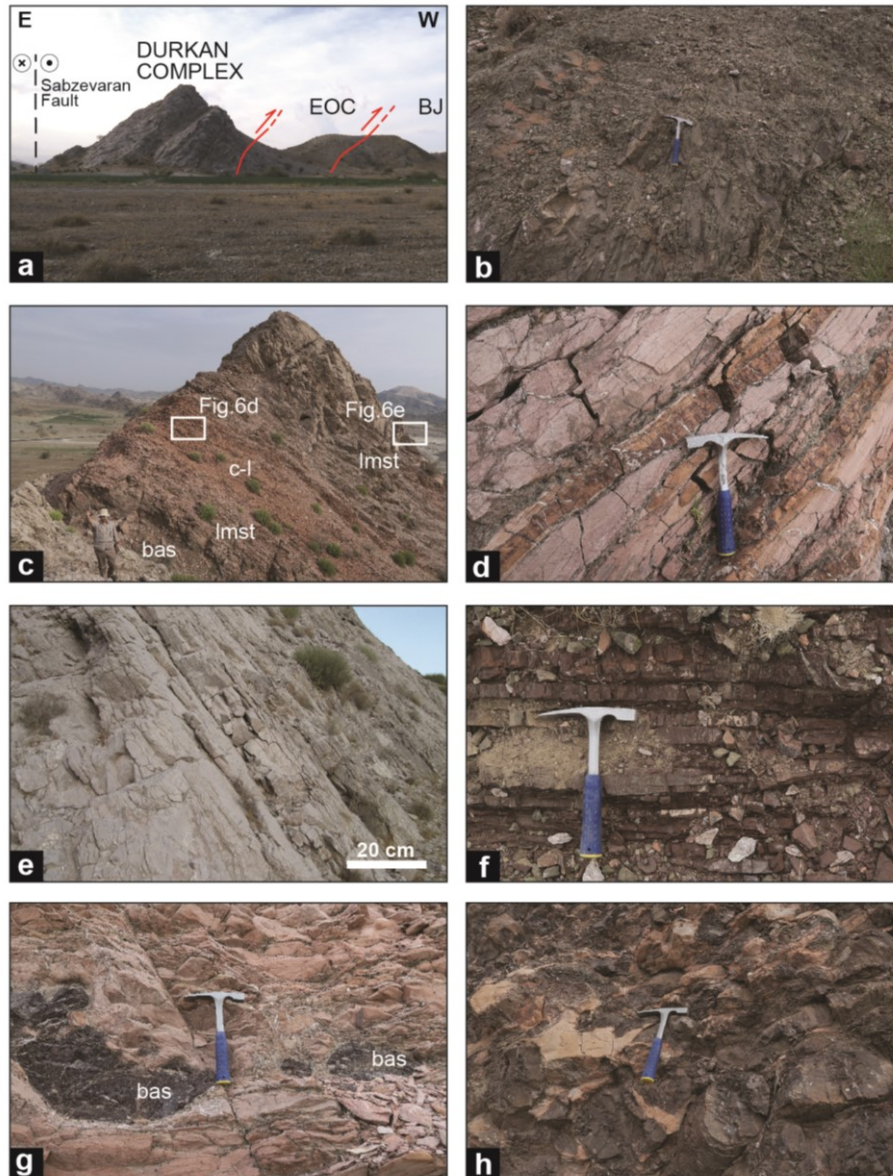


Figure 6.6. Field occurrence of the Durkan Complex in the Manujan transect: a) panoramic view of the reverse fault zone between the Bajgan Complex (BJ) and the Durkan Complex in the Manujan transect. A tectonic slice of Eocene siliciclastic succession (EOC) is interposed between the two Complexes. The location of the buried right-later Sabzevaran Fault is also shown; b) detail of greenish arenites within the Eocene succession tectonically juxtaposed to the Durkan Complex (hammer for scale); c) panoramic view of the pelagic sequence of the Cherty-Limestone and Basalt lithostratigraphic unit (bas: pillow basalt; lmst: limestone; c-l: cherty-limestone). The position of field occurrences shown in figures 6.6d, and 6.6e are also shown; d) alternating beds of pinkish cherty-limestone; e) whitish limestones from the Cherty-Limestone and Basalt; f) alternating chert and shale; g) detail of the pinch out of the pillow basalt flows (bas) within the pelagic sequence, suggesting primary stratigraphic relationships between lavas and pelagic sedimentary rocks; h) soft clasts of marly-limestone within pillow lava flows.

6.1.3. The Chah Shahi 1 transect

This transect is located just to the east of the village of Chah Shahi. It consists of three tectonic slices (Figs. 6.2, 6.3c). Two of the slices show similar stratigraphic successions and are tectonically juxtaposed by a NE-dipping thrust (Figs. 6.3c1, c2). The third succession crops out in the SSW sector showing stratigraphic features (see Fig. 6.3c3) that are quite different from those of the other two.

The westernmost and structurally lowermost unit (Figs. 6.3c3) includes a non-metamorphic succession, which consists of several levels of pillow lava flows associated with radiolarian cherts and volcanoclastic arenites (Fig. 6.7a), interlayered with red cherty-limestones, reddish shales and minor shaly-marls. This stratigraphic succession shows significant analogies with the Cherty-Limestone and Basalt lithostratigraphic unit of the Manujan transect (see section 6.2.2 and Fig. 6.3b3).

In contrast, the stratigraphic successions preserved in the other two slices of the Chah Shahi 1 transect are characterized by a Volcanic Sequence that stratigraphically passes to a Volcano-Sedimentary Sequence. The latter is, in turn, followed by a mainly carbonatic sedimentary succession (Fig. 6.7b), which only consists of one lithostratigraphic unit, hereafter named as Limestone and Shale (Figs. 6.3c1, c2). The Volcanic Sequence shows massive volcanic rocks (Fig. 6.7c) alternating with less abundant coarse-grained volcanoclastic arenites. The Volcano-Sedimentary Sequence is characterized by alternating volcanoclastic arenites (Fig. 6.7d) and varicoloured (greenish and purplish – to reddish) shales and siltstones (Figs. 6.7b, e). Compared to the Volcanic Sequence, this sequence is characterized by the subordinate abundance of massive volcanic rocks, as well as by the exclusive occurrence of purplish and greyish limestones, whose abundance increases toward the top of the succession (Figs. 6.3c1, c2; 6.7b, f). The succession of

the Limestone and Shale lithostratigraphic unit consists of greyish to light blue turbiditic limestones alternating with shaly-marls and shales, as well as less abundant cherty-limestones and volcanoclastic arenites (Figs. 6.3c1, c2; 6.7g, h). Locally, lenticular thick beds of whitish massive limestones and carbonatic breccia occur at the base of the succession (Fig. 6.3c2). The breccia shows clast-supported texture and its composition is largely characterized by white limestone clasts set in a fine-grained carbonatic matrix (Fig. 6.7i).

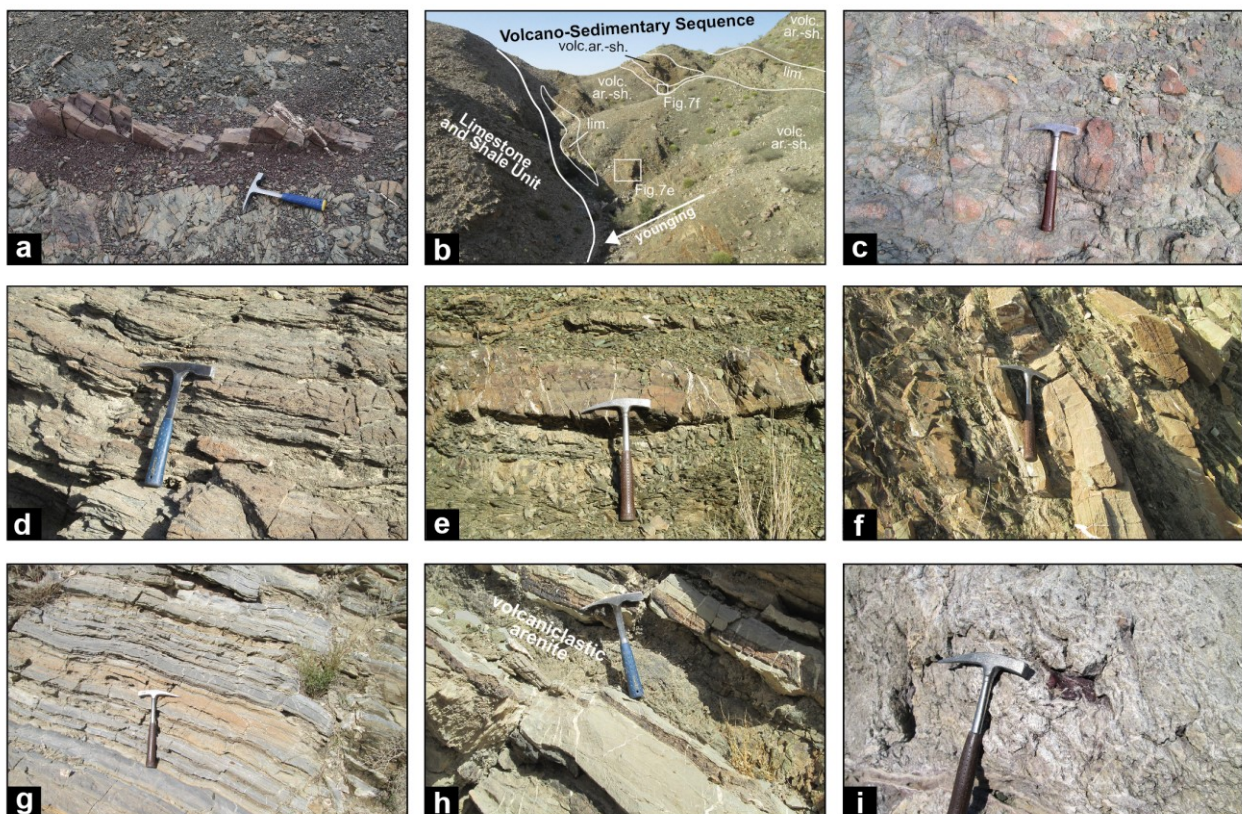


Figure 6.7. Field occurrence of the Durkan Complex in the Chah Shahi I transect: a) thin chert beds alternating with pillow basalt (hammer for scale); b) panoramic view of the stratigraphic transition from the Volcano-Sedimentary Sequence and the Limestone and Shale along an overturned fold limb; abbreviations: volc. ar.-sh.: volcanoclastic arenite and shale; lim.: limestone. The position of Figures 6.7e and 6.7f are indicated; c) volcanic rocks in the Volcanic Sequence; d) alternating volcanoclastic arenites and shales (Volcano-Sedimentary Sequence); e) volcanoclastic arenites alternating with greenish shale from the Meta Volcano-Sedimentary Sequence; f) greyish limestone alternating with greenish shale from the upper part of the Meta Volcano-Sedimentary Sequence; g) thin bedded limestones alternating with shaly-marls (Limestone and Shale); h) detail of greenish volcanoclastic arenites interbedded with cherty-limestone in the Limestone and Shale; i) clast-supported carbonatic breccia in the Limestone and Shale.

6.1.4. *The Chah Shahi 2 transect*

This transect is located few kilometres to the north of the village of Chah Shahi (Fig. 6.2). It is characterized by an uppermost tectonic slice showing a coherent stratigraphic succession bounded at the base by an NNW-striking thrust zone (Figs. 6.3d, 6.8a). This thrust zone displays a complex internal structure and juxtaposes the Durkan Complex to the Bajgan Complex (Fig. 6.3d). It displays interlacing faults segments that bound a series of lenticular slices of hundreds of metres in length (Fig. 6.8a). These tectonic slices show successions that differ in either lithostratigraphy or metamorphism. In the following discussion, I will summarize the complex field evidence by giving a schematic description of the main types of successions cropping out in this fault zone. For the sake of simplicity, I will describe first the successions tectonically deformed within the fault zone and then the coherent stratigraphic succession.

The structurally lowermost tectonic slice that is observable in the thrust zone is represented by a Meta Volcano-Sedimentary Sequence showing subgreenschist facies metamorphism. It consists of alternating marbles and shales with minor abundant massive meta-volcanic rocks and meta-volcaniclastic arenites (Fig. 6.3d1). This slice is overlain by a tectonic slice showing a non-metamorphic stratigraphic succession, which includes a Volcanic Sequence passing upward to a Volcano-Sedimentary Sequence (Fig. 6.3d2). A significant feature of this succession is the abundant occurrence of massive volcanoclastic breccias (Figs. 6.3d2, 6.8b). These breccias are characterized by fragments of aphyric, vesicular basalts, porphyritic basalts, mafic holocrystalline rocks (i.e., microgabbros and dolerites) as well as plurimillimetric pyroxene crystals (Fig. 6.8c). These fragments are set in a matrix exclusively made up of fine-grained volcanic material represented by crystals and altered volcanic glass (Fig. 6.8 c). The fault zone is characterized in the uppermost part by two distinct slices showing pervasive metamorphic recrystallization under

subgreenschist facies conditions (Figs. 6.3d3, d4). The lower slice is characterized by coarse-grained and sheared meta-volcaniclastic arenites alternating with meta-limestones and shales (Fig. 6.3d3). This succession shows many similarities with the succession of the Volcano-Sedimentary Sequence cropping out in other transects (e.g., Figs. 6.3c1, c2), as well as in other tectonic slices of this transect (e.g., Fig. 6.3d1). The meta-volcaniclastic rocks show a foliation defined by a fine-grained aggregate of chlorite, oxide, calcite and minor albite and quartz. The uppermost tectonic slice of the fault zone consists of a sequence of massive marble locally alternated with greenish meta-volcaniclastic arenites (Figs. 6.3d4, 6.8d). The same succession is also observed in some other tectonic slices within the fault zone and shows significant analogies with the Massive Marble lithostratigraphic unit cropping out in the Zandan transect (see Fig. 6.3a1).

The coherent succession consists of three lithostratigraphic units (Fig. 6.3d5). From the lower to the upper stratigraphic position, these units are: i) the Volcanic Sequence; ii) the Volcano-Sedimentary Sequence; iii) the Cherty-Limestone and Varicoloured Shale. The basal Volcanic Sequence includes massive volcanic rocks alternating with coarse-grained volcaniclastic breccias and arenites (Fig. 6.8e). The volcaniclastic breccia is characterized by clasts of aphyric, porphyritic and vesicular volcanic rocks, as well as either fractured or euhedral pyroxene crystals, up to 1-2 cm in size. These materials are set in a heterogeneous fine-grained and foliated matrix, mainly consisting of chlorite aggregate, clay mineral and less abundant calcite. The Volcanic sequence shows a stratigraphic and transitional passage to the Volcano-Sedimentary Sequence (Fig. 6.8f). The latter consists of greenish volcaniclastic arenites interbedded with varicoloured (purplish and reddish - to greenish) shales and siltstones, as well as purplish - to pinkish and light grey limestones (Figs. 6.3d5, 6.8f). In addition, thick lenticular beds of volcaniclastic breccias and polygenic breccias are interbedded in the sequence (Fig. 6.3d5). The volcaniclastic breccias observed in the Volcano-Sedimentary Sequence is texturally and compositionally comparable to

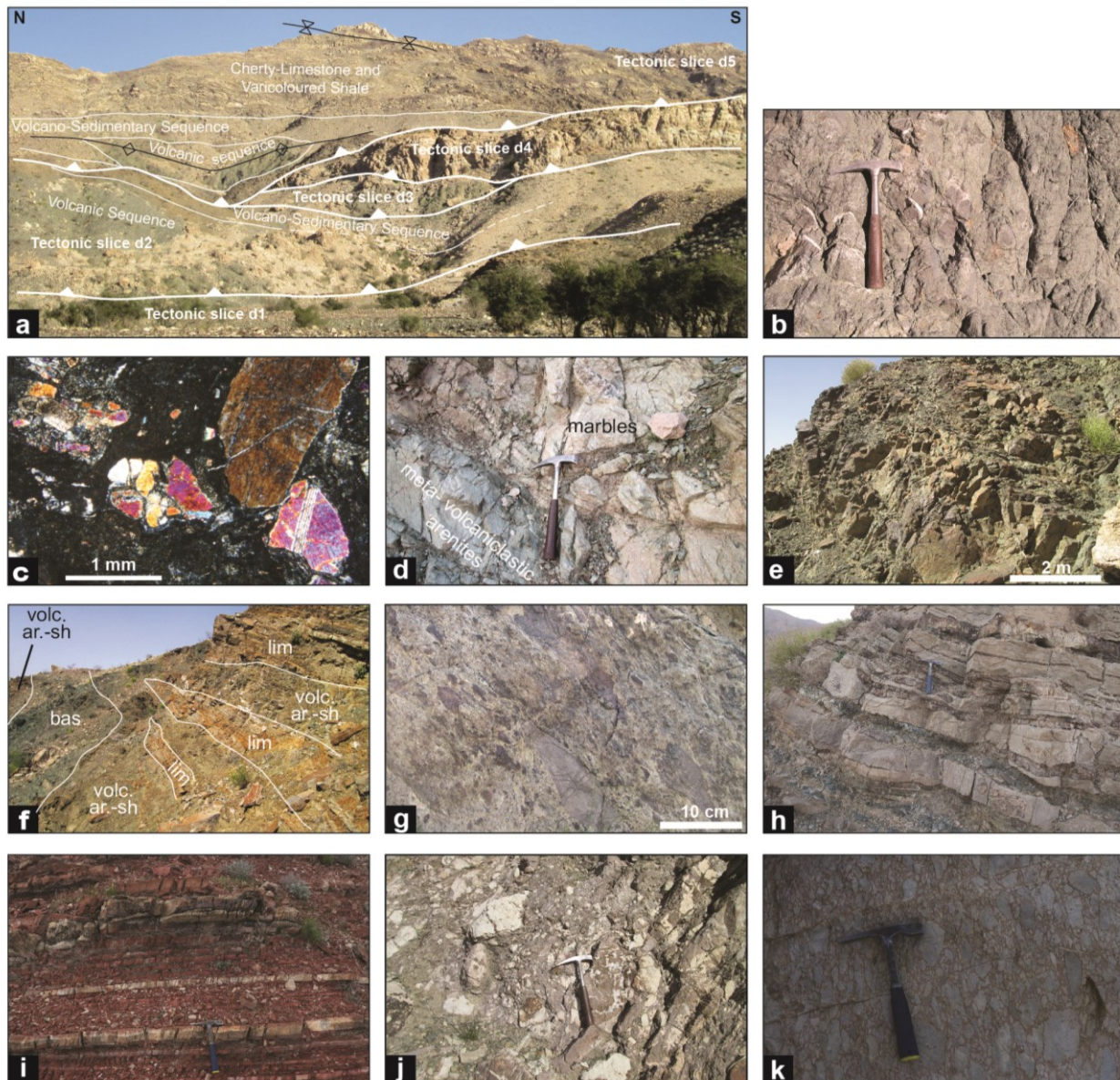


Figure 6.8. a) Panoramic view of the Chah Shahi 2 transect showing the thrust zone (tectonic slices d1 to d4) and the overlying coherent succession (tectonic slice d5). In the latter are also indicate the axial plane of macro-scale antiformal and synformal folds; Field occurrence and photomicrographs of the Durkan Complex in the Chah Shahi 2 transect (b-d: thrust zone; e-k coherent succession): b) volcaniclastic breccia showing clast of different types of volcanic rocks set within a greenish arenitic matrix (hammer for scale); c) photomicrograph of clast-supported volcaniclastic breccia, characterized by pyroxene crystals and volcanic fragments with different textures (aphyric, porphyritic and holocrystalline rocks) set in a fine-grained matrix made up of volcanic material (glass and microlite); d) massive marble showing stratigraphic relationships with meta-volcaniclastic arenite; e) massive volcanic rocks alternating with volcaniclastic arenites from the Volcanic Sequence; f) panoramic view of the Volcano-Sedimentary Sequence showing primary stratigraphic alternation of massive basaltic lava (bas), volcaniclastic arenites and greenish shale (volc. are.-sh.), and limestone and shale (lim.); g) matrix-supported breccia from the Volcano-Sedimentary Sequence showing limestone and shale clasts in a fine-grained greyish to greenish matrix; h) alternating cherty-limestone and varicoloured shale from the Cherty-Limestone and Varicoloured Shale; i) reddish cherts and shale alternating with brownish cherty-limestone; j) matrix-supported breccia showing decametric blocks enclosed within pinkish to greyish fine-grained carbonatic matrix; k) detail of the clast-supported breccias showing heterometric and angular clasts of carbonatic rocks set within a fine-grained matrix.

that observed in the underlying Volcanic Sequence. In contrast, the polygenetic breccias display matrix-supported texture with clasts up to 10-15 cm (Fig. 6.8g). The clasts include both volcanic and sedimentary rocks fragments (i.e., aphyric and vesicular basalts, grey limestone, reddish to purplish shale), and are embedded within a foliated, mainly carbonatic, fine-grained matrix. The succession continues upward with the Cherty-Limestone and Varicoloured Shale lithostratigraphic unit (Fig. 6.3d5). This unit is characterized by thin- to medium-thick beds of limestone, cherty limestone, and calcareous turbidites alternating with varicoloured shales (Figs. 6.3d5, 8h), reddish cherts and minor cherty-limestones (Fig. 6.8i), as well as minor volcanoclastic turbidites. Rare basaltic rocks intrude the successions, forming tabular sills. In addition, thick beds of breccias are interbedded within the successions of this lithostratigraphic unit at different stratigraphic level (Figs. 6.3d5, 6.8j). The breccias show both clast- and matrix-supported textures and are characterized by centimetric to decimetric limestone clasts and subordinate clasts of volcanic rocks. The clasts are angular to sub-angular in shape and are enclosed within a fine-grained and pinkish to reddish carbonatic matrix (Figs. 6.8j, k).

6.2. Biostratigraphy

Biostratigraphy is based on data from foraminifera, radiolarians and calcareous nannofossils analyses that were performed on a total of 37 samples taken from the studied transects. The aim of the biostratigraphic studies was to date the sedimentary rocks associated with the volcanic rocks, in order to provide age constraints for the magmatic activity. Due to the intense deformation that affected the successions of the Durkan Complex and resulted in a poor preservation of fossils, an integration of different biostratigraphic methods was needed for obtaining robust age data, as well as for correlating the different successions. Calcareous nannofossils, foraminifera, and radiolaria

were analysed on samples from Manujan and Chah Shahi 1 transects, whereas the Zandan transect has been investigated only by foraminifera. The detailed list of samples is given in [Appendix Table 6.1](#).

6.2.1. Foraminifera (courtesy of V. Luciani)

Foraminifera were analysed in thin sections. Unfortunately, the state of preservation is generally poor and foraminiferal tests are often recrystallized and/or deformed thus hampering in several cases a correct identification. The main results are reported below.

From the Zandan transect only samples MK901-904, and MK906 provided age information. Specifically, samples from MK901 to MK904 are from the Massive Limestone lithostratigraphic unit and they are grainstones-packstones with ooids and pisoids (MK904) containing shallow-water assemblages that include: *Corallinales*, benthic foraminifera such as common *Quinqueloculina* associated with textularids, *Pseudolituonella*, *Chrysalidina*, *Nezzazata* and *Pseudorhapydionina*. The last genus is stratigraphically restricted and indicates a late Cenomanian age ([Fig. 6.9](#)) ([Loeblich & Tappan, 1988](#); [Afgah et al., 2014](#)). Fossils from sample MK905 are very badly preserved to be recognizable with the exception of rare alveolinids. Sample MK906 that comes from a turbiditic level belonging to the Volcano-Sedimentary Sequence, includes slabs of mudstones showing deep recrystallization (dolomites?). Some of these slabs contain rare “ghost” of planktic foraminifera. The occurrence of one planktic foraminifer bearing double-keeled chambers suggests a Late Cretaceous age.

Samples MK822 and MK886 are grainstones with benthic foraminifera (miliolids, textularids) and red algae but age diagnostic taxa are lacking whereas the arenites MK887, MK888, MK893, MK897, MK897b do not display recognizable taxa.

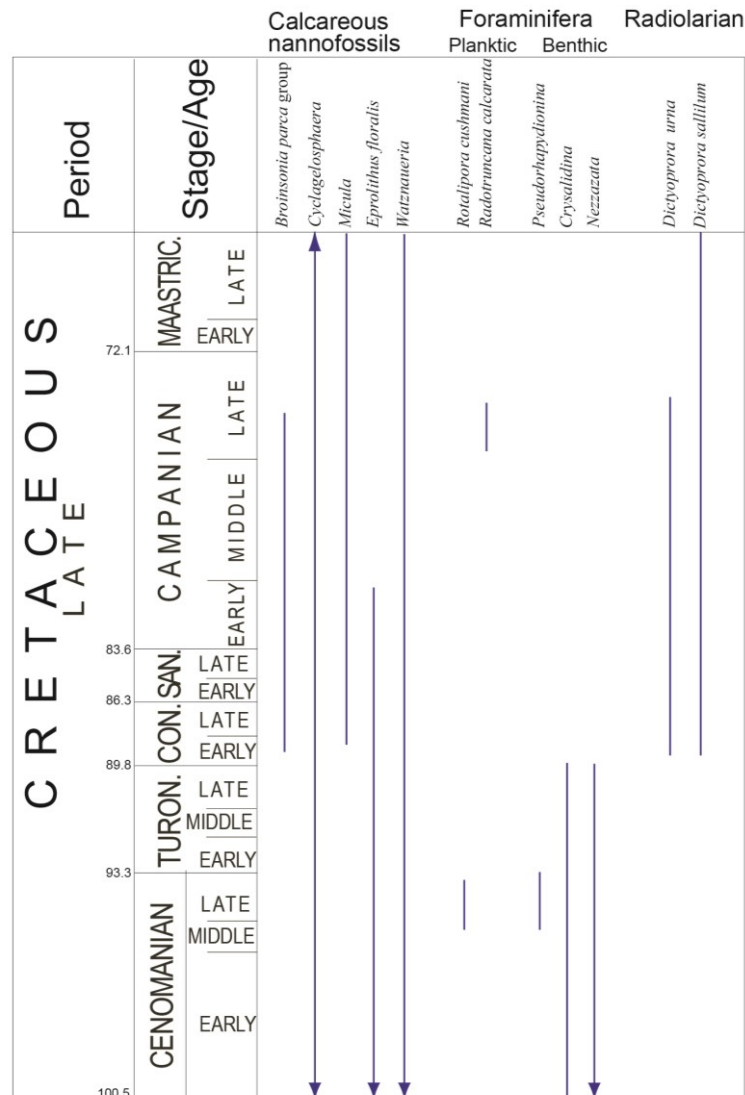


Figure 6.9. Range chart showing the distribution of calcareous nannofossil taxa, foraminifera taxa and radiolarian taxa recognized in the stratigraphic successions of the Durkan Complex. Chronostratigraphy and age of the stage boundaries after [Gradstein et al. \(2012\)](#).

The samples MK468 and MK472 from the siliciclastic successions in the Manujan transect are arenites preserving very rare alveoloinids and *Nummulites* of Eocene age. Sample MK362 is from the Cherty-Limestone and Basalt lithostratigraphic unit and it consists of a wackestone rich in planktic foraminifera that include *Globotruncanita stuarti*, *G. startiformis*, *Globotruncana arca*, *G. bulloides*, *G. falsostuarti*, *G. orientalis*, *Contusotruncana fornicata*, *C. plummeare*, *Rugoglobigerina rugosa*, *Ventibrella* sp. and *Radotruncana calcarata*. The occurrence of the last species allows us to refer the sample to the total range Zone *R. calcarata* ([Coccioni & Premoli](#)

Silva, 2015) of upper Campanian age (Fig. 6.9).

Only the samples MK854 and MK849 from the Volcano-Sedimentary Sequence in the Chah Shahi 1 transect provided age information. Specifically, the occurrence of rare specimens of *Rotalipora cushmani*, though poorly preserved, refers these samples to the Zone *R. cushmani* (Coccioni & Premoli Silva, 2015) of upper Cenomanian age (Fig. 6.9). These samples preserve several traces of organic carbon. Preservation of organic carbon is frequent in levels close to the sedimentary expression of the Oceanic Anoxic Event 2 that is recorded in the latest Cenomanian (Schlanger & Jenkyns, 1976). Samples MK847, MK852 and MK853 from the Limestone and Shale succession contain radiolarians but no recognizable planktic foraminifera. However, the microfacies of these samples that include numerous traces of organic carbon are similar to those from the previous samples containing *R. cushmani*. It is therefore possible to indicate a latest Cenomanian age also for the MK847, MK852 and MK853 samples.

Only the samples MK854 and MK849 from the Volcano-Sedimentary Sequence in the Chah Shahi 1 transect provided age information. Specifically, the occurrence of rare specimens of *Rotalipora cushmani*, though poorly preserved, refers these samples to the Zone *R. cushmani* (Coccioni & Premoli Silva, 2015) of upper Cenomanian age (Fig. 6.9). These samples preserve several traces of organic carbon. Preservation of organic carbon is frequent in levels close to the sedimentary expression of the Oceanic Anoxic Event 2 that is recorded in the latest Cenomanian (Schlanger & Jenkyns, 1976). Samples MK847, MK852 and MK853 from the Limestone and Shale succession contain radiolarians but no recognizable planktic foraminifera. However, the microfacies of these samples that include numerous traces of organic carbon are similar to those from the previous samples containing *R. cushmani*. It is therefore possible to indicate a latest Cenomanian age also for the MK847, MK852 and MK853 samples.

6.2.2. Calcareous nannofossils (courtesy of R. Catanzariti)

For the study of calcareous nannofossils, samples were prepared following standard preparation techniques for light microscopy observation (simple smear slide, as described in [Bown & Young, 1998](#)). Observations were performed through a Leitz-Laborlux12 POL microscopy with cross polarised light at 1250 magnification. Data were collected with the semi-quantitative counting method suggested by [Backman & Shackleton \(1983\)](#). In this study, specimens referable to the recognised taxa were counted on 200 fields of view and then were expressed relative to a unit area (number of specimens for mm²). Data are summarised in [Appendix Table 6.2](#), whereas microphotos of selected calcareous nannofossil taxa are shown in [Figure 6.10](#).

Calcareous nannofossils analyses were performed on 8 samples collected from the Cherty-Limestone and Basalt unit (Manujan transect), the Limestone and Shale (Chah Shahi 1 transect). Unfortunately, most of these samples were found to be barren and/or contain assemblages impossible to be recognized due to the high degree of diagenetic and/or metamorphic recrystallization. The samples from the marls of the Cherty-Limestone and Basalts lithostratigraphic unit (Manujan transect) contain assemblages very scarce and poorly preserved, but it was possible to recognize some useful taxa. On the contrary the samples from the Limestone and Shale unit in the Chah Shahi 1 transect were found to be barren. Assemblages present very low diversity; the only genera recognised were *Micula*, *Broinsonia*, *Cyclagelosphaera*, *Eprolithus*, *Thoracosphaera* and *Watznaueria*. More difficult was the identification of species because of diagenetic process that affected these calcareous fossils (heavily etched and overgrown). However, the common occurrence of *Micula* and the occurrence, even if rare, of *Broinsonia* belonging to the *parca* group, allow us to relate the Cherty-Limestone and Basalt lithostratigraphic unit to the Coniacian-Campanian time span ([Fig. 6.9](#)).

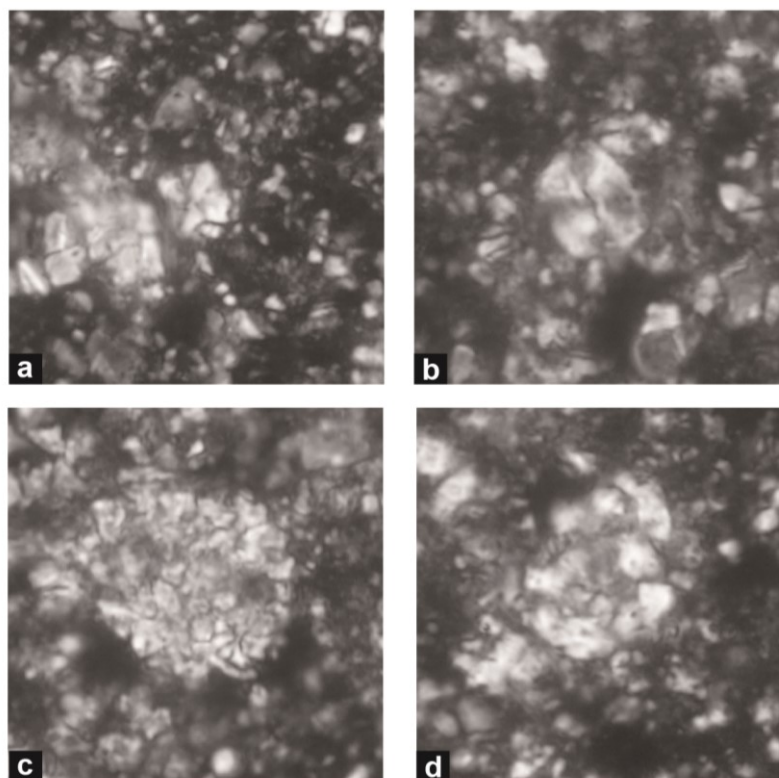


Figure 6.10. Microphotographs of selected calcareous nannofossil taxa. Light Microscope photographs are in Cross Polarized Light. a) *Micula*. Sample MK464. b) *Watznaueria* cf. *barnesiae*. Sample MK464. c) *Thoracosphaera*. Sample MK464. d) *Broinsonia* cf. *parca*. Sample MK464.

6.2.3. Radiolarian (courtesy of M. Chiari)

The sampled radiolarites were etched by a first treatment with hydrochloric acid at 3.7% for removing the carbonates present in some samples and for avoiding the formation of fluorite in the residues. The successive treatments, with hydrofluoric acid at 2%, permitted to extract radiolarians from the samples. The residues of the different treatments were preliminarily observed by means of a reflected light stereomicroscope then, the best-preserved radiolarians specimens were studied using a scanning electron microscope (SEM). The examined samples yielded radiolarians with very poor to moderate preservation and the principal radiolarian markers are shown in [Figure 6.11](#). References used for determining the first and last occurrence of the radiolarian taxa are given in the [Appendix Text 6.1](#).

Radiolarian determinations were performed on 8 samples collected from the Cherty-Limestone and Basalt lithostratigraphic unit in both the Manujan and Chah Shahi 1 transects. In detail, the samples MK363, MK367, MK466, MK469, and MK471 were collected in the Manujan transect whereas the samples MK 374, MK378, and MK796 were sampled in the Chah Shahi 1 transect. Unfortunately, the samples MK363, MK466, MKMK374, and MK378 were found to be barren or display very poor preservation of radiolarians hampering any age assignments. In the following sections, the results of radiolarian determinations are reported only for the samples meaningful for the age determinations.

6.2.3.1. Manujan transect

The sample MK367 yielded radiolarians with moderate preservation and the following taxa were determined: *Alievium* sp. cf. *A. murphyi* Pessagno, *Alievium* sp., *Archaeocenosphaera* (?) sp., *Archaeodictyomitra* sp. cf. *A. montisserei* (Squinabol), *Archaeodictyomitra* sp., *Becus* (?) sp., *Cryptamphorella macropora* Dumitrica, *Cryptamphoraella sphaerica* (White), *Cryptamphoraella* (?) sp., *Crucella* sp. cf. *C. messinae* Pessagno, *Dictyomitra formosa* (Squinabol), *Dictyomitra* sp. cf. *D. formosa* (Squinabol), *Dictyoprora sallilum* (Foreman), *Dictyoprora urna* (Foreman), *Dictyoprora* sp. aff. *D. urna* (Foreman), *Dictyoprora* sp. cf. *D. urna* (Foreman), *Foremanina* (?) sp., *Parvimitrella* sp. cf. *P. mediocris* (Tan) sensu O'Dogherty (1994), *Parvimitrella* sp. cf. *S. japonica* (Nakaseko & Nishimura), *Praeconocaryomma* (?) sp., *Pseudoaulophacus pargueraensis* Pessagno, *Pseudoaulophacus* sp. cf. *P. lenticulatus* (White), *Pseudoaulophacus* sp. cf. *P. putahensis* Pessagno, *Pseudoaulophacus* sp., *Rhopalosyringium* sp. The occurrence of *Dictyoprora sallilum* (Foreman) with *Dictyoprora urna* (Foreman) indicate early Coniacian-late Campanian age of the sample MK367 (Fig. 6.9).

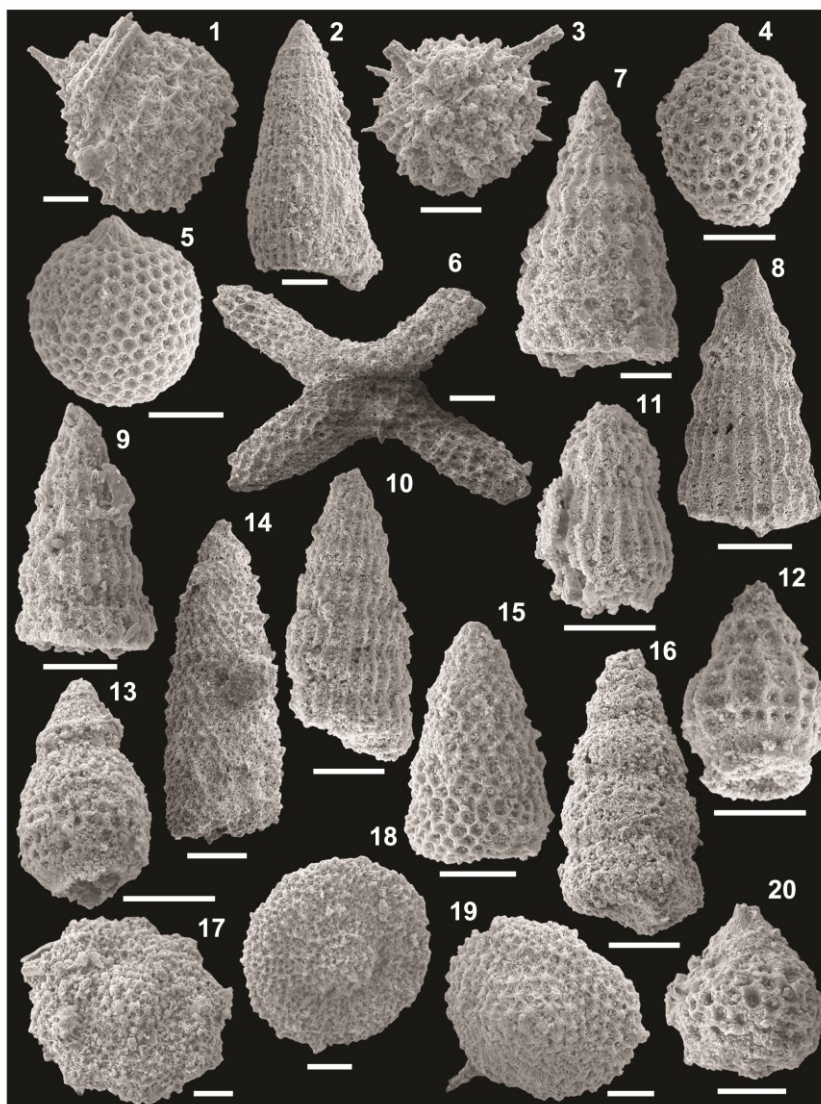


Figure 6.11. Scanning Electron Microscope (SEM) images of selected radiolaria taxa (scale bar 50 μ m). 1) *Alievium* sp. cf. *A. murphyi* Pessagno, MK367; 2) *Archaeodictyomitra* sp. cf. *A. regina* Campbell and Clark, MK469; 3) *Becus* (?) sp., MK367; 4) *Cryptamphorella macropora* Dumitrica, MK367; 5) *Cryptamphorella sphaerica* (White), MK367; 6) *Crucella* sp. cf. *C. messinae* Pessagno, MK367; 7) *Dictyomitra formosa* (Squinabol), MK367; 8) *Dictyomitra* sp. cf. *D. formosa* (Squinabol), MK367; 9) *Dictyomitra* sp. cf. *D. formosa* (Squinabol), MK469; 10) *Dictyomitra* sp. cf. *D. multicostata* Zittel, MK469; 11) *Dictyoprora sallilum* (Foreman), MK367; 12) *Dictyoprora urna* (Foreman), MK367; 13) *Dictyoprora urna* (Foreman), MK469; 14) *Foremanina* (?) sp., MK367; 15) *Parvimitrella* sp. cf. *P. mediocris* (Tan) sensu O'Dogherty (1994), MK367; 16) *Parvimitrella* sp., MK469; 17) *Pseudoaulophacus pargueraensis* Pessagno, MK367; 18) *Pseudoaulophacus* sp. cf. *P. lenticulatus* (White), MK367; 19) *Pseudoaulophacus* sp. cf. *P. putahensis* Pessagno, MK367; 20) *Rhopalosyringium* sp., MK367.

Range *Dictyoprora sallilum* (Foreman). Early Coniacian, *Theocampe urna* Zone of Riedel & Sanfilippo (1974) (*Theocampe urna* Zone: early Coniacian-late Santonian in Sanfilippo & Riedel, 1985) to late Maastrichtian, *Amphipyndax tylotus* zone of Foreman (1977) (*Amphipyndax tylotus*

Zone late Campanian-late Maastrichtian in Sanfilippo & Riedel, 1985).

Range Dictyoprora urna (Foreman). Early Coniacian, *Theocampe urna* Zone of Riedel & Sanfilippo (1974) (*Theocampe urna* Zone: early Coniacian-late Santonian in Sanfilippo & Riedel, 1985) to late Campanian, *Amphipyndax pseudoconulus* Zone after Riedel & Sanfilippo (1974) emended in Foreman (1977) (*Amphipyndax pseudoconulus* Zone: Campanian in Sanfilippo & Riedel, 1985).

The sample MK469 contained radiolarian in poor/moderate preservation and the following taxa were recognized: *Archaeodictyomitra* sp. cf. *A. regina* Campbell & Clark, *Dictyoprora urna* (Foreman), *Dictyomitra* sp. cf. *D. multicosata* Zittel, *Dictyomitra* sp. cf. *D. formosa* (Squinabol), *Dictyomitra* sp., *Parvimitrella* sp. It is possible to indicate an early Coniacian-late Campanian age for the sample MK469 due to the presence of *Dictyoprora urna* (Foreman) (range: *Theocampe urna* - *Amphipyndax pseudoconulus* Zones) (Fig. 6.9).

The sample MK471 contained radiolarians with poor preservation and the assemblage of this sample includes: *Alievium* (?) sp., *Archaeocenosphaera* sp., *Dictyoprora urna* (Foreman), *Praeconocaryomma* (?) sp. The age of the sample MK471 is early Coniacian-late Campanian (Fig. 6.9) for the presence of *Dictyoprora urna* (Foreman) (range: *Theocampe urna* - *Amphipyndax pseudoconulus* Zones).

6.2.3.2. Chah Shahi 1 transect

The sample MK796 contains radiolarians with poor/moderate preservation, and the assemblage includes the following taxa: *Alievium* sp., *Archaeodictyomita* sp., *Crucella* sp., *Dictyoprora urna* (Foreman), *Praeconocaryomma* (?) sp., *Pseudoaulophacus* sp. cf. *P. lenticulatus* (White), *Alievium* sp. The presence of *Dictyoprora urna* (Foreman) suggests an early Coniacian-late Campanian age

(range *D. urna*: *Theocampe urna*-*Amphipyndax pseudoconulus* Zones) for this samples (Fig. 6.9).

To summarize, the results of the radiolarians biostratigraphic study indicates early Coniacian - late Campanian age for the Cherty-Limestone and Basalt lithostratigraphic unit in both the Manujan and Chah Shahi 1 transects (Fig. 6.9).

6.3. Petrography of the Durkan Complex magmatic rocks

6.3.1. Magmatic texture

Most of the studied basalts are affected by variable degrees of alteration, which resulted in different extent of replacement of the primary magmatic minerals. Nonetheless, their original magmatic texture is still recognizable. Fresh plagioclase is very rare, and it is usually pseudomorphosed by fine grained assemblage of albite, calcite and sericite. Similarly, olivine crystals are commonly replaced by iddingsite and serpentine + Fe-Ti oxides (likely magnetite). Though fresh clinopyroxene crystals are present both as phenocrysts and groundmass minerals, clinopyroxene alteration commonly occur as pseudomorphic replacement by chlorite or actinolitic amphibole. Where volcanic glass is present, it has been generally replaced by an assemblage of chlorite and clay minerals.

The studied volcanic rocks are represented by basalts and a couple of differentiated rocks (a trachyte and an alkali-rhyolite). Four petrofacies types have been distinguished according to the textures observed and they are: 1) aphyric type; 2) porphyritic type; 3) sub-volcanic type; 4) metamorphic type.

The aphyric type petrofacies is characterized by basalts and a trachyte showing aphyric to slightly porphyritic texture ($PI < 10$) (Figs. 6.12a, b). In the basaltic rocks, the phenocrysts consist

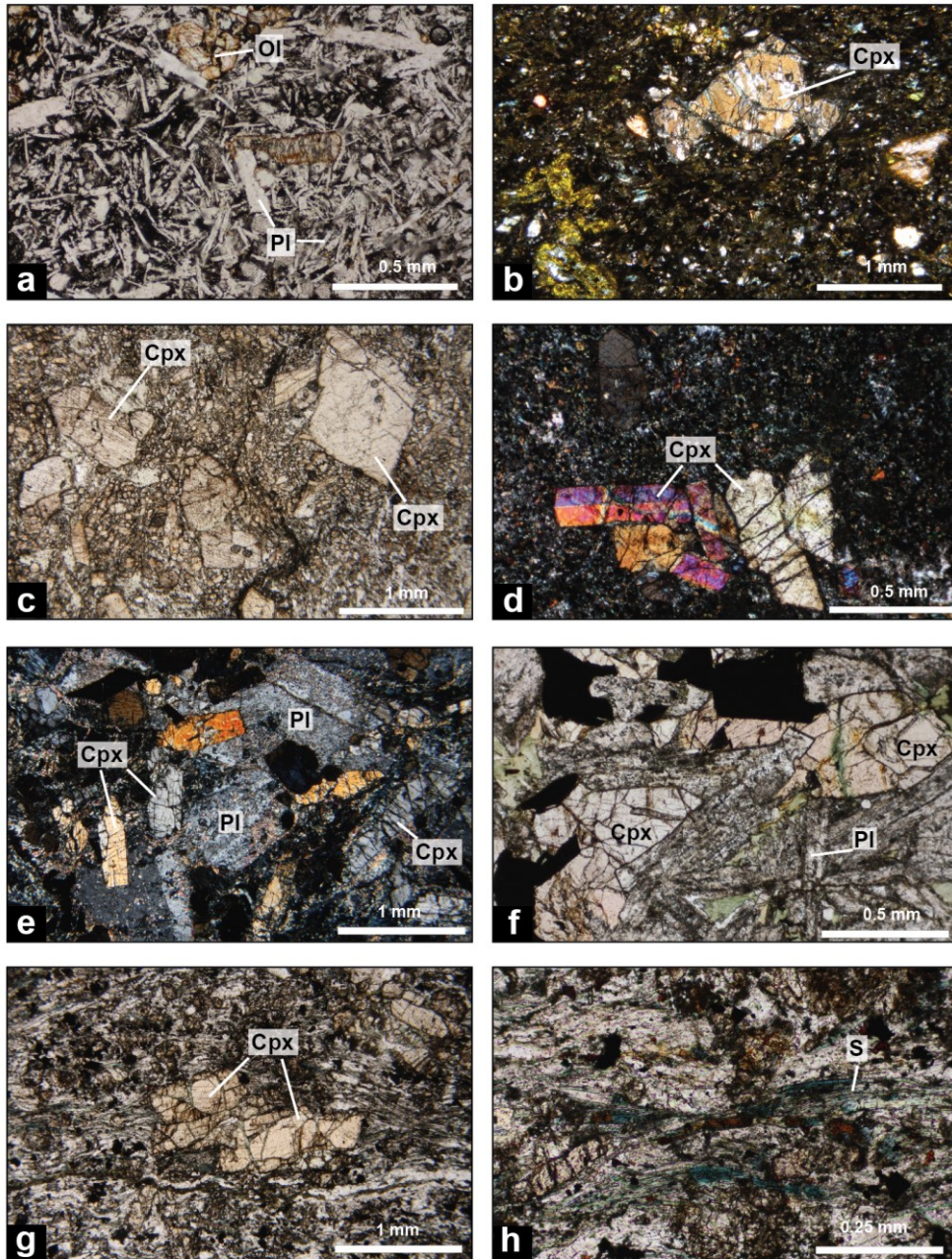


Figure 6.12. Photomicrographs of the magmatic rocks from the Durkan Complex: a-b) aphyric type petrofacies, c-d) porphyritic type petrofacies, e-f) sub-volcanic type petrofacies; g-h) metamorphic type petrofacies. a) basaltic rocks showing aphyric texture characterized by laths of plagioclase and altered olivine crystals within a hypocristalline ground mass; b) clinopyroxene phenocrysts set within ground mass showing intersertal to microcrystalline texture. In the ground mass occur microlite of plagioclase and clinopyroxene; c) porphyritic volcanic rocks characterized by pluri millimetric clinopyroxene phenocrysts set within microcrystalline ground mass. The ground mass includes clinopyroxene microlites, plagioclase, and oxides; d) volcanic rocks with glomeroporphyritic texture characterized by clinopyroxene phenocrysts set in a hypohyaline ground mass showing microlite and volcanic glass; e) highly porphyritic basalt showing clinopyroxene and plagioclase phenocrysts set within extremely altered hypohyaline ground mass; f) sub-volcanic rocks with holocrystalline and hypidiomorphic texture, characterized by euhedral altered plagioclase and subhedral to anhedral clinopyroxene and Fe-Ti oxides; g) relict magmatic clinopyroxene surrounded by fine grained foliation define by chlorite+actinolitic amphibole+epidote+albite; h) detail of the metamorphic foliation defined by chlorite, actinolitic amphibole, epidote, as well as minor albite and quartz.

of plagioclase laths, clinopyroxene crystals, and less abundant olivine (Fig. 6.12a). They are set in a hypocrystalline ground mass showing intersertal to microcrystalline texture with microlite of plagioclase, olivine, clinopyroxene and less abundant Fe-Ti oxides, surrounded by altered volcanic glass (Fig. 6.12b). In contrast, the trachyte is characterized by aphyric texture, showing micro-laths of plagioclase set in altered volcanic glass. Few samples of this petrofacies are characterized by amygdaloidal texture exhibiting vesicles filled by calcite and chlorite.

The porphyritic type petrofacies includes basalts showing porphyritic and glomeroporphyritic textures (Figs. 6.12c, d, e). In detail, the rocks of this petrofacies can be subdivided into two classes on the basis of the PI, which ranges from 15 - 30 and 35 - 60 (Figs. 6.12c, d, e). The phenocrysts are up to 5-6 mm in size and are mainly represented by clinopyroxene, as well as less abundant plagioclase, Fe-Ti oxides and rare olivine. Clinopyroxene phenocrysts show commonly a concentric zonation and a weak pleochroism, from pale yellow to pale pink. Fe-Ti oxides phenocrysts show both elongated-acicular and equidimensional crystalline habitus, likely representing ilmenite and magnetite, respectively. The phenocrysts are set in a hypohyaline groundmass showing intergranular to microcrystalline textures (Figs. 6.12c, d). Rarely intersertal texture can be observed in the groundmass. In the groundmass, clinopyroxene and plagioclase microliths can be recognized together with less abundant olivine microliths and subordinated altered volcanic glass. Some samples show amygdules (up to 30% in volume) filled by both quartz/chalcedony and calcite.

The sub-volcanic type is a peculiar petrofacies of the studied volcanic rocks. It includes dolerites showing holocrystalline, inequigranular and hypidiomorphic texture. In fact, they are characterized by euhedral plagioclase and euhedral to subhedral clinopyroxene crystals, up to 5 mm in size (Fig. 6.12f). Occasionally, the clinopyroxene partially includes the plagioclase, showing subophitic texture. These large crystals are surrounded by a fine-grained crystalline

aggregate consisting of euhedral to subhedral plagioclase, clinopyroxene as well as Fe-Ti oxides. The latter show the same features described for the porphyritic variety (see above). In addition, quartz (less than 5% in volume) occurs in interstitial position within the crystalline framework.

The slightly metamorphic type petrofacies includes basaltic rocks showing anastomosed foliation defined by fine-grained aggregate of chlorite, fibrous amphibole, Fe-Ti oxides, subordinate epidote, as well as by alignment of albite aggregate. The foliation envelops and surrounds relatively abundant relict of the magmatic clinopyroxene, and rarely plagioclase laths (Figs. 6.12g, h). In few samples, the metamorphic foliation is more developed, and it is marked by the alternation of millimetric-spaced and anastomosed domains with different mineralogical composition. In detail, albite-rich domains are alternated with domains represented by chlorite, epidote and relicts of magmatic clinopyroxene. The mineralogical paragenesis of these samples as well as the fine-grain of the metamorphic minerals indicate very low-degree of metamorphic overprint, likely in sub-greenschist-facies or prehnite-pumpellyite metamorphic condition.

6.3.2. *Vesicles content*

In section 6.4.1, it is outlined that some of the Durkan Complex basaltic rocks exhibit amygdaloidal texture. In volcanic rocks, the vesicles content per volume varies as a function of several factors, including the chemical affinity of the magma, its volatile content and their dissolution within the magma, as well as the water depth of eruption (Moore, 1970; Moore & Schilling, 1973; Memtimin et al., 2019). Among these factors, the magma affinity and water depth of eruption are believed to be strictly related (Moore 1970). In fact, the alkaline volcanic rocks are generally more vesicles-rich than those of tholeiitic chemical affinity, at a given eruption depth (Fig. 6.13). In addition, in both alkaline and tholeiitic volcanic rocks the increase of vesicularity is

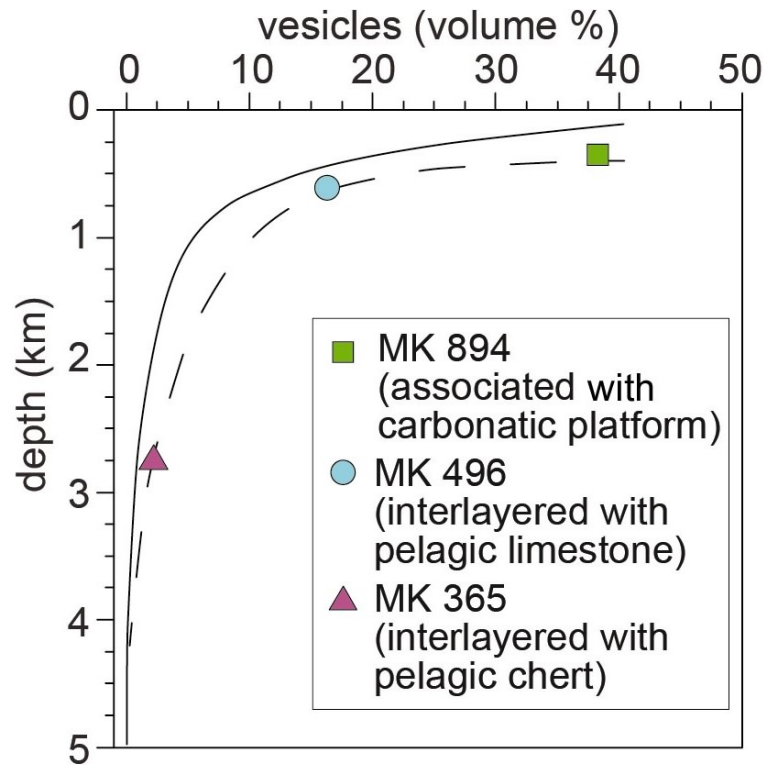


Figure 6.13. Relationships between water depth of eruption and vesicles content for the western Durkan Complex magmatic rocks. The different curves indicate the depth-vesicles percent for tholeiitic (solid line, from Moore & Schilling, 1973) and alkaline (dashed line, from Moore, 1970) volcanic rocks. The sedimentary rocks associated with each sample is also indicated for a better comparison of the depth of eruption deduced from the vesicles content with the sedimentary rocks paleo-depth indicators.

related to the decrease of the eruption depth (Fig. 6.13; Moore, 1970; Moore & Schilling, 1973; Memtimin et al., 2019). Geochemical data shown in section 6.5 indicate that the Durkan Complex magmatic rocks have alkaline affinity and quite comparable geochemical features. Therefore, the main parameter influencing the vesicles content can be assumed as related to the depth of eruption. Given these data, it is performed a comparative estimation of the vesicles per volume choosing samples associated with different sedimentary successions, which, in turn, indicate different depth of sedimentation (Fig. 6.13). The results show that the basaltic sample MK894 from the Volcano-Sedimentary Sequence, which is overlaying by the platform-derived Massive Limestone (Fig. 6.3a2), is characterized by a high amount of vesicles (~ 38%). This suggests eruption in shallow-water environment (Fig. 6.13). On the contrary, the basaltic sample MK365 is interlayered with the

pelagic succession of the Cherty-Limestone and Basalt lithostratigraphic unit (Fig. 6.3b3) and is characterized by a significantly lower percent of vesicles per volume (MK365, ~ 2%). This evidence indicates eruption in deep-water environment (Fig. 6.13). Finally, the basaltic sample MK496 from the Volcano-Sedimentary Sequence in the tectonic slice of Figure 6.3c2 is stratigraphically associated to pelagic limestone and shows a vesicles content per volume of ~ 16%, suggesting a relatively deep-water eruption environment (Fig. 6.13).

6.4. Geochemistry of the Durkan Complex magmatic rocks

As far as petrographic analyses indicate that most of the rocks from the Durkan Complex have undergone secondary alteration (e.g., sub-marine hydrothermal alteration, polyphase deformation, sub-greenschist facies metamorphism), some elements may have been remobilized. In fact, it is well known that large ion lithophile elements (LILE) and many major elements are commonly affected by alteration-induced mobilization (e.g., Cann, 1970; Pearce & Norry, 1979). In addition, light REE (LREE) may also be mobilized during secondary alteration processes (e.g., Valsami & Cann, 1992). In contrast, many incompatible elements (e.g., Ti, P, Zr, Y, Sc, Nb, Ta, Hf, Th), middle (M) and heavy (H) REE, as well as some transition metals (e.g., Ni, Co, Cr, V) are considered immobile during low-temperature alteration and metamorphism. These elements may exhibit clear mobility only in case of high temperature metamorphic events (i.e., for temperature approaching the melting points) and in case of processes occurring at high fluid/rock ratios (e.g., shear zones) (Hynes, 1980). For these reasons, the geochemical features of the Durkan Complex magmatic rocks are described using those elements considered immobile during alteration processes. In addition, to verify the amount of mobilization of Ba, Rb, Sr, SiO₂, Al₂O₃, FeO, CaO, Na₂O, K₂O, La, Ce some mobility tests were made by plotting them against some immobile

elements (e.g., Zr, Y) and then calculating the correlation coefficients (r^2) for the different group of rocks (not shown). These tests indicate that La (r^2 vs Zr = 0.85 – 0.89) and Ce (r^2 vs Zr = 0.80 – 0.85) show good correlation with immobile elements suggesting that the amount of mobilization of these elements was limited. SiO₂ (r^2 vs Zr = 0.63 – 0.91) and Rb (r^2 vs Zr = 0.70 – 0.88) resulted moderately mobilized in all the studied samples, therefore they can be used, thought with some caution. On the contrary, tests on Al₂O₃ (r^2 vs Zr = 0.40 – 0.51), Na₂O (r^2 vs Zr = 0.42 – 0.56), K₂O (r^2 vs Zr = 0.29 – 0.56), and Sr (r^2 vs Zr = 0.30 – 0.56) indicate that these elements were affected by high degrees of alteration-induced mobilization, and therefore, they cannot be used. Tests on FeO, CaO, and Ba returned different results depending on the rock-type. FeO was little mobilized only in samples of Group 1 (r^2 vs Zr = 0.67) and Group 2 (r^2 vs Zr = 0.64). Test on CaO indicate that this element was mobilized in all samples except for those of Group 1 (r^2 vs Zr = 0.77). Ba was affected by high degrees of secondary alteration in Group 1 (r^2 vs Zr = 0.58) and Group 3 (r^2 vs Zr = 0.44) rocks, whereas is moderately mobilized in Group 2 (r^2 vs Zr = 0.65) rocks. As a consequence of this variability of behaviour, I avoid using FeO, CaO and Ba for describing the geochemical features of the studied rocks. Based on the Nb/Y ratios (Winchester and Floyd, 1977; Pearce, 1996), we can distinguish three main groups of rocks (Fig. 6.14). Group 1 rocks show a transitional nature with Nb/Y ratios in the range 0.8-1.00, whereas Group 2 and 3 rocks show a clear alkaline affinity with Nb/Y ratios >1 (1.15-3.16).

6.4.1. Group 1 rocks

This group includes several basalts and one trachyte (sample MK795). The basalts display a transitional nature as testified by the relatively high Nb/Y ratios in the range 0.80 - 1.03 (Appendix Table 6.3, Fig. 6.14). Group 1 basalts show a wide range of composition in SiO₂ (43.3 – 53.3

wt%), MgO (4.93 – 11.9 wt%), Al₂O₃ (12.2 – 17.2 wt%), Mg# (47.8 – 75.4), likely reflecting different degrees of fractionation. By contrast, if compared to the basaltic samples the trachyte MK795 show higher and lower contents of SiO₂ and MgO, respectively (Appendix Table 6.3). The basaltic rocks are characterized by relatively high TiO₂ (1.20 – 2.29 wt%), P₂O₅ (0.23 – 0.51 wt%), Zr (73 – 220 ppm), Nb (13.5 – 32.6 ppm), and Ta (0.92 – 2.18 ppm) contents countered to relatively low abundance of Y, which range from 16.9 to 33.5 ppm. Compatible elements (such as Cr, V, Ni, and Co) contents are extremely variable, but generally high as expected for basaltic rocks (Appendix Table 6.3). These elemental contents reflect the relatively low Y/Nb ratio as well as the high Ti/V ratio (Appendix Table 6.3).

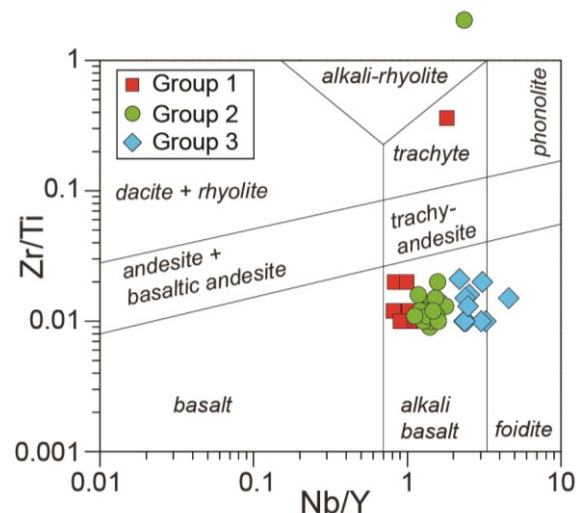


Figure 6.14. Nb/Y vs. Zr/Ti discrimination diagram of Winchester & Floyd (1977) modified by Pearce (1996) for volcanic, sub-volcanic and metavolcanic rocks from the Durkan Complex.

Normal type MORB (N-MORB) normalized incompatible elements spider-diagram displays decreasing patterns from Th to Yb, and, significantly, any negative anomalies in Ta, Nb, Ti and P (Fig. 6.15a). Only the sample MK 795 shows negative anomalies in Ti and P, likely reflecting the fractional crystallization of Fe-Ti oxides and apatite. Yb content is relatively low, ranging from 0.49 to 0.82 times N-MORB (Sun & McDounough, 1989) abundance in basaltic samples (Fig. 6.15a). The Group 1 rocks show significant LREE enrichment with respect to HREE, as well as

moderate depletion of HREE if compared to MREE (Fig. 6.15b). This is also testified by the $(La/Yb)_N$ and $(Sm/Yb)_N$ ratios, which are in the range 4.44 – 7.86 and 1.18 – 3.16, respectively (Fig. 6.16). The Yb and La contents range from ~ 11.7 to ~ 74.4 times chondrite abundance (Sun & McDonough, 1989), respectively (Fig. 6.15b). The overall chemical features of the Group 1 rocks

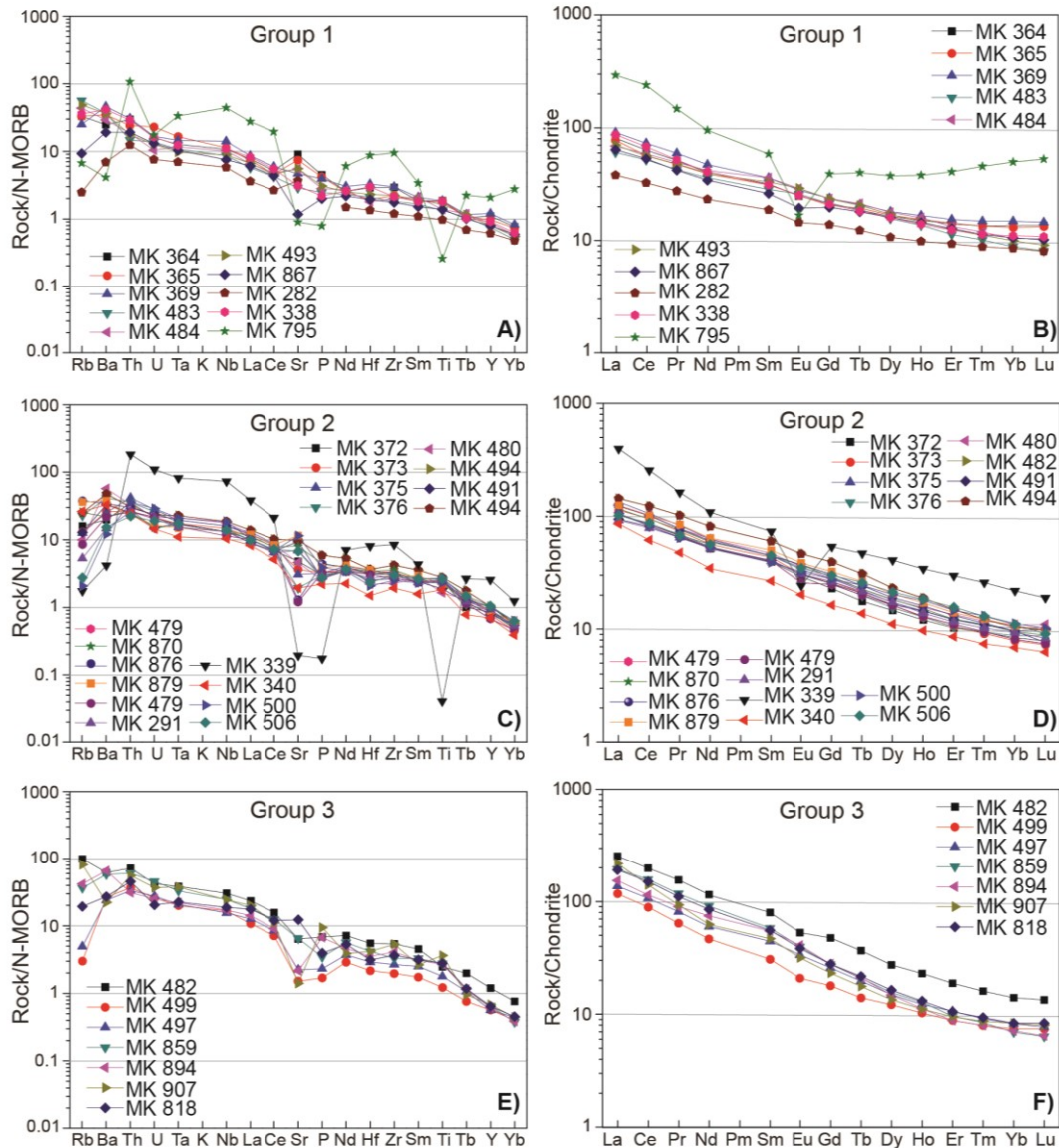


Figure 6.15. N-MORB normalized incompatible element patterns (A, C, and E) and Chondrite-normalized rare earth element (REE) patterns (B, D, and F) for volcanic, sub-volcanic and metavolcanic rocks from the Durkan Complex. Normalizing values are from Sun & McDonough (1989).

are intermediate between those of the typical P-MORB and within plate alkaline basalts, such as OIB (e.g., Sun & McDonough, 1989; Haase & Devey, 1996; Le Roex et al., 1983). Accordingly,

in the discrimination diagram shown in Fig. 6.17, these rocks plot in the fields for oceanic subduction-unrelated setting. In detail, they plot in the overlapping compositional variation field shared by typical P-MORB and Alkaline basalts (Fig. 6.17). These geochemical data collectively suggest a P-MORB affinity for the Group 1 rocks.

6.4.2. Group 2 rocks

The Group 2 rocks are distributed within all the recognized types of successions (Appendix Table 6.3). They include basalts showing a clear alkaline affinity as indicated by the higher Nb/Y ratios if compared to Group 1 rocks (Appendix Table 6.3, Fig. 6.14). In addition, this Group includes an extremely differentiated alkali-rhyolite, represented by the sample MK339 (Appendix Table 6.3, Fig. 6.14). Basalts are characterized by SiO₂ ranging from 41.9 to 52.8 wt% and Mg# ranging between 44.3 and 70.8 suggesting that these rocks represent melts at different stages of fractionation. This also indicates by the marked variation of MgO and Al₂O₃ contents (Appendix Table 6.3). The latter (Al₂O₃ = 12.6 – 15.9 wt%) is relatively low if compared to the Al₂O₃ contents in Group 1 rocks. By contrast, the differentiated sample MK339 show higher contents of SiO₂ and lower MgO abundance with respect to the basalts (Appendix Table 6.3). The basaltic rock of the Group 2 show relatively high contents of TiO₂ (2.03 – 5.13 wt%), P₂O₅ (0.23 – 0.66 wt%), Zr (139 – 303 ppm), Nb (23.6 – 44.0 ppm), Ta (1.42 – 2.94 ppm), as well as high Ti/V ratios (43 - 71). On the contrary, Y abundance is rather low, ranging from 18.5 to 33.0 ppm. Similarly to Group 1, these rocks show variable compatible elements, likely suggesting they represent basalts at different fractionation stage (Appendix Table 6.3). If compared to Group 1 rocks, the Zr/Y and Y/Nb incompatible elements ratios are higher and lower, respectively (Appendix Table 6.3). The N-MORB normalized incompatible elements spider diagrams (Fig. 6.15c) display strongly

decreasing patterns from Th to Yb. No Nb, Ta Ti and P negative anomalies can be seen, with the exception of the extremely fractionated sample MK339, which show Ti and P negative anomalies.

Yb content is ~ 0.6 times N-MORB abundance and is well comparable with those of Group 1

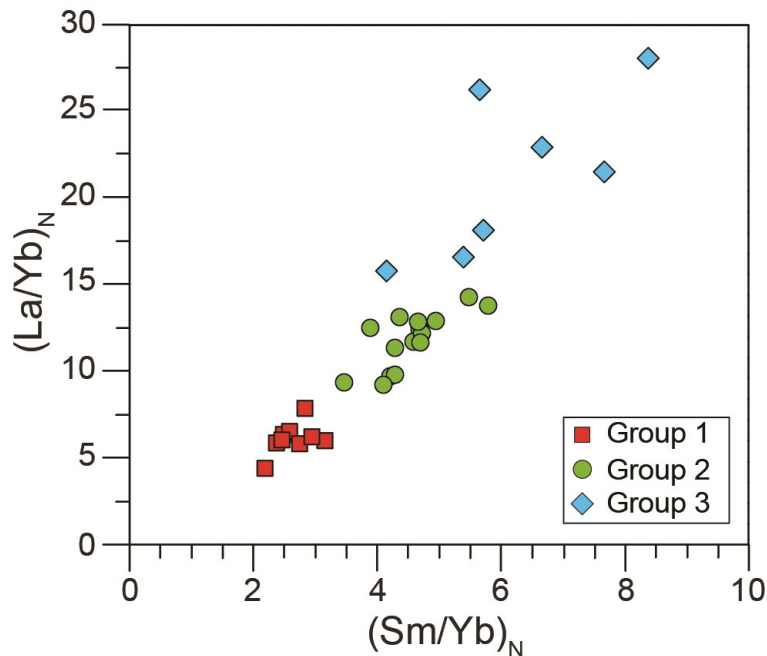


Figure 6.16. $(\text{Sm}/\text{Yb})_N$ vs $(\text{La}/\text{Yb})_N$ diagram for magmatic rocks of the Durkan Complex. Normalizing values are the chondrite abundances from Sun & McDonough (1989).

rocks. On the contrary, both Ta and Nb contents are generally slightly higher than those of Group 1 rocks (Figs. 6.15a, c). The REE-chondrite normalized patterns (Fig. 6.15d) are significantly decreasing from LREE to HREE ($\text{La}_N/\text{Yb}_N = 9.26 - 18.08$). In fact, the Yb and La contents ranges from ~ 9 to ~ 100 times chondrite composition, respectively (Sun & McDonough, 1989). In addition HREE show a marked depletion with respect to the MREE, as exemplified by the $(\text{Sm}/\text{Yb})_N$ ratios (3.35 – 5.79), which is comparable to Group 3 rocks and significantly higher with respect to the Group 1 rocks (Fig. 6.16, Appendix Table 6.3). The geochemical features of the Group 2 rocks are very similar to within-plates alkaline volcanic rocks, typical of oceanic islands (e.g., Wilson, 1989; Safonova et al., 2016). In the discrimination diagram of Figure 6.17, the Group 2 rocks plot close to the composition of the OIB (Sun & McDonough, 1989) and within the field

for subduction unrelated alkaline basalts, except for one samples plotting in the P-MORB composition field. If compared to Group 1 rocks, the Group 2 rocks show the increasing in OIB type chemical components (Fig. 6.17). In conclusion, the overall geochemical features indicate an OIB affinity for these rocks.

6.4.3. Group 3 rocks

The Group 3 rocks include basalts that are characterized by relatively high Nb/Y ratios indicating alkaline nature for these rocks (Appendix Table 6.3, Fig. 6.14). SiO₂ and MgO contents are in the range 42.1 – 53.5 to 3.39 – 13.61, respectively, suggesting that the Group 3 rock includes both rather primitive and differentiated rocks. Accordingly, Mg# shows a wide range of variation, from 39.4 to 74.9. The Group 3 basalts show relatively high contents of TiO₂ (1.55 – 4.61 wt%), P₂O₅ (0.20 – 1.11 wt%), Zr (148 – 403 ppm), Nb (36.5 – 71.7 ppm), and Ta (2.66 – 5.13 ppm) coupled with relatively low Y (15.9 – 33.7 ppm) abundance. Ni, Co, Cr and V abundances are extremely variable suggesting that these rocks represent basalts at different fractionation stages (Appendix Table 6.3). Ti/V ratios is relatively high and similar to those of Group 1 and 2 rocks (Appendix Table 6.3).

The Group 3 rocks show the highest Zr/Y ratios (9.30 – 20.6) among the studied rocks, except for the sample MK479 that has Zr/Y ratios comparable with that one of the Group 2 rocks (Appendix Table 6.3). Y/Nb ratios range from 0.32 to 0.47 and are significantly lower than the Group 1 rocks but is comparable with those of the Group 2 (Appendix Table 6.3). These rocks show marked enrichment of LILE with respect to HFSE (Fig. 6.15e), with abundance of Th and Yb ranging from ~ 35 to ~ 0.5 times N-MORB composition. In addition, the N-MORB normalized patterns from Ti to Yb of Group 3 rock are significantly steeper than those of the Group 1 and

slightly steeper than those of the Group 2 rocks (see and compare Figs. 6.15a, c, e). The Group 3 rocks show marked enrichment of LREE and MREE with respect to HREE (Fig. 6.15f), as exemplified by the high $(La/Yb)_N$ and $(Sm/Yb)_N$ ratios, which are in the range 15.8 – 28.07 and 4.15 – 8.37, respectively (Fig. 6.16, Appendix Table 6.3). Significantly, the MREE/HREE ratios for the Group 3 rocks are well comparable with those of Group 2 rocks, and considerably higher with respect those of the samples of the Group 1 (Fig. 6.16). Similarly to what was seen for the Group 2 rocks, the overall geochemical features of Group 3 rocks point out for an OIB chemical affinity (e.g., Wilson, 1989; Safonova et al., 2016). Accordingly, in Figure 6.17 they plot in the field for subduction unrelated rock, within the compositional field for alkaline basalts.

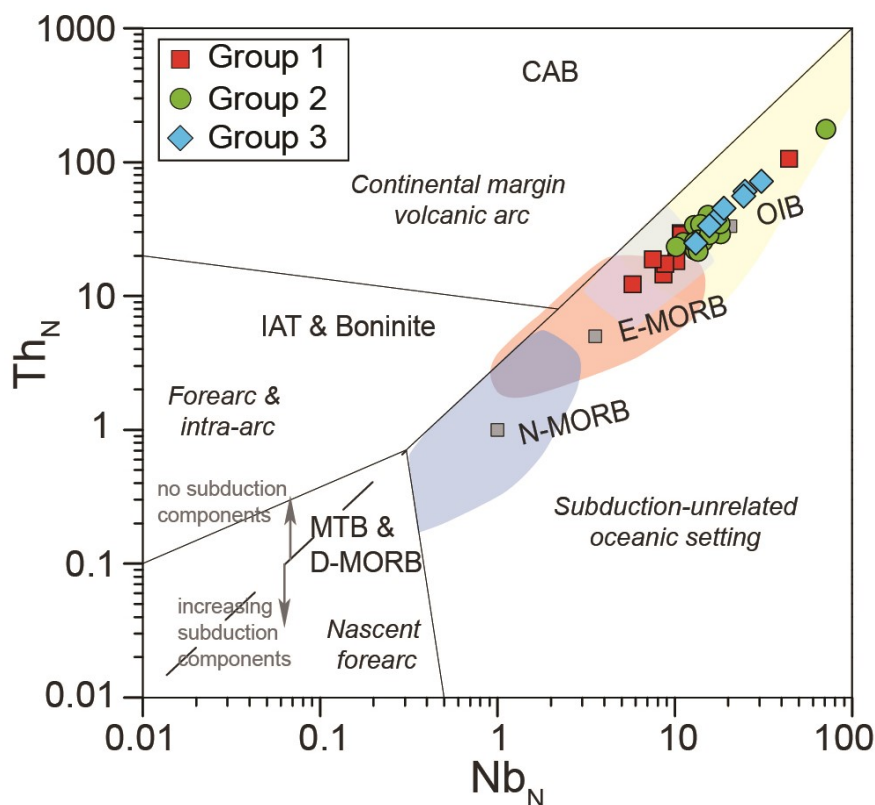


Figure 6.17. N-MORB normalized Th vs. Nb discrimination diagram of Saccani (2015) for volcanic, sub-volcanic and metavolcanic rocks from the Durkan Complex. Abbreviations, MORB: mid-ocean ridge basalt, N-: normal type, E-: enriched type, D-: depleted type, IAT: island arc tholeiite, CAB: calc-alkaline basalt; OIB: alkaline oceanic within-plate basalt; MTB: medium titanium basalt. Normalizing values, as well as the composition of typical N-MORB, E-MORB, and OIB (grey squares) are from Sun & McDonough (1989).

6.5. Mineral chemistry of clinopyroxene from the Durkan Complex

Many of the crystals in the studied rocks were not suitable for electron microprobe analysis, as a consequence of the secondary alteration. Olivine and plagioclase are always altered and were not analysed. In contrast, a detailed petrographic study allowed to identify some samples of basaltic rocks showing fresh clinopyroxenes that have been analysed by electron microprobe spectrometry. In detail, 39 representative major elements chemical analyses of clinopyroxenes from 8 samples are presented ([Appendix Table 6.4](#)). These samples are representative of all the rock groups identified by whole-rock chemical analyses. Thus, the dataset shown in [Appendix Table 6.4](#) allows us to discuss the variation of the chemical features of the pyroxene in relation to the whole-rock geochemistry of the hosting basaltic rocks. The clinopyroxene composition is strongly influenced, beside crystal-chemical constrain, by the composition of the magmas from which they crystallized. According to [Leterrier et al. \(1982\)](#) and [Beccaluva et al. \(1989\)](#), the clinopyroxene compositions represent a petrogenetic indicator of the chemical affinity of the magmatic melts that were in equilibrium with the crystals during their crystallization. Therefore, the mineral chemistry of clinopyroxene can provide robust constraints for the understanding of the tectono-magmatic setting of formation of primary basaltic melts. In the next section, the chemical composition of the clinopyroxene will be presented following the group of rocks identified according to the whole-rock chemical compositions (see section 6.5).

6.5.1. Clinopyroxene

Clinopyroxenes of Group 1 rocks were analysed in samples MK483 and MK485, which represent basalts with sub-volcanic texture. They show augitic composition with Enstatite end-member

ranging from 39.2 to 44.7 (Fig. 6.18; Appendix Table 6.4). Clinopyroxenes of Group 1 rocks show Mg# in the range 0.77 - 0.65, likely reflecting the crystallization from melts at different fractionation stages. CaO, Al₂O₃, and Cr₂O₃ decrease with decreasing of Mg#, whereas FeO_{tot} and TiO₂ generally increase with the decreasing of the Mg# (Appendix Table 6.4). The Group 1 clinopyroxenes display relatively low contents of TiO₂ (0.91 – 1.45 wt%), Na₂O (0.28 – 0.46 wt%) and CaO (19.26 – 21.11) if compared to the clinopyroxenes from Group 2 and 3 rocks (Appendix Table 6.4, Fig. 6.19). The Al₂O₃ (1.44 – 3.06 wt%) is lower than Group 2 and 3 clinopyroxenes at comparable value of Mg# (Appendix Table 6.4). The Cr₂O₃ contents are relatively low and show positive correlation with Mg# (Appendix Table 6.4). They are commonly unzoned, though three crystals show weak zoning. In the zoned crystal the core and rim show weak variation of their compositions (Appendix Table 6.4). In fact, in the samples MK483cr2 and MK485cr2 the core of the crystal shows slight lower Mg# with respect to the rim, whereas the core in samples MK483cr5 display slightly higher Mg# than the rim (Appendix Table 6.4). Using Ti – (Ca + Na) variation diagram the clinopyroxenes from Group 1 rocks plot in the field for clinopyroxene from sub-alkaline tholeiitic and calc-alkaline rocks and are clearly distinguished from clinopyroxenes from Group 2 and Group 3 rocks (Fig. 6.20). The (Ti + Cr) – Ca variation diagram shows that the clinopyroxenes from Group 1 rocks have a MORB affinity and are clearly distinct from clinopyroxenes crystallized from melts generated in volcanic arc settings (Fig. 6.20). Accordingly, in the discrimination diagram in Figure 6.21 they are distinct from clinopyroxene of basaltic rocks from subduction-related ophiolites, plotting in the field for clinopyroxene from MOR settings and within-plate oceanic settings.

Clinopyroxenes from the Group 2 rocks were analysed in the samples MK491 and MK479 that correspond to a sub-volcanic and an aphyric basaltic rocks, respectively. They mainly show an augitic composition, though few pyroxenes with diopsidic composition are present (Fig. 6.18). The

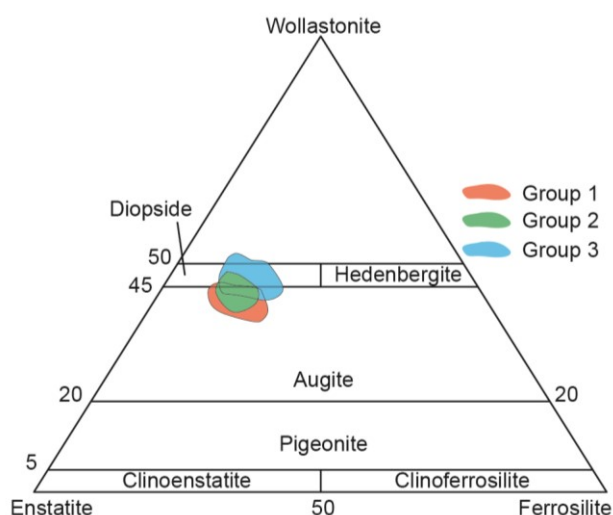


Figure 6.18. Pyroxene quadrilateral diagram (Morimoto, 1988) showing the compositional field of clinopyroxenes from sub-volcanic and volcanic rocks from the Durkan Complex.

Enstatite end-member range from 40.5 to 45.7 (Appendix Table 6.4). Mg# is generally high, ranging from 0.74 to 0.84 (Appendix Table 6.4). TiO₂ (1.01 – 2.1 wt%), Na₂O (0.33 – 0.5 wt%), CaO (21.02 – 22.3 wt%), and Al₂O₃ (2.66 – 4.39 wt%) contents are generally higher than clinopyroxenes from Group 1 rocks, whereas they are generally low with respect to the clinopyroxenes of Group 3 rocks (Appendix Table 6.4). For TiO₂, CaO and Na₂O these differences are particularly evident if clinopyroxene with comparable Mg# are exclusively taken into account (Fig. 6.19). Cr₂O₃ content is extremely variable (0.12 – 0.67 wt%) and gradually decreases with decreasing Mg#. The crystals from the sample MK479 are unzoned whereas those from the sample MK491 commonly show zoning. In the zoned clinopyroxene from the sample MK491 (i.e., crystals 3 and 6), the cores have quite narrow variation of chemical composition. However, the crystal 6 shows the core with Mg# higher than the rim. This variation is coupled with an increase of TiO₂, Al₂O₃, and FeO_{tot} contents, and a decrease of Cr₂O₃, MgO, CaO from core to rim (Appendix Table 6.4). These compositional variations likely reflect fractional crystallization processes during the growth of the crystals, as typically observed in clinopyroxenes from ophiolitic sequence (Beccaluva et al., 1989). In the Ti – (Ca + Na) variation diagram, the clinopyroxenes

from the Group 2 rocks plot in the field for pyroxene from alkaline rocks and are clearly distinguished from the clinopyroxenes of the Group 1 rocks (Fig. 6.20). In addition, they are also distinguished from the Group 3 rocks for the lower (Ca + Na) contents (Fig. 6.20). Accordingly, in the discrimination diagram of Beccaluva et al. (1989), they plot in the field for clinopyroxenes typical of plume-influenced Iceland basalts and within-plate oceanic basalts (Fig. 6.21).

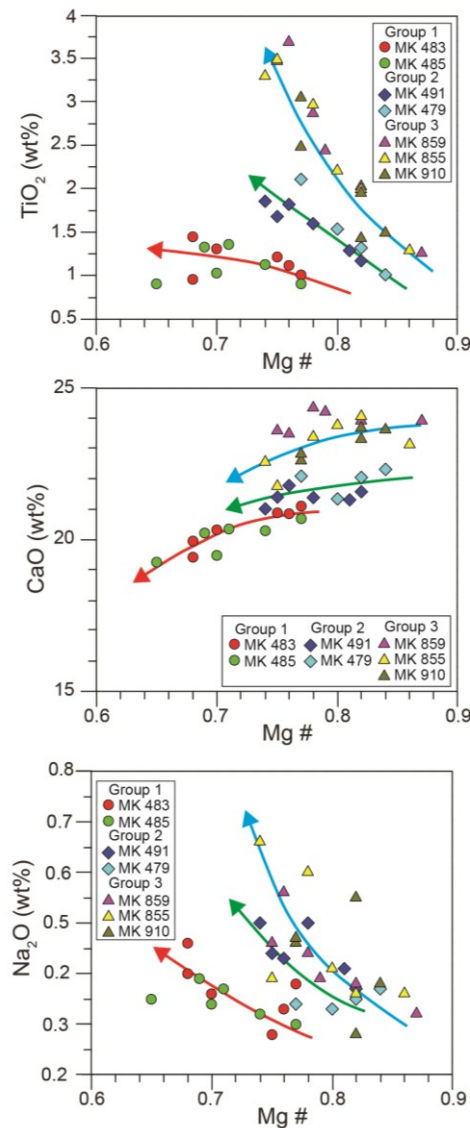


Figure 6.19. Clinopyroxene Mg# vs. TiO₂, CaO, and Na₂O for the clinopyroxene from the Durkan Complex. Arrows indicate the compositional trends for Group 1 (red arrow), Group 2 (green arrow), and Group 3 (blue arrow).

Clinopyroxene from the Group 3 rocks were analysed in the samples MK859, MK855, and MK910, which correspond to a porphyritic rock, an aphyric rock and a meta-volcanic rock,

respectively (Appendix Table 6.4). They mainly plot in the field for diopsidic clinopyroxene, despite some crystals show augitic composition (Fig. 6.18). The Enstatite end-member shows higher variation with respect to the other groups, ranging from 36.6 to 44.8 (Appendix Table 6.4). Mg# is generally high and quite variable (0.74 - 0.87). The Group 3 clinopyroxenes show variable

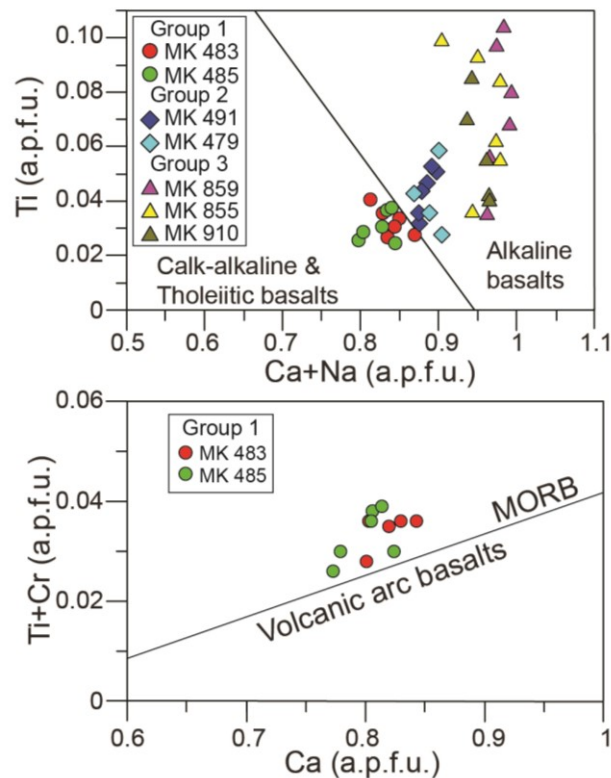


Figure 6.20. *Ti vs. (Ca + Na) and (Ti + Cr) vs. Ca discrimination diagrams of Leterrier et al. (1982) showing the composition of clinopyroxenes from the basalts of the Durkan Complex.*

and generally higher contents of TiO_2 (1.26 – 3.69 wt%), Na_2O (0.28 – 0.66 wt%), CaO (21.7 – 24.3 wt%), and Al_2O_3 (2.88 – 7.08 wt%) if compared to the clinopyroxenes from the other groups of rocks. This is particularly clear if the clinopyroxenes with comparable Mg# are exclusively considered (Fig. 6.19). Cr_2O_3 is positively correlated with Mg# and it is extremely variable, from 0.01 to 1.0. The crystals from this Group are frequently zoned, showing concentric zonation and multiple rims of growth that are clearly distinguishable also from the petrographic analysis. The zoning is associated to significant chemical variations of TiO_2 , CaO , Al_2O_3 , Na_2O , MgO , FeO_{tot} and Cr_2O_3 contents from core to rim (Appendix Table 6.4). Generally, the core of the crystals

shows higher MgO, Cr₂O₃, and CaO contents coupled with lower TiO₂, Al₂O₃, Na₂O, and FeO_{tot} contents with respect to the rim. However, some samples (i.e., MK855cr2 and MK855cr4) show an

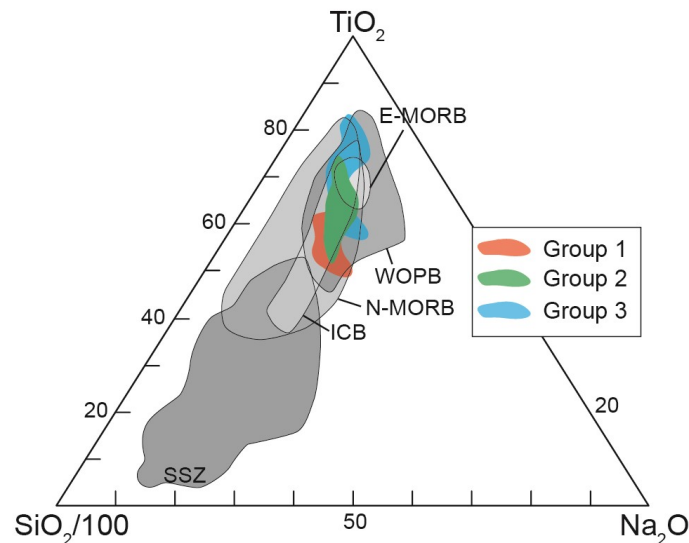


Figure 6.21. Ternary discrimination diagram (from *Beccaluva et al., 1989*) for clinopyroxenes from the basalts of the Durkan Complex.

opposite chemical variation of these elements, suggesting an inverse zonation in these crystals. In addition, some crystals show concentric and oscillatory zonation characterized by different rims of growth, showing rhythmic variation of TiO₂, CaO, Al₂O₃, Na₂O, MgO, FeO_{tot} and Cr₂O₃ contents ([Appendix Table 6.4](#)). This is particularly evident for the sample MK859cr1, in which TiO₂, Na₂O, MgO, and Cr₂O₃ show oscillatory chemical variation from the core to the rim of the crystal ([Appendix Table 6.4](#)). These features collectively indicate that the growth of the crystals occurred either from a progressively differentiating melt or from the equilibrium with different pulses of melts at different fractionation stages. The clinopyroxenes of the Group 3 rocks plot in the field for clinopyroxene of alkaline rocks and are clearly distinguished from the tholeiitic clinopyroxenes of the Group 1 rocks ([Fig. 6.20](#)). They are also characterized by higher (Ca + Na) contents, indicating a chemical distinction from the clinopyroxenes of the Group 2 rock ([Fig. 6.20](#)). An alkaline affinity for the clinopyroxenes of Group 3 rock is also suggested by the discrimination diagram in [Figure 6.21](#), where they are distinguished from the clinopyroxenes of the SSZ basaltic rocks and plot

within the field for plume-influenced Iceland and within-plate oceanic basalts.

6.5.2. Comparison between clinopyroxene composition and whole-rock geochemistry

As it is shown in the previous section, significant differences exist in the chemical composition of the clinopyroxenes of the western Durkan Complex in relation to the whole-rock geochemistry of the hosting rocks (Fig. 6.22). This feature is particularly evident for the TiO₂, CaO, Na₂O, and Al₂O₃ contents (Figs. 6.19, 6.20). In fact, the variation of TiO₂, CaO, Na₂O contents and the clinopyroxenes Mg# show different evolutionary trends for the clinopyroxenes from the three groups of rocks (Fig. 6.19). Extremely important is the variation in TiO₂ contents, which is commonly thought to reflecting the degree of depletion of the mantle source and the Ti activity of the parental mantle (Pearce & Norry, 1979). In detail, high TiO₂ content of clinopyroxenes indicate their crystallization from primary magmas generated from mantle sources, which did not undergo previous partial melting events (Pearce & Norry, 1979). The Figure 6.22 clearly shows a positive correlation with the Nb/Y ratios of the hosting rocks and the TiO₂, CaO, and Al₂O₃ contents of the clinopyroxene. This is particularly meaningful considering that the Nb/Y ratios for the volcanic rocks increase from the tholeiitic to the alkaline rocks (e.g., Winchester & Floyd, 1979; Pearce, 1996). The difference between tholeiitic and alkaline magmatic series is widely accepted as reflecting the partial melting of mantle sources with different composition and/or different degrees of partial melting (e.g., Wilson, 1989; Pearce, 2008; Saccani, 2015). In general, high value of the Nb/Y ratios are commonly associated to volcanic rocks generated from partial melting of rather enriched mantle sources, which did not undergo previous partial melting events (Winchester & Floyd, 1979; Pearce, 1996, 2014). All the evidence combined strongly point out for the crystallization of the three groups of clinopyroxenes from different fractionating parental melts,

which likely derived from different and not depleted mantle sources.

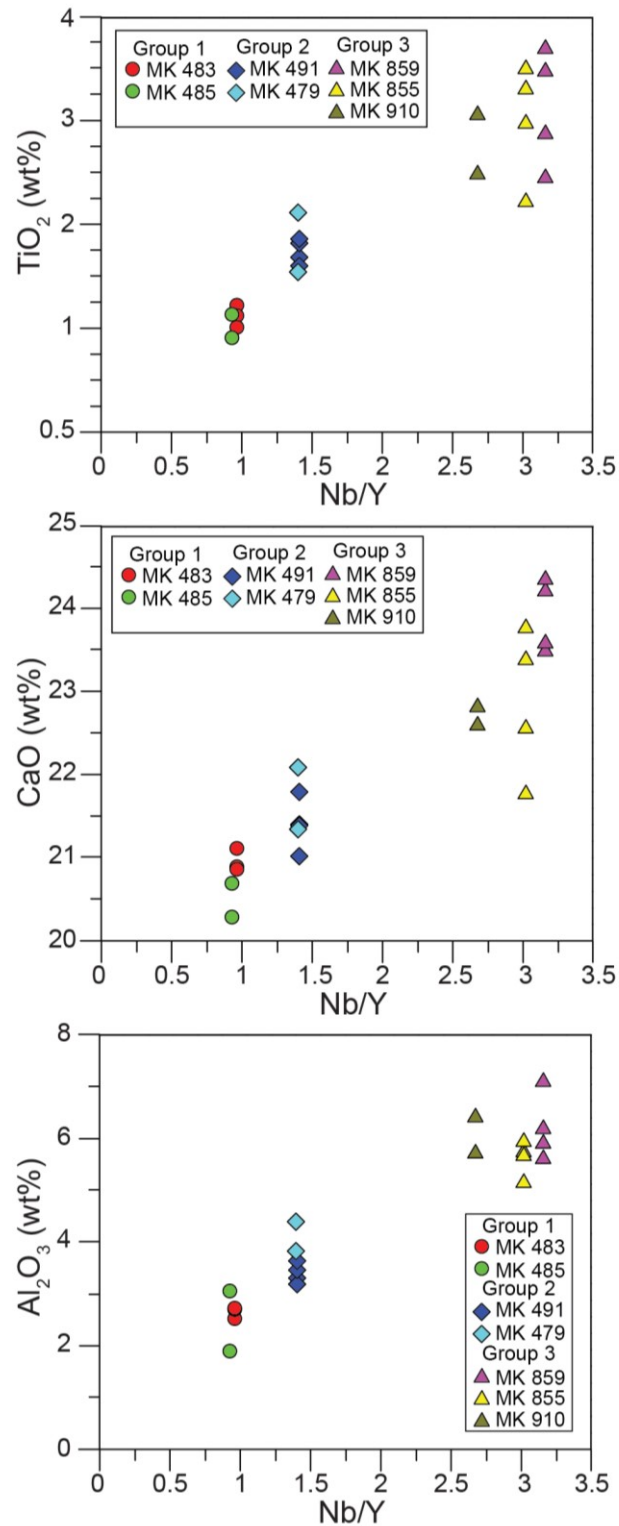


Figure 6.22. Variation diagrams showing Nb/Y ratio of the host rocks vs. TiO₂, CaO, and Al₂O₃ of the clinopyroxenes for the magmatic rocks from the Durkan Complex.

6.6. Discussion

6.6.1. Reconstruction of the stratigraphy of the western Durkan Complex

The integration of the stratigraphic and biostratigraphic data from different transects allows us to identify in the western Durkan Complex three main types of stratigraphic successions, which will be hereafter named as Type-I, Type-II and Type-III (Fig. 6.23). Basalts with P-MORB and alkaline geochemical affinity occur within all the three types of successions (section 6.5) and are associated with Late Cretaceous sedimentary rocks (Fig. 6.23). The geochemistry of the Durkan Complex basalts is compatible with their genesis in a within-plate oceanic setting.

6.6.1.1. Type-I stratigraphic succession

The Type-I succession is defined based on the stratigraphic features of the Cherty-Limestone and Basalt lithostratigraphic unit, which is preserved in the tectonic slice of the Manujan transect, as well as in the structurally lowermost tectonic slice of the Chah Shahi 1 transect (Fig. 6.3c3). It consists of a pelagic sequence including reddish cherts and pinkish to whitish cherty-limestones alternating with reddish shales as well as marls and silty-marls (Fig. 6.23). The integration of radiolarian, foraminifera and nannoplacton biostratigraphic data from the different tectonic slices indicates Coniacian - early Campanian age for this succession (Fig. 6.23). In addition, basaltic lava flows and less abundant volcanoclastic arenites are interbedded within the pelagic succession (Fig. 6.23). The low vesicularity of the lava flows within the Cherty-Limestone and Basalt lithostratigraphic unit (Fig. 6.13) suggests an eruption in a deep-marine environment with a relatively thick water column pressure (Moore, 1970; Moore & Schilling, 1973). All these data

support the emplacement of the magmatic rocks in a pelagic depositional setting during the Coniacian – early Campanian age.

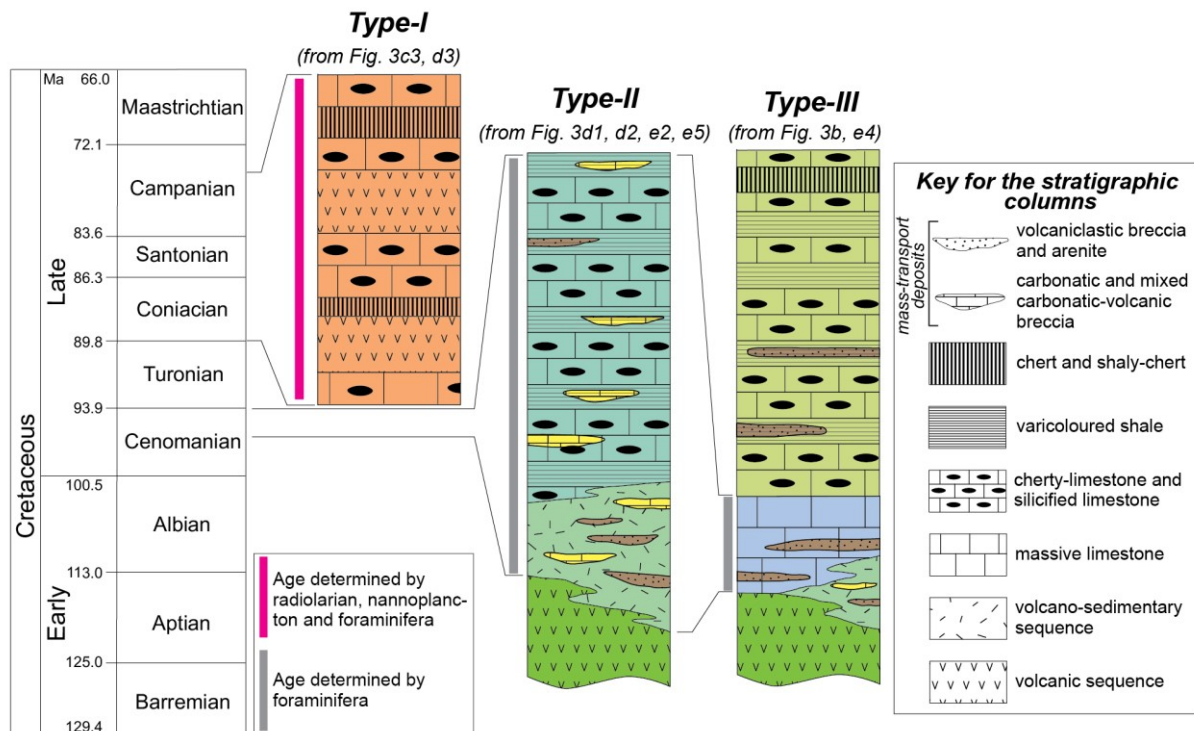


Figure 6.23. Schematic reconstructed stratigraphic columns and ages for the three different types of succession in the western Durkan Complex.

6.6.1.2. Type-II stratigraphic succession

The Type-II stratigraphic column (Fig. 6.23) has been reconstructed by integrating the stratigraphic features of the two uppermost tectonic slices of the Chah Shahi 1 transect (Figs. 6.3c1, c2), the uppermost tectonic slice of the Chah Shahi 2 transect (Fig. 6.3d5), as well as some tectonic slices in the thrust zone of the Chah Shahi 2 transect (Figs. 6.3d1, d2, d3). These tectonic slices are characterized by stratigraphic successions showing comparable stratigraphic features, which are: i) a basal Volcanic Sequence passing upward to a Volcano-Sedimentary Sequence; ii) a pelagic and hemipelagic sequences (i.e., Limestone and Shale, and Cherty-Limestone and

Varicoloured Shale lithostratigraphic units) resting above the Volcano-Sedimentary Sequence; iii) different types of mass-transport deposits interlayered at different stratigraphic levels (Fig. 6.23). In the tectonic slices within the thrust zone of the Chah Shahi 2 transect only the basal part of Type-II succession occurs most likely as a consequence of the tectonic deformation. The Volcanic Sequence and the Volcano-Sedimentary Sequence show transitional stratigraphic relationships, as suggested by the occurrence in both complexes of: i) basalts showing comparable intra-plate geochemical affinity (section 6.5); and ii) volcanoclastic breccias as well as volcanoclastic arenites. Following the diagnostic criteria proposed by McPhie et al. (1993), Fischer (1984), and Gutierrez et al. (2006), these sedimentary rocks could be defined as volcanogenic deposits and they likely represent the results of gravity-induced high density sedimentary processes (e.g., rock fall, grain flows, cohesive debris flows, hyperconcentrated flows, and/or high density turbiditic currents) operating on pre-existing volcanic series and/or volcanic reliefs. The volcanoclastic rocks become abundant in the Volcano-Sedimentary Sequence where they are interlayered with limestones, shales, and breccias, showing a mixed carbonatic-volcanic composition of both clasts and matrix (Fig. 6.23). These breccias likely represent the sedimentary products of mass-transport processes sourced from coeval volcanic and carbonatic debris. The limestones from the Volcano-Sedimentary Sequence in the Chah Shahi 1 transect exhibit Cenomanian pelagic foraminifera assemblages (Fig. 6.23), indicating relatively deep-water depositional setting for this sequence. This evidence is further supported by the analyses of vesicles contents of volcanic rocks from the Volcano-Sedimentary Sequence, which indicates eruption in relatively deep-water environment. The Type-II succession continues with a pelagic and hemipelagic sedimentary sequence (Fig. 6.23), whose stratigraphic features are defined on the basis of the succession of the Limestone and Shale, and Cherty-Limestone and Varicoloured Shale lithostratigraphic units (Figs. 6.3c1, c2, d5). Although these two lithostratigraphic units display some minor differences, they are comparable

for: i) the occurrence of pelagic limestones and pinkish to whitish cherty limestones interlayered with shales; ii) the stratigraphic position above the Volcano-Sedimentary Sequence; iii) the occurrence of calcareous turbidites and abundant carbonatic breccias and minor volcanoclastic arenites (Fig. 6.23). Unfortunately, the limestone from Limestone and Shale and the Cherty-Limestone and Varicoloured Shale underwent high degree of diagenetic and/or metamorphic recrystallization, hampering a biostratigraphic age determination. However, their stratigraphic position and their microfacies comparable with the Cenomanian limestones of the Volcano-Sedimentary Sequence suggest a latest Cenomanian or younger age (Fig. 6.23).

6.6.1.3. Type-III stratigraphic succession

The type III succession (Fig. 6.23) has been reconstructed from the integration of the stratigraphic features of the different successions preserved in the two tectonic slices of the Zandan transect (Fig. 6.3a), as well as within a slice of the thrust zone in the Chah Shahi 2 transect (Fig. 6.3d4). The structurally lowermost slice of the succession in the Zandan transect was metamorphosed under subgreenschist facies conditions as indicated by paragenesis of the metamorphic foliation in the meta-basalts; nonetheless, the stratigraphic features are fairly well preserved. The Massive Marble and the platform-derived Massive Limestone lithostratigraphic units (Fig. 6.23) could be correlated and they most likely represent comparable platform successions deformed at different depth into the accretionary wedge. In fact, as shown in Section 6.2.1, their correlation is suggested by: i) their similar lithostratigraphic architecture; ii) the occurrence of volcanoclastic debris in both the lithostratigraphic units; iii) their similar stratigraphic position above a volcanic stratigraphic interval, represented by the same alkaline volcanic rocks (Figs. 6.3a1, a2). The biostratigraphic data indicate a Cenomanian age for the platform-derived

Massive Limestone (Fig. 6.23). This age can possibly be extended to the Massive Marble lithostratigraphic unit from both the lower slice of the Zandan transect and the tectonic slice within the thrust zone in the Chah Shahi 2 transect (see Figs. 6.3a1, 6.3d4), whose metamorphism hamper any age determination. However, it is not possible to exclude that the Massive Marble facies could represent a platform succession of different ages. In the metamorphic and non-metamorphic successions of the Zandan transect, the platform successions stratigraphically overlie the Meta-Volcanic Sequence and the Volcano-Sedimentary Sequence, respectively (Figs. 6.3a1, a2). The occurrence in both sequences of volcanoclastic and volcanic rocks, the comparable geochemistry of their volcanic rocks, and their stratigraphic relationship between the overlaying platform successions seem to suggest both lateral and vertical stratigraphic transition between the two complexes (Fig. 6.23). In addition, lateral facies variation in the depositional basin before the onset of the platform sedimentation is further suggested by the occurrence in the Volcano-Sedimentary Sequence of massive limestone as well as mixed calcareous-volcanic turbidites. In the metamorphic slice of the Zandan transect, the platform succession of the Massive Marble lithostratigraphic unit is followed by the Meta Cherty-Limestone and Shale, which show a thinning upward trend. This lithostratigraphic unit likely represents a hemipelagic and pelagic succession indicating the drowning of the carbonatic platform (Fig. 6.23 see also Fig. 6.3a1). The non-metamorphic equivalent of this lithostratigraphic unit does not occur above the Massive Limestone, possibly as a consequence of a depositional hiatus or the elision for the tectonic deformation within the Makran Accretionary Prism. Unfortunately, due to the high metamorphic recrystallization of the limestone no biostratigraphic data are up to now available for the succession of the Meta Cherty-Limestone and Shale lithostratigraphic unit. However, its stratigraphic position (i.e., above the Massive Marble succession correlated with the Cenomanian platform succession of the Massive Limestone) suggests a Late Cretaceous age for this lithostratigraphic unit (Fig. 6.23).

6.6.2. Stratigraphic implications for the regional geology of the North Makran

The different types of successions of the Durkan Complex in the western sector of the North Makran record a complex interplay between sedimentation and alkaline magmatism during the Late Cretaceous. Unfortunately, in the western Durkan Complex the Late Cretaceous successions have been tectonically detached from their “basements” during their tectonic deformation in the Makran accretionary wedge. Nonetheless, it is worth to note that extremely subordinated tectonic slices showing Permian successions occur in the western Durkan Complex and they show tectonic relationship with the Cretaceous succession (McCall, 1985). This author has interpreted the Permian tectonic slices as the original stratigraphic base of the Cretaceous succession, though clear stratigraphic relationships were not observed. Therefore, this hypothesis should be re-investigated.

Figure 6.24 shows the tectono-sedimentary and magmatic stages recorded by the succession of the western Durkan Complex (this work) and those proposed in literature for the eastern part of the Durkan Complex (Hunziker, 2014; Hunziker et al., 2015). According to Hunziker et al. (2015), pre-Cretaceous rock assemblages are exposed in the eastern part of the Durkan Complex (i.e., Remeshk - Fannuj area). These authors reconstructed the Middle Jurassic - Early Cretaceous extensional history that affected the southern margin of the Lut block (i.e., the Eurasian margin; Fig. 6.24; McCall & Kidd, 1982; Burg, 2018 see also Hunziker et al., 2015 and Fig. 14 therein for further detail). This extensional tectonics led to the separation of the Bajgan-Durkan microcontinent from the southern margin of the Lut Block, and the subsequent opening of the North Makran Ocean during Early Cretaceous (Hunziker et al., 2015; Burg, 2018). The extensional tectonic stages were characterized by the emplacement of Early - Late Jurassic granitoid bodies into a Jurassic carbonatic platform (Fig. 6.24). These rocks were subsequently unconformably covered by Early Cretaceous pelagic sediments associated with alkaline and tholeiitic lavas, which

indicate the progressive deepening of the depositional setting (Fig. 6.24). In this scenario, the alkaline volcanic rocks in the eastern Durkan Complex represent within plate rift-related magmatism (Fig. 6.24), as commonly accepted in literature (Robertson, 2007; Pearce, 2008; Saccani, 2015; Saccani et al., 2015).

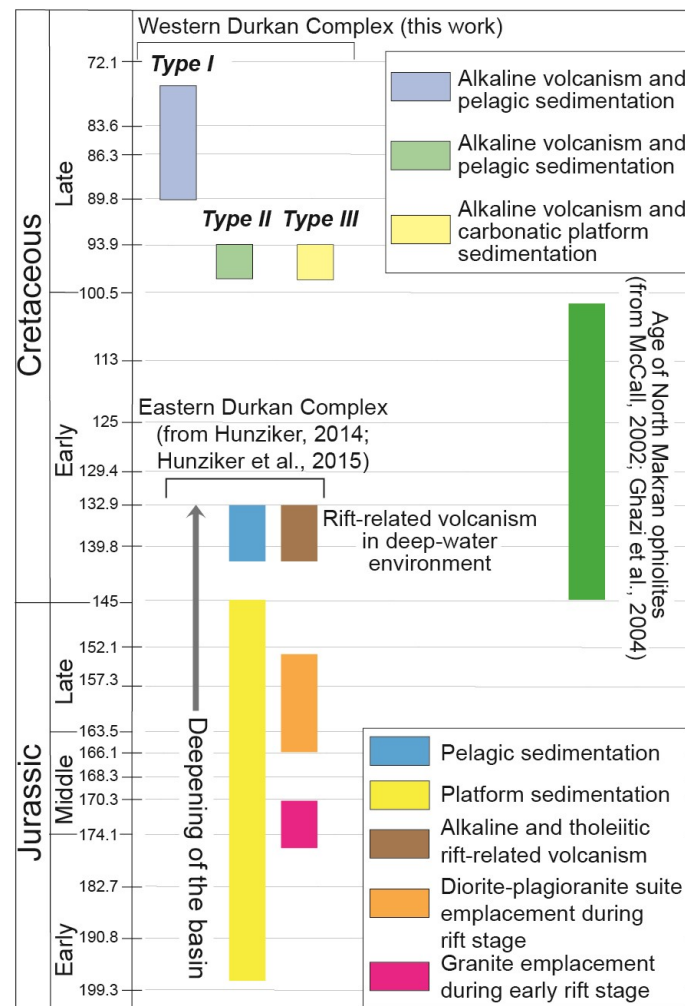


Figure 6.24. Comparison of the tectono-sedimentary and magmatic events recorded in the western Durkan Complex (this work) and the eastern Durkan Complex (Hunziker, 2014; Hunziker et al., 2015). Ages of the North Makran Ophiolites are also shown (data source: McCall, 2002; Ghazi et al., 2004).

The comparison of these previously published data and those presented in this work clearly outlines that the rift-related phases recorded in the eastern Durkan Complex are significantly older than the tectono-sedimentary and magmatic phases recognized for the western Durkan Complex (Fig. 6.24). This rises serious doubt about the interpretation of the western Durkan Complex as

remnants of a rifted continental margin domain. In fact, this interpretation implies a laterally diachronous rift of the southern margin of the Lut Block, which would have been active for 70-100 My, from Middle Jurassic - to Late Cretaceous (Fig. 6.24). This scenario seems to be quite unreasonable and it is in contrast with the Cretaceous regional-scale evolution of the northern part of the Neo-Tethys realm. In fact, the Late Cretaceous tectono-sedimentary evolution and the alkaline magmatism recorded by the western Durkan Complex post-dates the spreading stages of the North Makran Ocean, represented by the Early Cretaceous ophiolitic sequences (Fig. 6.24 and reference quoted therein). In addition, it is commonly accepted that starting from the Late Jurassic - Early Cretaceous the southern margin of the Eurasian plates (e.g., the Lut block in the Makran transect) was affected by the beginning of convergence kinematic rather than extensional tectonics (Dercourt et al., 1986; Sengör et al., 1988; Agard et al., 2011; Hassanzadeh & Wernicke, 2016; Barrier et al., 2018; Saccani et al., 2018; Burg, 2018; Rolland et al., 2020). This tectonic regime was associated with the northward motion of the Arabian Plate and the beginning of the northward subduction of the Neo-Tethys oceanic lithosphere and its minor branches, such as the North Makran Ocean, below the Eurasia continental margin (Hassig et al., 2013a, b; Monsef et al., 2019; Bonnet et al., 2020a, b). Another clue strongly suggesting that the western Durkan Complex may not represent a continental margin domain is the total lack of continental-derived debris within the clastic deposits. In fact, during the rifting stages the sediment supply of continental margin clastic successions is mainly represented by quartz-rich debris sourced from continental-derived rocks (Robertson, 2007 for exhaustive discussion; Berra et al., 2009; Festa et al., 2020). Such deposits are completely lacking in the western Durkan Complex successions, which, on the contrary, include mass-transport deposits showing volcanic, carbonatic, and mixed volcanic-carbonatic composition of the debris, without any kind of continental derived debris. In conclusion, the new data presented herein suggest that the stratigraphic successions and the alkaline volcanic rocks of

the western Durkan Complex do not represent remnants of a rifted continental margin.

It is widely accepted in literature that alkaline basaltic rocks erupted mainly in within-plate oceanic island setting (Pearce, 2008; Dilek & Furnes, 2011; Saccani, 2015; Saccani et al., 2015; Safonova & Santhos, 2014). Studies of modern oceanic setting indicate that the within-plate alkaline magmatic activity is commonly associated to the rising of mantle plume and/or hot spot magmatism (Morgan, 1971; Pearce, 2008). This magmatic activity results in the formation of volcanic reliefs and/or a chain of reliefs (i.e., seamounts or oceanic islands), which are built on older and pre-existing oceanic lithosphere (Morgan, 1971; Dilek & Furnes, 2011; Staudigel & Clague, 2010). Several recent studies document the occurrence of abundant alkaline magmatic rocks and OIBs within collisional and accretionary belts from Caucasus to Himalaya (Rolland et al., 2010; Hassig et al., 2013a,b; Saccani et al., 2013a; Yang & Dilek, 2015; Saccani et al., 2018; Azizi et al., 2018; Esmaeili et al., 2019; Rolland et al., 2020). Significantly, some of these alkaline and OIB rocks are Cretaceous in age and were interpreted as remnants of seamounts and/or oceanic plateau associated with plume-influenced magmatic activities in the northern sector of the Neo-Tethys Ocean at this time (Rolland et al., 2010; Saccani et al., 2013a; Saccani et al., 2018; Esmaeili et al., 2019; Rolland et al., 2020). Therefore, this regional-scale evidence strongly suggests that the Late Cretaceous sedimentary succession associated with alkaline magmatic rock in the western Durkan Complex could represent tectonically disrupted remnants of seamounts and/or oceanic islands, which existed in the northern sector of the Neo-Tethys. The wide age range indicated by biostratigraphic data suggests that this Complex is composed by fragments of distinct seamounts (i.e., a seamount chain) rather than the remnants of a unique seamount. In this interpretation, the Permian successions reported in the western Durkan Complex would represent exotic tectonic inclusions juxtaposed to the Cretaceous successions. Their paleogeographic origin is up to now unknown. Future stratigraphic and biostratigraphic studies on these assumed Permian slices are

needed to better constrain their ages and depositional settings. In the following sections, the stratigraphic record of the Durkan Complex successions will be compared with the stratigraphic architecture, volcanic facies as well as sedimentary and volcanic evolution proposed in literature for modern seamounts and oceanic islands in order to test the proposed hypothesis.

6.6.3. Petrological implications: melt petrogenesis of the magmatic rocks

The aim of the petrogenetic discussion is to identify the possible mantle sources for the magmatic rocks from the Durkan Complex and their melting conditions, in order to bring robust constraints for the tectono-magmatic setting of formation of this Complex. The modelling will be based on incompatible trace elements and REE ratios as they are believed to depend on the composition of the mantle source and its degree of partial melting rather than fractional crystallization and crustal assimilation (e.g., [Pearce, 1983](#); [Allègre & Minster, 1978](#); [Beker et al., 1997](#)). This assumption is particularly true if only primitive basaltic rocks (i.e., basalts with $Mg\# \sim 68$) are considered for the petrogenetic studies. In fact, incompatible trace elements and REE are moderately affected to the fractional crystallization of olivine, clinopyroxene and plagioclase (i.e., the typical paragenesis of basaltic rocks). As a consequence, the petrogenetic discussion will be carried out onto the less fractionated basalts from each group of rocks.

Sections 6.5 and 6.6 show that the magmatic rocks of the Durkan Complex exhibit transitional (i.e., Group 1 rocks) and alkaline affinities (i.e., Group 2 and 3 rocks). The different trace elements contents (e.g., Zr, Y, Nb) and REE patterns ([Fig. 6.15](#)) observed in the rocks of the three groups as well as their different incompatible elements (e.g., Zr/Y, Y/Nb, Th/Ta, Nb/Yb) and REE (i.e., La_N/Yb_N , Sm_N/Yb_N) ratios ([Appendix Table 6.3](#), [Fig. 6.16](#)) suggest that these rocks can derive from the partial melting of chemical distinct (although slightly) mantle sources and/or different

melting conditions. A first consideration about the petrogenesis of the Durkan Complex basalts can be derived from [Figure 6.25a](#), which shows that these basalts cannot be generated by a depleted MORB mantle (DMM)-type mantle source; in contrast the Zr and Nb contents indicate a genetic relationship with an enriched and/or transitional mantle source ([Fig. 6.25a](#)). The mineral chemistry of the clinopyroxenes and in particular their high TiO₂ contents also point out for the genesis of the Group 3 rocks from an enriched mantle source. [Figure 6.25b](#) further supports this conclusion; in fact the studied rocks plot along the mixing curve between N-MORB and OIB showing a composition shifted toward oceanic island basalts (OIB) endmember. Significantly, the influence of OIB-type chemical components increases from Group 1 to Groups 2 and 3, which, in contrast, are comparable to each other ([Fig. 6.25b](#)).

Further constraints on the possible mantle source for the Durkan Complex basalts can be seen in [Figure 6.25c](#), which shows that these rocks plot along the N-MORB – OIB trend and are well distinguished from basalts generated in continental margin and volcanic arc settings. These features collectively suggest the genesis of the studied rocks from the partial melting of mantle sources that have been influenced by OIB-type chemical components prior of the melting events without any contributions from subduction related chemical components and/or continental crust contamination.

Given these considerations, a semi-quantitative non-modal, batch partial melting modelling using both trace elements and REE has been performed ([Figs. 6.26, 6.27](#)) in order to find the mantle peridotite compositions that best fit the composition of the most primitive basalts of each geochemical Group. The Nb/Yb vs TiO₂/Yb modelling ([Fig. 6.26a](#), modified from [Pearce, 2008](#)) has the advantage of combining information about the enrichment of the source (i.e., variation of Nb/Yb) and the presence of residual garnet in the source (TiO₂/Yb). By contrast, the Zr vs Hf modelling ([Fig. 6.26b](#)) is particularly indicates to evaluate the enrichment of the mantle source

(Fig. 6.26b).

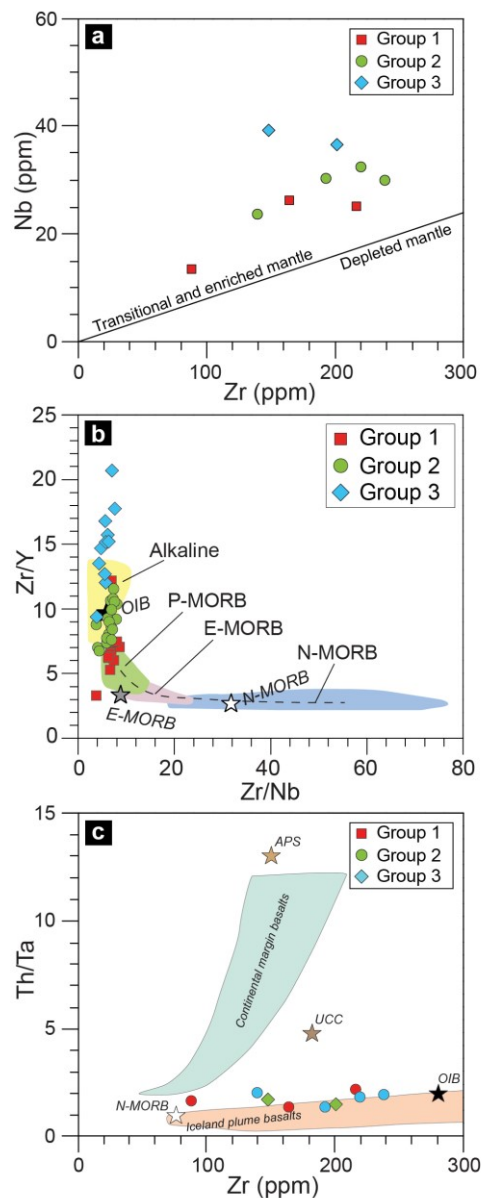


Figure 6.25. a) Nb vs Zr, b) Zr/Y vs Zr/Nb, and c) Th/Ta vs Zr diagrams for the magmatic rocks from the western Durkan Complex. Only the relatively less fractionated basalts are plotted. N-MORB, E-MORB and OIB end-members are from [Sun and McDonough \(1989\)](#). Fields indicate compositional variation for different types of basalts from subduction-unrelated ophiolites and modern oceanic setting (data from [Saccani et al., 2013b, 2014](#); [Le Roex et al., 1983](#); [Hanan et al., 2000](#); [Chauvet et al., 2011](#)). The dashed line represents the mixing curve calculated using OIB and N-MORB end-members (from [Le Roex et al., 1983](#)). Average pelitic sediments (APS) and upper continental crust (UCC) are from [Taylor & McLennan \(1985\)](#).

The results of incompatible elements modelling have been combined with the REE modelling ([Fig. 6.27](#)). The starting mantle source composition in the proposed modelling is the lherzolite ZB2 from the Northern Apennines ([Barbero et al., 2020](#)) that was metasomatized by various extent of

OIB-type chemical components. The latter has been assumed as the enriched mantle of [Lustrino et al. \(2002\)](#), which corresponds to the mantle source for alkaline basalts. The modal compositions of the assumed mantle sources, their chemical composition, the melting proportions and the REE and trace elements distribution coefficients used in the models are listed in [Appendix Table 6.5](#).

6.6.3.1. Group 1 rocks

The high Nb/Yb ratios implies the partial melting of a mantle source showing rather enriched composition ([Fig. 6.26a, b](#)). In fact, the Nb/Yb vs TiO₂/Yb model ([Fig. 6.26a](#)) shows that Group 1 rocks cannot be generated from the partial melting of sources with depleted composition as the DMM ([Workman & Hart, 2005](#)) or the lherzolite ZB2 ([Barbero et al., 2020](#)). By contrast, the geochemistry of Group 1 primitive basalts is compatible with the partial melting of a theoretically calculated S1 mantle source that is significantly more enriched in Nb/Yb with respect to the DMM and ZB2 sources ([Fig. 6.26a](#)). The high TiO₂/Yb ratios characterizing the Group 1 basalts can be explained by the presence of residual garnet in the mantle source ([Fig. 6.26a](#)). In detail, it can be explained by different melting combinations such as the partial melting at the garnet-facies, or the partial melting at both garnet- and spinel-facies with the mixing of the different melts produced ([Fig. 6.26a](#)). Accordingly, the Hf vs Zr petrogenetic model suggest that the compositions of Group 1 primitive basalts can be explained by the partial melting of a mantle source S1 that is rather enriched in Hf and Zr at both spinel- and garnet-facies and the mixing of the different melts produced ([Fig. 6.26b](#)). Partial melting degrees can be assumed as ~ 2% and ~ 7% in garnet- and spinel-facies, respectively ([Fig. 6.26b](#)).

The REE modelling confirms these results clearly indicating that the Group 1 primitive basalt derive from a mantle source S1 that is significantly enriched in LREE with respect to the DMM

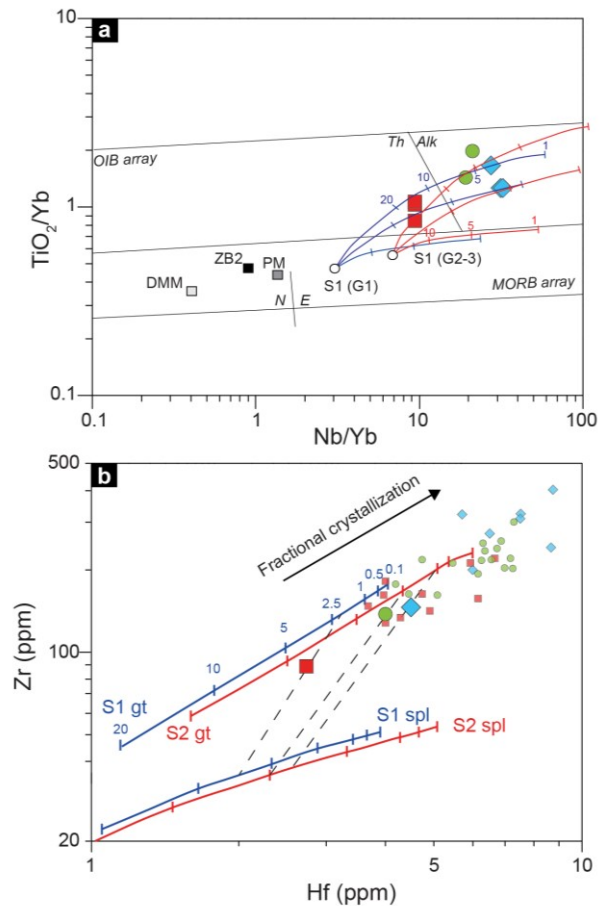


Figure 6.26. a) Nb/Yb vs. TiO_2/Yb diagram from [Pearce \(2008\)](#) for primitive basalts for each geochemical Group. Ticks on all melting curve indicate the same percentages of partial melting as shown for the melting curve of source S1 in garnet-facies and S2 in the spinel-facies (from [Pearce, 2008](#)); S1 and S2 represents theoretical mantle source calculated starting from the composition of the lherzolite ZB2 ([Barbero et al., 2020](#)) throughout the enrichment by OIB-chemical components. DMM and PM are shown from comparison (data from [Workman & Hart, 2005](#) and [Sun & McDonough, 1989](#), respectively); b) Zr vs Hf melting curve for the theoretical mantle source S1 and S2 calculated as explain for the model shown in [Figure 6.26a](#). For both a) and b) input parameters for the models (source modes, melting proportions, and partition coefficients, source compositions) are shown in [Appendix Table 6.5](#).

and ZB2 sources by OIB-type chemical components ([Fig. 6.26a](#)). The rather high $(Sm/Yb)_N$ ratio displayed by Group 1 rocks ([Figs. 6.15, 6.16](#)) suggest the involvement of residual garnet in the parental mantle source. In detail, the composition of Group 1 primitive basalt MK282 fits well with the melt calculated for 2.5% and 7.5% of partial melting of the S1 mantle source at garnet- and spinel-facies, respectively, with a mixing proportion between garnet and spinel melts of 50:50 ([Fig. 6.27a](#)). Different mixing proportions ([Fig. 6.27a₁](#)) and melting percentage (grey field of [Fig. 6.27a](#)) fail to reproduce the geochemical features of the Group 1 rocks.

6.6.3.2. Group 2 rocks

The high Nb/Yb ratios clearly indicates that the Group 2 rocks cannot derive from the partial melting of the depleted DMM and ZB2 mantle sources, implying an enriched source (Fig. 6.26a). Similarly to Group 1 rocks, the high TiO₂/Yb ratios of Group 2 rocks suggest residual garnet in the mantle source (Fig. 6.26a). The TiO₂/Nb vs Nb/Yb model suggests that the genesis of Group 2 rocks is related to the partial melting of a mantle source S2 that is more enriched with respect to the source S1 (Fig. 6.26a). In detail, this model suggests the partial melting at garnet-facies or a combination of partial melting in the garnet- and spinel-facies with the mixing of the melts produced (Fig. 6.26a). A similar conclusion can be drawn from the Zr vs Hf model that suggests for the genesis of Group 2 rocks the partial melting of S2 mantle at both garnet- and spinel-facies (~ 3 % at garnet-facies, 2.5 % at spinel-facies), with mixing proportions significantly shifted toward melt produced in the garnet-facies (Fig. 6.26b). These calculations fit well with the differences in term of incompatible elements that characterized the Group 2 rocks if compared to Group 1 rocks.

In term of REE, the high (Sm/Yb)_N and (La/Yb)_N ratios shown by Group 2 rocks (Figs. 6.15, 6.16) suggest residual garnet in the mantle source and a mantle source more enriched in LREE with respect to DMM (Workman & Hart, 2005), the lherzolite ZB2 (Barbero et al., 2020), and the calculated S1 source. The REE modelling indicates that the composition of primary melt of Group 2 rock (MK340) can be explained by the partial melting of the mantle source S2, which is enriched in LREE and MREE with respect to fertile lherzolite ZB2 by an OIB-like chemical components (Fig. 6.27b). In detail, the model indicate the ~ 2 % of partial melting at garnet-facies and ~ 5 % of partial melting at spinel-facies of this source, with mixing proportion of 60:40 in favour of melt produced at garnet-facies (Fig. 6.27b). Figure 6.27b also shows that different melting degrees of S2 source fail to reproduce the geochemical composition of the primary basalt of the Group 2.

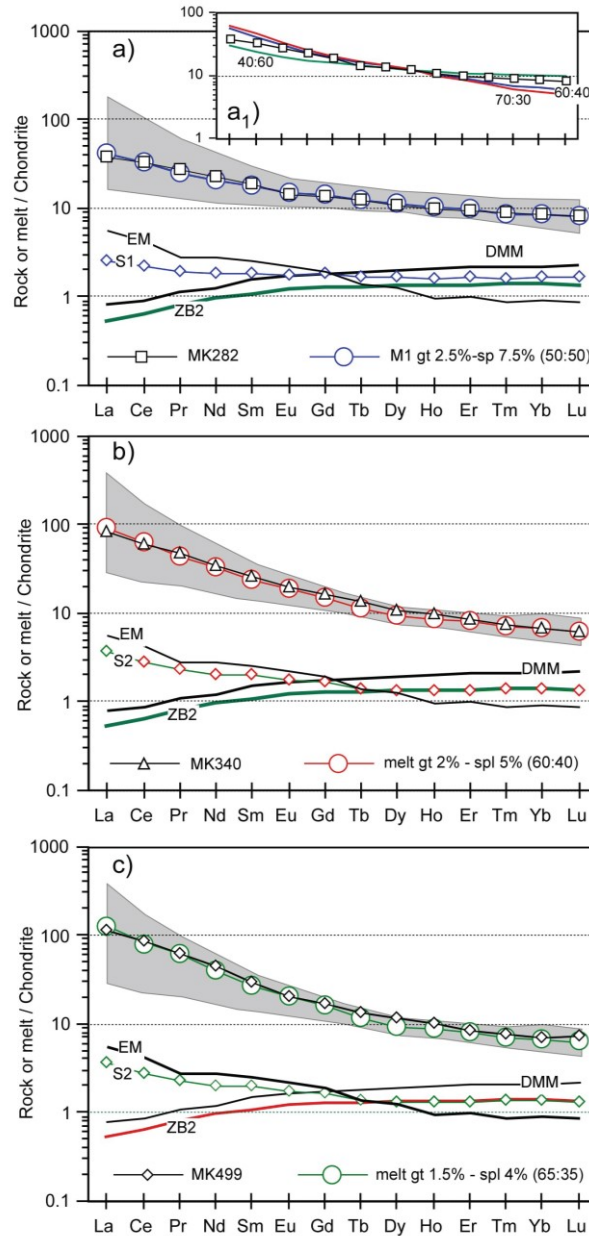


Figure 6.27. Calculated chondrite-normalized (Sun & McDonough, 1989) rare earth element (REE) liquid composition for parental melts derived from different mantle sources, assuming various degrees of non-modal batch partial melting. Abbreviations: EM: enriched mantle source (from Lustrino et al., 2002); DMM: depleted MORB mantle (Workman & Hart, 2005); S2: enriched mantle source S2. Input parameters for the REE models (source modes, melting proportions, and partition coefficients), as well as compositions of the different mantle sources are shown in Appendix Table 6.5.

6.6.3.3. Group 3 rocks

The high TiO_2/Yb and Nb/Yb ratios shown by primitive basalts of the Group 3 rocks indicate

residual garnet in the source during partial melting events and an enriched mantle source, respectively (Fig. 6.26a). The Nb/Yb vs TiO₂/Yb modelling suggests a parental mantle source more enriched than the one hypothesized for the genesis of Group 1 rocks. In detail, Group 3 rocks are compatible with the partial melting of the enriched source S2 either in the garnet-facies or in the garnet- and spinel-facies with the mixing of the different melts (Fig. 6.26a). A similar conclusion can be derived from the Zr vs Hf modelling, which shows how the Group 3 basalt was likely derived from the partial melting of a mantle source S2 that is significantly enriched in both elements with respect to mantle source S1 (Fig. 6.26b). In addition, this modelling implies the partial melting at both garnet- and spinel-facies (~ 1% at garnet-facies, ~ 4% at spinel-facies) and a mixing proportion in favour of garnet melt (Fig. 6.26b). The REE contents (Figs. 6.15, 6.16) of the Group 3 rocks clearly indicate residual garnet in the mantle source and a mantle source composition enriched in LREE with respect to the DMM (Workman & Hart, 2005) and the lherzolite ZB2 (Barbero et al., 2020). The REE modelling indicates that the composition of the Group 3 primitive basalt MK499 fits well with the composition of the calculated melt for ~ 1.5% and 4% of partial melting of the S2 source at garnet- and spinel-facies, respectively, with a mixing proportion between garnet- and spinel-melts of 65:35 (Fig. 6.27c). The theoretically calculated mantle source S2 displays HREE similar to the lherzolite ZB2 but is significantly enriched in LREE and MREE by OIB-like chemical components here considered as the enriched mantle EM of Lustrino et al. (2002) (Fig. 6.27c). As it is shown in Figure 6.27c, different degrees of partial melting with the same mixing proportions of the melts generated at spinel- and garnet-facies fail to reproduce the geochemical features of the Group 3 primitive basalt.

6.6.4. New definition of the Late Cretaceous tectono-sedimentary and volcanic environment for the western Durkan Complex

Data from present-day seamounts and their surrounding aprons have led to the recognition of two main stages of growth of seamounts, namely, the deep-water and the shallow-water shield stages (Staudigel & Schmincke, 1984; Moore & Clague, 1992; Gutierrez et al., 2006; Staudigel & Clague, 2010; Schnur & Gilbert, 2012). The deep-water stage (depths between ~ 2-3 km; Staudigel & Clague, 2010) is characterized by coeval pelagic sedimentation and non-explosive volcanic activity across and onto older oceanic crust and/or its sedimentary cover (Staudigel & Schmincke, 1984). This activity results in sills and dykes intruding the older crust and in a number of small coalescent volcanic reliefs formed by pillow lava flows, and less abundant pillow breccias and volcanoclastic rocks along the relatively slightly inclined flanks. In contrast, the shallow-water shield stage is marked by the seamount growth up to reach, at its summit, the critical depth for drastic increase in exsolution of magmatic volatiles (~ 700 of water-depth or less), which, in turn, results in explosive eruptions and/or subaerial eruptions in seamount emerged above the sea-level (Staudigel & Schmincke, 1984; Moore & Clague, 1992; Gutierrez et al., 2006; Staudigel & Clague, 2010; Schnur & Gilbert, 2012). The changing in the eruption style and the growth of the seamount cause: i) the significant increase of clastic volcanic and volcanoclastic rocks as a consequence of explosive volcanism and ii) the differentiation of seamount summit, seamount flanks, and deep-water apron depositional settings (Staudigel & Schmincke, 1984; Staudigel & Clague, 2010; Saint-Ange et al., 2013). The summit is characterized by shallow-water volcanic facies, such as highly vesicular pillow lava flows, pillow breccias, subaerial lava flows and pyroclastic deposits (Staudigel & Schmincke, 1984), and eventually by carbonatic platform deposits (Moore & Clague, 1992). In contrast, the flanks and their surrounding deep-water apron are mainly characterized by the

deposition of volcanoclastic mass-transport deposits, as response of the steepening of the seamount flanks and the gravitational instability of volcanic debris produced by explosive volcanism (Gutierrez et al., 2006; Saint-Ange et al., 2013; Quartau et al., 2018). In addition, lava flows and intrusions may occur in the flanks because of the downslope emplacement of flows from the summit and/or volcanic activity in minor eruptive centres along the flanks (Staudigel and Schmincke, 1984).

The stratigraphic features of the Type-I succession and their comparison with modern oceanic settings likely suggest that it represents the remnants of the deep-water stages of formation of a seamount (Fig. 6.28a). In fact, Type-I succession records sedimentation and volcanic activity in a deep-water setting below a thick water column. The minor occurrence of pillow breccias and thin volcanoclastic arenites would suggest the fragmentation and gravitational instability of basaltic lava

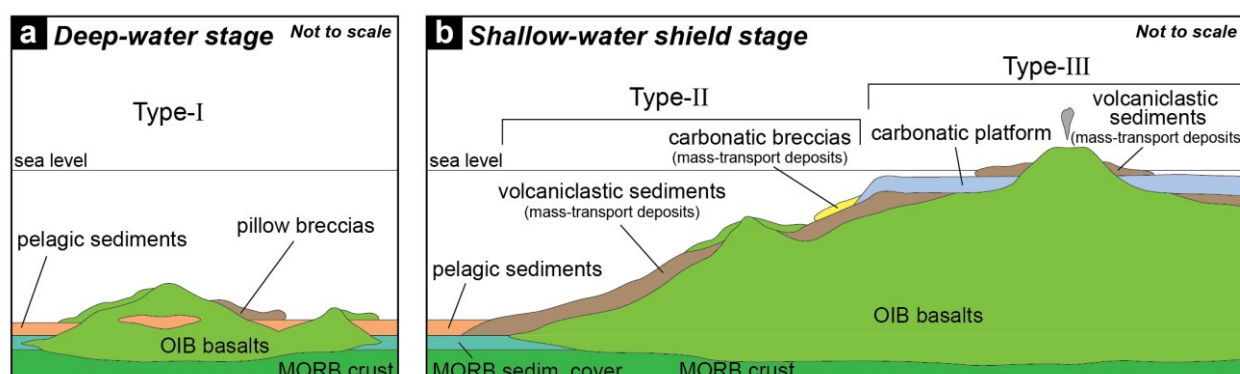


Figure 6.28. Schematic reconstruction of the depositional and eruptive setting of the Cretaceous successions of the western Durkan Complex during the deep-water stage (a) and the shallow-water shield stage (b).

flows along morphological relief(s), which were probably characterized by rather low inclination and little elevation (Fig. 6.28a). These reliefs were likely represented by some, but rather small in elevation, coalescent volcanic cones, which were formed by non-explosive and submarine basaltic volcanic activity (Fig. 6.28a). However, the relatively low abundance of pillow breccias and volcanoclastic arenites and their limited thickness compared to the basaltic lava flows suggest a depositional environment in which the gravity-driven sedimentary processes were subordinate (Fig.

6.28a) that is well comparable with the environment proposed for deep-water stage of growth of modern seamount (Staudigel & Schmincke, 1984).

The stratigraphic characteristics of the Type-II succession are well comparable with those of seamount flank settings forming in the shallow-water shield stage, as indeed observed in modern seamounts, as described above (Fig. 6.28b). In fact, Type-II succession records volcanic activity, pelagic sedimentation, as well as gravity-induced sedimentary processes in relatively deep-water depositional setting. The abundant occurrence of mass-transport deposits indicates that the depositional basin was influenced by morphological relief(s), which, according to the composition of mass-transport deposits, were characterized by heterogeneous volcanic and carbonatic rocks and/or unconsolidated carbonatic sediments (Fig. 6.28b). These reliefs likely corresponded to the flank and summit of the seamount, onto which a great amount of unconsolidated volcanic debris is produced by the explosive magmatism (Fig. 6.28b). In addition, in the seamount summit carbonatic platform sedimentation resulted in the production of carbonatic debris. All these material is prone to be resedimented by gravity flows along the flanks and in the deep-water apron at their base as a consequence of gravitational instability, possibly induced by both volcanic activity and the flanks steepening (Fig. 6.28b).

The stratigraphic features of the Type-III succession are comparable with the sedimentary and volcanic facies observed in seamount summit settings during the shallow-water shield stage (Fig. 6.28b). Indeed, Type-III succession records shallow-water carbonatic platform sedimentation and rather explosive volcanic eruptions under a relatively thin water column (Fig. 6.28b). In addition, the occurrence of volcanoclastic arenites interbedded within the platform sequence suggests the existence of exposed volcanic rocks and their sedimentary remobilization during platform deposition (Fig. 6.28b). During the shallow-water shield stage, the seamount summit is characterized by laterally heterogeneous articulated depositional setting, as response of the interplay

with the rate of the volcanic activity and its later migration, the platform sedimentation, and the erosion of pre-existing volcanic cones (Staudigel & Schmincke, 1984; Gutierrez et al., 2006; Saint-Ange et al., 2013). This, again, agrees with the stratigraphic features of the Type-III succession, which record interplay between volcanic activity, platform sedimentation and remobilization of volcanic debris along exposed volcanic relief (Fig. 6.28b). Finally, the upper part of the Type-III succession is characterized by hemipelagic and pelagic sequences, which stratigraphically rest above the Cenomanian carbonatic platform (Fig. 6.23). This evidence suggests that platform built on top of the seamount summit were progressively drowned, as commonly observed in modern oceanic island settings in response of a combination of several factors (e.g., ceasing volcanic activity, isostatic subsidence, erosion and collapse of seamount/s, global variation of sea level, see Moore & Clague, 1992; Staudigel & Clague, 2010). After their drowning, the seamount summit and flanks were draped by pelagic and hemipelagic deposits with minor intercalation of volcanoclastic arenites, similarly to what is observed in the stratigraphic record of the Type-III succession.

6.6.5. Tectono-magmatic significance of the basalts from the Durkan Complex

The geochemical and mineral chemistry data as well as the petrogenetic modelling presented here (sections 6.5, 6.6 and 6.7.3) suggest that the Durkan Complex is characterized by the association of P-MORB and alkaline basalts, which were formed by the partial melting of an OIB-like mantle source with variable contribution of melts formed at both garnet- and spinel-facies. The generation of basalts with OIB-like trace elements imprint could form in extremely variable tectonic settings and resulting from different processes such as: i) mid-ocean ridges associated to mantle heterogeneity of the asthenospheric sub-oceanic mantle (e.g., Hanan et al., 2000; Saccani et al., 2013b, 2014; Bortolotti et al., 2017; Esmaeili et al., 2019;), ii) oceanic within-plate magmatism

associated to rising of mantle plume or plume-proximal ridges showing interaction between asthenospheric sub-oceanic mantle and rising mantle plume chemical components and material (e.g., [Le Roex et al., 1983](#); [Lapierre et al., 2004](#); [Pearce, 2008](#); [Dilek & Furnes, 2011](#); [Chauvet et al., 2011](#); [Saccani et al., 2013a](#); [Rolland et al., 2020](#)); iii) continental within plate and /or rift-related magmatism showing the contribution from enriched sub-continental lithospheric mantle (e.g., [Robertson, 1998, 2007](#); [Fitton et al., 2000](#); [Mana et al., 2015](#); [Natali et al., 2018](#); [Brombin et al., 2019](#)).

Previous studies have suggested that the Durkan Complex represents the remnants of a continental margin domain tectonically deformed in the Makran Accretionary Prism ([McCall, 1985](#); [Hunziker et al., 2015](#)). However, the data presented in this thesis demonstrate that the Durkan Complex records a Late Cretaceous tectono-sedimentary and volcano-sedimentary evolution, which can be ascribed to the formation and development of seamounts chain. The detailed geochemical data and petrogenetic discussion presented in the section 6.7.3 strongly support the hypothesis that the Durkan Complex represents remnants of this Late Cretaceous seamounts chain. In fact, both the rock assemblages formed in mid-oceanic ridges setting and rift-related continental margins are different from the assemblages observed in the western Durkan Complex. In detail, the basaltic assemblages formed in plume-proximal mid-oceanic ridges and/or mid-oceanic ridges showing mantle heterogeneity of the asthenospheric sub-oceanic mantle are characterized by abundant N-MORB, E-MORB together with variable volumetric abundances of P-MORB and alkaline basalts ([Pearce, 2008](#); [Dilek & Furnes, 2011](#); [Saccani et al., 2013b, 2014](#); [Bortolotti et al., 2017](#); [Esmaeili et al., 2019](#)). Moreover, the continental margin volcanic rocks and continental within-plate magmatism are generally influenced by chemical components (e.g., Th, U, different partitioning between Th and Nb) derived from their interaction and contamination with the continental crust and/or with the lithospheric sub-continental mantle, which might bear inherited subduction-related

chemical components (see [Pearce, 2008](#) and reference therein). These features are never observed in the basalts of the Durkan Complex ([Figs. 6.17, 6.25b, 6.25c](#)). Further constraints on the interpretation of the Durkan Complex as a tectonically disrupted seamounts chain can be derived from the regional-scale evolution of the northern part of the Neo-Tethys realm during the Late Cretaceous (see section 6.7.2 for detailed discussion). In brief, Cretaceous alkaline and OIB rocks comparable with those of the Durkan complex found within the Neo-Tethys-related collisional belts from Armenia to Himalaya have been interpreted as remnants of seamounts and/or oceanic plateau associated with mantle-plume ([Rolland et al., 2010](#); [Saccani et al., 2013a](#); [Saccani et al., 2018](#); [Esmaeili et al., 2019](#); [Rolland et al., 2020](#)).

For these reasons and following the tectono-stratigraphic setting proposed in Section 6.7.4, a tectono-magmatic model is presented in [Figure 6.29](#) to schematically show the possible petrogenetic processes occurred during the formation of the Durkan seamounts chain. The Type-II and -III successions record the remnants of seamount slope and seamount summit depositional settings, respectively, and they were formed during the Cenomanian in the shallow-water stage of growth of a seamount ([Fig. 6.29a](#); see also [Fig. 6.28](#)). These types of successions are characterized by alkaline basalts of Group 2 and 3, whose geochemistry and melt petrogenesis (see Sections 6.7.3.2, 6.7.3.3) clearly indicate that they were derived from low degree of partial melting at both garnet- and facies-spinel of an extremely enriched mantle source S2 modified by OIB-type chemical components prior of the melting events ([Fig. 6.29a](#)). The petrogenetic models also show an increase of the volume percentages of melts formed at garnet-facies from the Group 2 and 3 ([Fig. 6.27](#)). By contrast, the Type-I succession represents the remnants of contemporaneous sedimentation and volcanism in a pelagic setting during Coniacian – early Campanian deep-water stage of growth of a seamount ([Fig. 6.29b](#); see also [Fig. 6.28](#)). This type of succession is mainly characterized by Group 1 rocks and minor Group 2 rocks, whereas Group 3 basalts are totally

lacking. According to the results of petrogenetic models, the deep-water stage of formation of the seamounts was characterized by the partial melting of a mantle region showing composite composition with enriched (S1) and strongly enriched (S2) mantle patches (Fig. 6.29b). These sources underwent low-degree of partial melting at both garnet- and spinel-facies (Fig. 6.29b). The lack of Group 3 rocks and the prevalence of Group 1 rocks likely suggest a relatively shallower melting during the deep-water stages with respect to the shallow-water stages of the growth of a seamount (Figs. 6.29a, b).

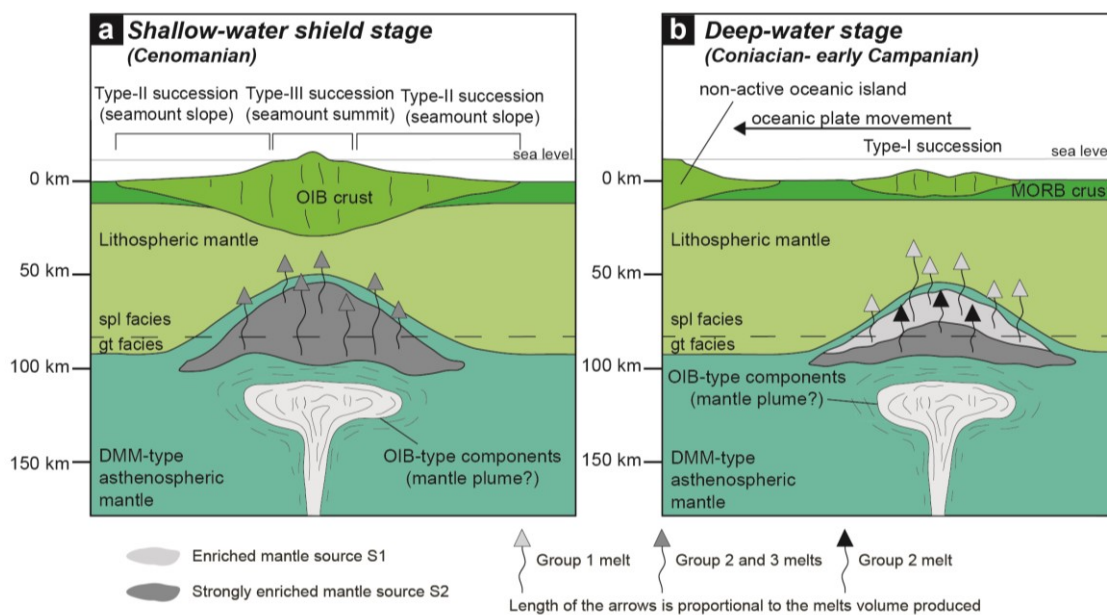


Figure 6.29. Conceptual cartoon showing the petrogenetic processes operating during the shallow-water (a) and deep-water (b) stages of growth of the Durkan seamounts chain. The depositional positions of the different Types of succession within the seamounts chain is from Fig. 6.28. Abbreviations: DMM: depleted MORB mantle; MORB: mid-oceanic ridge basalt; OIB: oceanic island basalt.

These features can be well explained by an oceanic within-plate magmatism, possibly related to the rising of deep and enriched mantle plume material (Figs. 6.29a, b). Indeed, mantle plume are likely the most effective means for transferring anomalous heat flux and enriched chemical components from the lower to the upper mantle (e.g., Regelous et al., 2003; Pearce, 2008; White, 2010; Kerr, 2014; Safonova & Santhos, 2014). The rising of mantle material that is more enriched and hotter than ambient mantle facilitates the starting of the partial melting at deeper level within

the garnet stability field (Figs. 6.29a, b). This can well explain the marked residual garnet geochemical signature shown by all the studied rocks. The presented data seem to suggest that slightly different basalts were produced during the shallow-water and deep-water stages of growth of a seamount (Figs. 6.29a, b). Understanding the processes responsible for the geochemical variation of the erupted basalts during the different stage of growth of the Durkan seamounts chain is extremely difficult. The main problem rises in the fact that the remnants of the Durkan seamounts chain have been severely deformed by multiple deformative events during the incorporation in the Makran Accretionary Prism (see section 6.6.4). However, it is commonly accepted that during the progressive growth of seamounts up to their emergence (i.e., shallow-water shield stage) above the sea level the volcanic product progressively changes from tholeiitic and less enriched rocks to alkaline and more enriched rocks (e.g., Moore & Clague, 1992; Regelous et al., 2003). The chemical variation of seamount basalts may be explained by the combination of several factors including: i) the increasing contribution from an enriched mantle source; ii) the decreasing of the contribution from the DMM-mantle; iii) the decreasing in partial melting degrees; iv) the deepening of the melting conditions (e.g., Regelous et al., 2003; Safonova et al., 2008; White, 2010; Safonova & Santhos, 2014). The clear recognition of the key factors controlling the change in geochemical features of Durkan Complex basalts is difficult to constrain. However, the recognition of Group 2 and 3 basalt within tectono-sedimentary assemblages recording shallow-water shield stage may suggest during this stage higher contributions of melting in garnet-facies and a strongly enriched mantle source (Fig. 6.29a). These features may in part be explained by the deepening of the partial melting region in response of the enhancing of the lithospheric load due to the growing and thickening of the OIB-crust together with a diffuse contribution from extremely enriched mantle source (Fig. 6.29a). By contrast, during deep-water stage the lithospheric load by the OIB-crust is significantly lower as response of a thinner OIB-crust (Fig. 6.29b) and the lower volume of melts

produced. In addition, the metasomatizing effect of the mantle plume is possibly still less diffuse and the mantle source show minor extent of enrichment of OIB-type chemical components (Fig. 6.29b). These effects combined likely result in the preferential partial melting at spinel-facies of a moderately enriched mantle source, though contribution from a strongly enriched mantle source are possible (Fig. 6.29b). This hypothesis agree with data from both modern and ancient seamount assemblages, which point out the importance of the lithospheric thickness in controlling the melting processes in the rising mantle plume (Regelous et al., 2003; Safonova et al., 2008; White, 2010). In detail, a thin lithosphere above a mantle plume cause the shallowing of partial melting combined with higher degree of the partial melting, producing melts less enriched in LREE with respect to M- and HREE. By contrast, higher thickness of lithosphere likely causes the deepening of the partial melting region combined with the decrease of the partial melting degree.

6.6.6. The role of seamount accretion in controlling the physiography and tectonic evolution of the Makran convergent margin

The entering of a seamount in the subduction complex can strongly influence the deformative processes operating in the frontal prism, as well as the anatomy of the whole convergent margin. For instance, it can produce: i) the reducing of the accretion and the enhancing of tectonic erosion of the basal part of the prism (Ranero & Von Huene, 2000; Bangs et al., 2006; Vannucchi et al., 2006; Clarke et al., 2018); ii) significant deformation of the upper plate, causing uplift and shortening of the already formed accretionary prism and the forearc-arc setting (Lallemand & Le Pichon, 1987; Lallemand et al., 1989; Dominguez et al., 1998); iii) the blocking of the subduction zone causing its change in polarity and/or its seaward subduction jump (Kerr, 2014; Rolland et al., 2010; Saccani et al., 2018); iv) gravitational instability of the frontal part of the subduction complex

(e.g., von Huene et al., 2004a, b; Ruh, 2016). In addition, convergence rate is believed to play a significant role in controlling the type and shape of frontal prisms (Clift & Vannucchi, 2004; Malatesta et al., 2013). In detail, slow convergence velocity (< 6 cm/yr) enhances the accretion, whereas high convergence rate (> 6 cm/yr) favour the tectonic erosion processes (Clift & Vannucchi, 2004; Malatesta et al., 2013).

The new data show that the different tectonic slices recognized in the western Durkan Complex represent remnants of the tectonic disruption of Late Cretaceous seamount and/or seamounts chain, which occurred during their incorporation in the Makran Accretionary Prism. In this interpretation, these seamounts were existing at this age in the northern sector of the Neo-Tethys. Here, it is presented a conceptual model for the processes responsible for this tectonic process (Figs. 6.30a, b, c). In the first stage, the accretionary wedge is formed from the accretion of fragments of the subducting oceanic lithosphere and its sedimentary cover, whereas the seamount chain is not yet involved in the deformation front (Fig. 6.30a). This stage was possibly characterized by the prevalence of subduction of oceanic lithosphere rather than accretion at shallow level of the wedge. The entering of the seamount chain in the subduction complex can likely change the deformation style within the frontal prism, enhancing the accretionary processes (Fig. 6.30b). The landward-side of the seamounts chain was accreted at different depth in the accretionary wedge (A in Fig. 6.30b). This process produced the progressive imbrication of several tectonic slices formed by different seamount-related successions (Fig. 6.28 and A, B, C in Fig. 6.30b). However, the entering in the subduction zone of extremely wide and high seamounts can also cause temporary and laterally variable re-organization of the shape and size of the frontal prism and/or collisional-like deformation of the already formed prism and the forearc region (Cloos, 1992). The evidence that part of the Durkan seamount chains was high enough to be covered by shallow-water platform succession suggests that the entering in the prism of the highest part of a seamount chain (B in Fig.

6.30b) can cause a shortening of the whole margin, the imbrication of the previously accreted units,

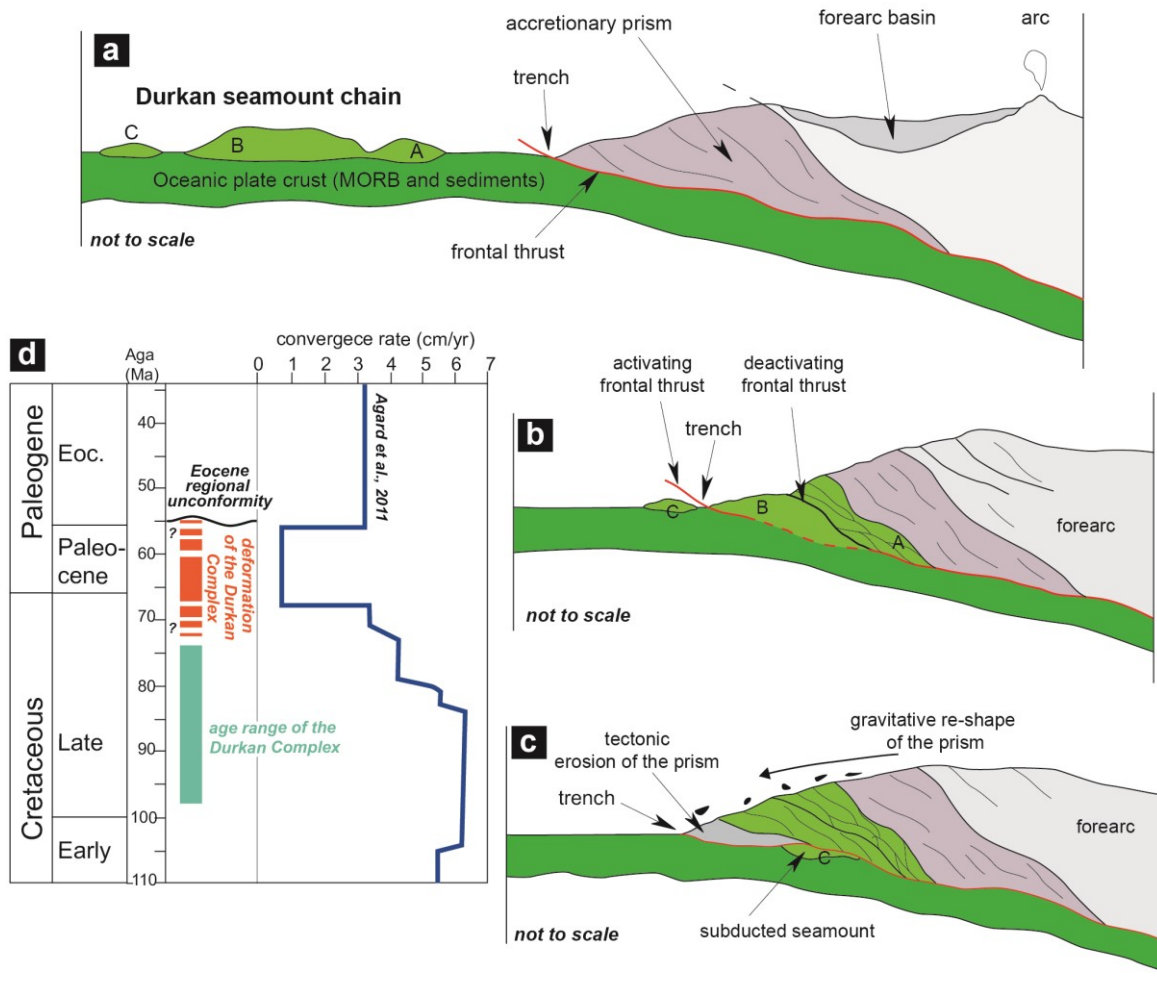


Figure 6.30. Conceptual model for the accretion of the Durkan seamount chain in the Makran Accretionary Prism: a) pre-accretion stage; b) accretion stage (imbrication of the prism); c) post-accretion stage and tectonic erosion of the prism. d) variation of plate convergence rate for the Arabia-Africa and Eurasia during the Late Cretaceous and Early Paleogene (from Agard et al., 2011) and its comparison with time of deformation of the Durkan Complex. Capital letters in panel a), b), and c) indicate different parts of the Durkan seamount chain deformed in different times in the accretionary prism, as discussed in the text.

as well as of the forearc-arc (Fig. 6.30b). Ultimately, these processes led to the growth of the frontal prism above a critical taper angle, which triggered the shift from tectonic accretion to erosion of the prism and related gravitational-induced deformation, in order to maintain its dynamic equilibrium (Figs. 6.30b, c). In fact, tectonic erosion of the prism and gravitational deformation are believed to represent the most effective processes to react to the overgrowth of the frontal prism (von Huene & Lallemand, 1990; von Huene et al., 2004b; Ranero & von Huene, 2000; Marroni & Pandolfi, 2001).

As a consequence, the final stages of the collision of the Durkan seamounts chain and the frontal prism can possibly be characterized by both basal erosion of the already accreted seamount fragments and gravitational instability of the frontal part of the prism (Fig. 6.30c).

Unfortunately, the new data presented together with those already published do not allow to properly constrain the absolute chronology of the described tectonic events. In fact, the age of very low-grade metamorphism is difficult to be constrained by radiometric dating. Similarly, biostratigraphic data are still poor as biostratigraphic marker are in general poorly preserved for the diagenetic recrystallization and low-grade metamorphism. The only available data to propose chronological constraints for the deformation of the Durkan Complex are the youngest age observed in its stratigraphic succession (i.e., late Campanian) and the oldest age of the deposits unconformably lying above it (i.e., early Eocene; Fig. 6.30d). According to these data, the incorporation of the Durkan seamounts chain in the Makran Accretionary Prism most likely occurred from the latest Cretaceous (i.e. Maastrichtian) to Paleocene or earliest Eocene (Fig. 6.30d). The probable age for the collision of the Durkan seamount coincides with a significant variation of the plate convergence rate in the Neo-Tethys realm (Fig. 6.30d). In fact, the late Maastrichtian - early Paleocene time span was characterized by very low convergence rate (< 1 cm/a) between the Arabia and Eurasia plates (Fig. 6.30a; see also Agard et al., 2011; Barrier et al., 2018). In many cases worldwide, the entry of seamounts and/or oceanic plateaux in the subduction zone significantly lowered the plate convergence rate (see Kerr, 2014 for an exhaustive review). Similarly, the lowering of the convergence rate in the Neo-Tethys observed at regional scale at the same time of the Durkan seamount(s) collision (Fig. 6.30d) suggests that this collisional event may have played a major role in controlling the convergence rate and the deformation style at the northern margin of the Neo-Tethys Ocean. Further investigations are however needed to better constrain this hypothesis.

APPENDIX

Appendix Table 6.1. List of samples studied for biostratigraphic analysis and relative coordinates (WGS84)

| limestone and meta-limestone for foraminifera biostratigraphy | | | marls for calcareous nannofossils biostratigraphy | | |
|---|-----------------|-----------------|---|---------------|---------------|
| Sample | Latitude | Longitude | Sample | Latitude | Longitude |
| Zandan transect | | | Manujan transect | | |
| MK822 | 27°15'20.49"N | 57°36'10.20"E | MK464 | 27°20'24.46"N | 57°30'05.11"E |
| MK886 | 27°16'21.29"N | 57°34'51.00"E | MK465 | 27°20'24.18"N | 57°30'05.23"E |
| MK887 | 27°16'23.09"N | 57°35'9.09"E | MK475 | 27°16'37.44"N | 57°38'41.49"E |
| MK888 | 27°16'23.09"N | 57°35'9.09"E | MK476 | 27°16'37.01"N | 57°38'41.47"E |
| MK893 | 27°16'26.41"N | 57°35'4.28"E | MK477 | 27°16'37.17"N | 57°38'41.44"E |
| MK897 | 27°16'26.58"N | 57°35'2.90"E | MK478 | 27°16'37.33"N | 57°38'41.38"E |
| MK897b | 27°16'26.56"N | 57°35'2.90"E | Chah Shahi 1 transect | | |
| MK901 | 27°16'26.66"N | 57°34'59.47"E | MK488 | 27°14'39.56"N | 57°32'11.01"E |
| MK902 | 27°16'27.20"N | 57°34'59.99"E | MK489 | 27°14'42.90"N | 57°32'10.78"E |
| MK903 | 27°16'26.75"N | 57°34'58.70"E | cherts for radiolarian biostratigraphy | | |
| MK904 | 27°16'25.76"N | 57°34'50.34"E | Sample | Latitude | Longitude |
| MK905 | 27°16'26.58"N | 57°34'22.28"E | Manujan transect | | |
| MK906 | 27°16'28.24"N | 57°34'20.86"E | MK363 | 27°20'28.12"N | 57°30'01.23"E |
| Manujan transect | | | MK367 | 27°20'28.19"N | 57°30'01.22"E |
| MK362 | 27° 20' 28.18"N | 57° 30' 01.34"E | MK374 | 27°13'50.66"N | 57°32'08.36"E |
| MK468 | 27° 20' 16.30"N | 57° 29' 56.12"E | MK378 | 27°13'52.34"N | 57°32'29.86"E |
| MK472 | 27° 20' 16.66"N | 57° 29' 56.77"E | MK466 | 27°20'24.20"N | 57°30'05.73"E |
| Chah Shahi 1 transect | | | MK469 | 27°20'16.19"N | 57°29'56.66"E |
| MK849 | 27°14'37.74"N | 57°32'11.71"E | MK471 | 27°20'16.25"N | 57°29'56.72"E |
| MK852 | 27°14'42.47"N | 57°32'10.07"E | Chah Shahi 1 transect | | |
| MK853 | 27°14'38.53"N | 57°32'10.62"E | MK796 | 27°13'51.34"N | 57°32'15.86"E |
| MK854 | 27°14'29.40"N | 57°32'8.40.55"E | Chah Shahi 2 transect | | |
| Chah Shahi 2 transect | | | MK847 | 27°14'31.25"N | 57°32'3.55"E |

Appendix Table 6.2. Calcareous nannofossils taxa with their relative abundances expressed as number of specimens for mm². All taxa are referenced in Young *et al.* (2017).

| Sample | Provenance | Abundance | Preservation | N°/mm ² | | | | | |
|--------|--------------|-----------|--------------|-------------------------------|-------------------------|---------------|--------------------------------|-----------------------|--------------------|
| | | | | <i>Broinsonia parca</i> group | <i>Cyclagelosphaera</i> | <i>Micula</i> | <i>Eprolithus cf. floralis</i> | <i>Thoracosphaera</i> | <i>Watznaueria</i> |
| MK464 | Manujan | Few | Very Poor | 0,5 | 0,5 | 15,5 | 0,5 | 1,0 | 8,0 |
| MK465 | | Few | Very Poor | 0,0 | 0,0 | 5,5 | 0,0 | 0,0 | 7,5 |
| MK488 | Chah Shahi 1 | Barren | | | | | | | |
| MK489 | | Barren | | | | | | | |

Appendix Table 6.3. (1/4) Major (wt.%) and trace (ppm) element composition of representative magmatic rocks from the western Durkan Complex. Abbreviations: bas: basalt; Tra: trachyte; aph: aphyric texture; sbv: sub-volcanic texture; MT-bas: meta-basalt; prh: porphyritic texture; XRF: X-ray fluorescence spectrometry; ICP-MS: inductively coupled plasma-mass spectrometry; n.d.: not detected. Mg# = $100 \times \text{MgO} / (\text{MgO} + \text{FeO})$. $\text{Fe}_2\text{O}_3 = 0.15 \times \text{FeO}$. Normalizing values for REE ratios from Sun & McDonough (1989).

| Geochemistry | Group 1 (P-MORB) | | | | | | | | | | |
|--------------------------------|------------------|------------------|------------------|------------------|------------------|------------------|------------------|------------------|------------------|-----------------|-----------------|
| Sample rock | MK364 aph bas | MK365 aph bas | MK369 aph bas | MK370 aph bas | MK483 sbv bas | MK484 sbv bas | MK485 sbv bas | MK493 sbv bas | MK867 aph bas | MK282 MT-bas | MK338 MT-bas |
| Note | | | | | | | | | | | |
| Succession | Type-I | Type-I | Type-I | Type-I | Type-II | Type-II | Type-II | Type-II | Type-II | Type-I | Type-II |
| <i>XRF analyses:</i> | | | | | | | | | | | |
| SiO ₂ | 53.3 | 51.4 | 43.3 | 51.8 | 47.2 | 44.6 | 47.2 | 47.6 | 49.5 | 52.3 | 50.9 |
| TiO ₂ | 2.29 | 2.27 | 2.19 | 2.27 | 1.64 | 1.68 | 1.90 | 2.01 | 1.69 | 1.20 | 2.24 |
| Al ₂ O ₃ | 16.5 | 14.8 | 15.9 | 16.4 | 15.6 | 16.3 | 17.2 | 16.7 | 14.9 | 12.2 | 13.3 |
| Fe ₂ O ₃ | 1.17 | 1.24 | 1.36 | 1.27 | 1.57 | 1.68 | 1.55 | 1.46 | 1.57 | 1.04 | 1.70 |
| FeO | 7.82 | 8.28 | 9.06 | 8.44 | 10.46 | 11.19 | 10.33 | 9.75 | 10.47 | 6.93 | 11.30 |
| MnO | 0.05 | 0.09 | 0.21 | 0.17 | 0.16 | 0.17 | 0.15 | 0.16 | 0.16 | 0.15 | 0.17 |
| MgO | 4.93 | 5.11 | 10.53 | 5.03 | 7.00 | 8.34 | 5.30 | 5.50 | 9.89 | 11.90 | 6.87 |
| CaO | 4.19 | 6.70 | 6.77 | 5.21 | 8.67 | 7.77 | 8.27 | 9.04 | 4.38 | 9.53 | 7.17 |
| Na ₂ O | 5.32 | 5.78 | 2.20 | 4.05 | 3.04 | 2.71 | 3.21 | 2.70 | 3.88 | 2.28 | 3.65 |
| K ₂ O | 0.97 | 0.81 | 1.28 | 1.40 | 1.59 | 1.11 | 1.54 | 1.28 | 0.18 | 0.09 | 0.97 |
| P ₂ O ₅ | 0.51 | 0.47 | 0.43 | 0.43 | 0.28 | 0.31 | 0.32 | 0.34 | 0.23 | | 0.25 |
| LOI | 2.54 | 2.69 | 6.57 | 3.43 | 2.99 | 3.6 | 2.99 | 3.03 | 2.92 | 2.31 | 1.67 |
| Total | 99.53 | 99.66 | 99.86 | 99.94 | 100.18 | 99.48 | 100.04 | 99.56 | 99.75 | 99.92 | 100.17 |
| Mg# | 52.9 | 52.4 | 67.4 | 51.5 | 54.4 | 57.0 | 47.8 | 50.1 | 62.7 | 75.4 | 52.0 |
| Zn | 202 | 170 | 120 | 118 | 102 | 114 | 107 | 106 | 104 | 60 | 112 |
| Cu | 72 | 59 | 60 | 75 | 123 | 125 | 125 | 125 | 113 | 75 | 105 |
| Sc | 29 | 26 | 35 | 30 | 26 | 25 | 21 | 24 | 34 | 34 | 45 |
| Ga | 17 | 17 | 22 | 19 | 20 | 19 | 23 | 21 | 16 | 12 | 19 |
| Ni | 56 | 47 | 214 | 101 | 66 | 55 | 30 | 32 | 84 | 108 | 28 |
| Co | 57 | 60.5 | 71.4 | 53 | 44.5 | 41.7 | 38.2 | 41.8 | 57.1 | 31.1 | 45.3 |
| Cr | 160 | 143 | 353 | 259 | 153 | 112 | 58 | 51 | 378 | 456 | 79 |
| V | 239 | 230 | 244 | 173 | 244 | 245 | 236 | 227 | 227 | 247 | 292 |
| Ba | 155 | 219 | 290 | 186 | 231 | 184 | 323 | 227 | 120 | 44 | 261 |
| Pb | 12 | 8 | 6 | 7 | 8 | 9 | 8 | 9 | 18 | 10 | 10 |
| <i>ICP-MS analyses:</i> | | | | | | | | | | | |
| Rb | 18.5 | 18.6 | 14.0 | (XRF) 27 | 31.7 | 24.4 | (XRF) 37 | 27.1 | 5.21 | 1.39 | 19.9 |
| Sr | 817 | 669 | 417 | 419 | 258 | 492 | 502 | 499 | 105 | 329 | 278 |
| Y | 30.9 | 26.9 | 33.5 | 25 | 20.8 | 23.8 | 23 | 22.2 | 21.9 | 17.0 | 25.4 |
| Zr | 216 | 164 | 220 | 182 | 134 | 149 | 143 | 164 | 130 | 88.0 | 157 |
| La | 19.1 | 18.2 | 21.4 | 20 | 14.2 | 16.2 | 20 | 16.6 | 15.1 | 8.95 | 20.5 |
| Ce | 38.7 | 34.5 | 44.4 | 48 | 31.6 | 35.8 | 45 | 34.3 | 32.4 | 19.8 | 41.3 |
| Pr | 4.84 | 4.48 | 5.63 | | 4.03 | 4.65 | | 4.52 | 3.98 | 2.60 | 4.90 |
| Nd | 18.6 | 18.2 | 21.9 | 21 | 16.7 | 19.5 | 16 | 18.5 | 15.9 | 10.8 | 18.8 |
| Sm | 4.84 | 4.74 | 5.48 | | 4.33 | 5.48 | | 5.03 | 3.97 | 2.85 | 4.76 |
| Eu | 1.43 | 1.46 | 1.61 | | 1.49 | 1.67 | | 1.68 | 1.12 | 0.834 | 1.46 |
| Gd | 4.41 | 4.21 | 4.86 | | 4.37 | 4.81 | | 4.81 | 4.05 | 2.83 | 4.31 |
| Tb | 0.695 | 0.723 | 0.778 | | 0.703 | 0.792 | | 0.766 | 0.671 | 0.458 | 0.681 |
| Dy | 4.13 | 4.25 | 4.57 | | 3.97 | 4.50 | | 4.32 | 4.06 | 2.71 | 4.06 |
| Ho | 0.854 | 0.870 | 0.941 | | 0.771 | 0.866 | | 0.827 | 0.812 | 0.556 | 0.785 |
| Er | 2.32 | 2.36 | 2.55 | | 1.98 | 2.19 | | 2.06 | 2.11 | 1.54 | 2.05 |
| Tm | 0.333 | 0.342 | 0.366 | | 0.281 | 0.303 | | 0.305 | 0.288 | 0.224 | 0.289 |
| Yb | 2.16 | 2.22 | 2.35 | | 1.75 | 1.93 | | 1.90 | 1.79 | 1.44 | 1.87 |
| Lu | 0.319 | 0.317 | 0.345 | | 0.257 | 0.279 | | 0.273 | 0.258 | 0.204 | 0.274 |
| Nb | 25.1 | 26.2 | 32.6 | 26 | 20.1 | 23.8 | 21 | 20.6 | 17.5 | 13.5 | 25.4 |
| Hf | 5.93 | 3.93 | 6.68 | 4 | 4.29 | 3.68 | 5 | 4.72 | 3.97 | 2.74 | 6.12 |
| Ta | 1.67 | 2.18 | 1.92 | | 1.42 | 1.53 | | 1.29 | 1.37 | 0.916 | 1.62 |
| Th | 3.58 | 2.89 | 3.66 | 3 | 1.76 | 2.21 | 2 | 2.12 | 2.28 | 1.49 | 3.48 |
| U | 0.748 | 1.08 | 0.783 | | 0.641 | 0.489 | | 0.593 | 0.613 | 0.356 | 0.764 |
| Nb/Y | 0.813 | 0.976 | 0.973 | 1.03 | 0.967 | 1.000 | 0.930 | 0.927 | 0.802 | 0.796 | 1.000 |
| Y/Nb | 1.23 | 1.02 | 1.03 | 0.973 | 1.03 | 1.00 | 1.08 | 1.08 | 1.25 | 1.26 | 1.00 |
| Zr/Y | 6.98 | 6.11 | 6.57 | 7.34 | 6.46 | 6.26 | 6.26 | 7.39 | 5.93 | 5.19 | 6.20 |
| Ti/V | 59.1 | 60.9 | 57.9 | 81.5 | 41.5 | 42.9 | 49.9 | 54.9 | 46.3 | 29.8 | 46.7 |
| (La/Sm) _N | 2.55 | 2.48 | 2.52 | | 2.12 | 1.91 | | 2.12 | 2.45 | 2.03 | 2.78 |
| (Sm/Yb) _N | 2.49 | 2.37 | 2.59 | | 2.75 | 3.16 | | 2.94 | 2.46 | 2.19 | 2.83 |
| (La/Yb) _N | 6.35 | 5.90 | 6.53 | | 5.83 | 6.03 | | 6.25 | 6.04 | 4.44 | 7.86 |

Appendix Table 6.3. (2/4)

| Geochemistry | Group 1 (P-MORB) | | Group 2 (Alkaline) | | | | | | | |
|--------------------------------|------------------|---------|--------------------|---------|---------|---------|---------|---------|---------|---------|
| Sample | MK795 | MK797 | MK372 | MK373 | MK375 | MK376 | MK490 | MK870 | MK876 | MK879 |
| rock | Tra | bas | aph bas | aph bas | aph bas | aph bas | sbv bas | prh bas | prh bas | sbv bas |
| Note | | | | | | | | | | |
| Succession | Type-I | Type-I | Type-I | Type-I | Type-I | Type-I | Type-II | Type-II | Type-II | Type-II |
| <i>XRF analyses:</i> | | | | | | | | | | |
| SiO ₂ | 66.9 | 51.1 | 47.6 | 48.2 | 46.3 | 46.2 | 45.1 | 46.5 | 45.6 | 47.9 |
| TiO ₂ | 0.32 | 1.23 | 2.96 | 2.72 | 3.09 | 3.00 | 5.13 | 2.60 | 3.21 | 2.65 |
| Al ₂ O ₃ | 14.7 | 13.9 | 14.2 | 14.3 | 14.5 | 15.0 | 13.9 | 12.6 | 15.9 | 13.2 |
| Fe ₂ O ₃ | 0.75 | 1.12 | 1.51 | 1.39 | 1.71 | 1.58 | 2.02 | 1.72 | 1.70 | 1.68 |
| FeO | 5.02 | 7.48 | 10.04 | 9.30 | 11.43 | 10.54 | 13.44 | 11.47 | 11.33 | 11.22 |
| MnO | 0.05 | 0.20 | 0.19 | 0.13 | 0.13 | 0.15 | 0.14 | 0.14 | 0.15 | 0.13 |
| MgO | 0.02 | 9.07 | 5.89 | 6.35 | 5.31 | 6.84 | 6.12 | 8.54 | 10.59 | 8.57 |
| CaO | 1.39 | 9.20 | 10.45 | 8.47 | 9.82 | 8.20 | 8.27 | 8.60 | 3.24 | 7.92 |
| Na ₂ O | 9.74 | 3.05 | 3.09 | 3.55 | 2.42 | 2.56 | 1.83 | 2.10 | 2.04 | 2.30 |
| K ₂ O | 0.06 | 1.08 | 0.65 | 0.38 | 0.56 | 1.34 | 0.89 | 0.24 | 1.54 | 0.94 |
| P ₂ O ₅ | 0.09 | 0.24 | 0.33 | 0.35 | 0.35 | 0.33 | 0.51 | 0.48 | 0.48 | 0.42 |
| LOI | 0.57 | 1.97823 | 2.80 | 4.27 | 4.10 | 3.88 | 2.04 | 4.91 | 4.13 | 3.05 |
| Total | 99.62 | 99.66 | 99.65 | 99.45 | 99.69 | 99.60 | 99.39 | 99.87 | 99.96 | 99.98 |
| Mg# | 0.7 | 68.4 | 51.1 | 54.9 | 45.3 | 53.6 | 44.8 | 57.0 | 62.5 | 57.7 |
| Zn | 133 | 52 | 97 | 105 | 113 | 119 | 148 | 79 | 113 | 54 |
| Cu | 3 | 74 | 38 | 93 | 59 | 112 | 158 | 65 | 24 | 9 |
| Sc | 1 | 31 | 24 | 23 | 31 | 32 | 34 | 29 | 23 | 27 |
| Ga | 37 | 14 | 20 | 16 | 27 | 23 | 25 | 23 | 24 | 24 |
| Ni | n.d. | 95 | 82 | 51 | 76 | 91 | 99 | 45 | 21 | 39 |
| Co | n.d. | 23.1 | 48 | 42 | 40 | 52 | 55 | 49 | 54 | 44 |
| Cr | 3 | 301 | 110 | 92 | 93 | 101 | 46 | 25 | 29 | 26 |
| V | 21 | 257 | 302 | 268 | 357 | 348 | 518 | 284 | 291 | 297 |
| Ba | 26 | 203 | 122 | 161 | 156 | 255 | 315 | 134 | 212 | 232 |
| Pb | 26 | 8 | 7 | 8 | 7 | 8 | 6 | 10 | 7 | 9 |
| <i>ICP-MS analyses:*</i> | | | | | | | | | | |
| | (XRF) | | (XRF) | | | | | | | |
| Rb | 3.7 | 28.0 | 8.76 | 7.16 | 6.94 | 12.4 | 22 | 13.8 | 20.6 | 19.7 |
| Sr | 80 | 193 | 422 | 318 | 270 | 170 | 701 | 705 | 114 | 1016 |
| Y | 58.0 | 22.6 | 23.1 | 21.2 | 27.9 | 24.0 | 28 | 28.4 | 23.9 | 23.9 |
| Zr | 701 | 73 | 238 | 242 | 223 | 219 | 295 | 259 | 220 | 204 |
| La | 68.9 | 12.0 | 24.7 | 26.6 | 31.6 | 24.2 | 32 | 27.3 | 28.9 | 29.3 |
| Ce | 145.5 | 23.1 | 51 | 58.0 | 64.1 | 50.9 | 75 | 57 | 61.3 | 61.6 |
| Pr | 13.93 | | 6.35 | 6.92 | 7.83 | 6.56 | | 7.17 | 7.31 | 7.95 |
| Nd | 44.0 | 8.0 | 23.9 | 26.2 | 29.0 | 24.8 | 25 | 27.4 | 28.1 | 29.7 |
| Sm | 8.91 | | 6.00 | 6.58 | 6.78 | 6.12 | | 6.82 | 6.76 | 7.60 |
| Eu | 0.97 | | 1.689 | 1.75 | 1.95 | 1.77 | | 2.14 | 2.14 | 2.22 |
| Gd | 7.96 | | 4.68 | 5.37 | 5.69 | 5.16 | | 5.95 | 6.24 | 6.60 |
| Tb | 1.488 | | 0.658 | 0.785 | 0.820 | 0.738 | | 0.841 | 0.903 | 0.981 |
| Dy | 9.45 | | 3.70 | 4.11 | 4.35 | 3.89 | | 4.63 | 4.80 | 5.20 |
| Ho | 2.131 | | 0.679 | 0.720 | 0.814 | 0.720 | | 0.852 | 0.905 | 0.964 |
| Er | 6.71 | | 1.69 | 1.73 | 2.00 | 1.73 | | 2.01 | 2.17 | 2.30 |
| Tm | 1.155 | | 0.238 | 0.232 | 0.272 | 0.239 | | 0.280 | 0.287 | 0.311 |
| Yb | 8.39 | | 1.42 | 1.33 | 1.73 | 1.48 | | 1.60 | 1.61 | 1.80 |
| Lu | 1.334 | | 0.199 | 0.183 | 0.263 | 0.220 | | 0.224 | 0.193 | 0.250 |
| Nb | 102.9 | 20.0 | 29.9 | 33.6 | 35.8 | 32.4 | 44 | 32.7 | 36.5 | 30.3 |
| Hf | 17.87 | 0.70 | 6.38 | 6.71 | 7.14 | 6.56 | 13 | 6.83 | 6.28 | 7.20 |
| Ta | 4.41 | | 2.16 | 2.21 | 2.52 | 2.33 | | 2.12 | 2.53 | 1.92 |
| Th | 12.85 | 2.00 | 4.11 | 3.11 | 4.89 | 4.15 | 6 | 3.20 | 3.49 | 2.69 |
| U | 0.809 | | 0.980 | 0.981 | 1.28 | 1.19 | | 0.685 | 1.07 | 0.752 |
| Nb/Y | 1.774 | 0.885 | 1.30 | 1.59 | 1.28 | 1.35 | 1.57 | 1.15 | 1.52 | 1.27 |
| Y/Nb | 0.56 | 1.13 | 0.772 | 0.629 | 0.781 | 0.743 | 0.636 | 0.869 | 0.656 | 0.790 |
| Zr/Y | 12.10 | 3.21 | 10.3 | 11.4 | 7.98 | 9.12 | 10.5 | 9.09 | 9.18 | 8.53 |
| Ti/V | 94.5 | 29.4 | 60.7 | 64.1 | 54.3 | 53.9 | 61.0 | 57.7 | 69.0 | 55.2 |
| (La/Sm) _N | 4.99 | | 2.66 | 2.61 | 3.01 | 2.55 | | 2.58 | 2.76 | 2.49 |
| (Sm/Yb) _N | 1.18 | | 4.68 | 5.48 | 4.36 | 4.59 | | 4.72 | 4.66 | 4.69 |
| (La/Yb) _N | 5.89 | | 12.4 | 14.3 | 13.1 | 11.7 | | 12.2 | 12.9 | 11.7 |

Appendix Table 6.3. (3/4)

| Geochemistry | Group 2 (Alkaline) | | | | | | | | | | |
|--------------------------------|--------------------|---------|---------|----------|---------|---------|---------|---------|---------|---------|---------|
| Sample | MK491 | MK480 | MK494 | MK479 | MK291 | MK339 | MK340 | MK342 | MK500 | MK506 | MK507 |
| rock | sbv bas | sbv bas | sbv bas | aph bas | MT-bas | MT-bas | MT-bas | MT-bas | aph bas | aph bas | aph bas |
| Note | | | | | | | | | | | |
| Succession | Type-II | Type-II | Type-II | Type-III | Type-II | Type-II | Type-II | Type-II | Type-II | Type-II | Type-II |
| <i>XRF analyses:</i> | | | | | | | | | | | |
| SiO ₂ | 44.3 | 52.8 | 46.9 | 51.7 | 46.4 | 66.8 | 41.9 | 45.4 | 42.0 | 46.4 | 45.7 |
| TiO ₂ | 2.25 | 2.04 | 3.34 | 3.06 | 2.91 | 0.05 | 2.03 | 3.65 | 2.60 | 3.15 | 2.75 |
| Al ₂ O ₃ | 14.3 | 14.5 | 13.7 | 13.9 | 14.5 | 15.2 | 13.4 | 13.3 | 14.1 | 13.6 | 14.8 |
| Fe ₂ O ₃ | 1.74 | 1.15 | 1.80 | 1.42 | 1.73 | 0.57 | 1.38 | 2.23 | 1.66 | 1.80 | 1.56 |
| FeO | 11.60 | 7.65 | 12.03 | 9.49 | 11.54 | 3.77 | 9.17 | 14.86 | 11.06 | 12.02 | 10.38 |
| MnO | 0.14 | 0.12 | 0.13 | 0.14 | 0.19 | 0.04 | 0.13 | 0.21 | 0.18 | 0.16 | 0.18 |
| MgO | 14.08 | 7.05 | 7.99 | 7.30 | 7.84 | 3.37 | 12.49 | 6.63 | 6.04 | 10.52 | 7.43 |
| CaO | 5.75 | 8.08 | 7.38 | 5.61 | 8.31 | 0.24 | 6.68 | 7.78 | 9.75 | 5.69 | 8.47 |
| Na ₂ O | 1.67 | 5.31 | 2.28 | 2.93 | 3.24 | 8.76 | 1.67 | 2.14 | 2.57 | 2.55 | 2.90 |
| K ₂ O | 0.44 | 0.38 | 1.03 | 0.29 | 0.02 | 0.10 | 0.66 | 0.22 | | 0.03 | 0.03 |
| P ₂ O ₅ | 0.30 | 0.28 | 0.66 | 0.35 | 0.32 | 0.02 | 0.23 | 0.38 | 0.40 | 0.30 | 0.30 |
| LOI | 3.13 | 1.30 | 2.37 | 3.51 | 2.96 | 1.18 | 9.97 | 2.76 | 9.13 | 3.47 | 5.21 |
| Total | 99.76 | 100.61 | 99.56 | 99.71 | 99.92 | 100.07 | 99.70 | 99.51 | 99.55 | 99.70 | 99.68 |
| Mg# | 68.4 | 62.2 | 54.2 | 57.8 | 54.8 | 61.4 | 70.8 | 44.3 | 49.3 | 60.9 | 56.1 |
| Zn | 122 | 39 | 137 | 126 | 141 | 208 | 86 | 167 | 110 | 110 | 119 |
| Cu | 116 | 56 | 91 | 44 | 110 | 5 | 147 | 121 | 71 | 93 | 101 |
| Sc | 27 | 22 | 23 | 27 | 33 | | 47 | 42 | 24 | 33 | 23 |
| Ga | 18 | 12 | 22 | 15 | 24 | 33 | 17 | 24 | 20 | 19 | 19 |
| Ni | 356 | 26 | 46 | 70 | 48 | | 97 | 36 | 59 | 38 | 45 |
| Co | 67 | 30 | 55 | 32 | 35 | | 51 | 50 | 53 | 36 | 39 |
| Cr | 412 | 237 | 19 | 193 | 94 | 40 | 152 | 54 | 65 | 38 | 94 |
| V | 294 | 265 | 310 | 267 | 315 | 42 | 312 | 376 | 318 | 325 | 277 |
| Ba | 204 | 351 | 293 | 135 | 91 | 26 | 202 | 198 | 74 | 95 | 90 |
| Pb | 9 | 10 | 7 | 7 | 8 | 5 | 9 | 8 | 9 | 9 | 10 |
| <i>ICP-MS analyses:*</i> | | | | | | | | | | | |
| Rb | 7.00 | 5.46 | 13.8 | 4.69 | 2.92 | 0.955 | 14.3 | 11 | 1.13 | 1.51 | 2 |
| Sr | 826 | 405 | 866 | 106 | 612 | 17 | 171 | 589 | 1010 | 595 | 588 |
| Y | 21.5 | 23.4 | 28.4 | 18.5 | 25.5 | 69.9 | 19.1 | 33 | 27.0 | 28.9 | 21 |
| Zr | 192 | 162 | 303 | 194 | 212 | 609 | 139 | 251 | 180 | 218 | 206 |
| La | 22.1 | 29.3 | 33.7 | 24.7 | 21.7 | 93.2 | 20.2 | 32 | 24.9 | 24.0 | 18 |
| Ce | 49.5 | 62.2 | 74.7 | 51.3 | 47.9 | 155 | 37.4 | 65 | 49.9 | 53.0 | 51 |
| Pr | 6.16 | 7.32 | 9.60 | 6.40 | 6.13 | 15.3 | 4.50 | | 6.08 | 6.41 | |
| Nd | 24.7 | 29.3 | 37.7 | 24.4 | 24.0 | 50.3 | 16.1 | 26 | 24.4 | 26.2 | 20 |
| Sm | 6.17 | 7.13 | 9.13 | 6.10 | 6.10 | 11.2 | 4.06 | | 5.91 | 6.85 | |
| Eu | 1.75 | 2.06 | 2.68 | 1.48 | 1.78 | 1.40 | 1.16 | | 1.86 | 2.00 | |
| Gd | 5.18 | 5.78 | 8.02 | 5.08 | 5.39 | 11.0 | 3.33 | | 5.68 | 6.12 | |
| Tb | 0.775 | 0.841 | 1.15 | 0.746 | 0.803 | 1.74 | 0.512 | | 0.909 | 0.964 | |
| Dy | 4.18 | 4.58 | 5.84 | 4.10 | 4.38 | 10.3 | 2.80 | | 5.11 | 5.40 | |
| Ho | 0.815 | 0.874 | 1.06 | 0.728 | 0.782 | 1.93 | 0.546 | | 1.01 | 1.04 | |
| Er | 2.00 | 2.22 | 2.46 | 1.81 | 1.90 | 4.88 | 1.41 | | 2.41 | 2.58 | |
| Tm | 0.278 | 0.299 | 0.309 | 0.241 | 0.258 | 0.654 | 0.188 | | 0.332 | 0.330 | |
| Yb | 1.63 | 1.85 | 1.75 | 1.37 | 1.58 | 3.70 | 1.16 | | 1.90 | 1.86 | |
| Lu | 0.252 | 0.278 | 0.249 | 0.188 | 0.210 | 0.477 | 0.158 | | 0.257 | 0.229 | |
| Nb | 30.2 | 40.6 | 42.4 | 26.0 | 30.0 | 165 | 23.6 | 43 | 41.9 | 31.5 | 30 |
| Hf | 5.09 | 4.45 | 7.29 | 6.12 | 5.45 | 16.2 | 3.00 | 6 | 4.18 | 4.72 | 7 |
| Ta | 2.24 | 2.71 | 2.94 | 2.02 | 1.98 | 10.5 | 1.42 | | 2.69 | 2.24 | |
| Th | 2.95 | 3.87 | 3.54 | 3.06 | 3.05 | 21.4 | 2.84 | 6 | 4.20 | 2.62 | 3 |
| U | 0.697 | 0.990 | 1.07 | 0.993 | 0.932 | 5.01 | 0.663 | | 1.33 | 0.869 | |
| Nb/Y | 1.41 | 1.74 | 1.49 | 1.40 | 1.18 | 2.37 | 1.24 | 1.31 | 1.55 | 1.09 | 1.44 |
| Y/Nb | 0.712 | 0.575 | 0.671 | 0.714 | 0.850 | 0.423 | 0.806 | 0.760 | 0.643 | 0.917 | 0.693 |
| Zr/Y | 8.94 | 6.95 | 10.7 | 10.5 | 8.33 | 8.71 | 7.31 | 7.68 | 6.69 | 7.53 | 9.83 |
| Ti/V | 47.6 | 46.4 | 66.6 | 71.3 | 57.0 | 6.94 | 43.5 | 60.1 | 54.2 | 60.6 | 63.1 |
| (La/Sm) _N | 2.31 | 2.66 | 2.38 | 2.62 | 2.30 | 5.39 | 3.21 | | 2.71 | 2.26 | |
| (Sm/Yb) _N | 4.21 | 4.28 | 5.79 | 4.95 | 4.28 | 3.35 | 3.89 | | 3.46 | 4.10 | |
| (La/Yb) _N | 9.74 | 11.4 | 13.8 | 12.9 | 9.84 | | 12.5 | | 9.40 | 9.26 | |

Appendix Table 6.3. (4/4)

| Geochemistry | | Group 3 (Alkaline) | | | | | | | | | |
|--------------------------------|------------------|--------------------|------------------|------------------|------------------|------------------|------------------|------------------|------------------|-----------------|------------------|
| Sample rock Note | MK482 sbv bas | MK496 prh bas | MK497 prh bas | MK499 prh bas | MK855 prh bas | MK859 prh bas | MK860 prh bas | MK894 aph bas | MK907 aph bas | MK910 MT-bas | MK818 aph bas |
| Succession | Type-II | Type-II | Type-II | Type-II | Type-II | Type-II | Type-II | Type-III | Type-III | Type-III | Type-III |
| <i>XRF analyses:</i> | | | | | | | | | | | |
| SiO ₂ | 48.6 | 46.7 | 50.8 | 48.4 | 45.1 | 42.1 | 45.4 | 51.8 | 51.8 | 53.5 | 53.1 |
| TiO ₂ | 3.06 | 3.41 | 2.25 | 1.55 | 3.28 | 3.41 | 3.77 | 3.41 | 4.61 | 3.98 | 3.54 |
| Al ₂ O ₃ | 15.8 | 15.2 | 14.2 | 14.9 | 12.8 | 13.1 | 13.8 | 14.8 | 14.2 | 13.0 | 12.8 |
| Fe ₂ O ₃ | 1.43 | 1.36 | 1.15 | 1.22 | 1.49 | 1.69 | 1.72 | 1.33 | 1.39 | 1.32 | 1.29 |
| FeO | 9.52 | 9.09 | 7.65 | 8.11 | 9.92 | 11.26 | 11.48 | 8.86 | 9.28 | 8.83 | 8.60 |
| MnO | 0.13 | 0.17 | 0.14 | 0.15 | 0.14 | 0.16 | 0.18 | 0.19 | 0.32 | 0.13 | 0.14 |
| MgO | 6.74 | 9.88 | 7.35 | 13.61 | 8.39 | 11.82 | 9.19 | 4.06 | 3.39 | 5.03 | 6.22 |
| CaO | 5.15 | 8.63 | 9.51 | 7.09 | 11.97 | 10.17 | 8.22 | 8.72 | 6.08 | 8.05 | 8.33 |
| Na ₂ O | 2.05 | 2.79 | 4.74 | 2.81 | 1.75 | 0.91 | 1.59 | 4.75 | 5.50 | 3.78 | 3.51 |
| K ₂ O | 3.08 | 0.25 | 0.12 | 0.11 | 1.79 | 1.80 | 2.10 | 0.54 | 1.08 | 0.76 | 0.66 |
| P ₂ O ₅ | 0.78 | 0.55 | 0.27 | 0.20 | 0.54 | 0.40 | 0.60 | 0.79 | 1.10 | 0.49 | 0.46 |
| LOI | 3.05 | 1.62 | 1.93 | 2.06 | 2.66 | 3.14 | 1.76 | 0.43 | 1.11 | 1.10 | 1.04 |
| Total | 99.44 | 99.65 | 100.11 | 100.25 | 99.87 | 99.97 | 99.85 | 99.62 | 99.89 | 99.96 | 99.63 |
| Mg# | 55.8 | 66.0 | 63.2 | 74.9 | 60.1 | 65.2 | 58.8 | 45.0 | 39.4 | 50.4 | 56.3 |
| Zn | 113 | 72 | 39 | 64 | 60 | 90 | 66 | 104 | 97 | 63 | 42 |
| Cu | 61 | 102 | 74 | 89 | 125 | 108 | 44 | 10 | 33 | 55 | 32 |
| Sc | 19 | 20 | 22 | 25 | 24 | 34 | 30 | 12 | 12 | 27 | 27 |
| Ga | 27 | 11 | 10 | 10 | 16 | 19 | 16 | 16 | 13 | 14 | 15 |
| Ni | 71 | 66 | 40 | 285 | 53 | 134 | 113 | | 33 | 28 | 15 |
| Co | 33 | 40 | 37 | 49 | 48 | 63 | 45 | 27 | 37 | 37 | 14 |
| Cr | 68 | 85 | 246 | 959 | 42 | 280 | 270 | 2 | 3 | 97 | 56 |
| V | 290 | 336 | 303 | 228 | 406 | 373 | 408 | 130 | 124 | 311 | 267 |
| Ba | 395 | 610 | 153 | 170 | 267 | 370 | 172 | 421 | 142 | 244 | 173 |
| Pb | 8 | 7 | 10 | 8 | 7 | 9 | 9 | 12 | 10 | 11 | 12 |
| <i>ICP-MS analyses:*</i> | | | | | | | | | | | |
| Rb | 55.8 | (XRF) 6 | 2.80 | 1.70 | (XRF) 36 | 20.7 | (XRF) 39 | 23.8 | 45.9 | (XRF) 16 | 11.0 |
| Sr | 581 | 570 | 204 | 138 | 584 | 591 | 192 | 198 | 128 | 1403 | 1123 |
| Y | 33.8 | 21 | 15.9 | 15.9 | 19 | 18.3 | 21 | 17.3 | 19.3 | 19 | 18.1 |
| Zr | 403 | 313 | 201 | 148 | 320 | 246 | 325 | 306 | 398 | 293 | 274 |
| La | 59.2 | 59 | 31.9 | 27.3 | 45.0 | 45.5 | 39 | 35.8 | 50.7 | 54 | 44.6 |
| Ce | 119 | 129 | 64.4 | 53.7 | 119 | 94.4 | 111 | 68.9 | 84.8 | 114 | 90.6 |
| Pr | 14.5 | | 7.58 | 5.99 | | 11.0 | | 8.41 | 8.72 | | 10.3 |
| Nd | 53.0 | 31 | 27.5 | 21.4 | 39 | 41.8 | 42 | 34.3 | 28.8 | 29 | 39.2 |
| Sm | 12.0 | | 6.69 | 4.63 | | 8.75 | | 8.24 | 7.05 | | 8.37 |
| Eu | 3.02 | | 1.92 | 1.19 | | 2.26 | | 2.33 | 1.81 | | 2.19 |
| Gd | 9.60 | | 5.21 | 3.62 | | 5.61 | | 5.65 | 4.68 | | 5.62 |
| Tb | 1.35 | | 0.722 | 0.516 | | 0.765 | | 0.774 | 0.651 | | 0.796 |
| Dy | 6.85 | | 3.73 | 3.03 | | 3.90 | | 3.70 | 3.37 | | 4.08 |
| Ho | 1.28 | | 0.681 | 0.572 | | 0.711 | | 0.624 | 0.620 | | 0.733 |
| Er | 3.07 | | 1.73 | 1.44 | | 1.57 | | 1.44 | 1.55 | | 1.73 |
| Tm | 0.402 | | 0.230 | 0.200 | | 0.212 | | 0.200 | 0.218 | | 0.235 |
| Yb | 2.34 | | 1.38 | 1.24 | | 1.16 | | 1.20 | 1.39 | | 1.40 |
| Lu | 0.336 | | 0.193 | 0.186 | | 0.159 | | 0.161 | 0.200 | | 0.208 |
| Nb | 71.8 | 67 | 36.5 | 39.2 | 58 | 57.9 | 54 | 40.3 | 57.1 | 52 | 44.0 |
| Hf | 11.4 | 8 | 6.00 | 4.48 | 8 | 8.66 | 6 | 7.33 | 8.71 | 14 | 6.50 |
| Ta | 5.13 | | 2.76 | 2.66 | | 4.39 | | 2.93 | 5.03 | | 3.01 |
| Th | 8.74 | 6 | 4.05 | 4.46 | 5 | 7.33 | 8 | 3.77 | 6.75 | 5 | 5.50 |
| U | 2.00 | | 1.31 | 1.23 | | 2.17 | | 1.20 | 1.76 | | 0.969 |
| Nb/Y | 2.13 | 3.13 | 2.29 | 2.47 | 3.02 | 3.16 | 2.60 | 2.33 | 2.96 | 2.68 | 2.43 |
| Y/Nb | 0.470 | 0.319 | 0.436 | 0.406 | 0.331 | 0.317 | 0.385 | 0.430 | 0.338 | 0.373 | 0.412 |
| Zr/Y | 11.9 | 14.6 | 12.6 | 9.30 | 16.7 | 13.4 | 15.6 | 17.7 | 20.6 | 15.1 | 15.1 |
| Ti/V | 65.6 | 62.1 | 45.3 | 41.4 | 49.9 | 56.7 | 56.6 | 159 | 225 | 77.7 | 80.7 |
| (La/Sm) _N | 3.17 | | 3.08 | 3.81 | | 3.35 | | 2.81 | 4.64 | | 3.44 |
| (Sm/Yb) _N | 5.72 | | 5.39 | 4.15 | | 8.37 | | 7.66 | 5.65 | | 6.66 |
| (La/Yb) _N | 18.2 | | 16.6 | 15.8 | | 28.1 | | 21.5 | 26.2 | | 22.9 |

Appendix Text 6.1. References for sample preparation and taxa determination in radiolarites

Radiolarites were etched following the method described by:

Dumitrica, P., 1970. Cryptocephalic and cryptothoracic Nassellaria in some Mesozoic deposits of Romania. *Revue Roumaine de Géologie, Géophysique et Géographie (série de Géologie)* 14, 45-124.

Pessagno, E.A., Newport, L.A., 1972. A technique for extracting Radiolaria from radiolarian chert. *Micropaleontology* 18, 231-234.

Baumgartner, P.O., Bjørklund, K.R., Caulet, J.P., De Wever P., Kellogg, D., Labracherie, M., Nakaseko K., Nishimura, A., Schaaf, A., Schimdt-Effing, R., Yao, A., 1981. Eurorad II, 1980. Second European meeting of radiolarian paleontologists: current research on Cenozoic and Mesozoic radiolarians. *Eclogae Geologicae Helveticae* 74, 1027-1061.

De Wever, P., 1982. Radiolaires du Trias et du Lias de la Téthys (Systématique, Stratigraphie). *Société Géologique du Nord* 7, 1-600.

Literature data used for determining the first and last occurrence of the radiolarian taxa we utilized the following papers:

Bak, M., 1996. Cretaceous Radiolaria from Niedzica Succession of the Pieniny Klippen Belt in Polish Carpathians. *Acta Palaeontologica Polonica* 41, (1), 91-110.

Bak, M., 1999. Cretaceous radiolarian zonation in the Polish part of the pienny Klippen Belt (Western carpathians). *Geologica Carpathica* 50 (1), 21-31

Bandini, A.N., Flores, K., Baumgartner, P.O., Jackett, S. J., Denyer, P., 2008. Late Cretaceous and Paleogene Radiolaria from the Nicoya Peninsula, Costa Rica: a tectonostratigraphic application. *Stratigraphy* 5 (1), 3-21.

Bragina, L.G., 2004. Cenomanian-Turonian radiolarians of Northern Turkey and the Crimean Mountains. *Paleontological Journal* 38 (4), 325-456.

Buchs, D. M., Baumgartner, P.O., Baumgartner-Mora, C., Bandini, A.N., Jackett, S.J., Diserens, M.O., Stucki, J., 2009. Late Cretaceous to Miocene seamount accretion and mélange formation in the Osa and Burica Peninsulas (Southern Costa Rica): episodic growth of a convergent margin. In: James, K., Lorente, M. A., Pindell, J. (Eds.), *The Origin and Evolution of the Caribbean Plate*, Geological Society of London Special Publications 328, 411-456.

Danelian, T., 2008. Diversity and biotic changes of Archaeodictyomitrid Radiolaria from the Aptian/Albian transition (OAE1b) of southern Albania. *Micropaleontology* 54 (1), 3-13.

De Wever, P., Grissac, C., Bourdillon-De, C., Beurrier, M., 1988. Radiolaires Sénoniens de la nappe de Samail (Oman). *Revue de Micropaleontologie* 31 (3), 166-179.

Foreman, H.P., 1977. Mesozoic radiolaria from the Atlantic Basin and its borderlands. In: Swain F.M. (Ed.), *Stratigraphic Micropaleontology of the Atlantic Basin and Borderlands*, 305-320.

Hashimoto, H., Ishida, K., Yamasaki, T., Tsujino, Y., Kozai T., 2015. Revised radiolarian zonation of the Upper Cretaceous Izumi inter-arc basin (SW Japan). *Revue de Micropaléontologie* 58, 29-50.

Hollis, C.J., Kimura, K., 2001. A unified radiolarian zonation for the Late Cretaceous and Paleocene of Japan. *Micropaleontology* 47 (3), 235-255.

Ishida, K., Hashimoto, H., 1998. Upper Cretaceous radiolarian biostratigraphy in selected chert-clastic sequences of the North Shimanto Terrane, East Shikoku. *News of Osaka Micropaleontologists Special volume* 1, 211-225.

O'Dogherty, L., Carter, E. S., Dumitrica, P., Goričan, Š., De Wever, P., Bandini, A.N., Baumgartner, P.O., Matsuoka, A., 2009. Catalogue of Mesozoic radiolarian genera. Part 2: Jurassic-Cretaceous. *Geodiversitas* 31 (2), 271-356

O'Dogherty, L., 1994. Biochronology and Paleontology of Mid-Cretaceous radiolarians from Northern Apennines (Italy) and Betic Cordillera (Spain). *Mémoires de Géologie (Lausanne)* 21, 1-413.

O'Dogherty, L., Goričan, S., Gawlick, H.J. 2017. Middle and Late Jurassic radiolarians from the Neotethys suture in the Eastern Alps. *Journal of Paleontology* 91 (1), 25-72.

- Pessagno, E.A. Jr., 1976. Radiolarian zonation and stratigraphy of the Upper Cretaceous portion of the Great Valley Sequence, California Coast Ranges. *Special Publication in Micropaleontology* 2, 1-95.
- Popova-Goll, I., Vishnevskaya V., Baumgartner, P.O., 2005. Upper Cretaceous (Santonian-Campanian) radiolarians from Voronezh Anticline, southwestern Russia. *Micropaleontology* 51 (1), 1-38.
- Riedel, W.R., Sanfilippo, A., 1974. 33. Radiolaria from the southern Indian Ocean, DSDP leg 26. In: Davis, T. A., Luyendyke, B. P. et al. (Eds), *Initial Reports of the Deep Sea Drilling Project*, U. S. Government Printing Office, Washington, 26, 771-783.
- Sanfilippo, A., Riedel, W.R., 1985. Cretaceous Radiolaria. In: Bolli, H. M., Saunders J. B. and Perch-Nielson K. (Eds.), *Plankton Stratigraphy*, Cambridge University Press, 573-630.
- Schaff, A., 1986. Radiolaria from Deep Sea Drilling Project Leg 891. In: Moberly, R., Schlanger. S. O., et al. (Eds.), *Initial Reports of DSDP*, Washington, U.S. Govt. Printing Office 89, 321-326.
- Taketani, Y., 1982. Cretaceous radiolarian biostratigraphy of the Urakawa and Obira areas, Hokkaido. *Science Reports of the Tohoku University* 52 (1-2), 1-75.
- Tekin, U.K., Ural, M., Göncüoğlu, M.C., Arslan, M., Kürüm, S., 2015. Upper Cretaceous Radiolarian ages from an arc-back-arc within the Yüksekova Complex in the southern Neotethys mélange, SE Turkey. *Comptes Rendus Palevol* 14, 73-84.
- Vishnevskaya, V.S., 2001. Jurassic to Cretaceous radiolarian biostratigraphy of Russia. *GEOS*, Moscow, pp. 376.
- Vishnevskaya, V.Y., De Wever, P., 1998. Upper Cretaceous Radiolaria from the Russian Platform (Moscow Basin). *Revue de Micropaleontologie* 41 (3), 235-265.

The names of genera have been updated according to:

- O'Dogherty, L., 1994. Biochronology and Paleontology of Mid-Cretaceous radiolarians from Northern Apennines (Italy) and Betic Cordillera (Spain). *Mémoires de Géologie (Lausanne)* 21, 1-413.
- O'Dogherty, L., Gorican, S., Gawlick, H.J. 2017. Middle and Late Jurassic radiolarians from the Neotethys suture in the Eastern Alps. *Journal of Paleontology* 91 (1), 25-72.

Appendix Table 6.4. (1/3) Representative analyses of clinopyroxene from the basalts forming the Durkan Complex. Atoms per formula units (a.p.f.u.) are calculated on the basis of four cations. The compositions of Fe^{3+} and Fe^{2+} were calculated from the measured total FeO according to Droop (1987); $Mg\# = 100 \times Mg / (Mg + Fe^{2+})$. Abbreviations, Wo: wollastonite; En: enstatite; Fs: ferrosilite.

| Rock geochem. | Group 1 | | | | | | | | | | | | Group 2 | | |
|--------------------------------|---------|-------|--------|-------|--------|-------|---------|-------|--------|-------|-------|-------|---------|--------|--------|
| rock | sbv bas | | | | | | sbv bas | | | | | | sbv bas | | |
| Sample | MK483 | MK483 | MK483 | MK483 | MK483 | MK483 | MK485 | MK485 | MK485 | MK485 | MK485 | MK485 | MK491 | MK491 | MK491 |
| Mineral-site | 2an1 | 2an10 | 3an2 | 4an4 | 5an3 | 5an8 | 2an2 | 2an6 | 1an2 | 4an2 | 5an7 | 6an2 | 1an3 | 3an1 | 3an7 |
| position | r | c | | | r | c | c | r | | | | | c | | r |
| note | | | | | | | | | | | | | | | |
| SiO ₂ | 50.50 | 49.84 | 50.94 | 48.59 | 49.94 | 48.85 | 50.00 | 50.08 | 49.64 | 49.02 | 49.77 | 50.00 | 50.269 | 49.326 | 48.755 |
| TiO ₂ | 1.22 | 0.96 | 1.12 | 1.45 | 1.31 | 1.01 | 0.91 | 1.03 | 1.33 | 1.36 | 1.13 | 0.91 | 1.165 | 1.675 | 1.823 |
| Al ₂ O ₃ | 2.53 | 2.40 | 2.70 | 2.51 | 2.53 | 2.73 | 1.44 | 1.74 | 2.63 | 2.83 | 3.06 | 1.90 | 2.978 | 3.301 | 3.189 |
| Cr ₂ O ₃ | 0.07 | 0.05 | 0.13 | 0.04 | 0.00 | 0.25 | 0.00 | 0.05 | 0.02 | 0.04 | 0.16 | 0.15 | 0.378 | 0.269 | 0.187 |
| FeO | 9.02 | 11.67 | 9.01 | 12.28 | 11.35 | 8.42 | 13.82 | 11.58 | 11.57 | 10.78 | 9.49 | 8.72 | 6.456 | 8.56 | 8.505 |
| Mno | 0.12 | 0.31 | 0.14 | 0.21 | 0.28 | 0.23 | 0.30 | 0.21 | 0.25 | 0.19 | 0.19 | 0.15 | 0.058 | 0.163 | 0.134 |
| MgO | 15.34 | 14.08 | 15.58 | 14.44 | 14.95 | 15.89 | 14.26 | 15.29 | 14.41 | 14.83 | 15.51 | 16.32 | 16.455 | 14.514 | 14.935 |
| CaO | 20.89 | 19.96 | 20.86 | 19.42 | 20.32 | 21.11 | 19.26 | 19.48 | 20.22 | 20.36 | 20.29 | 20.69 | 21.583 | 21.402 | 21.792 |
| Na ₂ O | 0.28 | 0.46 | 0.33 | 0.40 | 0.36 | 0.38 | 0.35 | 0.34 | 0.39 | 0.37 | 0.32 | 0.30 | 0.365 | 0.444 | 0.433 |
| K ₂ O | 0.00 | 0.00 | 0.01 | 0.00 | 0.02 | 0.01 | 0.01 | 0.00 | 0.01 | 0.02 | 0.03 | 0.04 | 0.004 | 0 | 0.003 |
| Totale | 99.95 | 99.73 | 100.81 | 99.33 | 101.07 | 98.88 | 100.36 | 99.80 | 100.46 | 99.80 | 99.94 | 99.17 | 99.711 | 99.654 | 99.756 |
| <i>A.p.f.u.</i> | | | | | | | | | | | | | | | |
| Si | 1.873 | 1.868 | 1.871 | 1.830 | 1.842 | 1.821 | 1.873 | 1.870 | 1.846 | 1.828 | 1.844 | 1.859 | 1.849 | 1.837 | 1.811 |
| Ti | 0.034 | 0.027 | 0.031 | 0.041 | 0.036 | 0.028 | 0.026 | 0.029 | 0.037 | 0.038 | 0.031 | 0.025 | 0.032 | 0.047 | 0.051 |
| Al | 0.110 | 0.106 | 0.117 | 0.111 | 0.110 | 0.120 | 0.064 | 0.076 | 0.115 | 0.125 | 0.134 | 0.083 | 0.129 | 0.145 | 0.140 |
| Cr | 0.002 | 0.001 | 0.004 | 0.001 | 0.000 | 0.007 | 0.000 | 0.001 | 0.001 | 0.001 | 0.005 | 0.004 | 0.011 | 0.008 | 0.005 |
| Fe ³⁺ | 0.095 | 0.136 | 0.100 | 0.175 | 0.159 | 0.202 | 0.165 | 0.150 | 0.145 | 0.170 | 0.135 | 0.166 | 0.124 | 0.112 | 0.163 |
| Fe ²⁺ | 0.185 | 0.230 | 0.176 | 0.212 | 0.191 | 0.060 | 0.268 | 0.212 | 0.215 | 0.166 | 0.159 | 0.105 | 0.074 | 0.155 | 0.101 |
| Mn | 0.004 | 0.010 | 0.004 | 0.007 | 0.009 | 0.007 | 0.009 | 0.007 | 0.008 | 0.006 | 0.006 | 0.005 | 0.002 | 0.005 | 0.004 |
| Mg | 0.848 | 0.787 | 0.853 | 0.810 | 0.822 | 0.883 | 0.796 | 0.851 | 0.799 | 0.824 | 0.857 | 0.905 | 0.902 | 0.806 | 0.827 |
| Ca | 0.830 | 0.801 | 0.820 | 0.783 | 0.803 | 0.843 | 0.773 | 0.779 | 0.806 | 0.814 | 0.805 | 0.824 | 0.850 | 0.854 | 0.867 |
| Na | 0.020 | 0.034 | 0.023 | 0.029 | 0.026 | 0.027 | 0.025 | 0.025 | 0.028 | 0.027 | 0.023 | 0.021 | 0.026 | 0.032 | 0.031 |
| K | 0.000 | 0.000 | 0.000 | 0.000 | 0.001 | 0.000 | 0.001 | 0.000 | 0.000 | 0.001 | 0.001 | 0.002 | 0.000 | 0.000 | 0.000 |
| Totale | 4.000 | 4.000 | 4.000 | 4.000 | 4.000 | 4.000 | 4.000 | 4.000 | 4.000 | 4.000 | 4.000 | 4.000 | 4.000 | 4.000 | 4.000 |
| Al (IV) | 0.110 | 0.106 | 0.117 | 0.111 | 0.110 | 0.120 | 0.064 | 0.076 | 0.115 | 0.125 | 0.134 | 0.083 | 0.129 | 0.145 | 0.140 |
| Al (VI) | 0.000 | 0.000 | 0.000 | 0.000 | 0.000 | 0.000 | 0.000 | 0.000 | 0.000 | 0.000 | 0.000 | 0.000 | 0.000 | 0.000 | 0.000 |
| Wo | 42.0 | 40.3 | 41.6 | 39.0 | 40.1 | 41.8 | 38.1 | 38.6 | 40.4 | 40.7 | 40.7 | 40.8 | 43.0 | 43.6 | 43.6 |
| En | 42.9 | 39.6 | 43.2 | 40.3 | 41.1 | 43.8 | 39.3 | 42.2 | 40.1 | 41.2 | 43.3 | 44.8 | 45.6 | 41.1 | 41.6 |
| Fs | 9.55 | 13.71 | 10.12 | 17.61 | 15.99 | 20.24 | 16.61 | 15.08 | 14.61 | 17.09 | 13.56 | 16.69 | 12.48 | 11.25 | 16.39 |
| Acm | 1.02 | 1.70 | 1.18 | 1.46 | 1.28 | 1.36 | 1.25 | 1.23 | 1.39 | 1.35 | 1.14 | 1.05 | 1.32 | 1.64 | 1.57 |
| Mg# wt% | 0.75 | 0.68 | 0.76 | 0.68 | 0.70 | 0.77 | 0.65 | 0.70 | 0.69 | 0.71 | 0.74 | 0.77 | 0.82 | 0.75 | 0.76 |

Appendix Table 6.4. (2/3)

| Rock geochem. | Group 2 | | | Group 2 | | | | Group 3 | | | | | | | |
|--------------------------------|------------------|---------|--------|---------|---------|--------|--------|---------|--------|---------|--------|---------|--------|--------|--------|
| rock | sbv bas | | | aph bas | | | | prh bas | | | | prh bas | | | |
| Sample | MK491 | MK491 | MK491 | MK479 | MK479 | MK479 | MK479 | MK859 | MK859 | MK859 | MK859 | MK859 | MK859 | MK855 | MK855 |
| Mineral-site | 5an3 | 6an1 | 6an4 | 3an3 | 4an3 | 5an3 | 12an3 | 1an10 | 1an14 | 1an7 | 1an13 | 4an2 | 5an1 | 1an5 | 1an12 |
| position | c | c | r | | | | | c | r1 | r2 | r3 | | | c | r |
| note | | | | | | | | | | | | | | | |
| | profile core-rim | | | | | | | | | | | | | | |
| SiO ₂ | 49.797 | 49.864 | 47.616 | 49.258 | 49.991 | 50.007 | 48.033 | 50.11 | 44.677 | 49.143 | 46.319 | 46.2 | 45.832 | 48.334 | 45.8 |
| TiO ₂ | 1.285 | 1.603 | 1.859 | 1.535 | 1.323 | 1.014 | 2.114 | 1.26 | 3.685 | 2.026 | 2.435 | 2.865 | 3.471 | 1.987 | 3.297 |
| Al ₂ O ₃ | 2.926 | 3.463 | 3.629 | 3.822 | 3.471 | 2.66 | 4.385 | 2.879 | 7.079 | 3.75 | 5.586 | 5.886 | 6.174 | 4.133 | 5.719 |
| Cr ₂ O ₃ | 0.404 | 0.414 | 0.279 | 0.262 | 0.362 | 0.674 | 0.117 | 0.975 | 0 | 0.371 | 0.415 | 0.309 | 0.009 | 0.198 | 0.072 |
| FeO | 6.765 | 7.788 | 8.601 | 6.982 | 6.488 | 5.753 | 7.779 | 4.252 | 7.121 | 5.829 | 6.485 | 6.72 | 7.57 | 5.871 | 8.084 |
| Mno | 0.188 | 0.124 | 0.149 | 0.072 | 0.164 | 0.129 | 0.1 | 0.098 | 0.072 | 0.076 | 0.074 | 0.119 | 0.094 | 0.076 | 0.092 |
| MgO | 16.093 | 15.27 | 14.044 | 15.881 | 16.216 | 16.681 | 14.912 | 16.023 | 12.522 | 15.087 | 13.665 | 13.518 | 12.754 | 14.599 | 13.158 |
| CaO | 21.315 | 21.393 | 21.019 | 21.34 | 22.051 | 22.32 | 22.09 | 23.905 | 23.483 | 23.905 | 24.195 | 24.342 | 23.581 | 24.055 | 22.545 |
| Na ₂ O | 0.407 | 0.499 | 0.498 | 0.329 | 0.352 | 0.368 | 0.339 | 0.315 | 0.558 | 0.381 | 0.393 | 0.441 | 0.462 | 0.361 | 0.663 |
| K ₂ O | 0 | 0 | 0.007 | 0.021 | 0.007 | 0.01 | 0.001 | 0 | 0 | 0 | 0 | 0.001 | 0 | 0 | 0 |
| Totale | 99.18 | 100.418 | 97.701 | 99.502 | 100.425 | 99.616 | 99.87 | 99.817 | 99.197 | 100.568 | 99.567 | 100.401 | 99.947 | 99.614 | 99.43 |
| <i>A.p.f.u.</i> | | | | | | | | | | | | | | | |
| Si | 1.845 | 1.834 | 1.809 | 1.821 | 1.828 | 1.837 | 1.779 | 1.839 | 1.675 | 1.801 | 1.722 | 1.706 | 1.708 | 1.789 | 1.713 |
| Ti | 0.036 | 0.044 | 0.053 | 0.043 | 0.036 | 0.028 | 0.059 | 0.035 | 0.104 | 0.056 | 0.068 | 0.080 | 0.097 | 0.055 | 0.093 |
| Al | 0.128 | 0.150 | 0.163 | 0.166 | 0.150 | 0.115 | 0.191 | 0.125 | 0.313 | 0.162 | 0.245 | 0.256 | 0.271 | 0.180 | 0.252 |
| Cr | 0.012 | 0.012 | 0.008 | 0.008 | 0.010 | 0.020 | 0.003 | 0.028 | 0.000 | 0.011 | 0.012 | 0.009 | 0.000 | 0.006 | 0.002 |
| Fe ³⁺ | 0.128 | 0.117 | 0.141 | 0.124 | 0.138 | 0.161 | 0.155 | 0.121 | 0.171 | 0.141 | 0.192 | 0.196 | 0.150 | 0.151 | 0.183 |
| Fe ²⁺ | 0.081 | 0.123 | 0.132 | 0.092 | 0.061 | 0.016 | 0.086 | 0.009 | 0.052 | 0.037 | 0.010 | 0.011 | 0.085 | 0.031 | 0.070 |
| Mn | 0.006 | 0.004 | 0.005 | 0.002 | 0.005 | 0.004 | 0.003 | 0.003 | 0.002 | 0.002 | 0.002 | 0.004 | 0.003 | 0.002 | 0.003 |
| Mg | 0.889 | 0.837 | 0.796 | 0.875 | 0.884 | 0.914 | 0.823 | 0.877 | 0.700 | 0.824 | 0.757 | 0.744 | 0.709 | 0.806 | 0.733 |
| Ca | 0.846 | 0.843 | 0.856 | 0.845 | 0.864 | 0.879 | 0.876 | 0.940 | 0.943 | 0.939 | 0.964 | 0.963 | 0.942 | 0.954 | 0.903 |
| Na | 0.029 | 0.036 | 0.037 | 0.024 | 0.025 | 0.026 | 0.024 | 0.022 | 0.041 | 0.027 | 0.028 | 0.032 | 0.033 | 0.026 | 0.048 |
| K | 0.000 | 0.000 | 0.000 | 0.001 | 0.000 | 0.000 | 0.000 | 0.000 | 0.000 | 0.000 | 0.000 | 0.000 | 0.000 | 0.000 | 0.000 |
| Totale | 4.000 | 4.000 | 4.000 | 4.000 | 4.000 | 4.000 | 4.000 | 4.000 | 4.000 | 4.000 | 4.000 | 4.000 | 4.000 | 4.000 | 4.000 |
| Al (IV) | 0.128 | 0.150 | 0.163 | 0.166 | 0.150 | 0.115 | 0.191 | 0.125 | 0.313 | 0.162 | 0.245 | 0.256 | 0.271 | 0.180 | 0.252 |
| Al (VI) | 0.000 | 0.000 | 0.000 | 0.000 | 0.000 | 0.000 | 0.000 | 0.000 | 0.000 | 0.000 | 0.000 | 0.000 | 0.000 | 0.000 | 0.000 |
| Wo | 42.9 | 43.1 | 43.6 | 43.1 | 43.8 | 44.0 | 44.6 | 47.7 | 49.5 | 47.7 | 49.4 | 49.5 | 49.1 | 48.5 | 46.6 |
| En | 45.0 | 42.8 | 40.6 | 44.7 | 44.8 | 45.8 | 41.9 | 44.5 | 36.7 | 41.9 | 38.8 | 38.2 | 36.9 | 41.0 | 37.9 |
| Fs | 12.86 | 11.72 | 14.17 | 12.45 | 13.78 | 16.12 | 15.53 | 12.12 | 17.11 | 14.14 | 19.16 | 19.61 | 15.09 | 15.12 | 18.36 |
| Acm | 1.48 | 1.82 | 1.87 | 1.20 | 1.27 | 1.31 | 1.24 | 1.14 | 2.13 | 1.38 | 1.45 | 1.62 | 1.74 | 1.32 | 2.48 |
| Mg# wt% | 0.81 | 0.78 | 0.74 | 0.80 | 0.82 | 0.84 | 0.77 | 0.87 | 0.76 | 0.82 | 0.79 | 0.78 | 0.75 | 0.82 | 0.74 |

Appendix Table 6.4. (3/3)

| Rock geochem. | Group 3 | | | | | | | | |
|--------------------------------|------------------|--------|--------|--------|--------|--------|--------|--------|--------|
| rock | prh bas | | | | MT-bas | | | | |
| Sample | MK855 | MK855 | MK855 | MK855 | MK910 | MK910 | MK910 | MK910 | MK910 |
| Mineral-site | 2an6 | 2an10 | 4an4 | 4an9 | 1an3 | 1an4 | 1an6 | 3an2 | 7an3 |
| position | c | r | r | c | c | e-c | r | | |
| note | profile core-rim | | | | | | | | |
| SiO ₂ | 45.548 | 45.777 | 49.726 | 48.154 | 47.658 | 46.062 | 45.404 | 48.72 | 49.02 |
| TiO ₂ | 2.969 | 3.489 | 1.29 | 2.211 | 1.951 | 2.477 | 3.047 | 1.492 | 1.43 |
| Al ₂ O ₃ | 5.921 | 5.647 | 2.915 | 5.127 | 4.378 | 5.698 | 6.386 | 3.542 | 3.298 |
| Cr ₂ O ₃ | 0.026 | 0.094 | 0.563 | 0.279 | 0.301 | 0.289 | 0.16 | 1 | 0.557 |
| FeO | 6.805 | 8.182 | 4.788 | 6.186 | 6.015 | 7.298 | 7.462 | 5.179 | 5.739 |
| Mno | 0.057 | 0.111 | 0.008 | 0.07 | 0.002 | 0.119 | 0.08 | 0.094 | 0.15 |
| MgO | 13.549 | 13.596 | 16.021 | 13.613 | 14.893 | 14.047 | 13.714 | 15.17 | 15.031 |
| CaO | 23.376 | 21.763 | 23.119 | 23.764 | 23.666 | 22.588 | 22.807 | 23.607 | 23.303 |
| Na ₂ O | 0.595 | 0.39 | 0.359 | 0.407 | 0.281 | 0.463 | 0.467 | 0.379 | 0.549 |
| K ₂ O | 0 | 0.017 | 0 | 0 | 0.009 | 0 | 0.005 | 0.015 | 0.023 |
| Totale | 98.846 | 99.066 | 98.789 | 99.811 | 99.154 | 99.041 | 99.532 | 99.198 | 99.1 |
| <i>A.p.f.u.</i> | | | | | | | | | |
| Si | 1.704 | 1.720 | 1.843 | 1.786 | 1.771 | 1.720 | 1.690 | 1.806 | 1.819 |
| Ti | 0.084 | 0.099 | 0.036 | 0.062 | 0.055 | 0.070 | 0.085 | 0.042 | 0.040 |
| Al | 0.261 | 0.250 | 0.127 | 0.224 | 0.192 | 0.251 | 0.280 | 0.155 | 0.144 |
| Cr | 0.001 | 0.003 | 0.016 | 0.008 | 0.009 | 0.009 | 0.005 | 0.029 | 0.016 |
| Fe ³⁺ | 0.206 | 0.138 | 0.125 | 0.102 | 0.170 | 0.195 | 0.198 | 0.148 | 0.163 |
| Fe ²⁺ | 0.007 | 0.119 | 0.024 | 0.090 | 0.017 | 0.033 | 0.034 | 0.013 | 0.015 |
| Mn | 0.002 | 0.004 | 0.000 | 0.002 | 0.000 | 0.004 | 0.003 | 0.003 | 0.005 |
| Mg | 0.756 | 0.762 | 0.885 | 0.753 | 0.825 | 0.782 | 0.761 | 0.839 | 0.831 |
| Ca | 0.937 | 0.876 | 0.918 | 0.944 | 0.942 | 0.904 | 0.910 | 0.938 | 0.926 |
| Na | 0.043 | 0.028 | 0.026 | 0.029 | 0.020 | 0.034 | 0.034 | 0.027 | 0.039 |
| K | 0.000 | 0.001 | 0.000 | 0.000 | 0.000 | 0.000 | 0.000 | 0.001 | 0.001 |
| Totale | 4.000 | 4.000 | 4.000 | 4.000 | 4.000 | 4.000 | 4.000 | 4.000 | 4.000 |
| Al (IV) | 0.261 | 0.250 | 0.127 | 0.214 | 0.192 | 0.251 | 0.280 | 0.155 | 0.144 |
| Al (VI) | 0.000 | 0.000 | 0.000 | 0.010 | 0.000 | 0.000 | 0.000 | 0.000 | 0.000 |
| Wo | 48.1 | 45.6 | 46.4 | 49.2 | 47.7 | 46.4 | 47.0 | 47.7 | 46.9 |
| En | 38.8 | 39.6 | 44.8 | 39.2 | 41.8 | 40.2 | 39.3 | 42.7 | 42.1 |
| Fs | 20.61 | 13.88 | 12.46 | 10.24 | 17.01 | 19.50 | 19.81 | 14.78 | 16.31 |
| Acm | 2.21 | 1.48 | 1.30 | 1.53 | 1.03 | 1.72 | 1.74 | 1.39 | 2.00 |
| Mg# wt% | 0.78 | 0.75 | 0.86 | 0.80 | 0.82 | 0.77 | 0.77 | 0.84 | 0.82 |

Appendix Table 6.5. Input parameters for the partial melting models used for the different volcanic rock-types from the Durkan Complex.

| Mantle source compositions | | | | | Partial melting parametres | | | | | | | | | |
|----------------------------|-------|-------|--------------|--------------|--|-------|-------|----|-----|------|------|-----|--|--|
| | ZB2* | EM** | Calculate S1 | Calculate S2 | Source mode (Thirlwall et al., 1994) | | | Ol | Opx | Cpx | Sp | Gt | | |
| La | 0.123 | 1.37 | 0.604 | 0.870 | Ol | 0.578 | 0.598 | La | (1) | (1) | (1) | (1) | | |
| Ce | 0.385 | 2.70 | 1.397 | 1.755 | Opx | 0.27 | 0.211 | Ce | (1) | (1) | (1) | (1) | | |
| Pr | 0.076 | 0.273 | 0.189 | 0.223 | Cpx | 0.119 | 0.076 | Pr | (1) | (1) | (1) | (1) | | |
| Nd | 0.448 | 1.33 | 0.873 | 0.966 | Sp | 0.033 | | Nd | (1) | (1) | (1) | (1) | | |
| Sm | 0.166 | 0.396 | 0.287 | 0.305 | Gt | | 0.115 | Sm | (1) | (1) | (1) | (1) | | |
| Eu | 0.069 | 0.128 | 0.102 | 0.104 | Melting mode (Thirlwall et al., 1994) | | | Eu | (1) | (1) | (1) | (1) | | |
| Gd | 0.263 | 0.407 | 0.374 | 0.345 | Ol | 0.1 | 0.05 | Gd | (1) | (1) | (1) | (1) | | |
| Tb | 0.049 | 0.055 | 0.063 | 0.053 | Opx | 0.27 | 0.2 | Tb | (1) | (1) | (1) | (1) | | |
| Dy | 0.344 | 0.329 | 0.435 | 0.340 | Cpx | 0.5 | 0.3 | Dy | (1) | (1) | (1) | (1) | | |
| Ho | 0.077 | 0.056 | 0.091 | 0.077 | Sp | 0.13 | | Ho | (1) | (1) | (1) | (1) | | |
| Er | 0.227 | 0.172 | 0.276 | 0.227 | Gt | | 0.45 | Er | (1) | (1) | (1) | (1) | | |
| Tm | 0.036 | 0.023 | 0.042 | 0.036 | | | | Tm | (1) | (1) | (1) | (1) | | |
| Yb | 0.237 | 0.156 | 0.281 | 0.237 | | | | Yb | (1) | (1) | (1) | (1) | | |
| Lu | 0.035 | 0.023 | 0.044 | 0.035 | | | | Lu | (1) | (1) | (1) | (1) | | |
| Ti | 555 | 950.0 | 750 | 792 | | | | Zr | (1) | (2) | (1) | (3) | | |
| Zr | 4.71 | 14.3 | 11.0 | 14.4 | | | | Nb | (1) | (5) | (6) | (7) | | |
| Nb | 0.202 | 2.00 | 0.852 | 1.64 | | | | Hf | (9) | (10) | (10) | (7) | | |
| Hf | 0.116 | 0.350 | 0.260 | 0.350 | | | | | | | | (8) | | |

1: Fujimaki et al. (1984) 6: Ewart & Griffin (1994)
2: Green et al. (1989) 7: Horn et al. (1994)
3: Klemme et al. (2006) 8: Green et al. (2000)
4: Klemme et al. (2002) 9: Adam & Green (2006)
5: Salters & Longhi (1999) 10: Kennedy et al. (1993)
11: Dunn & Sen (1994)

* Barbero et al. (2020)
** Lustrino et al. (2002)

Chapter 7. The Bajgan Complex

Associated manuscript:

Barbero E., Delavari M., Dolati A., Marroni M., Saccani E., Pandolfi L., Langone A., Tectono-magmatic significance of the Bajgan Complex in the North Makran domain (SE Iran): new constraints for its interpretation as Late Jurassic – Early Cretaceous meta-ophiolitic complex. In preparation

7.1. General field features

The Bajgan Complex is exposed in a triangular area to the north of Manujan (Fig. 7.1). In this area, this complex is bounded by the Sabzevaran Fault to the east and the Rudan Thrust to the south, which corresponds to the prolongation of the Bashakerd Thrust (Fig. 7.1; McCall, 1985). The Sabzevaran Fault corresponds to still active NNE-SSW trending dextral strike-slip faults, whereas the Rudan Thrust is an important km-thick brittle shear zone juxtaposing the Bajgan Complex onto the Sorkhband ultramafic slice and the Coloured Mélange Complex (Delavari et al., 2016).

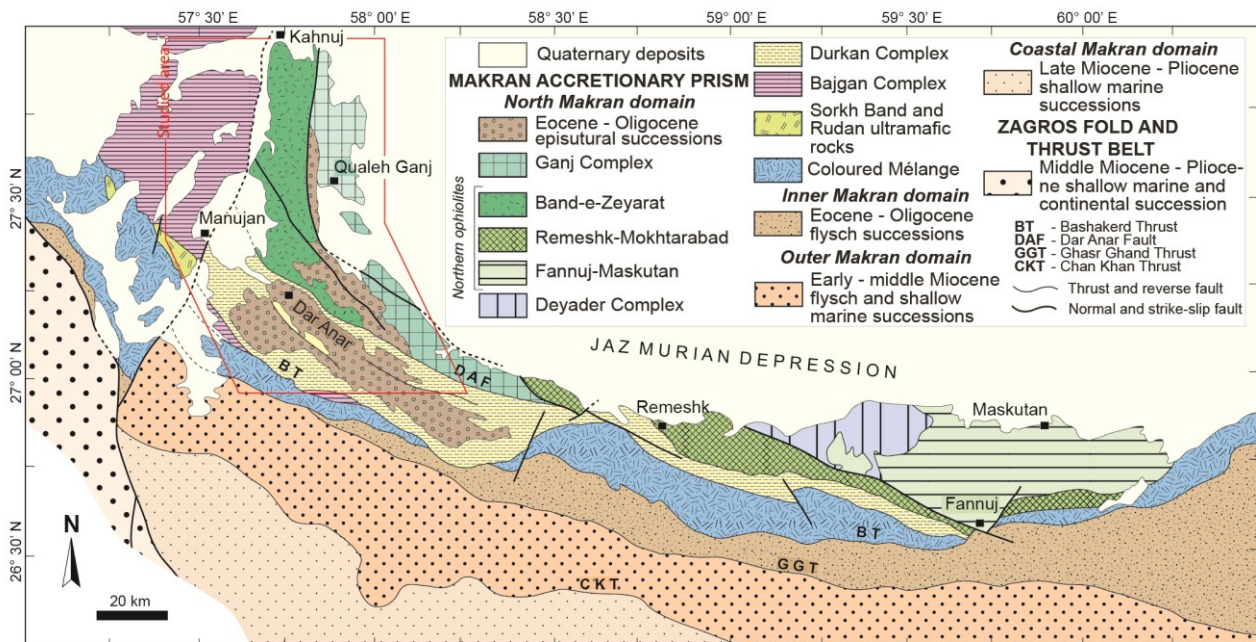


Figure 7.1. Simplified geological map of the North Makran Domain, modified from Eftekhar-Nezhad et al. (1979); Eftekhar-Nejad & McCall (1993); Burg (2018); Samimi Namin (1982, 1983). The box indicates the studied area.

This complex consists of an assemblage of metamorphic rocks aligned along a NW-SE trending main foliation and includes different slices separated by NW-SE trending mylonitic shear zones. The different slices include the same lithotypes the same metamorphic imprint. The main foliation and the shear zones in the Bajgan Complex are cut by swarm of not metamorphosed felsic dykes and covered by continental deposits Quaternary in age. This thesis focused on the general

lithostratigraphy of the Bajgan Complex, the geochemical features of the meta-igneous rocks, and the zircon dating of the magmatic protholits, in order to provide constraints for the tectono-stratigraphic and tectono-magmatic significance and the magmatic formation age of this complex. A detailed study of the structural setting as well as the metamorphic history of this complex will be the topic of future investigations.

7.2. Lithostratigraphy

The Bajgan Complex shows a wide range of metamorphic rocks spanning from meta-serpentinites to meta-igneous and meta-sedimentary rocks.

The meta-serpentinites, mainly located in the NE area of the Bajgan Complex, are represented by huge bodies with massive fabric surrounded by highly foliated zones. In the massive body the meta-serpentinites preserve relics of the primary assemblage represented by pyroxene minerals. Bands of chromitites are also recognized. The foliated meta-serpentinites lack of relics of primary mineral assemblage and the foliation is represented by anastomosed slip surfaces where the serpentine groups minerals are recrystallized.

The meta-igneous rocks are represented by both meta-volcanic and meta-intrusive rocks. The meta-intrusive mainly consists of meta-gabbros characterized by a strong partitioning of the deformation with poorly deformed meta-gabbros alternating with foliated meta-gabbros and mylonitic meta-gabbros. The poorly deformed meta-gabbros shows a well-preserved magmatic fabric with plagioclase and pyroxene as magmatic relics. The meta-gabbros show different grain-size and different mineralogical composition from gabbro, gabbro-norite, melagabbro up to anorthosite. A magmatic layering due to different mineralogical composition and/or different grain size has been also observed. The foliated meta-gabbros are instead characterized by a metamorphic

structure made without relict magmatic structures consisting of layers of green minerals, mainly elongated grains of amphibole, alternating with leucocratic layers consisting of plagioclase. These bands are strongly folded and boudinaged. The only relic of the magmatic minerals is represented by scattered pyroxenes in the green layers. The mylonitic meta-gabbro are fine-grained strongly foliated rocks with rare porphyroclasts of magmatic pyroxene. In association with meta-gabbros, also small stocks of meta-plagiogranites also occur.

The meta-volcanic rocks occur as thick lenticular bodies of banded, well foliated and lineated amphibolite. The bands show different mineralogical composition with amphibole- and plagioclase-rich mm-thick layers. No magmatic relics have been identified in the meta-volcanic rocks.

The meta-sedimentary rocks include meta-volcanoclastites, quartzites, micaschists, paragneisses, calcschists and impure marbles. The meta-volcanoclastites occur as foliated epidote- and albite-rich schists with variable percentage of mica-rich schists. The meta-volcanoclastites occur in association with quartzites, represented by quartz-rich layers alternating with thin layers of well-foliated micaschists. The impure marbles are instead composed of alternating fine-grained marble layers and calcschists layers. Fine- to medium-grained impure massive marbles are also recognized. Probably, at the top of the marbles, thin layers of micaschists occur. The micaschists are the most common lithology and they consist of monotonous thick layers of fine- to medium-grained, well foliated quartz-rich to quartz-free micaschists. The micaschists show a transition to thick layers of fine-grained mica-rich and fine- up coarse-grained, quartz-rich paragneisses.

7.3. Petrography and geochemistry of the meta-volcanic and meta-intrusive rocks

A total of thirty-one samples of metamorphic rocks derived from magmatic protoliths were taken for petrographic and whole-rock geochemical studies with the aim of assessing the

geochemical nature and the tectono-magmatic setting of formation of these rocks. The discussion will be therefore focused on the magmatic processes that can be inferred from these rocks, regardless of the late metamorphic processes that affected the Bajgan Complex rocks.

7.3.1. Petrography

The meta-ultramafic cumulates from the Bajgan Complex display a variety of textures ranging from non-pseudomorphic textures in which the texture of the protolith was totally obliterated by the metamorphic processes to pseudomorphic textures in which relics of the original magmatic textures can still be seen. In contrast, metamorphic processes have resulted in a severe recrystallization, so that it is almost impossible to determine the modal composition of the former peridotite. Most of the samples range in texture from mylonitic to grano-mylonitic and granoblastic with a fine-grained aggregate of chlorite, serpentine, and opaque minerals. In the mylonitic varieties, the opaque minerals are aligned along millimetre-spaced, lens-shaped foliation. In some of these samples, relics of the original cumulitic texture can be seen and consist of rounded, totally serpentinized grains. In a couple of samples showing granoblastic texture, the original cumulitic texture can be recognized because of the occurrence of relicts of cumulus clinopyroxene (sample MK274) or olivine (sample MK305). In these samples, the original intercumulus minerals cannot be recognized as they consist of a fine-grained aggregate of actinolite, tremolite, chlorite and Fe-Ti oxides. However, rare relicts of intercumulus clinopyroxene can still be seen in sample MK305. Sample MK316 shows lepidoblastic ocellar texture with layers of chlorite, serpentine, and opaque minerals surrounding augen-shaped aggregates of tremolite. Sample MK323 is represented by a talc schist with nematoblastic decussate texture. The mineral assemblage consists of talc, tremolite and rare chlorite in interstitial position. Finally, sample MK318 shows a mylonitic texture and, as

an exception with respect to the other samples, display a well-preserved original paragenesis, consisting of olivine and minor red-brown spinel. Olivine occurs as both coarse-grained lenses showing bookshelf texture and as fine-grained minerals aligned along the direction of shear. The occurrence of > 95 olivine in this rock points out for a cumulitic dunite protolith. In general, the textural evidence suggests that the protoliths of all the Bajgan meta-ultramafic rocks were represented by ultramafic cumulates.

The metaintrusive rocks include meta-anorthosite, metagabbro and metaplagiograntic varieties. The meta-anorthosite variety is represented by sample MK704 in which the main minerals are altered plagioclase, epidote, and minor quartz. This rock clearly shows a cumulitic texture with rounded crystals of plagioclase as the cumulus mineral and minor (ca.10% in volume) very altered and fine-grained intercumulus material in which only scarce apatite and zircon accessory phases can be recognized. Epidote and quartz are randomly scattered throughout the rock. Layers with different sizes of the plagioclase crystals mark the original magmatic layering. Meta-gabbros mainly show lepidoblastic and grano-lepidoblastic textures where the foliation is defined by layers of tremolitic / actinolitic amphibole and chlorite alternating with layers or lenses of albite, quartz and minor epidote. Sample MK254 also show augen-type (lens) texture, where lenses consist of large plagioclase crystal altered in a clay mineral assemblage. In this sample, the magmatic cumulitic texture is locally preserved and is defined by relicts of plagioclase (cumulus) and clinopyroxene (intercumulus) crystals. Clinopyroxene relicts can generally be observed in all meta-gabbros. In the grano-lepidoblastic varieties, foliation is feeble and marked by the alignment of actinolite crystals set in a granoblastic very fine-grained aggregate of chlorite, quartz, and albite. Meta-plagiogrinites are characterized by lepidoblastic augen texture. In sample MK508, the foliation is well developed and defined by muscovite, chlorite, and abundant epidote alternating with lenses of quartz, albite, and garnet. In sample MK701, the foliation is discontinuous and it is

defined by layers of green hornblende, chloritoid, and minor opaque minerals alternating with layers and lenses of quartz and albite. Apatite is a common accessory phase.

The texture of most of the metavolcanic rocks range from lepidoblastic to grano-lepidoblastic, in the lepidoblastic and grano-lepidoblastic varieties the foliation ranges from strong to feeble. In particular, samples showing alkaline affinity (see section 7.3.2 and [Appendix Table 7.1](#)), are represented by amphibolites with marked foliation defined by layers of green hornblende or actinolite and chlorite, and felsic, fine-grained layers of quartz, albite and minor epidote. The other samples showing lepidoblastic and grano-lepidoblastic textures are characterized by comparatively less marked foliation and mainly consist of tremolitic/actinolitic chlorite schist. The mineralogical paragenesis consists of albite + epidote + quartz + chlorite + actinolite/tremolite \pm opaque minerals \pm calcite. A couple of samples (MK254, MK269) show porphyroblastic texture. They are characterized by coarse-grained (2-3 mm) plagioclase porphyroblasts set in a very fine-grained granoblastic assemblage of tremolite, epidote, chlorite, and minor white mica, titanite, and opaque minerals. Sample MK513 exhibits nematoblastic decussate texture mainly defined by actinolite and chlorite crystals. The mineral paragenesis also includes albite, epidote and minor quartz, as well as abundant opaque minerals and leucoxene, as a distinctive feature.

7.3.2. *Geochemistry*

The extensive metamorphic imprint that affected the Bajgan rocks, as revealed by petrographic study, most likely resulted in the mobilization of some large ion lithophile elements (e.g., Rb, Ba, Sr) and most major elements. Instead, some incompatible elements and some transition metals (e.g., Y, Zr, Nb, Ta, Ti, REE, Ni, Co, Cr, V) are considered to be immobile during alteration and metamorphism ([Floyd & Winchester, 1978](#); [Pearce & Norrby, 1979](#)). Thus, the geochemical

characteristics and petrogenetic interpretations of the meta-magmatic rocks will be based on immobile elements.

In following sections, the chemical features of the magmatic protoliths will be discussed, regardless of their stratigraphic position. From a chemical point of view, three types of magmatic protoliths can be recognized. They are: 1) ultramafic cumulates; 2) mafic intrusive, volcanic, and subvolcanic rocks; 3) acidic intrusive rocks. Since the purpose of this section is to use the geochemical features of these rocks for assessing their tectono-magmatic setting of formation, mafic and acidic rocks will be further subdivided into three different chemical types that will be described in detail in the next sections (sections 7.3.2.2, 7.3.2.3, and 7.3.2.4). Unfortunately, the chemistry of ultramafic cumulitic rocks is of little help for interpreting the chemical affinity of their parental magmas, as well as the tectono-magmatic setting of formation. Therefore, these rocks will be described separately (section 7.3.2.1).

7.3.2.1. Ultramafic cumulitic protoliths

Meta-ultramafic cumulitic rocks were basically derived from peridotite and clinopyroxenite protoliths. They are characterized by low abundance of TiO_2 (0.01-0.46 wt%), and Al_2O_3 (1.14-6.29 wt%), whereas MgO contents, though variable in the different rock types, are generally high. In detail, they range from 35.6 to 41.0 wt% in the meta-peridotites and from 20.8 to 30.3 wt% in the meta-pyroxenite. CaO content should be used with caution, as it is very mobile during post-magmatic processes. Nonetheless, it is worth to note that its content is low in meta-peridotites, whereas in meta-pyroxenites it ranges from 11.22 to 12.2 wt%, reflecting the occurrence of clinopyroxene in the magmatic protoliths. Incompatible trace element contents are very low in all rock types (e.g., Zr = 0.17-19 ppm, Y = 0.47-6 ppm, Nb = 0.080-0.379 ppm, and Th = 0.008-0.044

ppm), as also exemplified in the N-MORB normalized incompatible element patterns in [Fig. 7.2a](#). By contrast, compatible elements, such as Cr (651-3488 ppm), Co (40-95 ppm), Ni (1070-2537 ppm), and V (29-265 ppm) show high abundance in all the studied rocks. No significant difference in compatible elements contents can be observed between the meta-peridotites and the meta-pyroxenites. In the chondrite-normalized REE diagram ([Fig. 7.2b](#)), the meta-peridotites show patterns rather depleted in both light REE (LREE) and heavy REE (HREE), with overall abundance lower than 1 time chondrite abundance. Some samples show LREE depleted patterns with respect to HREE whereas in other samples the LREE are slightly enriched with respect to MREE and HREE ([Fig. 7.2b](#)). In addition, most of the samples show Eu negative anomalies, but sample MK273 show positive Eu anomaly ([Fig. 7.2b](#)). The overall geochemical composition and the very depleted REE patterns of the meta-peridotite are compatible with compositions of the magmatic protoliths largely dominated by olivine with subordinate pyroxene and plagioclase. This conclusion is in agreement with the petrographic observation and therefore these rocks likely derived from cumulitic dunite protoliths.

7.3.2.2. Group 1 magmatic protoliths (N-MORB)

The protoliths of Group 1 rocks include basalt, ferrobasalt, troctolite, gabbro, and plagiogranite ([Appendix Table 7.1](#)). All these rocks display a clear sub-alkaline affinity, with Nb/Y ratio < 0.19 ([Fig. 7.3](#)). The meta-anorthosite MK704 shows high SiO₂, Al₂O₃, CaO, Na₂O, and Sr contents ([Appendix Table 7.1](#)) and low contents in trace elements, such as Th, Ta, Nb ([Fig. 7.2c](#)). The Chondrite-normalized REE pattern show moderate LREE/MREE and LREE/HREE enrichments (e.g., La_N/Sm_N = 1.93; La_N/Yb_N = 4.67), coupled with rather low HREE contents (e.g., Y_N = 4 times chondrite abundance, [Sun & McDonough, 1989](#)), as well as a marked Eu positive anomaly

(Fig. 7.2d). Due to its cumulitic nature, a definition of the magmatic affinity of this anorthosite cannot

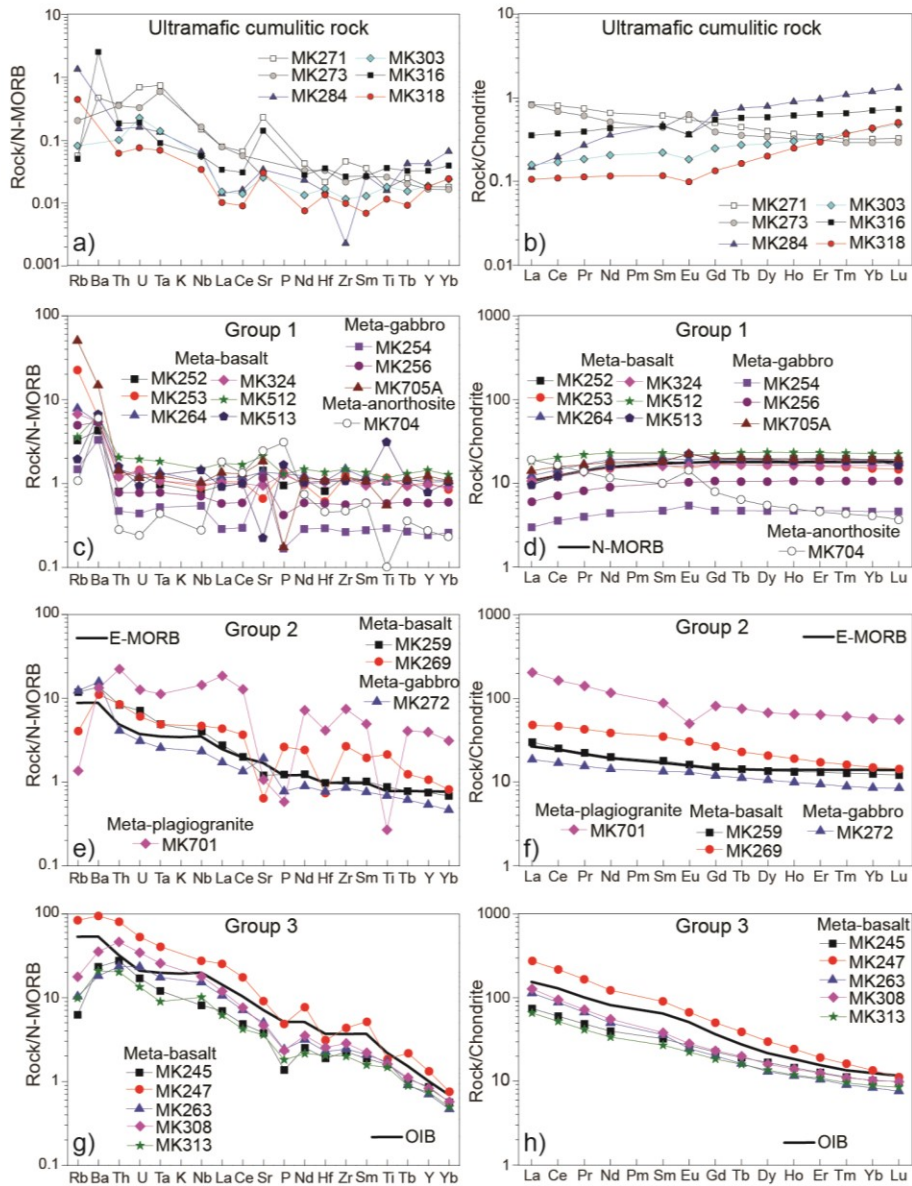


Figure 7.2. N-MORB normalized incompatible element patterns (left column) and chondrite-normalized REE patterns (right column) for meta-ophiolitic rocks from the Bajgan Complex. The compositions of modern normal-type (N-) and enriched-type (E-) mid-ocean ridge basalts (MORB), and alkaline ocean island basalt (OIB), as well as normalizing values are from Sun & McDonough (1989).

be straightforwardly determined. Nonetheless, the LREE/HREE enrichment and Th (0.03 ppm), Ta (0.06 ppm), and Nb (0.65 ppm) contents are very low compared to those of anorthosites derived from enriched-type magmas ($La_N/Yb_N = 10 - 35$; Th = 0.2 - 3 ppm; Ta = 0.15 – 1.4 ppm; Nb = 1.7

– 14.1 ppm; Mukherjee et al., 2005; Ghose et al., 2008; Shellnutt et al., 2020). The marked depletion of these elements suggests that the magmatic protolith of this meta-anorthosite was most likely formed from a depleted N-MORB type parental liquid. In addition, the (Th/Tb)/(Th/Ta) ratio (i.e., ratio of hygromagmatophile elements ratios) is 0.24, which is in the range of variation for Group 1 metagabbros and metabasalts (0.18 – 0.26), whereas it is much lower than those of anorthosites derived from enriched-type magmas (1.8 – 3.5; Shellnutt et al., 2020).

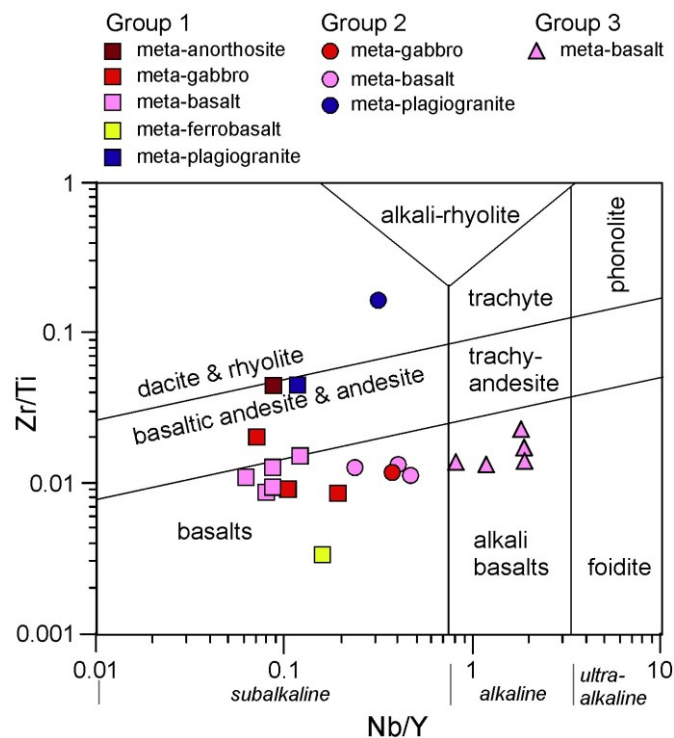


Figure 7.3. Nb/Y vs. Zr/Ti discrimination diagram of Winchester & Floyd (1977) modified by Pearce (1996) for meta-ophiolitic rocks from the Bajgan Complex.

Metagabbros are characterized by high MgO contents (10.9-14.8 wt%) and Mg# (84-69), as well as by high values of incompatible elements (e.g., Cr = 439-1069 ppm). By contrast, they show variable, but generally low abundances of incompatible elements (Appendix Table 7.1). These elements are particularly low in sample MK254 (e.g., TiO₂ = 0.36 wt%, P₂O₅ = 0.02 wt%, Zr=19.3 ppm, Y=6.68pp), which shows relicts of magmatic cumulitic texture, whereas they are comparatively higher in sample MK705A (e.g., TiO₂ = 0.67 wt%, Zr = 85.5 ppm, Y = 34.2ppm),

which is a meta-isotropic gabbro.

Compared to metagabbros, metabasalts show relatively lower MgO (7.88-10.5 wt%), and incompatible elements (e.g., Cr = 118-336 ppm) contents, as well as Mg# (67-54) coupled with generally higher abundance of incompatible elements (e.g., TiO₂ = 1.28-1.44 wt%, P₂O₅ = 0.11-0.15 wt%, Zr = 78.7-109 ppm, Y = 21.8-40.0 ppm; see also [Appendix Table 7.1](#)). The meta-ferrobasalt is characterized by very high TiO₂ (3.85 wt%), FeO_t (16.73 wt%), and V (453 ppm) coupled with low Mg# (54). These values are in agreement with the occurrence of abundant Fe-Ti oxides, as observed in thin sections. The incompatible elements spider diagrams show that Group 1 rocks share affinity with N-MORB basalts and gabbros, as suggested by flat N-MORB normalized patterns ([Fig. 7.2c](#)). High field strength elements (HFSE) contents range from ~0.2 to ~0.6 N-MORB abundance ([Sun & McDonough, 1989](#)) in the meta-cumulitic gabbro, whereas in meta-isotropic gabbros and meta-basaltic rocks they range from ~0.9 to ~1.6 times N-MORB abundance ([Fig. 7.2c](#)). The chondrite-normalized REE patterns further suggest an N-MORB affinity for Group 1 metagabbros and metabasalts. All these rocks show almost parallel patterns characterized by depletion of light REE (L-REE) with respect to medium (M-REE) and heavy (H-REE), with (La/Sm)_N = 0.53 – 0.79 and (La/Yb)_N = 0.51 – 0.81 ([Fig. 7.2d](#)). An N-MORB affinity for Group 1 rocks is further suggested by the discrimination diagram in [Figure 7.4a](#), in which these rocks plot in the field for subduction-unrelated settings, within the compositional field for typical N-MORB ([Saccani, 2015](#)). An N-MORB affinity is also suggested by the co-variation of Zr/Nb and Zr/Y ratios as shown in [Figure 7.4b](#), in which these rock plot in the field for N-MORB compositions.

The meta-plagiogranite is characterized by high SiO₂ content (72.58 wt%) and very low contents of TiO₂, P₂O₅, MgO, Cr, Co, Ni, and many other trace elements ([Appendix Table 7.1](#)). Given the very fractionated nature of this rock, Zr (83 ppm), Y (29 ppm), and Nb (3 ppm) contents are very low, thus suggesting an N-MORB affinity of its magmatic protolith.

7.3.2.3. Group 2 magmatic protoliths (E-MORB)

The protoliths of Group 2 rocks include basalt, gabbro, and plagiogranite ([Appendix Table 7.1](#)). All these rocks display a clear sub-alkaline affinity, with Nb/Y ratio ranging in mafic rocks from 0.24 to 0.37 ([Fig. 7.3](#)). Significantly, these values are intermediate between those of Group 1 and those of Group 3 rocks (see [Fig. 7.3](#) and section 7.3.2).

No significant chemical differences can be observed between the metagabbro MK272 and meta-basalts. The protolith of this meta-gabbro was represented by an isotropic gabbro whose composition was most likely reflecting (or very close to) those of the basaltic liquids. Therefore, the composition of this rock will be described together with those of meta-basalts. Group 2 mafic protoliths rocks show a small range of MgO (7.70- 10.55 wt%) and Mg# (74-63). Though fairly variable, TiO₂ (0.88-1.61 wt%), P₂O₅ (0.09-0.31 wt%), Nb (5.62-11.4 ppm), Y (15.5-30.9 ppm), and Zr (65.3-137 ppm) are generally high. In addition, the content of many trace elements is intermediate between that of Group 1 and that of Group 3 rocks. Compatible elements contents are also variable, depending on the degree of fractionations of the different rocks and they show good positive correlations with MgO contents ([Appendix Table 7.1](#)). The only exception is represented by the meta-gabbro MK272 in which Cr content (752 ppm) is fairly high in relation to the MgO value, possibly reflecting a small amount of Cr-spinel fractionation in the magmatic protolith. N-MORB normalized ([Sun & McDonough, 1989](#)) incompatible elements spider diagram for Group 2 meta-basalts and meta-gabbro show regularly decreasing pattern from Th (Th_N = 4-9) to Yb (Yb_N = 0.55-1.1) ([Fig. 7.2e](#)). These patterns are very similar to that of the typical enriched-type MORB (E-MORB) of [Sun & McDonough \(1989\)](#). Chondrite-normalized REE patterns are characterized by slight LREE enrichment with respect to MREE and HREE ([Fig. 7.2f](#)), as testified by the (La/Sm)_N and (La/Yb)_N ratios that are in the range 1.38-1.67 and 2.18-3.20, respectively. These patterns and

REE ratios are very similar to that of the typical E-MORB (Sun & McDonough, 1989).

In summary, the overall geochemical features of Group 2 meta-gabbro and meta-basalts point out for an E-MORB geochemical affinity of the magmatic protoliths, as also suggested by the diagrams in Figures 7.4a, b, where these rocks plot in the fields of typical E-MORB compositions (Sun & McDonough, 1989; Saccani, 2015).

The meta-plagiogranite is characterized by high SiO₂ content (71.19 wt%) and very low contents of TiO₂, P₂O₅, MgO, Cr, Co, Ni (Appendix Table 7.1). In contrast to the meta-plagiogranite of Group 1, this rock show high values of Y (115 ppm), Zr (374 ppm), Nb (35.1 ppm), Th (2.81 ppm), and Ta (1.56 ppm) at comparable degree of fractionation of the magmatic protoliths. The relatively high content in incompatible elements is exemplified in the N-MORB normalized incompatible elements pattern shown in Fig. 7.2e. Significantly, this pattern is characterized by negative anomalies of Ti and P, which reflect the crystallization of Fe-Ti oxides and apatite from a rather differentiated melt. The crystallization of these minerals is indeed observed in differentiated melt with ferrobasaltic-andesitic compositions in MORB-type magmatic series (e.g., Beccaluva et al., 1983). Though the overall REE content is significantly higher than those of meta-basalts and meta-gabbros, the meta-plagiogranite MK701 displays an REE pattern that is almost parallel to those of the meta-mafic rocks with slight LREE/MREE ($La_N/Sm_N = 2.31$) and LREE/HREE ($La_N/Yb_N = 3.54$) enrichments (Fig. 7.2f). However, this rock is characterized by a significant Eu negative anomaly, which reflect early crystallization and removal of plagioclase from the parental melt. The REE patterns (Fig. 7.2f) and the moderately high Nb, Ta, and Th abundances suggest that the magmatic protolith was formed as a consequence of extreme fractionation from an E-MORB type parental liquid.

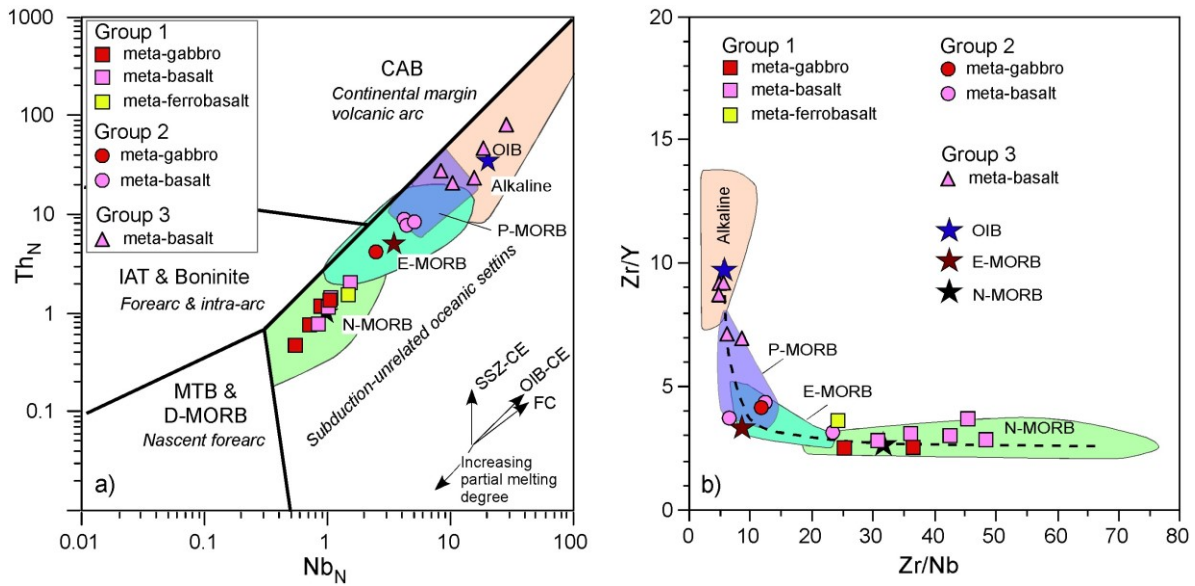


Figure 7.4. a) N-MORB-normalized Th vs. Nb discrimination diagram of [Saccani \(2015\)](#); b) Zr/Y vs. Zr/Nb diagram for meta-ophiolitic rocks from the Bajgan Complex. Abbreviations, MORB: mid-ocean ridge basalt, N-: normal type, E-: enriched type, P-: plume type, D-: depleted type, MTB: medium-Ti basalts, IAT: island arc tholeiite, CAB: calc-alkaline basalt; OIB: alkaline oceanic within-plate basalt, SSZ-CE: supra-subduction zone component enrichment trend, OIB-CE: OIB (plume-type) component enrichment trend, FC: fractional crystallization trend. The compositional variation of different types of volcanic rocks and dykes are also shown for comparison. Data for compositional fields in a) are from [Saccani \(2015\)](#). Fields in b) indicate the compositional variation for different types of basalts from the Zagros belt ophiolites ([Saccani et al., 2013b, 2014](#)); Oman ophiolites ([Chauvet et al., 2011](#); [Lapierre et al., 2004](#)), and Eastern Mediterranean ophiolites ([Saccani et al., 2003](#); [Bortolotti et al., 2004](#); [Chiari et al., 2011](#)). The dashed line in (b) represents the mixing line between OIB and N-MORB. Normalization values, as well as the composition of typical modern N-MORB, EMORB, and OIB (stars) are from [Sun & McDonough \(1989\)](#).

7.3.2.4. Group 3 protoliths (alkaline basalts)

This group includes five amphibolites derived from basaltic protoliths, which show alkaline affinity, as suggested by the high (i.e., > 0.79) Nb/Y ratio ([Appendix Table 7.1, Fig. 7.3](#)). Group 3 basalts display rather homogeneous compositions. MgO contents are in the range 7.30-10.9 wt% and Mg# is generally around 60, with the only exception of sample MK247 (MgO = 7.30 wt%) that has Mg# = 53, likely suggesting a moderately fractionated nature of its magmatic protolith. ([Appendix Table 7.1](#)). TiO₂ (1.84-2.33 wt%) and P₂O₅ (0.16-0.56 wt%) contents are relatively high in agreement with the alkaline affinity of these rocks and generally higher than those of Group 1 and 2 rocks. Similarly, these rocks show higher contents of Nb (19.0 - 65.2 ppm) and Zr (148-324

ppm) compared to the other groups, whereas Y (19.6-37.3 ppm) abundance is comparable with Group 2 rocks. Quite different contents of Cr (66-350 ppm) and Ni (27-141 ppm) are observed in the different rock types (Appendix Table 7.1). The incompatible elements spider diagrams are characterized by marked enrichment in LILE with respect to HFSE and regularly decreasing patterns from Rb to Yb (Fig. 7.2g). Significantly, these patterns are well comparable with those of OIB-type basalts (Sun & McDonough, 1989). The REE patterns are characterized by marked enrichment of LREE with respect to MREE and HREE (Fig. 7.2f), as exemplified by the $(La/Sm)_N$ and $(La/Yb)_N$ ratios that are in the range 2.29-3.33 and 7.24-20.1, respectively. In addition, a distinctive feature of the Group 3 rocks is the high MREE and HREE ratios ($Sm_N/Yb_N = 3.05 - 6.63$). As shown in Figure 7.2h, these features are collectively well comparable with those of the typical OIB of Sun & McDonough (1989). Accordingly, in the tectonic discrimination diagram of Figure 7.4a, the Group 3 rocks plot in the field for subduction-unrelated settings, namely within the compositional field for typical P-MORB and OIB (Saccani, 2015). A similar conclusion can be found out from the Zr/Nb vs. Zr/Y diagram (Fig. 7.4b) in which the rocks of Group 3 plot close to the composition of the typical alkaline OIB (Sun & McDonough, 1989).

7.4. U-Pb geochronology of the meta-intrusive rocks

Large part of the U-Pb data from MK704 and MK701 samples resulted severely discordant. The zircon grains from MK701 sample are generally euhedral and small ($<100\mu m$) with low aspect ratios. They are characterized by large homogeneous core surrounded by a brighter thin rim and rarely a faint oscillatory zoning is recognisable. Inclusions of apatite are common (CL features of: zrc55, 67, 50, 52). Nineteen U-Pb analyses on seventeen zircon grains were collected for the MK701 sample. Only 7 data provided a concordance $<8\%$ (Fig. 7.5) and a weighted average

$^{206}\text{Pb}/^{238}\text{U}$ age of $156\pm 6\text{Ma}$.

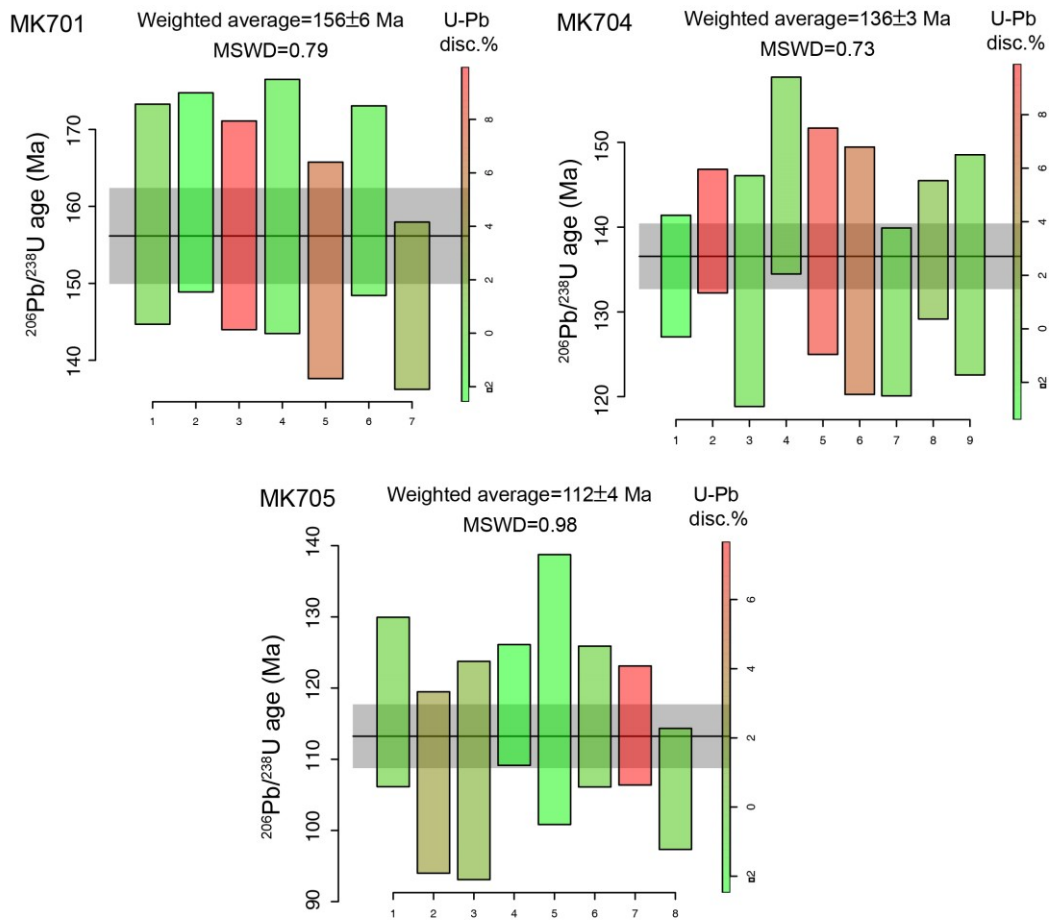


Figure 7.5. $^{206}\text{Pb}/^{238}\text{U}$ age distribution of concordant and sub-concordant (discordance $\leq \pm 10\%$) data. The weighted average age and the relative Mean Square Weighted Deviates (MSWD) are also reported.

The zircon grains from MK704 sample are generally small ($<75\mu\text{m}$) and stubby. They are characterised by darker core surrounded by brighter rims (Zrc 87, 88, 92, 104). Thirteen U-Pb data were collected for U-Pb analyses on fifteen zircon grains were performed for sample MK704. Nine U-Pb ratios with a concordance $<9\%$ provided a weighted average $^{206}\text{Pb}/^{238}\text{U}$ age of $136\pm 3\text{Ma}$ (Fig. 7.5).

The zircon grains from MK705 sample are euhedral, small ($<100\mu\text{m}$) and with low aspect ratios. Oscillatory zoning Zrc78, homogeneous large core (72, 76) 83. They may contain inclusions of apatite. Twelve U-Pb analyses on eleven zircon grains were collected for sample MK705. U-Pb

data showed a concordance better than that observed within other samples, generally <2%, with a weighted average $^{206}\text{Pb}/^{238}\text{U}$ age of eight data at $112\pm 4\text{Ma}$ (Fig. 7.5).

On the whole, the obtained ages range from $156\pm 6\text{Ma}$ to $112\pm 4\text{Ma}$ to, i.e. from Late Jurassic to uppermost Early Cretaceous.

7.5. Discussion

7.5.1. Tectono-magmatic significance

In the previous sections it has been suggested that, in contrast to previous interpretations, the metamorphic rocks of the Bajgan Complex were derived from Cretaceous magmatic protoliths displaying subduction-unrelated oceanic affinity (see Pearce, 2008, Dilek & Furnes, 2011; Saccani, 2015). Some trace-element ratios (e.g. Zr/Nb, Ce/Y, Th/Ta, Th/Tb) are little affected by fractional crystallization of predominantly olivine + clinopyroxene + plagioclase. Therefore, even in the presence of significant amounts of fractionation, they are believed to represent the elemental ratios in the source (e.g. Allègre & Minster, 1978). Ratios of incompatible elements (e.g., Zr/Nb, Th/Ta), ratios of hygromagmatophile element ratios ((Th/Ta)/(Th/Tb)) (Appendix Table 7.1), as well as distinct normalized multi-element and REE patterns (Fig. 7.2) suggest that the different Groups of magmatic protoliths from the Bajgan Complex have been originated from chemically distinct mantle sources. The Group 1 rocks show high Zr/Nb (23.6 -47.9) and (Th/Ta)/(Th/Tb) (3.6-5.6) ratios (Appendix Table 7.1, Fig. 7.4b) suggesting that the Group 1 basaltic protoliths were generated from a depleted-type mantle source. In contrast, Group 3 basaltic protoliths show low Zr/Nb (5.0 - 8.8) and (Th/Ta)/(Th/Tb) (0.2-0.5) ratios, suggesting that they were generated from an enriched-type mantle source (see Saccani et al., 2015, and references therein). The Group 2 mafic

protoliths show Zr/Nb (8.1 - 16.4) and (Th/Ta)/(Th/Tb) (0.80-1.29) ratios, which are generally low but intermediate between those of Group 1 and Group 3 rocks (Appendix Table 7.1, Fig. 7.4b). These elemental ratios suggest that Group 2 mafic rocks are compatible with a genesis from primary magmas originating from oceanic mantle source slightly enriched with respect to N-MORB sources. The Nb-Th co-variation (Fig. 7.4a) and the very low Th/Ta ratios (< 2 , Appendix Table 7.1) displayed by all rock groups indicate that they were originated from sub-oceanic mantle sources, with no influence of subduction-related or continental crust chemical components.

The high and very high LREE/HREE ratios ($La_N/Yb_N = 7.24-20.1$) displayed by the alkaline basalts of the Group 3 rocks (Fig. 7.2h, Appendix Table 7.1) suggest an involvement of a garnet-facies peridotite source. Moreover, the high absolute contents of La ($La_N = 65.5-271.8$) with respect to those of Yb ($Yb_N = 8.4-10.4$) imply a mantle source much more enriched in LREEs than the depleted N-MORB mantle (DMM). The Nb/Yb-Ti/Yb co-variation highlights depth of melting, as the variance of Ti/Yb values is almost entirely depending on garnet residues during melting, whereas the Nb/Yb variation mainly depends on source composition (i.e., depletion vs. enrichment) and melting degree (Pearce, 2008). In addition, according to Pearce (2008) and Saccani (2015), the Th-Nb co-variation (Fig. 7.4a) may be applied to determine whether or not basaltic rocks are truly oceanic, and then the $TiO_2/Yb - Nb/Yb$ diagram (Fig. 7.6) to determine the type of oceanic setting. In fact, on the $TiO_2/Yb - Nb/Yb$ diagram (Fig. 7.6), the Group 3 rocks have higher TiO_2/Yb ratios than MORB reflecting an alkaline OIB composition and deeper melting with involvement of a garnet-bearing mantle source. In addition, the Group 3 rocks show the higher Nb/Yb ratios, which clearly point out for a “plume-type” enriched mantle source. The Group 1 and Group 2 mafic rocks fall within the MORB array suggesting thus shallow melting in the spinel-facies mantle. The Group 2 rocks have Nb/Yb ratios higher than the Group 1 rocks and therefore it is suggested that these rocks were generated from partial melting of an E-MORB type mantle

source. Interestingly, the co-variation of TiO_2/Yb and Nb/Yb ratios of the Group 2 rocks reflects plume–ridge interaction (Fig. 7.6). In fact, Figure 7.4b shows that the Group 2 compositions conform extremely well to the mixing curve calculated using the OIB and N-MORB end-members. Such mixing relationships are consistent with either magma mixing or source region mixing (or eventually, a combination of both). Finally, the TiO_2/Yb and Nb/Yb ratios of the Group 1 rocks suggest a genesis from a depleted N-MORB type mantle source without any influence of plume-type chemical components (Fig. 7.6).

It has been demonstrated that different oceanic settings are characterized by distinct mantle source compositions, as well as distinctive petrogenetic processes (i.e., partial melting degrees, type and depth of melting, etc.) (see Pearce, 1983, 2008). In order to better constrain the type of oceanic setting in which the different Bajgan rocks were generated, non-modal, batch partial melting models have been performed (Fig. 7.7). In these models, plots of LREE/HREE (i.e. La/Yb) vs. MREE/HREE (i.e. Dy/Yb) ratios (Fig. 7.7a) and plots of Th vs. Nb/Yb ratio (Fig. 7.7b) are used. These plots are particularly useful for distinguishing between melting in the spinel and garnet stability fields (e.g., Thirlwall et al., 1994), whereas the abundance of Th and Nb (Fig. 7.7b) is particularly useful for evaluating the enrichment of the source (Saccani, 2015). In this Figures, three compositionally different mantle sources are considered based on the diagram in Figure 7.6: (1) a DMM source (Workman & Hart, 2005) melting in the spinel-facies; (2) a theoretical DMM source enriched in LREE and incompatible elements by a plume-type chemical component (i.e., plume-influenced source of Saccani (2015); or plume-proximal of Pearce (2008)) that melts in the spinel-facies. The composition of this source was assumed based on modelling, as presented by Saccani et al. (2013a, 2014, 2015); (3) an OIB-type source (Lustrino et al., 2002) that starts melting in the garnet-facies and continues to larger degrees into the spinel facies. In addition, it should be noted that Th and Nb are sensitive of fractional crystallization in shallow level magma

chambers. Therefore, fractional crystallization trends for primary melts generated from each mantle source are shown in Fig. 7.7b. They are calculated assuming the crystallization of olivine, plagioclase, clinopyroxene, and spinel in the proportions shown in Figure 7.7b.

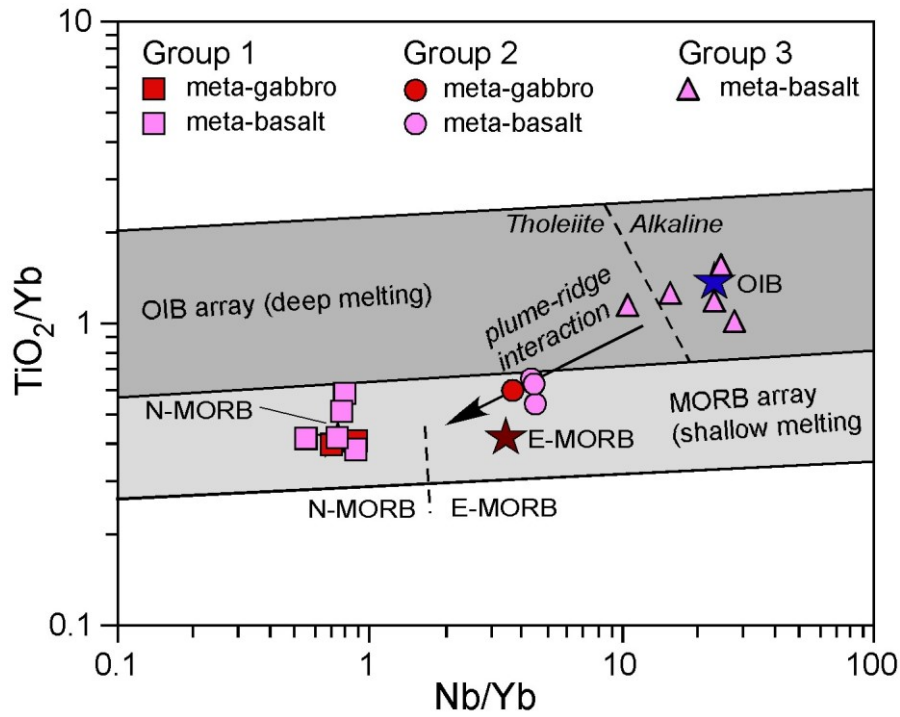


Figure 7.6. TiO_2/Yb vs. Nb/Yb diagram of *Pearce (2008)* for meta-ophiolitic rocks from the Bajgan Complex used for discriminating between deep (i.e., garnet-facies mantle) and shallow (i.e., spinel-facies mantle) melting, as well as between depleted (N-MORB type) and enriched mantle sources (OIB-type). Group 2 rocks plot in the region of compositions reflecting plume-ridge interaction.

The Group 1 mafic protoliths with N-MORB chemistry are compatible with melt generation from a depleted MORB-type mantle at shallow levels. In particular, both the REE ratios and Th-Nb-Yb composition of these rocks can be explained by high degrees (generally, 15 - 18 %) of partial melting of a DMM source in the spinel facies (Fig. 7.7). Both diagrams in Figure 7.7 show that primitive alkaline basalts of the Group 3 rocks are compatible with low degree partial melting (5 - 7%) of an OIB-type mantle source that starts to melt in the garnet-facies mantle (20-30% of the total melt) and it continues to melt to greater extent (70-80% of the total melt) in the spinel-facies (polybaric melting).

The modellings in Figures 7.7a and 7.7b show that E-MORB protoliths (Group 2) is

compatible with moderate degrees (~8 - 10 %) of partial melting in the spinel facies of a DMM source enriched in Th, Nb, and LREE by plume-type components. Alternatively, the Th-Nb-Yb composition of the Group 2 E-MORBs may have been derived from very high degrees (>20%) of polybaric melting of an alkaline OIB-type mantle source (Fig. 7.7b). However, the REE composition of these rocks cannot be explained by this melting process (Fig. 7.7a) and such a very high degree of melting is unreasonable in an oceanic subduction-unrelated setting.

In summary, the overall chemical composition of the metamorphic rocks from the Bajgan Complex (Figs. 7.4, 7.6) and the melting models shown in Figures 7.7 allow the following conclusions to be drawn: (1) the magmatic protoliths of these rocks were formed during Cretaceous times in a subduction-unrelated oceanic setting with no influence from either subduction or continental crust chemical components; (2) the chemically distinct groups of magmatic protoliths include tholeiitic N-MORBs and E-MORBs and alkaline OIBs that are related to different mantle source compositions, which are associated to distinct oceanic tectonic settings, such as mid-ocean ridge possibly influenced by plume-type components, for the tholeiitic rocks and within-plate seamounts, for the alkaline rocks.

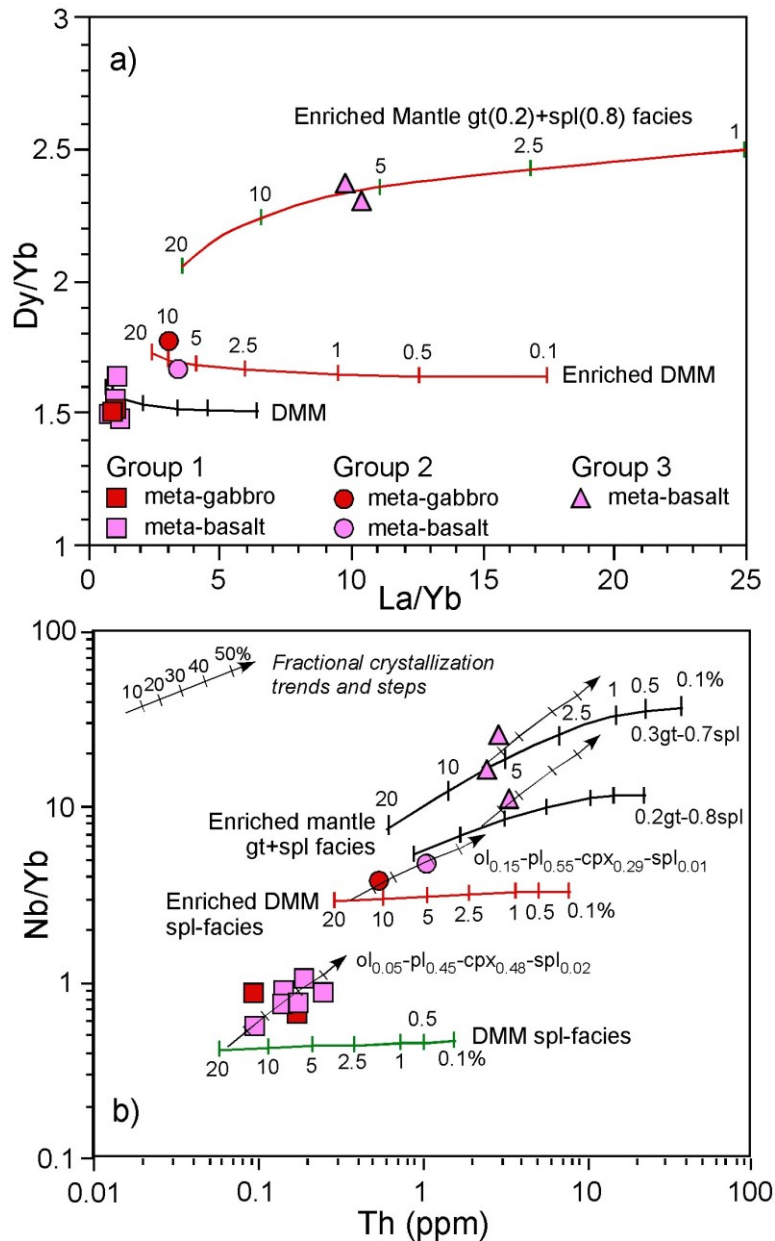


Figure 7.7. Non-modal, batch partial melting models using La/Yb vs. Dy/Yb (a) and Th vs. Nb/Yb (b). Relatively less fractionated mafic rocks from the Bajgan Complex are plotted in these diagrams. Both diagrams show the melting curves calculated for: depleted MORB mantle (DMM) in the spinel stability field; DMM enriched by OIB-type components in the spinel stability field; ocean island-type enriched mantle (OIB-type or plume-type mantle) in both garnet and spinel stability fields (proportions of melting in the garnet and spinel stability fields are shown in figure). Ticks on the DMM melting curve indicate the same percentages of melt fractions as shown for the other melting curves. Mantle source compositions, DMM: La = 0.222, Dy = 0.55, Yb = 0.353 ppm, Nb = 0.16 ppm, Th = 0.0068 ppm, (Workman & Hart, 2005); enriched DMM: La = 0.54, Dy = 0.58, Yb = 0.353 ppm, Nb = 1.2 ppm, Th = 0.1 ppm (based on models in Saccani et al., 2013a, 2014; 2015); Enriched (OIB-type) mantle: La = 0.75, Dy = 0.42, Yb = 0.347 ppm, Nb = 1.5 ppm, Th = 0.18 ppm (Lustrino et al., 2002). Source modes and melting proportions for the garnet-facies are: $Ol_{0.598}-Opx_{0.211}-Cpx_{0.076}-Grt_{0.115}$ and $Ol_{0.05}-Opx_{0.2}-Cpx_{0.3}-Grt_{0.115}$, respectively (Thirlwall et al., 1994). Source modes and melting proportions for the spinel-facies are: $Ol_{0.578}-Opx_{0.27}-Cpx_{0.119}-Spl_{0.033}$ and $Ol_{0.1}-Opx_{0.27}-Cpx_{0.5}-Spl_{0.13}$, respectively (Thirlwall et al., 1994). Fractional crystallization trends for primary melts are calculated assuming the crystallization of olivine (ol), plagioclase (pl), clinopyroxene (cpx), and spinel (spl) in the proportions shown in Figure. Partition coefficients are from McKenzie & O’Nions (1991) and Irving & Frey (1984).

7.5.2. *The Bajgan Complex re-interpreted as remnants of an Early Cretaceous oceanic lithosphere*

Results from this thesis indicate that the so far proposed interpretation of the Bajgan Complex as the pre-Mesozoic continental basement of a microcontinent (the so-called Bajgan-Durkan microcontinent (McCall, 1985; Hunziker et al., 2015; Burg, 2018; Saccani et al., 2018)) can be ruled out. Rather, the new data strongly suggest that the Bajgan Complex consists of the remnants of Late Jurassic to Early Cretaceous oceanic lithosphere. In fact, the geochemistry of the meta-igneous rocks from Bajgan Complex as well as the petrogenetic modelling indicate that these rocks formed in mid-oceanic ridge setting and they derive from the partial melting of DMM-type mantle sources influenced by OIB-chemical components. The occurrence of meta-basalts showing OIB chemical affinity may suggest a plume-influence mid-oceanic ridge or a polygenetic crust oceanic crust showing seamounts. The U/Pb zircon dating exclude a Paleozoic age of formation for the meta-igneous rocks of the Bajgan Complex. The collected data indicate an age ranging from 161 to 114 Ma, i.e. from Oxfordian to Aptian. The different ages detected in the meta-ophiolites are likely related to the occurrence of different slices, each bounded by mylonitic shear zones. These slices are likely derived by the deformation and metamorphism of distinct segments of the oceanic basin formed at different times. The coupling of geochemical and age data from Bajgan Complex imply the occurrence of remnants of a well-developed and thick oceanic crust that developed for a long time (more than 40 Ma) and produced MOR-type intrusive and effusive rocks. The presence of OIB and E-MOR meta-basalts point to a plume influenced magmatism in the Neo-Tethys oceanic Basin (see plume proximal oceanic lithosphere, see Pearce, 2008). Evidence of this Cretaceous oceanic within-plate basaltic magmatism in the Neo-Tethys oceanic basin have been indicated by several authors from Armenia to Himalaya (Saccani et al., 2013a; Yang & Dilek, 2015; Rolland et

al., 2020) and have been proposed in this thesis for the Late Cretaceous Durkan Complex (Chapter 6).

The conclusion derived by geochemical data are further supported by field data. In detail, the Bajgan Complex can be regarded as an assemblage of slices of both meta-igneous and meta-sedimentary rocks, which likely represent a meta-ophiolite and the related meta-sedimentary cover, respectively. The meta-ophiolites include the meta-serpentinites that can represent either the mantle section of the ophiolites or the lower part of the intrusive sequence. In the latter interpretation, the meta-serpentinites can correspond to cumulitic rocks forming the lower part of an intrusive sequence dominated by dunites and melagabbros. The upper part of the intrusive magmatic sequence is instead represented by the meta-intrusive rocks derived from metamorphism and deformation of a primary sequence of gabbro, gabbronorite, melagabbro and anorthosite but also including more felsic and evolved intrusive rocks as plagiogranites. The upper part of the oceanic crust can correspond to the meta-volcanic rocks, probably derived from massive and/or pillow-lava basalts. The occurrence of abundant meta-volcaniclastics associated to meta-volcanic rocks likely suggest a stratigraphic transition from the meta-ophiolitic rocks assemblage and its meta-sedimentary cover. The latter is composed by a succession consisting of quartzites, impure marbles, calcschists, fine - up medium-grained micaschists and fine- up coarse-grained paragneisses. These metamorphic rocks likely derived from a pristine succession including cherts, limestone and siliciclastic to mixed turbidites. All these lithologies are generally found in the sedimentary deposits at the top of the oceanic crust (Marroni & Pandolfi, 2007; Kusky et al., 2013; Wakita, 2015). The age of this assemblage cannot be detected by fossils because they have been totally recrystallized during the metamorphism, but an Early Cretaceous age can be proposed according to the Late Jurassic-Early Cretaceous age of meta-igneous rocks and the Early to Late Cretaceous age of the metamorphism.

To sum up, the new data presented in this thesis indicate that the Bajgan Complex represent an oceanic-derived tectonic element of the North Makran rather than the remnants of a micro-continent and it is composed by an assemblage of different slices of meta-ophiolites. These data suggest that the Cretaceous tectono-magmatic and geodynamic setting of the Makran sector of Neo-Tethys need to be re-evaluated with respect to previous interpretations (McCacll & Kidd, 1982; Hunziker et al., 2015; Burg, 2018; Saccani et al., 2018).

APPENDIX

Appendix Table 7.1. (1/3) Major (wt%) and trace (ppm) element analyses of meta-ophiolitic rocks from the Bajgan Complex. Abbreviations: XRF: X-ray fluorescence spectrometry; ICP-MS: inductively coupled plasma-mass spectrometry; b.d.l.: below detection limit. * Except when otherwise indicated. Mg# = 100 x Mg/(Mg+Fe). Fe₂O₃=0.15 x FeO. Normalizing values for REE ratios are from Sun & McDonough (1989). Abbreviations: n.d.: not detectable; b.d.l.: below detection limits. Mineral abbreviation (after Whitney and Evans, 2010). Ab: albite; Act: actinolite; Ap: apatite; Cal: calcite; Chl: Chlorite (group); Cld: chloritoid; Ep: epidote (Group); Grt: garnet (group); Hbl: green hornblende; Ms: muscovite (group); Ol: olivine (group); Op: opaque minerals (mostly Fe/Ti oxides); Pl: plagioclase (group); Px: Pyroxenes (group); Qz: quartz; Spl: spinel (group); Srp: serpentine (group); Tlc: talc; Tr: tremolite.

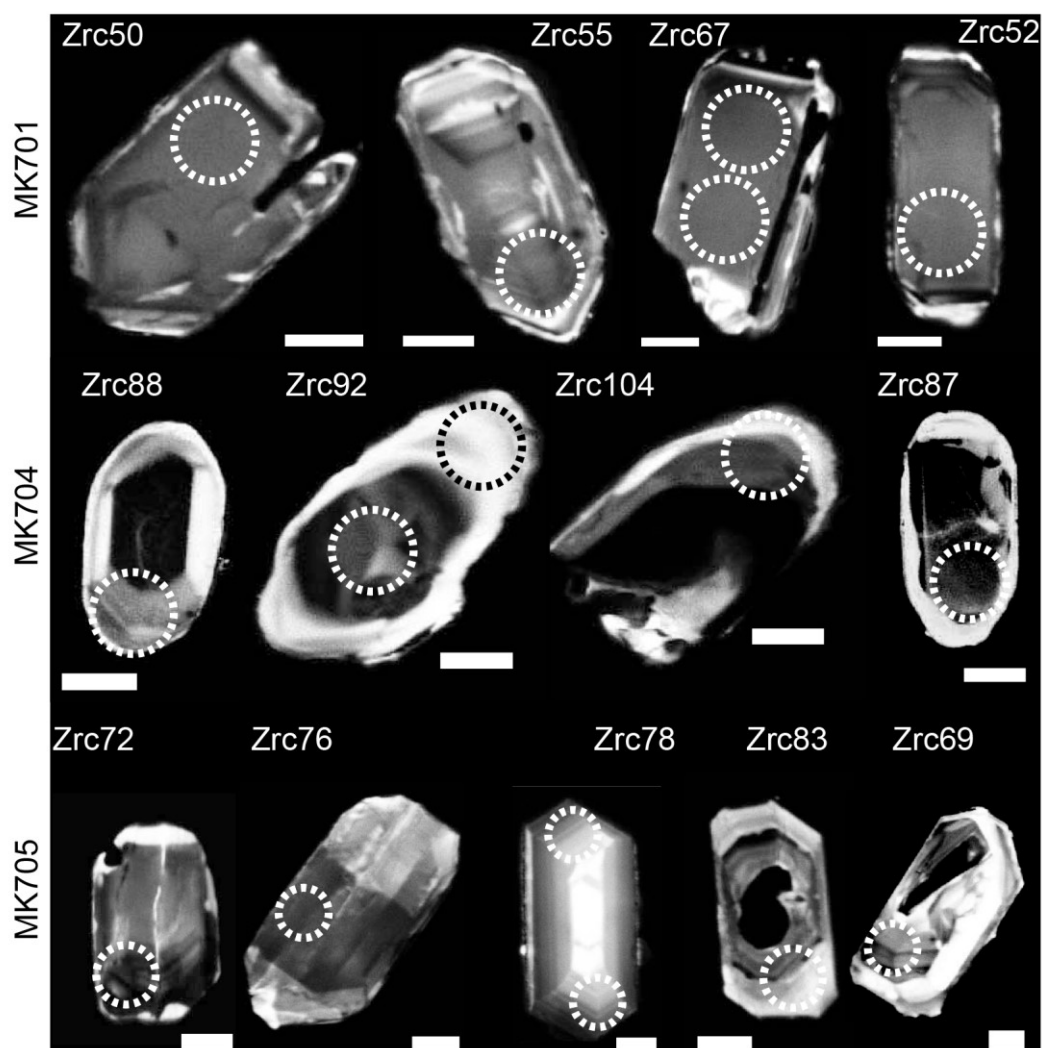
| MORB-type meta-ultramafic cumulitic rocks | | | | | | | | | | |
|---|------------|------------|-----------------|--------------|------------|--------------|---------------|------------|-----------------|------------|
| Sample | MK271 | MK273 | MK274 | MK284 | MK303 | MK305 | MK316 | MK318 | MK323 | MK330 |
| Protolith type | peridotite | peridotite | clinopyroxenite | peridotite | peridotite | peridotite | peridotite | peridotite | clinopyroxenite | peridotite |
| Texture | mylonitic | mylonitic | granoblastic | granoblastic | mylonitic | granoblastic | lepidoblastic | mylonitic | nematoblastic | mylonitic |
| Relict magmatic texture | cumulitic | n.d. | cumulitic | cumulitic | n.d. | cumulitic | n.d. | n.d. | n.d. | n.d. |
| Paragenesis | Srp-Chl-Op | Srp-Chl-Op | Px-Chl | Srp-Act-Chl | Srp-Chl-Op | Ol-Tr | Srp-Tr-Chl-Op | Ol-Spl | Tlc-Tr-(Chl) | Srp-Chl-Op |
| Note | | Px relicts | Px relicts | | | Px relicts | | | | |
| <i>Age</i> | | | | | | | | | | |
| <i>XRF analyses:</i> | | | | | | | | | | |
| SiO ₂ | 42.03 | 42.26 | 44.51 | 43.52 | 40.27 | 40.50 | 39.88 | 43.16 | 53.60 | 41.11 |
| TiO ₂ | 0.02 | 0.03 | 0.46 | 0.02 | 0.03 | 0.10 | 0.05 | 0.02 | 0.04 | 0.07 |
| Al ₂ O ₃ | 1.18 | 1.14 | 3.42 | 2.52 | 2.60 | 6.29 | 2.38 | 1.73 | 3.88 | 3.75 |
| Fe ₂ O ₃ | | | | | | | | | | |
| FeO | 4.86 | 5.90 | 6.52 | 6.68 | 5.90 | 7.97 | 7.31 | 7.52 | 6.13 | 4.03 |
| MnO | 0.07 | 0.07 | 0.09 | 0.00 | 0.08 | 0.13 | 0.07 | 0.11 | 0.22 | 0.09 |
| MgO | 39.18 | 39.03 | 26.92 | 35.60 | 39.62 | 30.31 | 38.90 | 41.04 | 20.82 | 38.68 |
| CaO | 0.33 | 0.17 | 12.18 | 0.75 | 0.21 | 5.71 | 0.16 | 1.41 | 11.22 | 0.10 |
| Na ₂ O | 0.01 | 0.01 | 0.11 | b.d.l. | 0.02 | 0.12 | 0.02 | 0.05 | 0.77 | 0.02 |
| K ₂ O | b.d.l. | b.d.l. | b.d.l. | b.d.l. | b.d.l. | b.d.l. | b.d.l. | b.d.l. | 0.12 | 0.01 |
| P ₂ O ₅ | b.d.l. | b.d.l. | b.d.l. | b.d.l. | b.d.l. | b.d.l. | b.d.l. | b.d.l. | b.d.l. | b.d.l. |
| LOI | 12.20 | 11.38 | 5.80 | 11.13 | 11.39 | 8.03 | 11.33 | 5.19 | 3.24 | 12.26 |
| Total | 99.88 | 99.99 | 100.01 | 100.21 | 100.11 | 99.17 | 100.09 | 100.22 | 100.04 | 100.11 |
| Mg# | 94.2 | 92.2 | 89.3 | 90.5 | 92.3 | 87.1 | 90.5 | 90.9 | 85.8 | 95.1 |
| Zn | 25 | 23 | 3 | 61 | 19 | 40 | 10 | 40 | 60 | 19 |
| Cu | 4 | 4 | 163 | 22 | b.d.l. | 31 | 33 | 13 | 187 | b.d.l. |
| Sc | 6 | 6 | 53 | 9 | 8 | 17 | 9 | 6 | 8 | 6 |
| Ga | b.d.l. | b.d.l. | 4 | b.d.l. | b.d.l. | b.d.l. | b.d.l. | b.d.l. | 5 | b.d.l. |
| Ni | 1457 | 1524 | 764 | 1832 | 1846 | 1410 | 1702 | 2537 | 1242 | 1492 |
| Co | 55 | 67 | 40 | 51 | 88 | 93 | 95 | 89 | 58 | 58 |
| Cr | 2661 | 2194 | 1267 | 1944 | 3021 | 3488 | 651 | 2989 | 1692 | 1661 |
| V | 42 | 29 | 265 | 34 | 36 | 84 | 32 | 46 | 63 | 46 |
| Ba | 3 | b.d.l. | 21 | b.d.l. | b.d.l. | 7 | 16 | b.d.l. | b.d.l. | 7 |
| Pb | 8 | 8 | 9 | 4 | 7 | 6 | 6 | 7 | 6 | 7 |
| <i>ICP-MS analyses:*</i> | | | | | | | | | | |
| Rb | 0.032 | 0.116 | 1 | 0.759 | 0.046 | b.d.l. | 0.028 | 0.252 | b.d.l. | b.d.l. |
| Sr | 20.9 | 2.37 | 11 | 3.08 | 2.30 | 46 | 12.83 | 2.73 | 3 | b.d.l. |
| Y | 0.506 | 0.471 | 5 | 1.19 | 0.529 | 4 | 0.92 | 0.510 | 4 | 6 |
| Zr | 3.41 | 1.61 | 15 | 0.169 | 0.861 | b.d.l. | 1.96 | 0.733 | 7 | 19 |
| La | 0.200 | 0.196 | b.d.l. | 0.035 | 0.038 | b.d.l. | 0.086 | 0.026 | b.d.l. | b.d.l. |
| Ce | 0.501 | 0.427 | b.d.l. | 0.122 | 0.106 | b.d.l. | 0.232 | 0.068 | b.d.l. | b.d.l. |
| Pr | 0.072 | 0.059 | | 0.026 | 0.018 | | 0.038 | 0.011 | | |
| Nd | 0.314 | 0.245 | b.d.l. | 0.170 | 0.098 | b.d.l. | 0.205 | 0.055 | b.d.l. | b.d.l. |
| Sm | 0.095 | 0.069 | | 0.072 | 0.034 | | 0.071 | 0.018 | | |
| Eu | 0.032 | 0.037 | | 0.021 | 0.011 | | 0.021 | 0.006 | | |
| Gd | 0.104 | 0.081 | | 0.135 | 0.052 | | 0.114 | 0.028 | | |
| Tb | 0.017 | 0.014 | | 0.028 | 0.010 | | 0.022 | 0.006 | | |
| Dy | 0.103 | 0.088 | | 0.203 | 0.071 | | 0.151 | 0.052 | | |
| Ho | 0.021 | 0.019 | | 0.051 | 0.017 | | 0.035 | 0.014 | | |
| Er | 0.058 | 0.053 | | 0.162 | 0.056 | | 0.107 | 0.050 | | |
| Tm | 0.008 | 0.008 | | 0.028 | 0.010 | | 0.017 | 0.010 | | |
| Yb | 0.055 | 0.050 | | 0.203 | 0.073 | | 0.121 | 0.075 | | |
| Lu | 0.008 | 0.008 | | 0.034 | 0.012 | | 0.019 | 0.013 | | |
| Nb | 0.348 | 0.379 | b.d.l. | 0.152 | 0.131 | b.d.l. | 0.132 | 0.080 | b.d.l. | 1 |
| Hf | 0.044 | 0.068 | | 0.031 | 0.035 | | 0.074 | 0.028 | | |
| Ta | 0.099 | 0.078 | | 0.018 | 0.019 | | 0.012 | 0.009 | | |
| Th | 0.044 | 0.043 | 1 | 0.018 | 0.012 | b.d.l. | 0.022 | 0.008 | 1 | b.d.l. |
| U | 0.033 | 0.016 | | 0.008 | 0.011 | | 0.009 | 0.004 | | |
| Ti/V | | | | | | | | | | |
| Nb/Y | 0.69 | 0.80 | | 0.13 | 0.25 | | 0.14 | 0.16 | | 0.23 |
| (La/Sm) _N | 1.36 | 1.84 | | 0.32 | 0.72 | | 0.78 | 0.90 | | |
| (Sm/Yb) _N | 1.90 | 1.52 | | 0.40 | 0.52 | | 0.65 | 0.27 | | |
| (La/Yb) _N | 2.59 | 2.81 | | 0.12 | 0.37 | | 0.51 | 0.25 | | |
| Zr/Nb | 9.79 | 4.25 | | 1.11 | 6.59 | | 14.85 | 9.16 | | 13.57 |
| Th/Ta | | | | | | | | | | |
| Th/Tb | | | | | | | | | | |
| (Th/Tb)/(Th/Ta) | | | | | | | | | | |

Table 7.1. (2/3)

| Sample | Group 1 (N-MORB) | | | | | | Meta-intrusive rocks | | | | MK 508 plagiogranite lepidoblastic augen |
|--------------------------------|------------------------|------------------------|---------------------------|------------------------|------------------------|---|---|--|----------------------------------|----------------------------------|--|
| | MK252 | MK253 | MK264 | MK324 | MK 512 | MK 513 | MK704 anorthositic meta-cumulitic | MK254 gabbro lepidoblastic augen | MK256 gabbro lepidoblastic | MK705A gabbro granoblastic | |
| Protolith type | basalt granoblastic | basalt granoblastic | basalt porphyroblastic | basalt granoblastic | basalt granoblastic | ferrobasalt nematoblastic decussate | | | | | |
| Texture | | | | | | | | | | | |
| Relict magmatic texture | n.d. | n.d. | n.d. | n.d. | n.d. | n.d. | n.d. | cumulitic | isotropic | isotropic | n.d. |
| Paragenesis | Qz-Ab-Act- Ep-Cal | Qz-Ab-Act- Ep | Pl-Chl-Ep- Tr | Qz-Ab-Act- Ep-Cal | Qz-Ab-Chl | Chl-Ab-Act- Ep-Qz-Lcx dolerite dyke | Pl-Ep-Qz | Pl-Tr-Op | Act-Ep- (Qz) Pl relicts | Srp-Qz- Act/Tr Px relicts | Ms-Chl-Ep- Qz-Ab-Grt |
| Note | | | | | | | | Px-Pl relicts | | | |
| Age | | | | | | | 136,6 Ma | | | 118,8 Ma | |
| XRF analyses: | | | | | | | | | | | |
| SiO ₂ | 49.09 | 50.25 | 48.35 | 49.00 | 47.79 | 42.48 | 60.16 | 48.21 | 49.83 | 49.61 | 72.58 |
| TiO ₂ | 1.28 | 1.43 | 1.29 | 1.35 | 1.44 | 3.85 | 0.12 | 0.35 | 0.71 | 1.27 | 0.29 |
| Al ₂ O ₃ | 13.43 | 14.72 | 14.29 | 13.81 | 14.18 | 12.25 | 17.31 | 15.53 | 14.61 | 14.92 | 11.23 |
| Fe ₂ O ₃ | 1.32 | 1.33 | 1.25 | 1.29 | 1.69 | 2.24 | 0.17 | 0.73 | 1.24 | 1.28 | 0.37 |
| FeO | 8.78 | 8.87 | 8.31 | 8.58 | 11.28 | 14.94 | 1.11 | 4.85 | 8.25 | 8.54 | 2.45 |
| MnO | 0.15 | 0.15 | 0.23 | 0.19 | 0.19 | 0.22 | 0.03 | 0.10 | 0.14 | 0.18 | 0.10 |
| MgO | 10.11 | 7.69 | 8.40 | 9.28 | 9.58 | 9.84 | 1.90 | 14.35 | 11.29 | 10.64 | 0.96 |
| CaO | 9.56 | 9.97 | 10.78 | 9.14 | 8.33 | 9.13 | 8.37 | 10.56 | 8.92 | 7.58 | 4.53 |
| Na ₂ O | 2.45 | 1.94 | 4.30 | 3.53 | 3.02 | 2.31 | 8.33 | 2.15 | 2.94 | 2.48 | 5.33 |
| K ₂ O | 0.16 | 1.03 | 0.30 | 0.36 | 0.14 | 0.33 | 0.13 | 0.13 | 0.24 | 0.63 | 0.80 |
| P ₂ O ₅ | 0.11 | 0.15 | 0.15 | 0.14 | 0.15 | 0.19 | 0.36 | 0.02 | 0.05 | 0.13 | 0.05 |
| LOI | 3.57 | 2.55 | 2.39 | 3.05 | 2.68 | 1.81 | 2.07 | 3.08 | 1.82 | 2.72 | 2.20 |
| Total | 100.01 | 100.08 | 100.03 | 99.72 | 100.47 | 99.59 | 100.07 | 100.06 | 100.05 | 100.68 | 100.89 |
| Mg# | 67.3 | 60.7 | 64.3 | 65.8 | 60.2 | 54.0 | 75.4 | 84.1 | 70.9 | 68.9 | 41.1 |
| Zn | 96 | 99 | 89 | 99 | 101 | 118 | 72 | 28 | 36 | 72 | 60 |
| Cu | 53 | 30 | 73 | 31 | 76 | 37 | 3 | 151 | b.d.l. | 3 | 10 |
| Sc | 33 | 31 | 29 | 41 | 37 | 36 | 9 | 34 | 39 | 28 | 11 |
| Ga | 15 | 17 | 14 | 15 | 19 | 18 | 14 | 10 | 13 | 20 | 10 |
| Ni | 126 | 111 | 44 | 44 | 33 | 86 | 2 | 213 | 89 | 102 | b.d.l. |
| Co | 37 | 42 | 35 | 57 | 35 | 53 | b.d.l. | 30 | 37 | 38 | 2 |
| Cr | 324 | 277 | 239 | 336 | 118 | 151 | 3 | 1069 | 439 | 847 | 5 |
| V | 288 | 331 | 211 | 242 | 330 | 453 | 28 | 172 | 287 | 193 | 20 |
| Ba | 27 | 40 | 34 | 34 | 41 | 42 | 39 | 21 | 34 | 94 | 100 |
| Pb | 9 | 6 | 8 | 8 | 9 | 7 | b.d.l. | 9 | 7 | 9 | 12 |
| ICP-MS analyses:* | | | | | | | | | | | (XRF) |
| Rb | 1.83 | 12.7 | 4.40 | 3.78 | 2.01 | 1.08 | 0.609 | 0.820 | 2.78 | 28.6 | 13 |
| Sr | 128 | 58.8 | 122 | 84.4 | 190 | 19.8 | 224 | 111 | 103 | 165 | 89 |
| Y | 31.0 | 28.7 | 29.0 | 26.6 | 40.0 | 21.8 | 7.69 | 6.68 | 16.1 | 34.2 | 29 |
| Zr | 88.8 | 88.8 | 109 | 80.3 | 109 | 78.7 | 35 | 19.3 | 40.7 | 85.5 | 83 |
| La | 2.32 | 2.62 | 2.92 | 2.52 | 4.34 | 2.26 | 4.61 | 0.705 | 1.44 | 3.34 | 6 |
| Ce | 7.37 | 7.77 | 8.86 | 7.37 | 12.5 | 7.47 | 10.2 | 2.19 | 4.39 | 9.70 | 18 |
| Pr | 1.35 | 1.32 | 1.60 | 1.30 | 2.09 | 1.36 | 1.32 | 0.380 | 0.779 | 1.58 | |
| Nd | 8.06 | 7.01 | 8.95 | 7.17 | 10.8 | 7.46 | 5.45 | 2.06 | 4.23 | 8.42 | 4 |
| Sm | 2.82 | 2.52 | 3.04 | 2.46 | 3.53 | 2.80 | 1.54 | 0.720 | 1.52 | 2.79 | |
| Eu | 1.01 | 0.877 | 1.11 | 0.936 | 1.27 | 1.30 | 0.835 | 0.314 | 0.595 | 1.30 | |
| Gd | 3.91 | 3.53 | 4.08 | 3.45 | 4.59 | 4.02 | 1.64 | 0.969 | 2.17 | 4.14 | |
| Tb | 0.717 | 0.622 | 0.734 | 0.621 | 0.868 | 0.721 | 0.241 | 0.176 | 0.394 | 0.745 | |
| Dy | 4.92 | 4.19 | 5.01 | 4.22 | 5.95 | 4.83 | 1.40 | 1.19 | 2.67 | 5.02 | |
| Ho | 1.11 | 0.940 | 1.11 | 0.936 | 1.32 | 1.04 | 0.286 | 0.267 | 0.607 | 1.10 | |
| Er | 3.29 | 2.66 | 3.22 | 2.67 | 3.85 | 3.14 | 0.764 | 0.783 | 1.75 | 3.22 | |
| Tm | 0.502 | 0.400 | 0.487 | 0.415 | 0.586 | 0.471 | 0.111 | 0.119 | 0.271 | 0.498 | |
| Yb | 3.26 | 2.55 | 3.20 | 2.77 | 3.84 | 3.15 | 0.709 | 0.779 | 1.80 | 3.28 | |
| Lu | 0.475 | 0.374 | 0.473 | 0.415 | 0.568 | 0.414 | 0.096 | 0.117 | 0.271 | 0.494 | |
| Nb | 1.85 | 2.10 | 2.42 | 2.25 | 3.46 | 3.34 | 0.649 | 1.25 | 1.62 | 2.36 | 3 |
| Hf | 1.65 | 1.23 | 2.17 | 2.10 | 2.77 | 2.19 | 0.948 | 0.592 | 1.17 | 2.22 | 2 |
| Ta | 0.128 | 0.1412 | 0.177 | 0.141 | 0.241 | 0.167 | 0.058 | 0.068 | 0.102 | 0.160 | |
| Th | 0.096 | 0.144 | 0.177 | 0.143 | 0.245 | 0.190 | 0.034 | 0.056 | 0.092 | 0.170 | 1 |
| U | 0.059 | 0.0676 | 0.058 | 0.065 | 0.091 | 0.044 | 0.011 | 0.020 | 0.036 | 0.054 | |
| Ti/V | 28 | 27 | 37 | 35 | 27 | 52 | 27 | 13 | 15 | 21 | |
| Nb/Y | 0.06 | 0.07 | 0.08 | 0.08 | 0.09 | 0.15 | 0.08 | 0.19 | 0.10 | 0.07 | 0.11 |
| (La/Sm) _N | 0.53 | 0.67 | 0.62 | 0.66 | 0.79 | 0.52 | 1.93 | 0.63 | 0.61 | 0.77 | |
| (Sm/Yb) _N | 0.96 | 1.10 | 1.05 | 0.99 | 1.02 | 0.99 | 2.42 | 1.03 | 0.94 | 0.95 | |
| (La/Yb) _N | 0.51 | 0.74 | 0.65 | 0.65 | 0.81 | 0.51 | 4.67 | 0.65 | 0.57 | 0.73 | |
| Zr/Nb | 47.9 | 42.3 | 45.1 | 35.7 | 31.3 | 23.6 | 54.9 | 15.4 | 25.1 | 36.2 | 25.2 |
| Th/Ta | 0.75 | 1.02 | 1.00 | 1.01 | 1.02 | 1.13 | | 0.82 | 0.91 | 1.06 | |
| Th/Tb | 0.13 | 0.23 | 0.24 | 0.23 | 0.28 | 0.26 | | 0.32 | 0.23 | 0.23 | |
| (Th/Tb)/(Th/Ta) | 0.18 | 0.23 | 0.24 | 0.23 | 0.28 | 0.23 | | 0.39 | 0.26 | 0.21 | |

Table 7.1. (3/3)

| Sample | Group 2 (E-MORB) | | | | | Group 3 (Alkaline basalts) | | | | |
|--------------------------------|-------------------------|---------------------------|-----------------------------------|-----------------------------------|---|----------------------------|--------------------------------------|-------------------------|--------------------------------------|-----------------------------------|
| | Meta-volcanic rocks | | | Meta-intrusive rock | | Meta-volcanic rocks | | | | |
| Protolith type | MK259 | MK269 | MK 509 | MK272 | MK701 | MK245 | MK247 | MK263 | MK308 | MK313 |
| Texture | basalt lepidoblastic | basalt porphyroblastic | basalt grano- lepidoblastic | gabbro grano- lepidoblastic | plagiogranite lepidoblastic augen | basalt lepidoblastic | basalt lepidoblastic decussate | basalt lepidoblastic | basalt lepidoblastic decussate | basalt grano- lepidoblastic |
| Relict magmatic texture | n.d. | n.d. | n.d. | isotropic | n.d. | n.d. | n.d. | n.d. | n.d. | n.d. |
| Paragenesis | Chl-Qz-Ab- Act-Ep | Pl-Chl-Tr-Ep- Qz | Chl-Qz-Ab- Op | Act-Chl | Hbl-Cld-Qz- Ab-Ab | Act-Chl-Qz- Ab | Hbl-Chl-Qz- Ab | Act-Chl-Qz- Ab+Ep | Hbl-Chl-Qz- Ab | Hbl-Chl-Qz- Ab |
| Note | | | | Px relicts | | | | | | |
| Age | | | | | 156,2 Ma | | | | | |
| <i>XRF analyses:</i> | | | | | | | | | | |
| SiO ₂ | 50.51 | 51.40 | 49.57 | 50.56 | 71.19 | 42.82 | 46.50 | 42.62 | 47.98 | 48.98 |
| TiO ₂ | 1.12 | 1.61 | 1.21 | 0.88 | 0.35 | 1.96 | 2.33 | 2.07 | 2.02 | 1.84 |
| Al ₂ O ₃ | 14.42 | 13.69 | 13.40 | 14.99 | 12.59 | 13.48 | 15.60 | 13.81 | 12.99 | 14.09 |
| Fe ₂ O ₃ | 1.30 | 1.20 | 1.20 | 0.99 | 0.59 | 1.88 | 1.76 | 1.62 | 1.53 | 1.53 |
| FeO | 8.65 | 7.99 | 8.00 | 6.58 | 3.94 | 12.52 | 11.72 | 10.77 | 10.18 | 10.19 |
| MnO | 0.16 | 0.10 | 0.15 | 0.13 | 0.02 | 0.17 | 0.13 | 0.36 | 0.19 | 0.21 |
| MgO | 9.31 | 10.02 | 7.70 | 10.55 | 1.02 | 10.16 | 7.30 | 10.90 | 8.91 | 8.72 |
| CaO | 8.40 | 7.29 | 11.69 | 9.49 | 3.17 | 10.73 | 7.44 | 10.53 | 10.44 | 9.15 |
| Na ₂ O | 3.77 | 2.82 | 4.11 | 3.35 | 6.59 | 2.55 | 3.65 | 2.57 | 2.98 | 3.29 |
| K ₂ O | 0.46 | 0.04 | 0.20 | 0.59 | 0.06 | 0.24 | 1.58 | 0.42 | 0.66 | 0.33 |
| P ₂ O ₅ | 0.15 | 0.31 | 0.15 | 0.09 | 0.07 | 0.16 | 0.56 | 0.27 | 0.27 | 0.21 |
| LOI | 1.87 | 3.08 | 3.55 | 1.85 | 0.49 | 3.38 | 1.49 | 4.11 | 1.46 | 1.54 |
| Total | 100.12 | 99.75 | 100.92 | 100.04 | 100.07 | 100.06 | 100.06 | 100.05 | 99.61 | 100.08 |
| Mg# | 65.7 | 69.1 | 63.2 | 74.1 | 31.5 | 59.1 | 52.6 | 64.3 | 60.9 | 60.4 |
| Zn | 100 | 74 | 104 | 58 | 175 | 110 | 100 | 156 | 96 | 94 |
| Cu | 50 | 38 | 28 | 77 | 5 | 97 | 108 | 27 | 92 | 86 |
| Sc | 41 | 49 | 30 | 41 | 9 | 48 | 14 | 17 | 40 | 47 |
| Ga | 14 | 9 | 15 | 14 | 3 | 17 | 23 | 18 | 16 | 14 |
| Ni | 28 | 36 | 41 | 85 | 5 | 141 | 27 | 78 | 119 | 58 |
| Co | 27 | 43 | 40 | 21 | 3 | 49 | 25 | 29 | 55 | 52 |
| Cr | 91 | 106 | 317 | 752 | 10 | 285 | 66 | 125 | 350 | 96 |
| V | 300 | 258 | 250 | 255 | 3 | 250 | 329 | 201 | 292 | 262 |
| Ba | 90 | 73 | 32 | 104 | 88 | 148 | 602 | 116 | 226 | 133 |
| Pb | 10 | 7 | 8 | 10 | b.d.l. | 11 | 13 | 11 | 10 | 9 |
| <i>ICP-MS analyses:*</i> | | | | | | | | | | |
| Rb | 6.95 | 2.35 | (XRF) 5 | 7.24 | 0.79 | 3.52 | 47.6 | 5.83 | 10.0 | 5.55 |
| Sr | 112 | 59.5 | 146 | 179 | 99.3 | 344 | 830 | 454 | 422 | 325 |
| Y | 21.7 | 30.9 | 25 | 15.5 | 115 | 24.2 | 37.3 | 19.6 | 23.1 | 20.8 |
| Zr | 79.3 | 137 | 98 | 65.3 | 374.0 | 167 | 324 | 181 | 211 | 148 |
| La | 7.15 | 11.4 | b.d.l. | 4.45 | 48.6 | 17.4 | 64.4 | 26.7 | 30.0 | 15.5 |
| Ce | 15.6 | 28.6 | 17 | 10.4 | 101 | 36.6 | 132 | 53.4 | 57.6 | 31.7 |
| Pr | 2.14 | 4.10 | | 1.48 | 13.5 | 4.60 | 15.7 | 6.31 | 6.79 | 3.92 |
| Nd | 9.36 | 17.5 | b.d.l. | 6.72 | 54.8 | 18.5 | 56.9 | 23.1 | 25.8 | 15.7 |
| Sm | 2.76 | 4.94 | | 2.06 | 13.6 | 4.92 | 13.7 | 5.50 | 5.82 | 4.13 |
| Eu | 0.947 | 1.79 | | 0.768 | 2.91 | 1.55 | 3.86 | 1.42 | 1.63 | 1.29 |
| Gd | 3.14 | 5.51 | | 2.46 | 16.7 | 4.61 | 10.3 | 4.13 | 4.76 | 3.78 |
| Tb | 0.538 | 0.862 | | 0.422 | 2.83 | 0.714 | 1.46 | 0.608 | 0.744 | 0.595 |
| Dy | 3.46 | 5.33 | | 2.71 | 17.2 | 4.25 | 7.61 | 3.31 | 4.06 | 3.45 |
| Ho | 0.757 | 1.09 | | 0.567 | 3.69 | 0.819 | 1.37 | 0.655 | 0.789 | 0.672 |
| Er | 2.19 | 2.89 | | 1.57 | 10.6 | 2.11 | 3.18 | 1.74 | 2.06 | 1.80 |
| Tm | 0.327 | 0.414 | | 0.227 | 1.56 | 0.286 | 0.411 | 0.231 | 0.280 | 0.245 |
| Yb | 2.15 | 2.56 | | 1.46 | 9.85 | 1.73 | 2.30 | 1.42 | 1.75 | 1.50 |
| Lu | 0.310 | 0.366 | | 0.217 | 1.43 | 0.251 | 0.283 | 0.193 | 0.251 | 0.215 |
| Nb | 9.77 | 11.4 | 6 | 5.62 | 35.1 | 19.0 | 65.2 | 35.8 | 42.1 | 23.7 |
| Hf | 2.07 | 1.55 | | 1.62 | 8.82 | 3.89 | 6.36 | 4.66 | 5.23 | 4.23 |
| Ta | 0.676 | 0.667 | | 0.352 | 1.56 | 1.60 | 5.44 | 2.32 | 3.42 | 1.19 |
| Th | 1.04 | 1.07 | b.d.l. | 0.512 | 2.81 | 3.34 | 9.80 | 2.85 | 5.60 | 2.45 |
| U | 0.350 | 0.295 | | 0.150 | 0.623 | 0.807 | 2.53 | 1.11 | 1.64 | 0.635 |
| Ti/V | 23 | 39 | 30 | 21 | | 49 | 43 | 65 | 42 | 43 |
| Nb/Y | 0.45 | 0.37 | 0.24 | 0.36 | 0.30 | 0.79 | 1.75 | 1.82 | 1.82 | 1.14 |
| (La/Sm) _N | 1.67 | 1.49 | | 1.39 | 2.31 | 2.29 | 3.03 | 3.13 | 3.33 | 2.43 |
| (Sm/Yb) _N | 1.43 | 2.15 | | 1.57 | 1.53 | 3.17 | 6.63 | 4.29 | 3.70 | 3.05 |
| (La/Yb) _N | 2.39 | 3.20 | | 2.18 | 3.54 | 7.24 | 20.1 | 13.4 | 12.3 | 7.42 |
| Zr/Nb | 8.1 | 12.1 | 16.4 | 11.6 | 10.7 | 8.8 | 5.0 | 5.1 | 5.0 | 6.2 |
| Th/Ta | 1.54 | 1.60 | | 1.46 | 1.81 | 2.09 | 1.80 | 1.23 | 1.64 | 2.05 |
| Th/Tb | 1.94 | 1.24 | | 1.21 | 0.99 | 4.81 | 6.70 | 4.68 | 7.52 | 4.11 |
| (Th/Tb)/(Th/Ta) | 1.26 | 0.77 | | 0.83 | 0.55 | 2.30 | 3.72 | 3.81 | 4.60 | 2.00 |



Appendix Figure 7.1. Representative CL images of zircon grains from the MK701, MK704 and MK705 samples. White bar is 20 μ m. Dotted circles refer to LA-ICP-MS spot locations.

Chapter 8. Structural setting

8.1. Structural setting of the Band-e-Zeyarat ophiolite

The Band-e-Zeyarat ophiolite consists of a N-S elongated tectonic unit bordered by high angle fault zones (Fig. 5.1). At map scale, this unit displays a domal antiformal structure showing a core composed of the intrusive complex and the sheeted dyke, whereas the borders are characterized by the volcanic sequence and the overlying pelagic sedimentary cover (Fig. 5.1). As already described by McCall (1985), mesoscale folding deformation are well recognizable in the pelagic sedimentary cover of the ophiolite; by contrast in the other stratigraphic units (i.e., volcanic sequence, sheeted dyke complex, and intrusive complex) the mesoscale structures are rarely observed due to the lack of clear stratigraphic markers for the deformation. For this reason, the structural investigation was carried out in selected areas in the northern sector, near the Kahnuj city, (Fig. 8.1) by analysing the pelagic sedimentary cover in detail. In this sector the pelagic sedimentary cover widely crops out and is unconformably covered by an Eocene succession consisting of conglomerates and arenites (Fig. 8.1). High angle strike-slip faults dismember the Band-e-Zeyarat unit in several fault-bounded blocks and they also deform the Eocene succession (Fig. 8.1). The structural analyses highlighted that the pelagic sedimentary cover is characterized by a multiphase deformative evolution consisting of two different deformative phases, namely D₁ and D₂ phases.

The D₁ phase is characterized by sub-isoclinal to close folds, showing fairly similar geometry with subrounded hinges (Fig. 8.2a). In the stratigraphic portion characterized by thin limestone beds, these folds locally display boudinage along the limbs and slightly thickened hinge zones (Fig. 8.2b). In the different tectonic slices, fold axes are rather dispersed as a consequence of the later deformative phases and faulting stage and possibly for the occurrence of non-cylindric folds (Fig. 8.1c). In the area close to the Sabzevaran Fault the axes mainly show N-S orientation (areas A1, A2; Fig. 8.1c); by contrast, moving away from the main fault (area A3 see Fig. 8.1c) and in the

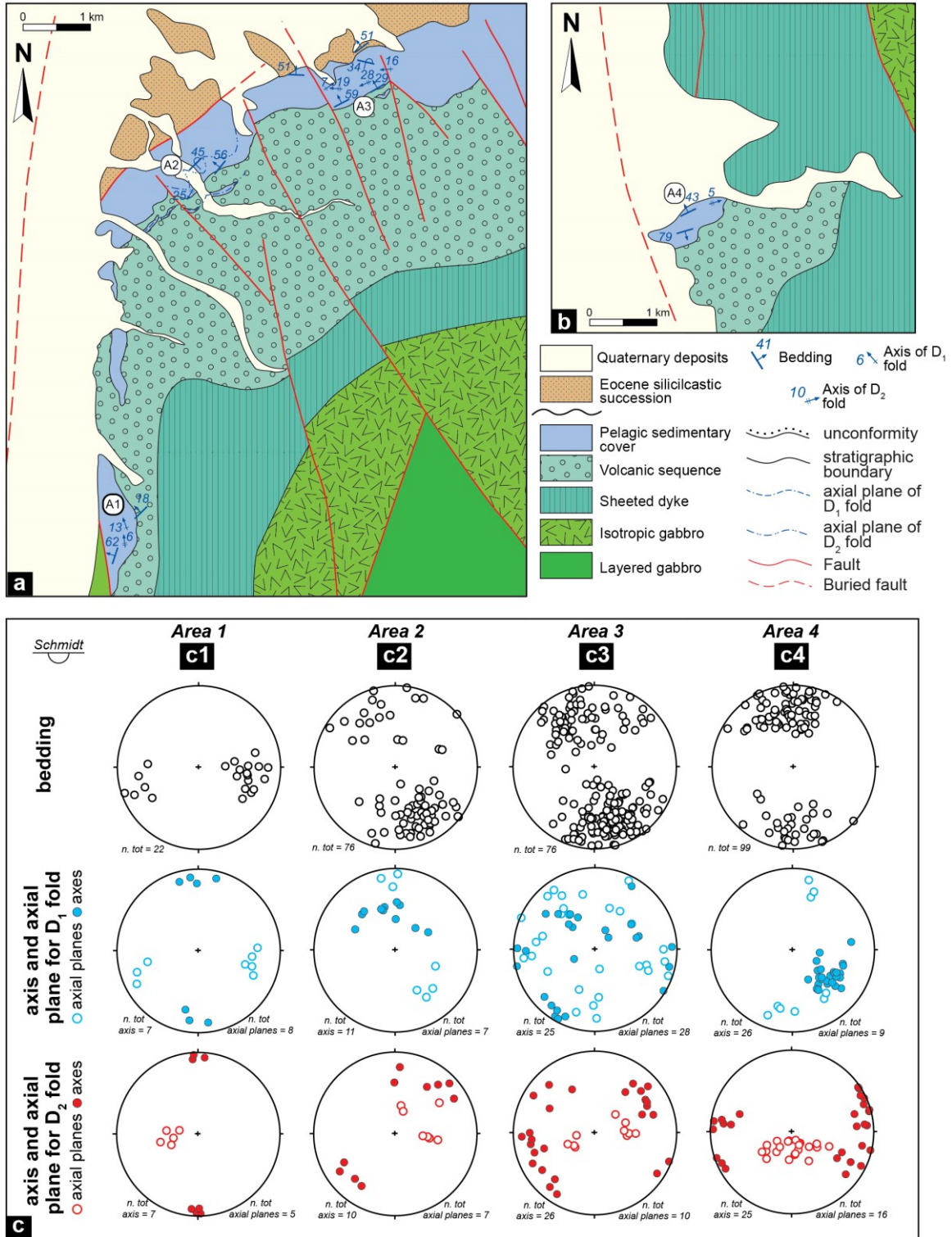


Figure 8.1. a), b) Simplified geological map of two selected areas to the south of the Kahnuj city (for their location see Figure 5.1) showing the structural setting (based on Samimi Namin, 1983 and modified according to original fieldwork and photointerpretation with satellite images). The location of four areas chosen for structural analysis are indicated; c) stereographic plot showing mesoscale data for the structural elements of D₁ and D₂ phases from four distinct studied area (locations shown in Fig. 8.1a).

core of the distinct tectonic slices (area A4 see Fig. 8.1c) the axes show clusters with mainly NE- to ESE and NW-SE orientation. This change in orientation outlines significant rotations due to post D_1 deformation along NNW- to NNE-striking strike-slip faults (Fig. 8.1a). The D_1 folds are associated with a foliation S_1 that represents the axial-plane foliation of these folds (Fig. 8.1c). S_1 is well developed in the marly beds where it represents a disjunctive cleavage generally at low angle with the bedding (S_0 ; Fig. 8.2c). In the hinge zone, an intersection lineation is locally observed within the marly horizons; it represents the intersection lineation between S_0 and S_1 and corresponds to the fold axis (Fig. 8.2a). In thin section, only a weak pressure solution locally occurs in the marl. By contrast, in the more competent limestone beds the foliation is only locally developed in the hinge zone as a disjunctive cleavage showing radial fanning around the hinge (Fig. 8.2d). This change in orientation is likely related to the refraction of the foliation as a consequence of the competence contrast between marl and limestone beds.

The D_2 phase is associated with the formation of open to close folds showing parallel geometry with rounded hinges (Fig. 8.2e). These folds are asymmetric and recumbent and are characterized by sub-horizontal axial planes (Figs. 8.2d, e; Fig. 8.1c). The D_2 folds are superimposed on the folds and structural elements D_1 , showing a type 3 interference pattern (Ramsey, 1967; Figs. 8.2e, g). The fold axes are sub-horizontal and variably oriented. They range from N- to NE-trends in the sectors close to the Sabzevaran Fault (areas A1, A2; Fig. 8.1c), whereas far from the main fault (area A3 see Fig. 8.1a) and within the core of the tectonic slices (area A4 see Fig. 8.1a) they show a complete distribution from NE-SW to SE-NW orientation (Fig. 8.1c). The asymmetry of D_2 folds indicate mainly N- to NW vergence, though W-verging folds have been observed close to the Sabzevaran Fault (in the area A1; Fig. 8.1a). Similarly to D_1 folds, this variation in orientation for structural elements of D_2 folds points out for significant rotations as a consequence of post- D_2 strike-slip faulting deformation (Fig. 8.1a). The D_2 folds are associated with a weakly

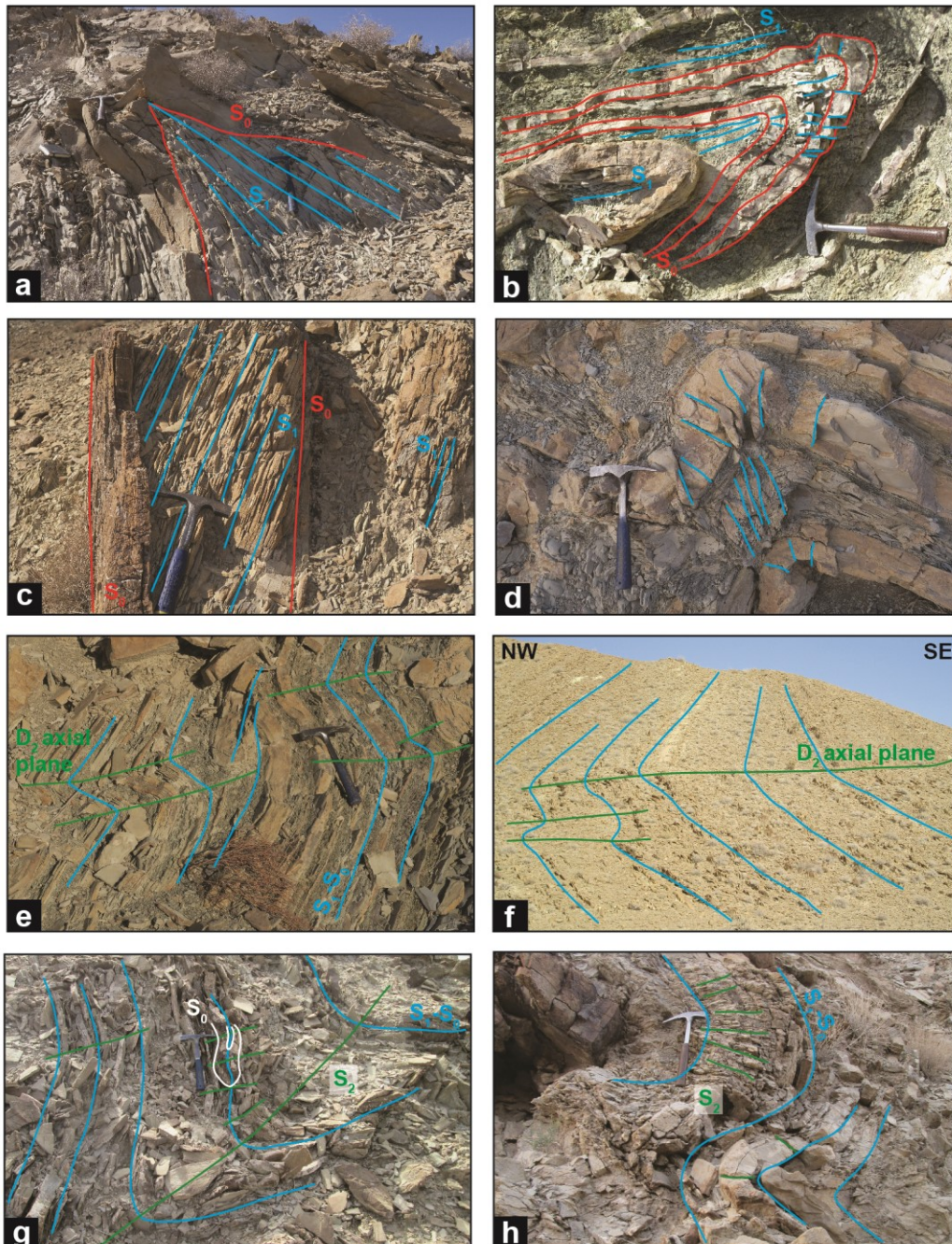


Figure 8.2. a-b) D_1 sub-isoclinal to tight folds showing axial plane foliation S_1 (indicated by light blue lines). The folded bedding S_0 is indicated by a red line; in figure b) is shown a close-up of the refraction of the S_1 foliation as a consequence of the competence of the deformed beds; c) structural relationships between S_1 foliation (light blue line) and S_0 bedding (red line) along the limbs of decametric isoclinal folds; d) hinge zone of D_1 fold showing the refraction of the foliation S_1 according to the competence of the deformed beds; mesoscale (e) and macroscale (f) D_2 asymmetric open folds that deform the composite surface S_1 - S_0 (light blue line) along a limb of a macroscale D_1 fold. D_2 axial surface is indicated by green lines; g) D_2 folds (green lines indicate D_2 axial planes) deforming the D_1 axial planes (light blue lines); h) hinge zone of a D_2 open fold showing fracture cleavage representing the axial plane foliation.

developed axial plane cleavage (S_2), which is mainly formed in the hinge zones of close folds. This cleavage corresponds to a centimetric spaced fracture cleavage and is sub-horizontal in all the studied areas (Fig. 8.2h; Fig. 8.1c).

In summary, both the D_1 and D_2 structure do not deform the Eocene succession, which is unconformably deposited above the Valanginian - Aptian pelagic (R. Catanzariti and V. Luciani personal communication) sedimentary cover of the Band-e-Zeyarat ophiolite (Fig. 8.1a). This evidence provides a time-constraint for the deformation of the Band-e-Zeyarat ophiolite, which likely occurred between Late Cretaceous and Paleocene - earliest Eocene.

8.2. Structural setting of the Durkan Complex

The Durkan Complex represents a key tectonic element of the western North Makran, which is bordered by the reverse Dar-Anar Fault, to the north, and the deformation zone associated with the Bashakerd Thrust, to the south (Fig. 6.1). As in part already described by McCall (1985), the map-scale structural setting of this complex is extremely articulated; in detail, the Durkan Complex is composed by several tectonic slices internally showing hundreds of metres thick successions that are characterized by polyphase folding. Given these structural complexities and the logistic difficulties in performing field studies in the studied area, the detailed mapping of the macro-scale structure throughout the whole studied area is extremely difficult. For these reasons, a structural study (from macro- to micro-scale) of the Durkan Complex in selected areas was performed to describe its structural setting and to reconstruct its deformation history. Nonetheless, these multiscale structural observations allow to propose a schematic and simplified structural map of a wider area to the south of Manujan (Fig. 8.3a), which shows some of the macro-scale folds (Fig. 8.4a) and the most important tectonic contacts. This structural study of the Durkan Complex allows

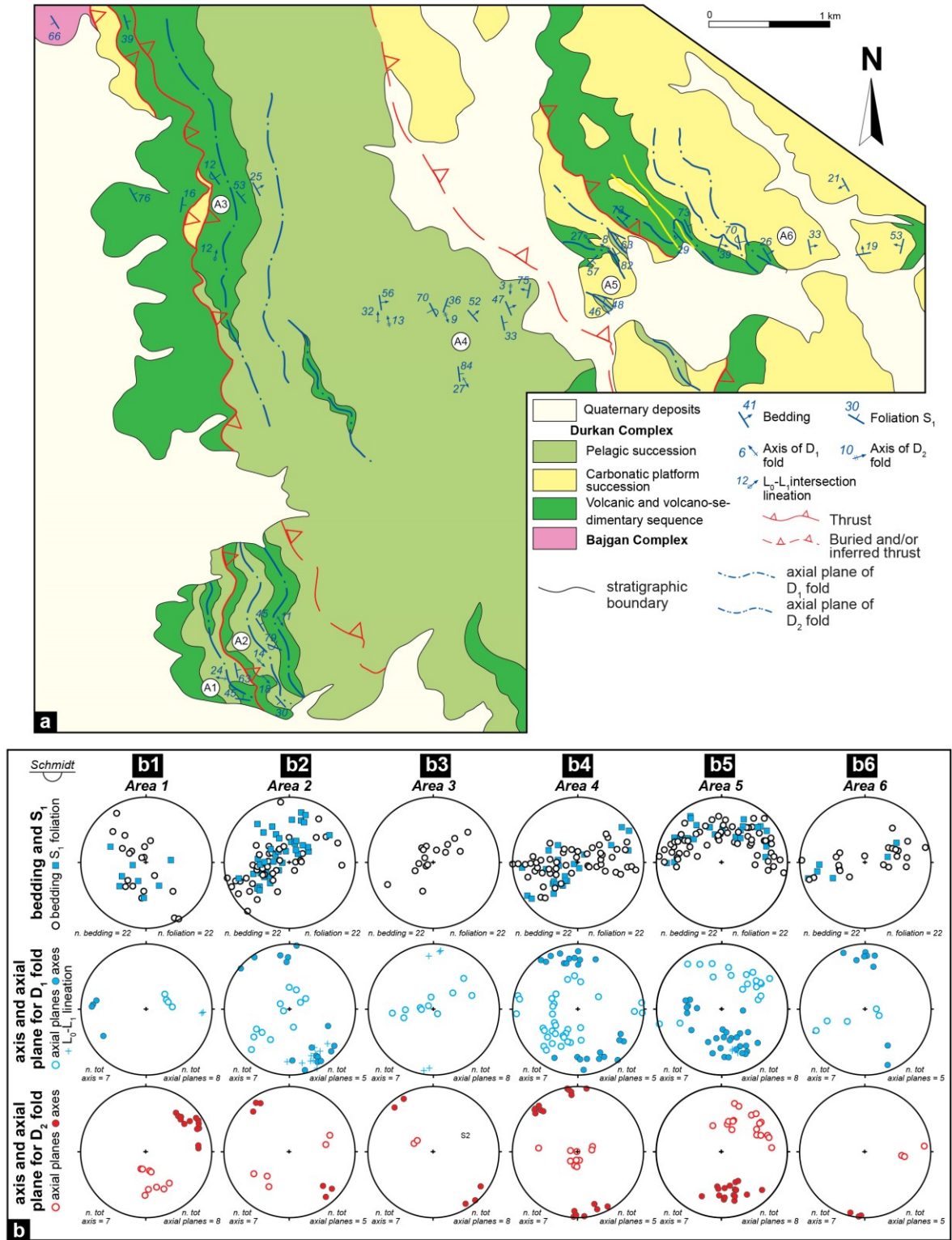


Figure 8.3. a) Simplified structural maps of the Durkan Complex to the south of Manujan city (see Fig. 6.2 for its location) showing the main tectonic contacts that border distinct tectonic units (based on Samimi Namin, 1983 and modified according to original fieldwork and photointerpretation with satellite images). The location of six areas chosen for detailed structural analysis are indicated; b) stereographic plots showing mesoscale data for the structural elements of D_1 and D_2 phases from six distinct studied area (locations shown in Fig. 8.3a).

to recognize a multiphase deformation evolution characterized by two deformative phases, namely D_1 and D_2 phases.

The D_1 deformation phase is associated with folds developed from macro- to micro-scale. These folds are isoclinal to sub-isoclinal and fairly non-cylindrical and show similar geometry (Figs. 8.4a, b, c). They are characterized by thickened and generally rounded hinge zones as well as strongly stretched and thinned limbs (Fig. 8.4b). In addition, in the sequence composed by alternating meta-limestone and shale, the limbs of the folds can be affected by boudinage of the competent beds. The D_1 folds show a general W-vergence and have in most of the tectonic slices sub-horizontal and mainly NW- to NNW-striking axes (Figs. 8.3b, 8.4a, b). However, locally NE-SW orientation can be observed likely as a consequence of passive rotations due to later deformative stages (Fig. 8.3b).

The D_1 folds are associated with an axial-plane foliation S_1 that is sub-parallel to or at low angle with the bedding S_0 (Figs. 8.4c, d; Fig. 8.3b). This spatial orientation of S_1 produce an intersection lineation between S_0 and S_1 (i.e., L_0-L_1), which is represented by either a marked colour variation along the foliation surface in the shale (Fig. 8.4e) or mullion structures where more competent beds are abundant in the deformed sequence (Fig. 8.4f). The L_0-L_1 lineation is generally parallel to the fold axes (Fig. 8.3b). The foliation shows different features and a differential development in the various lithologies. These differences can be seen both on mesoscopic and microscopic scale. In the shales it corresponds to a penetrative and mm-spaced slaty cleavage (Fig. 8.4d). In thin section, the S_1 is defined by aligned phyllosilicates (rare white mica + chlorite + clay minerals) that surround elongated quartz-albite aggregates showing crystallographic preferential orientation (Fig. 8.5a). By contrast, in the meta-limestone and/or meta-volcanoclastic arenite S_1 corresponds to a pressure solution cleavage (Fig. 8.5b). In thin section, this cleavage is characterized by elongated calcite grains as well as dissolutions seems of reddish to brownish clay minerals (Fig. 8.5b, c).

Rare white-mica and chlorite are found in the marble from the tectonic slices showing higher

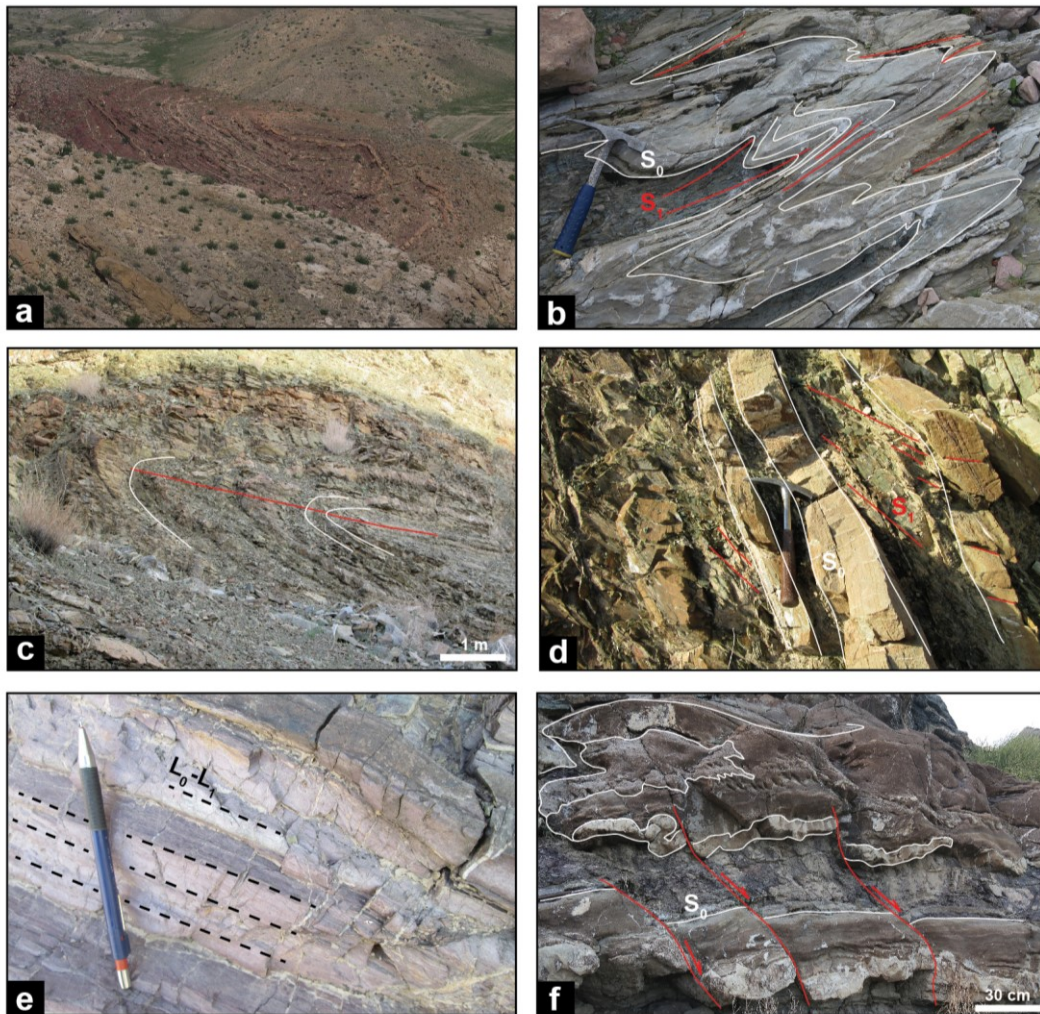


Figure 8.4. Macro-scale (a) and meso-scale (b) isoclinal folds formed during D1 phase. Close-up in (b) show the similar geometry of the folds and the thinning of their limb (white lines and red lines indicate bedding S_0 and axial plane foliation S_1 , respectively); c) D1 isoclinal folds associated with axial plane foliation S_1 (red line); d) structural relationships between bedding S_0 (white line) and foliation S_1 (red line) along a overturned beds of macro-scale anticline; e) shales showing colour variation on the S_1 foliation representing the intersection lineation L_0-L_1 ; f) isoclinal folds showing boudinage and mullion structures along the limbs (indicate by white line). The folds are crosscut by later extensional faults (red line).

extent of metamorphic recrystallization (Fig. 8.5d). However, in those tectonic slices characterized by weak metamorphism the S_1 foliation generally corresponds to a disjunctive cleavage in the more competent meta-limestone and meta-arenite (Fig. 8.4c).

The D2 deformation phase is characterized by the formation of heterogeneous folds in response of both the competence contrast of the beds and the metamorphic overprint of the folded

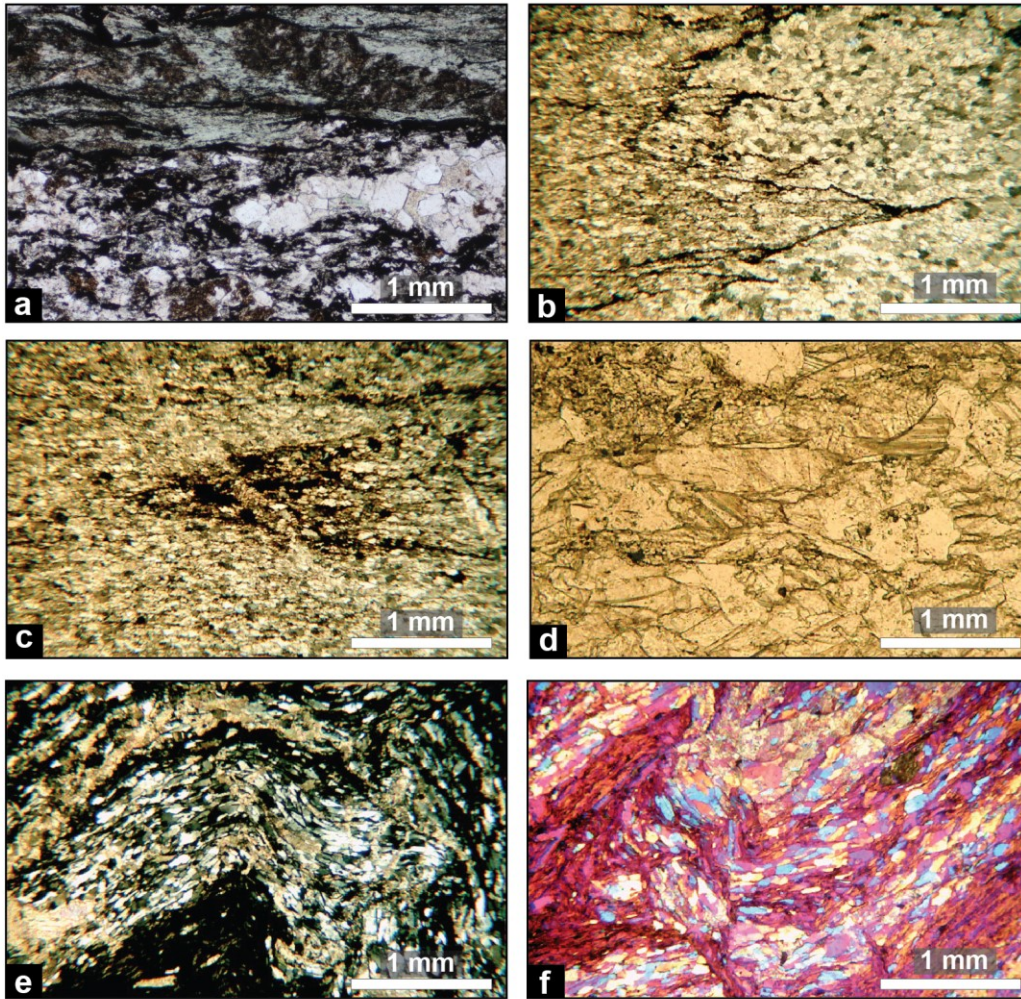


Figure 8.5. Photomicrographs of the D_1 and D_2 microstructures: a) S_1 foliation defined by chlorite and aggregate of albite and quartz; b-c) D_1 folds in meta-limestone showing different grain size and axial plane foliation represented by pressure solution cleavage; d) marble showing iso-oriented white mica crystals marking the S_1 foliation; e-f) D_2 open folds deforming the composite S_1 - S_0 surface. The D_2 folds are associated with an axial plane cleavage marked by reorientation of the phyllosilicates and micro-faults.

successions. D_2 folds range from open to close and generally asymmetric folds that are observed from macro- to micro-scale (Fig. 8.4a; Fig. 8.6a, b, Fig. 8.5e). They generally show a parallel geometry; however, where the folded sequence shows an increase of the shale/competent beds (e.g., meta-arenite and meta-limestone) ratios, D_2 folds are characterized by fairly similar geometry with acute hinge zones (Fig. 8.6c). Their superimposition on the folds and structural elements of D_1 produce a type 3 interference pattern (Ramsey, 1967) that can be recognized from macro- to meso-

scale (Fig. 8.4a; Fig. 8.6d). The axial planes of D_2 folds correspond to curvilinear surfaces at the meso-scale (Fig. 8.6c); they are generally slightly inclined, and their orientations are different in

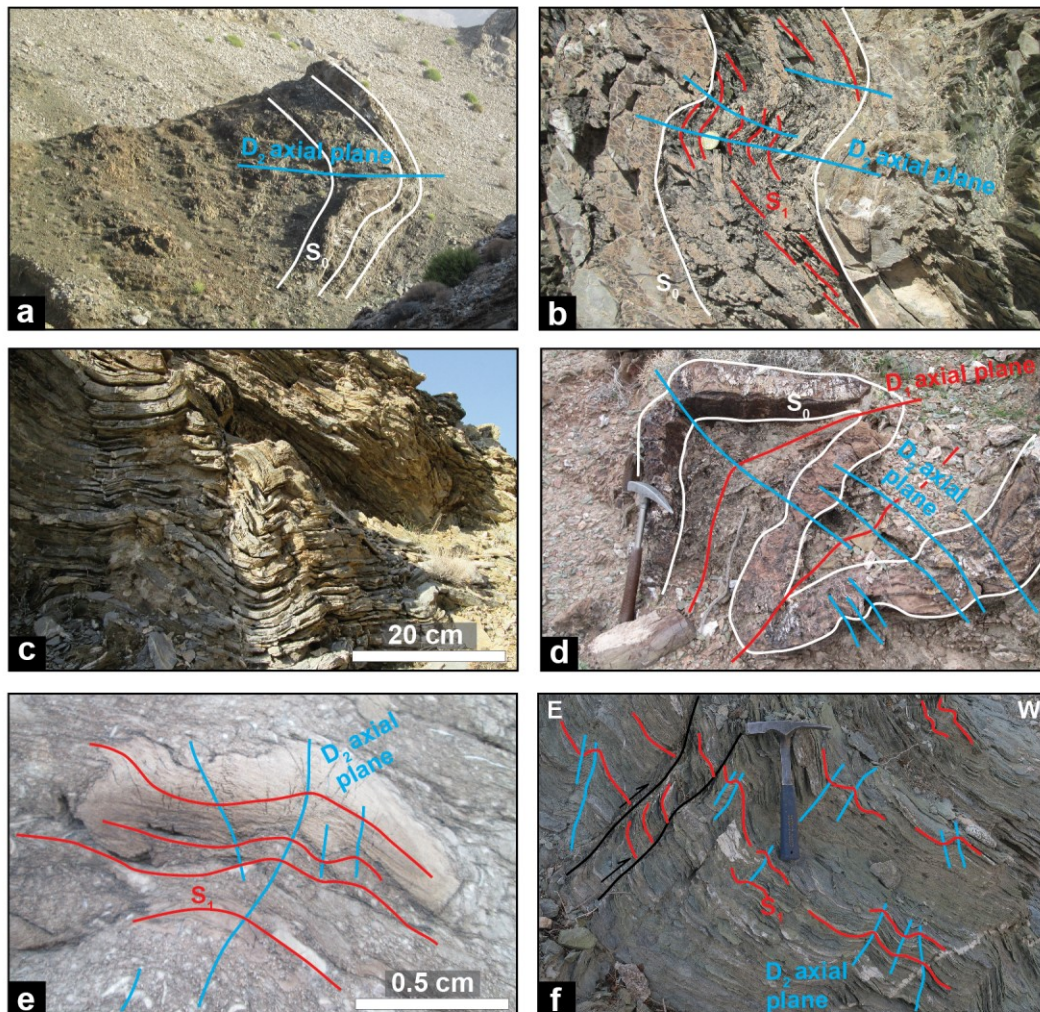


Figure 8.6. Macro-scale (a) and meso-scale (b) D_2 open and asymmetric folds (light blue lines represent axial plane, red lines represent S_1 foliation, and white lines correspond to bedding S_0); c) D_2 folds showing variation of the geometry from similar to parallel folds according to the thickness of the competent beds deformed; d) type 3 interference pattern between D_1 and D_2 folds. Symbols: red lines: D_1 axial plane; light blue lines: D_2 axial plane; white lines: bedding; e) detail of interference between D_1 and D_2 folds in a carbonatic meta-breccia. Symbols: red lines: D_1 axial plane; light blue lines: D_2 axial plane; f) D_2 E-verging crenulation folds (light blue lines represent axial planes) deforming the S_1 foliation (red lines) crosscut by W-verging reverse faults (black lines).

the various tectonic slices, ranging from NW-SE to W-E direction (Fig. 8.3b). The D_2 folds are associated with the development of an axial plane foliation S_2 that corresponds to a disjunctive cleavage in the most competent beds and to a crenulation cleavage in the shale (Fig. 8.6b, e, f). The axes of D_2 folds are generally sub-horizontal and show mainly NW-SE direction (Fig. 8.3b).

However, the striking of D₂ axes in some tectonic slices is mainly N-S (Fig 8.3b), likely suggesting rotation of the D₂ folds as a consequence of later deformative events. The asymmetry of the folds indicates a NE- to E-vergence (Fig. 8.6f). Locally the D₂ folds are associated with low-angle dipping faults showing the same direction of transport of the correlated folds. At micro-scale, the folds of the D₂ phase are well developed only in the shale, where they deform the composite surface defined by the S₁ foliation and the S₀ (Fig. 8.5e). The S₂ foliation is not associated with a metamorphic recrystallization; by contrast it is marked by the localized transposition and re-orientation of phyllosilicates (e.g., chlorite) of the S₁ foliation in the hinges zone and/or microfaults (Fig. 8.5f).

In conclusion, the structures of the D₁ and D₂ phases are sealed by the unconformable deposition of siliciclastic and carbonatic successions, which show Eocene or younger ages according to McCall (1985) and new preliminary data (see below). These data, together with the depositional age provided for the Durkan Complex (see section 6.3), suggest that the deformation of the Durkan Complex occurred from the latest Late Cretaceous to the Paleocene-earliest Eocene.

8.3. Post-Eocene deformation in the western North Makran

The post-Eocene deformation will be here briefly described as this thesis is not directly focused on this topic. However, a synthetic discussion based on preliminary new data and literature data (McCall, 1985) is useful to describe the possible structural evolution of the studied tectonic units in the western North Makran (see section 8.4).

The Eocene succession is well exposed to the east of Manujan and lies onto the Band-e-Zeyarat and the Durkan Complex with an angular and erosional unconformity (Figs. 8.7a, b). The stratigraphic analyses allow to reconstruct a succession showing extremely variable features and

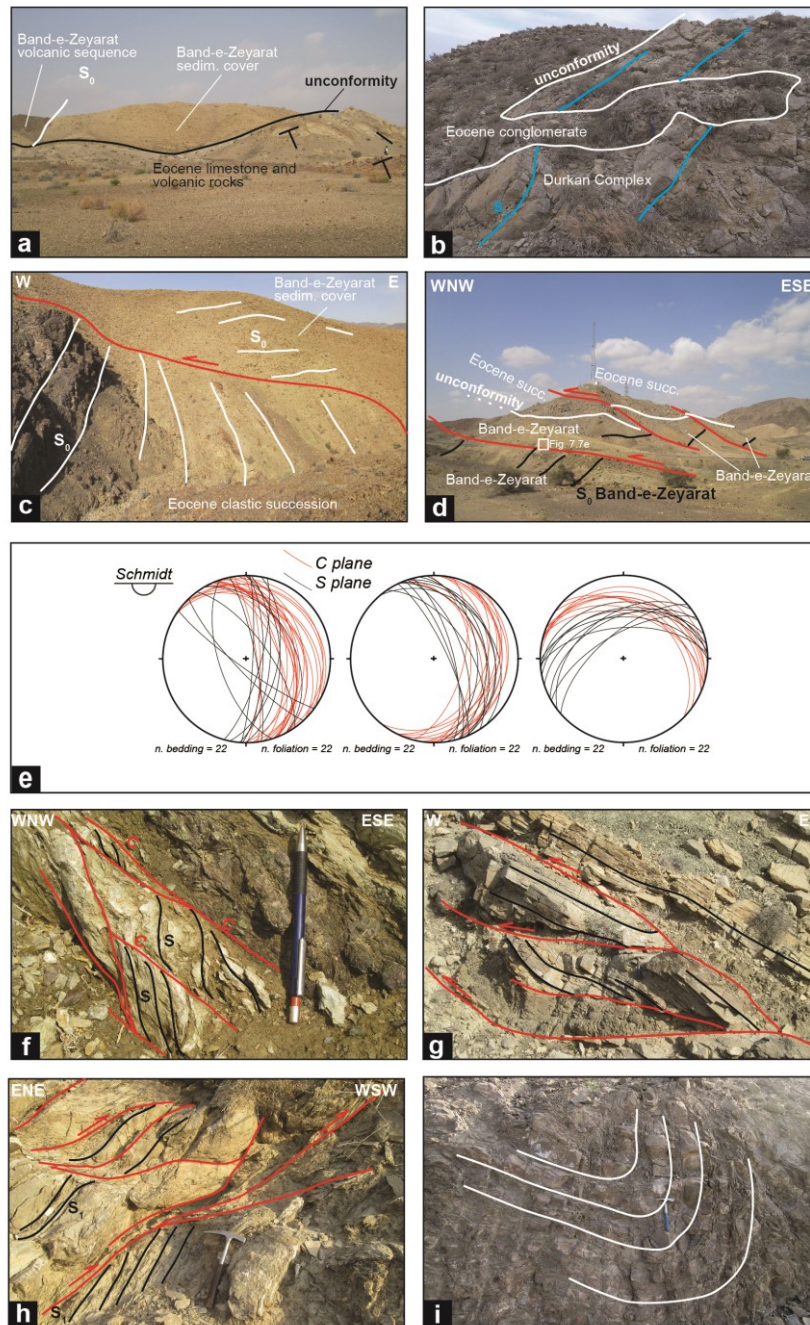


Figure 8.7. a) panoramic view of the unconformity surface separating the post-Eocene succession and the Band-e-Zeyarat ophiolite. The unconformity is indicated with black line whereas S_0 in the Band-e-Zeyarat ophiolite is represented with white line; b) close-up of the unconformable deposition of post-Eocene conglomeratic succession (unconformity indicated by white line) onto the deformed succession of the Durkan Complex (light blue line for the S_1 foliation); c) panoramic view of the internal part of a duplex structures showing the overthrusting of the Band-e-Zeyarat ophiolite onto the Eocene succession; d) Panoramic view of thrust-bounded tectonic slices including Band-e-Zeyarat ophiolite and the overlying Eocene succession; e) stereographic plot of thrust surface (C planes, red lines) and S-plane in S-C shear in different localities of the studied area; the transport direction range from WNW to SSE; f) S-C structures associated with a macro-scale thrust that indicate top-to WNW movement; g) meso-scale duplex in the Eocene succession (red lines: faults; black line: bedding); h) close-up showing the crosscutting relationships between the S_1 foliation in the Band-e-Zeyarat ophiolite and the thrust-related S-C shear zones; i) field occurrence of an upright folds associated with the $D_{1\text{post-eoc}}$ thrusts.

lateral-vertical changes of facies. These data agree with the previous published work by McCall (1985) and McCall (2002), which interpreted this succession as deposited in an articulated basin showing structural highs with platform sedimentation separated by rather deep basin showing fan-delta and turbiditic systems. As a general trend, this succession is characterized at the base by a laterally discontinuous clastic succession passing to a sequence showing the alternation of limestones, volcanic rocks and volcanoclastic rocks. The clastic succession is composed of alternating paraconglomerates, coarse-grained arenites, greenish shales and siltstones. The paraconglomerates are lenticular bodies and consists of a shaly matrix that includes up to plurimetric blocks of volcanic rocks, different varieties of limestones, and minor chert. The nature of the blocks and their abundance are strictly dependent on the substratum onto which the conglomerates are deposited. In particular, the clasts in the conglomerates are sourced from the erosion of the lithostratigraphic units lying below the unconformity. The arenites are quartz-rich and show abundant lithic fragments of volcanic rocks as well as limestones. The upper part of the succession continues with alternating limestone, coarse-grained calcarenites, thick basaltic lava flows and volcanoclastic breccias, arenites and shale. The calcarenites show fragments of carbonatic rocks, bioclasts and volcanic rocks. The preliminary structural analysis permit to identify in the Eocene succession two main deformation phases, namely $D_{1 \text{ post-eoc}}$ and $D_{2 \text{ post-eoc}}$ that are characterized by the structural association of faults and folds. Unfortunately, the data collected are up to now insufficient to better constrain the age of the deformation that can be ascribed to a generic post-Eocene according to the age of deformed rocks.

The $D_{1 \text{ post-eoc}}$ phase is characterized by map-scale thrust zones showing ramp-flat geometry (Fig. 8.7c). They are characterized by interlacing thrusts surfaces that define thrust-bounded tectonic slices (Fig. 8.7d), locally showing duplex geometry. The thrusts are mainly NNW-SSE to NNE-SSW oriented and show a general top-to-W sense of movement (Fig. 8.7c, d, e). At meso-

scale, the main deformation is localized along the main thrusts, where S-C shear zones and duplex structures can be observed (Fig. 8.7f, g). The shear zones clearly crosscut the S_1 foliation of the

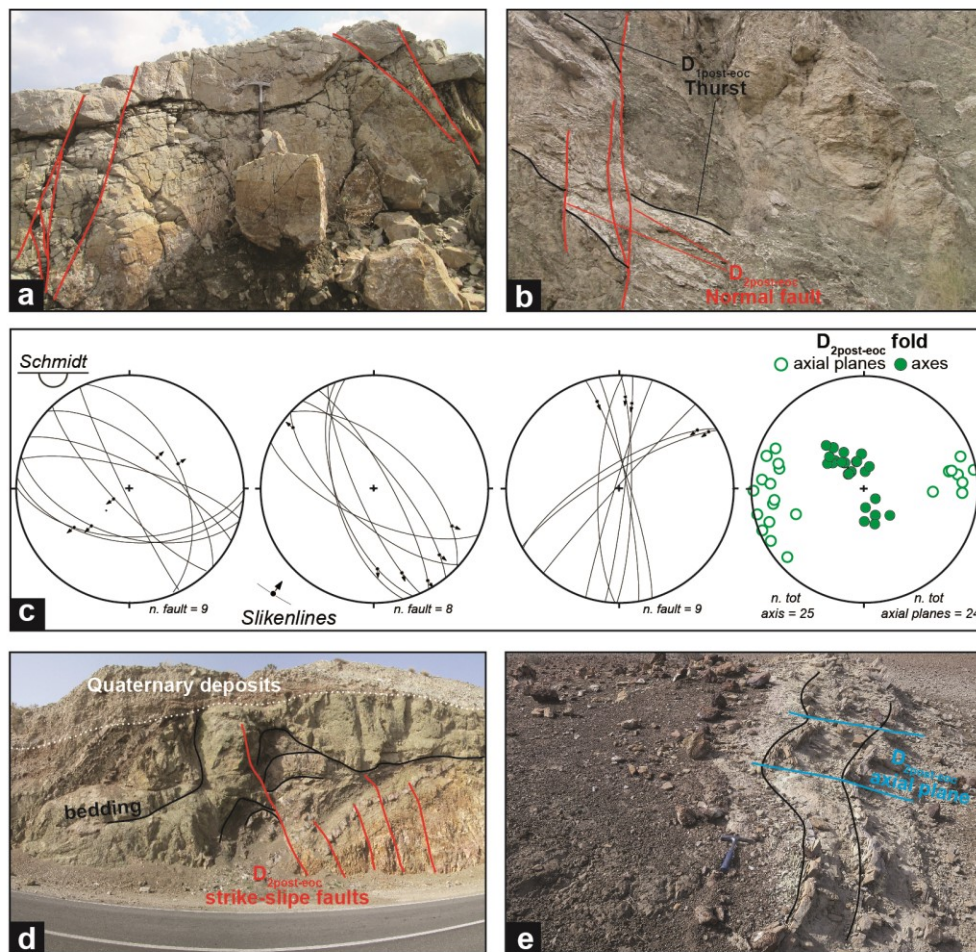


Figure 8.8. a) mesoscale conjugate normal faults in Eocene limestone; b) extensional fault crosscutting the deformation zones associated with $D_{1\text{ post-eoc}}$ thrust; c) stereographic plot showing representative data of normal faults (c1), strike-slip fault systems (c2, c3) and folds associated with strike-slip fault systems (c4). For the faults representative slickenlines are shown; d) faulting and folding deformation associated with dextral strike-slip fault zone; e) detail of folds associated with the strike-slip faulting.

Band-e-Zeyarat and the Durkan Complex, suggesting a relative chronological relationship (Fig. 8.7h). The thrust zones are locally associated with meso- to macro-scale folds (Fig. 8.7i). They are open to close asymmetric folds, showing a sub-vertical to rather inclined axial plane and sub-horizontal axis (Fig. 8.7i) and do not show axial plane foliation. These folds are well developed close to the main thrust surfaces indicating that they likely represent ramp-folds.

The D_2 post-eoc phase is typically characterized by high-angle normal and strike-slip faults developed from meso- to macro-scale. At meso-scale, the normal faults correspond to planar conjugate planes mainly showing NNW- to NW-strike (Figs. 8.8a, b, c). They crosscut the Eocene succession as well as the D_1 post-eoc structures (Fig. 8.8b). By contrast, two systems of strike-slip faults can be observed and they show NW-SE strike and N-S to NNE-SSW strike (Fig. 8.8c). They are represented by anastomosed planes forming interlacing lenticular tectonic slices and locally flower structures (Fig. 8.8d). These faults can be associated with folding and verticalization of the deformed sequence (Fig. 8.8d). The folds are observed in the proximity of the main faults and show sub-horizontal axis and sub-vertical axial plane. On the contrary, in the core and less deformed portions of the tectonic slices the succession is characterized by open to gentle folds showing NNW-trending and subvertical axes, as well as axial planes rather steep with mainly NW-SE strike (Fig. 8.8c). These folds display parallel geometry, rounded hinges and are locally associated with the development of a fracture cleavage as axial plane foliation (Fig. 8.8e). The character of these folds coupled with their axes orientation likely suggest that they formed to accommodate strike-slip movements along NNW-SSE striking faults.

8.4. Discussion: Structural evolution of the western North Makran

The structural data presented in this thesis together with those already published (see McCall (1985); see also section 2.3) outline for a long-lived and complex deformation history achieved during the Cretaceous – present day formation of the Makran Accretionary Prism. Data from both modern and fossil subduction complexes indicate that they are commonly characterized by a multistage deformation history showing various steps occurred at different depth and time during the accretion-subduction and the subsequent exhumation histories (Platt et al., 1985; Charvet &

Ogawa, 1994; Bettelli & Vannucchi, 2003; Clift & Vannuchhi, 2004; Marroni et al., 2004; Meneghini et al., 2009; Remitti et al., 2011; Wakabayashi, 2015; Kusky et al., 2013). In brief, the shallow level of the frontal part of a subduction complex, namely the frontal wedge, is characterized by the frontal accretion of non-consolidated or poorly consolidated deposits during their progressive lithification and dehydration alternated with tectonic erosion of the prism (Pini, 1999; Bettelli & Vannucchi, 2003; Remitti et al., 2011;). In general, at this shallow level within the frontal wedge the combination of tectonic, sedimentary, and diapir processes controls the deformation and commonly produces highly dismembered formation and composite chaotic units (i.e., broken formations and polygenetic mélanges; Bettelli & Vannucchi, 2003; Festa et al., 2012, 2013; 2019). By contrast, deformation at deeper level of the subduction complex is testified by the accretion (or underplating) of tectonic slices showing coherent successions that are characterized by non-coaxial folds, penetrative and continuous foliation as well as metamorphic recrystallization (Wakabayashi, 1992; Kusky et al., 1997; Marroni et al., 2004; Meneghini et al., 2020). In the case of underplating, the accretion in the prism is generally followed by exhumative deformation stage and/or stages that can be associated with an extensional tectonic regime within the prism in order to accommodate the thickening caused by the continuous underplating and/or post-collisional deformation (Marroni et al., 2004; Meneghini et al., 2020;). The structural data presented in this thesis indicate that the structural evolution of the studied sector of the North Makran can be subdivided in a pre-Eocene stage and a post-Eocene stage.

The pre-Eocene stage is recorded in the complex structural architecture of the Band-e-Zeyarat ophiolite and the Durkan Complex, which show a first phase of deformation characterized by the development of isoclinal folds associated with a pervasive and continuous axial plane foliation. This deformation style is consistent with the coherent underplating of these units in the Makran subduction complex. The different nature of the foliation in these two units, i.e., a disjunctive

cleavage in the Band-e-Zeyarat ophiolite and a sub-greenschist metamorphic foliation in the Durkan Complex, record their deformation at different depth within the Makran subduction complex. The asymmetry of the isoclinal folds indicates for the Durkan Complex and the Band-e-Zeyarat ophiolite a W-vergence and a S- to SE-vergence with respect to present-day coordinates, respectively. This phase of underplating was also possibly characterized by the localization of the deformation along discrete thrust zones and the imbrication of distinct tectonic slices. The thrusting of the Band-e-Zeyarat ophiolite onto the Durkan Complex possibly occurred during this phase, though post-Eocene thrust activity cannot be excluded. In addition, the entering of the Durkan seamounts chain in the prism could also cause a general shortening of the whole margin and the imbrication of the arc-forearc domain (see Chapter 6), now represented by the Ganj Complex. The underplating phase is followed in both units by a deformation phase showing folds with sub-horizontal axial plane and axes. This deformation style fits with the progressive exhumation of these units to shallower level of the accretionary prism. This is strongly supported by the features of the axial plane foliations formed in this stage and their comparison with those formed during the underplating stage; in fact the weak axial plane cleavage and the crenulation cleavage shown by D₂ folds in the Band-e-Zeyarat ophiolite and Durkan Complex, respectively, indicate an exhumation to shallow level after the D₁ deformation. In many cases worldwide, the exhumation of deeply accreted units occurred during the continent-continent collision (Platt, 1993; Marroni et al., 2004). However, triggering of exhumation and extension of the accretionary prism can also occur during subduction stages and it can be related to the overgrowth of the accretionary prism and the consequent accommodation to restabilize a critical taper angle (Platt, 1993; Marroni & Pandolfi, 1996). In the studied case, the accretion of fragments of the Durkan seamounts chain had likely induced the shifting from accretion to exhumation in order to balance the topographic overgrowth of the of the prism. In addition, possible contribution to the topographic thickening of the prism

may be related to the uplift of the whole prism in response the subduction of the highest parts of the Durkan seamount chain.

The unconformable deposition of the Eocene succession above the Band-e-Zeyarat unit and Durkan Complex (McCall, 1985) chronologically constrains the accretion and exhumation of these units during pre-Eocene times. This is also suggested by the occurrence of clasts of Band-e-Zeyarat unit and Durkan Complex lithologies within the Eocene basal conglomerate, as already described in the eastern Makran by Burg et al. (2013). The Eocene succession records the deposition within a basin showing articulated physiography likely inherited by previous tectonic stages. This kind of basin likely represents a wedge-top basin, which was characterized by the intercalations in the succession of volcanic and volcanoclastic rocks, suggesting a proximal active volcanic area. During the Eocene-Oligocene the deformation front of the Makran frontal wedge was migrating southward as indicated by the thrusting of the North Makran domain onto the progressively deformed Eocene – Miocene trench turbidites of the Inner Makran Domain (Dolati, 2010; Dolati & Burg, 2013; Burg et al., 2013). However, the new structural data outline a significative post-Eocene deformation of the previously accreted North Makran units and their overlying wedge-top successions. The post-Eocene thrusting stage (i.e., $D_{1\text{-post eoc}}$ phase) can be achieved during a shortening of the innermost part of the accretionary prism throughout the activation of out-of-sequence thrusts. During this stage, the reactivation of thrust zones formed during underplating of the North Makran units was probably diffuse as suggested by the common involvement of Eocene succession along the main tectonic boundary between the different tectonic units of the North Makran. The structural data indicates a W- to SSW vergence during this thrusting stage, with respect to present day coordinates. The great variation of tectonic transport direction can be a primary feature, implying an arc-shaped thrusts interlaced by lateral ramps and collectively accommodating oblique reverse kinematics. However, these different orientations can likely be a consequence of clockwise rotation

in response to $D_{2\text{post-eoc}}$ strike-slip faulting stages. This is also suggested by the comparison with structural data from the eastern North Makran that indicate mainly E-W trending of the thrusts (Dolati, 2010; Hunziker, 2014; Dolati & Burg, 2013; Burg et al., 2013), implying a possible clockwise rotation of the structures of the western North Makran. The comparison with regional-scale data suggest that these strike-slip activity and clockwise rotation can be related to the activation of the right-lateral Minab-Sabzevaran fault system during late Miocene – Pliocene (Stoneley, 2005; Regard et al., 2010). This fault system accommodates the different deformation style between the Zagros and the Makran that are characterized at this time by continent-continent collision and still active subduction, respectively.

*Chapter 9. Geodynamic implications and concluding
remarks*

9.1. Summary of the new data from the Ganj Complex, the Band-e-Zeyarat ophiolite, the Durkan Complex, and the Bajgan Complex in the western North Makran

In this thesis, new multidisciplinary field and lab-based data on the Ganj Complex, the Band-e-Zeyarat ophiolite, the Durkan Complex and the Bajgan Complex in the western North Makran have been presented. The Ganj Complex and the Band-e-Zeyarat ophiolites were formerly interpreted as the remnants of the North Makran Ocean, whereas the Durkan and the Bajgan Complexes were considered as the remnants of the southern continental margin of this basin.

This thesis provides new significant data to better understand the tectono-magmatic significance of these units and their role in the Late Cretaceous – Paleocene-early Eocene(?) convergence history. The main results are briefly summarized below:

- i) The Ganj Complex shows a Late Cretaceous volcano-sedimentary stratigraphic succession and the geochemistry of the magmatic rocks indicates that it represents a volcanic arc succession rather than an ophiolitic sequence. The characteristics of the succession suggest a rather shallow marine environment of deposition/eruption compatible with a Turonian - Coniacian intra-arc setting. The geochemical affinity of the magmatic rocks, which include IAT, calc-alkaline and rock with adakitic signature, indicates that the Ganj rocks derived from the partial melting of the sub-arc mantle wedge enriched by different types of chemical components released from the subducting slab. The occurrence of rocks with adakite-like chemical fingerprint implies the partial melting of the eclogitized subducting oceanic crust suggesting the subduction of a rather hot and/or young oceanic lithosphere. The present-day structural position of the Ganj Complex suggest that this arc was built close or onto the southern continental margin of the Lut block.
- ii) The Band-e-Zeyarat ophiolite shows crustal architecture, geochemical fingerprints of the

magmatic rocks, mineral chemistry of rock-forming minerals, as well as thermobarometric estimations, which indicate that it represents a MOR-type ophiolite (*sensu* Dilek & Furnes, 2011) formed during the Early Cretaceous. In particular, the petrogenetic studies indicate partial melting of sub-oceanic mantle in the spinel-facies and partial melting of sub-oceanic mantle bearing OIB-type chemical components for the genesis of the N-MORB and E-MORB type rocks, respectively. The significant contribution of partial melting in the garnet-facies shown by the E-MORB rocks suggest interaction of rising OIB-mantle patch with depleted sub-oceanic mantle. These processes strongly point out that the Band-e-Zeyarat ophiolites recorded Early Cretaceous oceanic crust formation dominated by plume-ridge interaction.

- iii) In the western North Makran, the Durkan Complex includes successions recording a Late Cretaceous interplay between alkaline magmatism and both shallow water and pelagic sedimentation. The geochemistry of the magmatic rocks, the mineral chemistry of clinopyroxene, and the petrogenetic study indicate that the Durkan Complex is characterized by the association of P-MORB and alkaline basalts, which were formed by partial melting of OIB-like mantle sources with variable contribution of melts formed at both garnet- and spinel-facies. The stratigraphic architecture and the geochemical features of the magmatic rocks suggest that the western Durkan Complex represents Late Cretaceous tectonically disrupted seamount fragments incorporated in the Makran Accretionary Prism. These findings strongly suggest that a mantle plume existed in the Makran sector of the Neo-Tethys during the Late Cretaceous and that it played a major role in influencing the volcanic activity and sedimentation.
- iv) The Bajgan Complex is composed by tectonic slices bordered by mylonitic shear zones. These slices show a wide range of metamorphic rocks including meta-serpentinites, meta-

intrusive rocks, meta-volcanic rocks and meta-sedimentary rocks. The meta-intrusive rocks mainly derived from different protoliths, ranging from gabbros, melagabbros, anorthosite, whereas meta-volcanic rocks likely derived from basalts and basaltic andesites. The meta-sedimentary rocks include meta-volcanoclastites, quartzites, micaschists, paragneisses, calcschists and impure marbles. This type of tectono-stratigraphic architecture is comparable with the MOR-type ophiolitic succession. The geochemistry of the meta-intrusive and meta-volcanic rocks indicate chemical affinities ranging from N-MORB to E-MORB and OIB. The petrogenetic study indicate that the N-MORB derived from partial melting of a sub-oceanic mantle source with a DMM composition (Workman & Hart, 2005), whereas E-MORB and OIB rocks derived from partial melting of a DMM-type mantle source modified by OIB-chemical components and an enriched OIB-type mantle source, respectively. Zircons dating on different meta-intrusive rocks point out for a Late Jurassic – Early Cretaceous ages for the protoliths proving that the Bajgan Complex do not represent a Paleozoic continental basement as proposed in literature (McCall, 1985). As a consequence, these new multidisciplinary data suggest that the Bajgan Complex represents an assemblage of different meta-ophiolitic tectonic slices, which were formed during the Late Jurassic to the Early Cretaceous in a MOR tectono-magmatic setting, possibly influenced by mantle plume activity.

- v) The structural data from the western North Makran outline a multiphase deformation history. The latest Late Cretaceous – Paleocene-earliest Eocene phase is characterized by the underplating and subsequent exhumation of the Band-e-Zeyarat and the Durkan Complex within the frontal part of an accretionary wedge. The entering of the Durkan seamount chain in the prism can likely have caused a diffuse shortening of the prism and the upper plate of the subduction system, such as the fore-arc and arc domain, now represented by the Ganj

Complex. The time constraint for this deformation stage is the unconformable deposition of the Eocene fore-arc succession above the Ganj Complex, the Band-e-Zeyarat ophiolite, and the Durkan Complex. In the studied sector of the North Makran domain, a significant post-Eocene deformation characterized by a thrusting stage followed by normal to strike-slip faulting stage has occurred. These stages likely testified for a deformation of the already formed and exhumed Cretaceous – Paleocene accretionary prism during the Oligocene – present day tectonic evolution of the Makran Accretionary Prism (Fig. 9.1).

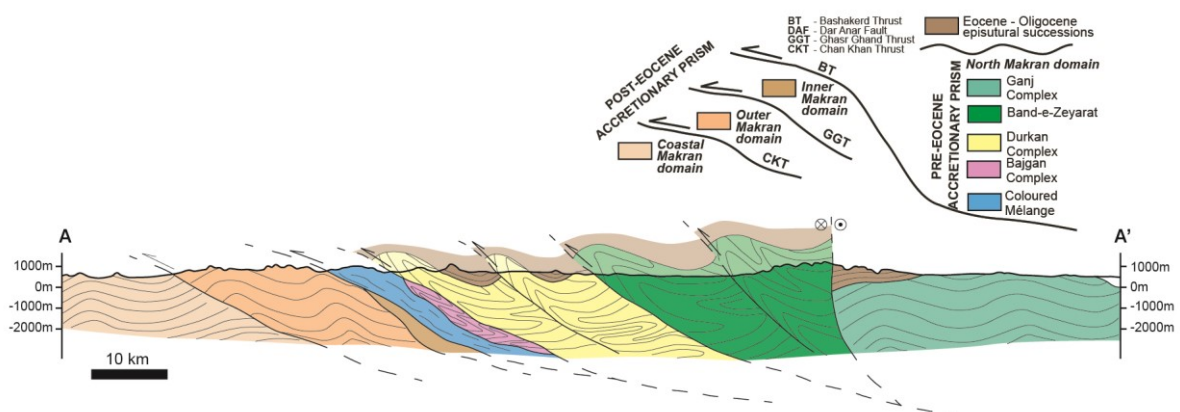


Figure 9.1. Simplified geological cross-section of the studied area (trace of cross-section shown in Figure 2.3) showing the structural relationships between the studied tectonic units and the structural domains of the Makran.

These new data from the western North Makran provide significant constraints for the understanding of the Late Jurassic - Cretaceous geodynamic and tectono-magmatic significance of the North Makran Ocean and its role during the convergent tectonic stages starting from the latest Late Cretaceous. The crucial conclusion is that the North Makran Ocean represents a rather “mature” oceanic seaway showing a complex Late Jurassic - Cretaceous tectono-magmatic evolution that was influenced by the rising of a mantle plume and the formation of a volcanic arc in the northern margin of the basin in response to the subduction of the lithosphere of the North Makran Ocean itself. In the following section, two-dimensional (2D) geodynamic reconstructions are presented with the aim to show a schematic synthesis of the Late Jurassic - Cretaceous tectono-magmatic and geodynamic evolution of the North Makran Domain.

9.2. Late Jurassic - Cretaceous tectono-magmatic and geodynamic model for the western North

Makran domain

The most recent geodynamic reconstruction for the North Makran Ocean proposed that this basin opened through an Early – Late Jurassic rift at the southern part of the Central Iran (i.e., Lut Block; see Fig. 2.4a; Hunziker et al., 2015). The existing geodynamic reconstructions have been well resumed by Burg (2018, Fig. 18); this figure is reported here in Fig. 9.2 for the reader convenience. The witnesses of the rifting stages are recorded in the eastern Durkan Complex and

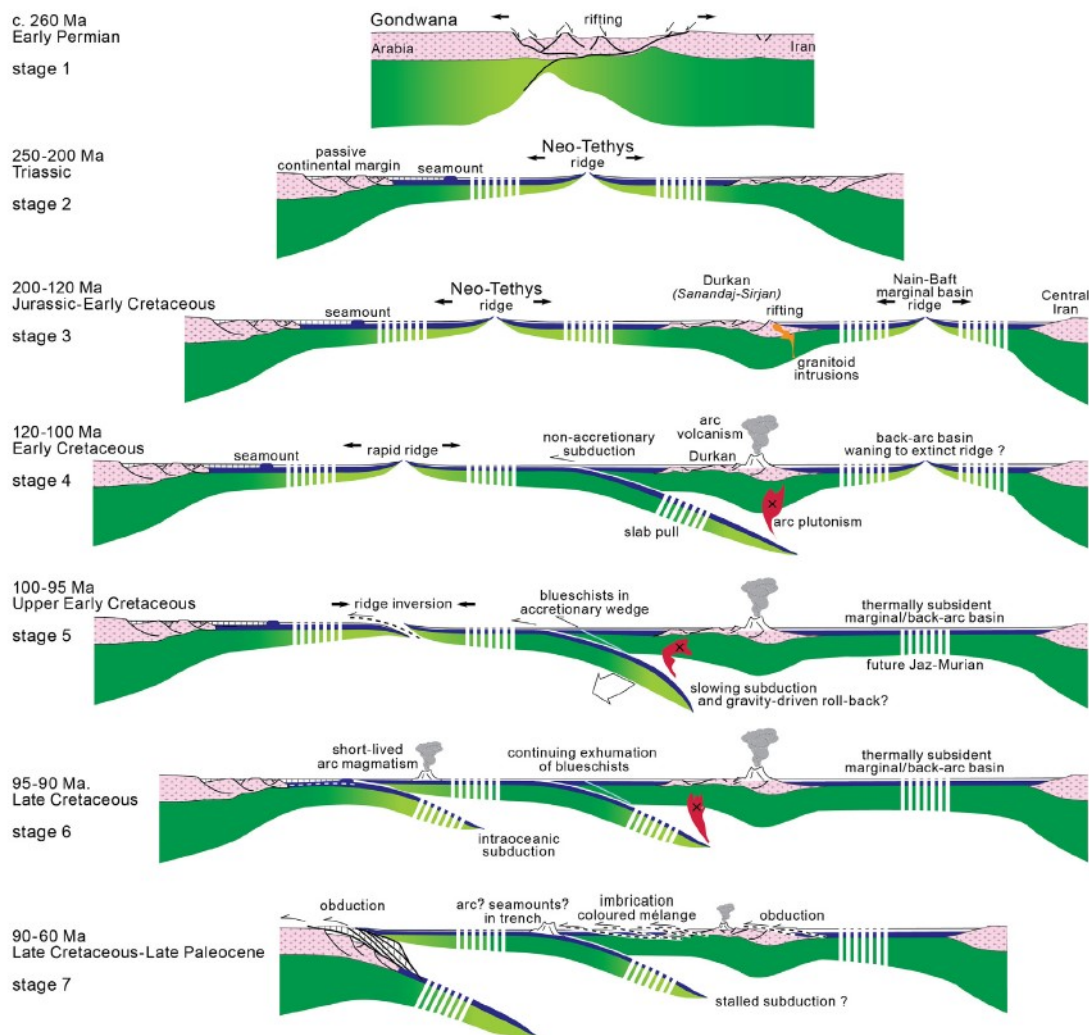


Figure 9.2. Tectonic reconstruction proposed by Burg (2018) along a N-S profiles of the Makran-Oman system. The tectonic evolution for the Makran sector is dominated by the presence of the Durkan microcontinental block.

correspond to a Jurassic suite of different granitoids. According to this model, the rifting stages caused the detachment of a microcontinent from the Lut Block, whose remnants were believed to correspond to the Durkan and Bajgan Complexes. The new data from these Complexes presented in this thesis indicate that this geodynamic model and the existence of a microcontinent (see model in [Fig. 9.2](#)) must be critically reevaluated. Starting from these new data, in the [Figure 9.3](#) three schematic 2D reconstructions for different ages are proposed.

During the Late Jurassic – Early Cretaceous a mid-oceanic ridge (MOR) was active as testified by the tectono-magmatic evolution of the Bajgan Complex ([Fig. 9.3a](#)). The Late Jurassic – Early Cretaceous oceanic lithosphere now preserved in the Bajgan Complex likely corresponds to fragments of the Neo-Tethys Ocean, which was separating during these ages the Lut Block and the Arabia Plate ([Fig. 9.3a](#)). This interpretation agrees with paleogeographic reconstruction for the Neo-Tethys realm during the Jurassic, which point out for a unique oceanic basin actively spreading between the Eurasian and the Arabian continental margin ([Barrier et al., 2018](#)). At this age, there is no evidence for active subduction zone and subduction-related magmatism in the Makran sector of the Neo-Tethys realm ([Fig. 9.3a](#)). By contrast, volcanic arc magmatic activity at 170-130 Ma is documented in the neighbouring Zagros-Sanandaj-Sirjan sector (see [Fig. 12](#) in [Agard et al., 2005](#)).

During the Late Cretaceous, there is a general agreement about the inception of convergent kinematics in the Neo-Tethys ocean ([McCall & Kidd, 1982](#); [Saccani et al., 2018](#); [Burg, 2018](#); [Barrier et al., 2018](#)). In the Makran sector of the Neo-Tethys realm, the convergence was accommodated by the formation of a north dipping intra-oceanic subduction zone ([Fig. 9.3b](#); see also [Saccani et al., 2018](#); [Burg, 2018](#)). This subduction was associated with Early Cretaceous subduction-related magmatism in the arc and fore-arc domains that is now testify in the Makran Accretionary Prism by the IAT and calc-alkaline volcanic rocks in the Coloured M \acute{e} lange ([Saccani et al., 2018](#)). This subduction identified two distinct branches of the Neo-Tethys in the Makran

according to their position with respect to the subduction zone, namely the southern Neo-Tethys Ocean and the North Makran Ocean, (Fig. 9.3b). The tectono-magmatic evolution of the North Makran Ocean was characterized at this age by a significant tectono-magmatic event, which is recorded by the Band-e-Zeyarat ophiolite and the Early Cretaceous meta-ophiolite in the Bajgan Complex. In detail, the geochemical, petrological, and geochronological data from Band-e-Zeyarat ophiolite and the Bajgan Complex likely indicate that a mid-oceanic ridge was active to the north of the intra-oceanic subduction and it was influenced by the embryonal activity of a mantle plume (Fig. 9.3b). Data from modern oceanic basin influenced by mantle plume, such as the Indian Ocean with the Reunion hotspot, indicate that the mantle plume activity can control the plate movements, as the plume head force is added to the ridge push (Cande & Stegman, 2011; Pusok & Stegman, 2020). The adding of this force can result in period showing fast and superfast spreading rate in the oceanic basin that can influence the convergence rate at tectonic plate scale (Cande & Stegman, 2011; van Hinsbergen et al., 2011). Therefore, the tectono-magmatic environment proposed for the Band-e-Zeyarat ophiolite and the Cretaceous meta-ophiolite in the Bajgan Complex suggests that the North Makran Ocean during the Early Cretaceous was a rather mature and wide oceanic basin showing an active mid-oceanic ridge likely characterized by fast-spreading rate and contemporaneous mantle plume activity and plume-ridge interaction (Fig. 9.3b).

The Late Cretaceous tectono-magmatic and geodynamic evolution of the North Makran Ocean is dominated by the contemporaneous closure of this ocean and diffuse mantle plume activity (Fig. 9.3c). These events are testified by the tectono-stratigraphic architecture and geochemical features of the Ganj Complex and the Durkan Complex. In fact, the Ganj Complex represents a volcanic arc formed close to the Eurasian margin in response of the northward subduction of the North Makran Ocean oceanic lithosphere below the Lut Block (Fig. 9.3c). By contrast, the Durkan Complex testify for a seamount chain in the North Makran Ocean that was formed by alkaline magmatism

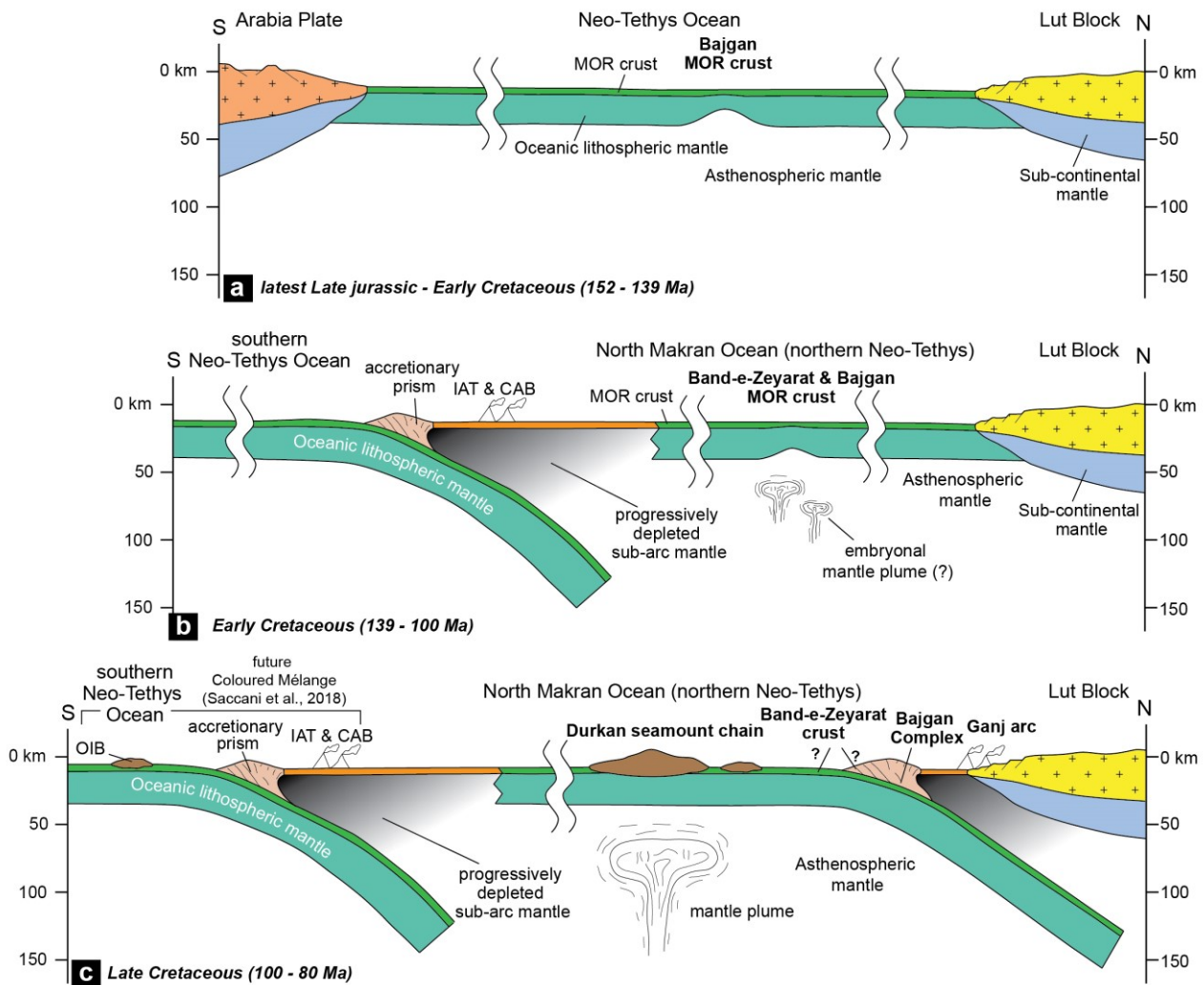


Figure 9.3. Tectono-magmatic and geodynamic reconstruction for the Makran sector of the Neo-Tethys realm during Late Jurassic – Early Cretaceous (a), Early Cretaceous (b), and Late Cretaceous (c). The reconstruction of the southern sector of the Neo-Tethys is based on [Saccani et al., \(2018\)](#) and [Burg, \(2018\)](#). Abbreviations: CAB: calc-alkaline basalt; IAT: island arc tholeiites; MOR: mid-ocean ridge; OIB: ocean island basalt.

likely related to a Late Cretaceous mantle plume (Fig. 9.3c). A further consequence of this mantle plume could possibly be a thermal perturbation of the oceanic lithosphere of the North Makran Ocean. In fact, mantle plumes are an excellent tool for transferring heat from the deep to the upper mantle and they commonly induce a positive perturbation of the thermal regime of the oceanic lithosphere ([White, 2010](#); [Kerr, 2014](#); [Safonova & Santhos, 2014](#)). For this reason, it can be postulated that the North Makran oceanic lithosphere was rather warm during the Late Cretaceous.

The subduction of such a warm oceanic lithosphere can explain the occurrence of volcanic rocks bearing adakite-like geochemistry in the Ganj arc as a consequence of chemical contribution from slab-melting facilitated by the anomalous warm temperature of the subducting slab (Fig. 9.3c). The Late Cretaceous IAT and calc-alkaline volcanic rocks nowadays preserved in the Coloured Mélange indicate that the intra-oceanic subduction of the Neo-Tethys and the related magmatism were still active to the south of the Bajgan microcontinent at this time (Fig. 9.3c; Saccani et al., 2018; Burg, 2018). Therefore, the Late Cretaceous was characterized by two different subduction zone in the Makran sector of the Neo-Tethys realm (Fig. 9.3c).

The present-day structural setting of the North Makran domain resulted from multiple deformative stages, which involved the deformation of the different units at different depth in an accretionary prism. The Figure 9.3c shows a complex architecture for the Markan sector of the Neo-Tethys at the end of the Late Cretaceous that possibly could influence the latest Late Cretaceous – Paleocene-earliest Eocene deformation history. In detail, the occurrence of different types of topographic reliefs on the subducting lithosphere of the North Makran Ocean, such as seamounts and volcanic arcs possibly controlled the deformation style of the convergent margin, causing the cycling transition from accretionary deformation to tectonic erosion (see Chapter 6.6.6). The interaction between this topographic reliefs and the frontal part of the accretionary prism (proto North Makran) could also have induced an intense shortening of the whole convergent margin, which lead to the final structuration of the North Makran that is unconformably sealed by the Eocene succession (Fig. 9.1).

9.3. Implications for the Cretaceous geodynamics of the Neo Tethys realm

Neo-Tethyan ophiolites occur within Alpine-Himalayan orogenic belts from the Mediterranean

region to the Middle East and Indonesia and mark the suture zones of different Neo-Tethyan sector and/or seaways (Stampfli & Borel, 2002; Dilek & Furnes, 2019; Furnes et al., 2020). The Neo-Tethys opened by Late Permian – Triassic continental rifting at the northern margin of Gondwana and continued to spread during the Jurassic (Dercourt et al., 1986; Sengör et al., 1988; Stampfli & Borel, 2002; Barrier & Vrielynck, 2008; Agard et al., 2011; Barrier et al., 2018). The Cretaceous evolution of the Neo-Tethys is dominated by the closure of the oceanic basin with the formation of multiple subduction zones to accommodate the changing in plate tectonic kinematics and the consequent inception of convergence between Africa-Arabia-India and Eurasia plates (Berberian et al., 1982; Dercourt et al., 1986; Sengör et al., 1988; Stampfli & Borel, 2002; Furnes et al., 2020; Martin et al., 2020).

Most of the geodynamic reconstructions so far proposed, though different in some aspects, agree with the interpretation that from Caucasus to Himalaya the closure of the Neo-Tethys occurred during Cretaceous with a northward subduction below the Eurasia margin and a coeval northward intra-oceanic subduction (Berberian et al., 1982; Agard et al., 2011; Yang & Dilek, 2015; Barrier et al., 2018; Marroni et al., 2020; Rolland et al., 2020; Hassig et al., 2020; Martin et al 2020). Since the earliest Late Cretaceous, the intra-oceanic subduction was associated with the formation of supra-subduction zone oceanic crust and was laterally continuous from the western and eastern sector of the Neo-Tethys (Fig. 9.4a). This continuity is testified by the abundant Late Cretaceous supra-subduction zone ophiolites and arc sequence preserved in the whole Alpine-Himalayan suture zones from Caucasus to Tibet-Himalaya (Pedersen et al., 2001; Mahéo et al., 2004; Saccani et al., 2013a; Goodenough et al., 2014; Kakar et al., 2014; Moghadam & Stern, 2015; Yang & Dilek, 2015; Monsef et al., 2018; Marroni et al., 2020; Rolland et al., 2010, 2020). In map-view geodynamic and paleogeographic reconstructions, the intra-oceanic subduction divided the Neo-Tethys Ocean in two different branches on the basis of their position (i.e., northward or southward)

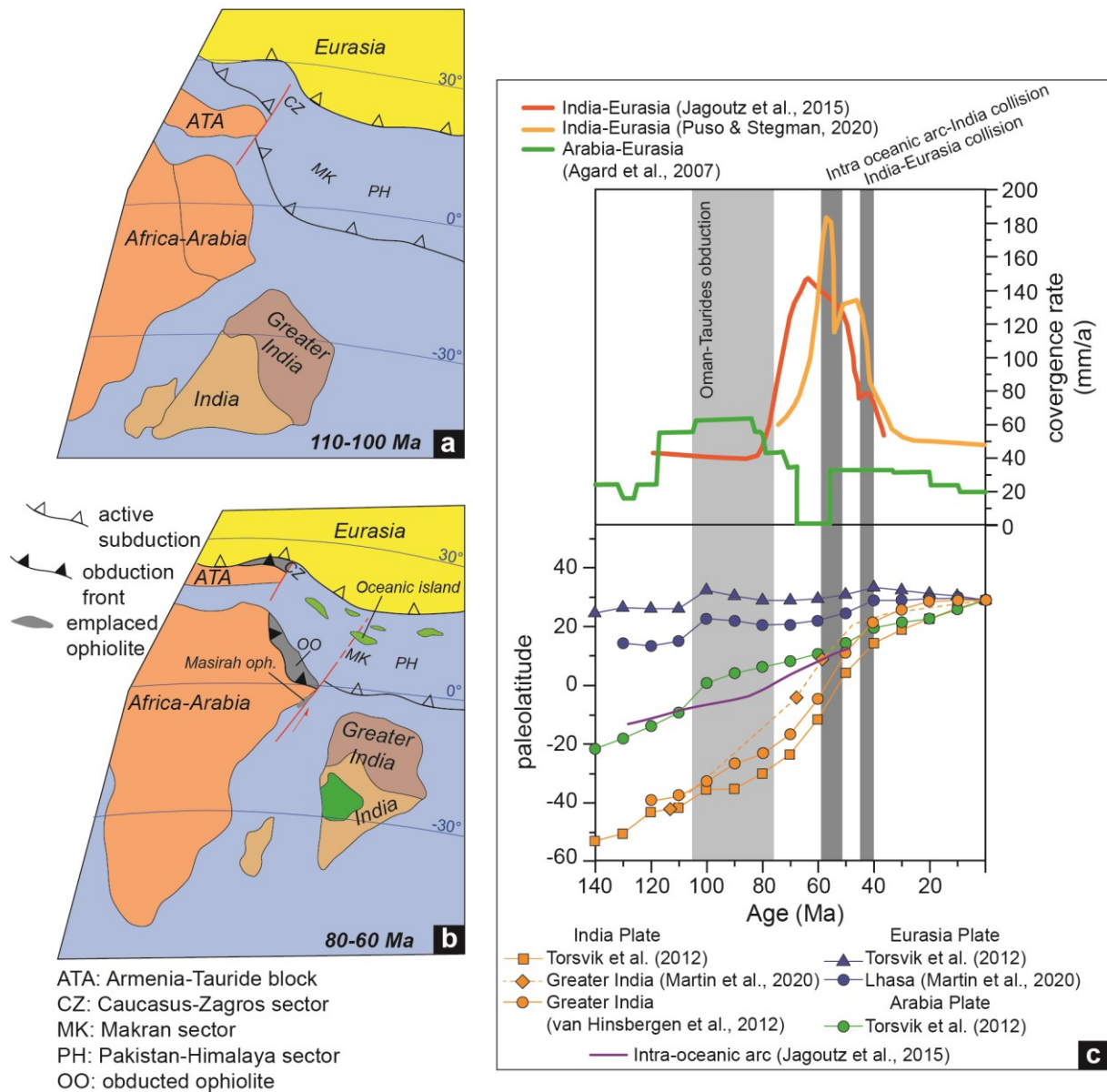


Figure 9.4. Paleogeographic maps for the latest Early Cretaceous (a) and Late Cretaceous – early Paleocene (b) for the Neo-Tethys Ocean (modified from Barrier & Vrielynck, 2008; Jagoutz et al., 2015; Barrier et al., 2018; Martin et al., 2020). c) Convergence rate (upper panel) and paleolatitude (lower panel) vs. age for Arabia, India, Eurasia and related microblocks (data from Agard et al., 2007; Torsvik et al., 2012; Jagoutz et al., 2015; van Hinsbergen et al., 2012; Martin et al., 2020; Pusok & Stegman, 2020). Ages for Oman-Taurides obduction are from Agard et al. (2007) and reference therein, whereas ages for India-intraoceanic arc and India-Eurasia are from Martin et al. (2020) and reference therein.

with respect to the intra-oceanic subduction (Fig. 9.4a). The 2D geodynamic models proposed for the Makran sector of the Neo-Tethys in the Figure 9.3 fit well with these regional-scale paleogeographic reconstructions. In fact, during the Cretaceous the North Makran Ocean likely

represented the oceanic seaway that was located to the north of the intra-oceanic subduction (Fig. 9.4a). This conclusion is strongly supported by the comparison of the tectono-magmatic evolution recognized in the North Makran Ocean and those described for the Caucasus, Zagros, and Himalaya sectors of the Northern Neo-Tethys. The most important aspect is the widespread occurrence of Early to Late Cretaceous OIB-type volcanic rocks associated to mantle plume in various ophiolitic units from Caucasus to Zagros (Rolland et al., 2010; Saccani et al., 2013a, 2014; Azizi et al., 2018). In addition, the ophiolite units and associated *mélange* in the Himalaya belt show the presence of OIB-type volcanic rocks, which are consistent with a similar tectono-magmatic evolution dominated by Cretaceous mantle plume activity (Yang & Dilek, 2015). These data indicate that the two Cretaceous subduction zones in the Neo-Tethys were separated by an oceanic lithosphere that likely recorded a complex and polygenetic tectono-magmatic evolution that is typical of mature and rather wide oceanic basin. An estimation of the dimension of this basin would be speculative. However, paleomagnetic data from the intra-oceanic arc and the arc formed onto the Eurasian margin in the Himalaya transect suggest a ~1500-3000 km width of the northern sector of the Neo-Tethys during the Cretaceous (Abrajevitch et al., 2005; van Hinsbergen et al., 2012; Jagoutz et al., 2015; Martin et al., 2020).

During the latest Late Cretaceous the evolution of the Neo-Tethys Ocean started to differentiate along strike from the western to the eastern sectors (i.e., Caucasus-Zagros; Pakistan-Himalaya, and Makran, see Fig. 9.4b). In fact, the Caucasus-Zagros sectors were characterized by the involvement within the intra-oceanic subduction of Arabian- and Gondwana-derived microcontinents (Fig. 9.4b; see also Barrier et al., 2018). This caused the almost synchronous (i.e., during Turonian – Late Maastrichtian, Agard et al., 2007) emplacement of Late Cretaceous supra-subduction zone ophiolites with their obduction above the northern continental margin of Arabia plate and Gondwana-derived microcontinent (Figs. 9.4b, c; Agard et al., 2011; Saccani et al.,

2013a; Moghadam & Stern, 2015; Goodenough et al., 2014; Kim et al., 2020; Marroni et al., 2020; Rolland et al., 2020). After the obduction, an oceanic basin was still opened in the northern sector and was consuming in the northward subduction below the Eurasian margin (Fig. 9.4b). The Pakistan-Himalaya sector of the Neo-Tethys was characterized by a similar tectonic evolution that, however, occurred at slightly younger ages (i.e., Late Cretaceous – Paleocene) than those of the Caucasus-Zagros sectors. In fact, paleogeographic reconstructions based on geological and paleomagnetic data suggest that the northern margin of the India plate collided with an intra-oceanic subduction zone and the related Ladakh – Kohistan arc during latest Paleocene (Fig. 9.4b; Searle & Treloar, 2010; Jagoutz et al., 2015; van Hinsbergen et al., 2012, 2019; Martin et al., 2020). This event led to the obduction onto India Plate of the arc and several supra-subduction zone ophiolites nowadays preserved in the eastern Pakistan and Himalaya (Burg, 2011; Kakar et al., 2014; Searle & Treloar, 2010; Yang & Dilek, 2015; Martin et al., 2020). Similarly to the Caucasus-Zagros sector, an ocean was still opened to the north of the suture zone between former intra-oceanic subduction and the India plates and its future complete subduction caused the collision between India and Eurasia plates during middle – late Eocene (Fig. 9.4b; Searle et al., 1997; Kakar et al., 2014; Jagoutz et al., 2015; Martin et al., 2020). At present, the Makran Accretionary Prism is characterized by still active subduction and it is separated from the Zagros and Himalaya collisional systems by two strike-slip fault systems (Burg, 2018; see Chapter 2). During the Cretaceous – Paleocene the Makran sector of the Neo-Tethyan intra-oceanic subduction likely represented the link between the Caucasus-Zagros and Pakistan-Himalaya sector (Fig. 9.4b). However, the main difference of the Makran sector could be that during the Late Cretaceous – Paleocene no obduction occurred in this southern part of the Neo-Tethys as no continental blocks and/or plate entered in the intra-oceanic subduction (Fig. 9.4b). This was likely related to the eastward termination of the Arabia plate and its separation from the India plate as a consequence of

the opening of the India Ocean from the Jurassic (Fig. 9.4b). This configuration likely allowed a continuous subduction of oceanic lithosphere from the Cretaceous to present-day to be active in the Makran sector (Fig. 9.4b). This hypothesis would require that during the Late Cretaceous a kinematic release of the subduction-dominated Makran sector from the neighbouring obduction-dominated sectors. It is hypothesised that such release could be represented by transform faults and/or strike-slip fault system (Fig. 9.4b). This hypothesis, though still preliminary and in some ways speculative, fits well with the evidence of Late Cretaceous – Paleocene transform boundary between Africa-Arabia and India plates (Gaina et al., 2015; Rodriguez et al., 2020). In detail, during Late Cretaceous – Paleocene these authors outlined the existence of laterally migrating sinistral strike-slip fault system along the eastern termination of the Arabia Plates that caused the emplacement of Masirah ophiolite onto the Arabian margin along a transpressive belt and accommodated the northward motion of Indian Plate (Fig. 9.4b).

A transform boundary between the Makran sector and Arabia during the latest Late Cretaceous - Paleocene is possibly suggested by the comparison of plate convergence rate and paleolatitude data for the Arabia and India plates with respect to Eurasia (Fig. 9.4c). These data suggest that during this period a major plate reorganization characterized by the significant increase of the rate of northward motion for the Indian Plate with respect to the rate of the Arabian plate (Fig. 9.4c; Torsvik et al., 2012; van Hinsbergen et al., 2012; Jagoutz et al., 2015; Martin et al., 2020). These data strongly suggest that these plates moved independently and were laterally released by a strike-slip/transform boundary (Fig. 9.4c). In this view, it is worth to note that the Makran sector could be influenced by this different kinematics and behaved during latest Late Cretaceous - Paleocene like a linkage between a slowing convergence system (Arabia-Eurasia) and an accelerating convergence system (India-Eurasia), accommodating continuous subduction of oceanic lithosphere since the Cretaceous.

9.4. Open problems and future perspective

This thesis provides multidisciplinary data that contribute to improve the knowledge of the Late Jurassic – Late Cretaceous tectono-magmatic and geodynamic evolution of the western North Makran and its latest Late Cretaceous – Paleocene-earliest Eocene deformation history. Nevertheless, this work still leaves many open problems that are worth to be investigated by future researches as summarized below.

- The structural setting of the Bajgan Complex should be investigated by combining field and microstructural data.
- The Durkan Complex is worth to be investigated to the east with respect to the area studied in this thesis. In particular, it is worth to obtain more age data of the alkaline magmatism in this complex for better define the age of the first occurrence of this type of magmatism in the North Makran Ocean.
- A detailed isotopic study of the volcanic and meta-volcanic rocks from the different tectonic units should be performed in order to assess the isotopic signature of these rocks. These data can help to perform further petrogenetic investigations and regional correlation between the different units.
- The detailed study of the metamorphism of the Bajgan Complex and the metamorphic slices in the Durkan Complex. These studies should identify the metamorphic evolution of these rocks, their P-T range, and their ages as these data are fundamental to better define the different stages of the convergence history.
- A detailed study of the post-Eocene succession and the associated magmatic rocks should be performed for better understanding their geological significance as well as the affinity and age of the magmatism.

References

- Abdetedal, M., Shomali, Z. H., Gheitanchi, M. R., 2015. Ambient noise surface wave tomography of the Makran subduction zone, south-east Iran: Implications for crustal and uppermost mantle structures. *Earthquake Science* 28(4), 235-251.
- Abrajevitch, A.V., Ali, J.R., Aitchison, J.C., Badengzhu Davis, A.M., Liu, J., Ziabrev, S.V., 2005. Neotethys and the India–Asia collision: insights from a palaeomagnetic study of the Dazhuqu ophiolite, southern Tibet. *Earth Planet. Sci. Lett.* 233, 87–102. <http://dx.doi.org/10.1016/j.epsl.2005.02.003>.
- Adam, J., Green, T.H., 1994. The effects of pressure and temperature on the partitioning of Ti, Sr and REE between amphibole, clinopyroxene and basanitic melts. *Chemical Geology* 117: 219-233. doi: 10.1016/0009-2541(94)90129-5.
- Afghah, M., Yousefzadeh, A., Shirdel, S., 2014. Biostratigraphic Revision of Middle Cretaceous Succession in South Zagros Basin (SW of Iran). *Journal of Earth Science & Climatic Change* 5 (8), <http://dx.doi.org/10.4172/2157-7617.1000216>
- Agard, P., Omrani, J., Jolivet, L., & Mouthereau, F., 2005. Convergence history across Zagros (Iran): constraints from collisional and earlier deformation. *International Journal of Earth Sciences*, 94(3), 401–419. <https://doi.org/10.1007/s00531-005-0481-4>
- Agard, P., Jolivet, L., Vrielynck, B., Burov, E., Monié, P., 2007. Plate acceleration: The obduction trigger? *Earth and Planetary Science Letters*, 258(3–4), 428–441. <https://doi.org/10.1016/j.epsl.2007.04.002>
- Agard, P., Omrani, J., Jolivet, L., Whitechurch, H., Vrielynck, B., Spakman, W., Monié, P., Meyer, B., Wortel, R., 2011. Zagros orogeny: a subduction-dominated process. *Geological Magazine* 148, 692–725. <https://doi.org/10.1017/S001675681100046X>
- Allègre, C.J., Minster, J.F., 1978. Quantitative models of trace element behavior in magmatic processes. *Earth Planet. Sci. Lett.* 38, 1-25.
- Anonymous, 1972. Penrose field conference on Ophiolites. *Geotimes*, 17, 24–25.
- Azizi, H., Lucci, F., Stern, R. J., Hasannejad, S., Asahara, Y., 2018. The Late Jurassic Panjeh submarine volcano in the northern Sanandaj-Sirjan Zone, northwest Iran: Mantle plume or active margin? *Lithos* 308–309, 364–380. <https://doi.org/10.1016/j.lithos.2018.03.019>
- Backman, J., Shackleton, N.J., 1983. Quantitative biochronology of Pliocene and Pleistocene calcareous nanofossils from the Atlantic, Indian and Pacific oceans. *Marine Micropaleontology* 8, 141-170.
- Bagheri, S., Stampfli, G., 2008. The Anarak, Jandaq and Posht-e-Badam metamorphic complexes in central Iran: New geological data, relationships and tectonic implications. *Tectonophysics* 451, p. 123–155. <https://doi.org/10.1016/j.tecto.2007.11.047>.
- Bangs, N. L. B., Gulick, S. P. S., Shipley, T. H., 2006. Seamount subduction erosion in the Nankai Trough and its potential impact on the seismogenic zone. *Geology*, 34(8), 701. <https://doi.org/10.1130/G22451.1>
- Barbero, E., Festa, A., Saccani, E., Catanzariti, R., & D’Onofrio, R., 2020. Redefinition of the Ligurian Units at the Alps–Apennines junction (NW Italy) and their role in the evolution of the Ligurian accretionary wedge: constraints from mélanges and broken formations. *Journal of the Geological Society*, 177(3), 562–574. <https://doi.org/10.1144/jgs2019-022>
- Barrier, E., Vrielynck, B., 2008. Paleotectonic Maps of the Middle East: Atlas of 14 Maps. Programme, Middle East Basin Evolution (MEBE).
- Barrier, E., Vrielynck, B., Brouillet, J.F., Brunet, M.F., 2018. Paleotectonic Reconstruction of the Central Tethyan Realm. Tectono-Sedimentary-Palinspastic maps from Late Permian to Pliocene. Atlas of 20 maps (scale: 1:15.000.000). CCGM/CGMW, Paris, <http://www.ccgmm.org>.
- Barth, M.G., Mason, P.R.D., Davies, G.R., Dijkstra A.H., Drury, M.R., 2003. Geochemistry of the Othris Ophiolite, Greece: Evidence for Refertilization? *Journal of Petrology*. 44, 1759-1785. DOI: 10.1093/petrology/egg058.

- Beccaluva, L., Macciotta, G., Piccardo, G.B., Zeda, O., 1989. Clinopyroxene composition of ophiolite basalts as petrogenetic indicator. *Chemical Geology*, 77(3–4), 165–182. [https://doi.org/10.1016/0009-2541\(89\)90073-9](https://doi.org/10.1016/0009-2541(89)90073-9)
- Beccaluva, L., Di Girolamo, P., Macciotta, G., Morra V., 1983. Magma affinities and fractionation trends in ophiolites. *Ofioliti* 8(3), 307-324.
- Beker, J.A., Menzies, M.A., Thirlwall, M.F., Macpherson, C.G., 1997. Petrogenesis of Quaternary intraplate volcanism, Sana'a, Yemen: implications for plume-lithosphere interaction and polybaric melt hybridization. *Journal of Petrology* 38, 1359-1390.
- Berberian, F., Muir, I.D., Pankhurst, R.J., Berberian, M., 1982. Late Cretaceous and early Miocene andean-type plutonic activity in northern Makran and Central Iran. *Journal of the Geological Society of London* 139, 605-614.
- Berra, F., Galli, M.T., Reghellin, F., Torricelli, S., Fantoni, R., 2009. Stratigraphic evolution of the Triassic-Jurassic succession in the Western Southern Alps (Italy): the record of the two-stage rifting on the distal passive margin of Adria. *Basin Research* 21 (3), 335–353. <https://doi.org/10.1111/j.1365-2117.2008.00384.x>
- Bettelli, G., Vannucchi, P., 2003. Structural style of the offscraped Ligurian oceanic sequences of the Northern Apennines: new hypothesis concerning the development of mélangé block-in-matrix fabric. *Journal of Structural Geology*, 25(3), 371–388. [https://doi.org/10.1016/S0191-8141\(02\)00026-3](https://doi.org/10.1016/S0191-8141(02)00026-3)
- Bonnet, G., Agard, P., Angiboust, S., Monié, P., Fournier, M., Caron, B., Omrani, J., 2020a. Structure and metamorphism of a subducted seamount (Zagros suture, Southern Iran). *Geosphere* 16, 62–81. <https://doi.org/10.1130/GES02134.1>
- Bonnet, G., Agard, P., Whitechurch, H., Fournier, M., Angiboust, S., Caron, B., Omrani, J., 2020b. Fossil seamount in southeast Zagros records intraoceanic arc to back-arc transition: New constraints for the evolution of the Neotethys. *Gondwana Research* 81, 423–444. <https://doi.org/10.1016/j.gr.2019.10.019>
- Bortolotti, V., Chiari, M., Göncüoğlu, M.C., Principi, G., Saccani, E., Tekin, U. K., Tassinari, R., 2017. The Jurassic–Early Cretaceous basalt–chert association in the ophiolites of the Ankara Mélange, east of Ankara, Turkey: age and geochemistry. *Geological Magazine*, 155, 451–478. <https://doi.org/10.1017/S0016756817000401>
- Bortolotti, V., Chiari, M., Kodra, A., Marcucci, M., Mustafa, F., Principi, G., Saccani, E., 2004. New evidence for Triassic MORB magmatism in the northern Mirdita Zone ophiolites (Albania). *Ofioliti*, 29, 243-246
- Bouma, A.H., 1962. *Sedimentology of some flysch deposits, a graphic approach to facies interpretation*. Elsevier Co., Amsterdam, pp. 168.
- Bown, P.R., 1998. *Calcareous nannofossil biostratigraphy*. British Micropalaeontology Society Publications Series. Chapman & Hall, London, pp. 328.
- Bown, P.R., Young J.R., 1998. Techniques. In: Bown, P.R. (Ed.), *Calcareous nannofossil biostratigraphy*. British Micropalaeontology Society Publications Series. Chapman & Hall, London, pp. 16-28.
- Brombin, V., Bonadiman, C., Jourdan, F., Roghi, G., Coltorti, M., Webb, L. E., Callegaro, S., Bellieni, G., De Vecchi, G., Sedeà, R., Marzoli, A. 2019. Intraplate magmatism at a convergent plate boundary: The case of the Cenozoic northern Adria magmatism. *Earth-Science Reviews*, 192, 355–378. <https://doi.org/10.1016/j.earscirev.2019.03.016>
- Burg, J.-P., 2018. Geology of the onshore Makran accretionary wedge: Synthesis and tectonic interpretation. *Earth Science Reviews*. 185, 1210-1231. <https://doi.org/10.1016/j.earscirev.2018.09.011>.
- Burg, J.-P., Bernoulli, D., Smit, J., Dolati, A., Bahroudi, A., 2008. A giant catastrophic mud-and-debris flow in the Miocene Makran. *Terra Nova* 20, 188-193. <http://doi.wiley.com/10.1111/j.1365-3121.2008.00804.x>
- Burg, J.-P., Dolati, A., Bernoulli, D., Smit, J., 2013. Structural style of the Makran tertiary accretionary complex in SE Iran. In: Al Hosani, K., Roure, F., Ellison, R., Lokier, S. (Eds.), *Lithosphere Dynamics and Sedimentary Basins: The Arabian Plate and Analogues*. *Frontiers in Earth Sciences*, Springer, Heidelberg, pp. 239-259. https://doi.org/10.1007/978-3-642-30609-9_12

- Burnett, J.A., 1998. Upper Cretaceous. In Bown, P.R., (ed.), *Calcareous Nannofossil Biostratigraphy*. British Micropalaeontological Society Publications Series. Chapman & Hall, London, pp. 132-199.
- Burns, L. E., 1985. The Border Ranges ultramafic and mafic complex, south-central Alaska: cumulate fractionates of island-arc volcanics. *Canadian Journal of Earth Sciences*, 22(7), 1020–1038. <https://doi.org/10.1139/e85-106>.
- Cande, S. C., Stegman, D. R., 2011. Indian and African plate motions driven by the push force of the Reunion plume head. *Nature* 475, 47-52.
- Cann, JR, 1970. Rb, Sr, Y, Zr and Nb in some ocean floor basaltic rocks. *Earth and Planetary Science Letters* 10, 7-11
- Casetta, F., Coltorti, M., Ickert, R. B., Bonadiman, C., Giacomoni, P.P., Ntaflos, T., 2018. Intrusion of shoshonitic magmas at shallow crustal depth: T–P path, H₂O estimates, and AFC modeling of the Middle Triassic Predazzo Intrusive Complex (Southern Alps, Italy). *Contributions to Mineralogy and Petrology*, 173(7), 57. <https://doi.org/10.1007/s00410-018-1483-0>
- Castillo, P.R., 2006. An overview of adakite petrogenesis. *Chinese Science Bulletin* 51(3), 257-268.
- Castillo, P.R., Janney, P.E., Solidum, R., 1999. Petrology and geochemistry of Camiguin Island, southern Philippines: insights into the source of adakite and other lavas in a complex arc tectonic setting, *Contrib. Mineral. Petrol.* 134, 33-51.
- Charvet, J., Ogawa, Y., 1994. Arc-trench tectonic. In: Hancock, P.L. (Ed.), *Continental Deformation*. Oxford, Pergamon Press, pp. 180–199.
- Chauvet, F., Lapiere, H., Maury, R. C., Bosch, D., Basile, C., Cotten, J., Brunet, P., Campillo, S., 2011. Triassic alkaline magmatism of the Hawasina Nappes: Post-breakup melting of the Oman lithospheric mantle modified by the Permian Neotethyan Plume. *Lithos*, 122, 122–136. <https://doi.org/10.1016/j.lithos.2010.12.006>
- Chiari, M., Djerić, N., Garfagnoli, F., Hrvatovic, H., Krstić, M., Levi, N., Malasoma, A., Marroni, M., Menna, F., Nirta, G., Pandolfi, L., Principi, G., Saccani, E., Stojadinović, U., Trivić, B., 2011. The geology of the Zlatibor-Maljen area (Western Serbia): A geotraverse across the Dinaric-Hellenic collisional belt. *Ofioliti*, 36, 139-166. A54
- Clarke, A.P., Vannucchi, P., Morgan, J., 2018. Seamount chain–subduction zone interactions: Implications for accretionary and erosive subduction zone behavior. *Geology* 46, 367–370. <https://doi.org/10.1130/G40063.1>
- Clift, P., Vannucchi, P., 2004. Controls on tectonic accretion versus erosion in subduction zones: Implications for the origin and recycling of the continental crust. *Reviews of Geophysics* 42 (2). <https://doi.org/10.1029/2003RG000127>
- Coccioni, R., Premoli Silva, I., 2015. Revised Upper Albian-Maastrichtian planktic foraminiferal biostratigraphy and magnetostratigraphy of the classical Tethyan Gubbio section (Italy). *Newsletter on Stratigraphy* 48 (1), 47-90.
- Coffin, M.F., Pringle, M.S., Duncan, R.A., 2002. Kerguelen hotspot magma output since 130 Ma. *Journal of Petrology*, 43, 1121–1139.
- Coleman, R.G., 1977. *Ophiolites*. Springer-Verlag, New York, 220 pp.
- Comas-Cufí, M, Thió-Henestrosa, S., 2011. CoDaPack 2.0: a stand-alone, multi-platform compositional software. In: Egozcue, J.J., Tolosana-Delgado, R., Ortego, M.I. (Eds.), *CoDaWork'11: 4th International Workshop on Compositional Data Analysis*. Sant Feliu de Guíxols.
- Davis, D., Suppe, J., Dahlen, F. A., 1983. Mechanics of fold-and-thrust belts and accretionary wedges. *Journal of Geophysical Research* 88 (B12), 1153–1172. <https://doi.org/10.1029/JB088iB02p01153>
- Defant, M.J., Drummond, M.S., 1990. Derivation of some modern arc magmas by melting of young lithosphere. *Nature* 347, 662-665.

- Defant, M.J., Drummond, M.S., 1993. Mount St. Helens: potential example of the partial melting of the subducted lithosphere in a volcanic arc. *Geology* 21, 541-550.
- Delaloye, M., Desmons, J., 1980. Ophiolites and Mélange terranes in Iran: a geochronological study and its paleotectonic implications. *Tectonophysics* 68, 83-111.
- Delavari, M., Dolati, A., Marroni, M., Pandolfi, L., Saccani E., 2016. Association of MORB and SSZ ophiolites along the shear zone between Coloured Mélange and Bajgan Complexes (North Maran, Iran): Evidence from the Sorkhband area. *Ofioliti* 41, 21-34.
- Dercourt, J., Zonenshian, L.P., Ricou, L.E., Kazmin, V.G., LePichon, X., Knipper, A.L., Grandjacquet, C., Sbertshikov, M., Geysant, J., Lepvrier, C., Pechersky, D.H., Boulin, J., Sibuet, J.C., Savostin, L.A., Sorokhtin, O., Westphal, M., Bazhenov, M.L., Lauer, J.P., Biju-Duval, B., 1986. Geological evolution of the Tethys Belt from the Atlantic to the Pamir since the Lias. *Tectonophysics* 123, 241-315.
- Desmons, J., Beccaluva, L., 1983. Mid-Ocean ridge and island-arc affinities in ophiolites from Iran: Palaeographic implications. *Chemical Geology* 39, 39-63.
- Dewey, J.F., Bird, J.M., 1971. The origin and emplacement of the ophiolite suite: Appalachian ophiolites in Newfoundland. *Journal of Geophysical Research*, 76, 3179–3206, doi: 10.1029/JB076i014p03179.
- Dickinson, W.R., 1970. Interpreting detrital modes of graywacke and arkose. *Jour. Sed. Petrol.*, 40, 695-707.
- Dickinson, W.R., 1995. Forearc basins. In: Busby, C.J., Ingersoll, R.V. (Eds.), *Tectonics of Sedimentary Basins*. Blackwell Science, Oxford, pp. 221-261.
- Dickinson, W.R., Beard, L.S., Breakenridge, J.L., Erjavec, R.C., Ferguson, K.F., Inman R.A., Knepp, F.A., Lindberg, F.A., Ryberg, P.T., 1983. Provenance of North American Phanerozoic sandstones in relation to tectonic setting. *Geol. Soc. Am. Bull.* 94, 222-235.
- Dilek, Y., Furnes, H., 2011. Ophiolite genesis and global tectonics: geochemical and tectonic fingerprinting of ancient oceanic lithosphere. *Geological Society of America Bulletin* 123, 387-411. 10.1130/B30446.1
- Dilek, Y., Furnes, H., 2014. Ophiolites and their origins. *Elements*, 10, 93–100, doi: 10.2113/gselements.10.2.93.
- Dilek, Y., Furnes, H., 2019. Tethyan ophiolites and Tethyan seaways. *Journal of the Geological Society*, 176(5), 899–912. <https://doi.org/10.1144/jgs2019-129>
- Dolati, A., 2010. Stratigraphy, Structure Geology and Low-temperature Thermochronology Across the Makran Accretionary Wedge in Iran. PhD thesis, ETH Zurich, 165 pp.
- Dolati, A., Burg, J.-P., 2013. Preliminary fault analysis and paleostress evolution in the Makran Fold-and-Thrust Belt in Iran. In: Al Hosani, K., Roue, F., Ellison, R., Lokier, S. (Eds.), *Lithosphere Dynamics and Sedimentary Basins: The Arabian Plate and Analogues*. *Frontiers in Earth Sciences*, Springer, Heidelberg, pp. 261–277. https://doi.org/10.1007/978-3-642-30609-9_13
- Dominguez, S., Lallemand, S.E., Malavieille, J., von Huene, R., 1998. Upper plate deformation associated with seamount subduction. *Tectonophysics* 293, 207–224. [https://doi.org/10.1016/S0040-1951\(98\)00086-9](https://doi.org/10.1016/S0040-1951(98)00086-9).
- Dorani, M., Arvin, M., Oberhänsli, R., Dargahi, S., 2017. P-T evolution of metapelites from the Bajgan complex in the Makran accretionary prism, south eastern Iran. *Geochemistry*, 77, 459–475. <https://doi.org/10.1016/j.chemer.2017.07.004>
- Draut, A.E., Clift, P.D., 2013. Differential preservation in the geologic record of intraoceanic arc sedimentary and tectonic processes. *Earth-Science Reviews* 116, 57-84, <http://dx.doi.org/10.1016/j.earscirev.2012.11.003>.
- Droop, G.T.R., 1987. A general equation for estimating Fe³⁺ concentrations in ferromagnesian silicates and oxides from microprobe analyses, using stoichiometric criteria. *Mineralogical Magazine*, 51, 431–435.
- Dunn, T., Sen, C., 1994. Mineral/Matrix Partition-Coefficients for Ortho-Pyroxene, Plagioclase, and Olivine in Basaltic to Andesitic Systems - a Combined Analytical and Experimental-Study. *Geochimica et Cosmochimica Acta*, 58, 717-733. doi: 10.1016/0016-7037(94)90501-0.

- Eftekhar-Nejad, J., McCall, G.J.H., 1993. Explanatory text of the Nikshahr quadrangle Map 1:250000. Geological survey of Iran N. L14.
- Eftekhar-Nezhad, J., Arshadi, S., Mahdavi, M.A., Morgan, K.H., McCall, G.J.H., Huber, H., 1979. Fannuj Quadrangle Map 1:250000. Ministry of Mines and Metal, Geological Survey of Iran, Tehran:
- Elliott, T., 2003. Tracers of the slab. In: Eiler, J. (Eds.), Inside the subduction factory. Geophysical Monograph Series AGU, Washington DC, Vol. 138, 23-45.
- Engdahl, E., Jackson, J.A., Myers, S.C., Bergman, E.A., Priestley, K., 2006. Relocation and assessment of seismicity in the Iran region. *Geophysical Journal International* 167 (2), 761–778. <https://doi.org/10.1111/j.1365-246X.2006.03127.x>
- Entezar-Saadat, V., Motavalli-Anbaran, S.H., Zeyen, H., 2017. Lithospheric structure of the Eastern Iranian plateau from integrated geophysical modeling: A transect from Makran to the Turan platform. *Journal of Asian Earth Sciences* 138, 357–366. <https://doi.org/10.1016/j.jseaes.2017.02.024>
- Esmaili, R., Xiao, W., Ebrahimi, M., Zhang, J., Zhang, Z., Abd El-Rahman, Y., Han, C., Wan, B., Ao, S., Song, D., Shahabi, S., Aouizerat, A., 2019. Makran ophiolitic basalts (SE Iran) record Late Cretaceous Neotethys plume-ridge interaction. *International Geology Review*, 1–21. <https://doi.org/10.1080/00206814.2019.1658232>
- Esmaili, R., Xiao, W., Griffin, W. L., Moghadam, H. S., Zhang, Z., Ebrahimi, M., Zhang, J., Wan, B., Ao, S., Bhandari, S., 2020. Reconstructing the Source and Growth of the Makran Accretionary Complex: Constraints From Detrital Zircon U-Pb Geochronology. *Tectonics* 39 (2). <https://doi.org/10.1029/2019TC005963>
- Ewart, A., Bryan, W.B., Gill, J.B., 1973. Mineralogy and geochemistry of the younger volcanic islands of Tonga, S.W. Pacific. *Journal of Petrology* 14, 429-465.
- Ewart, A., Griffin, W.L., 1994. Application of Proton-Microprobe Data to Trace-Element Partitioning in Volcanic-Rocks. *Chemical Geology*, 117, 251-284. doi: 10.1016/0009-2541(94)90131-7.
- Festa, A., Balestro, G., Borghi, A., De Caroli, S., Succo, A., 2020. The role of structural inheritance in continental break-up and exhumation of Alpine Tethyan mantle (Canavese Zone, Western Alps). *Geoscience. Frontiers* 11 (1), 167–188. <https://doi.org/10.1016/j.gsf.2018.11.007>
- Festa, A., Dilek, Y., Codegone, G., Cavagna, S., Pini, G. A., 2013. Structural anatomy of the Ligurian accretionary wedge (Monferrato, NW Italy), and evolution of superposed melanges. *Geological Society of America Bulletin*, 125(9–10), 1580–1598. <https://doi.org/10.1130/B30847.1>
- Festa, A., Dilek, Y., Mittempergher, S., Ogata, K., Pini, G. A., & Remitti, F., 2018. Does subduction of mass transport deposits (MTDs) control seismic behavior of shallow-level megathrusts at convergent margins?. *Gondwana Research*, 60, 186–193. <https://doi.org/10.1016/j.gr.2018.05.002>
- Festa, A., Dilek, Y., Pini, G. A., Codegone, G., Ogata, K., 2012. Mechanisms and processes of stratal disruption and mixing in the development of mélanges and broken formations: Redefining and classifying mélanges. *Tectonophysics*, 568–569, 7–24. <https://doi.org/10.1016/j.tecto.2012.05.021>
- Festa, A., Pini, G. A., Ogata, K., Dilek, Y., 2019. Diagnostic features and field-criteria in recognition of tectonic, sedimentary and diapiric mélanges in orogenic belts and exhumed subduction-accretion complexes. *Gondwana Research*, 74, 7–30. <https://doi.org/10.1016/j.gr.2019.01.003>
- Fisher, R. V., 1984. Submarine volcanoclastic rocks. *Geological Society of London Special Publications* 16 (1), 5–27. <https://doi.org/10.1144/GSL.SP.1984.016.01.02>
- Fitton, J.G., Godard, M., 2004. Origin and evolution of magmas on the Ontong Java Plateau. *Geological Society of London, Special Publications*, 229(1), 151–178. <https://doi.org/10.1144/GSL.SP.2004.229.01.10>
- Fitton, J. G., Larsen, L. M., Saunders, A. D., Hardarson, B. S., Kempton, P. D., 2000. Palaeogene Continental to Oceanic Magmatism on the SE Greenland Continental Margin at 63°N: a Review of the Results of Ocean

- Drilling Program Legs 152 and 163. *Journal of Petrology*, 41(7), 951–966. <https://doi.org/10.1093/petrology/41.7.951>
- Floyd, P. A., Winchester, J. A. 1978. Identification and discrimination of altered and metamorphosed volcanic rocks using immobile elements. *Chemical Geology*, 21(3–4), 291–306. [https://doi.org/10.1016/0009-2541\(78\)90050-5](https://doi.org/10.1016/0009-2541(78)90050-5)
- Foreman, H.P., 1977. Mesozoic radiolaria from the Atlantic Basin and its borderlands. In: Swain F.M. (Ed.), *Stratigraphic Micropaleontology of the Atlantic Basin and Borderlands*, 305-320.
- Fujimaki, H., Tatsumoto, M., Aoki, K., 1984. Partition coefficients of Hf, Zr, and REE between phenocrysts and groundmasses. *Journal of Geophysical Research* 89, Supl. B1, 662-672.
- Furnes, H., Dilek, Y., 2017. Geochemical characterization and petrogenesis of intermediate to silicic rocks in ophiolites: A global synthesis. *Earth-Science Reviews*, 166, 1–37. <https://doi.org/10.1016/j.earscirev.2017.01.001>
- Furnes, H., Dilek, Y., Zhao, G., Safonova, I., Santosh, M., 2020. Geochemical characterization of ophiolites in the Alpine-Himalayan Orogenic Belt: Magmatically and tectonically diverse evolution of the Mesozoic Neotethyan oceanic crust. *Earth-Science Reviews*, 208(July), 103258. <https://doi.org/10.1016/j.earscirev.2020.103258>
- Gaina, C., van Hinsbergen, D. J. J., Spakman, W., 2015. Tectonic interactions between India and Arabia since the Jurassic reconstructed from marine geophysics, ophiolite geology, and seismic tomography. *Tectonics*, 34(5), 875–906. <https://doi.org/10.1002/2014TC003780>
- Gansser, A., 1955. New aspects of the geology in central Iran. Paper presented at 4th World Petroleum Congress, Rome, pp. 279-300.
- Gazzi, P., 1966. Le arenarie del flysch sopracretaceo dell'Appennino modenese; correlazioni con il flysch di Monghidoro. *Mineral. Petrogr. Acta* 12, 69-97.
- Ghazi, A.M., Hassanipak, A.A., Mahoney, J.J., Duncon R.A., 2004. Geochemical characteristics, ^{40}Ar - ^{39}Ar ages and original tectonic setting of the Band-e-Zeyarat/Dar Anar ophiolite, Makran accretionary Prism, S.E. Iran. *Tectonophysics* 193, 175-196.
- Gill, J.B., 1981. *Orogenic Andesites and Plate Tectonics*, Berlin, Springer-Verlag, pp. 358.
- Glennie, K.W., Hughes Clarke, M.W., Boeuf, M.G.A., Pilaar, W.F.H., Reinhardt, B.M., 1990. Inter-relationship of Makran-Oman Mountains belts of convergence. *Geological Society of London Special Publications* 49, 773–786. <https://doi.org/10.1144/GSL.SP.1992.049.01.47>
- Ghose, N. C., Chatterjee, N., Mukherjee, D., Kent, R. W., Saunders, A. D., 2008. Mineralogy and Geochemistry of the Bengal Anorthosite Massif in the Chotanagpur Gneissic Complex at the Eastern Indian Shield Margin. *Journal of the Geological Society of India*, 72, 263-277.
- Goodenough, K. M., Thomas, R. J., Styles, M. T., Schofield, D. I., MacLeod, C. J., 2014. Records of Ocean Growth and Destruction in the Oman-UAE Ophiolite. *Elements*, 10(2), 109–114. <https://doi.org/10.2113/gselements.10.2.109>
- Govindaraju, K. 1994. compilation of working values and sample description for 383 geostandards. *Geostandard Newsletter*, Special Issue, 1994, 118, 158 p.).
- Gradstein, F.M., Ogg, J.G., Scmitz, M.D., Ogg G.M., 2012. *The Geologic Time Scheme*. Elsevier, Amsterdam, International Commission on Stratigraphy, pp.1144.
- Grando, G., McClay, K., 2007. Morphotectonics domains and structural styles in the Makran accretionary prism, offshore Iran. *Sedimentary Geology* 196, 157–179. <https://doi.org/10.1016/j.sedgeo.2006.05.030>
- Green, T., Blundy, J., Adam, J., Yaxley, G., 2000. SIMS determination of trace element partition coefficients between garnet, clinopyroxene and hydrous basaltic liquids at 2-7.5 Gpa and 1080-1200C. *Lithos*, 53, 165-187. doi: 10.1016/S0024-4937(00)00023-2.

- Green, T.H., Sie, S.H., Ryan, C.G., Cousens, D.R. 1989. Proton microprobe-determined partitioning of Nb, Ta, Zr, Sr and Y between garnet, clinopyroxene and basaltic magma at high pressure and temperature. *Chemical Geology* 74: 201-216. doi: 10.1016/0009-2541(89)90032-6.
- Gribble, R.F., Stern, R.J., Bloomer, S.H., Stuben, D., O'Hearn, T., Newman, S., 1996. MORB mantle and subduction components interact to generate basalts in the southern Mariana Trough back-arc basin. *Geochimica et Cosmochimica Acta* 60, 2153-2166.
- Gutierrez, M., Casillas, R., Fernandez, C., Balogh, K., Ahijado, A., Castillo, C., Colmenero, J.R., Garcia-Navarro, E., 2006. The submarine volcanic succession of the basal complex of Fuerteventura, Canary Islands: A model of submarine growth and emergence of tectonic volcanic islands. *Geological Society of America Bulletin* 118, 785–804. <https://doi.org/10.1130/B25821.1>
- Haase, K. M., Devey, C. W., 1996. Geochemistry of lavas from the Ahu and Tupa volcanic fields, Easter Hotspot, southeast Pacific: Implications for intraplate magma genesis near a spreading axis. *Earth and Planetary Science Letters*, 137(1–4), 129–143. [https://doi.org/10.1016/0012-821X\(95\)00217-Z](https://doi.org/10.1016/0012-821X(95)00217-Z)
- Haghipour, N., Burg, J.-P., Kober, F., Zeilinger, G., Ivy-Ochs, S., Kubik, P. W., Faridi, M. 2012. Rate of crustal shortening and non-Coulomb behaviour of an active accretionary wedge: The folded fluvial terraces in Makran (SE, Iran). *Earth and Planetary Science Letters*, 355–356, 187–198. <https://doi.org/10.1016/j.epsl.2012.09.001>
- Hanan, B. B., Blichert-Toft, J., Kingsley, R., Schilling, J.-G., 2000. Depleted Iceland mantle plume geochemical signature: Artifact of multicomponent mixing? *Geochemistry, Geophysics, Geosystems*, 1(4), <https://doi.org/10.1029/1999GC000009>
- Hassanzadeh, J., Wernicke, B.P., 2016. The Neotethyan Sanandaj-Sirjan zone of Iran as an archetype for passive margin-arc transitions. *Tectonics* 35, 586–621. <https://doi.org/10.1002/2015TC003926>
- Hässig, M., Rolland, Y., Sosson, M., Galoyan, G., Müller, C., Avagyan, A., Sahakyan, L., 2013a. New structural and petrological data on the Amasia ophiolites (NW Sevan–Akera suture zone, Lesser Caucasus): Insights for a large-scale obduction in Armenia and NE Turkey. *Tectonophysics* 588, 135–153. <https://doi.org/10.1016/j.tecto.2012.12.003>
- Hässig, M., Rolland, Y., Sosson, M., Galoyan, G., Sahakyan, L., Topuz, G., Çelik, Ö.F., Avagyan, A., Müller, C., 2013b. Linking the NE Anatolian and Lesser Caucasus ophiolites: evidence for large-scale obduction of oceanic crust and implications for the formation of the Lesser Caucasus-Pontides Arc. *Geodinamica Acta* 26, 311–330. <https://doi.org/10.1080/09853111.2013.877236>
- Hässig, M., Moritz, R., Ulianov, A., Popkhadze, N., Galoyan, G., Enukidze, O., 2020. Jurassic to Cenozoic Magmatic and Geodynamic Evolution of the Eastern Pontides and Caucasus Belts, and Their Relationship With the Eastern Black Sea Basin Opening. *Tectonics*, 39(10). <https://doi.org/10.1029/2020TC006336>
- Hébert, R., Laurent, R., 1990. Mineral chemistry of the plutonic section of the Troodos ophiolite: new constraints for genesis of arc-related ophiolites. In: *Proceedings of Troodos Ophiolite Symposium*; Malpas, J., Moores, E., Panayiotou, A., Xenophontos, C. Eds.; Cyprus, pp. 149-163.
- Hochstaedter, A., Gill, J., Peters, R., Broughton, P., Holden, P., Taylor, B., 2001. Across-arc geochemical trends in the Izu-Bonin arc: Contributions from the subducting slab. *Geochemistry, Geophysics, Geosystems* 2(7), Paper number 2000GC000105.
- Hoernle, K., Hauff, F., van den Bogaard, P., Werner, R., Mortimer, N., Geldmacher, J., Garbe-Schönberg, D., Davy, B., 2010. Age and geochemistry of volcanic rocks from the Hikurangi and Manihiki oceanic Plateaus. *Geochimica et Cosmochimica Acta*, 74(24), 7196–7219. <https://doi.org/10.1016/j.gca.2010.09.030>
- Hoffmann, G., Silver, E., Day, S., Driscoll, N., Appelgate, B., 2009. Drowned carbonate platforms in the Bismarck Sea, Papua New Guinea. *Marine Geophysical Researches* 30, 229-236.
- Horn, I., Foley, S.F., Jackson, S.E., Jenner, G.A., 1994. Experimentally determined partitioning of high field strength- and selected transition elements between spinel and basaltic melt. *Chemical Geology*, 117: 193-218. doi: 10.1016/0009-2541(94)90128-7.

- Hunziker, D., 2014. Magmatic and metamorphic history of the North Makran ophiolites and blueschists (SE Iran): Influence of Fe³⁺/Fe²⁺ ratios in blueschist facies minerals on geothermobarometric calculations. PhD Thesis, ETH Zurich, Switzerland, 364 pp.
- Hunziker, D., Burg, J.-P., Bouilhol, P., von Quadt, A., 2015. Jurassic rifting at the Eurasian Tethys margin: Geochemical and geochronological constraints from granitoids of North Makran, southeastern Iran. *Tectonics* 34, 571-593. [10.1002/2014TC003768](https://doi.org/10.1002/2014TC003768)
- Hynes, A., 1980. Carbonatization and mobility of Ti, Y, and Zr in Ascot Formation metabasalts, SE Quebec. *Contributions to Mineralogy and Petrology*, 75, 79-87.
- Ikeda, Y., Nagao, K., Ishii, T., Matsumoto, D., Stern, R.J., Kagami, H., Arima, M., Bloomer, S.H., 2016. Contributions of slab fluid and sediment melt components to magmatism in the Mariana Arc-Trough system: Evidence from geochemical compositions and Sr, Nd, and noble gas isotope systematics. *Island Arc* 25, 253-273.
- Ingersoll, R.V., Bullard, T.F., Ford, R.L., Grimm, J.B., Pickle, J.D., Sares, S.W., 1984. The effect of grain size on detrital modes: a test of the Gazzi-Dickinson point-counting method. *Journal of Sedimentary Petrology* 54, 103-116.
- Ingersoll, R.V., Suzcek, C.A., 1979. Petrology and provenance of Neogene sand from Nicobar and Bengal Fans, DSDP sites 211 and 218. *J. of Sedim. Petrol.* 49, 1217-1228.
- Irving, A. J., Frey, F. A., 1984. Trace element abundances in megacrysts and their host basalts: constraints on partition coefficients and megacryst genesis. *Geochimica et Cosmochimica Acta* 48, 1201-1221.
- Jagoutz, O., Royden, L., Holt, A. F., Becker, T. W., 2015. Anomalously fast convergence of India and Eurasia caused by double subduction. *Nature Geoscience*, 8(6), 475–478. <https://doi.org/10.1038/ngeo2418>
- Kakar, M. I., Kerr, A. C., Mahmood, K., Collins, A. S., Khan, M., McDonald, I., 2014. Supra-subduction zone tectonic setting of the Muslim Bagh Ophiolite, northwestern Pakistan: Insights from geochemistry and petrology. *Lithos*, 202–203, 190–206. <https://doi.org/10.1016/j.lithos.2014.05.029>
- Kanianian, A., Juteau, T., Bellon, H., Darvishzadeh, A., Sabzehi, M., Whitechurch, H., Ricou, L.-E., 2001. The ophiolite massif of Kahnuj (western Makran, southern Iran): new geological and geochronological data. *C. R. Acad. Sci. Ser. IIA Earth Planet. Sci.* 332, 543-552.
- Kelley, K.A., Plank, T., Grove, T.L., Stolper, E.M., Newman, S., Hauri E., 2005. Mantle melting as a function of water content beneath back-arc basins. *J. Geophys. Res.* 111, B09208, doi:10.1029/2005JB003732
- Kennedy, A.K., Lofgren, G.E., Wasserburg, G.J. 1993. An Experimental-Study of Trace-Element Partitioning between Olivine, Ortho-Pyroxene and Melt in Chondrules - Equilibrium Values and Kinetic Effects. *Earth and Planetary Science Letters* 115(1-4): 177-195. doi: 10.1016/0012-821X(93)90221-T.
- Kerr, A.C., 2014. Oceanic Plateaus. In: Holland, H.D., Turekian, K.K. (Eds.), *Treatise on Geochemistry*, Second edition vol. 4, Elsevier, Oxford, pp. 631–667.
- Kerr, A.C., White, R.V., Saunders, A.D., 2000. LIP Reading: Recognizing Oceanic Plateaux in the Geological Record. *Journal of Petrology*, 41(7), 1041–1056. <https://doi.org/10.1093/petrology/41.7.1041>
- Kim, S., Jang, Y., Kwon, S., Samuel, V. O., Kim, S. W., Park, S.-I., Santosh, M., Kokkalas, S., 2020. Petro-tectonic evolution of metamorphic sole of the Semail ophiolite, UAE. *Gondwana Research*, 86, 203–221. <https://doi.org/10.1016/j.gr.2020.05.013>
- Kinzler, R.J., 1997. Melting of mantle peridotite at pressures approaching the spinel to garnet transition: Application to mid-ocean ridge basalt petrogenesis. *Journal of Geophysical Research*, 102, doi: 10.1029/96JB00988. issn: 0148-0227.
- Klemme, S.; Gunther, D.; Hametner, K.; Prowatke, S.; Zack, T., 2006. The partitioning of trace elements between ilmenite, ulvospinel, armalcolite and silicate melts with implications for the early differentiation of the moon. *Chemical Geology*, 234, 251-263. doi: 10.1016/j.chemgeo.2006.05.005.

- Klemme, S., Blundy, J.D., Wood, B.J. 2002. Experimental constraints on major and trace element partitioning during partial melting of eclogite. *Geochimica et Cosmochimica Acta* 66: 3,109-3,123. doi: 10.1016/S0016-7037(02)00859-1.
- König, S., Schuth, S., Munker, C., Qopoto, C., 2007. The role of slab melting in the petrogenesis of high-Mg andesites: evidence from Simbo Volcano, Solomon Islands. *Contrib. Mineral. Petrol.* 153, 85-103. doi:10.1007/s00410-006-0136-x
- Kopp, C., Fruehn, J., Flueh, E.R., Reichert, C., Kukowski, N., Bialas, J., Klaeschen, D., 2000. Structure of the Makran subduction zone from wide-angle and reflection seismic data. *Tectonophysics* 329, 171–191. [https://doi.org/10.1016/S0040-1951\(00\)00195-5](https://doi.org/10.1016/S0040-1951(00)00195-5)
- Kostopoulos, D.K., Murton, B.J., 1992. Origin and distribution of components in boninite genesis: significance of the OIB component. In: Parson, L.M., Murton, B.J., Browning, P. (Eds.), *Ophiolites and their modern oceanic analogues: Geological Society of London, Special Publication 60*, pp. 133-154.
- Kusky, T.M., Bradley, D.C., Haeussler, P.J., Karl, S., 1997. Controls on accretion of flysch and mé'lange belts at convergent margins: evidence from the Chugach Bay thrust and Iceworm mé'lange, Chugach accretionary wedge, Alaska. *Tectonics* 16: 855–878
- Kusky, T.M., Windley, B.F., Safonova, I., Wakita, K., Wakabayashi, J., Polat, A., Santosh, M., 2013. Recognition of ocean plate stratigraphy in accretionary orogens through Earth history: A record of 3.8 billion years of sea floor spreading, subduction, and accretion. *Gondwana Research* 24, 501–547. <https://doi.org/10.1016/j.gr.2013.01.004>
- Lachance, G.R., Trail, R.J., 1966. Practical solution to the matrix problem in X-ray analysis. *Canadian Spectroscopy* 11, 43-48.
- Lallemand, S., Culotta, R., Von Huene, R., 1989. Subduction of the Daiichi Kashima seamount in the Japan Trench. *Tectonophysics* 160, 231-247.
- Lallemand, S., Le-Pichon, X., 1987. Coulomb wedge model applied to the subduction of seamounts in the Japan Trench. *Geology* 15 (11), 1065– 1069.
- Lapierre, H., Samper, A., Bosch, D., Maury, R.C., Béchenec, F., Cotten, J., Demant, A., Brunet, P., Keller, F., Marcoux, J., 2004. The Tethyan plume: geochemical diversity of Middle Permian basalts from the Oman rifted margin. *Lithos* 74, 167–198.
- Le Roex, A.P., Dick, H.J.B., Erlank, A.J., Reid, A.M., Frey, F.A., Hart, S.R., 1983. Geochemistry, Mineralogy and Petrogenesis of Lavas Erupted along the Southwest Indian Ridge Between the Bouvet Triple Junction and 11 Degrees East. *Journal of Petrology*, 24, 267–318. <https://doi.org/10.1093/petrology/24.3.267>
- Leterrier, J., Maury, R.C., Thonon, P., Girard, D., Marchal, M., 1982. Clinopyroxene composition as a method of identification of the magmatic affinities of paleovolcanic series. *Earth and Planetary Science Letters* 59, 139e154.
- Li, Y.H., 2000. *A Compendium of Geochemistry: from Solar Nebula to the Human Brain*. Princeton University Press, Princeton, pp. 440.
- Loeblich, A., Tappan, H., 1988. *Foraminiferal General and their Classification*, (2vols), Van Nostrand Reinhold ed., New York, 213 pp., 847 plates,
- Lustrino, M., Melluso, L., Morra, V., 2002. The transition from alkaline to tholeiitic magmas: a case study from the Orosei-Dorgali Pliocene volcanic district (NE Sardinia, Italy). *Lithos*, 63, 83–113. [https://doi.org/10.1016/S0024-4937\(02\)00113-5](https://doi.org/10.1016/S0024-4937(02)00113-5)
- Mahéo, G., Bertrand, H., Guillot, S., Villa, I. M., Keller, F., Capiez, P., 2004. The South Ladakh ophiolites (NW Himalaya, India): an intra-oceanic tholeiitic arc origin with implication for the closure of the Neo-Tethys. *Chemical Geology*, 203(3–4), 273–303. <https://doi.org/10.1016/j.chemgeo.2003.10.007>

- Malatesta, C., Gerya, T., Crispini, L., Federico, L., Capponi, G., 2013. Oblique subduction modelling indicates along-trench tectonic transport of sediments. *Nature Communications* 4 (1). <https://doi.org/10.1038/ncomms3456>
- Mana, S., Furman, T., Turrin, B. D., Feigenson, M. D., Swisher, C. C., 2015. Magmatic activity across the East African North Tanzanian Divergence Zone. *Journal of the Geological Society*, 172(3), 368–389. <https://doi.org/10.1144/jgs2014-072>
- Marroni, M., Pandolfi, L. 1996. The deformation history of an accreted ophiolite sequence: The internal Liguride units (northern Apennines, Italy). *Geodinamica Acta*, 9, 13–29, <https://doi.org/10.1080/09853111.1996.11417260>
- Marroni, M., Pandolfi, L., 2001. Debris flow and slide deposits at the top of the Internal Liguride ophiolitic sequence, Northern Apennines, Italy: A record of frontal tectonic erosion in a fossil accretionary wedge. *The Island Arc* 10 (1), 9–21. <https://doi.org/10.1046/j.1440-1738.2001.00289.x>
- Marroni, M., Pandolfi, L., 2007. The architecture of an incipient oceanic basin: a tentative reconstruction of the Jurassic Liguria-Piemonte basin along the Northern Apennines–Alpine Corsica transect. *International Journal of Earth Sciences*, 96(6), 1059–1078. <https://doi.org/10.1007/s00531-006-0163-x>
- Marroni, M., Meneghini, F., Pandolfi, L., 2004. From accretion to exhumation in a fossil accretionary wedge: a case history from Gottero unit (Northern Apennines, Italy). *Geodinamica Acta*, 17(1), 41–53. <https://doi.org/10.3166/ga.17.41-53>
- Marroni, M., Göncüoğlu, M. C., Frassi, C., Sayit, K., Pandolfi, L., Ellero, A., Ottria, G., 2020. The Intra-Pontide ophiolites in Northern Turkey revisited: From birth to death of a Neotethyan oceanic domain. *Geoscience Frontiers*, 11(1), 129–149. <https://doi.org/10.1016/j.gsf.2019.05.010>
- Martin, H., Smithies, R.H., Rapp, R.P., Moyen, J.-F., Champion, D.C., 2005. An overview of adakite, tonalite-trondhjemite-granodiorite (TTG) and sanukitoid: relationships and some implications for crustal evolution. *Lithos* 79, 1-24.
- Martin, C. R., Jagoutz, O., Upadhyay, R., Royden, L. H., Eddy, M. P., Bailey, E., Nichols, C. I. O., Weiss, B. P., 2020. Paleocene latitude of the Kohistan–Ladakh arc indicates multistage India–Eurasia collision. *Proceedings of the National Academy of Sciences*, 117(47), 29487–29494. <https://doi.org/10.1073/pnas.2009039117>
- McCall, G.J.H., 1983. Mélanges of the Makran, southeastern Iran. In: McCall, G.J.H. (Ed.), *Ophiolitic and related mélanges*, Benchmark Papers in Geology, Hutchinson Ross Publishing Company, Stroudsburg, Pennsylvania. 66, 292-299.
- McCall, G.J.H., 1985. Explanatory text of the Minab Quadrangle Map; 1:250,000; No. J13. Geological Survey of Iran, Tehran, pp. 530.
- McCall, G.J.H., 1997. The geotectonic history of the Makran and adjacent areas of southern Iran. *Journal of Asian Earth Sciences* 15, 517-531
- McCall, G.J.H., 2002. A summary of the geology of the Iranian Makran. *The Tectonic and Climatic Evolution of the Arabian Sea Region*. In: Clift, P.D. Kroon, D., Gaedicke, C., Craig, J. (Eds.), Oxford, Geological Society, London, Special Publications 195, 147-204.
- McCall, G.J.H., Kidd, R.G.W., 1982. The Makran southeastern Iran: the anatomy of a convergent margin active from Cretaceous to present. In: Leggett, J.K. (Ed.), *Trench-forearc geology: sedimentation and tectonics of modern and ancient plate margins*. Vol 10, 387-397.
- McKenzie, D., O'Nions, R.K., 1991. Partial melt distributions from inversion of rare earth element concentrations. *Journal of Petrology* 32, 1021-1091.
- McPhie, J., Doyle, M., Allen, R., 1993. *Volcanic textures: A guide to the interpretation of textures in volcanic rocks*. Hobart, Centre for Ore Deposit and Exploration Studies, University of Tasmania, Tasmanian Government Printing Office, 198 pp.

- Mentimin, M., Zhang, Y., Furnes, H., Pe-Piper, G., Piper, D.J.W., Guo, Z., 2019. Facies architecture of a subaqueous volcano–sedimentary succession on Bogda Mountains, NW China—Evidence of extension in Late Carboniferous. *Geological Journal* 55 (4), 3097–3111. <https://doi.org/10.1002/gj.3582>
- Meneghini, F., Marroni, M., Moore, J.C., Pandolfi, L., Rowe, C.D., 2009. The processes of underthrusting and underplating in the geologic record: structural diversity between the Franciscan Complex (California), the Kodiak Complex (Alaska) and the Internal Ligurian Units (Italy). *Geological Journal* 44 (2), 126–152.
- Meneghini, F., Pandolfi, L., Marroni, M., 2020. Recycling of heterogeneous material in the subduction factory: evidence from the sedimentary mélange of the Internal Ligurian Units, Italy. *Journal of the Geological Society*, 177(3), 587–599. <https://doi.org/10.1144/jgs2019-081>
- Mezzadri, G., Saccani, E., 1989. Heavy mineral distribution in Late Quaternary sediments of the Southern Aegean Sea: Implication for provenance and sediment dispersal in a sedimentary basin at active margins. *Journal of Sedimentary Petrology* 59, 412–422.
- Mibe, K., Kawamoto, T., Matsukage, K.N., Fei, Y., Ono, S., 2011. Slab melting versus slab dehydration in subduction-zone magmatism. *Proceedings of the National Academy of Sciences* 108, 8177–8182.
- Miyashiro, A., 1973. The Troodos complex was probably formed in an island arc. *Earth and Planetary Science Letters*, 19, 218–224, doi: 10.1016/0012-821X (73)90118-0.
- Moghadam, H. S., Stern, R. J., 2015. Ophiolites of Iran: Keys to understanding the tectonic evolution of SW Asia: (II) Mesozoic ophiolites. *Journal of Asian Earth Sciences*, 100, 31–59. <https://doi.org/10.1016/j.jseaes.2014.12.016>
- Mohammadi, A., Burg, J.-P., Winkler, W., Ruh, J., von Quadt, A., 2016. Detrital zircon and provenance analysis of Late Cretaceous–Miocene onshore Iranian Makran strata: Implications for the tectonic setting. *Geological Society of America Bulletin* 128, 1481–1499. <https://doi.org/10.1130/B31361.1>
- Monsef, I., Monsef, R., Mata, J., Zhang, Z., Pirouz, M., Rezaeian, M., Esmaeili, R., Xiao, W., 2018. Evidence for an early-MORB to fore-arc evolution within the Zagros suture zone: Constraints from zircon U-Pb geochronology and geochemistry of the Neyriz ophiolite (South Iran). *Gondwana Research*, 62, 287–305. <https://doi.org/10.1016/j.gr.2018.03.002>
- Monsef, I., Rahgoshay, M., Pirouz, M., Chiaradia, M., Grégoire, M., Ceuleneer, G., 2019. The Eastern Makran Ophiolite (SE Iran): evidence for a Late Cretaceous fore-arc oceanic crust. *International Geology Review*, 61 (11), 1313–1339. <https://doi.org/10.1080/00206814.2018.1507764>
- Moore, G.F., Shipley, T.H., Stoffa, P.L., Karig, D.E., Taira, A., Kuramoto, S., Tokuyama, H. & Suyehiro, K., 1990. Structure of the Nankai Trough accretionary zone from multichannel seismic reflection data. *Journal of Geophysical Research Solid-Earth* 95, 8753–8765. <https://doi.org/10.1029/JB095iB06p08753>
- Moore, J.G., 1970. Water Content of Basalt Erupted on the ocean floor. *Contribution to Mineralogy and Petrology* 28 (4), 272–279. <https://doi.org/10.1007/BF00388949>
- Moore, J.G., Clague, D.A., 1992. Volcano growth and evolution of the island of Hawaii. *Geological Society of America Bulletin* 104 (11), 1471–1484. [https://doi.org/10.1130/0016-7606\(1992\)104<1471:VGAEOT>2.3.CO;2](https://doi.org/10.1130/0016-7606(1992)104<1471:VGAEOT>2.3.CO;2)
- Moore, J.G., Schilling, J.G., 1973. Vesicles, water, and sulfur in Reykjanes Ridge basalts. *Contribution to Mineralogy and Petrology* 41 (2), 105–118. <https://doi.org/10.1007/BF00375036>
- Moores, E.M., Vine, F.J., 1971. The Troodos massif, Cyprus, and other ophiolites as oceanic crust: Evaluation and implications. *Philosophical Transactions of the Royal Society of London*, 268A, 443–466.
- Morgan, W.J., 1971. Convection Plumes in the Lower Mantle. *Nature* 230, 42–43. <https://doi.org/10.1038/230042a0>
- Morimoto, N., 1988. Nomenclature of Pyroxenes. *Mineralogy and Petrology*, 39(1), 55–76. <https://doi.org/10.1007/BF01226262>

- Moslempour, M.E., Khalatbari-Jafari, M., Ghaderi, M., Yousefi, H., Shahdadi, S., 2015. Petrology, geochemistry and tectonics of the extrusive sequence of Fannuj-Maskutan Ophiolite, southeastern Iran. *Journal of Geological Society of India* 85, 604–618.
- Motaghi, K., Shabanian, E., Nozad-Khalil, T., 2020. Deep structure of the western coast of the Makran subduction zone, SE Iran. *Tectonophysics* 776. <https://doi.org/10.1016/j.tecto.2019.228314>
- Moyen, J.-F., 2009. High Sr/Y and La/Yb ratios: The meaning of the “adakitic signature”. *Lithos* 112, 556-574.
- Moyen, J.-F., Stevens, G., 2006. Experimental constraints on TTG petrogenesis: implications for Archean geodynamics. In: Benn, K., Mareschal, J.-C., Condie, K.C. (Eds.), *Archean geodynamics and environments*. monographs. AGU, pp. 149-178.
- Mukherjee, D., Ghose, N. C., Chatterjee, N., 2005. Crystallization history of a massif anorthosite in the eastern Indian shield margin based on borehole lithology. *Journal of Asian Earth Sciences*, 25, 77–94.
- Murton, B.J., 1989. Tectonic controls on boninite genesis. In: Saunders, A.D., Norry, M.J. (Eds.), *Magmatism in the Ocean Basins*. Geological Society of London, Special Publications 42, pp. 347-377.
- Mutti E., 1992. *Turbidite Sandstones*. AGIP (Ed.), San Donato Milanese. 275pp.
- Natali, C., Beccaluva, L., Bianchini, G., Siena, F., 2018. Coexistence of alkaline-carbonatite complexes and high-MgO CFB in the Paranà-Etendeka province: Insights on plume-lithosphere interactions in the Gondwana realm. *Lithos*, 296–299, 54–66. <https://doi.org/10.1016/j.lithos.2017.11.001>
- O'Dogherty, L., 1994. Biochronology and Paleontology of Mid-Cretaceous radiolarians from Northern Apennines (Italy) and Betic Cordillera (Spain). *Mémoires de Géologie (Lausanne)* 21, 1-413.
- Omrani, H., Moazzen, M., Oberhänsli, R., Moslempour, M.E., 2017. Iranshahr blueschist: subduction of the inner Makran oceanic crust. *Journal of Metamorphic Geology* 35(4), 373-392.
- Parkinson I.J., Pearce J.A., 1998. Peridotites from the Izu-Bonin-Mariana forarc (ODP Leg 125): evidence for mantle melting and melt-mantle interaction in a suprasubduction zone setting. *J. Petrol.* 39, 1577-1618.
- Parlak, O., Bağcı, U., Rızaoğlu, T., Ionescu, C., Önal, G., Höck, V., Kozlu, H., 2020. Petrology of ultramafic to mafic cumulate rocks from the Göksun (Kahramanmaraş) ophiolite, southeast Turkey. *Geoscience Frontiers*, 11(1), 109–128. <https://doi.org/10.1016/j.gsf.2018.11.004>
- Pearce J. A., 2014. Immobile element fingerprinting of ophiolites. *Elements*, 10: 101-108.
- Pearce J.A., 1996. A user's guide to basalt discrimination diagrams. In: Bailes, A.H., Christiansen, E.H., Galley, A.G., Jenner, G.A., Keith, J.D., Kerrich, R., Lentz, D.R., Leshner, C.M., Lucas, S.B., Ludden, J.N., Pearce, J.A., Peloquin, S.A., Stern, R.A., Stone, W.E., Syme, E.C., Swinden, H.S., Wyman, D.A., (Eds.), *Trace element geochemistry of volcanic rocks: applications for massive sulphide exploration*. Short Course Notes. Geol. Assoc. Canada 12, 79-113.
- Pearce, J.A., 1983. Role of the Sub-continental Lithosphere in Magma Genesis at Active Continental Margin. In: Hawkesworth, C.J., Norry, M.J. (Eds.), *Continental Basalts and Mantle Xenoliths*. Cheshire, United Kingdom, Shiva Publishing, pp. 230-249.
- Pearce, J.A., 2008. Geochemical fingerprinting of oceanic basalts with applications to ophiolite classification and the search for Archean oceanic crust. *Lithos* 100, 14–48. <https://doi.org/10.1016/j.lithos.2007.06.016>
- Pearce, J.A., Norry, M.J., 1979. Petrogenetic implications of Ti, Zr, Y, and Nb variations in volcanic rocks. *Contributions to Mineralogy and Petrology* 69, 33-47.
- Pearce, J.A., Parkinson I.J., 1993. Trace element models for mantle melting: application to volcanic arc petrogenesis. In Princiard, H.M., Alabaster, T., Harris, N.B.W., Neary, C.R. (Eds.), *Magmatic processes and plate tectonics*. London, Geol. Soc. Sp. Publ. 76, 373-403.
- Pedersen, R. B., Searle, M. P., Corfield, R. I., 2001. U–Pb zircon ages from the Spontang Ophiolite, Ladakh Himalaya. *Journal of the Geological Society*, 158(3), 513–520. <https://doi.org/10.1144/jgs.158.3.513>

- Penney, C., Copley, A., Oveisi, B., 2015. Subduction tractions and vertical axis rotations in the Zagros–Makran transition zone, SE Iran: the 2013 May 11 M w 6.1 Minab earthquake. *Geophysical Journal International* 202, 1122–1136. <https://doi.org/10.1093/gji/ggv202>
- Penney, C., Tavakoli, F., Saadat, A., Nankali, H.R., Sedighi, M., Khorrami, F., Sobouti, F., Rafi, Z., Copley, A., Jackson, J., Priestley, K., 2017. Megathrust and accretionary wedge properties and behaviour in the Makran subduction zone. *Geophysical Journal International* 209, 1800–1830. <https://doi.org/10.1093/gji/ggx126>
- Pini, G. A., 1999. Tectonosomes and olistostromes in the argille scagliose of the Northern Apennines, Italy. In *Tectonosomes and Olistostromes in the Argille Scagliose of the Northern Apennines, Italy* (Vol. 335, pp. 1–70). Geological Society of America. <https://doi.org/10.1130/0-8137-2335-3.1>
- Pirnia, T., Saccani, E., Torabi, G., Chiari, M., Gorican, S., Barbero, E., 2020. Cretaceous tectonic evolution of the Neo-Tethys in Central Iran: Evidence from petrology and age of the Nain-Ashin ophiolitic basalts. *Geoscience Frontiers* 11 (1), 57-81, <https://doi.org/10.1016/j.gsf.2019.02.008>
- Platt, J.P. 1993. Exhumation of high-pressure rocks: A review of concepts and processes. *Terra Nova*, 5, 119–133, <https://doi.org/10.1111/j.1365-3121.1993.tb00237.x>
- Platt, J.P., Leggett, J.K., Young, J., Raza, H., Alam, S., 1985. Large-scale sediment underplating in the Makran accretionary prism, southwest Pakistan. *Geology* 13, 507. [https://doi.org/10.1130/0091-7613\(1985\)13<507:LSUITM>2.0.CO;2](https://doi.org/10.1130/0091-7613(1985)13<507:LSUITM>2.0.CO;2)
- Pusok, A. E., Stegman, D. R., 2020. The convergence history of India-Eurasia records multiple subduction dynamics processes. *Science Advances*, 6(19), eaaz8681. <https://doi.org/10.1126/sciadv.aaz8681>
- Putirka, K.D., 2008. Thermometers and Barometers for Volcanic Systems. *Reviews in Mineralogy and Geochemistry*, 69(1), 61–120. <https://doi.org/10.2138/rmg.2008.69.3>
- Putirka, K.D., Johnson, M., Kinzler, R., Longhi, J., Walker, D., 1996. Thermobarometry of mafic igneous rocks based on clinopyroxene-liquid equilibria, 0-30 kbar. *Contributions to Mineralogy and Petrology*, 123(1), 92–108. <https://doi.org/10.1007/s004100050145>
- Putirka, K.D., Mikaelian, H., Ryerson, F., Shaw, H., 2003. New clinopyroxene-liquid thermobarometers for mafic, evolved, and volatile-bearing lava compositions, with applications to lavas from Tibet and the Snake River Plain, Idaho. *American Mineralogist*, 88(10), 1542–1554. <https://doi.org/10.2138/am-2003-1017>
- Putirka, K.D., Perfit, M., Ryerson, F.J., Jackson, M.G., 2007. Ambient and excess mantle temperatures, olivine thermometry, and active vs. passive upwelling. *Chemical Geology*, 241(3–4), 177–206. <https://doi.org/10.1016/j.chemgeo.2007.01.014>
- Quartau, R., Ramalho, R.S., Madeira, J., Santos, R., Rodrigues, A., Roque, C., Carrara, G., Brum da Silveira, A., 2018. Gravitational, erosional and depositional processes on volcanic ocean islands: Insights from the submarine morphology of Madeira Archipelago. *Earth and Planetary Science Letters* 482, 288–299. <https://doi.org/10.1016/j.epsl.2017.11.003>
- Ramsay, J.G., 1967. *Folding and Fracturing of Rocks*. Mc Graw and Hill ed., 568 pp.
- Ranero, C. R., von Huene, R., 2000. Subduction erosion along the Middle America convergent margin. *Nature* 404 (6779), 748–752. <https://doi.org/10.1038/35008046>
- Rapp, R., Shimizu, N., Norman, M.D., Applegate, G.S., 2000. Reaction between slab-derived melts and peridotite in the mantle wedge: experimental constraints at 3.8 GPa. *Chemical Geology* 160, 335-356.
- Regard, V., Hatzfeld, D., Molinaro, M., Aubourg, C., Bayer, R., Bellier, O., Yamini-Fard, F., Peyret, M., & Abbassi, M., 2010. The transition between Makran subduction and the Zagros collision: recent advances in its structure and active deformation. *Geological Society of London Special Publications* 330(1), 43–64. <https://doi.org/10.1144/SP330.4>
- Regard, V., Bellier, O., Thomas, J.-C., Abbassi, M. R., Mercier, J., Shabanian, E., Feghhi, K., Soleymani, S., 2004. Accommodation of Arabia-Eurasia convergence in the Zagros-Makran transfer zone, SE Iran: A

- transition between collision and subduction through a young deforming system. *Tectonics*, 23(4), <https://doi.org/10.1029/2003TC001599>
- Regelous, M., Hofmann, A.W., Abouchami W., Galer, S.J.G., 2003. Geochemistry of Lavas from the Emperor Seamounts, and the Geochemical Evolution of Hawaiian Magmatism from 85 to 42 Ma. *Journal of Petrology*, 44(1), 113–140. <https://doi.org/10.1093/petrology/44.1.113>
- Remitti, F., Vannucchi, P., Bettelli, G., Fantoni, L., Panini, F., Vescovi, P., 2011. Tectonic and sedimentary evolution of the frontal part of an ancient subduction complex at the transition from accretion to erosion: The case of the Ligurian wedge of the northern Apennines, Italy. *Geological Society of America Bulletin*, 123(1–2), 51–70. <https://doi.org/10.1130/B30065.1>
- Riaz, M.S., Bin, S., Naeem, S., Kai, W., Xie, Z., Gilani, S.M.M., Ashraf, U., 2019. Over 100 years of faults interaction, stress accumulation, and creeping implications, on Chaman Fault System, Pakistan. *International Journal of Earth Sciences* 108 (4), 1351–1359. <https://doi.org/10.1007/s00531-019-01710-0>
- Richards, J.P., Kerrich R., 2007. Adakite-Like Rocks: Their Diverse Origins and questionable role in metallogenesis. *Economic Geology* 102: 537-576.
- Ricou, L.E., 1994. Tethys reconstructed: plates continental fragments and their boundaris since 260Ma from Central America to South-eastern Asia. *Geodinamica Acta* 7, 169-218.
- Riedel, W.R., Sanfilippo, A., 1974. 33. Radiolaria from the southern Indian Ocean, DSDP leg 26. In: Davis, T. A., Luyendyke, B. P. et al. (Eds), *Initial Reports of the Deep Sea Drilling Project*, U. S. Government Printing Office, Washington, 26, 771-783.
- Robertson, A., 1998. Rift-related sedimentation and volcanism of the north-Indian margin inferred from a Permian–Triassic exotic block at Lamayuru, Indus suture zone (Ladakh Himalaya) and regional comparisons. *Journal of Asian Earth Sciences*, 16(2–3), 159–172. [https://doi.org/10.1016/S0743-9547\(98\)00009-9](https://doi.org/10.1016/S0743-9547(98)00009-9)
- Robertson, A.H.F., 2007. Overview of tectonic settings related to the rifting and opening of Mesozoic ocean basins in the Eastern Tethys: Oman, Himalayas and Eastern Mediterranean regions. *Geological Society of London Special Publications* 282, 325–388. <https://doi.org/10.1144/SP282.15>
- Rodriguez, M., Huchon, P., Chamot-Rooke, N., Fournier, M., Delescluse, M., Smit, J., Plunder, A., Calvès, G., Ninkabou, D., Pubellier, M., François, T., Agard, P., Gorini, C., 2020. Successive shifts of the India-Africa transform plate boundary during the Late Cretaceous-Paleogene interval: Implications for ophiolite emplacement along transforms. *Journal of Asian Earth Sciences*, 191(December 2019), 104225. <https://doi.org/10.1016/j.jseaes.2019.104225>
- Rolland, Y., Galoyan, G., Sosson, M., Melkonyan, R., Avagyan, A., 2010. The Armenian Ophiolite: insights for Jurassic back-arc formation, Lower Cretaceous hot spot magmatism and Upper Cretaceous obduction over the South Armenian Block. *Geological Society of London Special Publications* 340, 353–382. <https://doi.org/10.1144/SP340.15>
- Rolland, Y., Hässig, M., Bosch, D., Bruguière, O., Melis, R., Galoyan, G., Topuz, G., Sahakyan, L., Avagyan, A., Sosson, M., 2020. The East Anatolia–Lesser Caucasus ophiolite: An exceptional case of large-scale obduction, synthesis of data and numerical modelling. *Geoscience Frontiers* 11 (1), 83–108. <https://doi.org/10.1016/j.gsf.2018.12.009>
- Rollinson, H., 1993. *Using geochemical data: evaluation, presentation, interpretation*. Longman Scientific, Harlow, pp. 352.
- Rollinson, H., 2009. New models for the genesis of plagiogranites in the Oman ophiolite. *Lithos*, 112(3–4), 603–614. <https://doi.org/10.1016/j.lithos.2009.06.006>
- Ross, K., Elthon, D., 1993. Cumulates from strongly depleted mid-ocean-ridge basalt. *Nature*, 365(6449), 826–829. <https://doi.org/10.1038/365826a0>

- Rossetti, F., Nasrabad, M., Theye, T., Gerdes, A., Monié, P., Lucci, F., Vignaroli, G., 2014. Adakite differentiation and emplacement in a subduction channel: the late Paleocene Sabzevar magmatism (NE Iran). *Geological Society of America Bulletin* 126, 317-343.
- Ruh, J. B., 2016. Submarine landslides caused by seamounts entering accretionary wedge systems. *Terra Nova* 28 (3), 163–170. <https://doi.org/10.1111/ter.12204>
- Saccani, E., 2015. A new method of discriminating different types of post-Archean ophiolitic basalts and their tectonic significance using Th-Nb and Ce-Dy-Yb systematics. *Geoscience Frontiers* 6, 481-501. [10.1016/j.gsf.2014.03.006](https://doi.org/10.1016/j.gsf.2014.03.006)
- Saccani, E., Allahyari, K., Beccaluva, L., Bianchini, G., 2013a. Geochemistry and petrology of the Kermanshah ophiolites (Iran): Implication for the interaction between passive rifting, oceanic accretion, and OIB-type components in the Southern Neo-Tethys Ocean. *Gondwana Research* 24, 392–411. <https://doi.org/10.1016/j.gr.2012.10.009>
- Saccani, E., Azimzadeh, Z., Dilek, Y., Jahangiri, A., 2013b. Geochronology and petrology of the Early Carboniferous Misho Mafic Complex (NW Iran), and implications for the melt evolution of Paleo-Tethyan rifting in Western Cimmeria. *Lithos*, 162–163, 264–278. <https://doi.org/10.1016/j.lithos.2013.01.008>
- Saccani, E., Beccaluva, L., Photiades, A., Zeda, O., 2011. Petrogenesis and tectono-magmatic significance of basalts and mantle peridotites from the Albanian-Greek ophiolites and sub-ophiolitic mélanges. New constraints for the Triassic-Jurassic evolution of the Neo-Tethys in the Dinaride sector. *Lithos* 124, 227-242.
- Saccani, E., Delavari, M., Dolati, A., Marroni, M., Pandolfi, L., Chiari, M., Barbero E., 2018. New insights into the geodynamics of Neo-Tethys in the Makran area: Evidence from age and petrology of ophiolites from the Coloured Mélange Complex (SE Iran). *Gondwana Research* 62, 306-327. [10.1016/j.gr.2017.07.013](https://doi.org/10.1016/j.gr.2017.07.013)
- Saccani, E., Dilek, Y., Marroni, M., Pandolfi, L., 2015. Continental margin ophiolites of Neotethys: Remnants of Ancient Ocean–Continent Transition Zone (OCTZ) lithosphere and their geochemistry, mantle sources and melt evolution patterns. *Episodes* 38, 230–249. <https://doi.org/10.18814/epiugs/2015/v38i4/82418>
- Saccani, E., Dilek, Y., Photiades A., 2017. Time-progressive mantle-melt evolution and magma production in a Tethyan marginal sea: A case study of the Albanide-Hellenide ophiolites. *Lithosphere* 10: 35-53, <https://doi.org/10.1130/L602.1>.
- Saccani, E., Allahyari, K., Rahimzadeh, B., 2014. Petrology and geochemistry of mafic magmatic rocks from the Sarve-Abad ophiolites (Kurdistan region, Iran): Evidence for interaction between MORB-type asthenosphere and OIB-type components in the southern Neo-Tethys Ocean. *Tectonophysics*, 621, 132–147. <https://doi.org/10.1016/j.tecto.2014.02.011>
- Saccani, E., Photiades, A., Padoa, E., 2003. Geochemistry, petrogenesis and tectono-magmatic significance of volcanic and subvolcanic rocks from the Koziakas Mélange (Western Thessaly, Greece). *Ophiolites*, 28, 43-57. A22
- Saffer, D.M., Tobin, H.J., 2011. Hydrogeology and mechanics of subduction zone forearcs: fluid flow and pore pressure. *Annual Review of Earth and Planetary Sciences* 39, 157-186.
- Safonova, I., Maruyama, S., Kojima, S., Komiya, T., Krivonogov, S., Koshida, K., 2016. Recognizing OIB and MORB in accretionary complexes: A new approach based on ocean plate stratigraphy, petrology and geochemistry. *Gondwana Research* 33, 92–114. <https://doi.org/10.1016/j.gr.2015.06.013>
- Safonova, I.Y., Santosh, M., 2014. Accretionary complexes in the Asia-Pacific region: Tracing archives of ocean plate stratigraphy and tracking mantle plumes. *Gondwana Research* 25, 126–158. <https://doi.org/10.1016/j.gr.2012.10.008>
- Saint-Ange, F., Bachèlery, P., Babonneau, N., Michon, L., Jorry, S.J., 2013. Volcaniclastic sedimentation on the submarine slopes of a basaltic hotspot volcano: Piton de la Fournaise volcano (La Réunion Island, Indian Ocean). *Marine Geology* 337, 35–52. <https://doi.org/10.1016/j.margeo.2013.01.004>
- Salter, V., Longhi, J., 1999. Trace element partitioning during the initial stages of melting beneath mid-ocean ridges. *Earth and Planetary Science Letters*, 166, 15-30. doi: 10.1016/S0012-821X(98)00271-4.

- Samimi Namin, M., 1982. Geological Map of Taherui 1:250000 Scale. Tehran: Ministry of Mines and Metal, Geological Survey of Iran.
- Samimi Namin, M., 1983. Geological Map of Minab 1:250000 Scale. Tehran: Ministry of Mines and Metal, Geological Survey of Iran.
- Sanfilippo, A., Riedel, W.R., 1985. Cretaceous Radiolaria. In: Bolli, H. M., Saunders J. B. and Perch-Nielson K. (Eds.), *Plankton Stratigraphy*, Cambridge University Press, 573-630.
- Schlanger, S. O., Jenkyns, H. C., 1976, Cretaceous oceanic anoxic events: causes and consequences. *Geologie en Mijnbouw* 55, 179–184.
- Schnur, S.R., Gilbert, L.A., 2012. Detailed volcanostratigraphy of an accreted seamount: Implications for intraplate seamount formation. *Geochemistry, Geophysics, Geosystems* 13, 1–13, <https://doi.org/10.1029/2012GC004301>.
- Searle, M.P., Treloar, P.J., 2010. Was late cretaceous-Paleocene obduction of ophiolite complexes the primary cause of crustal thickening and regional metamorphism in the Pakistan Himalaya? *Geol. Soc. Lond., Spec. Publ.* 338, 345–359. <http://dx.doi.org/10.1144/SP338.16>.
- Searle, M., Corfield, R. I., Stephenson, B., McCarron, J., 1997. Structure of the North Indian continental margin in the Ladakh–Zaskar Himalayas: implications for the timing of obduction of the Spontang ophiolite, India–Asia collision and deformation events in the Himalaya. *Geological Magazine*, 134(3), 297–316. <https://doi.org/10.1017/S0016756897006857>
- Şengör, A.M.C., Altın, D., Cin, A., Ustaömer, T., Hsü, K.J., 1988. Origin and assembly of the Tethyside orogenic collage at the expense of Gondwana Land. *Geological Society of London Special Publications* 37, 119–181. <https://doi.org/10.1144/GSL.SP.1988.037.01.09>
- Sepidbar, F., Lucci, F., Biabangard, H., Zaki Khedr, M., Jiantang, P., 2020. Geochemistry and tectonic significance of the Fannuj-Maskutan SSZ-type ophiolite (Inner Makran, SE Iran). *International Geology Review*, 1-28. <https://doi.org/10.1080/00206814.2020.1753118>
- Shafaii Moghadam, H., Stern, R. J., 2015. Ophiolites of Iran: Keys to understanding the tectonic evolution of SW Asia: (II) Mesozoic ophiolites. *Journal of Asian Earth Sciences* 100, 31-59.
- Shaker-Ardakani, A.R., Arvin, M., Oberhänsli, R., Mocek, B., Moeinzadeh, S.H., 2009. Morphology and petrogenesis of pillow lavas from the Ganj Ophiolitic Complex, Southeastern Kerman, Iran. *Journal of Sciences, Islamic Republic of Iran* 20, 139-151.
- Shellnutt, J. G., Dostal, J., Keppie, J. D., Keppie, D. F., 2020. Formation of Anorthositic Rocks within the Blair River Inlier of Northern Cape Breton Island, Nova Scotia (Canada). *Lithosphere*, 2020(1), 1–21. <https://doi.org/10.2113/2020/8825465>
- Shervais, J. W., 2001. Birth, death, and resurrection: The life cycle of suprasubduction zone ophiolites. *G3-Geochemistry, Geophysics, Geosystems*, 2, doi:10.1029/2000GC000080.
- Sisson, T. W., Grove, T. L., 1993. Experimental investigations of the role of H₂O in calc-alkaline differentiation and subduction zone magmatism. *Contributions to Mineralogy and Petrology*, 113(2), 143–166. <https://doi.org/10.1007/BF00283225>
- Stakes, D.S., Taylor, H.P., 2003. Oxygen isotope and chemical studies on the origin of large plagiogranite bodies in northern Oman, and their relationship to the overlying massive sulphide deposits. *Geological Society London Special Publications*, 218(1), 315–351. <https://doi.org/10.1144/GSL.SP.2003.218.01.17>
- Stampfli, G., Borel, G., 2002. A plate tectonic model for the Paleozoic and Mesozoic constrained by dynamic plate boundaries and restored synthetic oceanic isochrons. *Earth and Planetary Science Letters*, 196(1–2), 17–33. [https://doi.org/10.1016/S0012-821X\(01\)00588-X](https://doi.org/10.1016/S0012-821X(01)00588-X)
- Staudigel, H., Clague, D.A., 2010. The geological history of deep-sea volcanoes: Biosphere, hydrosphere, and lithosphere interactions. *Oceanography* 23, 58–71. <https://doi.org/10.2307/24861062>

- Staudigel, H., Schmincke, H.-U., 1984. The Pliocene seamount series of La Palma/Canary Islands. *Journal of Geophysical Research Solid-Earth* 89 (B13), 11195–11215. <https://doi.org/10.1029/JB089iB13p11195>
- Stoneley, R. 2005. The Zendan Fault of southern Iran. *Proceedings of the Geologists' Association*, 116(3–4), 311–313, [https://doi.org/10.1016/S0016-7878\(05\)80049-5](https://doi.org/10.1016/S0016-7878(05)80049-5)
- Sun, S.S., McDonough, W.F., 1989. Chemical and isotopic systematics of oceanic basalts: implications for mantle composition and processes. In: Saunders, A.D., Norry, M.J. (Eds.), *Magmatism in the Ocean Basins*. Geological Society Special Publication, London 42, 313-345.
- Taylor, S.R., McLennan, S.M., 1985. *The Continental Crust: its composition and evolution: an examination of the geochemical record preserved in sedimentary rocks*. Oxford, Blackwell Scientific Publication, pp. 312.
- Thirlwall, M.F., Upton, B.G.J., Jenkins, C., 1994. Interaction between Continental Lithosphere and the Iceland Plume – Sr-Nd-Pb Isotope Geochemistry of Tertiary Basalts, NE Greenland. *Journal of Petrology*, 35(3), 839–879. <https://doi.org/10.1093/petrology/35.3.839>
- Tinterri R., 2011. Combined flow sedimentary structures and the genetic link between sigmoidal- and hummocky-cross stratification. *GeoActa* 10, 1-43.
- Torsvik, T. H., Van der Voo, R., Preeden, U., Mac Niocaill, C., Steinberger, B., Doubrovine, P. V., van Hinsbergen, D. J. J., Domeier, M., Gaina, C., Tohver, E., Meert, J. G., McCausland, P. J. A., Cocks, L. R. M., 2012. Phanerozoic polar wander, palaeogeography and dynamics. *Earth-Science Reviews*, 114(3–4), 325–368. <https://doi.org/10.1016/j.earscirev.2012.06.007>
- Ulmer, P., 1989. Partitioning of high field strength elements among olivine, pyroxenes, garnet and calc alkaline picobasalt: experimental results and an application. *International Journal of Mass Spectrometry and Ion Physics*, 42-47.
- Valsami, E., Cann, J.R., 1992. Mobility of rare earth elements in zones of intense hydrothermal alteration in the Pindos ophiolite, Greece. In: Parson, L.M., Murton, B.J., Browning, P. (Eds.), *Ophiolites and Their Modern Oceanic Analogues*. *Geol. Soc. London Spec. Publ.* 60, pp. 219-232.
- Vannucchi, P., Fisher, D.M., Bier, S., Gardner, T.W., 2006. From seamount accretion to tectonic erosion: Formation of Osa Mélangé and the effects of Cocos Ridge subduction in southern Costa Rica. *Tectonics* 25 (2). <https://doi.org/10.1029/2005TC001855>
- van Hinsbergen, D. J. J., Steinberger, B., Doubrovine, P. V., Gassmöller, R., 2011. Acceleration and deceleration of India-Asia convergence since the Cretaceous: Roles of mantle plumes and continental collision. *Journal of Geophysical Research*, 116(B6), B06101. <https://doi.org/10.1029/2010JB008051>
- van Hinsbergen, D. J. J., Lippert, P. C., Dupont-Nivet, G., McQuarrie, N., Doubrovine, P. V., Spakman, W., Torsvik, T. H., 2012. Greater India Basin hypothesis and a two-stage Cenozoic collision between India and Asia. *Proceedings of the National Academy of Sciences*, 109(20), 7659–7664. <https://doi.org/10.1073/pnas.1117262109>
- van Hinsbergen, D. J. J., Lippert, P. C., Li, S., Huang, W., Advokaat, E. L., Spakman, W., 2019. Reconstructing Greater India: Paleogeographic, kinematic, and geodynamic perspectives. *Tectonophysics*, 760(April 2018), 69–94. <https://doi.org/10.1016/j.tecto.2018.04.006>
- von Huene, R., Lallemand, S., 1990. Tectonic erosion along the Japan and Peru convergent margins. *Geological Society of America Bulletin* 102 (6), 704-720.
- von Huene, R., Ranero, C. R., & Watts, P., 2004a. Tsunamigenic slope failure along the Middle America Trench in two tectonic settings. *Marine Geology* 203, 303-317. [https://doi.org/10.1016/S0025-3227\(03\)00312-8](https://doi.org/10.1016/S0025-3227(03)00312-8)
- von Huene, R., Ranero, C.R., Vannucchi, P., 2004b. Generic model of subduction erosion. *Geology* 32, 913–916. 10.1130/G20563.1

- Wakabayashi, J., 1992. Nappes, tectonics of oblique plate convergence, and metamorphic evolution related to 140 million years of continuous subduction, Franciscan Complex, California. *Journal of Geology* 100: 19–40.
- Wakabayashi, J., 2015. Anatomy of a subduction complex: Architecture of the Franciscan Complex, California, at multiple length and time scales. *International Geology Review*. <https://doi.org/10.1080/00206814.2014.998728>
- Wakabayashi, J., Dilek, Y., 2003. What constitutes “emplacement” of an ophiolite?: Mechanisms and relationship to subduction initiation and formation of metamorphic soles. in Dilek, Y. and Robinson, P.T., eds., *Ophiolites in Earth History: Geological Society of London Special Publication 218*, p. 427–448.
- Wakita, K., 2015. OPS mélange: a new term for mélanges of convergent margins of the world. *International Geology Review*, 57(5–8), 529–539. <https://doi.org/10.1080/00206814.2014.949312>
- Wanless, V.D., Behn, M.D., 2017. Spreading rate-dependent variations in crystallization along the global mid-ocean ridge system. *Geochemistry, Geophysics, Geosystems*, 18(8), 3016–3033, <https://doi.org/10.1002/2017GC006924>
- Warren, J. M., 2016. Global variations in abyssal peridotite compositions. *Lithos*, 248–251, 193–219. <https://doi.org/10.1016/j.lithos.2015.12.023>
- White, W. M., 2010. Oceanic Island Basalts and Mantle Plumes: The Geochemical Perspective. *Annual Review of Earth and Planetary Sciences*, 38(1), 133–160. <https://doi.org/10.1146/annurev-earth-040809-152450>
- White, R.S., Klitgord, K., 1976. Sediment deformation and plate tectonics in the Gulf of Oman. *Earth and Planetary Science Letters* 32, 199–209. [https://doi.org/10.1016/0012-821X\(76\)90059-5](https://doi.org/10.1016/0012-821X(76)90059-5)
- Wilson, M., 1989. *Igneous Petrogenesis: A Global Tectonic Approach*. Chapman & Hall, pp 466.
- Winchester, J.A., Floyd, P.A., 1977. Geochemical discrimination of different magma series and their differentiation products using immobile elements. *Chemical Geology* 20, 325-343.
- Workman, R.K., Hart, S.R., 2005. Major and trace element composition of the depleted MORB mantle (DMM). *Earth and Planetary Science Letters* 231, 53-72.
- Xia, L., Li, X., 2019. Basalt geochemistry as a diagnostic indicator of tectonic setting. *Gondwana Research*, 65, 43–67. <https://doi.org/10.1016/j.gr.2018.08.006>
- Yang, G., Dilek, Y., 2015. OIB- and P-type ophiolites along the Yarlung- Zangbo Suture Zone (YZSZ), Southern Tibet: Poly- Phase melt history and mantle sources of the Neotethyan oceanic lithosphere. *Episodes* 38, 250–265. <https://doi.org/10.18814/epiiugs/2015/v38i4/82420>
- Young, J.R., Bown, P.R., Lees, J.A., 2017. Nannotax3 website. International Nannoplankton Association. Accessed 21 Apr. 2017. URL: <http://www.mikrotax.org/Nannotax3>
- Zanchetta, S., Berra, F., Zanchi, A., Bergomi, M., Caridroit, M., Nicora, A., Heidarzadeh, G., 2013. The record of the Late Palaeozoic active margin of the Palaeotethys in NE Iran: Constraints on the Cimmerian orogeny. *Gondwana Research* 24, 1237-1266, <https://doi.org/10.1016/j.gr.2013.02.013>
- Zuffa, G.G., 1980. Hybrid arenites: their composition and classification. *J. Sed. Petr.* 49, 21-29.
- Zuffa, G.G., 1987. Unravelling hinterland and offshore palaeogeography from deep-water arenites. In: Legget J.K., Zuffa G.G., (Eds.), *Marine Clastic Sedimentology, models and case studies (a volume in memory of C. Tarquin Teale)*, Graham and Trotman, London, pp. 39-61.

Acknowledgements

First of all, I would like to express my gratitude to my supervisors Emilio Saccani and Luca Pandolfi for giving me the opportunity to work on Makran ophiolites and for their continuous support during my PhD thesis. Emilio and Luca helped me both in the field, in the lab and during the writing of the thesis, guiding me in this “three-years journey”. I learned a lot from them on both geology and other things and I will be always grateful for this, for their friendship, and for having transmitted me their passion for ophiolites.

A special thank goes to Morteza Delavari, Asghar Dolati and Michele Marroni for their continuous support during my PhD and for the passionate discussion about Makran geology. My fieldwork would have been impossible without the help of Morteza and Asghar. They got the domestic fly tickets, managed the car and driver for the fieldwork, always found five-stars hotels for the night and so on. I will never forget the fun talk and laugh drinking hundreds of boiling *chai* and I will always thank them for their friendships. I wish to thank Michele for the time he dedicated to me for discussing structural evolution and geodynamic reconstructions of the Makran.

I would like to thank Federica Zaccarini and all the staff of the Leoben University for hosting me during my research period abroad. Federica opened to me the microprobe lab and I thank her for the hundreds analyses and the fun times and good company. A special thanks go to Renzo Tassinari for hundreds (maybe even thousand) XRF and ICP-MS analyses and for his teaching about samples preparation in the lab and to Renzo Tamoni for thin sections preparation. I am thankful for the collaboration with Rita Catanzariti, Marco Chiari, Valeria Luciani, and Antonio Langone who provided me biostratigraphic and radiometric dating.

I desire to acknowledge Professor Andrea Zanchi and Osman Parlak who kindly review my thesis reading more than 300 hundred pages. I really appreciated their suggestions and comments that significantly improved the final version of this thesis.

I spent three great years at the Physics and Earth Science Department of the Ferrara University. I guess because I met good people there. In particular. I would like to thank Beatrice, Chiara, Enrico, Federico, Gabriella, Giacomo, Gian Marco, Giulio, Luca, Marcello, Maria, Mattia, Mina, Negar, Pier Paolo, Roberta, Valentina, Valeria for the time spent together, they will be always in my thoughts. I want to thank also the professors Bonadiman, Bianchini, Coltorti and Gianolla for their teaching and friendship during this period.

I want to thank my family for their continuous support and their love during this intense period during which we have been distance.

Last but not least, I would like to thank all the Iranian people that helped me during the fieldwork in the Makran, I will never forget their hospitality and generosity. With most of them I could not communicate as I can't speak Farsi. Thanks to them I learnt that a smile and handshake can say more things than thousands of words. They will be always in my heart and I hope a good future for them. A special mention goes to Ahmad

Behboodi (Haji) for his unconditioned help for organizing the fieldwork and finding accommodation for the night, to the PhD student Ahmad Nateghpour for the help in the field and for his company and friendship, to Massoud and Majid the best drivers of the Kerman province.



**Università
degli Studi
di Ferrara**

Ph.D. course in Earth and Marine Science

Cycle XXXIII

Report of activities attended during the Ph.D. course

Ph.D. candidate: Edoardo Barbero

Personal details:

Name: Edoardo Barbero

Place and date of birth: Cremona (Italy), 19th September 1991

Email: edoardo.barbero@unife.it

Spoken languages: Italian (native), English (B2).

Education: 2013-2016 master's degree in Applied Earth Sciences – University of Torino, Italy

Short courses and workshops

2020:

Il magmatismo Cenozoico innescato dalla convergenza Africa-Arabia-Eurasia – (**workshop**) held online 2 July 2020, Dr. Agostini Samuele (Consiglio Nazionale delle Ricerche, Pisa)

Unlocking the secrets of slow slip events: the role of lithological and geometric heterogeneity of the subducting plate - (**workshop**), held online 28 May 2020, Prof. Francesca Meneghini (University of Pisa)

Online seminar series on rift and rifted margins – (**workshop**) Short presentations by Mike Kendall (University of Oxford), Cécile Doubre (University of Strasbourg), Sarah Jaye Oliva (University of Tulane).

The structure and growth of fault zones – (**short course**) held online 11-12-13 May 2020, Dr. Giovanni Camanni (University of Napoli)

2019:

Workshop UZAG, PhD Short Course on the electron microprobe – (**short course**) Leoben end of September 2019, Dr. Federica Zaccari (Montan Universität, Leoben)

Breaking apart: the influence of magmatism in continental rifting – (**workshop**) Torino 25 Giugno 2019, Dr. Sara Mana (Salem State University, USA)

2018:

Tectonics during early stages of continental collision and similarities to subduction zones: insights from the Central European Alps – (**workshop**) Modena, 18/06/2018, Dr. Armin Dielforder (Helmholtz Centre Potsdam, GFZ German Research Centre for Geosciences)

Petrologia delle rocce metamorfiche: Modellizzazione termodinamica utilizzando THERMOCALC – (**short course**) Pisa, from 21/05/2018 to 24/05/2018, Dr. Gisella Rebay (University of Pavia)

2017:

Caos e tettonica a zolle: i mélanges nei prismi di accrezione e nelle catene collisionali – (**workshop**) Ferrara, 18/12/2017, Prof Gian Andrea Pini (University of Trieste)

Significance of Tectonic Geomorphology and Palaeoseismology for infrastructure design – (**workshop**) Ferrara, 27/11/2017, Prof. Ioannis Koukouvelas (University of Patras, Greece)

Fault geometry across the Hellenides - (**workshop**) Ferrara, 28/11/2017 (University of Patras, Greece)

Research period abroad

September – October 2019 (40 days): electron microprobe analytical stage at University of Leoben (Austria).

January – February 2019 (25 days): Field-work in the Makran area (SE Iran) with the collaboration of the Kahrazmi University, Tehran (Iran).

January – February 2018 (16 days): Field-work in the Makran area (SE Iran) with the collaboration of the Kahrazmi University, Tehran (Iran).

Attendance to national and international congresses and meetings

- EGU 2020 online, 4-8 May 2020.
Online presentation: Barbero E., Delavari M., Dolati A., Pandolfi L., Marroni M., Saccani E., Chiari M., Luciani V. & Catanzariti R. - The Durkan Complex in the western Makran Accretionary Prism (SE Iran): Evidence for a Late Cretaceous tectonically disrupted oceanic seamount
- SIMP-SGI-SOGEI Congress (3 days), Parma 17-19 September 2019, Il tempo del pianeta Terra e il tempo dell'uomo: le geoscienze fra passato e futuro.
Oral presentation: Barbero E., Delavari M., Dolati A., Pandolfi L., Marroni M., Saccani E. & Catanzariti R. - The Ganj Ophiolitic Complex reinterpreted as a Late Cretaceous volcanic arc: implications for the geodynamic evolution of the North Makran domain (SE Iran), session S20. Orogenesis and orogenic wedges: a multiscale and multitechnique approach.
Poster presentation: Barbero E., Delavari M., Dolati A., Pandolfi L., Marroni M., Saccani E., Chiari M., Luciani V. & Catanzariti R. - Preliminary stratigraphic and petrological data on the Durkan Complex (Makran accretionary wedge, SE Iran), session S20. Orogenesis and orogenic wedges: a multiscale and multitechnique approach
- Annual meeting of Gruppo Italiano di Geologia Strutturale (GIGS) - San Giovanni Valdarno 12-15 June 2018: Convegno ed escursione lungo il crinale dell'Appennino tosco-emiliano e nelle Alpi Apuane
Poster presentation: Barbero, E., Saccani, E., Pandolfi, L., Marroni, M., Delavari, M., Dolati, A., Catanzariti, R., Preliminary petrological and stratigraphic data on the Band-e-Zeyarat ophiolite (Makran accretionary wedge, SE Iran).

Scientific papers

Barbero E., Delavari M., Dolati A., Marroni M., Saccani E., Pandolfi L., Langone A., *Tectono-magmatic significance of the Bajgan Complex in the North Makran domain (SE Iran): new constraints for its interpretation as Late Jurassic – Early Cretaceous meta-ophiolitic complex*. **In preparation**

Barbero E., Delavari M., Dolati A., Marroni M., Saccani E., Pandolfi L., Zaccarini F., Tectonically disrupted remnants of a Late Cretaceous plume-influenced seamounts chain in the Neo-Tethys realm: new petrological constraints from the western Durkan Complex (Makran Accretionary Prism, SE Iran). **In preparation**

Barbero E., Pandolfi L., Delavari M., Dolati A., Saccani E., Catanzariti R., Luciani V., Chiari M., Marroni M., **2021**. *The western Durkan Complex (Makran Accretionary Prism, SE Iran): a Late Cretaceous tectonically disrupted seamounts chain and its role in controlling deformation style*. *Geoscience Frontiers*, 12(3), <https://doi.org/10.1016/j.gsf.2020.12.001>.

Barbero E., Delavari M., Dolati A., Vahedi L., Langone A., Marroni M., Pandolfi L., Zaccarini F., Saccani E., **2020**. *Early Cretaceous Plume–Ridge Interaction Recorded in the Band-e-Zeyarat Ophiolite (North Makran, Iran): New Constraints from Petrological, Mineral Chemistry, and Geochronological Data*. *Minerals*, 10(12), 1100, doi:10.3390/min10121100.

Barbero E., Delavari M., Dolati A., Saccani E., Marroni M., Catanzariti R., Pandolfi L., **2020**. *The Ganj Complex reinterpreted as a Late Cretaceous volcanic arc: Implications for the geodynamic evolution of the North Makran domain (southeast Iran)*. *Journal of Asian Earth Sciences*, 195, <https://doi.org/10.1016/j.jseaes.2020.104306>

Scholarships

2019:

Abroad Mobility Grant by University of Ferrara, supporting the research period at University of Leoben (Austria) for performing electron microprobe analyses.

Other activities

2020:

Tutor for the Bachelor's Degree course "Geological Mapping" (Prof. Piero Gianolla)

Teaching assistant for the Bachelor's Degree course "Laboratory of Petrography" (Prof. Emilio Saccani)

2019:

Tutor and teaching assistant for the Bachelor's Degree course "Geological Mapping" (Prof. Piero Gianolla)

Tutor for the Bachelor's Degree course "Laboratory of Petrography" (Prof. Emilio Saccani)

Dottorati di ricerca

Il tuo indirizzo e-mail

brbdrd@unife.it

Oggetto:

Dichiarazione di conformità della tesi di Dottorato

Io sottoscritto Dott. (Cognome e Nome)

Barbero Edoardo

Nato a:

Cremona

Provincia:

Cremona

Il giorno:

19/09/1991

Avendo frequentato il Dottorato di Ricerca in:

Scienze della Terra e del Mare

Ciclo di Dottorato

33

Titolo della tesi:

Geological and petrological investigation of the western North Makran ophiolites (SE Iran): new constraints for the Late Jurassic – Cretaceous tectono-magmatic and geodynamic evolution of the Neo-Tethys Ocean

Titolo della tesi (traduzione):

Tutore: Prof. (Cognome e Nome)

Saccani Emilio

Settore Scientifico Disciplinare (S.S.D.)

GEO/07

Parole chiave della tesi (max 10):

Ophiolites, North Makran domain, Iran, Tectono-magmatic evolution, Geodynamics, Neo-Tethys, Mesozoic

Consapevole, dichiara

ed uso di atti falsi, decade fin dall'inizio e senza necessità di alcuna formalità dai benefici conseguenti al provvedimento emanato sulla base di tali dichiarazioni; (2) dell'obbligo per l'Università di provvedere al deposito di legge delle tesi di dottorato al fine di assicurarne la conservazione e la consultabilità da parte di terzi; (3) della procedura adottata dall'Università di Ferrara ove si richiede che la tesi sia consegnata dal dottorando in 2 copie, di cui una in formato cartaceo e una in formato pdf non modificabile su idonei supporti (CD-ROM, DVD) secondo le istruzioni pubblicate sul sito : <http://www.unife.it/studenti/dottorato> alla voce ESAME FINALE – disposizioni e modulistica; (4) del fatto che l'Università, sulla base dei dati forniti, archiverà e renderà consultabile in rete il testo completo della tesi di dottorato di cui alla presente dichiarazione attraverso l'Archivio istituzionale ad accesso aperto "EPRINTS.unife.it" oltre che attraverso i Cataloghi delle Biblioteche Nazionali Centrali di Roma e Firenze. DICHIARO SOTTO LA MIA RESPONSABILITA': (1) che la copia della tesi depositata presso l'Università di Ferrara in formato cartaceo è del tutto identica a quella presentata in formato elettronico (CD-ROM, DVD), a quelle da inviare ai Commissari di esame finale e alla copia che produrrà in seduta d'esame finale. Di conseguenza va esclusa qualsiasi responsabilità dell'Ateneo stesso per quanto riguarda eventuali errori, imprecisioni o omissioni nei contenuti della tesi; (2) di prendere atto che la tesi in formato cartaceo è l'unica alla quale farà riferimento l'Università per rilasciare, a mia richiesta, la dichiarazione di conformità di eventuali copie. PER ACCETTAZIONE DI QUANTO SOPRA RIPORTATO

Dichiarazione per embargo

12 mesi

Richiesta motivata embargo

1. Tesi in corso di pubblicazione

Liberatoria consultazione dati Eprints

Consapevole del fatto che attraverso l'Archivio istituzionale ad accesso aperto "EPRINTS.unife.it" saranno comunque accessibili i metadati relativi alla tesi (titolo, autore, abstract, ecc.)

Firma del dottorando

Ferrara, li 22/04/2021 Firma del Dottorando __Edoardo Barbero__

Firma del Tutore

Visto: Il Tutore Si approva Firma del Tutore __Emilio Sacconi__